Methods in
Molecular Biology 2431

Springer Protocols

Alessio Vagnoni *Editor*

Axonal Transport

Methods and Protocols

Humana Press

METHODS IN MOLECULAR BIOLOGY

Series Editor
John M. Walker
School of Life and Medical Sciences
University of Hertfordshire
Hatfield, Hertfordshire, UK

For further volumes:
http://www.springer.com/series/7651

For over 35 years, biological scientists have come to rely on the research protocols and methodologies in the critically acclaimed *Methods in Molecular Biology* series. The series was the first to introduce the step-by-step protocols approach that has become the standard in all biomedical protocol publishing. Each protocol is provided in readily-reproducible step-by-step fashion, opening with an introductory overview, a list of the materials and reagents needed to complete the experiment, and followed by a detailed procedure that is supported with a helpful notes section offering tips and tricks of the trade as well as troubleshooting advice. These hallmark features were introduced by series editor Dr. John Walker and constitute the key ingredient in each and every volume of the *Methods in Molecular Biology* series. Tested and trusted, comprehensive and reliable, all protocols from the series are indexed in PubMed.

Axonal Transport

Methods and Protocols

Edited by

Alessio Vagnoni

Department of Basic and Clinical Neurosciences, Maurice Wohl Clinical Neuroscience Institute, Institute of Psychiatry, Psychology and Neuroscience, King's College London, London, UK

Humana Press

Editor
Alessio Vagnoni
Department of Basic and Clinical
Neurosciences
Maurice Wohl Clinical Neuroscience Institute
Institute of Psychiatry
Psychology and Neuroscience
King's College London
London, UK

ISSN 1064-3745 ISSN 1940-6029 (electronic)
Methods in Molecular Biology
ISBN 978-1-0716-1989-6 ISBN 978-1-0716-1990-2 (eBook)
https://doi.org/10.1007/978-1-0716-1990-2

© The Editor(s) (if applicable) and The Author(s), under exclusive license to Springer Science+Business Media, LLC, part of Springer Nature 2022
7 chapters are licensed under the terms of the Creative Commons Attribution 4.0 International License (http://creativecommons.org/licenses/by/4.0/). For further details see license information in the chapters.
This work is subject to copyright. All rights are solely and exclusively licensed by the Publisher, whether the whole or part of the material is concerned, specifically the rights of translation, reprinting, reuse of illustrations, recitation, broadcasting, reproduction on microfilms or in any other physical way, and transmission or information storage and retrieval, electronic adaptation, computer software, or by similar or dissimilar methodology now known or hereafter developed.
The use of general descriptive names, registered names, trademarks, service marks, etc. in this publication does not imply, even in the absence of a specific statement, that such names are exempt from the relevant protective laws and regulations and therefore free for general use.
The publisher, the authors and the editors are safe to assume that the advice and information in this book are believed to be true and accurate at the date of publication. Neither the publisher nor the authors or the editors give a warranty, expressed or implied, with respect to the material contained herein or for any errors or omissions that may have been made. The publisher remains neutral with regard to jurisdictional claims in published maps and institutional affiliations.

This Humana imprint is published by the registered company Springer Science+Business Media, LLC, part of Springer Nature.
The registered company address is: 1 New York Plaza, New York, NY 10004, U.S.A.

Preface

It is hard not to be startled when looking through the eyepiece of a microscope down onto a live cell, in isolation or embedded in a tissue, that presents the observer with a vast array of intricate dynamics. The trafficking of cellular components is essential for any cell to function properly, and understanding the logic governing this process is a fundamental aspect of biology. Intracellular transport is especially important in neurons due to their peculiar architecture with long and specialized axons and dendrites. Much research has focused on the transport within the axonal compartment, not least because of the strong correlation between damage to axonal transport and the pathogenesis of several neurodegenerative diseases. Above all, the axons of neurons are beautiful cellular structures that, due to their stereotypical microtubule orientation, naturally lend themselves to studying the logic of cargo transport.

Cargo transport through axons directly or indirectly supports every neuronal function and, over the last ~50 years, many methods and models have been developed to study this process. The interest in studying axonal transport is reflected by the breadth of contributions to this series, which fittingly starts with a method describing the use of the forefather of all models for axonal transport studies, the squid giant axon. Methods in *Aplysia* and *Xenopus* follow before several protocols to study transport in rodent and human models are presented. These precede a series of methods developed in zebrafish, *Drosophila*, and *C. elegans*. In some instances, novel observations are also reported as the result of the application of these methodologies. The series ends with two studies of *in vitro* reconstitution of mRNA and mitochondrial motility using purified components. Although these methods were not originally devised to study axonal transport, they are an outstanding example of the ever-expanding array of methodologies that can be applied to understanding the logic of neuronal cargo transport.

Overall, the book aims to provide a comprehensive overview and introduction to methods and protocols to study axonal transport. It will be useful both as a reference for experts in the field and as an introduction for scientists who would like to venture in this fascinating research field.

Cambridge, UK *Alessio Vagnoni*

Contents

Preface . . . . . *v*
Contributors . . . . . *xi*

PART I SQUID, APLYSIA, AND XENOPUS

1 The Giant Axon of the Squid: A Simple System for Axonal Transport Studies 3
Joseph A. DeGiorgis, Marcus Jang, and Elaine L. Bearer

2 Live Imaging and Quantitative Analysis of Organelle Transport in Sensory Neurons of *Aplysia Californica* 23
Kerriann Badal, Yibo Zhao, Kyle E. Miller, and Sathyanarayanan V. Puthanveettil

3 Live Imaging of RNA Transport and Translation in *Xenopus* Retinal Axons 49
Julie Qiaojin Lin and Jean-Michel Cioni

PART II MOUSE IN VIVO AND EX VIVO

4 Imaging Axonal Transport in Ex Vivo Central and Peripheral Nerves 73
Stacey Anne Gould, Robert Adalbert, Stefan Milde, and Michael Coleman

5 In Vivo Imaging of Axonal Organelle Transport in the Mouse Brain 95
Johannes Knabbe, Jil Protzmann, and Thomas Kuner

6 Studying Axonal Transport in the Brain by Manganese-Enhanced Magnetic Resonance Imaging (MEMRI) 111
Elaine L. Bearer, Xiaowei Zhang, and Russell E. Jacobs

PART III RODENT PRIMARY NEURONS

7 Microfluidic Neuromuscular Co-culture System for Tracking Cell-to-Cell Transfer and Axonal Transport of Labeled Proteins 145
Ariel Ionescu and Eran Perlson

8 Imaging Diversity in Slow Axonal Transport 163
Archan Ganguly and Subhojit Roy

9 Methods and Applications of Campenot Trichamber Neuronal Cultures for the Study of Neuroinvasive Viruses 181
Wesley M. Tierney, Ian A. Vicino, Stella Y. Sun, Wah Chiu, Esteban A. Engel, Matthew P. Taylor, and Ian B. Hogue

10 Molecular Analysis of Axonal Transport Dynamics upon Modulation of Microtubule Acetylation 207
Silvia Turchetto, Romain Le Bail, Loic Broix, and Laurent Nguyen

11 Live-Cell Imaging of RNA Transport in Axons of Cultured Primary Neurons 225
J. Tabitha Hees and Angelika B. Harbauer

12 Visualizing Vesicle-Bound Kinesins in Cultured Hippocampal Neurons 239
Andrew Montgomery, Alex Garbouchian, and Marvin Bentley

13 Retrograde Axonal Transport of Neurotrophins in Basal Forebrain Cholinergic Neurons 249
Arman Shekari and Margaret Fahnestock

14 Use of Microfluidics Chambers to Image Axonal transport in Adult Sensory Neurons 271
Maria Fransiska Emily, Lokesh Agrawal, Paolo Barzaghi, Miki Otsuki, and Marco Terenzio

Part IV Human-Derived Neurons

15 High-Resolution Imaging of Mitochondria and Mitochondrial Nucleoids in Differentiated SH-SY5Y Cells 291
Emily Annuario, Kristal Ng, and Alessio Vagnoni

16 Assessment of Mitochondrial Trafficking as a Surrogate for Fast Axonal Transport in Human Induced Pluripotent Stem Cell–Derived Spinal Motor Neurons 311
Arpan R. Mehta, Siddharthan Chandran, and Bhuvaneish T. Selvaraj

Part V Zebrafish

17 In Vivo Live Imaging of Axonal Transport in Developing Zebrafish Axons 325
Melody Atkins, Jamilé Hazan, and Coralie Fassier

18 Visualizing the Intracellular Trafficking in Zebrafish Mauthner Cells 351
Rongchen Huang, Yang Xu, Min Chen, Leiqing Yang, Xinliang Wang, Yueru Shen, Yubin Huang, and Bing Hu

Part VI Drosophila In Vivo, Ex Vivo, and Primary Neurons

19 Dissection and Direct Imaging of Axonal Transport in *Drosophila* Segmental Nerves 367
William M. Saxton, Angeline Lim, and Inna Djagaeva

20 Detailed Imaging of Mitochondrial Transport and Precise Manipulation of Mitochondrial Function with Genetically Encoded Photosensitizers in Adult *Drosophila* Neurons 385
Francesca Mattedi, George Chennell, and Alessio Vagnoni

21 Mitochondrial DNA Transport in *Drosophila* Neurons 409
Joseph M. Bateman

22 Live Imaging of Axonal Transport in the Adult *Drosophila* Central Nervous System 417
Wayne Robinson and Tanja A. Godenschwege

23 *Drosophila* Primary Neuronal Cultures as a Useful Cellular Model to Study and Image Axonal Transport 429
André Voelzmann and Natalia Sanchez-Soriano

24 High-Resolution Live Imaging of Axonal RNP Granules in *Drosophila* Pupal Brain Explants 451
Caroline Medioni, Jeshlee Vijayakumar, Anne Ephrussi, and Florence Besse

Part VII C. elegans

25 Analyzing the Impact of Gene Mutations on Axonal Transport in *Caenorhabditis Elegans* 465
Yuzu Anazawa and Shinsuke Niwa

26 Methods to Quantify and Relate Axonal Transport Defects to Changes in *C. elegans* Behavior 481
Syed Nooruzuha Barmaver, Muniesh Muthaiyan Shanmugam, and Oliver Ingvar Wagner

27 Imaging Intracellular Trafficking in Neurons of *C. elegans* 499
Sravanthi S. P. Nadiminti and Sandhya P. Koushika

Part VIII In vitro Reconstitution Assays

28 In Vitro Reconstitution of Molecular Motor-Driven Mitochondrial Transport 533
Verena Puttrich, Jakub Rohlena, Marcus Braun, and Zdenek Lansky

29 In Vitro Reconstitution of Kinesin-Based, Axonal mRNA Transport 547
Julia Grawenhoff, Sebastian Baumann, and Sebastian P. Maurer

Index *569*

Contributors

Robert Adalbert • *Department of Anatomy, Histology and Embryology, Faculty of Medicine, University of Szeged, Szeged, Hungary*

Lokesh Agrawal • *Molecular Neuroscience Unit, Okinawa Institute of Science and Technology Graduate University, Okinawa, Japan*

Yuzu Anazawa • *Department of Biology, Faculty of Sciences, Tohoku University, Tohoku, Japan*

Emily Annuario • *Department of Basic and Clinical Neurosciences, Maurice Wohl Clinical Neuroscience Institute, Institute of Psychiatry, Psychology and Neuroscience, King's College London, London, UK*

Melody Atkins • *Sorbonne Université, UPMC-Université Paris 6, INSERM U1130, CNRS UMR8246, Neuroscience Paris Seine—Institut de Biologie Paris-Seine (NPS-IBPS), Paris, France; INSERM, UMR-S 1270, Institut du Fer à Moulin, UMR-S 1270 Sorbonne Université, Paris, France*

Kerriann Badal • *Department of Neuroscience, The Scripps Research Institute, Scripps Florida, Jupiter, FL, USA; Integrated Biology Program, Florida Atlantic University, Jupiter, FL, USA*

Syed Nooruzuha Barmaver • *Department of Life Science, Institute of Molecular and Cellular Biology, National Tsing Hua University, Hsinchu, Taiwan*

Paolo Barzaghi • *Imaging Section, Okinawa Institute of Science and Technology Graduate University, Okinawa, Japan*

Joseph M. Bateman • *Maurice Wohl Clinical Neuroscience Institute, King's College London, London, UK*

Sebastian Baumann • *Centre for Genomic Regulation (CRG), The Barcelona Institute of Science and Technology (BIST), Barcelona, Spain*

Elaine L. Bearer • *Marine Biological Laboratory, Woods Hole, MA, USA; Brown University, Providence, RI, USA; Department of Pathology, University of New Mexico Health Sciences Center, Albuquerque, NM, USA; Biology and Biological Engineering and the Beckman Institute, California Institute of Technology, Pasadena, CA, USA*

Marvin Bentley • *Department of Biological Sciences and the Center for Biotechnology and Interdisciplinary Studies, Rensselaer Polytechnic Institute, Troy, NY, USA*

Florence Besse • *Université Côte d'Azur, CNRS, Inserm, Institut de Biologie Valrose, Nice, France*

Marcus Braun • *Institute of Biotechnology, Czech Academy of Sciences, BIOCEV, Prague West, Czech Republic*

Loïc Broix • *GIGA-Stem Cells and GIGA-Neurosciences, Interdisciplinary Cluster for Applied Genoproteomics (GIGA-R), University of Liège, CHU Sart Tilman, Liège, Belgium*

Siddharthan Chandran • *UK Dementia Research Institute at the University of Edinburgh, Edinburgh, UK; Centre for Clinical Brain Sciences, University of Edinburgh, Edinburgh, UK; Euan MacDonald Centre for Motor Neuron Disease Research, University of Edinburgh, Edinburgh, UK; Anne Rowling Regenerative Neurology Clinic, University of Edinburgh, Edinburgh, UK*

Min Chen • *Hefei National Laboratory for Physical Sciences at the Microscale, Chinese Academy of Sciences Key Laboratory of Brain Function and Disease, School of Life Sciences, Division of Life Sciences and Medicine, University of Science and Technology of China, Hefei, P.R. China*

George Chennell • *Department of Basic and Clinical Neurosciences, Maurice Wohl Clinical Neuroscience Institute, Institute of Psychiatry, Psychology and Neuroscience, King's College London, London, UK; Wohl Cellular Imaging Centre, Maurice Wohl Clinical Neuroscience Institute, Institute of Psychiatry, Psychology and Neuroscience, King's College London, London, UK*

Wah Chiu • *Department of Bioengineering, Department of Microbiology and Immunology, Division of CryoEM and Bioimaging, SSRL, SLAC National Accelerator Laboratory, Stanford University, Menlo Park, CA, USA*

Jean-Michel Cioni • *Division of Neuroscience, IRCCS San Raffaele Scientific Institute, Milan, Italy*

Michael Coleman • *Department of Clinical Neurosciences, John van Geest Centre for Brain Repair, University of Cambridge, Cambridge, UK*

Joseph A. DeGiorgis • *Biology Department, Providence College, Providence, RI, USA; Marine Biological Laboratory, Woods Hole, MA, USA; Brown University, Providence, RI, USA*

Inna Djagaeva • *Department of Molecular, Cell and Developmental Biology, University of California Santa Cruz, Santa Cruz, CA, USA*

Maria Fransiska Emily • *Molecular Neuroscience Unit, Okinawa Institute of Science and Technology Graduate University, Okinawa, Japan*

Esteban A. Engel • *Department of Molecular Biology and Princeton Neuroscience Institute, Princeton University, Princeton, NJ, USA*

Anne Ephrussi • *European Molecular Biology Laboratory (EMBL), Heidelberg, Germany*

Margaret Fahnestock • *Department of Psychiatry and Behavioural Neurosciences, McMaster University, Hamilton, ON, Canada*

Coralie Fassier • *Sorbonne Université, UPMC-Université Paris 6, INSERM U1130, CNRS UMR8246, Neuroscience Paris Seine—Institut de Biologie Paris-Seine (NPS-IBPS), Paris, France; Sorbonne Université, INSERM UMR_S 968, CNRS UMR_7210, Institut de la Vision, Paris, France*

Archan Ganguly • *Department of Pharmacology and Physiology, University of Rochester Medical Center, Rochester, NY, USA*

Alex Garbouchian • *Department of Biological Sciences and the Center for Biotechnology and Interdisciplinary Studies, Rensselaer Polytechnic Institute, Troy, NY, USA*

Tanja A. Godenschwege • *Department of Biological Sciences, Florida Atlantic University, Jupiter, FL, USA*

Stacey Anne Gould • *Department of Clinical Neurosciences, John van Geest Centre for Brain Repair, University of Cambridge, Cambridge, UK*

Julia Grawenhoff • *Centre for Genomic Regulation (CRG), The Barcelona Institute of Science and Technology (BIST), Barcelona, Spain*

Angelika B. Harbauer • *Max Planck Institute for Neurobiology, Martinsried, Germany*

Jamilé Hazan • *Sorbonne Université, UPMC-Université Paris 6, INSERM U1130, CNRS UMR8246, Neuroscience Paris Seine—Institut de Biologie Paris-Seine (NPS-IBPS), Paris, France*

J. Tabitha Hees • *Max Planck Institute for Neurobiology, Martinsried, Germany*

Ian B. Hogue • *Center for Immunotherapy, Vaccines, and Virotherapy, Biodesign Institute, and School of Life Sciences, Arizona State University, Tempe, AZ, USA*

Bing Hu • *Hefei National Laboratory for Physical Sciences at the Microscale, Chinese Academy of Sciences Key Laboratory of Brain Function and Disease, School of Life Sciences, Division of Life Sciences and Medicine, University of Science and Technology of China, Hefei, P.R. China*

Rongchen Huang • *Hefei National Laboratory for Physical Sciences at the Microscale, Chinese Academy of Sciences Key Laboratory of Brain Function and Disease, School of Life Sciences, Division of Life Sciences and Medicine, University of Science and Technology of China, Hefei, P.R. China*

Yubin Huang • *Hefei National Laboratory for Physical Sciences at the Microscale, Chinese Academy of Sciences Key Laboratory of Brain Function and Disease, School of Life Sciences, Division of Life Sciences and Medicine, University of Science and Technology of China, Hefei, P.R. China*

Ariel Ionescu • *Department of Physiology and Pharmacology, Sackler Faculty of Medicine, Tel-Aviv University, Tel Aviv, Israel*

Russell E. Jacobs • *Zilkha Neurogenetic Institute, Keck School of Medicine, University of Southern California, Los Angeles, CA, USA*

Marcus Jang • *Brown University, Providence, RI, USA*

Johannes Knabbe • *Department of Functional Neuroanatomy, Institute for Anatomy and Cell Biology, Heidelberg University, Heidelberg, Germany; Center for Psychosocial Medicine, Department of General Psychiatry, Heidelberg University Hospital, Heidelberg, Germany*

Sandhya P. Koushika • *Department of Biological Sciences, Tata Institute of Fundamental Research, Mumbai, India*

Thomas Kuner • *Department of Functional Neuroanatomy, Institute for Anatomy and Cell Biology, Heidelberg University, Heidelberg, Germany*

Zdenek Lansky • *Institute of Biotechnology, Czech Academy of Sciences, BIOCEV, Prague West, Czech Republic*

Romain Le Bail • *GIGA-Stem Cells and GIGA-Neurosciences, Interdisciplinary Cluster for Applied Genoproteomics (GIGA-R), University of Liège, CHU Sart Tilman, Liège, Belgium*

Angeline Lim • *Department of Molecular, Cell and Developmental Biology, University of California Santa Cruz, Santa Cruz, CA, USA*

Julie Qiaojin Lin • *Department of Clinical Neurosciences and UK Dementia Research Institute at the University of Cambridge, Cambridge, UK*

Francesca Mattedi • *Department of Basic and Clinical Neurosciences, Maurice Wohl Clinical Neuroscience Institute, Institute of Psychiatry, Psychology and Neuroscience, King's College London, London, UK*

Sebastian P. Maurer • *Centre for Genomic Regulation (CRG), The Barcelona Institute of Science and Technology (BIST), Barcelona, Spain; Universitat Pompeu Fabra (UPF), Barcelona, Spain*

Caroline Medioni • *Université Côte d'Azur, CNRS, Inserm, Institut de Biologie Valrose, Nice, France*

Arpan R. Mehta • *UK Dementia Research Institute at the University of Edinburgh, Edinburgh, UK; Centre for Clinical Brain Sciences, University of Edinburgh, Edinburgh, UK; Euan MacDonald Centre for Motor Neuron Disease Research, University of*

Edinburgh, Edinburgh, UK; Anne Rowling Regenerative Neurology Clinic, University of Edinburgh, Edinburgh, UK

Stefan Milde • *The ALBORADA Drug Discovery Institute, University of Cambridge, Cambridge, UK*

Kyle E. Miller • *Department of Integrative Biology, Michigan State University, East Lansing, MI, USA*

Andrew Montgomery • *Department of Biological Sciences and the Center for Biotechnology and Interdisciplinary Studies, Rensselaer Polytechnic Institute, Troy, NY, USA*

Muniesh Muthaiyan Shanmugam • *Department of Life Science, Institute of Molecular and Cellular Biology, National Tsing Hua University, Hsinchu, Taiwan*

Sravanthi S. P. Nadiminti • *Department of Biological Sciences, Tata Institute of Fundamental Research, Mumbai, India*

Kristal Ng • *Department of Basic and Clinical Neurosciences, Maurice Wohl Clinical Neuroscience Institute, Institute of Psychiatry, Psychology and Neuroscience, King's College London, London, UK*

Laurent Nguyen • *GIGA-Stem Cells and GIGA-Neurosciences, Interdisciplinary Cluster for Applied Genoproteomics (GIGA-R), University of Liège, CHU Sart Tilman, Liège, Belgium*

Shinsuke Niwa • *Frontier Research Institute for Interdisciplinary Sciences (FRIS), Tohoku University, Tohoku, Japan*

Miki Otsuki • *Molecular Neuroscience Unit, Okinawa Institute of Science and Technology Graduate University, Okinawa, Japan*

Eran Perlson • *Department of Physiology and Pharmacology, Sackler Faculty of Medicine, Tel-Aviv University, Tel Aviv, Israel; The Sagol School of Neuroscience, Tel-Aviv University, Tel Aviv, Israel*

Jil Protzmann • *Department of Functional Neuroanatomy, Institute for Anatomy and Cell Biology, Heidelberg University, Heidelberg, Germany; Karolinska Institutet, Department of Medical Biochemistry and Biophysics, Stockholm, Sweden*

Sathyanarayanan V. Puthanveettil • *Department of Neuroscience, The Scripps Research Institute, Scripps Florida, Jupiter, FL, USA*

Verena Puttrich • *Institute of Biotechnology, Czech Academy of Sciences, BIOCEV, Prague West, Czech Republic*

Wayne Robinson • *Department of Biological Sciences, Florida Atlantic University, Jupiter, FL, USA*

Jakub Rohlena • *Institute of Biotechnology, Czech Academy of Sciences, BIOCEV, Prague West, Czech Republic*

Subhojit Roy • *Department of Pathology, University of California, San Diego, La Jolla, CA, USA*

Natalia Sanchez-Soriano • *Department of Molecular Physiology & Cell Signalling, Institute of Systems, Molecular & Integrative Biology, University of Liverpool, Liverpool, UK*

William M. Saxton • *Department of Molecular, Cell and Developmental Biology, University of California Santa Cruz, Santa Cruz, CA, USA*

Bhuvaneish T. Selvaraj • *UK Dementia Research Institute at the University of Edinburgh, Edinburgh, UK; Centre for Clinical Brain Sciences, University of Edinburgh, Edinburgh, UK; Euan MacDonald Centre for Motor Neuron Disease Research, University of Edinburgh, Edinburgh, UK*

Arman Shekari • *Department of Psychiatry and Behavioural Neurosciences, McMaster University, Hamilton, ON, Canada*
Yueru Shen • *Hefei National Laboratory for Physical Sciences at the Microscale, Chinese Academy of Sciences Key Laboratory of Brain Function and Disease, School of Life Sciences, Division of Life Sciences and Medicine, University of Science and Technology of China, Hefei, P.R. China*
Stella Y. Sun • *Department of Bioengineering, Department of Microbiology and Immunology, Division of CryoEM and Bioimaging, SSRL, SLAC National Accelerator Laboratory, Stanford University, Menlo Park, CA, USA*
Matthew P. Taylor • *Department of Microbiology and Cell Biology, Montana State University, Bozeman, MT, USA*
Marco Terenzio • *Molecular Neuroscience Unit, Okinawa Institute of Science and Technology Graduate University, Okinawa, Japan*
Wesley M. Tierney • *Center for Immunotherapy, Vaccines, and Virotherapy, Biodesign Institute, and School of Life Sciences, Arizona State University, Tempe, AZ, USA*
Silvia Turchetto • *GIGA-Stem Cells and GIGA-Neurosciences, Interdisciplinary Cluster for Applied Genoproteomics (GIGA-R), University of Liège, CHU Sart Tilman, Liège, Belgium*
Alessio Vagnoni • *Department of Basic and Clinical Neurosciences, Maurice Wohl Clinical Neuroscience Institute, Institute of Psychiatry, Psychology and Neuroscience, King's College London, London, UK*
Ian A. Vicino • *Center for Immunotherapy, Vaccines, and Virotherapy, Biodesign Institute, and School of Life Sciences, Arizona State University, Tempe, AZ, USA*
Jeshlee Vijayakumar • *Université Côte d'Azur, CNRS, Inserm, Institut de Biologie Valrose, Nice, France*
André Voelzmann • *School of Biological Sciences, Faculty of Biology, Medicine and Health, The University of Manchester, Manchester, UK*
Oliver Ingvar Wagner • *Department of Life Science, Institute of Molecular and Cellular Biology, National Tsing Hua University, Hsinchu, Taiwan*
Xinliang Wang • *Hefei National Laboratory for Physical Sciences at the Microscale, Chinese Academy of Sciences Key Laboratory of Brain Function and Disease, School of Life Sciences, Division of Life Sciences and Medicine, University of Science and Technology of China, Hefei, P.R. China*
Yang Xu • *Hefei National Laboratory for Physical Sciences at the Microscale, Chinese Academy of Sciences Key Laboratory of Brain Function and Disease, School of Life Sciences, Division of Life Sciences and Medicine, University of Science and Technology of China, Hefei, P.R. China*
Leiqing Yang • *Hefei National Laboratory for Physical Sciences at the Microscale, Chinese Academy of Sciences Key Laboratory of Brain Function and Disease, School of Life Sciences, Division of Life Sciences and Medicine, University of Science and Technology of China, Hefei, P.R. China*
Xiaowei Zhang • *Department of Radiology, UC San Diego School of Medicine, San Diego, CA, USA*
Yibo Zhao • *Department of Neuroscience, The Scripps Research Institute, Scripps Florida, Jupiter, FL, USA*

Part I

Squid, *Aplysia*, and *Xenopus*

Chapter 1

The Giant Axon of the Squid: A Simple System for Axonal Transport Studies

Joseph A. DeGiorgis, Marcus Jang, and Elaine L. Bearer

Abstract

The squid giant axon has a long history of being a superb experimental system in which to investigate a wide range of questions concerning intracellular transport. In this protocol we describe the method used for dissecting the axon to preserve its viability in vitro, and the technique for injecting exogenous materials into the living axon. Now that the squid genome is emerging, and the CRISPR/cas9 system has been successfully applied to knock-out squid genes, the giant axon will resume its place in the scientific pantheon of powerful experimental systems in which to address biological questions pertaining to all eukaryotes.

Key words Axonal transport, Intracellular transport, Kinesin, Amyloid precursor protein, Microtubule-based transport, Herpes simplex virus type 1, *Doryteuthis (Loligo) pealei*, Giant axon, Cytoskeleton

1 Introduction

The giant axon of the squid made a name for itself when Hodgkin and Huxley received the 1963 Nobel prize for their work discovering the molecular basis for neuronal electrical action potentials [1]. This discovery was made possible by the large size of the axon, up to 1 mm in diameter and 7 cm in length, which allowed electrodes to be placed inside and outside of the axon to measure the electrical potential across the axonal plasma membrane for the first time. Decades later other scientists, working at the Marine Biological Laboratory in Woods Hole, Massachusetts, with the squid *Doryteuthis (Loligo) pealei* (Fig. 1), discovered that intracellular transport of cytoplasmic organelles moved bidirectionally in the excised axon in a process referred to as fast axonal transport [2, 3]. Using video enhanced differential interference contrast (DIC) light microscopy, movements of these organelles could be imaged and their rate of motility measured. These movements also occurred in extruded axoplasm lacking cell body or plasma

Alessio Vagnoni (ed.), *Axonal Transport: Methods and Protocols*,
Methods in Molecular Biology, vol. 2431, https://doi.org/10.1007/978-1-0716-1990-2_1,
© The Author(s), under exclusive license to Springer Science+Business Media, LLC, part of Springer Nature 2022

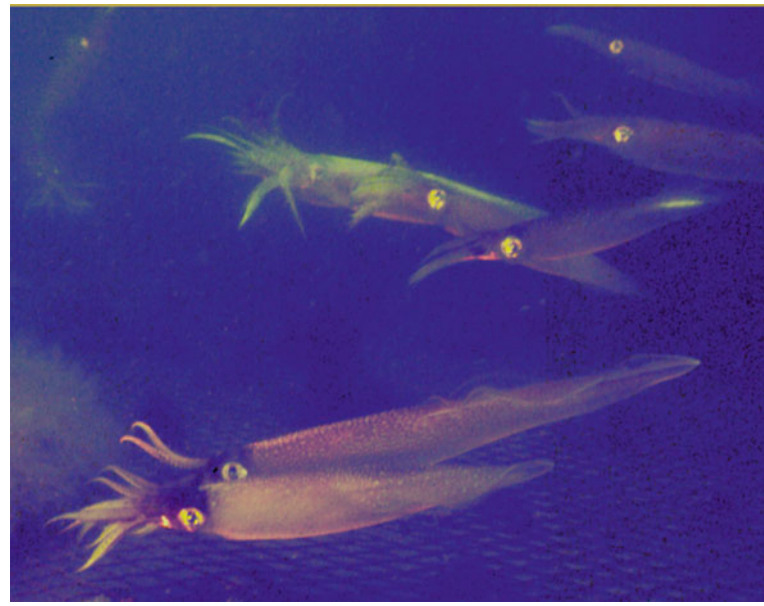

Fig. 1 Live squid, *Doryteuthis pealei*, whose species is known as long-finned inshore squid, imaged in the collecting net during capture, are transported to the Marine Resources Center (MRC) at the Marine Biological Laboratory, Woods Hole, Massachusetts

membrane and were found to occur bidirectionally along single microtubules in an ATP dependent process [4]. This led to an intensive search for the molecular motors that power these movements. Ultimately Vale, Reese, and Sheetz, building on their earlier observations with Bruce Schnapp [4], identified the first microtubule-based motor from the squid, which they named kinesin (Kinesin-1) [4]. Following on this discovery, many other microtubule-based motors were uncovered within neurons in squid [5] suggesting a complex transport system. In squid this included a Kinesin-3 that was shown to be tightly bound to KI treated organelles isolated from squid axoplasm that move at a rate of 2.0μm/s [6], four times faster than the rate of purified Kinesin-1 and the rate at which organelles move in the intact squid giant axon.

The intracellular transport mechanisms, originally identified in the squid giant axon, have turned out to be ubiquitous processes occurring in many types of eukaryotic cells. Some investigators have pursued the interaction of the motor domain of this force generating protein, while others explored cofactors regulating its activity. In these studies, the squid giant axon played a minor role.

By the early 2000s a major remaining question was how these motors interact with their cargo. Our initial exploration exploited the neurotropic herpes simplex virus type one (HSV1) together with the squid axon to investigate the interaction of an intracellular particle with the axonal transport machinery [7–10]. Taking

another leaf from marine biological Nobel-winning work identifying fluorescent proteins initially from jellyfish [11] also at Woods Hole, we tagged human herpes simplex virus type 1 (HSV-1) with green fluorescent protein and injected labeled virus into the excised giant axon [7, 8, 10]. Genetic manipulations of the virus and biochemical treatment of labeled viral particles prior to injection allowed us to identify surface receptors interacting with transport machinery, as extraction of membranes from intracellular HSV stripped its anterograde motility capacity [9, 10].

These experiments pointed to a role of amyloid precursor protein as a motor receptor, which had been suggested by others [12–16]. Continuing to use the experimental strategy of injecting particles into the living giant axon, we coated fluorescent beads with peptides derived from amyloid precursor protein and demonstrated a 15 amino acid peptide that was sufficient to drive transport of beads in the anterograde direction toward the synapse in the axon [17]. Cloning and sequencing the squid amyloid precursor protein (APP) revealed high degree of homology particularly in the motor binding domain across multiple species throughout the evolutionary tree from yeast to human [17]. Recently this homology has been further revealed to be functionally equivalent in mouse [18–20] and in human iPS neurons [21, 22]. Which motor binds this domain remains a question. While some investigators identified Kinesin-1 [15, 23], others were unable to confirm an interaction [24]. Interestingly, APP localizes in a cluster at the interface between the microtubule and KI-washed isolated squid organelles known to bind to microtubules through Kinesin-3 [25]. It has also been suggested that no motor binds directly to APP and the interaction between APP and motors is indirect, mediated by other proteins such as Jun-interacting proteins, JIP1–2 [26–31], and JIP3 [32].

Many questions remain that could be answered in the squid giant axon, especially now that sequencing of expressed sequence tags [5, 33, 34] and genomic DNA (http://ivory.idyll.org/blog/2014-loligo-transcriptome-data.html) and (https://spartanideas.msu.edu/2014/02/18/loligo-pealeii-squid-data-dump/) is underway and that genetic manipulations via the CRISPR/cas9 system are possible [35]. The giant axon provides a unique system of an intact neuronal process with all of its inner machinery intact in its native chemical environment, large enough to inject and transparent enough for optical imaging. The ability to inject purified well-characterized components is a special feature hard to achieve in cultured cells. A drawback of working in the squid giant axon is the seasonal availability of the Atlantic long-finned squid in the Woods Hole waters, plentiful in summer and sparse in winter. The Marine Biological Laboratory, with its powerful resources including both a fishing vessel, the research vessel (R.V.) Gemma (Fig. 2), to hunt and capture the squid, running seawater tanks to maintain squid in

Fig. 2 The R.V. Gemma. Squid are collected by the research fishing vessel, R.V. Gemma, daily Monday through Friday, beginning late April into early December. After capture, they are maintained in tanks at the Marine Resources Center at the MBL

the laboratory, wet bench space for visiting investigators, and state-of-the-art laser scanning confocal microscopy facilities, is the premiere site for squid giant axon biology. Ongoing efforts to breed and raise the long-finned squid in captivity continue and may come to fruition soon. We hope this protocol will inspire others with crucial biomedical questions to address them in the powerful experimental system, the squid giant axon.

Here we describe our method of dissecting the squid giant axon and injecting the living axon with exogenous probes.

2 Materials

2.1 Dissection of the Squid Giant Axon

1. Squid (Fig. 3), preferably captured not more than 48 h previously and maintained in running seawater tanks at ocean temperatures.
2. Squid dissecting table with running seawater (Fig. 4).
3. Large sharp scissor.
4. Spools of black and white sewing thread.
5. Roboz Surgical Castroviejo Micro Dissecting Scissors RS-5658.
6. 2 Dumont #5 Forceps Inox Tips Roboz RS-5-15.
7. Push pins.

Fig. 3 *Doryteuthis (Loligo) pealei*, photographed in the lab

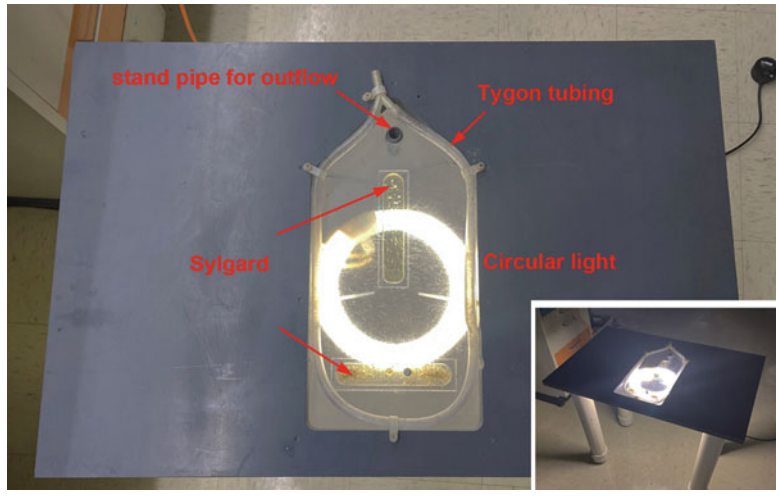

Fig. 4 The squid dissecting table is illuminated from underneath with a circular light, on which the squid mantle can be pinned onto Sylgard™ silicone. The table itself was custom made with PVC and the dissection area made of clear molded plexiglass. Running water fills the dissecting area, flowing out from Tygon tubing, and draining out through a standpipe at the head of the table. The table measures 21 × 32 in., and stands 32 in. tall. The open dissecting area measures 8 × 16 in. Tubing is 5/8 in. internal diameter, with holes in it like a sprinkler system. The light is an 8-in. circular fluorescent bulb connected to a foot switch

8. Large petri dish with Sylgard 184 elastomer ½ in. coating the bottom.
9. Stainless steel micro pins.
10. Large rubber stopper.
11. Parafilm.
12. 10μL micropipettes and tips.
13. Ca^{++}-free seawater.
14. Dental wax.

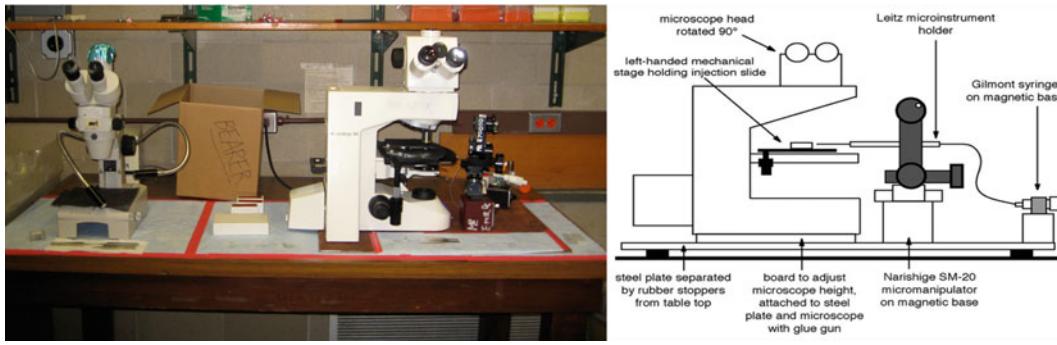

Fig. 5 Microscope setup in the Bearer Lab space at MBL. (**a**) To the left, the dissecting scope for removal of connective tissue and cleaning of the axon. To the right, the injection setup with a microscope and 10× lens. (**b**) Diagram of the injection setup. Modified after Jaffe and Terasaki [40]

15. 1/2× buffer: 10 mM HEPES–KOH (pH 7.2), 175 mM L-aspartic acid, 65 mM taurine, 85 mM betaine, 25 mM glycine, 6.5 mM $MgCl_2$, 5 mM EGTA 0.5 mM D-glucose, 1.5 mM $CaCl_2$ with 1 mM DTT and 10 mM each of benzamidine, leupeptin, pepstatin A, aprotinin, and phenanthroline.

2.2 Microinjection Materials Needed for the Squid Axon Injections (See Note 1)

1. Dissecting microscope (*see* Fig. 5 for microscope setup).
2. Upright microscope (black simple upright scope) with a 10× objective with phase rings and a phase condenser.
3. Micromanipulator (Narishige SM20) Model SM-20.
   (a) Magnetic base: Flexbar Machine Corp. Model 11002.
4. Micropipette puller (Narishige or other).
5. Micrometer syringe—Gilmont S-1200 Cat.no. GS-1200 *Note: see World Precision Instruments (WPI) for different syringes.*
6. Magnetic stand for holding micrometer syringe Flexbar Cat. no. 11004.
7. Leica micro-instrument holder.
   (a) Kramer Scientific Cat.no. 520145.
   (b) W832688 Tubing replacement.
   (c) 026-350-012-007 Brass collar replacement.
8. Syringe needle adapter Thomas Scientific Cat.no. 8960-D59.
9. Teflon tubing 20 guage, 24" length from either Scientific Commodities or Hamilton Company. You can also use polyethylene or teflon tubing, with cut off syringe needles pushed into the ends, for making the connections to the syringe and microinstrument holder.
10. Steel plate goes underneath scope and supports micromanipulator stability.
11. Watchmakers forceps.

12. Small scissors.
13. Hamilton Syringe (10μL) Fisher Scientific Cat.no. 14-824-54A.
    (a) Mercury (In room with injections—be careful, very toxic).
14. Fluorinert oil Sigma F9880.
15. Silicon grease.
16. Sylgard.
17. Glass capillary tubing for pipets (1 mm in diameter, 6 cm long).
    (a) Drummond Scientific, Cat. No. 1-000-0500.
18. Diamond knife.
19. Microscope slides with frosted end.
20. Ca^{++}-free seawater.
21. Double stick tape.
22. No. 0 and No. 1 glass coverslips.

3 Methods

3.1 Dissection of the Squid Giant Axon

1. Live squid (*Doryteuthis pealei)* are obtained from the Marine Resources Center (MRC) at the Marine Biological Laboratory, Woods Hole, Massachusetts. Squid are collected daily Monday through Friday from late April until early December by the research vessel (R.V.) Gemma (Fig. 2). Squid are maintained in tanks at the MRC for scientific investigation and fished from the tank in a long handled scoop net (Fig. 3).
2. To begin the dissection, the squid is decapitated with a large pair of sharp scissors with one quick cut.
3. The squid mantle is then cut open with a longitudinal cut along the ventral surface.
4. The skin and fins are removed by hand.
5. The mantle is opened up and pinned down on the dissecting table with push pins (Figs. 4 and 6). The table has a 1-in. deep well and is filled with fresh well-oxygenated seawater from an open seawater system made available in individual laboratories at Marine Biological Laboratory. The seawater flows through Tygon tubing into the well and over the squid mantle, then down a short standpipe. There is continuous flow through system to maintain aeration.
6. The internal organs including the gills, brachial and systemic hearts, digestive and reproduction systems, and the syphon are dissected out with scissors. The remaining mantle contains a series of third order giant axons. The squid is bisymmetric so there are two sets of axons that innervate the mantle muscle

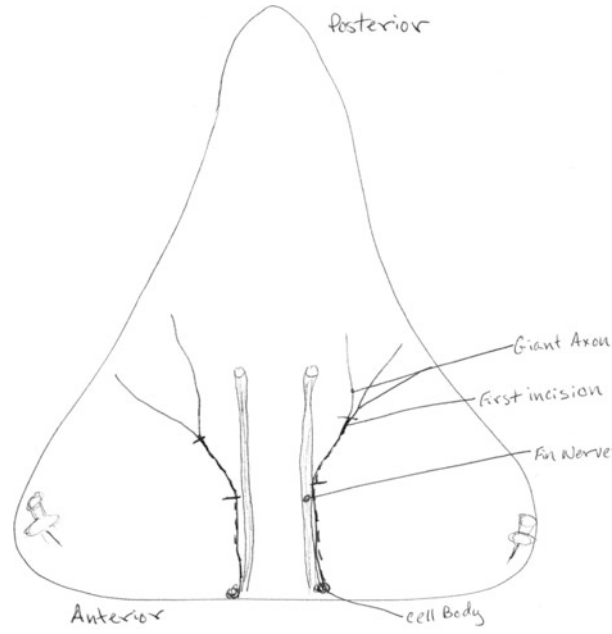

Fig. 6 Squid mantle diagram indicating the giant axon, other nerve bundles, and placement of pins

and are responsible for a coordinated muscle contraction in the process of swimming forward and a jet action that moves the squid backwards, mantle first, through the water column.

7. The squid dissecting table possesses a glass bottom that allows the mantle to be illuminated from below using transmitted light to make the mantle and giant axons visible (*see* Fig. 4). The axon itself lies within a cavity within the mantle and is surrounded with connective tissue (Fig. 6). To open the cavity an incision is made in the mantle just above the axon and near the axons cell body with surgical scissors. With the incision the mantle opens up exposing the axon and connective tissue. From this initial incision the mantle is cut along the entire length of the axon to the first bifurcation. A pair of forceps is used to reach under the axon just prior to the bifurcation and the end of black sewing thread is grabbed by the forceps and the thread pulled underneath the axon. The thread is tied tight around the axon collapsing the cell membrane holding the cytoplasm within the axon.
8. The axon is cut on the distal side of the ligation at the bifurcation and then the black thread is used to pull the axon from the mantle cavity. The proximal side of the axon is tied off with white thread just before the cell body and the cell body is cut away from the axon. The black and white threads distinguish the proximal and distal end of the axon.

9. Once removed from the mantle, the axon is placed in a petri dish lined with Sylgard a silicon-based elastomer. The axon is stretched out on the Sylgard and pinned down with small dissecting pins through the thread into the Sylgard. The petri dish is then filled with fresh well-aerated seawater.
10. Using Dumont #5 Forceps the connective tissue is pulled off of the axon. This step is also described below, and necessary for injections.
11. One way to extrude is begin by stretching parafilm across a large rubber stopper. The axon is cut at the black thread at the distal end of the axon. The axon is placed on the parafilm and a glass rod is used to extrude the cytoplasm. The glass rod is pressed down across the axon just distal to the white thread collapsing the cell membrane and then the rod is rolled down the axon. The axoplasm begins to emerge from the cell membrane and continues as the rod rolls along the membrane surface, like forcing toothpaste out of a tube. Typically, axoplasm is extruded into 50μL of 1/2× buffer [4].
12. Alternatively, extrusion can be performed by holding the axon at the cell body end with one forceps and sliding another forceps down its length while exerting pressure by squeezing, as in Fig. 7.
13. Extruded axoplasm contains about 50μg of protein per microliter. The volume that can be extruded is about 0.7μL/cm of axon length.
14. Extruded axoplasm can be studied in a variety of ways: live video-assisted DIC or confocal fluorescence microscopy for recording of organelle movements [2, 3, 7–10, 17], isolation of subcomponents such as organelles and motors [4, 6], or touch preps for negative-stained EM of cytoskeletal elements [36] (Fig. 8).
15. Instead of extruding the axoplasm, the axon can be injected with exogenous materials and studied intact for motility of endogenous organelles, such as mitochondria, or of exogenous particles tracked either by DIC [3, 37] or by time-lapse laser scanning confocal microscopy [7–10, 17, 23]. Peptides and other small molecules can also be added to the extruded axoplasm on injected to study their effect on motility of various components, exogenous or endogenous [9, 17, 38, 39].

3.2 Squid Axon Injections

3.2.1 Prepare micropipettes

1. Pull micropipette tubes to make needles with micropipette puller. Make long thin points.

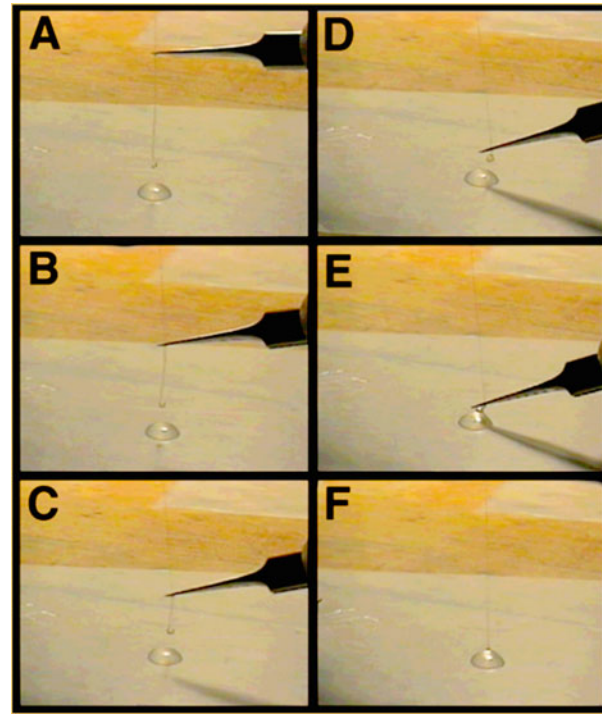

Fig. 7 An axon being extruded. Extrusion of axoplasm can be done simply, by holding the axon at the cell body end with one forceps pair while sliding another pair of forceps down its length, squeezing gently like squeezing toothpaste out of the tube from the far end. A 50μL droplet of 1/2× buffer receives the axoplasm on a sheet of dental wax. Axoplasm extruded this way is useful for biochemistry as well as microscopy [9, 17, 23, 41–44]

2. Back fill pipette needles with a small drop of mercury using a Hamilton syringe.
3. Mount pipette needle in micromanipulator.

3.2.2 Make capillary loading stage-3 glass slides staked together using silicon grease, with a dab of silicon grease in the center of the top slide (Fig. 9).

1. Cut a capillary tube in half with diamond pencil and use one half to load sample.
2. Load capillary tube with a 20μL pipetteman (*see* **Note 2**).
   (a) 2–3μL of dimethylpolysiloxane (oil).
   (b) 2–3μL of sample (use 2–3μL of oil to separate different samples).
   (c) Cap tube with 2–3μL of dimethylpolysiloxane.
3. Place capillary tube on "capillary loading stage" using the drop of silicon to secure it and place on microscope stage.

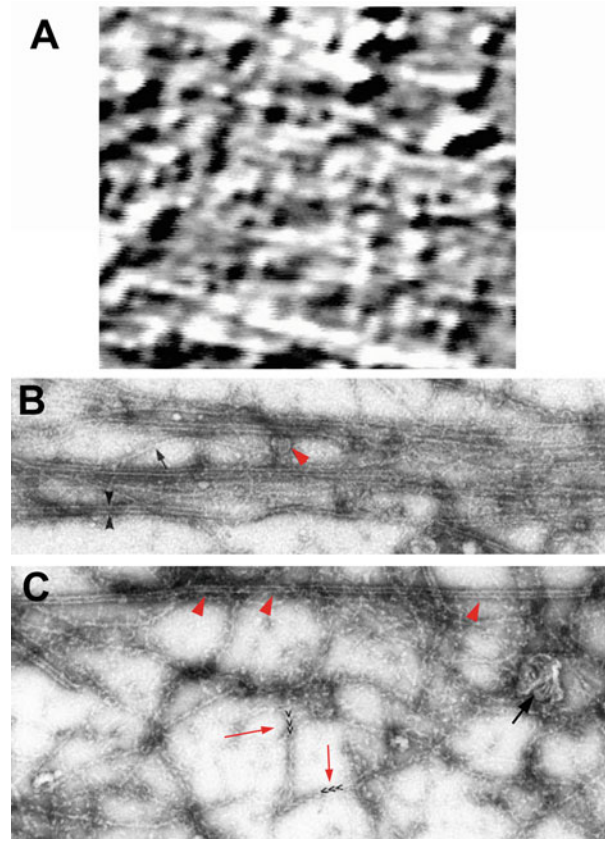

Fig. 8 Examples of microcopy of extruded axoplasm. (**a**) An example of a frame from a video obtained by DIC microscopy of vesicles and filaments in extruded axoplasm. (**b**) An example of electron-microscopy of a negative-stained touch prep of extruded axoplasm. Black arrowheads indicate a microtubule, red arrowhead indicates an organelle adjacent to a microtubule, black arrow indicates another type of filament, either neurofilament or actin. (**c**) Another example of an electron-micrograph of a negative-stained touch prep of extruded axoplasm after treatment with the S1 fragment of myosin that decorates actin filaments and distinguishes them from neurofilaments. Red arrowheads indicate a microtubule; red arrows indicate actin filaments decorated with the S1 fragment of myosin which forms the classic arrowheads along actin filaments (indicated by black "V" chevrons) along examples of two decorated filaments; black arrow indicates an organelle. (**b**) and (**c**): Modified from Bearer and Reese [36]

4. Focus microscope on the oil meniscus in the capillary tube (*see* Fig. 10).
   - Bring the pipette into the field of view and bring the pipette into focus by using the micromanipulator to move the tip up or down.

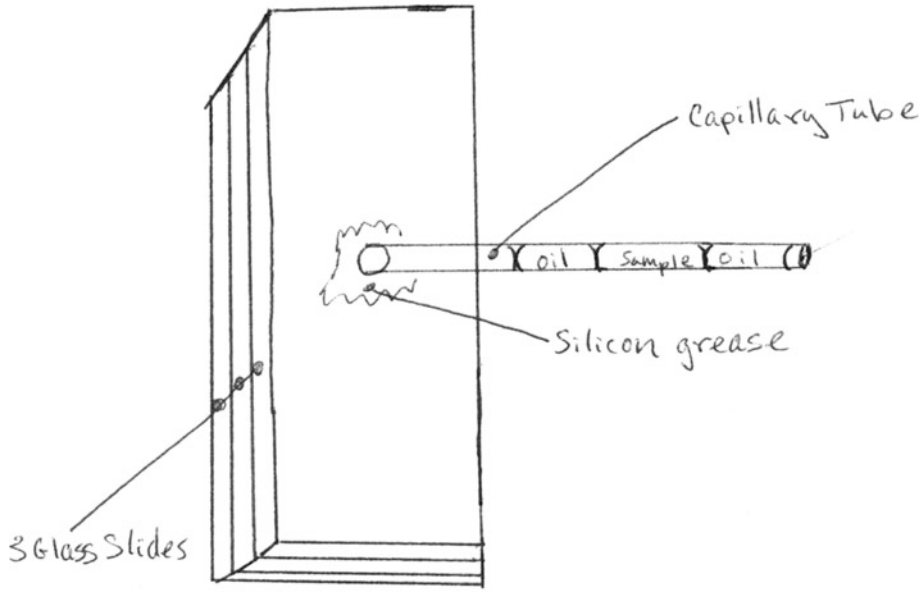

Fig. 9 The capillary loading stage is made by stacking 3 glass slides greased together with silicone, and then a dab of silicone grease in the center of the top slide. The capillary tube is then loaded with a 20μL pipetteman, first with 2–3μL of dimethylpolysiloxane, then 2–3μL of sample (use 2–3μL of oil to separate different samples), and finally capped with 2–3μL of dimethylpolysiloxane

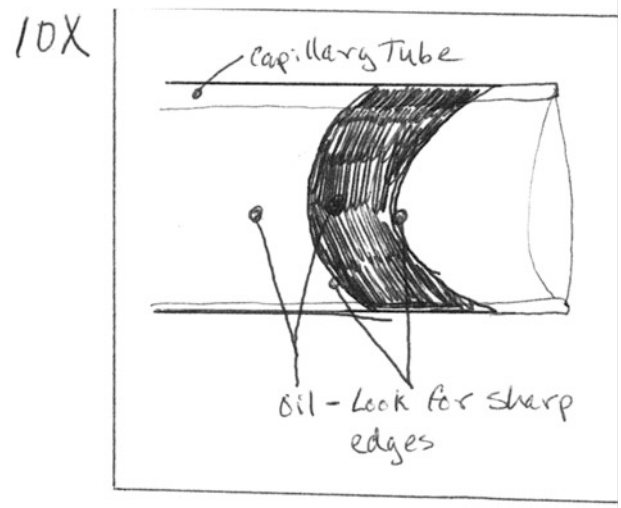

Fig. 10 Capillary tube. Focus the microscope on the oil meniscus in the loaded capillary tube, which is on the microscope stage, and use the micromanipulator to move the tip of the micropipette up or down to bring it into focus. Keep the focus of the microscope on the capillary tube

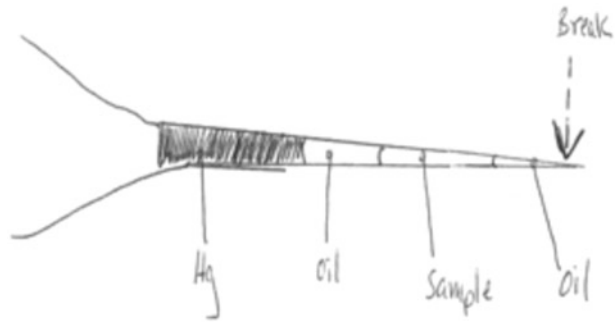

Fig. 11 Loaded micropipette. Place the tip of the pipette into the capillary tube, and suck up 5–10 units of oil, 10 units of sample, and 5 units of oil in sequence

- Break ½ mm off the tip of the pipette by touching it to the edge of the capillary tube to open it up and sharpen the glass tip to penetrate the axon.
- Push the mercury to the tip of the pipette. Fluorinert is the oil in the micrometer syringe used to load the capillary tube.
- Put the tip of the pipette into the capillary tube and suck up 5–10 units of oil, 10 units of sample, and 5 units of oil in sequence. (Fig. 11).
- Use a unit bar, reticule, in the oculars of the microscope to measure the amount of each component in the micropipette.

3.2.3 Clean off the connective tissue under observation in the dissecting scope, using a Sylgard coated petri dish filled with Ca^{++}-free seawater. Once the connective tissue is removed, it is imperative to maintain the axon in Ca^{++}-free seawater, as any calcium entry through the smallest nick will induce neurofilament disassembly and axon death [36].

3.2.4 Set up "axon injection stage"-3 glass slides greased together, 1 strip of Teflon running close to one side of the slide and square of Teflon in the middle (Figs. 12 and 13). The Teflon creates a backboard to push the axon against when injecting (*see* **Note 3**).

- Put bolus of Ca^{++}-free seawater along the strip of Teflon.
- Place freshly dissected squid axon along Ca^{++}-free seawater with the cell body toward the frosted end of the slide, to maintain axonal orientation.
- Cover axon with a cover slip and add more Ca^{++}-free seawater to chamber as needed (Fig. 12).
- Focus on the axon so that the sides of the axon are two clear edges running parallel to each other (Fig. 13).

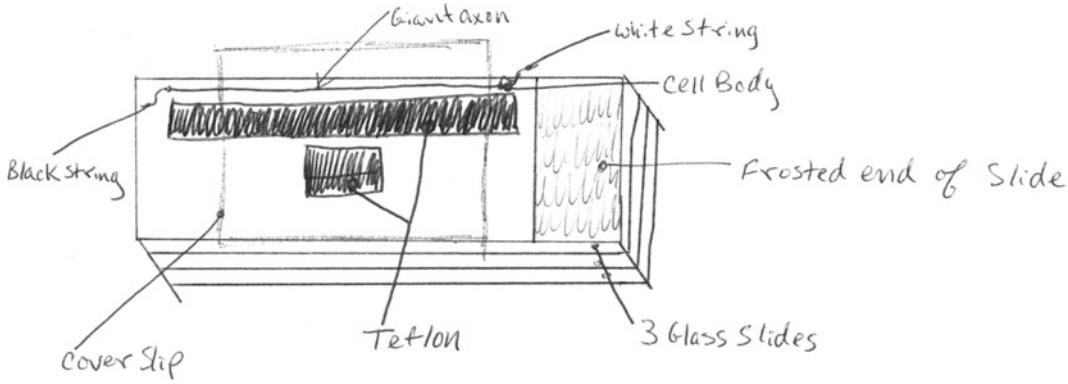

Fig. 12 Injection chamber, low mag. Setting up the axon injection stage requires the 3 glass slides greased together, a strip of Teflon running close to one side of the slide, and a Teflon square in the center of the slide mount. The axon will lie on the far edge of the slide along the edge of the Teflon strip, with the cell body toward the frosted end. The injection chamber is then placed on the microscope stage

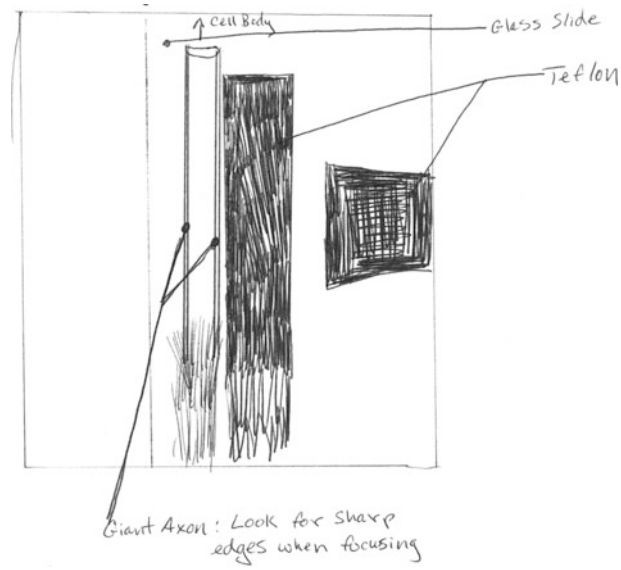

Fig. 13 Injection chamber, focusing. Once covered with a cover slip and the addition of more Ca^{++}-free seawater to the chamber until no air bubbles exist in the injection stage, focus on the axon until both sides of the axon appear as two clear edges running parallel to each other on the prepped glass slide. Adjustments to the condenser may be needed for sharp focus

- Look for a healthy place on the axon stripped of sheath to make injection.
- Use the micromanipulator to focus the pipette without changing the focus on the microscope—so that both are in the same focal plane.

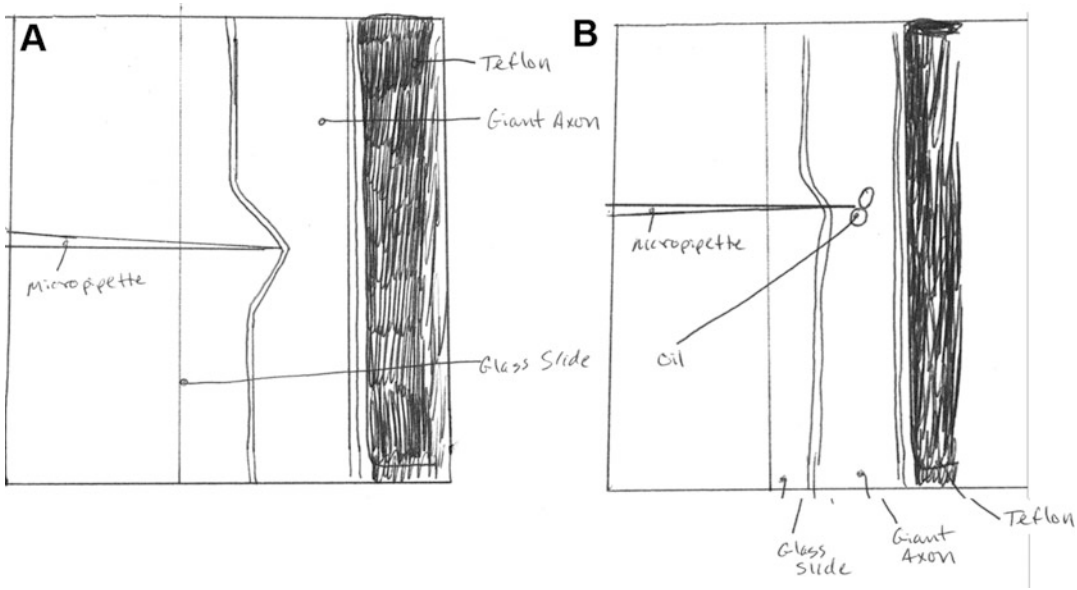

Fig. 14 Injection. (**a**) Bring the micropipette into focus using the micromanipulator. This will adjust the micropipette to be in the same focal plane as the axon that has just been brought into focus on the microscope stage. Advance the micropipette with the micromanipulator until it presses into the side of the axon. If the axon rolls, pull back, and readjust the focus of the microscope on the axon, then readjust the micropipette position with the micromanipulator. It may be necessary to stretch the axon using the strings at either end to lessen rolling and enhance penetration. (**b**) Advance the micropipette steadily until indentation is halfway into the axon, then gently tap the butt of the micromanipulator dial until the micropipette pops into the axon

- Move the axon and pipette tip toward each other using the stage *x*, *y* manipulators to adjust the axon and the micromanipulator to adjust the pipette as needed.
- Make sure the pipette is still in the same focal plane as the axon (use micromanipulator to focus the micropipette, do not re-adjust the microscope)—this ensures easier injections, otherwise the axon may roll when you try to "stick" it.
- Use the stage and micromanipulator to touch the axon with the pipette creating an indentation in the axon (Fig. 14a**).**
- Using the micromanipulator try to push the pipette into the axon. Tapping the side of the micromanipulator may help to pop the needle into the axon.
- -After "sticking" the axon, slowly inject sample using the micrometer syringe while observing through the microscope and then remove the pipette. You should see the oil droplet form within the axon as you inject (Fig. 14b**)**. Make sure not to inject the mercury.

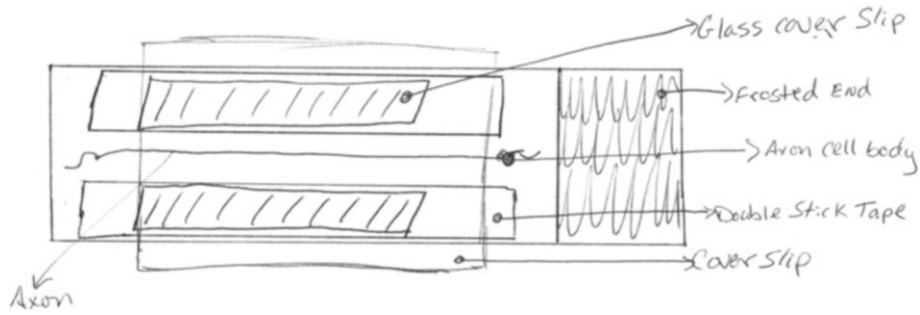

Fig. 15 Mounting injected axon for confocal imaging. Quickly mount the axon on the axon imaging slide chamber. The chamber has two strips of double stick tape running along each side, and half a No. 1 coverslip placed on top of each tape strip, creating a well down the center of the slide. Holding the threads, place the axon in the well between the mounted tape strips, with the cell body toward the frosted end of the slide. Fill the well with Ca^{++}-free seawater and cover the assemblage with a No. 0 coverslip (*see* **Note 4**)

- Quickly mount axon on the "axon imaging slide chamber"—one glass slide with two strips of double stick tape running along each side, creating a space down the middle. Cut a No. 1 cover slip in half lengthwise with the diamond knife and stick one half to each side of the slide, creating a well so that the axon is not squished and can be submerged in Ca^{++}-free seawater (Fig. 15).
- Add Ca^{++}-free seawater to the well and place the axon so that the cell body is toward the frosted end of the slide.
- Gently place cover slip over the axon and fill the space with more Ca^{++}-free seawater (*see* **Note 4**).

3.2.5 Place the axon in its chamber into a slide carrier box and carry it over to the confocal microscope. Bring along 5 mL of Ca^{++}-free seawater to add to the chamber to prevent drying, and forceps to reposition the axon in case it shifts.

4 Notes

1. This protocol was developed with guidance from Mark Terasaki and Laurinda Jaffe who had developed and published a protocol for egg and embryo injections [40]. That protocol contains additional details that may help when setting up injections of the giant axon.
2. When injecting more than one sample, as in co-injection of two colors of peptide-coated beads, or beads plus soluble peptide, it is important to separate the two samples with another small bolus of oil, and to inject in both sequences, with sample A first and sample B second and vice versa [9, 17]. It is also imperative to have some control that axon viability (i.e., active transport) is

still occurring following dissection, as any nick in the plasma membrane can result in lethal damage. We have used DIC microscopy [8, 41], fluorescence labeling of mitochondria with a dye that only fluoresces in metabolically active mitochondria [10], or negatively charged 100 nm fluorescent polystyrene beads [23]. We also monitor the oil droplet from drift. Any drift in the oil droplet indicates that the axonal cytoskeleton is disassembling. The neurofilaments that stabilize the cytoskeleton are exquisitely sensitive to Ca^{++} and will come apart if any has leaked into the axon [37].

3. Check that the connective tissue is fully removed, being careful not to injure the axonal membrane. If connective tissue is still surrounding the axon, it will be very difficult to pierce it with the micropipette for injection.
4. The thickness of the coverslip over the axon should be determined by the confocal microscope, the lenses, and the magnification desired for imaging. For the Zeiss 510 and 710 in the MBL Microscope Facility, the No. 0 coverslip was best. For imaging fluorescence by confocal, a water-immersion lens with a long focal distance (like the ZEISS Achroplan ×40 80/W lens with numerical aperture of 0.8 and working distance of 3.6 mm used with a No. 0 coverslip) is necessary, as the axon is too thick for short working distance lenses with higher magnifications. The transport machinery is in the deeper regions of the axon, which is 1.0 mm thick. Hence a minimum working distance that includes the thickness of the coverslip plus at least 0.3 mm allows imaging without exerting pressure on the axon during focusing. It is best to confirm the injection site by finding the oil droplet with low magnification (×10) phase microscopy before trying to image transport by fluorescence at higher magnification.

Acknowledgments

We are grateful to Prasanna Satpute-Krishnan, Derek Nobrega, and Michael P. Conley for development of this protocol and some of the drawings, to Thomas S. Reese for inspiration and guidance, to Jim Galbraith for construction of the squid table, to Mark Terasaki and Laurinda Jaffe for injection advice, and to the Marine Biological Laboratory Embryology Course for loan of the micromanipulator and other injection equipment. We also thank Paulette Ferland for technical assistance. We co-authors were all at Brown University when this work was developed and we remain Brown Alumni. We are grateful to Brown University for the extraordinary opportunity afforded us to work together: Bearer as tenured professor and PI, DeGiorgis as PhD candidate, and Jang in the BA-MD program.

This work was funded by Frederick Bang Summer Whitman Fellowships from MBL (E.L.B.), the Dart Foundation (E.L.B.) as well as NIGMS RO1 GM47368, NINDS RO1 NS046810 and RO1 NS062184 (E.L.B.), and the National Science Foundation under EPSCoR Cooperative Agreement #OIA-1655221 (J.A.D.).

References

1. Hodgkin A, Huxley A (1952) A quantitative description of membrain current and its application to conduction and excitation in nerve. J Physol 117:500–544
2. Allen RD, Metuzals J, Tasaki I, Brady ST, Gilbert SP (1982) Fast axonal transport in squid giant axon. Science 218(4577):1127–1129
3. Brady ST, Lasek RJ, Allen RD (1982) Fast axonal transport in extruded axoplasm from squid giant axon. Science 218(4577): 1129–1131
4. Vale RD, Schnapp BJ, Reese TS, Sheetz MP (1985) Movement of organelles along filaments dissociated from the axoplasm of the squid giant axon. Cell 40(2):449–454. https://doi.org/10.1016/0092-8674(85)90159-X. [pii]
5. DeGiorgis JA, Cavaliere KR, Burbach JPH (2011) Identification of molecular motors in the Woods Hole squid, Loligo pealei: an expressed sequence tag approach. Cytoskeleton 68(10):566–577. https://doi.org/10.1002/cm.20531
6. DeGiorgis JA, Petukhova TA, Evans TA, Reese TS (2008) Kinesin-3 is an organelle motor in the squid giant axon. Traffic 9(11): 1867–1877. https://doi.org/10.1111/j.1600-0854.2008.00809.x
7. Bearer EL, Breakefield XO, Schuback D, Reese TS, LaVail JH (2000) Retrograde axonal transport of herpes simplex virus: evidence for a single mechanism and a role for tegument. Proc Natl Acad Sci U S A 97(14):8146–8150. https://doi.org/10.1073/pnas.97.14.8146. [pii]
8. Bearer EL, Schlief ML, Breakefield XO, Schuback DE, Reese TS, LaVail JH (1999) Squid axoplasm supports the retrograde axonal transport of herpes simplex virus. Biol Bull 197(2): 257–258
9. Bearer EL, Wu C (2019) Herpes simplex virus, Alzheimer's disease and a possible role for Rab GTPases. Front Cell Dev Biol 7. https://doi.org/10.3389/fcell.2019.00134
10. Satpute-Krishnan P, DeGiorgis JA, Bearer EL (2003) Fast anterograde transport of herpes simplex virus: role for the amyloid precursor protein of Alzheimer's disease. Aging Cell 2(6):305–318
11. Shimomura O (2009) Discovery of green fluorescent protein (GFP) (Nobel lecture). Angew Chem Int Ed Engl 48(31):5590–5602. https://doi.org/10.1002/anie.200902240
12. Gunawardena S, Goldstein LS (2001) Disruption of axonal transport and neuronal viability by amyloid precursor protein mutations in Drosophila. Neuron 32(3):389–401. https://doi.org/10.1016/S0896-6273(01)00496-2. [pii]
13. Kamal A, Goldstein LS (2000) Connecting vesicle transport to the cytoskeleton. Curr Opin Cell Biol 12(4):503–508
14. Kamal A, Goldstein LS (2002) Principles of cargo attachment to cytoplasmic motor proteins. Curr Opin Cell Biol 14(1):63–68
15. Kamal A, Stokin GB, Yang Z, Xia CH, Goldstein LS (2000) Axonal transport of amyloid precursor protein is mediated by direct binding to the kinesin light chain subunit of kinesin-I. Neuron 28(2):449–459
16. Kamal A, Almenar-Queralt A, LeBlanc JF, Roberts EA, Goldstein LS (2001) Kinesin-mediated axonal transport of a membrane compartment containing beta-secretase and presenilin-1 requires APP. Nature 414(6864): 643–648
17. Satpute-Krishnan P, DeGiorgis JA, Conley MP, Jang M, Bearer EL (2006) A peptide zipcode sufficient for anterograde transport within amyloid precursor protein. Proc Natl Acad Sci U S A 103(44):16532–16537
18. Bearer EL, Falzone TL, Zhang X, Biris O, Rasin A, Jacobs RE (2007) Role of neuronal activity and kinesin on tract tracing by manganese-enhanced MRI (MEMRI). NeuroImage 37(Suppl 1):S37–S46
19. Cromberg LE, Saez TMM, Otero MG, Tomasella E, Alloatti M, Damianich A, Pozo Devoto V, Ferrario J, Gelman D, Rubinstein M, Falzone TL (2019) Neuronal KIF5b deletion induces striatum-dependent locomotor impairments and defects in membrane presentation of dopamine D2 receptors.

J Neurochem 149(3):362–380. https://doi.org/10.1111/jnc.14665

20. Saez TMM, Fernandez Bessone I, Rodriguez MS, Alloatti M, Otero MG, Cromberg LE, Pozo Devoto VM, Oubiña G, Sosa L, Buffone MG, Gelman DM, Falzone TL (2020) Kinesin-1-mediated axonal transport of CB1 receptors is required for cannabinoid-dependent axonal growth and guidance. Development 147(8). https://doi.org/10.1242/dev.184069
21. Lacovich V, Espindola SL, Alloatti M, Pozo Devoto V, Cromberg LE, Carná ME, Forte G, Gallo JM, Bruno L, Stokin GB, Avale ME, Falzone TL (2017) Tau isoforms imbalance impairs the axonal transport of the amyloid precursor protein in human neurons. J Neurosci 37(1):58–69. https://doi.org/10.1523/jneurosci.2305-16.2016
22. Pozo Devoto VM, Dimopoulos N, Alloatti M, Pardi MB, Saez TM, Otero MG, Cromberg LE, Marín-Burgin A, Scassa ME, Stokin GB, Schinder AF, Sevlever G, Falzone TL (2017) αSynuclein control of mitochondrial homeostasis in human-derived neurons is disrupted by mutations associated with Parkinson's disease. Sci Rep 7(1):5042. https://doi.org/10.1038/s41598-017-05334-9
23. Seamster PE, Loewenberg M, Pascal J, Chauviere A, Gonzales A, Cristini V, Bearer EL (2012) Quantitative measurements and modeling of cargo-motor interactions during fast transport in the living axon. Phys Biol 9(5):055005. https://doi.org/10.1088/1478-3975/9/5/055005
24. Lazarov O, Morfini GA, Lee EB, Farah MH, Szodorai A, DeBoer SR, Koliatsos VE, Kins S, Lee VM, Wong PC, Price DL, Brady ST, Sisodia SS (2005) Axonal transport, amyloid precursor protein, kinesin-1, and the processing apparatus: revisited. J Neurosci 25(9):2386–2395. https://doi.org/10.1523/jneurosci.3089-04.2005
25. Lakshmana MK, Stevenson JW, Conaty EA, Walsh RB, Poidomani PJ, Samoriski CM, Scollins BJ, DeGiorgis JA (2016) The amyloid precursor protein of Alzheimer's disease clusters at the organelle/microtubule interface on organelles that bind microtubules in an ATP dependent manner. PLoS One 11(1):e0147808. https://doi.org/10.1371/journal.pone.0147808
26. M-m F, Holzbaur ELF (2013) JIP1 regulates the directionality of APP axonal transport by coordinating kinesin and dynein motors. J Cell Biol 202(3):495–508. https://doi.org/10.1083/jcb.201302078
27. Hammond JW, Griffin K, Jih GT, Stuckey J, Verhey KJ (2008) Co-operative versus independent transport of different cargoes by Kinesin-1. Traffic 9(5):725–741
28. Horiuchi D, Barkus RV, Pilling AD, Gassman A, Saxton WM (2005) APLIP1, a kinesin binding JIP-1/JNK scaffold protein, influences the axonal transport of both vesicles and mitochondria in Drosophila. Curr Biol 15(23):2137–2141
29. Horiuchi D, Collins CA, Bhat P, Barkus RV, Diantonio A, Saxton WM (2007) Control of a kinesin-cargo linkage mechanism by JNK pathway kinases. Curr Biol 17(15):1313–1317
30. Muresan Z, Muresan V (2005) Coordinated transport of phosphorylated amyloid-beta precursor protein and c-Jun NH2-terminal kinase-interacting protein-1. J Cell Biol 171(4):615–625. https://doi.org/10.1083/jcb.200502043. [pii]
31. Muresan Z, Muresan V (2005) c-Jun NH2-terminal kinase-interacting protein-3 facilitates phosphorylation and controls localization of amyloid-beta precursor protein. J Neurosci 25(15):3741–3751
32. Bowman AB, Kamal A, Ritchings BW, Philp AV, McGrail M, Gindhart JG, Goldstein LS (2000) Kinesin-dependent axonal transport is mediated by the sunday driver (SYD) protein. Cell 103(4):583–594
33. Liscovitch-Brauer N, Alon S, Porath HT, Elstein B, Unger R, Ziv T, Admon A, Levanon EY, Rosenthal JJC, Eisenberg E (2017) Trade-off between transcriptome plasticity and genome evolution in cephalopods. Cell 169(2):191–202. e111. https://doi.org/10.1016/j.cell.2017.03.025
34. Vallecillo-Viejo IC, Liscovitch-Brauer N, Diaz Quiroz JF, Montiel-Gonzalez MF, Nemes SE, Rangan KJ, Levinson SR, Eisenberg E, Rosenthal JJC (2020) Spatially regulated editing of genetic information within a neuron. Nucleic Acids Res 48(8):3999–4012. https://doi.org/10.1093/nar/gkaa172
35. Crawford K, Diaz Quiroz JF, Koenig KM, Ahuja N, Albertin CB, Rosenthal JJC (2020) Highly efficient knockout of a squid pigmentation gene. Curr Biol 30(17):3484–3490. e3484. https://doi.org/10.1016/j.cub.2020.06.099
36. Bearer EL, Reese TS (1999) Association of actin filaments with axonal microtubule tracts. J Neurocytol 28(2):85–98
37. Lasek RJ, Brady ST (1985) Attachment of transported vesicles to microtubules in axoplasm is facilitated by AMP-PNP. Nature 316(6029):645–647. https://doi.org/10.1038/316645a0

38. Brady ST, Pfister KK, Bloom GS (1990) A monoclonal antibody against kinesin inhibits both anterograde and retrograde fast axonal transport in squid axoplasm. Proc Natl Acad Sci U S A 87(3):1061–1065. https://doi.org/10.1073/pnas.87.3.1061
39. Galbraith JA, Reese TS, Schlief ML, Gallant PE (1999) Slow transport of unpolymerized tubulin and polymerized neurofilament in the squid giant axon. Proc Natl Acad Sci U S A 96(20): 11589–11594. https://doi.org/10.1073/pnas.96.20.11589
40. Jaffe LA, Terasaki M (2004) Quantitative microinjection of oocytes, eggs, and embryos. Methods Cell Biol 74:219–242
41. Bearer EL, DeGiorgis JA, Bodner RA, Kao AW, Reese TS (1993) Evidence for myosin motors on organelles in squid axoplasm. Proc Natl Acad Sci U S A 90(23):11252–11256
42. DeGiorgis JA, Reese TS, Bearer EL (2002) Association of a nonmuscle myosin II with axoplasmic organelles. Mol Biol Cell 13(3): 1046–1057
43. Bearer EL, DeGiorgis JA, Medeiros NA, Reese TS (1996) Actin-based motility of isolated axoplasmic organelles. Cell Motil Cytoskeleton 33(2):106–114. https://doi.org/10.1002/cm.970330202
44. Bearer EL, DeGiorgis JA, Jaffe H, Medeiros NA, Reese TS (1996) An axoplasmic myosin with a calmodulin-like light chain. Proc Natl Acad Sci U S A 93:6064–6068. https://doi.org/10.1002/cm.970330202

Chapter 2

Live Imaging and Quantitative Analysis of Organelle Transport in Sensory Neurons of *Aplysia Californica*

Kerriann Badal, Yibo Zhao, Kyle E. Miller, and Sathyanarayanan V. Puthanveettil

Abstract

Axonal transport moves proteins, RNAs, and organelles between the soma and synapses to support synaptic function and activity-dependent changes in synaptic strength. This transport is impaired in several neurodegenerative disorders such as Alzheimer's disease. Thus, it is critical to understand the regulation and underlying mechanisms of the transport process. *Aplysia californica* provides a powerful experimental system for studying the interplay between synaptic activity and transport because its defined synaptic circuits can be built in-vitro. Advantages include precise pre- and postsynaptic manipulation, and high-resolution imaging of axonal transport. Here, we describe methodologies for the quantitative analysis of axonal transport in *Aplysia* sensory neurons.

Key words Organelle transport, Aplysia, Mitochondria, Kymograph, Live imaging, Transport quantification, Bidirectional transport, Organelle density

1 Introduction

Axonal transport delivers cargoes for cellular functions, recycles exhausted organelles to maintain neuronal health [1], and carries signals for cell-to-cell communication [2]. Studying neuronal cell-specific transport is essential for a better understanding of the role of communication between the soma and the synapse in synaptic remodeling and plasticity. However, few model systems can be used for these studies since most in vitro cultures are composed of mixed populations of neuronal types and support cells [3]. As a result, discrimination of specific types of pre- and postsynaptic neurons typically requires fluorescence, electrophysiological, or cytochemistry techniques [4–6]. Studying cell-specific axonal transport is simplified with the sea hare model organism, *Aplysia californica*, where neurons are identified, named, and can be isolated individually during dissection to create defined cultures [7]. Furthermore,

Alessio Vagnoni (ed.), *Axonal Transport: Methods and Protocols*,
Methods in Molecular Biology, vol. 2431, https://doi.org/10.1007/978-1-0716-1990-2_2,
© The Author(s), under exclusive license to Springer Science+Business Media, LLC, part of Springer Nature 2022

Aplysia neurons are very large in general; some cell bodies as large as 1 mm in diameter. Collectively these properties make *Aplysia* neurons an ideal system for understanding the interplay between axonal transport and synaptic function.

The mechanism underlining axonal transport is conserved across species. It is mediated by the molecular motors kinesin and dynein, which transport cargoes in the anterograde and retrograde directions, respectively [1]. Organelles, such as mitochondria and lysosomes, are transported bidirectionally by these molecular motors along microtubules aided by adaptor proteins [8, 9]. Mitochondria within neurons are essential for ATP production, intracellular calcium ion sequestering, neuronal health and homeostasis, synapse formation, function, and plasticity [10].

Apart from the significance of transport in synapse function and plasticity, axonal transport is also implicated in several neuropsychiatric disorders (reviewed in [11]). For example, defects in the axonal transport of cargoes such as RNA, proteins, and organelles contribute to many neurological disorders and diseases such as Alzheimer's, Huntington's disease, and Parkinson's disease [11, 12]. Cargo organelles such as mitochondria and lysosomes are transported to maintain neuronal health and functions; however, disruption in their transport can be detrimental. For example, altered axonal mitochondrial transport may lead to diseases such as Charcot–Marie–Tooth Disease or neuroinflammation [13, 14]. Moreover, improper delivery of lysosomes or their substrates contributes to diseases such as Alzheimer's and age-related defects [15, 16]. Specifically, defects in the retrograde transport of lysosomes contribute to Alzheimer's disease amyloid plaque buildup and blockades within the axon [9]. Lysosomes contribute significantly to neuronal health and toxicity control [15, 17, 18]. Understanding the mechanisms of regulation, critical signal mediation, and activity-dependent trafficking patterns of the axonal transport of mitochondria and lysosomes will contribute to our knowledge of neuronal health, plasticity, and neurodegenerative diseases.

A rigorous framework for describing axonal transport requires a full understanding of flux (F). Flux is a measure of the number of objects that pass a point on a line, a line across a two-dimensional surface, or a plane across a three-dimensional volume over a given period. Theoretically, there are two approaches for measuring flux: one can measure the number and speed that organelles pass a point (Eq. 1), or one can track the total number and full velocity profiles of organelles over a segment of axon (Eq. 2). While in our initial studies of mitochondrial transport, we used the later [19], we now favor the former [20] because it provides a direct estimate of kinesin and dynein velocity and requires less effort to attain an estimate of flux. Therefore, it is highly important to study the rate

of transport of different organelles to better understand synapse function, plasticity, neuronal health and disorders.

In practice, transport is measured by drawing a line across the center of a kymograph and then counting the number of organelles that cross that line over time to measure flux (F) and the speed at which they cross the line to measure instantaneous velocity (V_{INT}). Using Eq. 1, the concentration of moving organelles (C_{MOV}) is estimated by dividing flux by V_{INT} (Eq. 1). To confirm the estimate, the concentrations of moving (C_{MOV}) and total organelles (C_{TOT}) are then measured directly by counting the number of each along a segment of the axon. From these measurements, the ratio of moving to stationary organelles (R_{MOV}) is calculated (Eq. 3) and can be used to estimate average velocity V_{AVE} (Eq. 4). Collectively these equations provide a complete understanding of transport.

$$F = V_{\mathrm{INT}}\, C_{\mathrm{MOV}} \tag{1}$$

$$F = V_{\mathrm{AVE}}\, C_{\mathrm{TOT}} \tag{2}$$

$$R_{\mathrm{MOV}} = \mathrm{C_{MOV}}/\mathrm{C_{TOT}} \tag{3}$$

$$V_{\mathrm{AVE}} = V_{\mathrm{INT}}\, R_{\mathrm{MOV}} \tag{4}$$

Two concrete examples provide a helpful way to understand these equations. First, consider a group of scientists discussing whether "transport" is higher along an open highway or in the middle of a city. The first notes that on the highway ten cars pass a point over 10 min (Flux, 1 car/min), each moving with an instantaneous velocity of 1 km/min, with a density (or concentration) of 1 car/km. The second points out that in the city, ten cars pass a point over 10 min (Flux, 1 car/min), going only 0.1 km/min, but are packed at a density of 10 car/km. The first person claims transport is higher on the highway based on velocity, while the second argues the same for the city based on car density. A third person notes because the same number of cars pass a point along the road over a given period in time, the flux, and thus the traffic in both locations is the same. A broader view is that no single variable is "most" important; knowledge of each is needed for a complete description of transport.

A more subtle aspect of transport concerns the difference between average and instantaneous velocity (Eq. 1 vs. Eq. 2). For example, in the classic children's story, "The Tortoise and the Hare," the tortoise travels at a slow pace without stopping, while the hare moves rapidly but stops to take breaks. Counter-intuitively the tortoise wins the race because it maintains a higher average velocity (V_{AVE}); nonetheless, when the hare is in motion, it has a higher instantaneous velocity (V_{INT}). Using Eq. (2) and noting that the total concentration (C_{TOT}) of hares and tortoise are equal to each other, it also follows that "tortoise flux" is higher than "hare flux." Arguably, part of what makes this story enjoyable

is that it plays with our notions of what it means to be fast. While our focus here is on measuring V_{INT}, V_{AVE} can be measured using particle-tracking software or by completely tracing the path of all organelles: both docked and moving. Using the ratio of moving and stationary organelles, V_{INT} is calculated using Eqs. 3 and 4. Objectively, both V_{INT} and V_{AVE} are valid metrics of transport, so long as care is taken in understanding their differences.

Importantly, because each variable corresponds to a different underlying biological mechanism, usually one is of primary interest. Because a significant function of axonal transport is to deliver or to remove material from the growth cone or synapse, flux is often a biologically important variable. When finding there is a change in flux, it is natural to ask if it occurs because of a change in velocity or concentration. A change in C_{MOV} might suggest that either biogenesis or docking is altered, which, in turn, can be resolved by examining the ratio of C_{MOV} over C_{TOT}. An alteration in V_{INT} indicates that the stepping by dynein or kinesin along MTs changes directly. In light of this, flux, V_{INT}, and the ratio of moving and stationary organelles are often the most relevant measures of transport.

Here we describe our method for studying mitochondrial and lysosomal transport in *Aplysia* neurons. In brief, we discuss how to prepare cultures, to isolate the hemolymph needed for healthy cultures, the use of electrophysiology to measure synaptic strength in co-cultures of sensory and motor neurons [7], and the fluorescent labeling of lysosomal-related organelles (LROs) and mitochondria for the live imaging of their transport. Finally, we then describe methods for quantitative transport analysis.

2 Materials

Prepare all solutions in sterile glassware. While some solutions are stored in −80, −20, or 4 °C, all solutions must be thoroughly thawed to room temperature before being used for culture preparation and imaging acquisition.

2.1 Animals, Culture Medium, and Culture Preparation

1. 10–15 *Aplysia*, 1–4 g heavy.
2. *Aplysia*, 80–120 g heavy, 6–9-month-old.
3. Modified L15: 500 mL L15, 744 mg calcium chloride hydrate, 6250 mg sodium chloride, 3120 mg dextrose, 3120 mg magnesium sulfate, 172 mg potassium chloride, 96 mg sodium chloride, 2850 mg magnesium chloride, 1800 mg HEPES, 5 mL Penicillin-Streptomycin, pH = 7.6, adjustable with sodium hydroxide.
4. Hemolymph isolated from wild-caught *Aplysia*.

5. 35 mm poly-L-lysine treated glass-bottom petri dish.
6. Dispase II: 1 mg Dispase II/7.5 mL modified L15.
7. L-glutamine: (200 mM) stock, (5 mM) working.
8. Silicone-bottom petri dish (working dish).
9. Inverted dissection microscope with a wide stage.
10. 35 mm sterile Petri dishes.
11. Fine Science Tools Dumont M5S forceps.
12. Fine Science Tools Item Number 15000–08 spring scissors.
13. Waxed dissection pan.
14. Dissection scissors.
15. Dissection forceps.
16. Pins 0.10 mm thick.
17. 0.38 M magnesium chloride in water (anesthetic reagent).
18. Glass electrode: Glass 8250 with filament.
19. 10 μm pipette.
20. 10 μm pipette tips.
21. 34.5 °C incubator.
22. 17.8 °C incubator.

2.2 Electrophysiology

23. 2.3 M potassium chloride intracellular solution.
24. AxoGraph software (https://axograph.com/download).
25. Glass electrodes (1.50 OD, 0.86 ID, 100 mm length).
26. Sutter puller Model P-97.
27. Microinjector syringe.
28. Silver bare wire 0.010″ thick.
29. Electrophysiology rig (Fig. 1).

2.3 Imaging

30. MitoTracker Green FM (300 nM) ThermoFisher Scientific Cat#M7514.
31. Lysotracker Deep Red (75 nM) ThermoFisher Scientific Cat#L12492.
32. 880 confocal Zeiss inverted microscope.

3 Methods

3.1 Medium Preparation: Hemolymph and Modified L15

1. Solution preparation: Isolate and process fresh hemolymph from wild-caught *Aplysia* (*see* **Note 1**) or thaw stored aliquot to room temperature. Thaw L-glutamine, mix thoroughly until particles are fully dissolved. Keep the modified-L15 medium aliquot at room temperature.

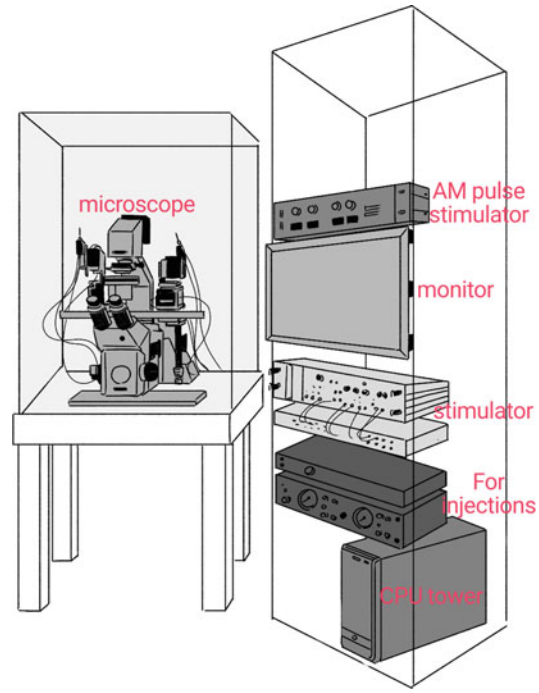

Fig. 1 Cartoon illustration of a typical electrophysiology setup for studying *Aplysia* neurons

2. 25–50% medium: One quarter to one half of the final medium should consist of hemolymph (*see* **Note 2**). Make up the rest of the medium with modified-L15 medium. Add 5 mM L-glutamate. Invert the tube to mix thoroughly.

3.2 Isolating Ganglia and Individual Neurons

1. Abdominal ganglia: Motor neurons L7 and L11 isolated from the abdominal ganglia of 1–4 g heavy animals (Fig. 2). Carefully inject 10–15 animals with 60% 0.38 M $MgCl_2$ volume/ animal body weight (g) and wait until animals are anesthetized and dissect out the abdominal ganglia. Place abdominal ganglia in modified L15.
2. Pleural ganglia: Sensory neurons are isolated from the pleural ganglia of 80–120 g heavy animals that are between 6 and 9 months old. The pleural ganglia are connected to the pedal ganglia that are connected to the cerebral ganglia, together the three pairs of ganglia make up the "CNS ring." Inject one animal with 60% 0.38 M $MgCl_2$ volume/ animal body weight (g), wait until anesthetized, and remove the CNS ring. Place ring in modified L15.
3. Protease treatment: 7.5 mg/mL Dispase II is used to digest Aplysia ganglia. To dissolve dispase II, use modified L15. Once completely dissolved, transfer ganglia into dispase. Incubate

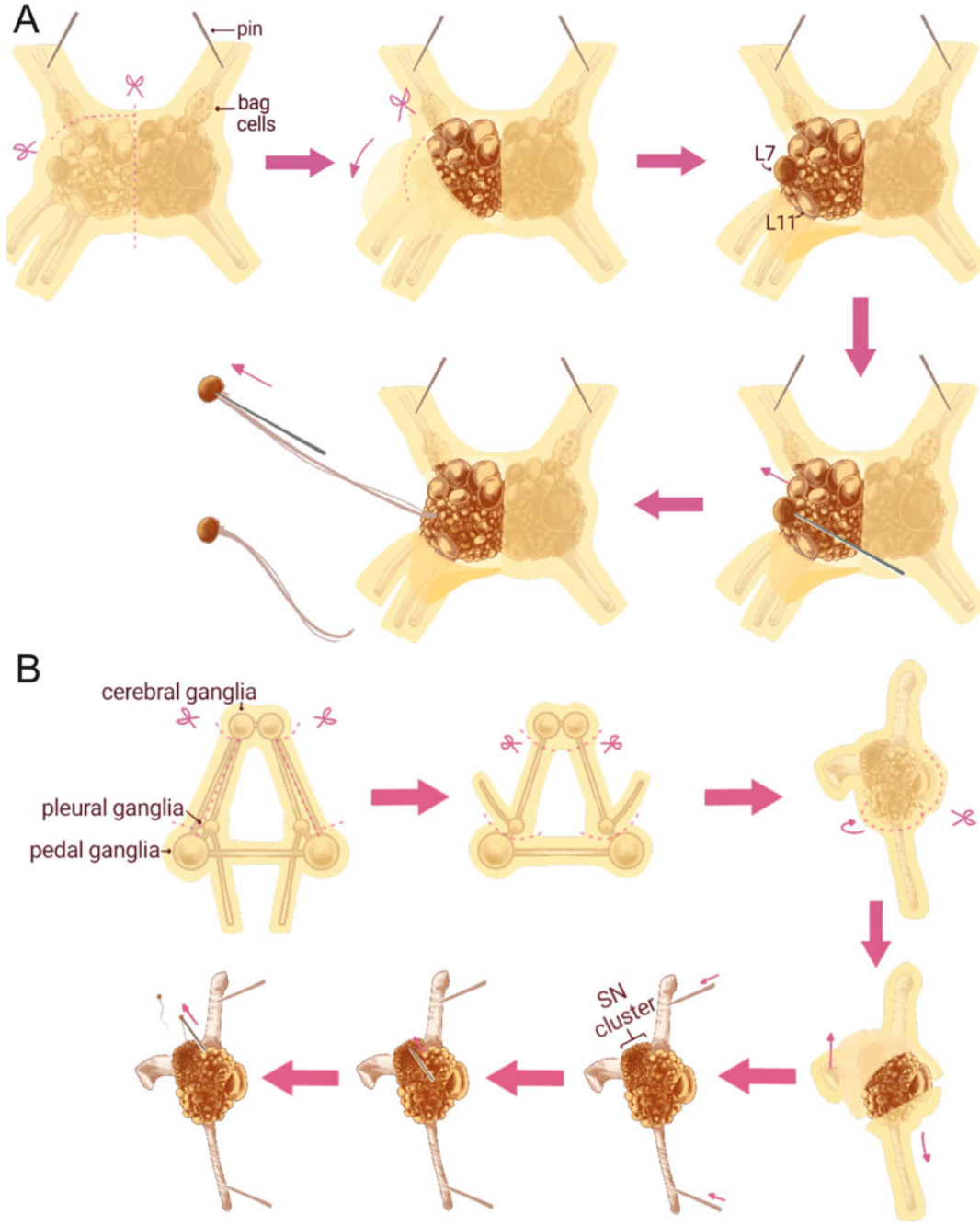

Fig. 2 Preparation of *Aplysia* sensory and motor neuron cultures. (**a**) L7 motor neuron isolation illustration. Abdominal ganglia are dissected from *Aplysia* (1–4 g) and digested in 7.5 mg/mL dispase for 1 h and 40 min. The ganglia are then washed three times with modified L15 medium. The abdominal ganglion is oriented so that the lightly pigmented neuron cell bodies are on the left and the darker-pigmented cell bodies are on the right. The ganglia are pinned down through the connective tissue above the bag cells and the sheath of tissue covering the ganglia is removed. First, an incision is made down the middle of the ganglia, cutting the connective tissue as you move down the middle of the ganglia. It is important to remove the sheath without disturbing the neurons. The remaining tissue sheath on the left side of the ganglion is removed to expose the neurons. A glass electrode is used to remove the L7MN from the ganglion by gently touching the cell body of

abdominal ganglia for 1 h 40 min at 34.5 °C. Incubate CNS ring for 2 h at 34.5 °C.

4. At least 1 h before cells are removed from the incubator, add 1.5 mL of 25–50% medium to 35 mm poly-L-lysine treated glass-bottom dish.
5. Add 25–50% medium to sylgard working dish.
6. Coat 10 μm pipette tip with 25–50% medium by pipetting up the medium and keeping it in the tip. This will prevent the cells from sticking to the tip.
7. Prepare three 35 mm dishes of modified L15 for rinsing ganglia. Once abdominal ganglia protease treatment is complete, rinse ganglia by dipping and transferring ganglion one by one in and out of three dishes of modified L15. Transfer all ganglia to the working dish.
8. Orient the ganglia so that L neurons are on the left, R neurons are on the right, and bag cells are on top. See Fig. 2a for a detailed illustration.
9. With two small forceps and ganglia still oriented, as explained in **step 7**, wrap the connective tissue around the pins. Ganglia must be stiff and easy to cut, so wrap the connective tissue tightly.
10. Using the small spring scissors, cut down the center of the ganglia, along the top and the bottom of the left ganglia, and peel the sheath away from the center to expose the neurons cell bodies. Do not cut too close to the ganglia, or you will puncture the cells. Cut away any lingering tissue from the ganglia.
11. Identify the L7 cell body [7, 21, 22]. This will be the second-largest cell body in the bottom half of the left ganglia. Use the glass electrode and aim at the base of the L7 neuron. Carefully move the electrode to the left to remove the motor neuron from the ganglia. Drag the neuron away from the ganglia to avoid degradation from residual protease on the ganglia. Repeat for remaining ganglia.

Fig. 2 (continued) the neuron and pulling the neuron away from the ganglion. L7MN has the second-largest cell body in the lower-left hemisphere of the abdominal ganglia (L11MN has the largest cell body in the lower-left hemisphere). L7MN has a relatively long axon with many branches. (**b**) Sensory neuron isolation illustration. The pleural-pedal-cerebral ganglia "CNS ring" are dissected from *Aplysia* (80–120 g), making sure to keep the integrity of the ring structure. The tissue is then digested in 7.5 mg/mL dispase for 2 h at 34.5 °C. The CNS ring is then washed three times with modified-L15 medium. The pleural ganglion is isolated from the ring by cutting the connections between the pedal and cerebral ganglia. The sheath of tissue covering the pleural ganglion is removed with forceps and fine scissors to expose the neurons. The pleural ganglion is oriented so that the sensory neuron cluster is visible. The ganglion is pinned down via the connection tissues. A glass electrode is used to remove single sensory neurons from the ganglion by gently touching the cell body of the sensory neuron and pulling the sensory neuron away from the ganglion

12. Slowly pipette up individual neurons and pipette them out into a glass-bottom dish.
13. Use a glass electrode to detangle the axon of the motor neuron. Slightly press down on along the length of the axon to help it stick to the glass bottom.
14. Wait at least 1 h before adding sensory neurons to the motor neuron.
15. Clear the dish of abdominal ganglia by removing and discarding ganglia.
16. After motor neurons have adhered to the glass bottom, start preparing sensory neurons. Wash the CNS ring in three dishes of modified L15.
17. In the last dish, remove the pleural ganglia from the ring, keeping its long connective tissues.
18. Transfer pleural ganglia to the working dish.
19. De-sheath pleural ganglia by making an incision at the top of the ganglia and pulling away the tissue. De-sheath some of the connective tissue. See Fig. 2b for a detailed illustration.
20. Pin down the ganglia by inserting the glass electrodes into the connective tissues. Ganglia must be pinned down tightly.
21. Identify sensory neurons [7, 21].
22. Use a glass electrode to pull and isolate sensory neurons.
23. Once 2–4 sensory neurons with long axons have been isolated, use the micropipette to transfer the sensory neurons to the glass-bottom dish with a single motor neuron.
24. Use the glass electrode to untangle sensory neurons.
25. Overlay the axons of the sensory neurons on the motor neuron axon.
26. Gently push the dish away and repeat for the remaining dishes of motor neurons.
27. Leave the dishes on the microscope overnight.
28. The next day, transfer the dishes to the 17.8 °C incubator.

3.3 Electrophysiology Recordings

Representative images of SN-L7MN cultures are shown in Fig. 3. Excitatory postsynaptic potentials (EPSPs) are recorded from SN-L7MN cultures between DIV4–7 to ensure the formation of synaptic connections.

1. Load an intracellular solution of 2.3 M KCl into a recording electrode that has a resistance between 7 and 11 MΩ.
2. A silver-painted electrode containing modified L15 is used as the stimulating electrode. The electrode must have a silver wire

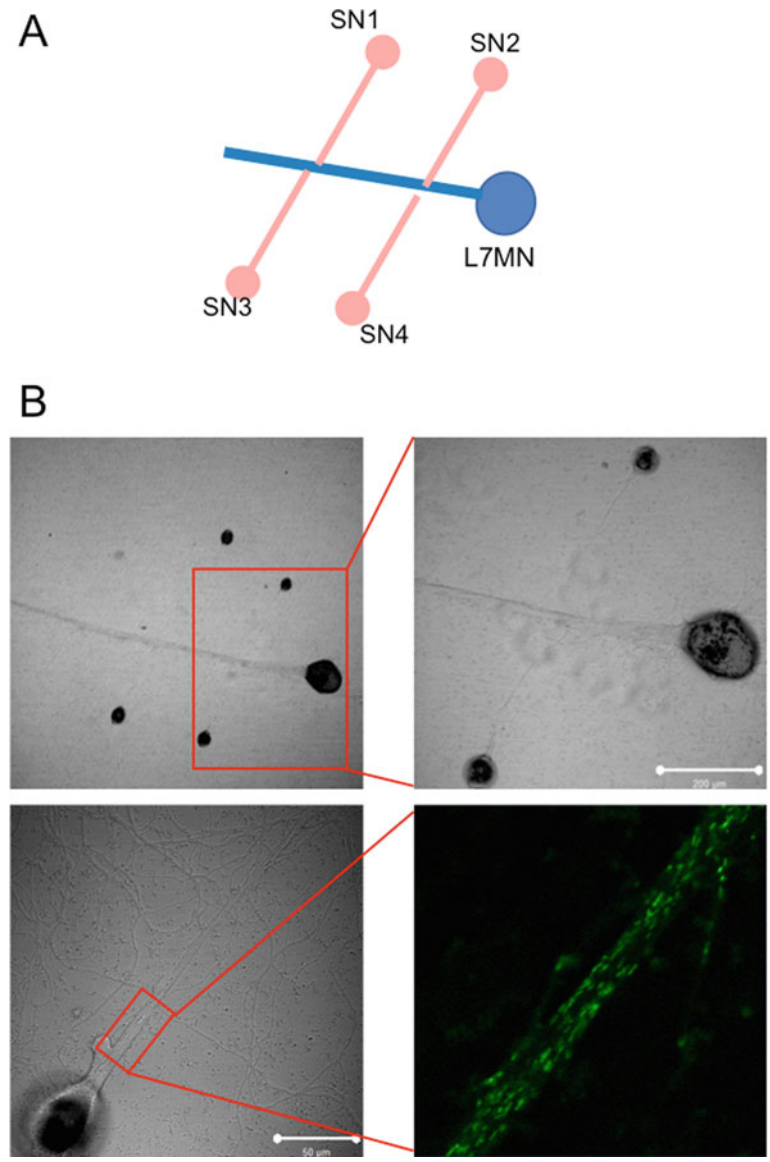

Fig. 3 *Aplysia* SN-L7MN co-cultures. (**a**) Basic schematic of SN-L7MN with sensory neurons (SN) and motor neuron (MN) identified. (**b**) Co-culture at ×10 (top left panel), ×20 (top right panel), ×63 (bottom left panel), and ×63 with 3.0 digital zoom magnification (bottom right panel). The fourth panel shows axonal mitochondria stained with MitoTracker

wrapped around the outer wall and a silver wire inserted in the electrode, touching the inner wall.

3. Using AxoGraph, run the protocol for 1 ms stimulation and 2-s recording.

4. Place the dish on the electrophysiology rig and insert the silver wire grounding electrode in the media in the dish to complete the circuit.
5. Balance the recording electrode to 0 mV.
6. Insert the recording electrode into the cell body of the motor neuron.
7. Buzz the cell with low to medium stimulation, inject negative current, and adjust the cell membrane to a voltage between −80 and −85 mV.
8. Touch the stimulating electrode to the cell body of the sensory neuron.
9. Starting with a current of 1 mA, stimulate the sensory neuron. Increase stimulation by 1 mA intervals until the motor neuron produces an EPSP. EPSPs ≥3 mV can be used for experiments.
10. Repeat for all of the sensory neurons within the dish and all remaining co-cultures.

3.4 Live-Cell Imaging of Mitochondrial and Lysosomal Axonal Transport

Mitochondrial and lysosomal transport videos are acquired using a ×63 NA 1.4 oil objective at 3.0 digital zoom. In a typical experiment, 300 images are captured at ~500 ms intervals using the highest scan speed. Mitotracker Green FM is excited using 488 nm light with the laser power set to 1.5% of power. Lysotracker Deep Red is excited using 561 nm light and a laser power of 1.2% of power (*see* **Note 3**).

1. Forty minutes before imaging, *Aplysia* neurons are incubated at 17.8 °C with 300 nM Mitotracker Green FM and/or 75 nM Lysotracker Deep Red (*see* **Note 4**).
2. Images of transport within the axons of sensory neurons are collected using the parameters noted above. Representative images of mitochondrial and lysosome imaging are shown in Figs. 3 and 4.

3.5 Quantitative Analysis of Live Imaging Data

All image processing is conducted in ImageJ or FIJI (Fiji Is Just ImageJ).

1. Movies in proprietary formats (e.g., CZI) are opened in FIJI using the Bio-Formats Importer plugin. The individual channels are separated, converted to a concatenated stack, and are then saved as a tiff. Figure 5a shows the three channels for a sample movie. To speed processing, in this and other steps, folders of movies are processed using the Process > Batch > Macro function.
2. Individual stacks are opened one at a time in ImageJ, and the movie is played back and forth to find a segment of the axon where organelles are in focus (*see* **Note 5**). An axonal segment

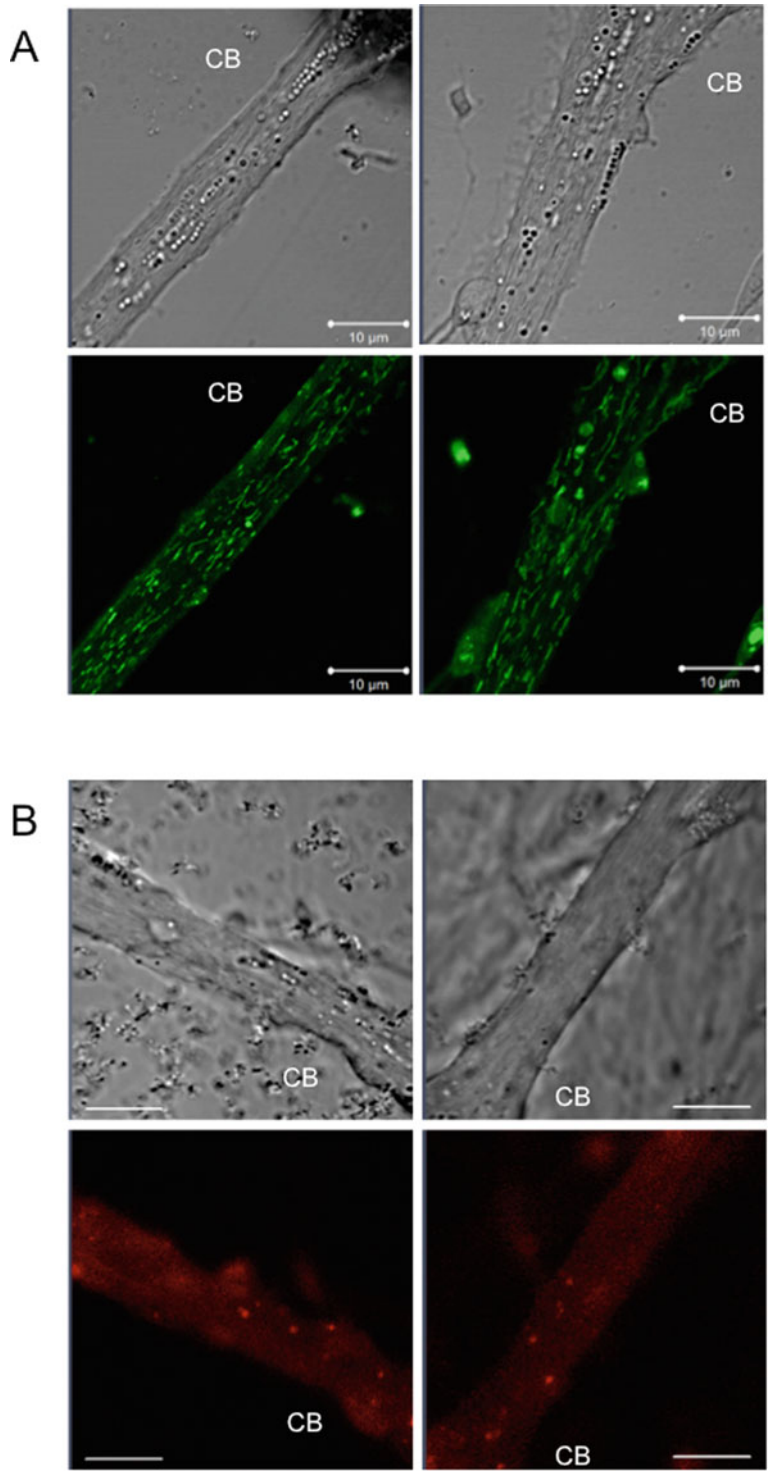

Fig. 4 Representative images of organelle transport in sensory neurons. (**a**) DIC (top row) and MitoTracker fluorescence images (bottom row) of mitochondrial transport within SNs axons at $\times 63$ with 3.0 digital zoom. CB represents the cell body of the SN to label transport orientation. (**b**) DIC (top row) and LysoTracker fluorescence images (bottom row) of lysosomal-related organelle (LROs) transport within SNs axons at $\times 63$ with 3.0 zoom. CB represents the cell body of the SN to label transport orientation. Scale bar $= 10$ μm

that is straight is selected, and the angle of the segment is measured using the Straight Line tool. The stack is then rotated such that the cell body is toward the left, and the axon runs horizontally using the Rotate function with the settings Bicubic and Enlarge. The rotated stack is then saved (*see* **Note 6**).

3. Individual rotated stacks are opened, a 300 × 200 selection rectangle is generated, placed over a region of the axon of interest, adjusted such that the Y-axis matches the width of the axon (Fig. 5b). Then the region of the axon is cropped and saved.
4. The stacks of movies that contain multiple channels are processed to split and save the individual channels. To better preserve pixel intensity data, the stacks are converted to a 32-bit format. Pixel dimension data from the metadata are overwritten in ImageJ using the Analyze > Set Scale > Click to Remove Scale function. This sets the pixel length to a value of one in both the time and space dimensions. This helps to prevent possible errors when using the measure tool in the measurement of flux and velocity from kymographs, which outputs results based on pixel dimension.
5. *Aplysia* axons are too thick to generate kymographs from which transport can be analyzed. Thus, a single axon is split into multiple kymographs (Fig. 5c, d), with a thickness of approximately 1 μm, by running a script which: converts the movies to 300 × 200 pixels; reslices the movie to generate a stack consisting of 200 kymographs; drawing a center line on the kymographs which will be used to measure flux and velocity; converting the stack from 200 kymographs to 20 kymographs by Z-projecting groups of ten slices using the Max Intensity setting; rotating the stack such that the time axis is on the x-axis; stretching the time axis by a factor of two to optimize the slope of the lines, and resetting the pixel dimension data to ensure correct measurements in the next step (*see* **Notes 7**, **8**).
6. Axonal width is measured by batch processing image stacks, which were cropped to match the width of the axon (Fig. 5b). The width of each stack is then exported to Excel for later processing.
7. To analyze kymographs, the brightness and contrast settings must be applied consistently across the data (*see* **Note 9**). As a first step, a couple of movies and kymographs are opened. The movies are played back and forth beside the kymographs, and the brightness and contrast are adjusted until settings are found that allow traces to be followed across the set of test movies. These values are then noted and applied in the next step. Viewing kymographs on a high-quality monitor is recommended to ease eye strain.

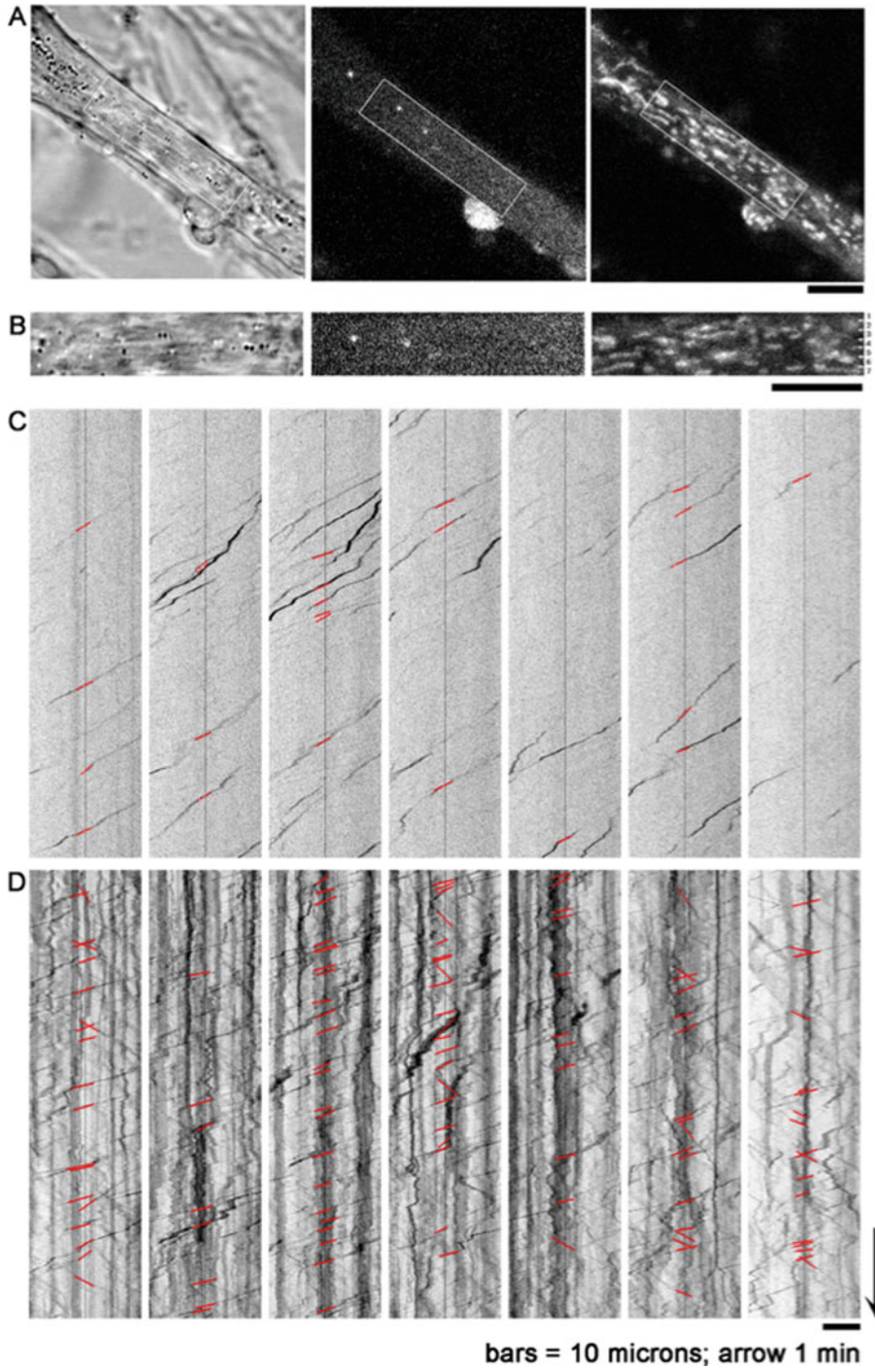

Fig. 5 Mitochondrial and LROs flux analysis. (**a**) Full DIC (left panel), LROs (middle panel), and MitoTracker (right panel) fluorescent images. The cell body is toward the upper left. (**b**) Cropped regions for flux analysis. The axon is divided into seven areas, indicated by the arrows on the right. (**c**) LROs multi-kymograph. A vertical line is drawn down the center of each kymograph. LROs that pass the centerline are marked in red. The slopes of the tracks are used to determine velocity. (**d**) The MitoTracker kymograph was marked in the same manner. All bars are 10 μm; arrow $=$ 1 min

8. To process multi-kymographs, stacks are opened, and the brightness and contrast are set. Based on the processing described above, time is on the *x*-axis, width on the *y*-axis, the cell body is toward the bottom of the screen, and there is a white line running horizontally in the middle of the axon. Organelles that move in the retrograde direction have traces that slope to the right, and those that move in the anterior direction slope to the left. A Wacom drawing tablet is used to measure traces. It is configured such that the hotkeys run the fill function (command F), the measure function (command M), the Next Slice (<), and Previous Slice (>) commands. With the Straight Line cursor selected, lines are selected over traces that pass the centerline (Fig. 5c, d). These are then filled to prevent double-counting of traces and to provide a visual record of what was measured. The line segments are then measured, and the length and slope of the line, along with the file name, and slice number are temporarily stored in a Results Table. After marking the traces in the first slice of the multi-kymograph, the stack is advanced to the next slice. Potential traces are considered, then the stack is briefly stepped back to confirm it has not been marked and then stepped forward for marking and measurement. When mistakes are made, incorrect entries are deleted in the results table. To ensure that traces are accurately reflecting the motion of organelles, the movies are opened and played back and forth beside the kymograph. After analysis, the data in the results table (for example, see Table 1) are saved and imported into an Excel file (*see* **Notes 10, 11**).
9. Post-processing and Statistical Analysis. The results data are posted into the Excel file template and sorted by file name. The pixel dimensions in terms of microns per pixel and time per pixel are entered. For each trace, the velocity and direction of transport are calculated. For each neuron, these are automatically tabulated based on the file name, to generate the raw anterograde and retrograde fluxes in units of mitochondria/min and average instantaneous velocity in units of μm/s. Because mitochondrial flux is positively correlated with the width of *Aplysia* neurons, the raw flux values are divided by the width of the axon in microns to give adjusted flux in units of mitochondria/min microns. These values are then sorted and pooled based on the experimental condition. To determine the density of mitochondria in motion, adjusted flux is divided by velocity, which generates units of mitochondria per square micron. Statistical analysis for simple conditions is conducted in Excel, for example, by Student's *t*-tests. If multiple conditions are analyzed, the data is exported to MiniTab for one-way ANOVA with the post-hoc Tukey test.

Table 1
Descriptive information for the example of mitochondrial transport

Descriptive information	
Number of movie frames	600
Time interval between frames	0.57 s
Total time of the movie	342 s; 5.7 min
Axon width	5.6 μm
Axon length observed	29.3 μm
Axon area observed	164 μm^2
Flux and velocity analysis	
Number of anterograde moving mito	20
Number of retrograde moving mito	96
Raw anterograde flux	3.5 mito/min
Raw retrograde flux	16.8 mito/min
Axon width adjusted anterograde flux	0.63 mito/μm min
Axon width adjusted retrograde flux	3.0 mito/μm min
Density of anterograde transport	0.017 mito/μm^2
Density of retrograde transport	0.042 mito/μm^2
Total density in motion	0.06 mito/μm^2
Average anterograde velocity	0.6 μm/s
Average retrograde velocity	1.2 μm/s
Density analysis	
Number of stationary mito	39
Number of moving mito	10
Total number of mito	49
Percentage in motion	20%
Density of stationary mito	0.24 mito/μm^2
Density of moving mito	0.06 mito/μm^2
Total density	0.3 mito/μm^2
Total length of stationary mito	67 μm
Total length of moving mito	6.7 μm
Percentage of mito mass in motion	9%

3.6 Measuring Mitochondrial Density

Understanding the biological mechanisms that modulate organelle transport often requires measurement of the concentration of moving, stationary, and total mitochondria. While the flux analysis described above assesses the density of moving mitochondria,

determination of the percentage of mitochondria in motion or the percentage of mitochondrial mass in motion requires additional analysis. In cases where axons are thin (i.e., approximately 1 μm in diameter) and the density of docked mitochondria is low, it is relatively straightforward to draw a line across the kymograph, count the number of docked mitochondria, and to divide by the length measured to determine the density of docked mitochondria in units of mitochondria/μm of the axon. In turn, further dividing this by the average width of the axon yields units of mito/μm^2. Nonetheless, because of the large width of *Aplysia* axons and the high density of mitochondria, a more sophisticated approach is required to address questions about mitochondrial density and motion (Fig. 6). In brief, the method we describe uses median *Z*-projection of a time-lapse series to generate an image of docked mitochondria (Fig. 6c). Image math that subtracts docked mitochondria from total mitochondria to produce an image of moving mitochondria (Fig. 6e). Then hand tracing of the length and number of docked and moving mitochondria to generate the results for statistical analysis (Fig. 6d, f). In more detail:

1. To generate an image of docked mitochondria, an 11-frame sequence from the middle of the movie (i.e., frames 295 to 305 from a 600 frame movie) is *Z*-projected using a median filter (Fig. 6c). Because the median filter sorts the intensity values of the set of pixels and returns the middle value, if a mitochondrion is stationary for less than half the number of frames, it is "removed" from the image. Because the images in the example are acquired at two frames a second, here, the algorithm "defines" a mitochondrion as being stationary if it remains in place for more than 5 s. It follows that the choice of the number of frames to median project depends on the frame rate of image acquisition (*see* **Note 12**).
2. To generate an image of total mitochondrial mass, a single frame from the middle of the movie is copied (Fig. 6a). Because this image will be used to generate an image of moving mitochondria through image subtraction of docked mitochondria, it is processed with a Gaussian blur (1.2 pixels) to remove high-frequency noise (Fig. 6b). To determine the proper setting, try different values, and then do the image calculation. Optimal values produce images where the blurred image of total mitochondrial mass looks similar to the image of docked mitochondria generated by the median *Z*-projection (Fig. 6c) (*see* **Note 13**).
3. To generate an image of moving mitochondrial mass (Fig. 6e), the image of docked mitochondrial mass (Fig. 6c) is subtracted from the image of total mitochondrial mass (Fig. 6b) using the Process > Image calculator function in ImageJ.

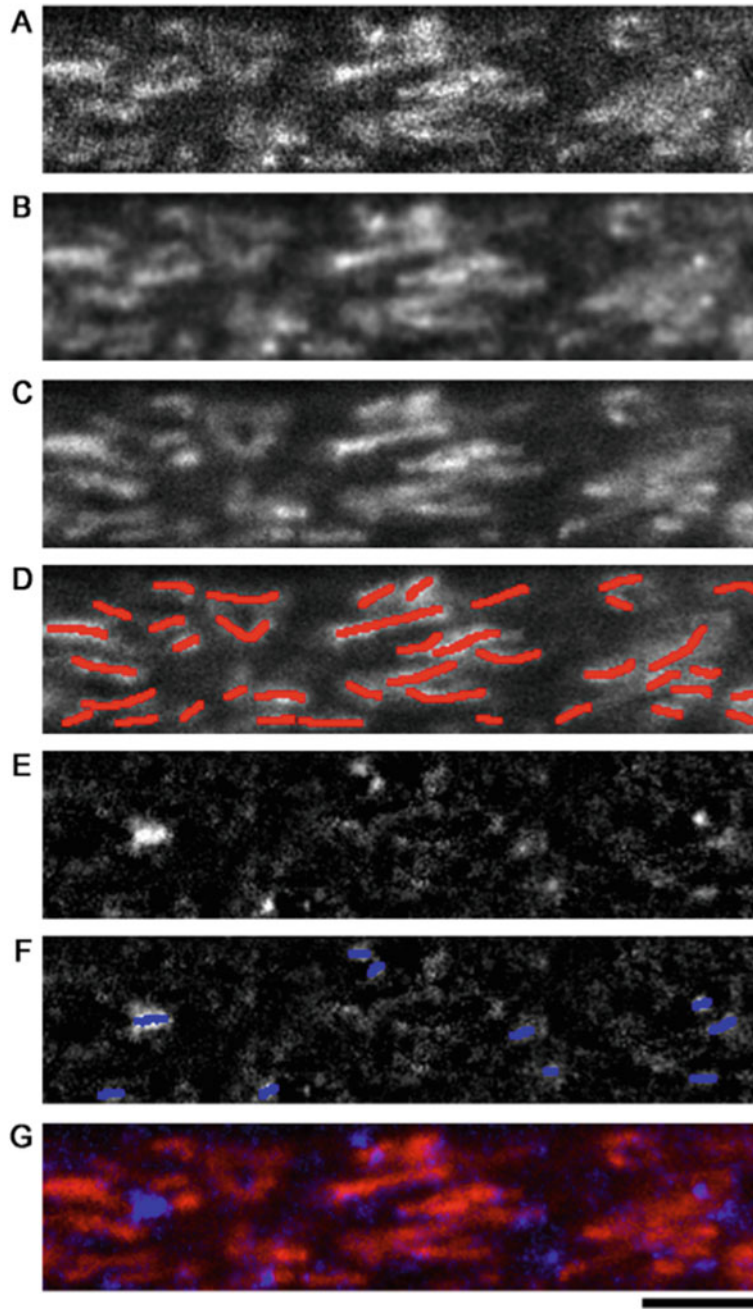

Fig. 6 Analysis of docked and stationary mitochondria. (**a**) Unprocessed image of a single frame in the middle of a movie showing the distribution of total mitochondria. (**b**) Image after Gaussian Blur. (**c**) Median Z-projection of 11 frames from transport video to show the distribution of docked mitochondria. (**d**) The same image after tracing. (**e**) An image of the moving mitochondria generated by subtracting the image of docked mitochondria from total mitochondria. (**f**) The same image after tracing. (**g**) Overlay of stationary mitochondria (red) and moving mitochondria (blue). Scale bar = 5 μm

4. To measure the length and number of docked mitochondria, the freehand line tool is selected in ImageJ and used to draw paths over the docked mitochondria (Fig. 6d). Each line is marked with the fill tool, and the length of the line is saved using the measure function to the results table. This data is then copied into Excel. To measure the length and number of moving mitochondria, this process is repeated (Fig. 6f). When marking mitochondria, playing the movie back and forth helps in verifying that moving and docked mitochondria are correctly marked.
5. For visualization, it may be helpful to display a color overlay of docked and moving mitochondria (Fig. 6g) using the Image > Color > Merge Channel tool.
6. Depending on the experiment, knowledge of either the percentage of moving mitochondria or the percentage of total mitochondrial mass in motion may be more useful. In these terms, because the length of a docked mitochondrion is typically longer than a moving mitochondrion, the percentage of mitochondria in motion tends to be higher than the mass of mitochondria in motion. To calculate the percentage of moving mitochondria in Excel, the number of moving mitochondria is divided by the sum of the docked and moving mitochondria. To calculate the percentage of mitochondrial mass in motion, the total length of moving mitochondria is divided by the sum of the total length of moving and docked mitochondria. To convert these values to the same units as in the flux analysis, divide the number of mitochondria by the area of the images analyzed. For the example shown, the percentage of mitochondria in motion is 20%, and the mass of mitochondria in motion is 9%. From the flux and density analysis, the total concentration of mitochondria in motion for this example was 0.06 mito/μm^2 in both cases. That independent means of analysis yields the same value increases confidence in the reliability of the assessment of mitochondrial transport (Table 1) (*see* **Notes 14, 15**).

4 Notes

1. It is crucial to select high-quality neurons for imaging experiments. This begins with selecting healthy animals for neuron isolations. A healthy animal should not be translucent in appearance. The gill of the animal should be a dark purple color and should not be visible once the parapodia are closed. Animals should be fed between 1 and 3 days before being used for cultures. Healthy neuronal cultures show neurite growth as early as four hours after plating. Neurons should have a

circular/oblong cell body. When making cultures, it is critical to avoid damaging the axon because it can lead to axon degradation. An intact axon can exhibit damage caused by touching the axon with the glass electrode and causing damage to the axonal integrity. This damage can be noted by excess damage around the axon that can obstruct the axonal imaging quality. Poor neuronal health will lead to low image quality and fragmented axonal mitochondria. To avoid damaging the neuron cell body and axon, use glass electrodes that have a fine, thin, flexible tip. One should be able to bend the tip of the axon along the bottom of the culturing dish without breaking or fragmenting the glass electrode.

2. Wild Aplysia californica (500–1000 g) caught off the coast of California are acquired for hemolymph isolation. After at least a 48 h acclimation period, animals are prepared for hemolymph isolation. A demonstration and description of hemolymph isolation is shown in [23]. Batch to batch hemolymph variation is a major problem for Aplysia experiments; therefore, it is essential to use optimal hemolymph. Good hemolymph, when initially extracted, is translucent and has a light purple hue. Once stored at −80 °C, it should be pink to purple. Do not use hemolymph that contains ink or is brown. Hemolymph should be centrifuged at 1000 x *g* for 10 min, so that blood cells are removed. Additionally, if precipitates or debris remain in the medium, it should be filtered using a 0.45 μm pore size, to improve imaging quality.

   To reduce the effects of hemolymph variation on experimental conditions, a few quality controls should be considered before starting experimental studies.

   Can isolated sensory neurons and motor neurons (cultured separately) thrive within the hemolymph-L15 medium? Neurons cultured in sub-optimal hemolymph start to die hours after plating with the axon shrinking into the neuronal cell body. If this occurs, a new batch of hemolymph should be prepared.

   Are the basal electrophysiological measurements stable? Healthy neurons grown in ideal hemolymph-L15 medium will give stable, similar EPSP measurements (with little variation, ~5 mV difference) when measured daily.

   Are mitochondria healthy? Mitochondria should not be fragmented; instead, they should have a long rod-like structure with roughly 20% of the total being in motion. A neuron with mostly stalled or fragmented mitochondria indicates poor neuronal health.

   Optimally, one batch of isolated hemolymph stored in 5 mL aliquots should be used for the duration of a project.

However, if it is insufficient, a different hemolymph batch may be used as long as it passes these quality control checks.

3. Microscopy troubleshooting: Balancing adequate illumination with phototoxicity is a core challenge in live imaging. If the laser power is too low, the motion of organelles will be difficult to quantify. If it is too high, cell health can decline rapidly. When beginning experiments, it may be useful to collect a series of movies where the laser power is incrementally increased. Converting these movies to kymographs then allows a determination of a power range that generates useful kymographs with a minimal negative impact on neuronal health and photobleaching. Gain is more flexible but should not be increased if the laser power is increased.
4. Staining troubleshooting: Staining issues will arise if the concentrations of MitoTracker or LysoTracker are too high. A high concentration will result in saturation, causing the dye to spread to regions beyond mitochondria or lysosomes. Incubation times for the dyes are also important. Excess dye and prolonged incubation substantially enhance the background signals. MitoTracker that has been incubated for too long compromises neuronal health and leads to mitochondrial fragmentation. Rinsing the neurons with fresh hemolymph-L15 medium after the appropriate incubation time will resolve saturation issues, allowing for longer imaging time. MitoTracker Green and LysoTracker Red will not create signaling crosstalk if applied at optimal concentrations.
5. If the signal to noise ratio is low, images can be processed with a Gaussian blur filter to suppress shot noise (typically with a setting in the 0.6–1.2-pixel range), before generating kymographs. A straightforward way to find the optimal setting is to take a single movie, apply various degrees of blur, save the movies to a folder, and then process the set of movies to make kymographs with the various settings.
6. Stage drift or other sources of motion can make it very difficult to generate kymographs. If this is a problem, the StackReg plugin is a reliable way to correct this problem. As large movies can take a relatively long time to process, running this as an overnight batch macro may be recommended.
7. When doing the Grouped *Z*-projections for the multi-kymographs, it is recommended that a range of settings are used on one or more images before processing the data. If too many slices are grouped, the signal to noise ratio falls. Likewise, transport can be obscured by stationary or other transported organelles. In turn, if the number of grouped images is too small, a single organelle will appear on multiple kymographs, which increases the risk that it will be counted twice. A starting

point is to find the average width of the organelle in pixels and then *Z*-project roughly three times the number of slices. For example, if an organelle appears to be three pixels wide, set the group number to nine or ten. In general, *Z*-projecting slices that cover roughly 1 μm of the axon is an excellent starting point for analyzing mitochondrial transport.

8. Depending on the data set, *Z*-projection using the StDev setting may give better results than using the Max Intensity setting. The Max Intensity function returns the brightest pixel for a given coordinate in the stack, whereas the StDev setting returns the standard deviation of the average pixel intensity. For data sets where the signal to noise ratio is low, the Max intensity in the shot noise can approach the intensity of the signal and thus obscure it. The StDev function, in essence, averages out the shot noise and returns a value that is proportional to the difference between the background level of intensity and the signal of labeling for the organelle. From experience, it is suggested to try both settings for a couple of movies before processing the complete data set.
9. The brightness and contrast settings one uses to analyze kymographs are critical. Optimally, the same settings should be used for all of the kymographs in a batch (i.e., the settings should be written down and applied to all kymographs). If the brightness is too low, faintly labeled objects will be missed. If the contrast is too high, spurious tracks may be made. To find the proper settings, open a movie and a kymograph simultaneously and play the movie back and forth. Make sure that what is seen in the movie as moving organelles, corresponds with what is being measured in the kymograph.
10. Kymographs provide the best estimates of velocity when the slopes of the measured lines are at approximately 45°. This arises because as the slope approaches 90°, small changes in angle equate to large differences in velocity. This is further exacerbated because measurements are made on digitized images. For example, if movies are acquired at a low acquisition rate such that organelles move a distance of 50 pixels per frame, the rise to run ratio is 1:50. As a result, an error of one pixel in the rise measurement can lead to a considerable error in the velocity measurement. Likewise, the same problem exists for slowly moving organelles. Thus, for a given data set, the time or distance axis is typically stretched such that the rise to run ratio is roughly 1:5 or approximately 10° for the fastest moving organelles.

    The best solution for generating kymographs with the optimal rise to run ratio is to ensure that the acquisition rate of the movies is high enough that the fastest moving organelles generate kymographs where the rise to run ratio is less than

5 pixels per frame. For example, if the pixel size is 0.1 μm, and organelles are moving at 1 μm/s. One image per sec yields a rise to run of 1:10. Thus it would be suggested to acquire two images per sec.

A secondary and related problem is that if the time interval between frames is too long, a trace appears as a diagonal series of dots. While these can be linked together by eye in simple movies, in cases where multiple organelles are in motion, the data can be overlooked, leading to an underestimate of velocity and flux.

11. In practice, there are limitations on the rate of image acquisition that arise from hardware constraints and phototoxicity. Two approaches to addressing these problems are to use an objective with lower magnification, but the same NA and binning. In our experience, a ×63 1.4 NA objective typically generates better kymographs than a ×100 1.4 NA objective. Presumably, this is because it both increases the micron to pixel ratio and increases the signal to noise because a higher number of photons are hitting a given pixel in the camera. The other approach is to use ×2 or ×4 binning, which increases S/N at the hardware level, increases image throughput on the camera (where the rate of data storage is limiting), reduces file size, and can permit the use of less intense illumination to generate usable data. This, of course, must be balanced by the loss of resolution.
12. The described approach assumes that the density of transported and docked mitochondria is relatively constant during the time-lapse acquisition. From personal experience, if there are no issues with phototoxicity, this generally seems to hold for mitochondria and can be verified by examination of the kymographs from a given experiment. Nonetheless, if this is a concern, multiple time points in a time-lapse sequence can be assessed and averaged.
13. There are several caveats and cautions to be considered when doing the density analysis. Perhaps the most important is that mitochondria have a diameter of approximately 200 nm, whereas the resolution of a conventional light microscope is roughly 250 nm (when using green light). Because two mitochondria that are closer than 250 nm cannot be resolved, there is a tendency to undercount the number of docked mitochondria. Likewise, when a mitochondrion is shorter than 250 nm, it will appear to be 250 nm long, which will tend to lead to an overestimation in mitochondrial length. Because of these factors, the utility of the described approach lies more in determining if there are significant differences between two experimental conditions, than providing an absolute measure of the length and number of mitochondria. If such an approach

is needed, super-resolution microscopy will provide more accurate estimates.

14. Though this approach is somewhat labor-intensive and time-consuming as images are analyzed by hand, it has the advantages of being direct, readily understandable, easy to verify by visual inspection of the processed data. As a case in point, one can simply look at the images in Fig. 6 and count the number of mitochondria by eye to confirm that roughly 20% of the mitochondria are in motion. While automated methods of analysis, such as using the difference tracker plugin in ImageJ, can rapidly process large data sets with minimal effort, this must be balanced with time it takes to determine the proper settings for the software using a "ground truth" reference. As well as the consideration that one should compare the output of the software with a manual analysis of the data as a "reality" check.
15. It is easy to make mistakes when quantitatively measuring velocity and flux, as the final measurements depend on the objective, camera, frame rate, binning, the speed the computer can store images and any processing of the kymographs. In terms of best practices, it is highly recommended that time stamps for image acquisition are examined in the metadata to verify the frame rate. A common problem is that while the microscope is set to record, for example, one image per sec, in actuality, it takes slightly longer because of time lag associated with changing filters and opening and closing shutters. Likewise, it is highly recommended that pixel size is directly measured with a micrometer for the exact settings (i.e., objective, binning, image magnifier) used to acquire the images. For example, if one acquires images using $\times 2$ binning, but uses the pixel dimensions for $\times 1$ binning in the analysis, velocities and flux will be off by a factor of two. Likewise, a simple error in the post-processing spreadsheet will lead to incorrect results. In these terms, it is highly recommended that the velocity of one or more organelles is directly measured by hand from the movie and that the velocities are directly compared with the measured velocities from a fully processed kymograph.

5 Summary and Conclusions

Using Aplysia sensory neurons as a model for live imaging of organelles, we have outlined methodologies for quantitative analysis of anterograde and retrograde transport of fluorescently tagged organelles. Because this transport is a critical point of regulation for synapse formation and maintenance, we have also described analysis methodologies to distinguish between stalled and mobile organelles and density analysis. These methodologies could be easily

adapted to similar studies in other neurons, hence will be highly useful for studying the regulation of transport to understand the health and plasticity of neurons.

Acknowledgments

We gratefully acknowledge funding support from NIH (5R01MH094607-05, 5R21MH108929-02), and NSF (Award number 1453799) to carry out this work.

References

1. Maday S, Twelvetrees AE, Moughamian AJ, Holzbaur ELF (2014) Axonal transport: cargo-specific mechanisms of motility and regulation. Neuron 84(2):292–309. Epub 2014/10/22. https://doi.org/10.1016/j.neuron.2014.10.019
2. Brown A (2013) Axonal transport. In: Pfaff DW (ed) Neuroscience in the 21st century: from basic to clinical. Springer, New York, NY, pp 255–308
3. Roppongi RT, Champagne-Jorgensen KP, Siddiqui TJ (2017) Low-density primary hippocampal neuron culture. J Vis Exp 122:55000. https://doi.org/10.3791/55000
4. Verstraelen P, Van Dyck M, Verschuuren M, Kashikar ND, Nuydens R, Timmermans J-P, De Vos WH (2018) Image-based profiling of synaptic connectivity in primary neuronal cell culture. Front Neurosci 12:389. https://doi.org/10.3389/fnins.2018.00389
5. Letellier M, Levet F, Thoumine O, Goda Y (2019) Differential role of pre- and postsynaptic neurons in the activity-dependent control of synaptic strengths across dendrites. PLoS Biol 17(6):e2006223. https://doi.org/10.1371/journal.pbio.2006223
6. Glasgow SD, McPhedrain R, Madranges JF, Kennedy TE, Ruthazer ES (2019) Approaches and limitations in the investigation of synaptic transmission and plasticity. Front Synaptic Neurosci 11:20. https://doi.org/10.3389/fnsyn.2019.00020
7. Montarolo PG, Goelet P, Castellucci VF, Morgan J, Kandel ER, Schacher S. A critical period for macromolecular synthesis in long-term heterosynaptic facilitation in Aplysia. Science 1986;234(4781):1249–54. Epub 1986/12/05. doi: https://doi.org/10.1126/science.3775383
8. Lin M-Y, Sheng Z-H (2015) Regulation of mitochondrial transport in neurons. Exp Cell Res 334(1):35–44. Epub 2015/01/19. https://doi.org/10.1016/j.yexcr.2015.01.004
9. Ferguson SM (2018) Axonal transport and maturation of lysosomes. Curr Opin Neurobiol 51:45–51. Epub 2018/03/09. https://doi.org/10.1016/j.conb.2018.02.020
10. Devine MJ, Kittler JT (2018) Mitochondria at the neuronal presynapse in health and disease. Nat Rev Neurosci 19(2):63–80. https://doi.org/10.1038/nrn.2017.170
11. Liu X-A, Rizzo V, Puthanveettil SV (2012) Pathologies of axonal transport in neurodegenerative diseases. Transl Neurosci 3(4):355–372. https://doi.org/10.2478/s13380-012-0044-7
12. Chevalier-Larsen E, Holzbaur ELF. Axonal transport and neurodegenerative disease. Biochim Biophys Acta 2006;1762(11):1094–108. doi: https://doi.org/10.1016/j.bbadis.2006.04.002
13. Errea O, Moreno B, Gonzalez-Franquesa A, Garcia-Roves PM, Villoslada P (2015) The disruption of mitochondrial axonal transport is an early event in neuroinflammation. J Neuroinflammation 12(1):152. https://doi.org/10.1186/s12974-015-0375-8
14. Baloh RH, Schmidt RE, Pestronk A, Milbrandt J (2007) Altered axonal mitochondrial transport in the pathogenesis of Charcot-Marie-tooth disease from mitofusin 2 mutations. J Neurosci 27(2):422–430. https://doi.org/10.1523/jneurosci.4798-06.2007
15. Lie PPY, Nixon RA (2019) Lysosome trafficking and signaling in health and neurodegenerative diseases. Neurobiol Dis 122:94–105. Epub 2018/05/30. https://doi.org/10.1016/j.nbd.2018.05.015
16. Guo W, Stoklund Dittlau K, Van Den Bosch L (2020) Axonal transport defects and neurodegeneration: Molecular mechanisms and therapeutic implications. Semin Cell Dev Biol 99:

133–150. https://doi.org/10.1016/j.semcdb.2019.07.010

17. Li X, Jiang L-H (2018) Multiple molecular mechanisms form a positive feedback loop driving amyloid β42 peptide-induced neurotoxicity via activation of the TRPM2 channel in hippocampal neurons. Cell Death Dis 9(2): 195. https://doi.org/10.1038/s41419-018-0270-1
18. Fricker M, Tolkovsky AM, Borutaite V, Coleman M, Brown GC (2018) Neuronal cell death. Physiol Rev 98(2):813–880. https://doi.org/10.1152/physrev.00011.2017
19. Miller KE, Sheetz MP (2004) Axonal mitochondrial transport and potential are correlated. J Cell Sci 117(13):2791. https://doi.org/10.1242/jcs.01130
20. Badal KK, Akhmedov K, Lamoureux P, Liu X-A, Reich A, Fallahi-Sichani M, Swarnkar S, Miller KE, Puthanveettil SV. Synapse formation activates a transcriptional program for persistent enhancement in the bi-directional transport of mitochondria. Cell Rep. 2019;26(3):507–17.e3. doi: https://doi.org/10.1016/j.celrep.2018.12.073
21. Zhao Y, Wang DO, Martin KC (2009) Preparation of Aplysia sensory-motor neuronal cell cultures. J Vis Exp 28:1355. https://doi.org/10.3791/1355
22. Frazier WT, Kandel ER, Kupfermann I, Waziri R, Coggeshall RE. Morphological and functional properties of identified neurons in the abdominal ganglion of *aplysia californica*. J Neurophysiol 1967;30(6):1288–351. doi: https://doi.org/10.1152/jn.1967.30.6.1288
23. Zhao Y, Wang DO, Martin KC (2009) Preparation of aplysia sensory-motor neuronal cell cultures. J Vis Exp (28):e1355. https://doi.org/10.3791/1355

Chapter 3

Live Imaging of RNA Transport and Translation in *Xenopus* Retinal Axons

Julie Qiaojin Lin and Jean-Michel Cioni

Abstract

In neurons, specific mRNAs are transported into axons, where their local translation supports essential cellular functions. Over the years, our knowledge of the molecular mechanisms underlying axonal mRNA translation has rapidly expanded. However, tools to study mRNA localization and translation in real time with high spatial precision were not available until recently. Here, we present a live imaging approach to examine axonal mRNA trafficking and translation simultaneously in *Xenopus* retinal ganglion cells (RGCs), using in vitro synthesized fluorescently labeled mRNAs coupled with a genetically encoded protein tagging system to visualize synthesizing peptides at single-molecule resolution. We further describe the process of image analysis in detail, thus providing a methodology that can be used to investigate new research questions in the field.

Key words mRNA transport, mRNA translation, Live imaging, Axon, *Xenopus*, Retinal ganglion cell

1 Introduction

Axonal mRNA translation enables precise spatiotemporal control of the proteome in this specialized compartment. This regulatory process has now been proven to be essential to support a wide variety of neuronal functions during development and at the adult stage, including fast responses to changes in the extracellular environment and tight control of neuronal homeostasis [1]. However, the molecular principles that restrict translation of specific mRNAs to selected axonal sites remain largely unknown

The past two decades have witnessed a rapid development of live imaging approaches to study local protein synthesis in neuronal compartments. Classically, fluorescence recovery after photobleaching (FRAP) on fluorescent protein reporters fused to a protein of interest (POI) was used to monitor mRNA translation activity in living cells [2]. Later, the introduction of photoconvertible fluorescent proteins, such as Kaede, Dendra2, mEos2, and

Alessio Vagnoni (ed.), *Axonal Transport: Methods and Protocols*,
Methods in Molecular Biology, vol. 2431, https://doi.org/10.1007/978-1-0716-1990-2_3,
© The Author(s) 2022

mMaple, greatly improved our toolkit of fluorescent reporters to visualize de novo protein synthesis at subcellular locations [3–5]. However, real-time visualization of translation events at single-molecule resolution has become possible only recently. For instance, visualization of single protein synthesis events in dendrites and axons have been accomplished by using the fast-folding, fast-photobleaching bright yellow fluorescent protein derivative, Venus, as a translation reporter [6–9]. Moreover, another method "SunTag" has been adapted into various cellular systems, including neurons [10–13].

The SunTag system is based on the principle of signal amplification via protein multimerization. It uses a recombinant single-chain variable fragment (scFv) antibody fused to a fluorescent protein (e.g., superfolder GFP (sfGFP)) that recognizes 24 tandem repeats of a yeast leucine zipper motif (GCN4 dimerization domain) inserted at the N-terminus of the POI [14]. When the two fusion proteins are expressed, pre-formed scFv-sfGFP will immediately bind to nascent peptides, reducing delays in signal detection associated with protein synthesis and folding and providing strong signal-to-noise ratio to identify single-molecule translation events.

In addition to requiring protein engineering, the SunTag method also requires the labeling of the mRNA encoding for the POI, to enable event identification via colocalization. Indeed, only peptides detected by scFv-sfGFP that colocalize with labeled mRNAs represent nascent peptides: when translation is completed, the mRNA and peptide signals dissociate from each other, as the fully formed protein is released from the ribosome. Notably, this technical particularity can be used to study mRNA trafficking in the same experimental setup, expanding information gained from a single experiment.

Co-labeling of mRNA and peptides poses a technical challenge in certain model systems. mRNAs encoding for the POI can be tagged by using the MS2 or PP7 system [11–13]. However, this requires the genetic engineering of the mRNA to add the stem-loop coding sequences to the construct (multiple MS2 hairpins) and the introduction of an additional construct expressing stem-loop-binding fluorophores in the cellular system (MS2 coat proteins fused to a fluorescent protein). Interestingly, previous studies in *Xenopus* retinal ganglion cells (RGCs) have shown that in vitro synthesized mRNAs can be fluorescently labeled by mixing fluorescently conjugated UTP molecules into the reaction mixture [15], and that the mRNA product is translated in neurons following injection [16]. Therefore, this model system is particularly suited for dual mRNA tracking and translation experiments using SunTag.

In this protocol, we provide a step-to-step guide to perform SunTag-based real-time single-molecule imaging in *Xenopus* RGC axons. Using *laminB2* as an example of gene of interest (GOI), we

further describe how the use of synthetic fluorescent UTP-conjugated mRNAs allows simultaneous analysis of mRNA trafficking and translation in axons.

2 Materials

2.1 Reagents

1. Experimental constructs: 5′UTR-SunTag-GOI-3′UTR and scFv-GCN4-sfGFP-GB1 cloned into the appropriate vectors (made as described in Subheading 3.1).
2. Fluorescently conjugated UTP (e.g., Cy5/Cy3-UTP, PerkinElmer).
3. In vitro transcription kit (e.g., mMessage mMachine SP6/T7/T3 Transcription Kit, Thermo Fisher Scientific).
4. Poly(A) tailing kit (e.g., Poly(A)Tailing Kit, Thermo Fisher Scientific).
5. RNA purification kit (e.g., RNeasy Mini Kit, Qiagen).
6. Sylgard 184 kit.
7. Microloader pipette tips.
8. Mineral oil.
9. Antibiotic–antimycotic (e.g., Antibiotic–antimycotic (100×), GIBCO, which contains 10,000 units/mL penicillin, 10,000 μg/mL streptomycin, and 25 μg/mL amphotericin B as fungizone).
10. Poly-L-lysine.
11. Laminin.
12. Leibovitz's L-15 Medium, preferably without phenol red (e.g., Gibco Leibovitz's L-15 Medium, no phenol red, Thermo Fisher Scientific).
13. 3-Aminobenzoic acid ethylester methanesulfonate (MS-222).
14. Microtubule-depolymerizing drugs (e.g., nocodazole, colchicine).
15. Puromycin.

2.2 Buffers

1. 10× Modified Barth's Solution (MBS): 880 mM NaCl, 10 mM KCl, 24 mM $NaHCO_3$, 100 mM HEPES, 8.2 mM $MgSO_4$, 3.3 mM $Ca(NO_3)_2$, 4.1 mM $CaCl_2$. Adjust the pH to 7.5. Sterilize and store at 4 °C for up to 3 months.
2. 0.1× MBS for raising *Xenopus* embryos: Prepare 1 L of the solution by diluting 10 mL of 10× MBS in 990 mL of water. The pH value of the concentrated buffer lowers after dilution. Add 1 M NaOH drop by drop, stirring at the same time, to adjust the pH to 7.5. Store at room temperature for up to 3 months.

3. 2% (wt/vol) L-cysteine solution for microinjection: Freshly prepare 50 mL of the solution on the day of injection by adding 1 g of L-cysteine to 1× MBS. Adjust the solution to pH 8 by adding 5 M NaOH drop by drop. Cysteine solution has to be freshly prepared, and the correct pH level is critical to effective de-jellying.
4. 4% (wt/vol) Ficoll solution for microinjection: Prepare 250 mL of the solution by mixing 10 g of Ficoll PM 400 into 250 mL of 0.1× MBS with 1% (vol/vol) antibiotic–antimycotic. Adjust the pH to 7.5 by adding 1 M NaOH. Store at 4 °C for up to 3 months.
5. 0.04% (wt/vol) MS-222 solution for electroporation: Freshly prepare 50 mL of the solution by mixing 20 mg of MS-222 in 50 mL of 1× MBS. Adjust pH to 7.5 with 1 M NaOH. Keep the solution protected from light.
6. 0.1× MBS for culture (embryo wash solution): Under sterile conditions, prepare 250 mL of the solution with 1% (vol/vol) antibiotic–antimycotic. Adjust the pH to 7.5 by adding 1 M NaOH and filter the solution with a 0.22-μm filtration system. Store at 4 °C for up to 3 months.
7. Culture medium: Under sterile conditions, prepare 250 mL of 60% (vol/vol) L-15 medium with 1% (vol/vol) antibiotic–antimycotic. Adjust the pH to 7.6–7.8 and filter the solution with a 0.22-μm filtration system. Store at 4 °C for up to 3 months.
8. 0.04% (wt/vol) MS-222 solution for culture: Under sterile conditions, prepare 50 mL of the solution by mixing 20 mg of MS-222 in 50 mL of 1× MBS with 1% (vol/vol) antibiotic–antimycotic. Adjust pH to 7.5 with 1 M NaOH. Filter the solution with a 0.22-μm filtration system. Store at 4 °C for up to 1 month.

2.3 Equipment

1. Cooling incubator (set at temperature between 16 and 20 °C).
2. Micropipette puller (e.g., PUL-1 Micropipette Puller, World Precision Instruments).
3. Borosilicate glass capillary tubing: (a) 1.0 mm outer diameter × 0.5 mm inner diameter, 100 mm length (for microinjection), (b) 1.0 mm outer diameter × 0.78 mm inner diameter, 100 mm length (for electroporation).
4. Microloader tips (e.g., Eppendorf Microloader Pipette Tips 20 μL, Thermo Fisher Scientific).
5. Setup for microinjection: Assemble the following components of the microinjector and connect to a pressure pump/inert gas supply (Fig. 1a):

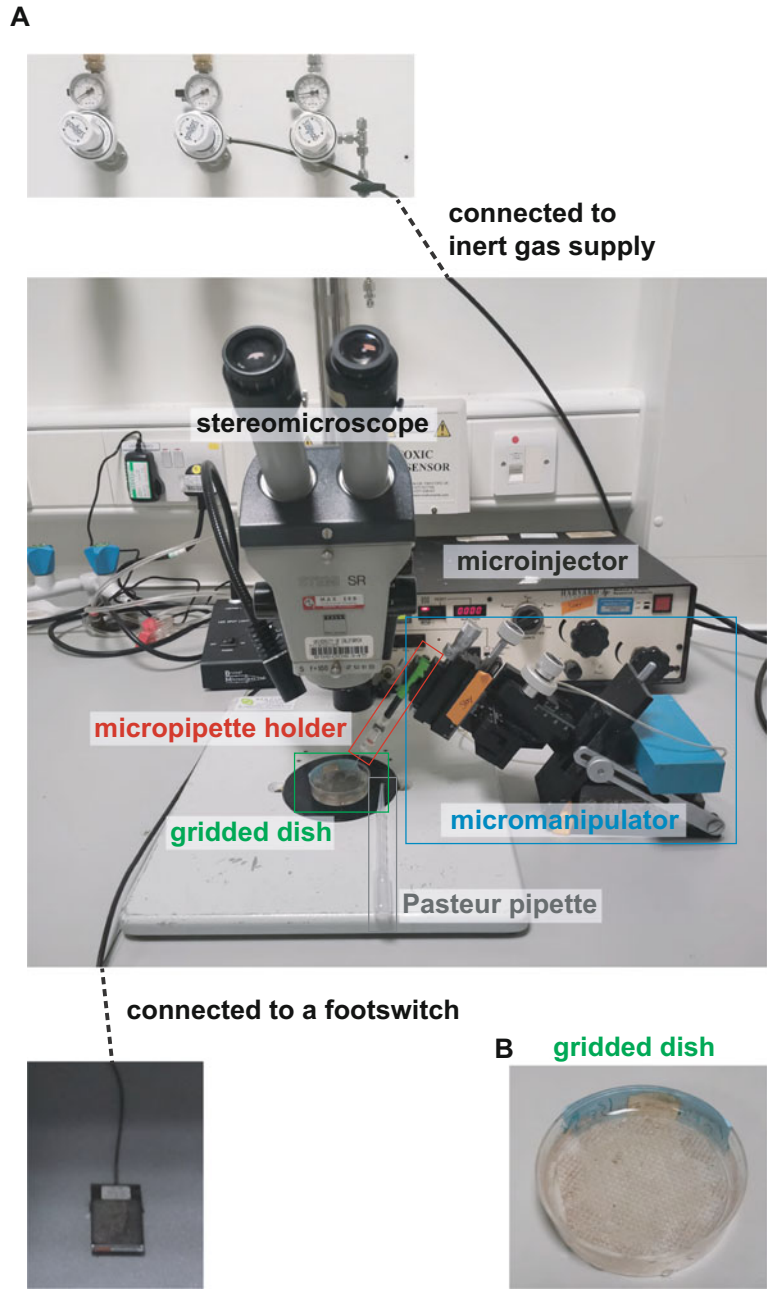

Fig. 1 *Xenopus* blastomere injection setup. (**a**) Key components and connections of the injection setup. (**b**) Gridded dish used for embryo alignment. The grid sizes are 1.5 × 1.5 mm

(a) Microinjector (e.g., PLI-100 Pico-Injector, Harvard Apparatus, or Picospritzer III, Parker) connected to a footswitch.

(b) Manual micromanipulator.

(c) Micropipette holder (e.g., Microelectrode Holder, World Precision Instruments).

6. Stereomicroscope with light source and a graticule attached to an eyepiece.
7. 50 mm Petri dishes.
8. Gridded dish for holding embryos in place for injection (Fig. 1b): Cut a circle of 56 mm diameter from Nitex mesh (1.5 × 1.5 mm) and glue it into a 60-mm Petri dish using waterproof glue. Allow it to dry before use. The gridded dishes can be cleaned with water and ethanol and reused.
9. Disposable Pasteur pipettes.
10. Fine-pointed forceps.
11. Setup for electroporation (also see ref. [17]): Assemble the following components of the microinjector and connect to a pressure pump/inert gas supply (Fig. 2a):
    (a) Microinjector.
    (b) Manual micromanipulator.
    (c) Micropipette holder for the glass micropipette (e.g., Microelectrode Holder, World Precision Instruments) connected to a footswitch.
    (d) Micropipette holder and electrode adaptor for electrodes.
    (e) Square wave pulse generator (e.g., TSS20 Programmable Square Wave Electroporator, Intracel) connected to a handswitch.
    (f) A pair of flat-ended platinum electrodes (Fig. 2b).
12. Glass rod with an angled round end (Fig. 2c).
13. Electroporation chamber: Make reusable molds with the indicated dimensions by polycarbonate 3D printing (Fig. 3). Mix the base and curing agent of the Sylgard 184 kit according to the manufacturer's manual and pour the Sylgard mixture to fill the center of the mold (do not overfill). Leave the mixture to set overnight. Fit and fix the chamber into a 35 mm Petri dish.
14. Laminar flow hood.
15. Pin holders (e.g., Nickel Plated Pin Holder, Fine Science Tools).
16. 0.1–0.2 mm dissection pins (e.g., Minutien Pins, Fine Science Tools).
17. Glass bottom dish (e.g., 35 mm Glass Bottom Dish, MatTek).
18. 35 mm Petri dishes.
19. Fluorescence dissecting stereomicroscope for examining fluorescent protein expression in embryos.

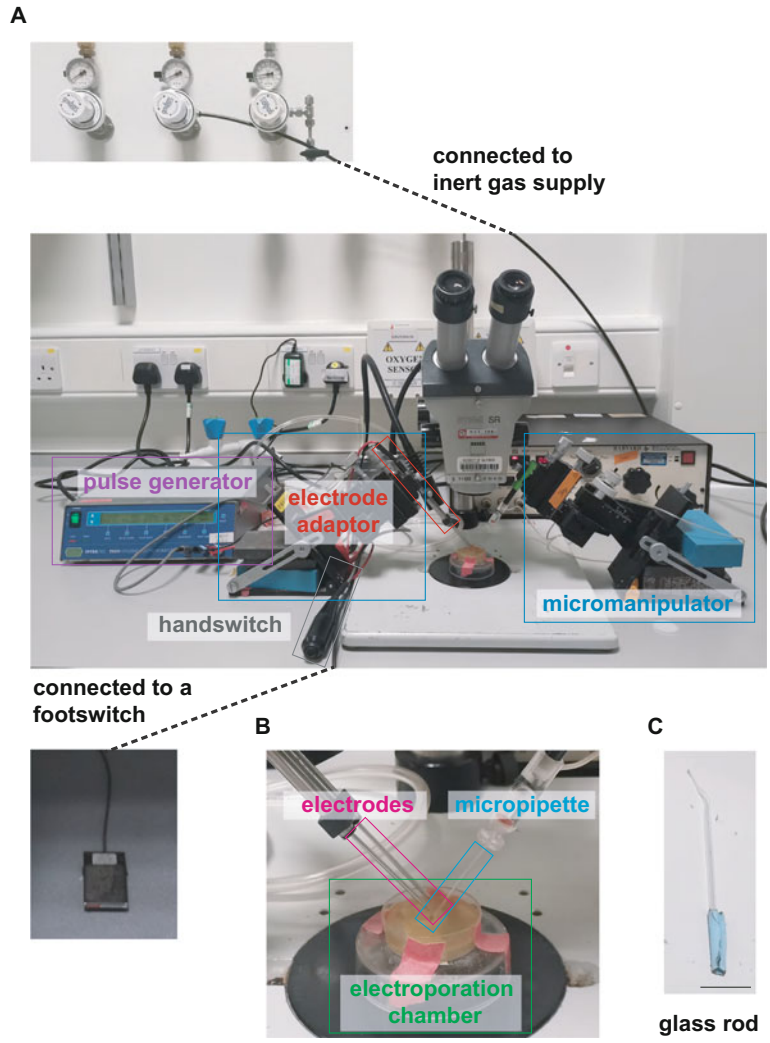

Fig. 2 *Xenopus* embryo electroporation setup. (**a**) Key components and connections of the electroporation setup. (**b**) Correct positioning of the electrodes, the glass micropipette, and the electroporation chamber. (**c**) Schematic to indicate the shape of the glass rod. Scale bar: 1 cm

20. Fluorescent inverted microscope for live imaging of RGC axons: The microscope should be equipped with ×60 or ×100 water or oil immersion objective, an automatic shutter system, fluorescent light source with excitation wavelengths at 488, 560, and 640 nm, appropriate emission filters, and a sensitive camera for low-light high-speed imaging. As two examples:
    (a) Spinning disk or high-speed laser scanning confocal microscope with standard Argon and Helium–Neon lasers for excitation connected to an inverted microscope with

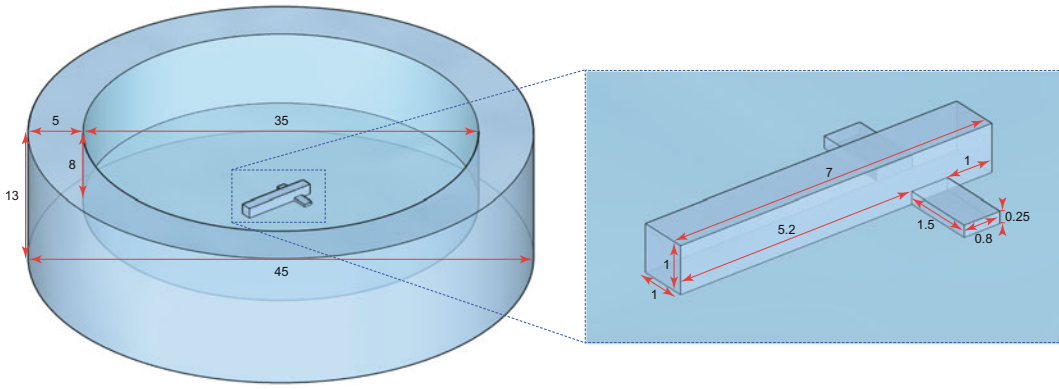

Fig. 3 Design and dimensions of a 3D-printed reusable mold to cast electroporation chambers for stage 26–30 *Xenopus* embryo eye-targeted electroporation. Numbers are indicated in mm

the appropriate camera and objective (×60 or ×100 1.4NA oil or silicon).

(b) Inverted fluorescent microscope with a LED illumination system.

2.4 Xenopus laevis Embryos

Xenopus laevis eggs were fertilized in vitro and embryos were raised in 0.1× MBS at 16–20 °C, and staged according to the tables of Nieuwkoop and Faber [18] (*see* **Note 1**).

3 Methods

3.1 Plasmid Construction

1. 5′UTR-SunTag-GOI-3′UTR (e.g., pCS2+-5′UTR-SunTag-*lmnb2*-3′UTR). With high-fidelity Gibson Assembly (e.g., NEBuilder HiFi DNA Assembly Cloning Kit, NEB), assemble the following fragments (a–c) into the multiple cloning site (MCS) of the mammalian expression vector pCS2+ (*see* **Note 2**) linearized by restriction enzymes (BamHI and XhoI) in the indicated order (Fig. 4a):

   (a) The 5′ untranslated region (UTR) of *Xenopus laminb2* (*lmnb2*).

   (b) The SunTag sequence (24 GCN4 peptide tandem repeats).

   (c) The coding sequence (CDS) and 3' UTR of *Xenopus lmnb2*.

   Fragments (a) and (c) as part of the gene of interest (GOI) can be obtained by PCR from a cDNA library synthesized from *Xenopus laevis* embryo RNA extracts using a commercially available cDNA synthesis kit (e.g., SuperScript IV First-Strand Synthesis System, Thermo Fisher Scientific) (*see* **Note 3**).

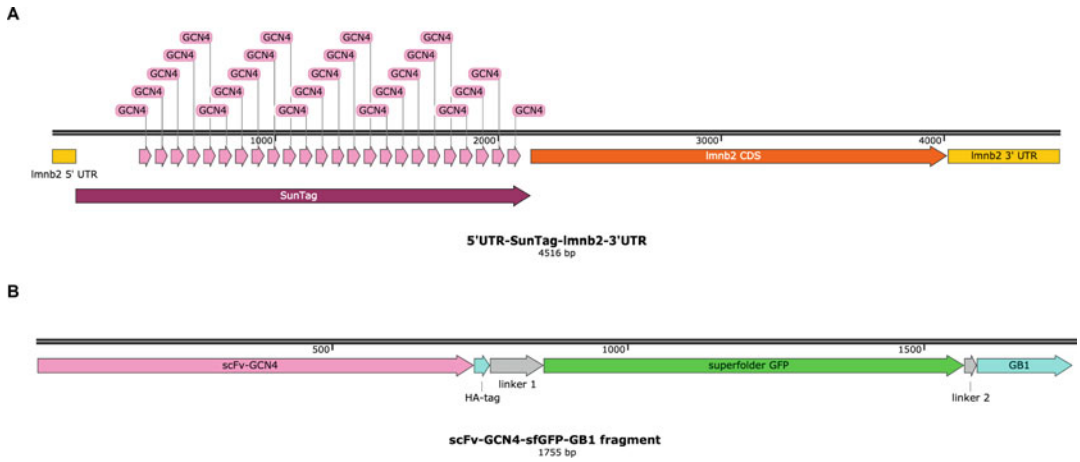

Fig. 4 Maps for constructs used in this protocol. (**a**) The insert region of the pCS2+-5′UTR-SunTag-*lmnb2*-3′UTR plasmid, containing the 5′ UTR of Xenopus *laminb2* (*lmnb2*), a SunTag sequence (24 GCN4 peptide tandem repeats) and a coding sequence and a 3′ UTR of *lmnb2*. (**b**) The insert region of the pCS2+-scFv-GCN4-sfGFP-GB1 plasmid, containing a scFv-GCN4 sequence to encode a GCN4-recognizing single-chain variable fragment, and a superfolder GFP

Fragment (b) can be obtained from the pcDNA4TO-24xGCN4_v4-kif18b-24xPP7 plasmid (#74928, Addgene) by PCR, using this primer pair:

Forward primer:

5′-(sequence of the 20–30 bp at the 3′ end of the GOI 5′UTR) TCTGGAGGAGAAGAACTTTTGAGC -3′.

Reverse primer:

5′-(reverse complement sequence of the 20–30 bp at the 5′ end of the GOI CDS) AGAACCCTTTTTAAGTCGGGCTAC -3′.

2. pCS2+-scFv-GCN4-sfGFP-GB1

scFv-GCN4-sfGFP-GB1 fragment (Fig. 4b) is amplified from pHR-scFv-GCN4-sfGFP-GB1-dWPRE (#60907, Addgene) by PCR, using the following primer pair:

Forward primer:

5′-(sequence of the 20–30 bp on the linearized plasmid immediately upstream of the first cutting site) CGCGTGCCAC CATGGGCCCCGACAT-3′.

Reverse primer:

5′-(reverse complement sequence of the 20–30 bp on the linearized plasmid immediately downstream of the second cutting site) ACTAGTTTATTCGGTTACCGTGAAG-3′.

The fragment is then cloned into pCS2+ vector linearized by BamHI and EcoRI by Gibson Assembly to

Table 1
Primers for cloning pCS2+-5′UTR-SunTag-*lmnb2*-3′UTR and pCS2+-scFv-GCN4-sfGFP-GB1 plasmids

Plasmid	Amplified fragment	Forward (F)/ reverse (R)	Primer sequences (5′ to 3′) (sequences complementary to the template)
pCS2+-5′UTR-SunTag-*lmnb2*-3′UTR	*lmnb2* 5′UTR	F	GCTACTTGTTCTTTTTGCAGGATCC GAGTCCCGCCATTGAATGAAGGGAC
		R	CCCACCGTACACGCCTACCGCCCAT ATTCCGGTAAAATATTCCCGCCAAAC
	SunTag	F	GTTTGGCGGGAATATTTTACCGGAAT ATGGGCGGTAGGCGTGTACGGTGGG
		R	GACCGACTTGGTGTAGCAGTAGCCAT TTTGAATTCTGACCGGTGCGGCCGC
	lmnb2 CDS +3′UTR	F	GCGGCCGCACCGGTCAGAATTCAAA ATGGCTACTGCTACACCAAGTCGGTC
		R	GGGCTGCAGAATCTAGAGGCTCGAG TAATTTGATGTGTGAAAAACTTCAG
pCS2+-scFv-GCN4-sfGFP-GB1	scFv-GCN4-sfGFP-GB1	F	TTCTTTTTGCAGGATCCCATCGATT CGCGTGCCACCATGGGCCCCGACAT
		R	CTAGAGGCTCGAGAGGCCTTGAATT ACTAGTTTATTCGGTTACCGTGAAG

generate the plasmid pCS2+-scFv-GCN4-sfGFP-GB1 that can be used for in vitro mRNA synthesis (*see* **Note 4**).

3. Primers for cloning pCS2+-5′UTR-SunTag-*lmnb2*-3′UTR and pCS2+-scFv-GCN4-sfGFP-GB1 plasmids (Table 1).

3.2 In Vitro mRNA Synthesis

1. In vitro transcribe capped mRNAs of 5′UTR-SunTag-GOI-3′UTR (e.g., 5′UTR-SunTag-*lmnb2*-3′UTR) and scFv-GCN4-sfGFP-GB1 using mMessage mMachine SP6 (or T7/T3 depending on the RNA polymerase promoter in the plasmid) Transcription Kit. For fluorescently labeled 5′UTR-SunTag-GOI-3′UTR mRNA synthesis, 1 μL of fluorophore-conjugated UTP (e.g., Cy5-UTP) should be added to the reaction mixture. The reaction should be finished with 15-min DNase treatment to remove template plasmids.
2. Polyadenylate DNase-treated reactions using a Poly(A) Tailing Kit to increase the mRNA stability. The size of the mRNA before and after polyadenylation should be checked on an RNase-free agarose gel to ensure the mRNA is not degraded (*see* **Note 5**).
3. Clean up mRNA using an RNA purification kit.
4. Measure RNA concentration with NanoDrop.

3.3 Blastomere Injection

1. Freshly prepare 2% L-cysteine solution on the day of injection.
2. Fill gridded dishes with room-temperature 4% Ficoll solution.

3. Prepare and calibrate glass capillary micropipettes before injection.
   (a) Two micropipettes with long sharp tips are pulled from a borosilicate glass capillary (1.0 mm outer diameter × 0.5 mm inner diameter, 100 mm length) using a micropipette puller by following the manufacturer's instructions to adjust the settings. The optimal shape of the micropipette is a 10–15 mm taper length and a < 5 μm tip diameter.
   (b) Use a microloader pipette tip to fill the micropipette with 3–5 μL of injection solution containing 100–300 ng/μL of pCS2+-scFv-GCN4-sfGFP-GB1 in vitro synthesized mRNA (*see* **Note 6**). Avoid introducing air bubbles by inserting the tip to the end of the micropipette and releasing the solution slowly.
   (c) Mount the micropipette onto the micropipette holder.
   (d) Use a pair of fine forceps to break the tip of the micropipette (break off around 200 μm). Check the solution forms a drop upon triggering of the pressure pulse using the connected footswitch.
   (e) Prepare a dish of mineral oil. Lower the micropipette using the manual micromanipulator until the tip is immersed in mineral oil.
   (f) Under mineral oil, adjust the drop volume to 5 nL (diameter of the spherical drop = 212 μm) with an eyepiece graticule by adjusting the duration of the pressure pulse. If the drop is too small, it is recommended to break the tip further to avoid later clogging of the micropipette.
4. De-jelly stage 3 (4-cell) embryos with 2% L-cysteine solution (3–5 min at room temperature with constant swirling). Embryos should reach stage 3 approximately 90 min post-fertilization at room temperature.
5. Wash de-jellied embryos three times with 0.1× MBS in 50 mm dishes or a 250 mL beaker to remove residual L-cysteine.
6. Align embryos in rows and columns in a gridded dish in 4% Ficoll solution, with animal poles facing up and dorsal blastomeres (lighter and often smaller two cells) on the right.
7. Inject 5 nL of the injection solution into each of the two dorsal blastomeres (*see* **Note 7**).
8. 1 h after injection, embryos are washed three times with 0.1× MBS and placed in 35–100 mm Petri dishes with 0.1× MBS, in an incubator set at a temperature of 16–20 °C.

3.4 Targeted Eye Electroporation

1. Wait for injected embryos to reach stage 26–30 (*see* **Notes 8** and **9**).
2. Prepare and calibrate glass capillary micropipettes before electroporation.
   (a) Pull two micropipettes with long sharp tips from a borosilicate glass capillary (1.0 mm outer diameter × 0.78 mm inner diameter, 100 mm length) using a micropipette puller by following the manufacturer's instructions to adjust the settings. The optimal shape of the micropipette is a 10–15 mm taper length and a < 5 μm tip diameter.
   (b) Use a microloader pipette tip to fill the micropipette with 5 μL of Cy5-conjugated in vitro-transcribed 5′UTR-Sun-Tag-GOI-3′UTR mRNA, diluted to 800–2000 ng/μL (*see* **Note 10**). Avoid introducing air bubbles.
   (c) Mount the micropipette onto the micropipette holder.
   (d) Use a pair of fine forceps to break the tip of the micropipette (break off around 200 μm). Check the solution forms a drop upon triggering the pressure pulse using the connected footswitch.
   (e) Prepare a dish of mineral oil. Lower the micropipette using the manual micromanipulator until the tip is immersed in mineral oil.
   (f) Under mineral oil, adjust the drop volume to 5 nL (diameter of the spherical drop = 212 μm) with an eyepiece graticule by adjusting the duration of the pressure pulse. If the drop is too small, it is recommended to break the tip further to avoid later clogging of the micropipette.
3. Mount the electrodes into the electrode adaptor.
4. Set the pulse generator with the following parameters: voltage = 18 V; pulse number = 8; duration = 50 ms; intervals = 1 s.
5. Freshly prepare 0.04% (wt/vol) MS-222 solution before electroporation.
6. Select stage 26–30 embryos with positive GFP fluorescence in the retinal primordium using a fluorescence dissecting stereomicroscope.
7. Remove embryos' jelly coats using forceps in 0.1× MBS.
8. Anesthetize de-jellied embryos in MS-222 solution (*see* **Note 11**).
9. Add 0.5 mL of MS-222 solution to the center of the electroporation chamber to completely cover the central "†" compartment. Remove any air bubbles in the "†" compartment with a glass rod.

10. Transfer an anesthetized embryo to the "†" compartment. Avoid exposing the embryo to air and air-liquid interfaces during this process.
11. Reposition the embryo using the glass rod so that it sits in the longer channel of the "†" compartment with the dorsal side facing up and the retinal primordia positioned within the shorter channel.
12. Remove excess MS-222 solution in the electroporation chamber while ensuring that the embryo is not exposed to air.
13. Insert the glass micropipette into the retinal primordium closer to the positive electrode.
14. Deliver 8 injection pulses using the connected footswitch.
15. Withdraw the glass micropipette at once.
16. Deliver the electric pulses immediately after the last injection pulse by pressing the handswitch.
17. When the electric pulses are completed, gently transfer the embryo into a Petri dish containing 0.1× MBS.
18. Before electroporating the next embryo, check the micropipette is not clogged by delivering a pulse in air.
19. Once the desired number of embryos have been electroporated, keep them in a 14–20 °C incubator and protect them from light.

3.5 Xenopus Retinal Culture

1. Wait for injected and electroporated embryos to reach stage 34.
2. Coat glass bottom dishes with 10 μg/mL poly-L-lysine and incubate for 4 h to overnight at room temperature.
3. Remove poly-L-lysine from the dishes, then rinse three times with sterile water and leave in the hood until dry.
4. Coat the dried dishes with 10 μg/mL laminin in L-15 medium for 1–3 h at room temperature.
5. During laminin incubation, wash embryos three times by transferring them sequentially between three dishes containing embryo wash solution, using a sterile Pasteur pipette.
6. Anesthetize washed embryos in a dish containing an equal volume of culture medium and 0.04% (wt/vol) MS-222 solution for culture.
7. Transfer the embryos to a Sylgard dish containing the solution used in the previous step.
8. Dissect out the electroporated eye primordia using two 0.1–0.2 mm minutien pins attached to pin holders.
9. Carefully transfer the dissected eyes to three 35 mm Petri dishes containing culture medium sequentially using a P200

pipette, to wash away any residual skin tissue attached to the eyes.

10. Remove the laminin-coating solution in the glass bottom dishes and wash once with culture medium. Immediately add 400–500 μL culture medium to the center of each dish. Avoid drying during this process.
11. Plate the washed eyes onto the glass bottom dishes and incubate in a 20 °C incubator. Protect the culture from light.

3.6 Imaging Protocol

1. After 24 h, set up a fluorescence microscope (*see* **Note 12**) for imaging live RGC axons at room temperature:
   (a) Use an objective with high magnification (×60–×100).
   (b) By imaging a few axons in a "test" dish, adjust the illumination intensity of lasers or lamp/LED light sources at the corresponding excitation wavelengths (Cy3 at 560 nm or Cy5 at 640 nm, and sfGFP at 488 nm) to avoid bleaching of the signal over the acquisition period.
   (c) Adjust the exposure time to ensure sufficiently high signal-to-noise ratios for fluorescent puncta without introducing a significant time delay between channels when acquiring images at different excitation wavelengths sequentially.
2. Acquire a 1–2 min continuous time-lapse movie for each axon segment using the same acquisition settings.
3. When performing this protocol for the first time, it is recommended that the following control conditions are included in addition to the experimental treatments:
   (a) Pre-incubate the culture with microtubule-depolymerizing drugs. The percentage of stationary/oscillatory Cy3/5-RNA granules in axons is expected to be higher compared to the untreated condition, as microtubule-based directed transport of RNA granules is disrupted.
   (b) Pre-incubate the culture with the protein synthesis inhibitor puromycin (100 μM) to verify that the SunTag signal represents the genuine population of synthesizing peptides. The number of sfGFP-positive puncta colocalized with Cy3/5-RNA granules should decrease upon the protein synthesis inhibitor treatment (*see* **Note 13**).

3.7 Quantifying RNA Granule Movement, mRNA Localization, and the Local Synthesis Rate of POI in Axons

1. Generate kymographs from time-lapse image stacks.
   (a) Open the ImageJ/FIJI program and import an image stack as a hyperstack (channels and time) using the "Bio-Formats Importer" plugin (*see* **Note 14**) (Fig. 5a).

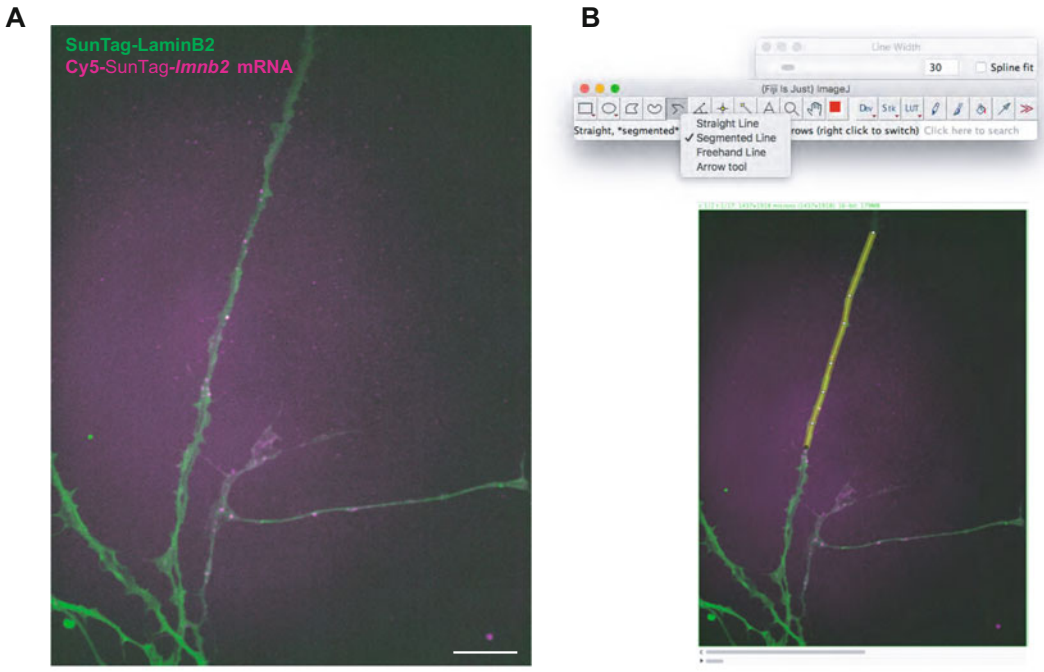

E

track number	KymoButler Direction	pixelsize time= 0.6 sec Av frame2frame velocity [um/sec]	pixelsize space= 0.0957 um track duration [sec]	minimum frames= 3 track total displacement [um]	minimum obj size= 3 Start2end velocity [um/sec]	threshold= 0.15
1	-1	0.0553	30	1.6269	0.0542	
2	1	0.1196	3	0.2871	0.0957	
3	0	0	29.4	0	0	
4	1	1.1656	8.4	9.0915	1.0823	
5	-1	0.3828	6.6	2.2968	0.348	
6	1	0.1385	23.4	3.1581	0.135	
7	0	0	12	0	0	
8	1	0.1387	28.2	3.828	0.1357	
9	0	0	5.4	0	0	
10	1	0.1861	11.4	2.0097	0.1763	
11	-1	0.1196	5.4	0.5742	0.1063	
12	0	0	2.4	0	0	
13	-1	0.0456	25.8	1.1484	0.0445	
14	-1	0.3722	4.2	1.3398	0.319	
15	1	0.5981	3	1.4355	0.4785	

Fig. 5 Analysis of axonal mRNA trafficking using Kymobutler. (**a**) The first frame of a representative time-lapse movie imaging scFv-GCN4-sfGFP-labeled SunTag-LaminB2 puncta and Cy5-conjugated SunTag-*Imnb2* mRNA. Scale bar: 10 μm. (**b**) Example of how to generate a kymograph using the segmented line tool in ImageJ/FIJI for subsequent Cy5-RNA movement analysis. (**c**) Example of a kymograph of Cy5-SunTag-*Imnb2* mRNA granules generated by the ImageJ/FIJI "KymographBuilder" plugin from the axon segment indicated by a yellow segmented line in (B) over a 1-min movie. Vertical lines as a result of camera "hot pixels" are indicated by red arrowheads. (**d**) A resulted kymograph generated by Kymobutler with identified tracks and the track numbers labeled in color. (**e**) An example table listing movement parameters (direction, velocity, duration, displacement) associated with individual tracks indicated in (**d**). The three tracks colored in red (#3, #7, and #12) do not pass the post-analysis manual tracking, as they are artifacts due to camera hot pixels, and therefore should be excluded from further analysis

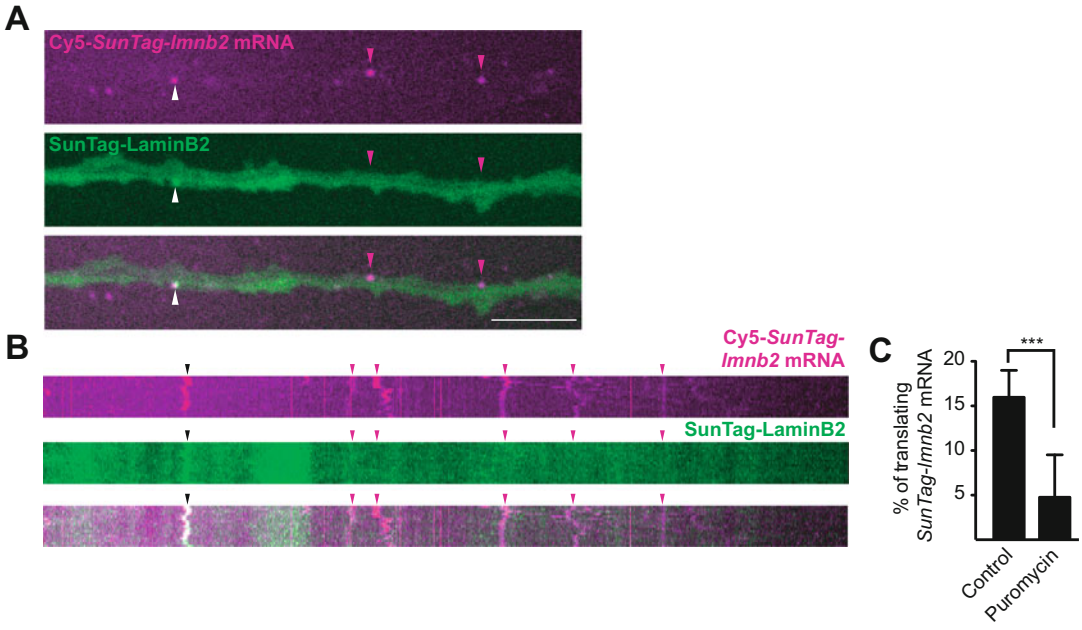

Fig. 6 Visualization of synthesizing SunTag-LaminB2 peptides in axons. (**a**) An axon segment containing three Cy5-SunTag-*Imnb2* granules (white and magenta arrowheads in the middle image). One of them is actively translated in this snapshot (white arrowhead) and the other two are not seen to be translated (magenta arrowheads). Scale bar: 5 μm. (**b**) Kymographs showing the SunTag-LaminB2 protein and Cy5-SunTag-*Imnb2* mRNA granules present in the axon segment shown in Fig. 5b over a 1-min movie. The track of the GFP-positive SunTag-LaminB2 granule colocalizes with that of the Cy5-SunTag-*Imnb2* granule (black arrowhead), revealing there is a synthesizing peptide present in this axon. The other Cy5-SunTag-*Imnb2* mRNAs are not translationally active (magenta arrowheads). (**c**) Quantification of LaminB2 synthesis rate in the untreated axons and axons pre-incubated with protein synthesis inhibitor puromycin at the concentration of 100 μM ($n = 39$ control and 21 puromycin-treated axons).

(b) Use the "segmented line" tool to trace a segment of the axon, following a proximal (start) to distal (end) orientation (Fig. 5b).

(c) Adjust the line width of the segmented line by double clicking the "line" tab to cover the width of the axon (Fig. 5b).

(d) Generate kymographs for all channels using the KymographBuilder plugin (Plugins > Kymograph > KymographBuilder).

(e) Split channels and save each channel separately (Figs. 5c and 6c).

2. Retrieve information of granule movements using the automated kymograph analysis program "Kymobutler" [19].

(a) Open the cloud-based interface of the program (http://kymobutler.deepmirror.ai).

(b) Following the instructions, upload the saved kymograph images one at a time.

(c) After uploading, the preliminary results will be displayed—successfully identified tracks are labeled in color (Fig. 5d). Adjust the parameters, accordingly, including detection sensitivity (threshold for track detection), granule size (minimum size of detected objects), and track duration (minimum number of consecutive frames per track).

(d) Set the pixel sizes correctly in distance (μm) and time (seconds).

(e) After submission, download the "Results.zip" folder for the kymograph.

(f) Unzip the folder, which contains a table summarizing key parameters related to the granule movement (overall moving direction, frame-to-frame velocity, track duration, total displacement along the axon, and start-to-end velocity) extracted from the kymograph (Fig. 5e) and a table listing coordinates of all identified tracks. The track numbers can be correlated to the tracks labeled in color and marked with numbers in the "overlaylabeled" image file for post-analysis checking.

(g) In some kymographs, hot pixels caused by long exposures during acquisition may lead to bright vertical straight lines (Fig. 5c, lines indicated by red arrowheads), which may be mistaken as a stationary track by the program. Removing such tracks by post-analysis manual checking is required to improve the accuracy of the motion type analysis.

(h) Extract information relevant to the study from the summary table.

3. To investigate whether a specific treatment alters the localization of the fluorescently labeled mRNA, the granule density of a kymograph is computed by dividing the number of identified tracks (after removing tracks generated by hot pixels) by the length of the axon (width of the kymograph in μm). Averaging the granule density of axons in each treatment group allows comparison between experimental conditions.

4. The local synthesis rate of the POI is determined by the percentage of Cy5-RNA granules that are GFP-positive, representing synthesizing peptides on ribosome-associated RNA granules (Fig. 6a–c). Averaging measurements obtained from multiple axons in each treatment group allows comparison between experimental conditions (Fig. 6d shows the quantification of LaminB2 synthesis rate in the untreated and puromycin-treated axons) (*see* **Note 15**).

4 Notes

1. The local government regulations regarding experimental animal usage should be carefully observed. All animal experiments reported in this chapter were approved by the University of Cambridge Ethical Review Committee in compliance with the University of Cambridge Animal Welfare Policy. This research has been regulated under the Animals (Scientific Procedures) Act 1986 Amendment Regulations 2012, following ethical review by the University of Cambridge Animal Welfare and Ethical Review Body (AWERB).
2. The cloning procedure can be tailored to investigate the translation of other genes of interest (GOI). As a requirement of the subsequent in vitro transcription, when choosing the cloning vector, it is essential that the vector contains a promoter for a bacteriophage DNA-dependent RNA polymerase (a SP6, T7 or T3 promoter), located adjacent to the 5′ end of the 5′UTR of the GOI. For instance, pCS2+ vector contains an SP6 promoter upstream of the MCS. However, a mammalian expression promoter, such as a CMV promoter, is not required.
3. An alternative to amplifying the GOI from the cDNA library is to obtain the corresponding fragments from an IMAGE cDNA clone if available.
4. The scFv-GCN4-sfGFP-GB1 construct can be introduced into cells either in its mRNA or DNA form. The percentage of RGC axons expressing the construct can reach 90% by mRNA injection, while this percentage is 30–60% when DNA is injected. If using DNA, it is important that the cloning vector contains an appropriate expression promotor, such as CMV, and a SV40 polyadenylation site appended to the scFv-GCN4-sfGFP-GB1. The sequence of a signal peptide targeting the fusion protein to specific subcellular compartments, such as nuclear localization sequence and organelle-targeting signals, can be added to the construct in order to visualize synthesizing peptides at specific subcellular locations. If the channel (excitation at 488 nm) is required for imaging other fluorescent molecules in the cell, super-folded GFP (sfGFP) in the plasmid can be replaced by other fluorophores.
5. Some RNA may appear as multiple size bands on the gel due to RNA secondary structures, which can be eliminated by denaturing RNA at 70 °C for 10 min.
6. Multiple concentrations of the mRNA injected should be tested in pilot experiments.
7. Injection of embryos needs to be completed within 45 min at room temperature before they reach stage 5. According to

Nieuwkoop and Faber's Table, stage 3 (4-cell) embryos develop to stage 4 (8-cell) in 15 min and stage 5 (16-cell) in another 30 min at room temperature. When the embryos reach stage 4, the lighter two blastomeres on the animal side (at the top) should be injected. This could limit the number of embryos that can be injected during one experiment, which may in turn limit the number of conditions that can be included.

8. The percentage of RGCs expressing the electroporated constructs typically decreases as the embryo ages. Eye-targeted electroporation can be performed as early as stage 24, although eye primordia can be more easily identified at and after stage 26.
9. mRNA molecules in cells are not as stable as DNA plasmids and their expression lag time is much shorter (as there is no delay due to a transcription step). Therefore, it is recommended to minimize the time between when they are first introduced intracellularly and when the imaging is performed by electroporating the fluorescently labeled mRNA at a stage closer to the culture and imaging as opposed to blastomere injection.
10. In pilot experiments, multiple concentrations of Cy5-mRNA should be tested in embryos injected with different concentrations of pCS2+-scFv-GCN4-sfGFP-GB1 mRNA to determine the optimal concentrations for both synthetic mRNAs.
11. Avoid anesthetizing too many embryos at the same time. The experimenter should aim to electroporate all anesthetized embryos within 30 min, as prolonged anesthetization harms axon and embryo health.
12. As axons are thin structures, various illumination and acquisition modes are suitable for live axon imaging, including confocal, widefield/epifluorescence, total internal reflection fluorescence (TIRF), and highly inclined and laminated optical sheet (HILO).
13. In contrast to puromycin, the commonly used protein synthesis inhibitor cycloheximide has little, or even the opposite effect on the number of sfGFP-positive puncta colocalized with Cy3/5-RNA granules. This is due to the differences in mechanism of action between puromycin and cycloheximide: puromycin dissociates ribosomal subunits and releases the mRNA and the synthesizing peptide, while cycloheximide freezes ribosomes on the mRNA being translated due to the blocking of the translocation step during elongation [13].
14. Importing the image stack with "Bio-Formats Importer" plugin ensures the correct organization of the hyperstack using the information generated by the acquisition program.

15. When combined with additional cellular structure markers, such as the late endosome marker RFP-Rab7a [20], this technique can be applied to visualize local protein synthesis at specific subcellular locations.

Acknowledgments

The authors thank Francesca W. van Tartwijk for valuable comments on the manuscript. This work was supported by a Sir Henry Wellcome Postdoctoral Fellowship from the Wellcome Trust (to J. Q.L.) and a Career Development Award from the Giovanni Armenise-Harvard Foundation (J.-M.C.). This research was funded in whole, or in part, by the Wellcome Trust [215943/Z/19/Z]. For the purpose of open access, the author has applied a CC BY public copyright license to any Author Accepted Manuscript version arising from this submission.

References

1. Holt CE, Martin KC, Schuman EM (2019) Local translation in neurons: visualization and function. Nat Struct Mol Biol 26:557–566
2. Kourtis N, Tavernarakis N (2009) Cell-specific monitoring of protein synthesis in vivo. PLoS One 4:e4547
3. Leung KM, van Horck FP, Lin AC, Allison R, Standart N, Holt CE (2006) Asymmetrical beta-actin mRNA translation in growth cones mediates attractive turning to netrin-1. Nat Neurosci 9:1247–1256
4. McEvoy AL, Hoi H, Bates M, Platonova E, Cranfill PJ, Baird MA, Davidson MW, Ewers H, Liphardt J, Campbell RE (2012) mMaple: a photoconvertible fluorescent protein for use in multiple imaging modalities. PLoS One 7:e51314
5. Wang DO, Kim SM, Zhao Y, Hwang H, Miura SK, Sossin WS, Martin KC (2009) Synapse- and stimulus-specific local translation during long-term neuronal plasticity. Science 324: 1536–1540
6. Ifrim MF, Williams KR, Bassell GJ (2015) Single-molecule imaging of PSD-95 mRNA translation in dendrites and its dysregulation in a mouse model of fragile X syndrome. J Neurosci 35:7116–7130
7. Strohl F, Lin JQ, Laine RF, Wong HH, Urbancic V, Cagnetta R, Holt CE, Kaminski CF (2017) Single molecule translation imaging visualizes the dynamics of local beta-actin synthesis in retinal axons. Sci Rep 7:709
8. Tatavarty V, Ifrim MF, Levin M, Korza G, Barbarese E, Yu J, Carson JH (2012) Single-molecule imaging of translational output from individual RNA granules in neurons. Mol Biol Cell 23:918–929
9. Yu J, Xiao J, Ren X, Lao K, Xie XS (2006) Probing gene expression in live cells, one protein molecule at a time. Science 311: 1600–1603
10. Tanenbaum ME, Gilbert LA, Qi LS, Weissman JS, Vale RD (2014) A protein-tagging system for signal amplification in gene expression and fluorescence imaging. Cell 159:635–646
11. Wang C, Han B, Zhou R, Zhuang X (2016) Real-time imaging of translation on single mRNA transcripts in live cells. Cell 165: 990–1001
12. Wu B, Eliscovich C, Yoon YJ, Singer RH (2016) Translation dynamics of single mRNAs in live cells and neurons. Science 352: 1430–1435
13. Yan X, Hoek TA, Vale RD, Tanenbaum ME (2016) Dynamics of translation of single mRNA molecules in vivo. Cell 165:976–989
14. Worn A, Auf der Maur A, Escher D, Honegger A, Barberis A, Pluckthun A (2000) Correlation between in vitro stability and in vivo performance of anti-GCN4 intrabodies as cytoplasmic inhibitors. J Biol Chem 275: 2795–2803
15. Leung KM, Lu B, Wong HH, Lin JQ, Turner-Bridger B, Holt CE (2018) Cue-polarized transport of beta-actin mRNA depends on

3'UTR and microtubules in live growth cones. Front Cell Neurosci 12:300

16. Wong HH-W, Lin JQ, Ströhl F, Roque CG, Cioni J-M, Cagnetta R, Turner-Bridger B, Laine RF, Harris WA, Kaminski CF et al (2017) RNA docking and local translation regulate site-specific axon remodeling in vivo. Neuron 95:852–868.e858
17. Wong HH, Holt CE (2018) Targeted electroporation in the CNS in Xenopus embryos. Methods Mol Biol 1865:119–131
18. Nieuwkoop PD, Faber J (1994) Normal table of Xenopus laevis (Daudin) : a systematical and chronological survey of the development from the fertilized egg till the end of metamorphosis. Garland, New York
19. Jakobs MA, Dimitracopoulos A, Franze K (2019) KymoButler, a deep learning software for automated kymograph analysis. Elife 8: e42288. https://doi.org/10.7554/eLife.42288
20. Cioni JM, Lin JQ, Holtermann AV, Koppers M, Jakobs MAH, Azizi A, Turner-Bridger B, Shigeoka T, Franze K, Harris WA et al (2019) Late endosomes act as mRNA translation platforms and sustain mitochondria in axons. Cell 176(56–72):e15

Open Access This chapter is licensed under the terms of the Creative Commons Attribution 4.0 International License (http://creativecommons.org/licenses/by/4.0/), which permits use, sharing, adaptation, distribution and reproduction in any medium or format, as long as you give appropriate credit to the original author(s) and the source, provide a link to the Creative Commons license and indicate if changes were made.

The images or other third party material in this chapter are included in the chapter's Creative Commons license, unless indicated otherwise in a credit line to the material. If material is not included in the chapter's Creative Commons license and your intended use is not permitted by statutory regulation or exceeds the permitted use, you will need to obtain permission directly from the copyright holder.

Part II

Mouse *In Vivo* and *Ex Vivo*

Chapter 4

Imaging Axonal Transport in Ex Vivo Central and Peripheral Nerves

Stacey Anne Gould, Robert Adalbert, Stefan Milde, and Michael Coleman

Abstract

Neurones are highly polarized cells with extensive axonal projections that rely on transport of proteins, RNAs, and organelles in a bidirectional manner to remain healthy. This process, known as axonal transport, can be imaged in real time through epifluorescent imaging of fluorescently labeled proteins, organelles, and other cargoes. While this is most conveniently done in primary neuronal cultures, it is more physiologically relevant when carried out in the context of a developed nerve containing both axons and glia. Here we outline how to image axonal transport ex vivo in sciatic and optic nerves, and the fimbria of the fornix. These methods could be altered to image other fluorescently labeled molecules, as well as different mechanisms of intracellular transport.

Key words Epifluorescence microscopy, Sciatic nerve, Tibial nerve, Fimbria, Fornix, Axonal transport, Imaging, Ex vivo, Live imaging

1 Introduction

Imaging axonal transport is useful to help build an understanding of the role particular organelles, proteins, or other biological molecules play in axon health and disease. The ex vivo imaging system we outline here combines several advantages of in vitro and in vivo systems, while eliminating some of the disadvantages outlined in **Note 1**. This protocol enables movement of fluorescently tagged molecules to be easily imaged in fully developed adult mouse nerves and fimbria, without the need for expensive in vivo imaging equipment or specialized training in mouse surgical techniques. However, it is important to remember that there are a number of limitations that arise, including physical axonal injury due to excision of nervous tissue from the mouse, a change in the environment

Supplementary Information The online version of this chapter (https://doi.org/10.1007/978-1-0716-1990-2_4) contains supplementary material, which is available to authorized users.

Alessio Vagnoni (ed.), *Axonal Transport: Methods and Protocols*,
Methods in Molecular Biology, vol. 2431, https://doi.org/10.1007/978-1-0716-1990-2_4,
© The Author(s), under exclusive license to Springer Science+Business Media, LLC, part of Springer Nature 2022

that the tissue is in, and loss of blood supply and input from other nerves and tissue in the body. These factors lead to a gradual decline in the rate of axonal transport and axons eventually die [1].

The methods described here were optimized for imaging CFP-labeled mitochondria and Venus-labeled NMNAT2 in the nervous system of genetically modified mice [2, 3]. However, the principles would apply to imaging other fluorescently labeled molecules (proteins, RNA, or other organelles), such as peroxisomes [4] and endosomes [5]. Fluorescently labeled p75 neurotrophin receptor or binding fragment of the tetanus toxin has also successfully been used to image bidirectional transport in vivo after uptake at the neuromuscular junction [5–7], as has application of lipophilic dyes to the sciatic nerve [8, 9]. One could experiment with these kinds of label and apply them to this ex vivo imaging protocol, enabling other forms of intracellular transport, such as endosomal uptake and cell-protein sorting mechanisms to be explored.

The technique described here has successfully been used to study the effects of normal mouse aging as well as dietary nutrient availability on both mitochondrial and NMNAT2 transport [10, 11]. In a disease context, the effects of familial Alzheimer's disease-related genes on mitochondrial transport have also been explored [12, 13]. Further applications could be to study the effects of neurotoxic injuries, such as occurs in chemotherapy-induced peripheral neuropathy, or nervous system disorders, such as neuropathy caused by metabolic disease or viral infection. Effects of drugs or therapeutics when pre-administered in vivo or after application to the excised nerve could also be explored (though the latter brings with it several caveats outlined in **Note 2**).

There is a plethora of factors which can affect the rate of axonal transport of various cargoes. Some of these include glucose and nutrient availability, exposure to neurotoxins (such as vincristine), age, anesthesia, and electrical activity, as well as disease and injury status. Ex vivo, temperature changes, pressure applied to the nerve, calcium influx at the sites of cut, and nutrient availability are amongst environmental factors that will alter the rate of mitochondrial and NMNAT2 transport, with raised intracellular calcium levels being known to arrest movement of mitochondria and anchor them to regions of high calcium concentration [14–17]. The imaging system we outline here allows exploration of these factors and many others, but this also means it is sensitive to them. Therefore, careful design of experiments and consistency between experimental and control samples, as well as between imaging sessions is crucial for obtaining reliable results.

2 Materials

2.1 Consumables

1. Neurobasal A medium.
2. Pressurized oxygen.
3. Pipette tip and tube (or equivalent) to facilitate movement of oxygen from the canister into the medium.
4. Suitable imaging surface to place the nerve and medium on, for example, glass bottomed cell culture dish.
5. 70% ethanol to sterilize mouse skin and remove residual fur.
6. Bijou vials to securely transport warm oxygenated medium and the dissected tissue.
7. Sterile tubes to warm and oxygenate medium in.
8. Petri dishes for fimbria dissection.

2.2 Equipment

1. Water bath to heat the medium to 37 °C.
2. Dissection tools.
   - Large scissors to remove the head and fur.
   - Tape to hold the hindlimbs in place for sciatic and tibial nerve dissections.
   - Small scissors to cut the skull for access to the optic nerves/brain.
   - Scalpel to cut the skin (alternatively use forceps and small spring-loaded scissors).
   - Small spring-loaded scissors to dissect the nerve.
   - Curved scissors or forceps to gently balance the nerve(s) on to transfer them into the medium.
3. Weight to hold tissue in place during imaging session (*see* **Note 3**).

2.3 Mice

1. Mice hemizygous for *Nmnat2*-Venus, or *mito*CFP (*see* **Note 4** for colony maintenance and genotyping).
2. Other genetically modified mice with fluorescently tagged molecules, as required.
3. Ensure animal breeding and humane methods of culling are appropriately authorized according to the relevant animal welfare legislation in the country/institute where research is being conducted.

2.4 Microscope

1. Live imaging inverted epifluorescence microscope. Confocal microscopy could be used instead of epifluorescence, but at a potential cost to the temporal resolution.
2. Image detection camera and capture software.

3. Environment chamber to maintain constant 37 °C temperature (or temperature of interest).
4. Immersion oil for high magnification imaging.

3 Methods

It is important to remember that many variables such as temperature, pressure, nutrient availability, and time taken to collect and image the tissue can alter the rate of axonal transport. Try to minimize these variables to avoid confounding results (*see* **Note 5** for more detailed advice). Importantly, in each imaging session, aim to image an equal number of control and experimental nerves to minimize the possibility of day-to-day environmental variation confounding the results.

3.1 Set Up the Microscope, Environmental Chamber, and Imaging Software Parameters

1. A setup similar to that shown in Fig. 1 is required for ex vivo live imaging.
2. Prior to culling mice and collecting tissue, set up your imaging parameters on the microscope software (this may require pre-optimization experiments).

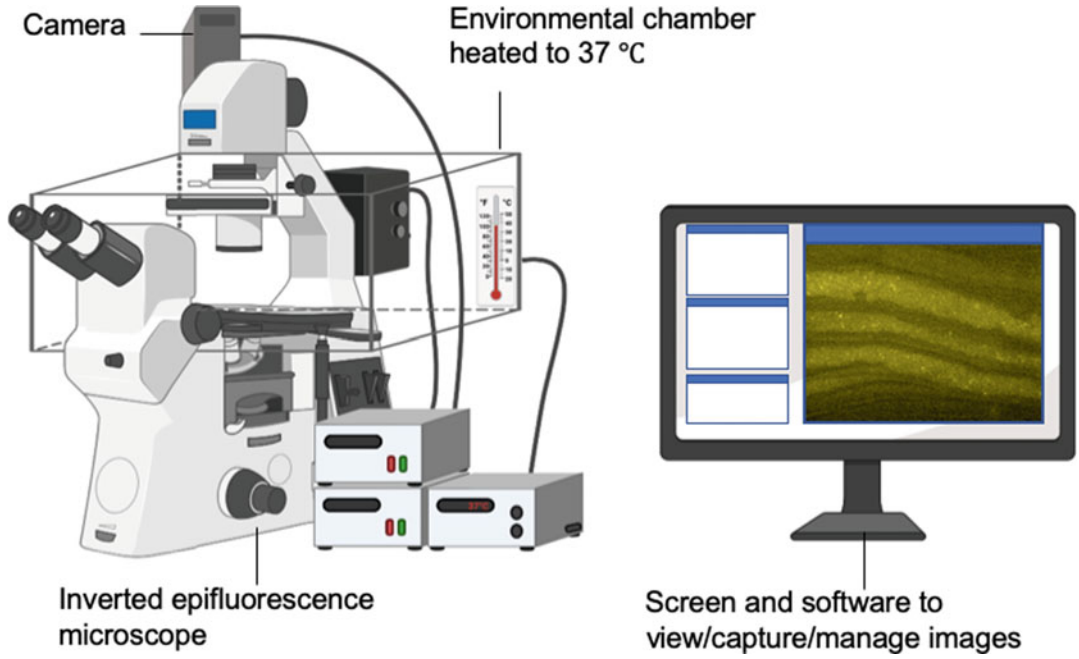

Fig. 1 Example inverted epifluorescence microscope and associated equipment needed for live imaging of ex vivo nerves and fimbria

3. Image mitochondrial or NMNAT2-Venus transport at a rate of two frames per second. You may need to modify or empirically determine these parameters for different cargoes and rates of transport.

3.2 Prepare Medium for Nerve/Fimbria Collection and Imaging

1. Warm Neurobasal A medium in a 37 °C water bath.
2. While warming medium, place a pipette tip attached to a tube providing the pressurized oxygen into the medium for at least 30 min before tissue dissection. Secure the tip in place (with parafilm, or a suitable alternative) to infuse the medium with oxygen, as shown in Fig. 2.
3. Keep the medium warm and ensure there is a continuous supply of oxygen to medium that will be used in later dissections and/or during the fimbria dissection.

3.3 Cull the Mice

1. Only cull mice and collect tissue after the microscope, dissection space, and medium have been prepared and are ready to use, as minimising time between culling the mouse and imaging the nerve is crucial, as explained in more detial in **Note 6**.

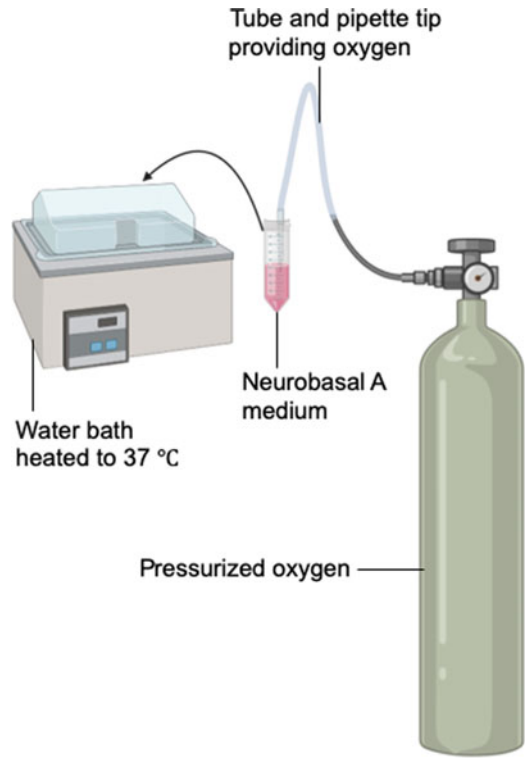

Fig. 2 An example of how to oxygenate and prewarm Neurobasal A medium

2. Humanely sacrifice the mouse whose tissue will be imaged—*see* **Note 7** for considerations on which method of euthanasia is appropriate.
3. If imaging the fimbria and optic nerves, ensure the method of euthanasia does not involve squashing or destruction of the brain.

3.4 Dissecting the Sciatic Nerve (Fig. 3)

1. For sciatic and tibial nerve collection, after culling the mouse, tape the feet down, as indicated in Fig. 3a.
2. Remove the fur covering the hind limbs and lower back and clean the muscle underneath with 70% ethanol, as indicated in Fig. 3b.
3. Palpate to locate the hip and hold the muscle just below the hip with forceps while cutting along the length of the leg (as indicated in Fig. 3c–f).
4. The sciatic nerve should be immediately visible in the space under the incision, as indicated by the arrow in Fig. 3e.
5. Carefully, without pulling the nerve, track back to the sciatic notch and cut the nerve where it exits the notch, Fig. 3g.
6. Follow the nerve along the length of the leg to the ankle, gently removing any non-nervous tissue along the way, and cut the nerve at the ankle, Fig. 3h.
7. It is important to include the section of tibial nerve after the sciatic nerve trifurcates (at the knee), even if only imaging the sciatic nerve, since this will enable orientation of the nerve and allow you to distinguish between anterograde and retrograde transport and provide enough tissue to avoid imaging in a region near the cut sites affected by calcium influx.
8. Remove any tissue holding the nerve in place and try to avoid collecting any lumps of fat or non-nervous tissue with the nerve.
9. Balance the nerve on curved scissors or forceps (Fig. 3i) and place it into freshly oxygenated pre-warmed Neurobasal A medium for transfer to the microscope.
10. Aim to complete this process within 3 min. It is important to collect as much of the nerve as possible to allow imaging of regions that are not affected by the immediate increase in calcium influx next to the cut sites.

3.5 Dissecting the Optic Nerve (Fig. 4)

1. Place the whole head of the mouse immediately in pre-oxygenated Neurobasal A medium warmed to 37 °C.
2. Transfer the head to the dissection microscope and keep the tissue at 37 °C for the duration of the dissection, replacing Neurobasal A medium with warm freshly oxygenated medium regularly throughout the dissection.

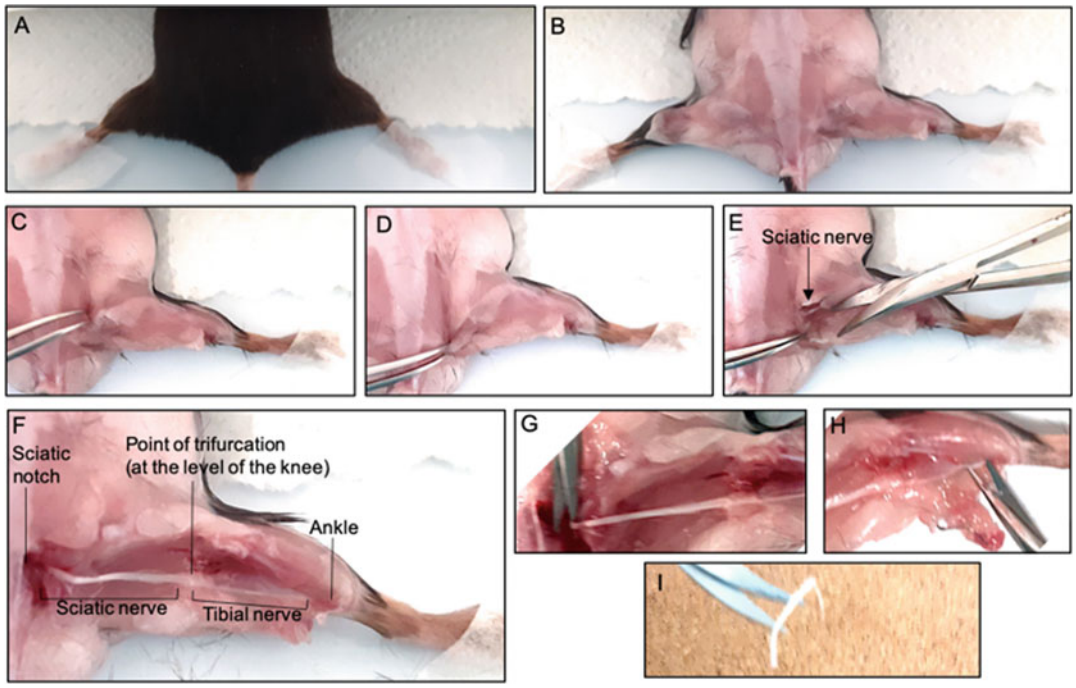

Fig. 3 How to dissect the sciatic and tibial nerves. After the mouse has been humanely culled, tape the paws down (**a**) and remove the fur (**b**). Palpate to locate the hip bone (**c**), then pull the tissue taut (**d**). Cut the tissue and this should reveal the sciatic nerve (**e**) indicated by the arrow. Cut away the overlying tissue from the spine to the ankle to reveal the entire nerve (**f**). Cut the nerve at the sciatic notch (**g**) and ankle (**h**), then gently collect it using bent scissors or forceps (**i**) to transfer it into prewarmed oxygenated Neurobasal A medium

3. Remove the skin and fur from the head, as shown in Fig. 4a–b.
4. Cut the skull along the sagittal suture, starting at the cranio-vertebral junction (foramen occipitale magnum) through the occipital, parietal, and frontal bones. Then cut along the sides of the skull from the foramen occipitale magnum through the temporal bones to the eye, ideally at a level adjacent to the center of the eye, taking care not to squash the brain (Fig. 4c).
5. Peel the skull from the brain using forceps, taking care not to squash the brain (Fig. 4d).
6. Remove the brain by lifting the frontal cortex with forceps and tipping the brain back, leaving the optic nerves with the optic chiasm attached in the skull (Fig. 4e–f).
7. Remove the upper and lower eyelids and transect the extraocular eye muscles (Fig. 4g).
8. Sever the nerves below the optic chiasm to separate the nerves from the brain, then transect the optic chiasm longitudinally at the midline (Fig. 4g). This will allow the optic nerves to be removed individually.

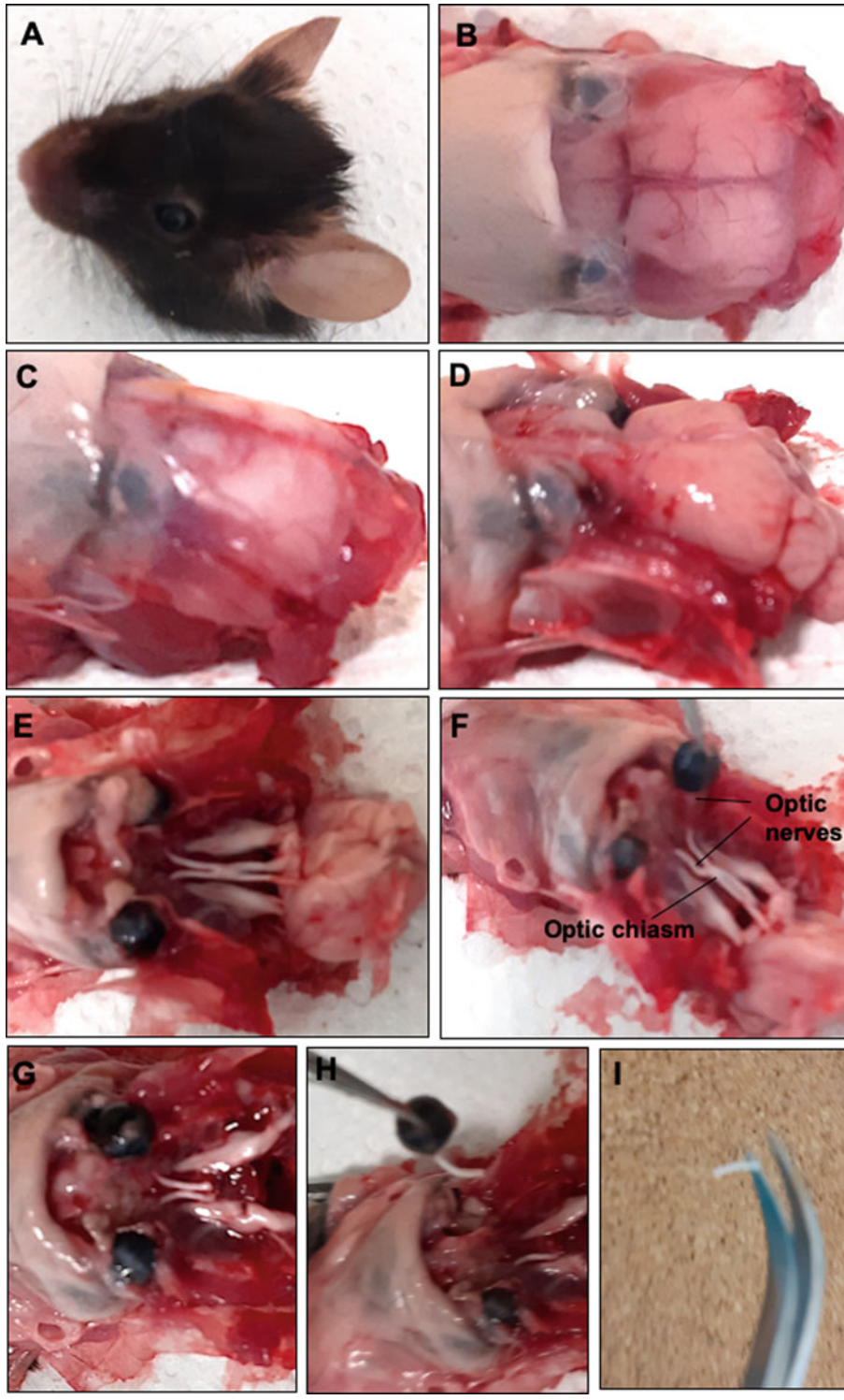

Fig. 4 How to dissect the optic nerves. Remove the head of a humanely culled mouse (**a**) and peel the skin back towards the nose to reveal the skull (**b**). Cut along the midline of the skull and each side of the skull towards the eye (**c**) and use forceps to remove the skull (**d**). Remove the extraocular muscles and then tip the brain backwards to reveal the optic chiasm and nerves (**e**) and locate the optic nerves (**f**). Cut below the optic

9. Remove the eye globes with the optic nerves attached by gently pulling them out from the eye socket (Fig. 4h).
10. Transect the optic nerves behind the eye globe (Fig. 4i).
11. Place the nerve into freshly oxygenated pre-warmed Neurobasal A medium and transfer it to the microscope. If you have dissected both the sciatic and tibial nerve, you will notice that the tibial nerve (post trifurcation) is thinner than the sciatic nerve (pre-trifurcation). Use this to orientate the nerve; anterograde transport moves in the direction towards tibial nerve and retrograde transport moves in the direction towards sciatic nerve.

3.6 Dissecting the Fimbria (Fig. 5)

1. For fimbria collection, place the whole head of the mouse immediately in pre-oxygenated Neurobasal A medium warmed to 37 °C.
2. Transfer the head to the dissection microscope and keep the tissue at 37 °C for the duration of the dissection and replace Neurobasal A dissecting medium with freshly oxygenated medium regularly throughout the dissection.
3. Remove the brain from the skull, as described for the optic nerve dissection (Subheading 3.5, **steps 3–6**), then place the brain into fresh warm, oxygenated Neurobasal A medium.
4. Remove the cortex and striatum on both hemispheres of the brain. After removing these structures, the hippocampi become visible (Fig. 5a–b).
5. Dissect out the hippocampi to expose the right and left side fimbria and the body of fornix (Fig. 5c).
6. Carefully, without pulling, remove fimbria and body of fornix and clean them of any attached gray matter (Fig. 5d–f).
7. Place the explant into freshly oxygenated pre-warmed Neurobasal A medium and transfer to the microscope.
8. Image the ventral (Fig. 5g) not dorsal (Fig. 5h) side of the explant.

3.7 Imaging the Sciatic and Optic Nerves, or Fimbria

1. Once the tissue has been dissected and transported to the microscope, gently transfer it from the oxygenated medium to an imaging dish—avoid clamping the tissue too hard with forceps and try to only handle it at the edges avoiding the central region to be imaged.

Fig. 4 (continued) chiasm to remove the connections to the brain, and then cut the optic chiasm longitudinally to separate the nerves (**g**). Gently remove the eye from its socket and the nerve should remain attached (**h**). Finally, cut the nerve close to the eyeball and transfer it using curved scissors or forceps (**i**) into prewarmed oxygenated Neurobasal A medium

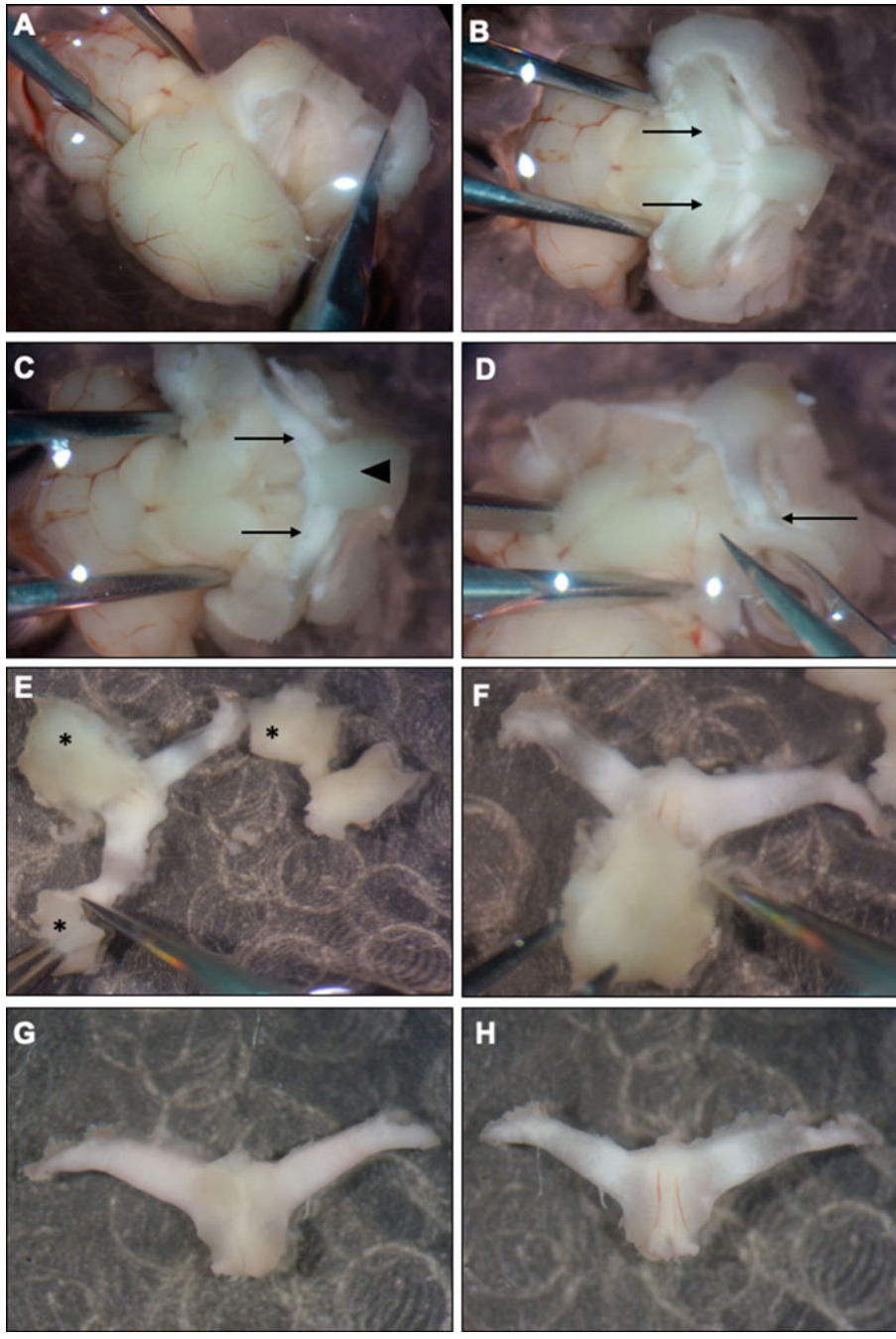

Fig. 5 How to dissect the fimbria. Maintain the extracted brain in oxygenated Neurobasal A medium and begin to remove the cortex and striatum (**a**). When the cortex and striatum are removed bilaterally, hippocampi become visible, as indicated by arrows (**b**). Removal of hippocampi exposes the right and left side fimbria (indicated by arrows) and the body of fornix (indicated by the arrowhead) (**c**). Gently remove the fimbria (right-side fimbria, indicated by arrow) from remainder of the brain (**d**). Once the fimbria and body of fornix are removed from the brain, several pieces of gray matter usually remain attached, indicated by asterisks in (**e**), which need to be removed before imaging. The final stage of the dissection involves removal of the gray matter (triangular septal nuclei) from the dorsal side of the fornix (**f**). Live images will be taken from the ventral side of the completed explant, as shown in (**g**). The dorsal side of the explant is indicated in (**h**)

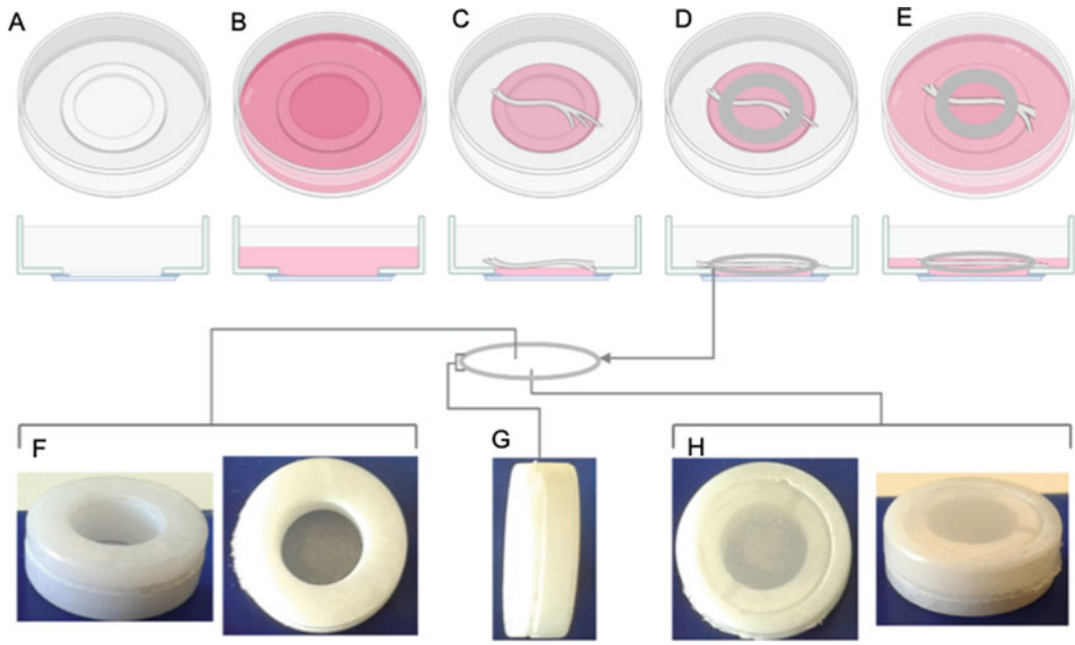

Fig. 6 How to plate the tissues for imaging (**a–e**) using a weighted disk (**f–h**). A glass bottomed cell culture dish (**a**) is flooded with Neurobasal A medium (**b**) which is then mostly aspirated from the dish leaving a shallow covering on the glass portion (**c**). The tissue is placed gently into this medium (**c**) and a plastic weight placed on top to flatten the nerve against the glass imaging surface (**d**). Fresh warm oxygenated Neurobasal A medium is then pipetted onto the weight and into the imaging dish at a volume that only just covers the nerve (**e**). The custom-made weight, viewed from the top (**f**), side (**g**), and bottom (**h**) was made using mesh from a 100 μm cell strainer placed taut over a custom-made plastic disk with the following measurements: outside diameter (1.5 cm), inside diameter (0.8 cm), width (0.5 cm), and weight 870 g

2. Add just enough fresh prewarmed oxygenated medium to cover the sample, but not so much that the sample starts to float.
3. The sample will need to be secured in place to prevent it drifting during image acquisition, as suggested in Fig. 6.
4. Place the sample inside the preheated environment chamber into the microscope's dish holder and allow it to acclimatize to the controlled environment for 10 min.
5. If imaging sciatic or optic nerves, ensure you are aware of the orientation of the nerve and how this translates to the image conveyed on the screen so you can determine the proportions of anterograde and retrograde transport during analysis, *see* **Note 8** for more details.
6. When selecting fields to image, aim to capture several axons running in parallel.
7. Image at least five separate fields of view, ideally from different axons for analysis.

8. The first images of sciatic nerves should be made no more than 20 minutes after the mouse was culled, including the acclimatization period.
9. Imaging sciatic nerves at a rate of two frames per second for 2 min is optimal for Venus-labeled NMNAT2 and CFP-labeled mitochondria at ×100 magnification.
10. The first images of optic nerves should be made no more than 20 min after the mouse was culled, including the acclimatization period.
11. The first images of the fimbria should be made no more than 30 min after the mouse was culled, including the acclimatization period.
12. Imaging optic nerves and/or fimbria at a rate of two frames per second for 1 min is optimal for Venus-labeled NMNAT2 at ×100 magnification.
13. Ensure the samples are maintained in Neurobasal A medium and that the environment chamber remains at 37 °C for the duration of imaging.
14. Remember to image an equal number of control and test samples each day. Since the rate of axonal transport and number of moving particles declines the longer the tissue is ex vivo, the total time spent imaging should not exceed 45–60 min for sciatic nerves, or 30–45 min for optic nerves and fimbria (*see* **Note 9** for tips on how to achieve this).

3.8 Quantifying the Videos

1. Videos will capture a combination of particles that are stationary and those which are moving in anterograde or retrograde directions (Fig. 7; Video 1). These can be analyzed using a combination of the ImageJ Straighten plugin and DifferenceTracker plugin (see Figs. 8 and 9; Videos 2–3) designed to generate aggregate statistics relating to particle movement [18].
2. Combined, these plugins enable identification of stationary and moving particles in each frame, and if tissue is orientated correctly during image acquisition, the proportion of anterograde and retrograde movement. If tissue was not orientated correctly, the Straighten plugin can be used to correct this, as described in **Note 10**.
3. The output from the combined plugins provides a tracked particle video (Fig. 10; Video 3), kymographs from the straightened and tracked videos (Fig. 11), and two .txt files (difference filter.txt and mass particle tracker.txt) containing statistics. Particle movement should be normalized to axon length and presented as particle count per second per 100 μm axon length.

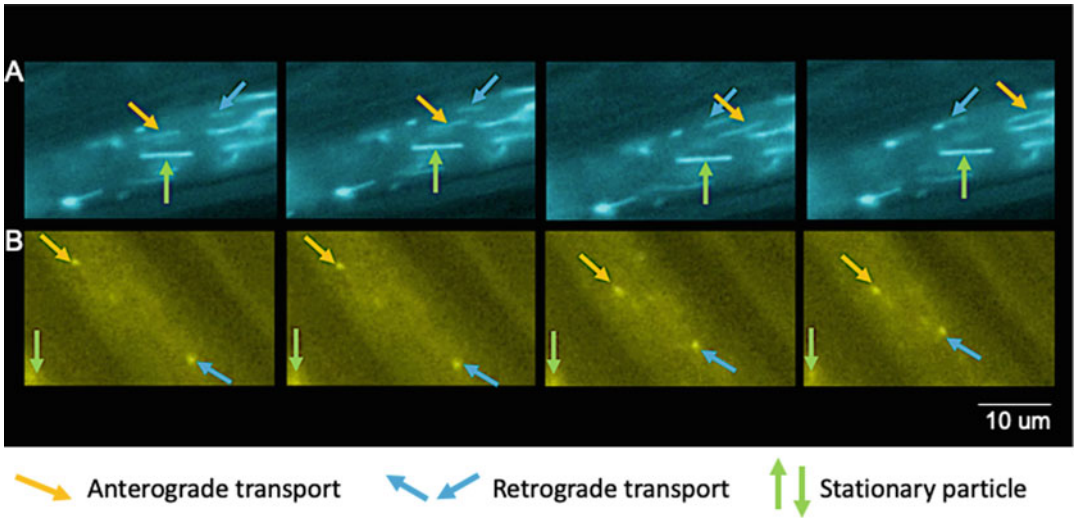

Fig. 7 Sequential frames from videos of mitochondrial and NMNAT2 vesicle transport in sciatic nerves from *mitoCFP* (**a**) and *Nmnat2*-Venus (**b**) mice**.** This shows that it is possible to track anterograde and retrograde transport of fluorescently labeled mitochondria (**a**) and NMNAT2 (**b**). Stills were taken approximately eight frames apart from a two frame per second video. Arrows pointing from left to right (orange) indicate anterograde transport, arrows pointing from right to left (blue) indicate retrograde transport, and arrows pointing vertically (green) indicate stationary particles

4 Notes

1. In vivo imaging ensures maintenance of blood supply (thus endogenous nutrient availability and access to other cell types such as monocytes), sensory input (i.e., from other nerves/tissues), and avoids the physical injury caused by explanting the nervous tissue being imaged. If compounds are administered to mice prior to imaging, effects of the compound on the nerves, as well as metabolites and effects caused by other cell types can be assessed. However, animals need to be anesthetized and fully immobilized for the duration of the experiment bringing issues of animal welfare, as well as potential confounds of anesthetic actions on nerve function and axonal transport. Even breathing and the effects of blood flow can be a problem. In addition, surgically skilled experimenters, expensive equipment, and a time-consuming low-throughput protocol limit uses of in vivo nervous system imaging. Injury to other sites is still required to gain access. In vitro systems overcome some of these problems, enabling higher throughput of experiments at lower cost, easier manipulation of genes, penetration of drugs, and the ability to assess direct actions of compounds on neurones without other cell types present in vivo. Many of these caveats can be eliminated in non-mammalian in vivo model

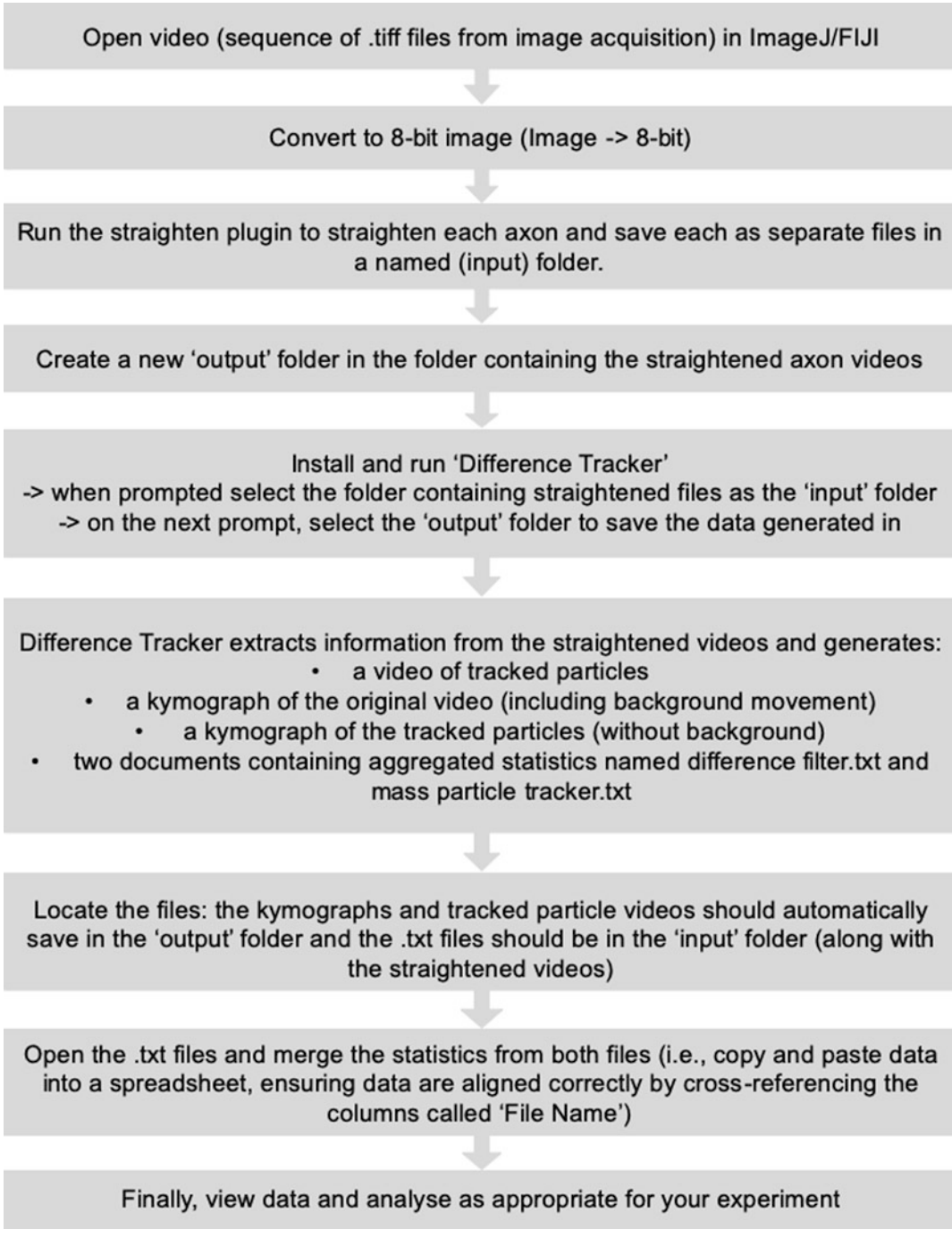

Fig. 8 Flow diagram describing the ImageJ (Fiji) video analysis protocol step-by-step

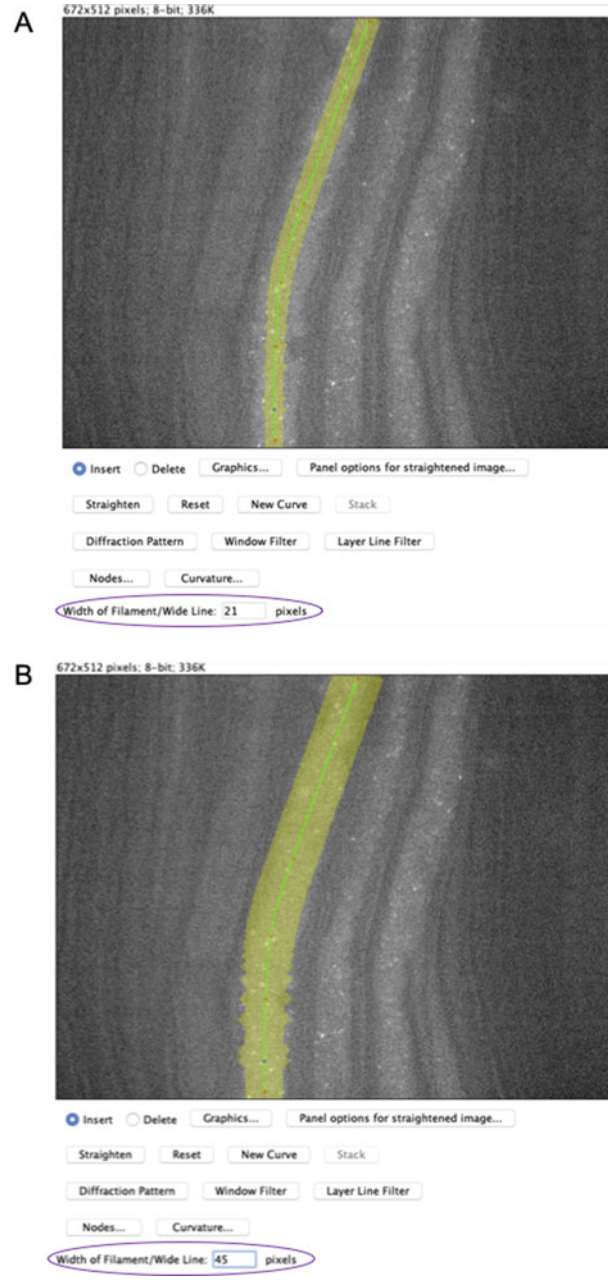

Fig. 9 Screenshot of the ImageJ straightening function when used on a video of axon transport. Once you have manually drawn a line down the center of the axon, ensure the highlighted section covers the entire width of the axon. The image in (**a**) is insufficiently highlighted. This can be rectified by altering the pixel width of the line, as indicated in the purple circles. Iteratively alter the pixel width until the entire axon is highlighted, as indicated in (**b**). By doing this, you avoid losing particles during the tracking process

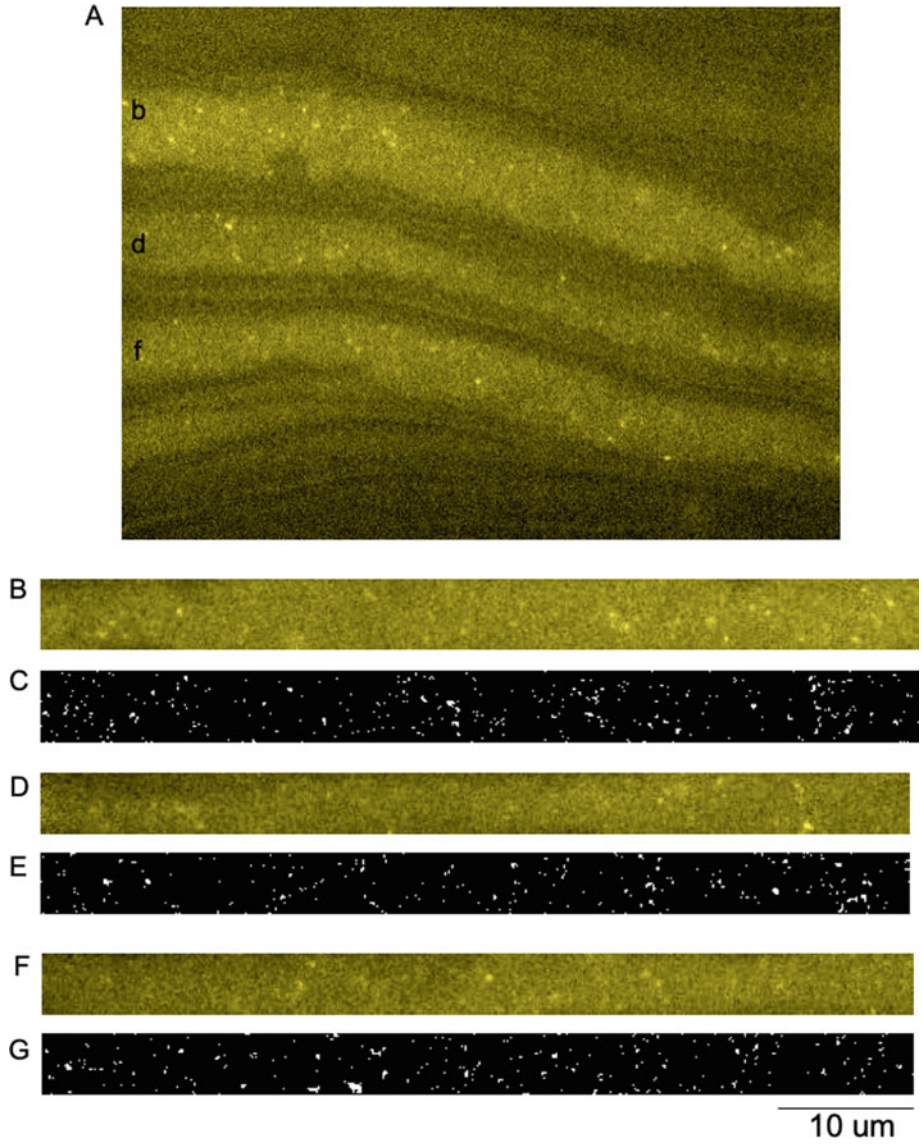

Fig. 10 Original videos are converted into straightened axons and then videos of tracked particles. Original video contains three separate axons (**a**) from which three separate straightened axon videos are generated (**b**, **d**, and **f**; yellow panes). Each of these straightened videos are analyzed and their corresponding tracked particle videos generated (black). Axons labeled b, d, and f in the original video (**a**) correspond the straightened videos B, D, and F

systems, such as zebrafish embryos and *Drosophila* wing or larvae. However, these model systems have other drawbacks, such as being non-mammalian systems and are often limited to specific developmental stages.

2. Drugs or compounds applied ex vivo may not permeate the nerve fully. Since there is a limited time during which the nerve

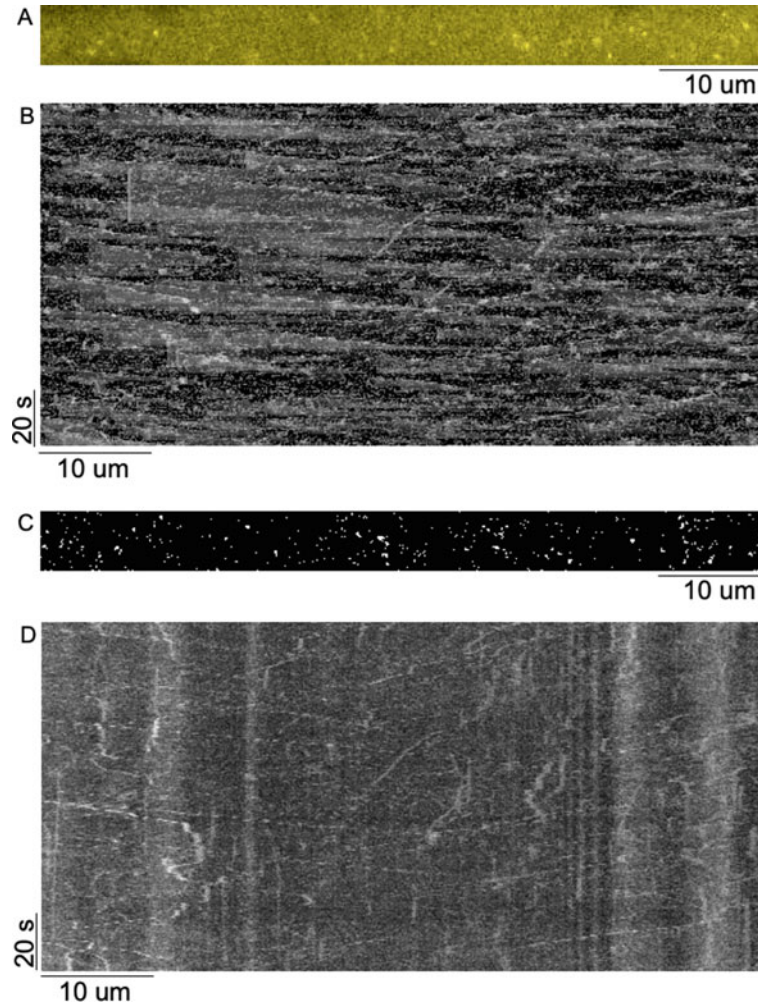

Fig. 11 Kymographs generated from raw videos and tracked particles. Video of straightened axon (**a**) and the kymograph generated from it (**b**). Tracked particle video (**c**) generated from its straightened axon (**a**) and the kymograph generated from tracked particles (**d**)

can be imaged, this limits the length of time the nerve can be infused with the compound before imaging, and subsequently the length of time the compound has to act on its target. In unpublished data, we found that some inhibitors are able to permeate into the excised nerve and act within 15 min of application, though others could not (unpublished data). Therefore, experiments aiming to explore direct effects of compounds on excised nerves will require optimization before performing. De-sheathing the nerve (removing the epineurium) may facilitate permeation of the compounds into the nerve, but care is needed to avoid stretching the nerve during this dissection.

3. The weight to hold the ex vivo tissue in place during image acquisition was custom-made using mesh from a 100 μm cell strainer placed taut over a custom-made plastic disk weighing 870 mg, as shown in Fig. 6f–h.
4. Mito-CFP and *Nmnat2*-Venus colonies are maintained by crossing hemizygous breeders with wild-type (C57BL/6) mice. Litters are then genotyped to select for hemizygous experimental mice using the genotyping primers and PCR amplification protocol detailed in Table 1.
5. Controlling for factors affecting axonal transport: Dissect and image the explants in the quickest possible time to avoid capturing images at the point of natural decline in axonal transport that occurs the longer tissue is ex vivo. Avoid stretching or applying pressure to the explants during excision or movement between animal, medium, and the microscope imaging platform. Since crush injuries interrupt axonal transport and trigger axon degeneration, avoid picking up the tissue using a pinching action with the forceps—instead, gently scoop the tissue onto curved forceps or scissors. Mitochondrial movement is more sensitive to axon damage than movement of NMNAT2, which could be due to calcium influx which occurs at sites of transection and the known sensitivity of mitochondrial trafficking to raised calcium levels. Therefore, ensure that the length of the sciatic/tibial or optic nerves explanted are as long as possible and comparable between experimental conditions to enable imaging of transport away from the physically damaged regions. The length of nerve explants should be a minimum of 4 mm for axonal transport to be detectable. For analysis of CNS axonal transport in explanted tissue, NMNAT2-Venus mice are a more robust and reliable model than MitoCFP mice. Reliable quantification of mitochondrial transport in optic nerves and fimbria is hard to achieve, as frequently little or no movement of mitochondria can be observed. Finally, minimize movement of explants through different temperatures by placing the excised tissue into warm medium as soon after the mouse is culled as possible. Keep the medium warm during transport to the microscope's controlled prewarmed environment chamber.
6. It is optimal to complete imaging the nerve as soon after culling the mouse as possible (within 45–60 min for sciatic and tibial nerves, and within 30–45 min for the optic nerves and fimbria, which is a more complex time-consuming dissection). Aim to submerge the nerves in pre-warmed and oxygenated medium within 2–3 min and the head within 30 s of culling the mouse.
7. Mice must be euthanized according to the legislation in place in the respective country. From a technical viewpoint, bear in

Table 1
Genotyping information for mitoCFP and *Nmnat2*-Venus transgenic mice

Gene	Fragment size (base pairs)	Forward primer sequence/reverse primer sequence (both 5′–3′)	PCR amplification protocol
mitoCFP	~200 (Tg) no band (wt)	CGCCAAGATCCATTCGTT/GAACTT CAGGGTCAGCTTGC	Step 1: 93 °C, 5 m; Step 2. 93 °C, 30 s; Step 3. 57 °C, 30 s; Step 4. 68 °C, 30 s; Repeat 2–4 35×; 68 °C 2 m 4 °C
Nmnat2-Venus	170 (Tg) 300 (wt)	ATGGAAGTGATTGTTGGGGAC/CTGCTCTT GGTGGAGCTGAC	Step 1. 95 °C, 2 m; Step 2. 95 °C, 30 s; Step 3. 64 °C, 20 s; Step 4. 72 °C, 75 s; Repeat 2–4 39×; 72 °C, 5 m; 4 °C
Nmnat2-Venus	~1000 (Tg) <200 (wt)	CACCTGTCCTACCAGCTGGCTG/ GTGGCC GTTTACGTCGCCGTC	Step 1. 95 °C, 2 m; Step 2. 95 °C, 30 s; Step 3. 64 °C, 20 s; Step 4. 72 °C, 75 s; Repeat 2–4 39×; 72 °C 5 m; 4 °C

Tg transgenic, wt wild-type, m minutes, s seconds

mind that culling mice by CO_2 or anesthetic overdose can cause changes in cortisol, blood glucose levels, and direct actions on the nerve which could affect the rate at which your molecule of interest is transported. While these effects are controlled for somewhat by having control and test subjects, it is best to use the method of culling that causes the fewest disturbances and least stress to mice.

8. How to orientate the tissue for videos: If the region of sciatic or optic nerve closest to the cell bodies are orientated such that in the video they would be to the left of the axon, then the output from the analysis method used will quantify movement from the left of the video to the right as anterograde transport, and right to left as retrograde. It is not possible to know direction of transport in the fimbria due to the presence of multi-directional axons.
9. In order to obtain the maximum amount of information from each animal, and thus reduce the overall number of animals needed, it is advisable to use all desired samples for your study (i.e., sciatic nerve, optic nerve, fimbria) from each animal. Given the requirement for immediate imaging following completion of the dissection, we have found it helpful to have one person carrying out the dissections sequentially on each animal (in the order sciatic nerve–optic nerve–fimbria) while a second person images the samples on the microscope as soon as each piece of tissue is successfully dissected.
10. If videos run from top to bottom rather than left to right (or in the opposite directions to those described in **Note 8**), this can be corrected using the "Straighten" plugin by selecting the end of the axon closest to the cell body (rather than the distal ends) at the beginning of the "Straighten" function and selecting the end of the axon that is closer to the distal end (rather than the cell body end) last. The straightened video generated would then show anterograde transport moving from left to right and retrograde in the opposite direction.

References

1. Sajic M, Mastrolia V, Lee CY, Trigo D, Sadeghian M, Mosley AJ et al (2013) Impulse conduction increases mitochondrial transport in adult mammalian peripheral nerves in vivo. PLoS Biol. 11(12):e1001754. https://doi.org/10.1371/journal.pbio.1001754
2. Milde S, Fox AN, Freeman MR, Coleman MP (2013) Deletions within its subcellular targeting domain enhance the axon protective capacity of Nmnat2 in vivo. Sci Rep 3:2567–2567
3. Misgeld T, Kerschensteiner M, Bareyre FM, Burgess RW, Lichtman JW (2007) Imaging axonal transport of mitochondria in vivo. Nat Methods 4(7):559–561. https://doi.org/10.1038/nmeth1055
4. Sorbara CD, Wagner NE, Ladwig A, Nikić I, Merkler D, Kleele T et al (2014) Pervasive axonal transport deficits in multiple sclerosis models. Neuron. 84(6):1183–1190. https://doi.org/10.1016/j.neuron.2014.11.006
5. Gibbs KL, Kalmar B, Sleigh JN, Greensmith L, Schiavo G (2016) In vivo imaging of axonal transport in murine motor and sensory neurons. J Neurosci Methods 257:26–33.

https://doi.org/10.1016/j.jneumeth.2015.09.018

6. Bilsland LG, Sahai E, Kelly G, Golding M, Greensmith L, Schiavo G (2010) Deficits in axonal transport precede ALS symptoms in vivo. PNAS 107(47):20523–20528
7. Sleigh JN, Tosolini AP, Gordon D, Devoy A, Fratta P, Fisher EMC et al (2020) Mice carrying ALS mutant TDP-43, but not mutant FUS, display in vivo defects in axonal transport of signaling endosomes. Cell Reports 30(11):3655–3662.e2. https://doi.org/10.1016/j.celrep.2020.02.078
8. Kalinski AL, Kar AN, Craver J, Tosolini AP, Sleigh JN, Lee SJ et al (2019) Deacetylation of Miro1 by HDAC6 blocks mitochondrial transport and mediates axon growth inhibition. J Cell Biol 218(6):1871–1890. https://doi.org/10.1083/jcb.201702187
9. Sleigh JN, Tosolini AP, Schiavo G (2020. [cited 2021 Jan 28]. p. 271–92. (Methods in Molecular Biology). Available from:) In vivo imaging of anterograde and retrograde axonal transport in rodent peripheral nerves. In: Babetto E (ed) Axon degeneration: methods and protocols [Internet]. Springer, New York, NY. https://doi.org/10.1007/978-1-0716-0585-1_20
10. Gould S (2021) Exploring SARM1 as a target to delay programmed axon degeneration [Internet] [Thesis]. University of Cambridge. [cited 2021 Jan 27]. Available from: https://www.repository.cam.ac.uk/handle/1810/316071
11. Milde S, Adalbert R, Elaman MH, Coleman MP (2015) Axonal transport declines with age in two distinct phases separated by a period of relative stability. Neurobiol Aging 36(2):971–981. https://doi.org/10.1016/j.neurobiolaging.2014.09.018
12. Adalbert R, Milde S, Durrant C, Ando K, Stygelbout V, Yilmaz Z et al (2018) Interaction between a MAPT variant causing frontotemporal dementia and mutant APP affects axonal transport. Neurobiol Aging 68:68–75. https://doi.org/10.1016/j.neurobiolaging.2018.03.033
13. Gilley J, Seereeram A, Ando K, Mosely S, Andrews S, Kerschensteiner M et al (2012) Age-dependent axonal transport and locomotor changes and tau hypophosphorylation in a "P301L" tau knockin mouse. Neurobiol Aging 33(3):621.e1–621.e15. https://doi.org/10.1016/j.neurobiolaging.2011.02.014
14. Mandal A, Drerup CM (2019. [cited 2021 Jan 29];13. Available from: https://www.frontiersin.org/articles/10.3389/fncel.2019.00373/full#B135) Axonal transport and mitochondrial function in neurons. Front Cell Neurosci. https://doi.org/10.3389/fncel.2019.00373
15. Smith GM, Gallo G (2018) The role of mitochondria in axon development and regeneration. Dev Neurobiol 78(3):221–237. https://doi.org/10.1002/dneu.22546
16. Zhang CL, Ho PL, Kintner DB, Sun D, Chiu SY (2010) Activity-dependent regulation of mitochondrial motility by calcium and Na/K-ATPase at nodes of ranvier of myelinated nerves. J Neurosci 30(10):3555–3566. https://doi.org/10.1523/JNEUROSCI.4551-09.2010
17. Saotome M, Safiulina D, Szabadkai G, Das S, Fransson Å, Aspenstrom P et al (2008) Bidirectional Ca2+-dependent control of mitochondrial dynamics by the Miro GTPase. PNAS. 105(52):20728–20733
18. Andrews S, Gilley J, Coleman MP (2010) Difference tracker: ImageJ plugins for fully automated analysis of multiple axonal transport parameters. J Neurosci Methods 193(2):281–287. https://doi.org/10.1016/j.jneumeth.2010.09.007

Chapter 5

In Vivo Imaging of Axonal Organelle Transport in the Mouse Brain

Johannes Knabbe, Jil Protzmann, and Thomas Kuner

Abstract

Visualization and analysis of axonal organelle transport has been mostly conducted in vitro, using primary neuronal cell cultures, although more recently, intravital organelle imaging has been established in model organisms such as drosophila, zebrafish, and mouse. In this chapter, we describe a method to visualize axonal transport of cellular organelles such as dense core vesicles or mitochondria in the living mouse brain in order to study organelle transport in its native environment. We achieve this goal by injecting adeno-associated viruses expressing fluorescently tagged marker proteins into thalamic nuclei of mice, thereby transducing neurons that project to the surface of the brain. Axonal projections and trafficking of organelles can be imaged with a 2-photon microscope through a chronically implanted window in the mouse skull in anesthetized as well as awake mice.

Key words Axonal transport, In vivo imaging, Cranial window surgery

1 Introduction

Visualizing axonal transport of cell organelles is vital for understanding the basic functions of neurons. Yet, axonal transport has also been shown to be impaired in multiple neurological diseases [1] such as Huntington's disease [2], Alzheimer's disease [3], multiple sclerosis [4] or during aging [5]. While a lot of work has been done in cultured primary neurons, intravital imaging of axonal organelle transport has been established in different model organisms such as drosophila [6], zebrafish [7], or mammals. In mice, in vivo axonal transport has been first visualized in spinal cord neurons using transgenic mouse lines with genetically labeled mitochondria [4, 8]. Furthermore, mitochondrial transport has been analyzed in retinal ganglion cells [9] and in cortical neurons using in utero electroporation in Layer 2/3 collaterals [10] or visual cortex [11]. In vivo imaging has been also established in the sciatic nerve after injection of fluorescent probes [12].

Alessio Vagnoni (ed.), *Axonal Transport: Methods and Protocols*,
Methods in Molecular Biology, vol. 2431, https://doi.org/10.1007/978-1-0716-1990-2_5,
© The Author(s), under exclusive license to Springer Science+Business Media, LLC, part of Springer Nature 2022

We established an in vivo axonal transport imaging approach using chronically implanted cranial windows and 2-photon microscopy in anesthetized as well as awake mice to image axonal transport in situ in the living mammalian brain. We injected a combination of at least two different adeno-associated viruses (AAVs) expressing fluorescently tagged proteins in thalamic nuclei projecting to layer I of the cortex to label axonal projections as well as the organelles of interest with different fluorescent marker proteins (Fig. 1). AAVs were constructed by inserting a marker protein such as neuropeptide Y for dense core vesicles (DCVs) [13], mitoGFP [14] for mitochondria, or MacF18 for microtubule plus ends [15] after a neuronal promoter such as the synapsin promoter (Fig. 1a). As the mitoGFP construct that we used was Cre-dependent, we co-injected a virus expressing the Cre recombinase. Simultaneous labeling of the axons was achieved by expressing mCherry in the cytosol under a strong and ubiquitous promoter such as the CAG promoter. To label presynaptic boutons, we used synaptophysin as a marker, fused to mCherry (alternatively, a different suitable fluorescent protein can be used, depending on the experimental paradigm). In principle, a neuronal promoter is not even needed, because the virus particles are injected deeply into the brain and only a few axonal projections reach its surface where imaging is performed. However, it is possible to target specific subtypes of neurons with the use of subtype-specific promoters or by combining Cre-dependent AAVs with a subtype-specific Cre-driver line. The axonal projections that can be imaged are sparse enough to be separated and reidentified over the course of many weeks (Fig. 2) which would not be the case if the viruses had been injected directly into the cortex. In addition, many of the axonal stretches run in parallel to the surface so that time-lapse imaging can be performed without changing the z-position of the objective, facilitating post-processing.

With this chronic imaging approach, it is possible to analyze transport over the course of many weeks as well as during different experimentally induced conditions in the same animals and thus increasing statistical strength. As we are using virally encoded marker proteins, in principle any organelle or cargo that can be visualized in vitro can also be visualized in vivo, precluding the need to create new reporter mouse lines. However, existing mouse lines can be used when suitable or efficiently combined with viral approaches. In our laboratory, we successfully imaged transport of DCVs [16] as well as mitochondria [17] and the dynamics of microtubule plus ends [16] both in anesthetized and awake mice. Other laboratories have been imaging transport of endosomes and lysosomes using our technique as well (personal communication). By choosing different promoters, markers, and fluorescent proteins, the system can easily be adapted for imaging other cell organelles, presynaptic boutons, or axons in specific neuronal

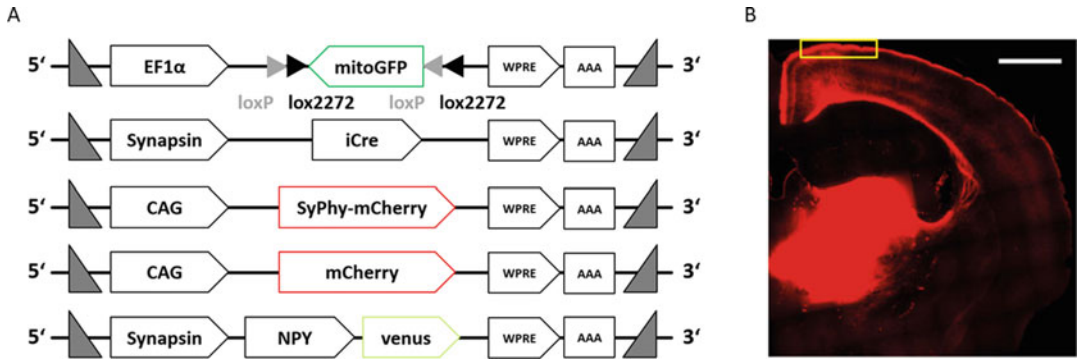

Fig. 1 (**a**) AAVs expressing fusion proteins to label distinct axonal organelles. NPY-venus is a fusion protein with neuropeptide Y and labels DCVs, mitoGFP labels mitochondria in neurons concurrently expressing iCre. In addition, another AAV can be injected that labels the axon (either mCherry or GFP, scheme in right panel) or presynaptic boutons (SyPhy-mCherry, a fusion protein of synaptophysin, labels synaptic vesicles). *See* **Note 1** for further details. (**b**) Thalamic injection site and axonal projection emanating from it. The yellow box depicts the imaging area. Wide-field epifluorescence imaging of an 80 μm thick section; scale bar, 1 mm

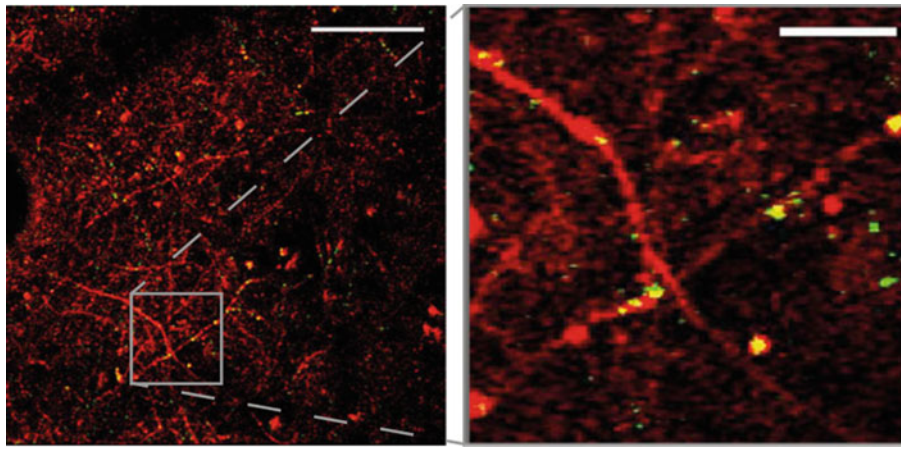

Fig. 2 Example image of a single frame used for in vivo 2-photon time-lapse imaging 40 μm below the pial surface. mCherry-labeled axons (red) and NPY-venus-labeled DCVs (green), DCVs in labeled axons appear yellow. Scale bar, 50 μm. Right panel: magnified view of region marked in the left panel. Scale bar, 10 μm

subtypes. To analyze alterations in axonal transport in different genetically encoded disease models, disease-specific mouse lines can be used for imaging as well. Thus, our approach offers a wide range of options to study organelle transport in vivo.

2 Materials

2.1 Cranial Window Surgery

1. Electric shaver.
2. Stereotaxic apparatus.
3. Fine marker pen.

4. 1% xylocaine as local anesthetic.
5. 70% ethanol for disinfection.
6. Eye ointment (Bepanthen with 5% Dexpanthenol).
7. Gel foams to stop bleedings (Equispon, Equimedical B.V., Zwanenburg, Netherlands).
8. Cotton swabs.
9. Normal Rat Ringer (NRR) solution: 135 mM NaCl, 5.4 KCl, 1.8 mM $CaCl_2$, 1.0 mM $MgCl_2$, 5.0 mM Hepes, pH 7.2.
10. Anesthesia mix in 0.9% saline: 0.5 mg/kg fentanyl (0.5 µl/g body weight of 1 mg/ml fentanyl), 9.5 mg/kg midazolam (1.9 µl/g body weight of 5 mg/ml midazolam), 0.75 mg/kg medetomidin (0.75 µl/g body weight of 1 mg/ml medetomidin).
11. Antagonistic mix in 0.9% saline: 0.75 mg/kg naloxone (1.86 µl/g body weight of 0.4 mg/ml naloxone), 0.03 mg/kg flumazenil (0.3 µl/g body weight of 0.1 mg/ml flumazenil), 1.5 mg/kg antipamezole (0.3 µl/g body weight of 5 mg/ml antipamezole), 3.72 µl of 0.9% saline per gram of body weight.
12. Pain medication post surgery: 5 mg/kg carprofen in 0.9% saline.

2.2 Craniectomy

1. Dental drill.
2. Forceps for removal of the skull flap (straight Dumont #2, Fine Science Tools Inc. Heidelberg, Germany).
3. Forceps for removal of the dura mater (straight Dumont #5, Fine Science Tools Inc. Heidelberg, Germany).
4. Cover slip (6 mm diameter, number 0 (85–130 µm thickness)).
5. Dental acrylic cement (glue: Cyano, Hager Werken, Duisburg, Germany; powder: Paladur, Heraeus, Hanau, Germany).

2.3 Viral Injection

1. Injection glass micropipette (5 µl).
2. Adeno-associated viruses (AAVs). Production of the AAVs is not the focus of this protocol and can be performed as described in [18]. Further information regarding selection of fluorophores can be found in **Note 1**.

2.4 2-Photon Microscopy

2.4.1 2-Photon Microscope

1. TriM Scope II microscope (LaVision BioTec GmbH, Stuttgart, Germany) equipped with a tunable pulsed Ti:Sapphire laser (Chameleon Ultra II; Coherent, Santa Clara, CA, USA).
2. Mirrors: 560 nm dichroic mirror, 535/70 nm emission filter for GFP or venus signal, 645/75 nm emission filter for mCherry signal.

3. Photomultiplier tube: (PMTs, H7422–40-LV 5 M; Hamamatsu).
4. Objective: 25×, 1.1 NA, apochromatic, water immersion, working distance 2 mm (Nikon).
5. Epifluorescent lamp.
6. USB camera.

2.4.2 Imaging Session

1. Isoflurane in medical O_2.
2. Vaporizer.
3. Heating pad.
4. Infra-red LED light source.

3 Methods

3.1 Preparation for Cranial Window Surgery

1. Deeply anesthetize the mouse by intraperitoneally (i.p.) injecting a dose of 3.1 μl/g anesthesia mix. *See* **Note 2** for this and the subsequent steps. *See* **Note 3** with regard to the type of anesthesia. For further details regarding the surgery *see* **Note 4**.
2. Protect the eyes of the mouse from dehydration and irritation by applying eye ointment.
3. Keep the mouse on 35 °C by a feedback-controlled heating pad throughout the surgery.
4. Shave the head of the mouse at the site of the surgery with an electric hair shaver (*see* **Note 5**).
5. Mount the mouse in a stereotaxic apparatus.
6. Inject xylocaine subcutaneously (s.c.) at the site of surgery.
7. Disinfect the scalp with 70% ethanol.
8. Lift the skin with a forceps and make a small cut in the medial-lateral direction with a small scissors. Proceed with a longer cut in the anterior-posterior direction until reaching the line between both eyes.
9. Remove a flap of the scalp, approximately 1 cm^2, as well as the subjacent gelatinous periosteum using surgical scissors.
10. Clean the skull with Normal Rat Ringer (NRR) solution and dry it with cotton swabs.
11. Level the mouse skull to Cartesian coordinates centered at bregma.
12. Mark bregma with a fine tipped pen.
13. Align the head horizontally in the stereotactic apparatus.

14. Target the right-hemispheric medio-dorsal (MD) nucleus of the thalamus using the coordinates relative to bregma:
    (a) 0.82 mm in the anterior-posterior axis
    (b) 1.13 mm in the medial-lateral axis
    (c) 3.28 mm in the dorso-ventral axis
15. Mark this point on top of the skull with a fine tipped pen.

3.2 Viral Injection

1. Aspirate the viral particles with an injection glass micropipette connected to a 10 ml syringe via a three-way valve (*see* **Note 6**).
2. Apply negative pressure via the syringe and wait until liquid has flown into the micropipette.
3. Drill a small hole into the skull where you marked the position of the MD thalamus before with a dental drill without hurting the surface of the brain (see Fig. 3, left panel).
4. Slowly lower the AAV-containing glass capillary at the target coordinates into the brain and wait for 5 min.
5. Inject around 800 nl AAV solution into the medio-dorsal thalamus with a speed of 0.4 µl/min by manually controlling the pressure using the 10 ml syringe. For slowly injecting the AAV, apply a weak positive pressure by moving the syringe stamp from 4 to 3 and wait for 2–3 min. If the meniscus does not move, apply more pressure for a short time, set the pressure to zero again and start from beginning.

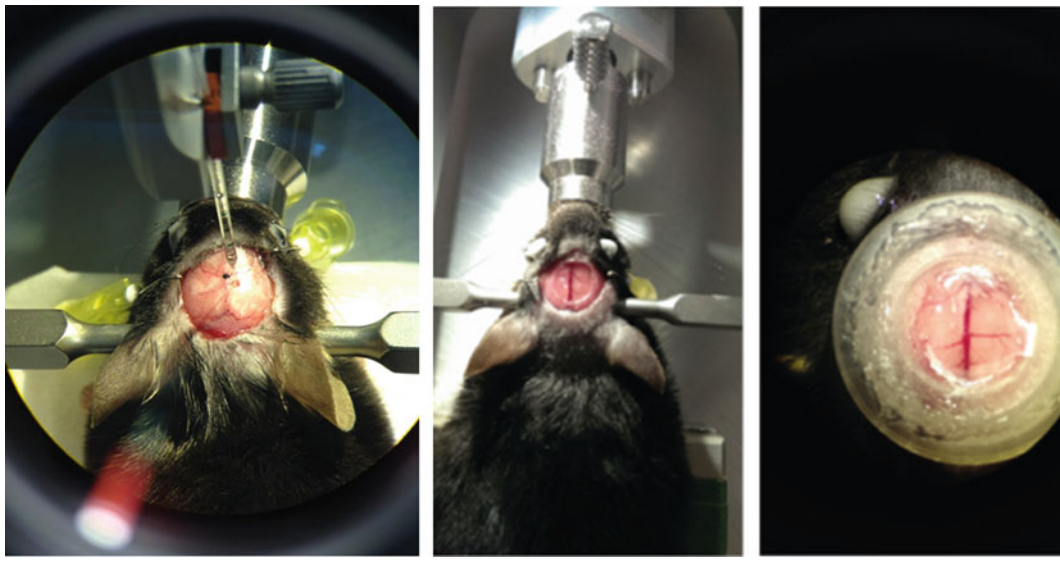

Fig. 3 Chronic window surgery. Left panel shows the stereotactic delivery of the viral particles. Middle panel shows a mouse in the stereotactic holder after removal of skull bone. Right panel depicts a close-up of the holding "crown" and the window after the surgery

6. After completion of the injection, wait for 10 min to prevent backflow of the virus, then remove the capillary slowly from the brain.

3.3 Craniectomy and Implantation of Chronic Cranial Window

1. Place the coverslip centrally over the injection site and draw the outline of the coverslip with a fine marker onto the skull (*see* **Note 7**).
2. Roughen the skull by drilling superficial grooves into the surface of the skull leading to a better bonding with the dental cement applied later in the procedure.
3. Do not drill too long at one point to prevent heating of the skull.
4. Remove a circular part of the skull, with a diameter of ~6.5–7 mm by drilling a deep groove into the outline of the circle until the groove almost reaches the dura mater (*see* **Note 8**). Remove the skull debris with an air duster during this process. The cortical surface vasculature should become visible under the circular groove, especially when buffer is applied. Expect to encounter some bleeding from the skull owing to tearing off the vascular plexus in the trabecular section of the cranial bone.
5. Apply a drop of buffer on top of the skull island to achieve successful removal of the skull. As one edge of the skull is lifted with the forceps later on, the fluid helps the flap of skull to detach from the dura (*see* **Note 9**).
6. Carefully remove the flap of the skull with a #2 forceps by inserting one tip of the forceps into the skull flap. Keep the tip in a horizontal position and try to avoid direct perforation of the thinned bone with the forceps, which could injure the dura. Slowly lift the central island of skull bone, exposing the dura (Fig. 3, middle panel, *see* **Note 10**).
7. If bleeding occurs, place hemostatic gel foams soaked in NRR on the brain.
8. Carefully remove the dura mater with a very fine #5 forceps (*see* **Note 11**).
9. Under ideal circumstances the dura should not bleed (*see* **Notes 12** and **13**).
10. Carefully and gently remove any blood on the surface of the brain with wet gel sponges.
11. Carefully remove small bone dust particles from the skull opening or at the edge of the skull with a very fine forceps as they could later on lead to bleedings.

12. Place a glass coverslip inside the opening and glue it to the skull with dental cement powder mixed in acrylic glue (*see* **Notes 14–17**).
13. Glue the 3D-printed plastic "crown" over the glass coverslip with dental acrylic cement leaving enough space for imaging afterward. Instructions for 3D-printing of crowns as well as an imaging holder can be requested from the corresponding author. Alternatively use any commercially available head-mounting system (Fig. 3, right panel).
14. Wait until the dental acrylic cement has dried out.
15. Terminate the anesthesia by injecting a dose of 3.1 μl/g antagonistic mix s.c..
16. Peri-operative care: Inject carprofen s.c.
17. If possible, keep the mouse in a heated cage set to 37 °C overnight.
18. Post-operative care: Inject carprofen s.c. every 12 h for the next 2 days (if bleeding occurs beneath the cranial window during this time *see* **Note 18** for further measures).

3.4 In Vivo 2-Photon Microscopy

1. Wait 4–8 weeks for the glial inflammatory reaction to cease.
2. Anesthetise the mouse with 5% isoflurane in medical O_2 using a vaporizer.
3. Head-fix the crown into a custom-built holder or commercial mounting system.
4. Clean the cover glass thoroughly with distilled water.
5. Use immersion liquid according to the specifics of the objective.
6. Maintain isoflurane at 0.8–1.5% with a flow rate of 0.5 l/s.
7. Monitor the breathing rate using an infra-red camera and an infra-red LED light source, both mounted within the enclosed microscope setup.
8. Keep the body temperature of the animal at 37 °C with a heating pad.
9. Check the viral expression prior to the experiment using epi-fluorescent illumination (*see* **Note 19**).

3.5 Visualizing Axonal Organelle Transport In Vivo

1. Tune the 2-photon laser to the desired wavelength. We use 960 nm for simultaneous excitation of mCherry and eGFP or Venus.
2. Use an objective optimized for multiphoton imaging with a large numerical aperture and a high working distance. In our hands, a Nikon objective with ×25 magnification, a numerical

aperture of 1.1, and a working distance of 2 mm produced the best results.

3. Image axonal organelle trafficking in Layer 1 of motor cortex, 50–100 μm below the pial surface.
4. Perform dual color imaging for imaging the axons at the same time as the respective organelles (*see* **Note 20**).
5. Look for areas where you can already see long axonal stretches in one image and start acquiring images there. For small organelles sometimes movement of particles can only be detected after post-processing.
6. Set the imaging parameters optimized for the expected speed and size of the organelles (*see* also **Notes 21–23**):
   (a) Mitochondria:
      - Take frames from an area of 436 × 436 μm, at 1024 × 1024 pixel resolution (resulting in 0.426 μm/pixel resolution).
      - Image with a frame rate of 0.6 Hz.
   (b) Dense core vesicles:
      - Take frames from an area covering 200 × 200 μm at 1071 × 1071 pixel resolution (resulting in 0.19 μm/pixel resolution).
      - Image with a frame rate of 0.9 Hz.
7. Image with the lowest laser power possible to avoid bleaching stationary structures or the axonal filling protein over time. We typically use 5–15% laser power (note that the intensity applied in the focal plane depends on the depth of the imaging area relative to the surface of the brain, the intensity of the fluorescence signal, the sensitivity of the detectors, and on many microscope-specific properties).

3.6 Post-processing and Visualization

3.6.1 Correct for Movement Artifacts

1. Open a time series in Fiji [19].
2. To correct for movement artifacts that occur with breathing, register the acquired time-lapse movies in xy with the Fiji plugin "moco" [20] (see Fig. 4).
3. Select a template image from the time-lapse, the algorithm compares every possible translation of every image of the time-lapse to the template image and chooses the translation with minimized template-to-frame difference (see Fig. 4).

3.6.2 Visualization

Kymographs can be used to reduce a 3D image with two spatial and one time dimension (*xyt*) to two dimensions. In a kymograph, the time (*t*) is plotted on the *y*-axis, while the length of an axon (*xy*) is linearized and plotted on the *x*-axis. Stationary structures will thus be depicted as straight vertical bars, while moving structures are

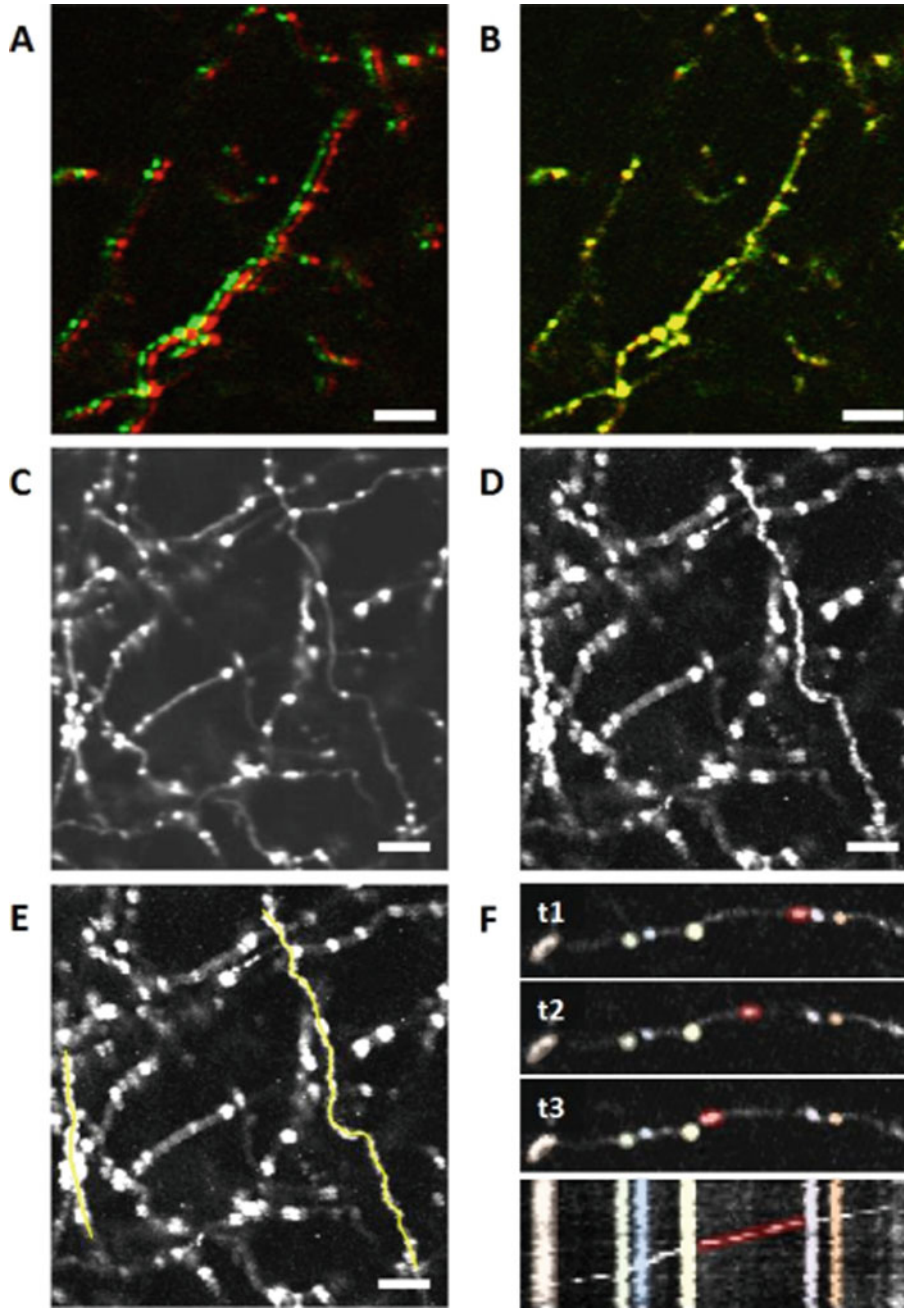

Fig. 4 Motion correction. Data processing implied template-based registration with the Fiji plugin "moco" [19] and subsequent region of interest (ROI) selection in the maximum intensity projection (MIP) in which, in contrast to the average intensity projection (AIP), movement of organelles can be detected. (**a**) Two planes of a time-lapse before registration. Movement artifacts are evident by lack of overlap. (**b**) Same planes as in (**a**) after registration. (**c**) AIP of time-lapse shows outlines of axons as well as stationary mitochondria. (**d**) MIP of time-lapse reveals mitochondrial trafficking through axons. (**e**) ROI selection was done in MIP in order to pick those axons which show mitochondrial trafficking (yellow). (**f**) Principle of a kymograph: in kymographs, time is shown on the *y*-axis and fluorescence intensity along the *x*-axis. Stationary mitochondria will thus be seen as vertical lines, while a moving mitochondrion (red label) is visible as a diagonal line. Scale bars 10 μm

visible as diagonal lines. The slope of the diagonal line is equivalent to the speed of the particle, the steeper the slope, the higher the speed. Mean speed can be calculated by measuring the traveled distance of the particle on the *x*-axis of the kymograph as well as the time on the *y*-axis.

1. Open a time series in Fiji.
2. Visualize the movement of the organelles along the axon with a kymograph that can be generated with the Multi Kymograph tool in Fiji [19] (see Fig. 5).
3. Mark the axon of interest with the "Segmented Line" tool in Fiji and select the "Multi Kymograph" tool, then select the linewidth depending on your pixel size.

4 Notes

1. Be careful to always select two fluorophores that can be excited with one wavelength, but have emission wavelengths that are sufficiently separated. Following this strategy, spectral demixing of the fluorescence signals is not required. In our hands the combination of GFP and mCherry consistently produced excellent results, while other bright fluorophores, such as tdTomato, resulted in strong bleed-through into the GFP channel.
2. Always wear gloves and a surgical mask while doing the surgery to prevent infections, the chronical windows should stay clear for months.
3. If you use isoflurane during the surgery, you might encounter swelling of the brain, try to use injectable anesthesia or a combination of isoflurane and injectable drugs. Injecting 2 mg/kg dexamethasone before the anesthesia can help with brain swelling.
4. Cranial window surgery was adapted from published work [21].
5. Be very careful to remove all hair after shaving to avoid having them on top of the brain later on. Alternatively use a shaving cream.
6. For aspirating the viral particles, connect a tube airtight with the back of the glass pipette. Then connect a three-way valve with a 10 ml syringe to the tube. Put 1–2 μl of virus solution on parafilm, then lower the tip of the glass pipette into the drop. While aspirating the viral particles, check with binoculars if the tip of the glass pipette is still inside the drop. Be very careful not to suck air into the glass pipette.
7. It is possible to use smaller coverslips (3 mm, 5 mm) to avoid bleeding from vessels that run through the skull near bregma

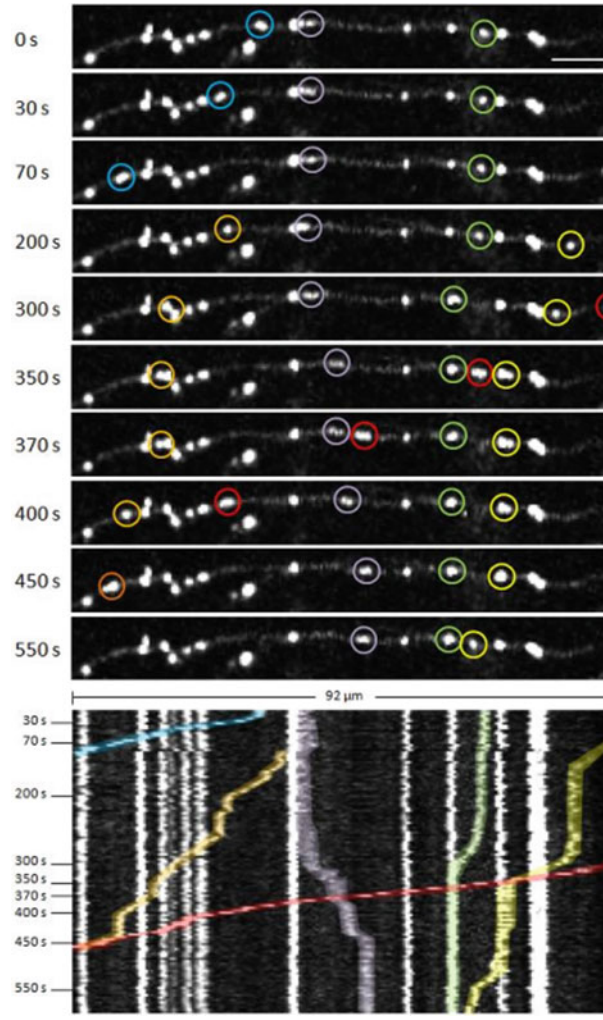

Fig. 5 Mitochondrial transport kymographs. The upper panels show snapshots of an axonal stretch at different time points during a time-lapse of 600 s, while the lower panel shows the corresponding kymograph. The time points at which the snapshots were taken are marked in the kymograph. A previously stable mitochondrion became mobile (10 s, blue). A mitochondrion underwent fission (300 s, purple), its mobile part became stationary at a different location (450 s). Two mitochondria fuse or overlap spatially (300 s, green). A mobile mitochondrion became temporarily stable (100–200 s) and temporarily fused or overlapped (350–550 s) with a stationary one before moving on (yellow). Slow mitochondrial trafficking (orange). Fast mitochondrial trafficking (red). The red and orange mitochondria fused or overlapped while being transported (450 s, dark orange). Transport occurs in anterograde and retrograde directions (compare purple to other colors). Scale bar 10 µm

(emissary veins). Smaller windows run the risk of becoming ingrown with bone.

8. Take great caution to not accidently injure the brain with the drill before removing the skull. A thin layer of bone covering the brain should remain. Check the thickness of the skull in the groove by gently pushing onto the central island of the cranial bone with a fine probe. If the island moves when lightly touched, it is ready to be removed. Drilling across bone sutures might cause excessive bleedings and should be avoided. When taking out the skull flap, this small layer of bone should be thin enough to easily be ripped apart without too much force.
9. After grabbing the skull flap, remove it while holding it as it might hurt the surface of the brain when it falls back onto it.
10. Always keep the brain surface wet after removal of the skull flap by placing a wet hemostatic gel sponge (equispon) on top of the brain surface.
11. Be very careful with the removal of the dura, the upper layer of the brain can easily be damaged. Look for small holes in the dura where you can grab the dura with the forceps #5 and strip large parts of it away.
12. When during removal of the dura a superficial capillary is torn, put a wet hemostatic gel sponge on top of the brain and wait some minutes for the bleeding to stop. Prepare small sponge blocks before and put them into buffer to soak. Be careful not to apply any pressure to the brain when putting the sponge on top of it. Do not use any cotton swabs or tissue paper on top of the brain!
13. If you see the surface of the brain getting hurt at one point and diffusely bleeding, do not clean it there anymore as you might damage it even more.
14. When implanting the large 6 mm coverslip over both hemispheres, it is easier to only remove the dura on the side of the brain where the virus has been injected.
15. Disinfect the coverslip with ethanol and clean it with lens cleaning tissue before putting it on top of the brain.
16. Before placing the coverslip onto the brain, dip one side of the coverslip in NRR or PBS and then place this side on top of the brain. Try to leave the other side of the coverslip dry, as the cement might otherwise mix with the solution and overflow the top of the cover slip.
17. If cement flows onto the coverslip, let it dry a little bit and then remove it with a scalpel or a small needle.
18. If the brain shows heavy bleeding days after the surgery, daily subcutaneous injection of 2 mg/kg dexamethasone should help.

19. Use vessels visible in the epifluorescent image for orientation and relocation to the same imaging site during every imaging session.
20. Try to use emission filters with wide bandwidths to catch as much fluorescence as possible of the labeled organelles.
21. If you encounter heavy movement artifacts during imaging, try to increase the isoflurane concentration for deeper anesthesia.
22. If you see any round fluorescent structures in the brain, make sure to check if they are autofluorescent by imaging them in multiple channels at once as these might be lipofuscine granula occurring during the aging process and not the structures of interest.
23. Very small moving particles (e.g., dense core vesicles) could only be detected after post-processing of the time-lapses after imaging. Do not give up if you cannot see organelles immediately during the imaging session.

References

1. Vitet H, Brandt V, Saudou F (2020) Traffic signaling: new functions of huntingtin and axonal transport in neurological disease. Curr Opin Neurobiol 63:122–130. https://doi.org/10.1016/j.conb.2020.04.001
2. Li XJ, Orr AL, Li S (2010) Impaired mitochondrial trafficking in Huntington's disease. Biochim Biophys Acta 1802(1):62–65. https://doi.org/10.1016/j.bbadis.2009.06.008
3. Wang ZX, Tan L, Yu JT (2015) Axonal transport defects in Alzheimer's disease. Mol Neurobiol 51(3):1309–1321. https://doi.org/10.1007/s12035-014-8810-x
4. Sorbara CD, Wagner NE, Ladwig A, Nikic I, Merkler D, Kleele T, Marinkovic P, Naumann R, Godinho L, Bareyre FM, Bishop D, Misgeld T, Kerschensteiner M (2014) Pervasive axonal transport deficits in multiple sclerosis models. Neuron 84(6):1183–1190. https://doi.org/10.1016/j.neuron.2014.11.006
5. Mattedi F, Vagnoni A (2019) Temporal control of axonal transport: the extreme case of organismal ageing. Front Cell Neurosci 13:393. https://doi.org/10.3389/fncel.2019.00393
6. Vagnoni A, Bullock SL (2016) A simple method for imaging axonal transport in aging neurons using the adult Drosophila wing. Nat Protoc 11(9):1711–1723. https://doi.org/10.1038/nprot.2016.112
7. Drerup CM, Nechiporuk AV (2016) In vivo analysis of axonal transport in zebrafish. Methods Cell Biol 131:311–329. https://doi.org/10.1016/bs.mcb.2015.06.007
8. Misgeld T, Kerschensteiner M, Bareyre FM, Burgess RW, Lichtman JW (2007) Imaging axonal transport of mitochondria in vivo. Nat Methods 4(7):559–561. https://doi.org/10.1038/nmeth1055
9. Takihara Y, Inatani M, Eto K, Inoue T, Kreymerman A, Miyake S, Ueno S, Nagaya M, Nakanishi A, Iwao K, Takamura Y, Sakamoto H, Satoh K, Kondo M, Sakamoto T, Goldberg JL, Nabekura J, Tanihara H (2015) In vivo imaging of axonal transport of mitochondria in the diseased and aged mammalian CNS. Proc Natl Acad Sci U S A 112(33):10515–10520. https://doi.org/10.1073/pnas.1509879112
10. Lewis TL Jr, Turi GF, Kwon SK, Losonczy A, Polleux F (2016) Progressive decrease of mitochondrial motility during maturation of cortical axons in vitro and in vivo. Curr Biol 26(19):2602–2608. https://doi.org/10.1016/j.cub.2016.07.064
11. Smit-Rigter L, Rajendran R, Silva CA, Spierenburg L, Groeneweg F, Ruimschotel EM, van Versendaal D, van der Togt C, Eysel UT, Heimel JA, Lohmann C, Levelt CN (2016) Mitochondrial dynamics in visual cortex are limited in vivo and not affected by axonal structural plasticity. Curr Biol 26(19):2609–2616. https://doi.org/10.1016/j.cub.2016.07.033

12. Sleigh JN, Tosolini AP, Schiavo G (2020) In vivo imaging of anterograde and retrograde axonal transport in rodent peripheral nerves. In: Babetto E (ed) Axon degeneration: methods and protocols. Springer, New York, NY, pp 271–292. https://doi.org/10.1007/978-1-0716-0585-1_20
13. Dominguez N, van Weering JRT, Borges R, Toonen RFG, Verhage M (2018) Dense-core vesicle biogenesis and exocytosis in neurons lacking chromogranins A and B. J Neurochem 144(3):241–254. https://doi.org/10.1111/jnc.14263
14. Kitay BM, McCormack R, Wang Y, Tsoulfas P, Zhai RG (2013) Mislocalization of neuronal mitochondria reveals regulation of Wallerian degeneration and NMNAT/WLD(S)-mediated axon protection independent of axonal mitochondria. Hum Mol Genet 22(8):1601–1614. https://doi.org/10.1093/hmg/ddt009
15. Honnappa S, Gouveia SM, Weisbrich A, Damberger FF, Bhavesh NS, Jawhari H, Grigoriev I, van Rijssel FJ, Buey RM, Lawera A, Jelesarov I, Winkler FK, Wuthrich K, Akhmanova A, Steinmetz MO (2009) An EB1-binding motif acts as a microtubule tip localization signal. Cell 138(2):366–376. https://doi.org/10.1016/j.cell.2009.04.065
16. Knabbe J, Nassal JP, Verhage M, Kuner T (2018) Secretory vesicle trafficking in awake and anaesthetized mice: differential speeds in axons versus synapses. J Physiol 596(16):3759–3773. https://doi.org/10.1113/JP276022
17. Protzmann J, Jaiswal A, Rohr K, Kuner T, Cambridge S, Knabbe J (2019) Acute ethanol intoxication induces preferred loss of presynaptic boutons devoid of mitochondria in vivo. bioRxiv:536334. https://doi.org/10.1101/536334
18. Schwenger DB, Kuner T (2010) Acute genetic perturbation of exocyst function in the rat calyx of held impedes structural maturation, but spares synaptic transmission. Eur J Neurosci 32(6):974–984. https://doi.org/10.1111/j.1460-9568.2010.07391.x
19. Schindelin J, Arganda-Carreras I, Frise E, Kaynig V, Longair M, Pietzsch T, Preibisch S, Rueden C, Saalfeld S, Schmid B, Tinevez JY, White DJ, Hartenstein V, Eliceiri K, Tomancak P, Cardona A (2012) Fiji: an open-source platform for biological-image analysis. Nat Methods 9(7):676–682. https://doi.org/10.1038/nmeth.2019
20. Dubbs A, Guevara J, Yuste R (2016) Moco: fast motion correction for calcium imaging. Front Neuroinform 10:6. https://doi.org/10.3389/fninf.2016.00006
21. Holtmaat A, Bonhoeffer T, Chow DK, Chuckowree J, De Paola V, Hofer SB, Hubener M, Keck T, Knott G, Lee WC, Mostany R, Mrsic-Flogel TD, Nedivi E, Portera-Cailliau C, Svoboda K, Trachtenberg JT, Wilbrecht L (2009) Long-term, high-resolution imaging in the mouse neocortex through a chronic cranial window. Nat Protoc 4(8):1128–1144. https://doi.org/10.1038/nprot.2009.89

Chapter 6

Studying Axonal Transport in the Brain by Manganese-Enhanced Magnetic Resonance Imaging (MEMRI)

Elaine L. Bearer, Xiaowei Zhang, and Russell E. Jacobs

Abstract

From the earliest notions of dynamic movements within the cell by Leeuwenhoek, intracellular transport in eukaryotes has been primarily explored by optical imaging. The giant axon of the squid became a prime experimental model for imaging transport due to its size, optical transparency, and physiological robustness. Even the biochemical basis of transport was identified using optical assays based on video microscopy of fractionated squid axoplasm. Discoveries about the dynamics and molecular components of the intracellular transport system continued in many model organisms that afforded experimental systems for optical imaging. Yet whether these experimental systems reflected a valid picture of axonal transport in the opaque mammalian brain was unknown.

Magnetic resonance imaging (MRI) provides a non-destructive approach to peer into opaque tissues like the brain. The paramagnetic ion, manganese (MnII), gives a hyperintense signal in T_1 weighted MRI that can serve as a marker for axonal transport. Mn(II) enters active neurons via voltage-gated calcium channels and is transported via microtubule motors down their axons by fast axonal transport. Clearance of Mn(II) is slow. Scanning live animals at successive time points reveals the dynamics of Mn(II) transport by detecting Mn(II)-induced intensity increases or accumulations along a known fiber tract, such as the optic nerve or hippocampal-forebrain projections. Mn(II)-based tract tracing also reveals projections even when not in fiber bundles, such as projections in the olfactory system or from medial prefrontal cortex into midbrain and brain stem. The rate of Mn(II) accumulation, detected as increased signal intensity by MR, serves as a proxy for transport rates. Here we describe the method for measuring transport rates and projections by mangeses-enhanced magnetic resonance imaging, MEMRI.

Key words Axonal transport, Intracellular transport, Stereotactic injection, Micropipettes, Manganese, Magnetic resonance imaging (MRI), Neuronal projections, Tract tracing, Kinesin, Statistical parametric mapping, Time-lapse MRI, T_1-weighted MRI

1 Introduction

Manganese as a contrast agent for magnetic resonance imaging (MRI) was first suggested by Nobel laureate, Paul Lauterbur, in the 1970s [1, 2]. Alan Korestsky and his group followed up on

Alessio Vagnoni (ed.), *Axonal Transport: Methods and Protocols*,
Methods in Molecular Biology, vol. 2431, https://doi.org/10.1007/978-1-0716-1990-2_6,
© The Author(s), under exclusive license to Springer Science+Business Media, LLC, part of Springer Nature 2022

these suggestions with two seminal papers describing the use of manganese-enhancement in MRI as a biomarker, first for neural activity [3, 4] and secondly for neuronal tract tracing [5]. "Tract tracing" refers to a contrast agent traveling within a neuron from one location to another, thereby delineating the projection of that neuron's axons. Tract tracing has long been used with histologic reagents, such as horseradish peroxidase or fluorescent dextrans, that trace neuronal projections as witnessed by optical microscopy [6, 7]. Obviously, these exogenous tract tracers rely on endogenous axonal transport systems to travel within axons and thereby trace their projections.

Early on, investigators realized that Mn(II) enters active neurons and travels within them to distant locations and thus could be used as a tract tracer in living brains detected by MRI [5, 8, 9]. Initially, investigators developed a manganese-based tract-tracing technique in well-characterized systems, particularly the optic nerve [5, 10, 11] and olfactory system [9]. These technical studies revealed that Mn(II) is a trans-synaptic tracer dependent on neural activity for distal accumulation [10, 12]. Technical development was succeeded by applications of MEMRI tract tracing to observe connections and projections within the central nervous system, such as projections from the amygdala to the hippocampus [13], and the intricate tracing of the songbird's vocal control and the plasticity of songbird learning centers [14–21]. More recently, Mn(II)-based tract tracing revealed that functional projections from the medial prefrontal cortex into the deeper brain are altered by deregulation of the serotonergic, dopaminergic, or noradrenergic systems [22–24]. Most recently, tract tracing in the mouse hippocampal-forebrain projections revealed the effects of genetic alterations of amyloid precursor protein (APP) on transport dynamics and destination within this important memory circuit [25, 26].

Knowledge of the molecular mechanisms of axonal transport began with discovery of the first microtubule-based motor, kinesin, from the giant axon of the squid [27]. Much subsequent work focused on mechanistic descriptions of this motor—protein conformation of the force-producing "head," how it moves along the microtubule at the molecular level, whether it is conserved across species, and what the rates of cargo transport are. These studies ultimately resulted in identification of numerous members of a large kinesin family [28]. Of these, only three appear to be enriched in axons: Kif1, Kif2, and Kif5. These studies were mainly carried out in vitro.

Despite meticulous molecular studies, how axonal transport works within the mammalian brain remained an open question until time-lapse MEMRI was developed to address it [10, 29]. Unlike in vitro optical assays, where motility of individual particles can be tracked, MEMRI is more similar to the radioactive

tracer studies [30–33] that detect changes over time rather than individual cargo movements. For MEMRI, intensity changes likely represent a Mn(II) being carried in a mixture of different subcellular components. Thus only an average transport rate and not an instantaneous velocity can be measured, similar to the measurements made originally by autoradiography of radioactive tracers, as performed in goldfish optic nerve [31]. A limitation for any MR imaging strategy is its inherently low signal-to-noise ratio (SNR), which determines the length of time needed to acquire an image. Proton MR signal intensity depends on the number of water molecular in each voxel, which influences the resolution. Witnessing dynamic processes is especially challenging since the animal must be kept alive and still within the scanner, limiting the amount of time that an image can be safely captured. Fortunately, Mn (II) produces a robust signal at safe doses [34], which can overcome this limitation to some extent [35].

Hence, using a tract-tracing protocol coupled with time-lapse MEMRI, we were first able to follow Mn(II) progress along the optic nerve in 3D after $MnCl_2$ injection into the vitreous of the eye by capturing a slab image across the optic tract at 6 min intervals [10]. By reducing the field of view and deploying Mn(II), enough intensity change was collected to compare normal Mn(II) transport in wild-type optic nerve to that of mice deleted in one of kinesin-1 light chains (KLC-1). We reported that conventional kinesin is a participant but not essential to neuronal transport of Mn(II) in the optic tract [10]. Subsequently we used intracerebral stereotactic injection of Mn(II) to follow transport dynamics in fiber bundles of hippocampal-forebrain projections [25, 26, 29, 36, 37], and to projections not bundled, such as those emanating from the medial prefrontal cortex [22–24, 38]. Differing rates of transport were inferred from mapping and measuring distal accumulations of Mn (II)-dependent MR signal over time. Resulting images are quantitatively evaluated for statistically significant intensity changes by voxel-wise statistical parametric mapping [39–42] and region-of-interest intensity measurements [10, 36, 37].

Here we describe our method to perform MEMRI for either tract tracing or axonal transport dynamics in the mouse's living brain.

2 Materials

2.1 Solutions

All solutions should be made in double-distilled sterilized water, and all pipettes and tubes should be autoclaved before use. It is important to avoid contamination by either pathogens or bacterial wall lipopolysaccharides (LPS) that induce inflammatory reactions (*see* **Note 1**).

2.1.1 Materials and Supplies

1. $MnCl_2$-tetrahydrate.
2. Dextran-tetramethylrhodamine-3000 k-lysine fixable (RDA) (ThermoFisher Catalog number D3308).
3. Distilled water, autoclaved.
4. 10× sterile phosphate buffered saline, pH 7.4.
5. Red food coloring.
6. 5 μm syringe filters.
7. 10 mL conical tubes, sterilized.
8. 1 mL Eppendorf tubes, sterilized.
9. 0.6 mL Eppendorf tubes, sterilized.
10. Pipetters and sterilized pipette tips.
11. Weigh balance and weigh boats.
12. Small metal spatulas.

2.1.2 Solution Composition

1. For ocular injection: Mn(II) stock solution: $MnCl_2$–$4H_2O$ solution: The concentration of the stock depends on the dose to be used. Different stock concentrations of $MnCl_2$ that are typically used are: 0.2, 0.4, 0.6, 0.8, 1.0, and 1.2 M $MnCl_2$. Prepare by dissolving appropriate amount of $MnCl_2$–$4H_2O$ in 10 mL sterilized (double distilled) H_2O. See Table 1 for weights to add for each molarity. These stock solutions are prepared in 10 mL portions and stored at −80 °C where they are stable for at least a year (*see* **Note 1**).
2. For intracerebral injection, $MnCl_2$ concentrations in the injectate can range from 200 to 600 mM. Start with a 2× solution of $MnCl_2$ as described above and dilute half-half with RDA solution (*see* **Note 2**).
3. Rhodamine-dextran-amine (RDA) solution: Resuspend 10 mg of dextran-tetramethylrhodamine-3000 k-lysine fixable (RDA) (ThermoFisher Catalog number D3308) in 1 mL of sterile H_2O to reach a 10 mg/mL solution and prepare labeled tubes with 10 μL aliquots. Store at −20 °C. Typically the entire vial of dry RDA from the vendor is resuspended in the appropriate volume of sterile H_2O for a 10 mg/mL final stock solution.

2.2 Preparation of Injection Micropipettes

1. Quartz capillary tubes: Outer diameter ~1 mm and internal diameter ~0.7 mm, 100 mm length (Drummond 50 μL microcaps Cat # 1-000-0500 work well).
2. 4 × 20 mL glass bottles.
3. 20 mL 6N HCl.
4. 100 mL distilled H_2O, autoclaved.

Table 1
$MnCl_2$ solutions

Molarity	Amount of $MnCl_2$–$4H_2O$ (MW = 197.91 g/mol) in 10 mL H_2O
400 mM	0.79 g
600 mM	1.19 g
800 mM	1.58 g
1 M	1.98 g
1.2 M	2.36 g

5. 20 mL Hexamethyldisiloxane (HMDS, 10% in Chloroform). Make this up in a fume hood and store separate from corrosives in the fume hood. Check your lab's safety manual for storage of flammables.
6. Hamilton gastight 1.0 μL with 19-gauge needle to fit the tubing (https://www.hamiltoncompany.com/laboratory-products/product-specs/51867).
7. Tubing: 0.01"ID PEEKTM (polyetheretherketone) tubing to connect the capillary tube to the Hamilton syringe.
8. Plastic petri dish with putty for storage of micropipettes.
9. Micropipette puller: We use P-2000 from Sutter Instruments (Novato, CA).
10. Microsyringe Pump: We use World Precision Instruments Inc. (Sarasota, Florida).
11. Silicon oil #1 (Dimethyl polysiloxane, DMPS-1C) or Fluorinert oil—type FC-70. Do not mix these oils. Silicon oil is used to fill the tubing.
12. Silicon Oil #2. (Octamethyltrisiloxane, viscosity 1 cSt) which is used to cap the Mn(II)/RDA solution in the micropipette which controls volume of injectate.
13. Dissecting microscope with eyepiece reticle to calibrate the micropipettes. The reticle should have a 10–12 mm scale (12 mm is better), divided in 100–120 divisions.

2.3 For Intravitreal Eye Injections

Materials and supplies:

1. A fine steel needle (30 gauge, 0.3 mm) to bore into the sclera.
2. A glass micropipette with tip diameter <10 μm, calibrated to inject 125–250 μL.
3. Tubing to fit the blunt end of the capillary tube/micropipette and connect it to the Hamilton syringe needle.

4. Microinstrument holder to connect the micropipette to the tubing to the Hamilton syringe, or to a tail-vein catheter tip (SAI Inc., IL, USA) for intravitreal injections.
5. Anesthesia: 1.5% isoflurane delivered through a nose cone; or 7.5 mg ketamine plus 5 mg xylazine per kg, intraperitoneal.
6. Stereotaxic head frame. We used the Kopf Instruments head frame (Tujunga, CA). The frame should have a bar to hold the teeth and ear stabilizers that pin the bone behind the ears.
7. Ophthalmic gel.

2.4 For Intracerebral Stereotaxic Injections

Materials and supplies in addition to those needed for preparation and calibration of the micropipettes and eye injections:

1. Leica Angle Two small animal stereotaxic injection apparatus with atlas integration. This instrument must be aligned before commencing the procedure and whenever changing the probe. For details about the alignment procedure, please refer the Angle Two User's Manual at https://www.leicabiosystems.com/research/neuroscience/products/leica-angle-two/downloads/.

   This device does not calibrate the micropipette volumes but does use a digital atlas to position the injection site in the mouse brain accurately and reproducibly.
2. Scalpel, sterilized.
3. Forceps, sterilized.
4. Phosphate buffered saline, autoclaved and sterile.
5. Cotton swabs, sterile.
6. Hand drill on the stereotactic apparatus (cleaned and sterilized) (this may be a component of the Angle Two).
7. Betadine solution (10% providone-iodine), or cyclohexadine, and 75% alcohol solution.
8. Glass micropipette with tip diameter <4 μm, calibrated to inject 3–5 nL.
9. Heparin saline (5 units/mL).
10. Isoflurane.
11. Ketoprofen of buprenorphine for analgesia if planning survival afterwards.
12. Ophthalmic ointment.
13. Bupivacaine.
14. Bone wax.
15. Surgical glue.
16. Pillow/warming pad.
17. Lactated Ringer's solution and 1 mL syringe with 19-gauge needle.

3 Method

3.1 Preparation of Injection Micropipettes

1. Immerse 10 capillary tubes in the 20 mL of 6 N HCL_2 contained in glass tube for 30 min in room temperature. Use the Hamilton syringe to flush the capillaries 2–3 times with 6 N HCl_2.
2. Move the capillary tubes to another glass tube and flush them 3 times with sterile H_2O.
3. Move the washed capillary tubes to another glass tube. Using the Hamilton syringe from the slowly pull 20 mL of HMDS (10% in Chloroform) into tube to make sure the capillaries filled with the solution, if there is bubble inside tube, flush it with a syringe. **Note**: This step must be performed in a fume hood. The chloroform is toxic.
4. Move the capillaries to the fourth glass tube and dry them with blooming air. **Note:** The inside of the capillary tubes should be dry, otherwise a wet condition will impair pulling.
5. Store washed micropipettes in the Petri dish lined up on strips of modeling clay or putty and covered in a dry place. These can be prepared in advance.
6. Pull a fine tip on each capillary tube. The micropipettes are fashioned from washed 1 mm OD quartz capillary that are pulled to approximately 40 μm internal diameter bore near the tip with a micropipette puller.

3.2 Micropipette Calibration

1. Calibrate each pipette by drawing a 4 mm length of saline or water into the end of the micropipette using a microsyringe pump with digital display driving a 1.0 μL Hamilton syringe fitted to the micropipette via mineral oil-filled 0.01"ID PEEKTM (polyetheretherketone) tubing (Upchurch Scientific Inc, Oak Harbor, WA) under observation with the reticle on a dissecting scope (Figs. 1, 2).
2. Gently expel the solution into a puddle of oil on a glass slide and measure the diameter of the droplet with the reticle. See Tables 2 and 3 for correlation of diameter to volume. Correlate the length of solution in the pipette with the size of the droplet it makes when expelled (Fig. 1).

3.3 Prepare Injectate

3.3.1 For Eye Injection

1. In a 1 mL sterilized Eppendorf tube, dilute 1 M $MnCl_2$ stock to 0.25 mM by pipetting 0.25 μL into 0.75 μL distilled H_2O.
2. Pass through a 5 μm filter. See Table 4 for typical concentrations and volumes used for intravitreal injections. We demonstrated that 0.125–0.25 μL of 200 mM aqueous Mn(II) had minimal effects on visual evoked potentials and was sufficient to produce measurable intensity changes by T1-weighted MR (*see* **Note 2**).

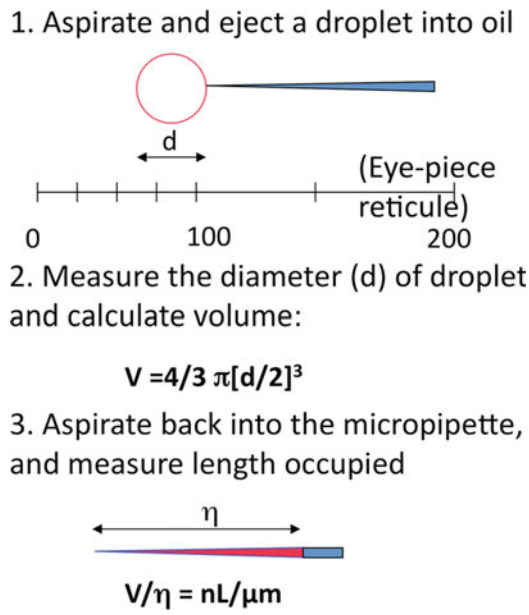

Fig. 1 Calibrating micropipettes. Aspirate a small amount of aqueous solution and eject a droplet into a puddle of silicon oil on the microscope stage. Using the ruler in the reticle of the microscope eyepiece, measure the diameter (d) of the droplet and calculate its volume. Aspirate the droplet back into the micropipette and measure the length of tubing it occupies. Make a note of these measurements for each micropipette

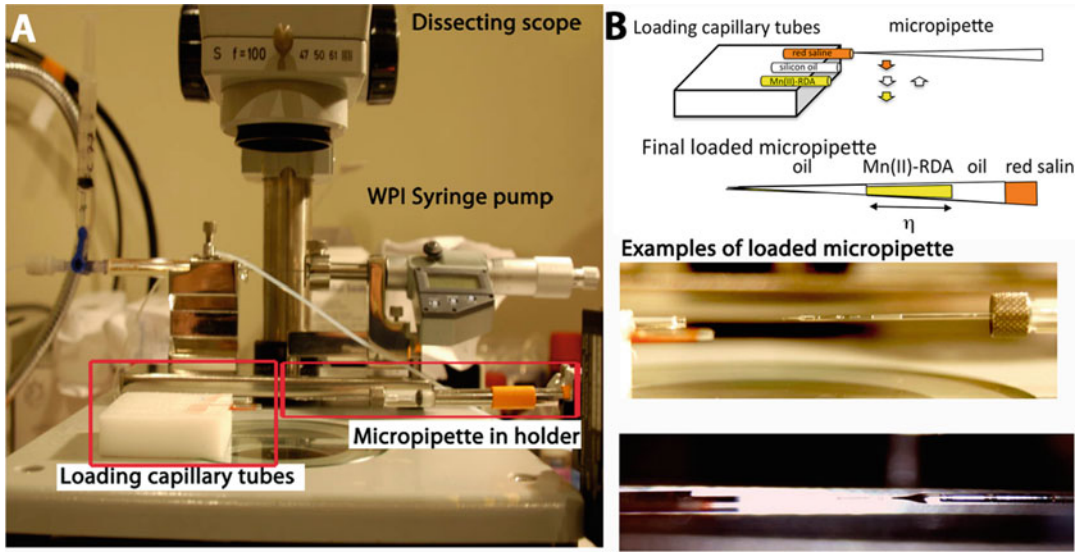

Fig. 2 Loading micropipettes. (**a**) Setup of the dissecting scope stage for loading the micropipettes. (**b**) Diagram of the procedure and examples of filled micropipettes. Create three loading capillaries tubes, one filled with red-food-color/saline; a second with $MnCl_2$-RDA; and the third with silicon oil. Under the dissecting microscope sequentially add first the red solution then the silicon oil, then the exact amount of $MnCl_2$ solution that is equivalent to 3–5 nL according to the reticle. Finally cap the tip with another bolus of silicon oil

Table 2
Comparison of the volume calculations by oil drop sphere and by capillary ID and length

Eye piece units	$MnCl_2$ drop in Oil (diameter in μm)	Volume (nL)
5		
10	50	**0.065**
15	62.5	**0.128**
20	75	**0.221**
30	100	**0.524**
40	130	**1.15**
50	162.5	**2.247**
60	200	**4.18**
70	250	**8.18**

Volume calculation by oil drop sphere (Nanoliter vol = $(1/6)\pi d^3$)

Table 3
Examples of volume calculation per capillary length (20 units = 1 mm)

Eye piece Units	Capillary ID (μm)	Capillary radius	Height (mm)	Volume (nL)
5				
10	12.5	0.0062	0.5	6.14E-05
15	15	0.0075	0.75	0.133
20	20	0.01	1	0.314
30	25	0.0125	1.5	0.7366
40	30	0.015	2	1.14
50	35	0.0175	2.5	2.401
60	45	0.0225	3	4.77
70	55	0.0275	3.5	8.31

3.3.2 For Intracerebral Injection

For 200 mM $MnCl_2$ with 0.5 mg/mL RDA in PBS, pH 7.4 (*see* **Note 3**).

1. Make 400 mM $MnCl_2$ in PBS. In a 1.5 mL Eppendorf, add 0.5 mL 800 mM $MnCl_2$, 0.1 mL 10× PBS, and 0.4 mL H_2O.
2. Check the pH and adjust, if necessary, with phosphoric acid or sodium hydroxide in 1–2 μL increments.
3. Dilute 10 mg/mL RDA stock to 1 mg/mL by adding 10 μL of 10× PBS and 80 μL of H_2O to 10 μL of thawed aliquot from stock. This makes 100 μL volume.

Table 4
Concentrations of MnC_{l2} for intravitreal injections for optic nerve imaging

Stock	Amount injected/time	Check for	Reference
0.8 mmol in 1 mL H_2O	1–2 μL, slowly	MRI immediately post-injection	Pautler et al. [5]
1 M $MnCl_2$ in H_2O	0.1 μL, over 5 min, leave needle in place for 15 min	Pupillary light response	Watanabe et al. [1]
200 mM $MnCl_2$ in H_2O	0.125–0.5 μL over 3 min	Visual evoked potentials; MR immediately following	Bearer et al. [10, 25, 37]
200 mM $MnCl_2$ in H_2O	0.250 μL,	MRI immediately post-injection	Gallagher et al. [26]

4. Vortex thoroughly to ensure uniform suspension.
5. Mix 50 μL of 1 mg/mL RDA with 50 μL of 400 mM $MnCl_2$ stock solution to obtain 200 mM $MnCl_2$ with 0.5 mg/mL 3K RDA.

If higher concentrations of Mn(II) are desired, select an aqueous $MnCl_2$ stock solution that is 4× the required final concentration, bring to 1× PBS and then mix 1:1 with RDA.

You will plan to inject 3–5 nL (*see* **Note 4**).

3.4 Load the Injection Micropipette

The tubing in the injection system should be filled with Pure Silicon Fluid (100% Dimethyl Polysiloxane, viscosity 5 cSt) with no air bubbles.

3.4.1 For Intravitreal Injection

Mn(II) solution does not contain RDA and is loaded directly into the micropipette or the tail-vein catheter tip in the injection apparatus. Alternatively, this injection can be performed manually.

3.4.2 For Intracerebral Injection

The micropipette contains a series of oil, saline with food coloring and Mn(II)-RDA solutions (*see* Fig. 2). The micropipette loading procedure described below ensures that a precise amount of Mn (II) solution will be injected.

1. Create three "loading capillary tubes."
2. Block the end of three cleaned capillary tubes with putty or modeling clay.
3. Using the Hamilton syringe fill each capillary tube with the following:
   (a) Pure Silicon Fluid (Octamethyltrisiloxane, viscosity 1 cSt).
   (b) Mn(II)-RDA solution (the tracers).

(c) Saline with a drop of red food coloring which function as the moving mark during the injection.

Tape the three tubes side-by-side on the plastic block on the dissecting scope platform, pointing the open end across the field of view (*see* Fig. 2b).

4. Load the micropipette by withdrawing solutions from the capillary tube.

This should be done under direct observation in the microscope. Mount the micropipette onto the injection system and secure the holder to a micromanipulator so that the micropipette is aimed at the openings of the three loading capillary tubes. Advance the micropipette towards the loading tubes.

(a) Adjust syringe meter reading to 0.0000 units.

(b) First, enter the loading tube with the saline-red solution and draw up 20 units on the monitor mark (20 units). Withdraw the micropipette from this capillary tube.

(c) Next, insert the micropipette into the 1cSt Pure Silicon Fluid tube and draw up 10 units of oil to isolate red saline from $MnCl_2$ solution. Withdraw the micropipette and re-adjust syringe meter reading to 0.0000 units.

(d) Then insert into Mn(II)-RDA solution and withdraw desired amount previously determined by your calibration under observation in the microscope using the reticle eyepiece and your calibration of that particular micropipette to determine exact amount to load. You are aiming for 3–5 nL volume of Mn(II)-RDA. Withdraw the micropipette.

(e) Finally, return to the first capillary tube with silicon oil and draw up 10 units of 1cSt Pure Silicon Fluid to fill the tip of the micropipette. This oil limits any leakage of tracer along the injection track during insertion of the micropipette into the brain, helps to identify the injection site subsequently, and probably reduces clotting during micropipette insertion into the brain.

3.5 Anesthetize Mouse and Place in the Stereotaxic Apparatus

The following is a brief description for installing the mouse into the Angle Two stereotactic injection apparatus. For more detailed description, refer to the Angle Two manual (https://www.leicabiosystems.com/research/neuroscience/products/leica-angle-two/).

1. Mouse is put down with 1.5% isoflurane in an anesthesia chamber.
2. Pull out the incisor bar from anesthesia chamber, hook the incisor teeth over the incisor bar and push the nose down and

Fig. 3 Infusion pump and micropipette holder. Various infusion pumps are possible. We used the Harvard Apparatus. It is important that the pump can reproducibly delivery 3–10 nL volumes at rate of 1–2 nL/min [37]

then slide the bar back until the nose is inside the anesthesia chamber.

3. Place both side ear bars 2 mm front ear canals and against the lower jaws, and affix both ear bars in the same positions. **Note:** The animal's head must be securely and symmetrically affixed in the stereotaxic instrument, reproducibly aligned with the movement axes of the manipulator section.
4. Shave the head with a scalpel and sterilize the skin with Betadine solution (10% providone-iodine) and 75% alcohol solution.
5. Infuse 1 mg/kg 0.25% bupivacaine, which lasts 48–72 h, along the skin margin of the scalp prior to surgery (Fig. 3).
6. Pull the skin tight by pressing caudally and cut a small midline incision with a scalpel. Retract the skin with forceps. Scrape the scalp membranes away from the midline with forceps and fully expose the bone. The midline, bregma and lambda should be visible on the skull (Fig. 4). Swab off any blood with a cotton swab and wetted with saline.
7. Install the hand-drill on the stereotaxic apparatus.
8. Touch the drill bit down at Bregma and at lambda and take a vertical reading on the dorsal-ventral location at each point. By trial and error, adjust the vertical position of the incisor bar until bregma and lambda get the same vertical reading. This is the "Skull Flat" reference plane and is very important to tip the underlying brain according to the atlas.
9. Drill a hole at the place above where you plan to inject. For CA3 of the hippocampus, this is 3.2 mm (midline), −4.1 mm (bregma); for medial prefrontal cortex, 0.8 mm (midline), 1.9 mm (bregma). Other locations can also be selected. It is

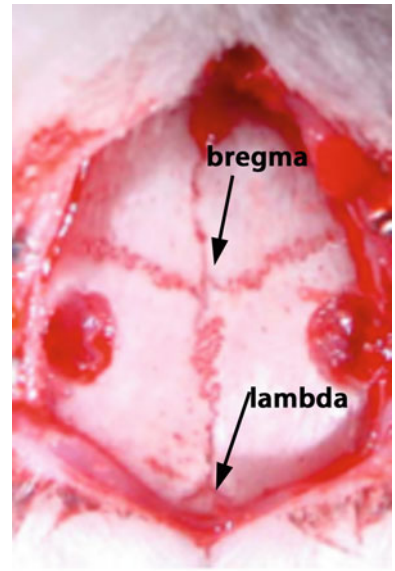

Fig. 4 Surgical preparation. Mouse head with the scalp laid back. Bregma and lambda are labeled. It is important for these two locations be level (same vertical distance) for the deeper structures in the brain to correlate with the atlas

best to make as small a hole in the skull as possible and position this hole over the brain location of interest.

Click “set target”

Find the site to be injected in the Atlas

Click “zero Bregma”

Touch the drill down at Bregma

Click “zero Bregma"

Click “to target”

Move the hand-drill to the target site. Under the microscopy move the drill down and touch the drill tip to the surface of the skull, slowly turn the drill and make a hole by adding a light pressure on the drill with left finger. Stop turning as soon as the CSF can be seen. The skull is very thin and the space between skull and brain is very small.

10. Check that the skull is still “Flat”—Bregma and lambda at the same vertical position.

3.6 Inject

3.6.1 For Intravitreal Injection

1. Induce and maintain anesthesia with 1.5% isoflurane in room air.
2. With a fine steel needle (30 gauge, 0.3 mm) bore a hole in the sclera through which the Mn(II) solution is then injected.

3. Insert the micropipette or tail-vein catheter through the hole in the sclera. Using the WPI pump, inject slowly over 3–5 min, and leave the micropipette in the eye for 5–15 min after completing the injection. Maintain the animal under anesthesia, put ophthalmic gel over both eyes, and mount the animal into the probe support for the scanner. Scanning should begin within 30 min of the injection and reviewed to confirm integrity of the eye. At the conclusion of this initial scan, awaken the mouse. Check pupillary constriction (shine a light and watch the pupil contract) to confirm that the eye has not been compromised.

3.6.2 For Intracerebral Injection

1. Maintain the mouse under anesthesia in the stereotaxic frame after peeling back the scalp to bare the skull.
2. Install the MnCl2-RDA loaded micropipette on the stereotaxic instrument.
3. Under the microscope move the micropipette tip down and very gently touch the Bregma to instruct the stereotaxic apparatus.

   Click “set target”

   Click “zero Bregma”

   Click “zero Bregma”

   Click “to target”
4. Move the micropipette back up and dip the tip in an Eppendorf tube containing heparin saline (5 units/mL). Swab off any blood in the drilled hole of the skull with heparin saline using a sterile cotton swab.
5. Move the micropipette to the target site. Under the microscope move the micropipette down to the surface of the hole in the skull, and then slowly lower the micropipette into the brain until reaching the desired depth (dorsal-ventral). For CA3 of hippocampus, −3.4 mm (down), and for medial prefrontal cortex, −1.8 mm (down). Other locations can be programmed into the stereotactic apparatus. By following the atlas in the Angle Two stereotaxic apparatus, these and other locations can be selected. Alternatively, if a computerized injector apparatus with pre-programmed locations, the online Paxinos mouse brain atlas (http://labs.gaidi.ca/mouse-brain-atlas) can help determine precise coordinates to target specific brain structures.

   Slowly screw in the syringe until 0.000 units showed in reading meter and continue to screw in the syringe with additional pressure (0.5 units). Under the microscope, monitor the infusion by observing the flow of saline-food red mark in the capillary.

Note: Infusion is usually slow. It is necessary to wait for at least 10 min after finishing the injection before withdrawing the micropipette from the brain.

Slowly (1 min/mm) withdraw the micropipette and check whether the Mn(II)-RDA has been completely infused by examining the micropipette tip in the microscope. The meniscus between the Mn(II) aqueous solution and the silicon oil should be apparent if any is left in the micropipette.

6. Repair the skull with bone wax. Glue the skin incision back together with surgical glue.

   Inject the mouse with glycopyrrolate (0.02 mg/kg) subcutaneously and give lactated Ringer's solution at 10 mL/kg/h intraperitoneal. Maintain anesthesia (1.5% isoflurane in room air) and place in the MR scanner (*see* **Note 4**).

7. Monitor for infection of the wound or brain, for wound dehiscence of the surgery site, or for unexpected reaction to the procedure. Manifestations could be decreased activity, lethargy, inflammation, or even pus from the wound and would be followed by seeking advice from the attending veterinarian.

4 Imaging and Data Collection

Many different hardware options are available for mouse brain imaging. Mn(II) enhancement has been detected in scanners with B-fields ranging from 1.5 to 11.7T. Some have a vertical bore and some horizontal. The mouse holder should have the appropriate dimensions to fit into the radiofrequency (RF) coil within the scanner bore. We have experience with the Bruker 11.7T 89 mm vertical bore BioSpin Avance DRX500 scanner, the Bruker 7T 40-cm horizontal bore, with a 11.4 cm (inner diameter) 660 mT/m gradient scanner, and the MR Solutions Powerscan Preclinical MRI System 7.0T horizontal 24 cm bore scanner. The 11.7T scanner equipped with a Micro2.5 gradient system was used to acquire in vivo mouse brain images with a 35 mm linear birdcage RF coil.

The mouse holder, RF coils, and gradients are all unique to each scanner. Provided below are the setting we used in the 11.7T scanner and some tips for optimizing scanning parameters when using other filed strengths, RF coils, and gradients. The best whole head images are likely to be captured with a whole heard volume coil for brain-wide imaging with a diameter of 20 mm around the head, and 35 mm (Fig. 5). The mouse holder should provide for monitoring of physiologic measurements of body temperature, respirations and heart rate, as well as a nose cone for anesthesia and a heating pad.

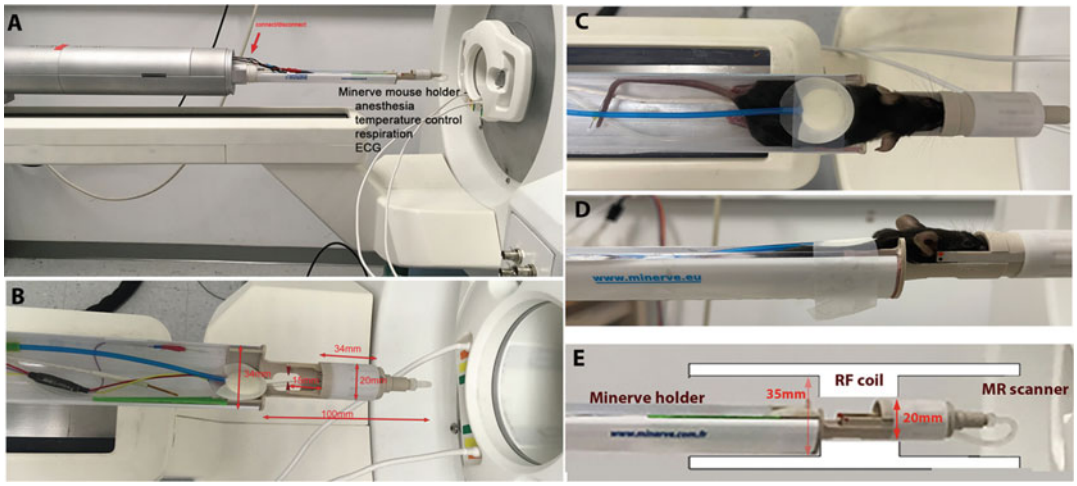

Fig. 5 Mouse holder and RF coil dimensions. Shown is an example of a mouse holder for the horizontal 7T MR scanner with a 24 cm bore. (**a**) The Minerva mouse holder includes a nose cone for anesthesia, temperature control pad, and monitors for respiration and electrocardiogram. Connections are indicated with the red arrow. (**b**) The dimensions of the holder show 1000 mm length that inserts into the RF coil inside the scanner, 20 mm diameter × 34 mm length of the nose cone, 15 mm from the cone to the ear bars to stabilize the head, and 34 cm internal diameter for the mouse body. (**c** and **d**) A C57B//6 mouse positioned in the holder viewed from top (**c**) and side (**d**). Tape encircles the mouse/temperature pad/holder. (**e**) Diagram of the RF coil dimensions showing how the holder fits within the scanner. Note that the RF coil around the head has an internal 20 mm diameter

4.1 Inserting the Animal into the Scanner

This should be done as soon as possible after completion of the $MnCl_2$ injection.

1. Place the anesthetized mouse in the holder. Use tape to secure the body. Connect the physiologic monitoring devices and ensure that the isoflurane is being delivered into the nose cone. Keep the mouse ventilated via the nose cone with 1–1.5% isoflurane in room air.
2. Slide the holder into the MR Scanner.
3. Maintain body temperature at 37.5 °C using the heating pad. Monitor physiology (*see* **Note 5**).

4.2 Scanning Parameters

We have used a variety of scanning parameters in the 11.7T Bruker, and these differ with those in our two other 7T scanners (*see* Table 5).

4.2.1 Optic Nerve Transport Rates from Time-Lapse MR After Intravitreal Injection [10]

In this case, no more than 0.125 μL of 50 mM $MnCl_2$ in buffered saline pH 7.4 is injected intravitreal, i.e. behind the lens. Check the pupil for light response.

1. Time-lapse MRI: Capture slab images of the optic tract (0.45 cm thick slab with 32 axial slices) at 6-min intervals for 2 h (20 images total) beginning 30 min post-injection.

Table 5
Examples of parameters for Mn(II) image optimization

Scanner	Sequence	TR	TE	Flip angle	Rare factor	Number of averages	Scan time
11.7T Bruker	3D FLASH	25 ms	5 ms	20	na	2	34 min
7T Bruker	3D FLASH	25 ms	5 ms	30	na	4	46 min
	3D FLASH	15 ms	2.8 ms	30	na	8	45 min
	3D RARE	250 ms	12 ms	90	4	2	23 min
7T MR Solutions	FSE	300 ms	26 ms	90	na	3	80 min

FLASH fast low angle shot, *RARE* rapid acquisition with relaxation enhancement, *FSE1* fast or turbospin echo, *TR* relaxation time, *TE* echo time, *CNR* SNR+ Mn(II) minus SNR no Mn(II), where SNR is mean intensity divided by standard deviation of the noise.

2. Adjust the field of view to encompass the optic nerves from the eyes to the optic chiasm. The optic nerve dips down towards the chiasm and then up afterwards. Hence you cannot capture its full length in this slab. A larger slab may need longer acquisition for sufficient contrast.
3. 3D RARE sequence: TR/TE 300/5 ms, 4 echoes, 1 average.
4. FOV = $1.5^2 \times 0.45$ cm, and $128^2 \times 32$ matrix size for a voxel size of $140 \times 110 \times 140$ μm.

4.2.2 Whole Brain Images After Stereotactic Mn(II) Injection

In this case, rates along axons are difficult to calculate because of the complexity of the projections. Instead, rates of Mn (II) accumulations along the known projections from the injection site are measured. Projections from CA3 of the hippocampus presented an especially attractive target to measure transport by MEMRI, as they coalesce into a robust fiber bundle that courses into the fimbria of the hippocampus and down the fornix through septal regions to mammillary bodies. Retrograde transport of nerve growth factor from septal nuclei back up to the hippocampus via the fornix has been studied by radiographic tracers [43]. It is critical to collect a pre-injection image without Mn(II) contrast prior to injections.

4.2.3 For Measuring Transport in the Hippocampal Projections

1. Collect a pre-injection image using the same parameters as will be used for alignments of the post-Mn-injection images.
2. Perform the stereotactic injection as described above.
3. Place the anesthetized mouse in the scanner and capture an image within 30 min of the injection. This image will

determine that the injection site is placed as expected. The high concentration of Mn(II) in the injection site will appear as a small dark sphere within the halo of hyperintensity due to the Mn(II) in the image.

4. Remove the mouse from the scanner, monitor its recovery in a fresh cage. It can be returned to the home cage once it walks around freely without wobbling, typically 30 min after cessation of the isoflurane.
5. Repeat imaging at successive time points, such as 6 h and 24 h, or 4, 8 and 24 h. In between sessions, the mouse should be freely moving in its home cage with ad libitum water and food.

4.2.4 Examples of Imaging Parameters in 11.7T Bruker for Whole Brain MEMRI

1. 3D RARE imaging sequence with RARE factor of 4, 4 averages, TR/TEeff = 300 ms/21 ms; matrix size of 256 × 160 × 128; FOV 23 mm × 14.4 mmÅ~11.5 mm; yielding 90 μm isotropic voxels with 102 min scan time [25, 29, 36].
2. 3D RARE imaging sequence with RARE factor of 4, 4 averages, TR/TEeff = 250 ms/12 ms; matrix size of 160 × 128 × 88; FOV 16 mm × 12.8 mm × 8.8 mm; yielding 100 μm isotropic voxels with a 46 min scan time [26, 37].
3. 3D RARE imaging sequence with RARE factor of 4, 4 averages, TR/TEeff = 250 ms/24 ms; matrix size of 160 × 128 × 78; FOV 16 mm × 12.8 mm × 7.8 mm; yielding 100 μm isotropic voxels with 40 min scan time [22–24].

4.2.5 Optimization of Signal from Mn(II) Enhancement

The goal in optimization of imaging parameters is to obtain the largest intensity difference between non-Mn(II) and with Mn(II). You will need either living mice before and after $MnCl_2$ injection, or fixed head/brains with and without $MnCl_2$. Typical parameters that might work best in your specific hardware are 3D FLASH and 3D RARE pulse sequences. Fast turbospin echo (FSE) is also useful. Alternative to optimizing imaging in the live mouse include fixing the mouse brains or preparing phantoms in capillary tubes with varying $MnCl_2$ concentrations in buffered saline. If a fixed brain is used, it can either be imaged before and after $MnCl_2$ injection, or two sets of fixed brains one with and the others without $MnCl_2$. Principally specimens with and without $MnCl_2$ are needed for this step. Below is a protocol for performing optimization of imaging parameters on living mice. Also see Table 5 for pulse sequence parameters to explore.

1. Begin by imaging the mouse head without Mn(II). This provides the baseline intensity values. Use a range of pulse sequences (*see* Table 5 for examples).

2. Inject the smallest amount (3–5 nL of 250 mM) in CA3 of the hippocampus, the mPFC, or 0.125 μL of 50 mM $MnCl_2$ into the vitreous of the eye.
3. Set the FOV to encompass the brain as tightly as possible. Typically, a field of view (FOV) of 200 × 124 × 82 slices for a matrix size of 20 mm × 12 mm × 8 mm will encompass the brain, aiming for 100 μm isotropic voxel resolution. For live imaging aim for the best pulse sequence in the least amount of time.
4. Wait 24 h and then image with the same range of pulse sequences.
5. Transfer images from scanner to your computer workstation. All images should be the same size and type. Convert from Bruker or DICOM or other capture format to NIfTI, which can be done in Fiji/ImageJ from NIH (https://imagej.net/Fiji).
6. Select region of interest (ROI) with at least 9 voxels in the region you expect axonal transport to deliver Mn(II) in the pre-injected and post-injected images. For example, this ROI should be the medial septum after hippocampal injection, the thalamus after mPFC, or the superior colliculus after eye injections. Intensity measurements are then normalized for noise. There are multiple methods to perform this. For the purpose of optimizing the Mn(II) signal from your scanner, a quick, simple method is to calculate the mean intensity in your ROI and divide it by the pooled standard deviation (noise). For noise, you can also select a non-tissue region in the same image to calculate a standard deviation of the intensity.
7. The aim is to find the pulse sequence that gives the biggest difference between the normalized intensity value (SNR) for post-Mn compared to pre-Mn in the region where Mn(II) is expected to accumulate. These measurements can be tricky in images that are not aligned and scaled. If a strong effect of Mn (II) is not detected with any of the parameters, review the images visually to be sure that the ROI is not just misplaced, or that the noise is properly accounted for. It is also helpful to perform this test on 3–5 animals and compare results for consistency.
8. Results from these measurements can be used to inform a power analysis for a Students *t*-test, the most often used statistic for parametric mapping that tests the hypothesis that any change is due to chance. For this analysis, the mean intensity and the standard deviation can be entered into online statistical calculators, such as http://powerandsamplesize.com or http://statulator.com/SampleSize/ss2PM.html [44, 45]. Assuming a

power of 0.8–0.95 at a 95% confidence level, the sample size needed for most MEMRI experiments is 10–15 animals.

9. Once the imaging parameters are established, MR images that follow the progress of the Mn(II) signal at successive time points can be captured. Again, it is critical to obtain pre-Mn (II) injected images for each animal as computational analysis will otherwise be compromised (see below). For intravitreal transport rates, images should be collected as a slab as described above with as short a time difference as possible between scanning. We were able to get enough contrast in 6 min images using the 3D RARE sequence [10]. For cerebral tracing and rates of accumulation, images can be captured at 2–6 h or longer intervals [22–26, 29, 36, 37, 46]. After 24 h the Mn (II) signal begins to dissipate.

5 Confirmation of the Injection Sites

It is critical to confirm that all injections were delivered as expected, and cluster tightly within a small volume (Fig. 6**).**

1. Examine the 0.5 h post-injection MR image for the dark center of the hyperintense Mn(II) sphere. The center of that black sphere is the location of the injection (Fig. 6a).
2. For each 0.5 h image, measure the distance from the midline (lateral, *x*), from in front of or behind bregma (anterior-posterior, *y*) and the distance from the top of the brain (*z*). These will be the *x,y,z* coordinates.
3. Calculate the centroid of all these measurements, and the distances from the centroid in each *x.y.z* direction of each injection site. Any mouse with an injection site at a distance more than 1 mm outside the general injection volume should be carefully considered and possibly removed from the dataset.
4. Display the injection sites on the MDA as "landmarks" in Amira or Aviso [26] (Fig. 6b), or in a 3D graph [29].
5. At the conclusion of imaging, perform cardiac perfusion to fix the brain, embed fixed brains, and section them. We typically send our samples to NeuroScience Associates, Inc. (https://www.neuroscienceassociates.com/) for embedding and sectioning. They can embed up to 25 brains in the same clock and serially section them in register.
6. Identify the injection site by the co-injected RDA in fluorescence microscopy (Fig. 6c, d).
7. Identify injection sites in histology section by bright field microscopy. The oil droplet also leaves a small lacuna which

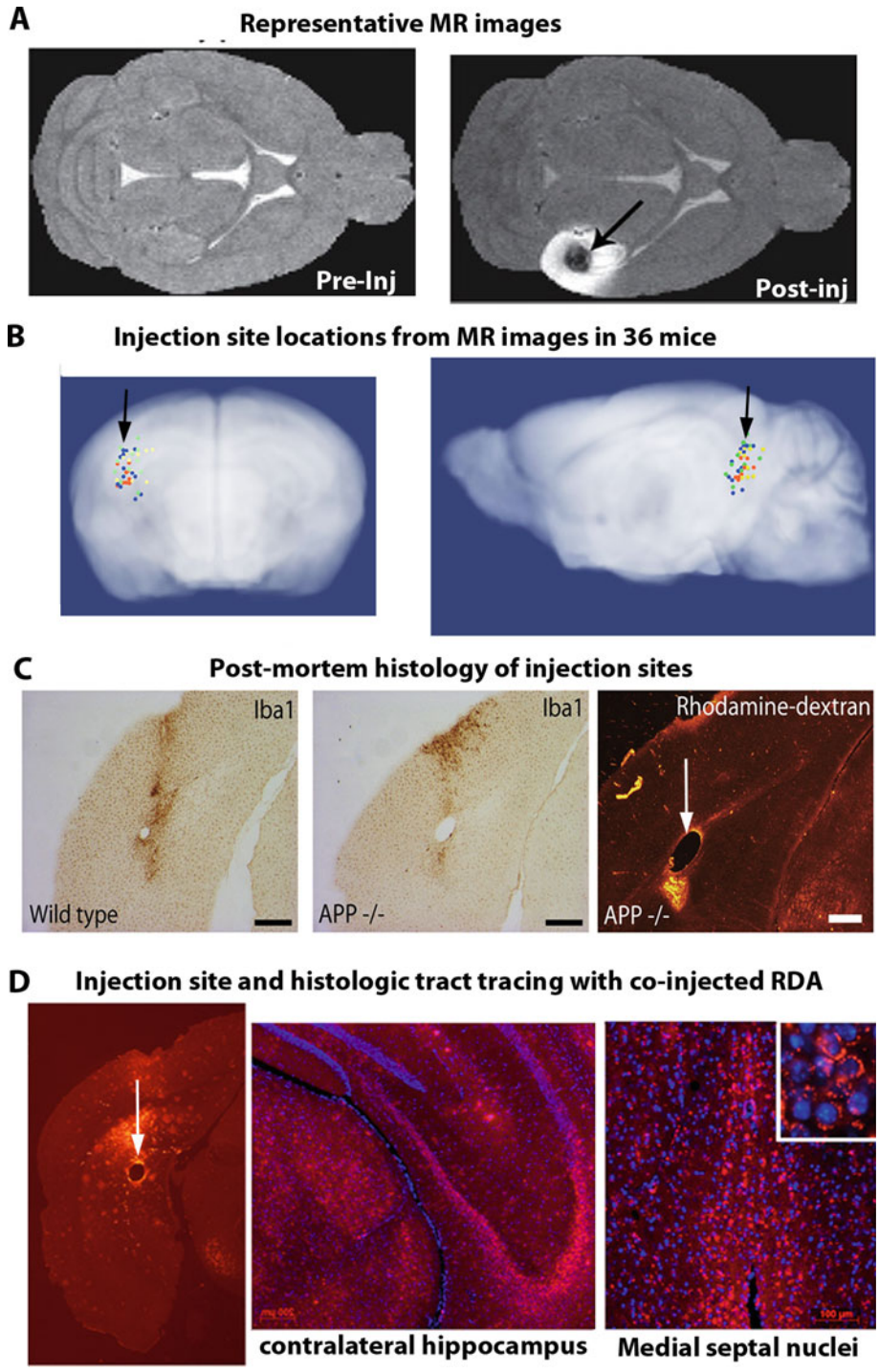

Fig. 6 Confirmation of the injection site. (**a**) The injection site should be obvious in the 0.5 h post-injection image (black arrow). These are images of a single animal after skull-tripping and normalization to the dataset. Pre-injection (left) and 0.05 h post-injection (right). Adapted from Gallagher et al. [26]. (**b**) The injection site is localized in each animal and the distance from Bregma, midline, and anterior posterior coordinates calculated from the aligned images. Shown is a projection of landmarks on a full thickness gray scale image of the MDA. There are 36 animals in four different cohorts, color-coded. Adapted from Medina et al. 2019 [47]. (**c**)

allows identification of the injection site [22–26, 29, 36, 47] (Fig. 6c).

8. Stain sections for various markers, such as Iba1 by immunohistochemistry to detect inflammation around the injection sides (Fig. 6c)[26].
9. Trace the RDA to determine that the expected projections were labeled by examining serial sections with fluorescence microscopy for rhodamine signal. Secondary staining with Dapi facilitates identifying the anatomy (Fig. 6d)[25, 36].

6 Computational Image Analysis

1. Ensure all images are in the same format and all brains have the same orientation. Most of the software was been developed for NIfTI formats which have a header that can be viewed, duplicated, and transferred to all images. If images are collected with different resolutions (voxel size), this must be corrected. The dimensions (number of slices in each of the 3 coordinates) of the images must also be identical. Analysis is easiest on images originally collected with identical format, resolution, and dimensions. These can be monitored by examination of the header.
2. Preprocessing. There are a variety of methods for preprocessing, including ours [48, 49], to prepare the images for statistical analysis. When capturing images of living mice, the whole head will be in the image. There are some specific preprocessing steps for MEMRI, especially after Mn(II) stereotactic injection because the hyperintense signal at the injection site can distort intensity-based automated alignments. Also important is to perform any necessary corrections of intensity inhomogeneities arising in the acquisition, such as N3 [50, 51] correction (updated to N4ITK [52]) on raw whole head images, as these corrections can efface real Mn(II)-dependent intensities.
3. Skull stripping. The oblong shape of the mouse brain and the small distance between the brain and skull complicate masking of non-brain head tissue, which is present in images of living animals. To overcome these issues, we developed a simple approach that utilizes a reference whole head image and its

Fig. 6 (continued) Histology of sections through the injection site stained for Iba1, a marker of microglial activation seen in inflammation and tissue injury. Minor amounts of staining occur in the needle track. That the injection site is accurately identified is confirmed with fluorescence of the rhodamine dextran. Adapted from Gallagher et al. [26]. (**d**) Rhodamine fluorescence at the injection site (left, white arrow), RDA transported to the contralateral hippocampus (middle panel), and to the medial septal nuclei (right panel). Inset shows higher magnification of RDA fluorescence inside neurons. Blue: Dapi stained nuclei. Adapted from Bearer et al. [54]

respective mask as templates. The reference image is aligned to the new image and the warp field applied to the reference mask, creating a new warped mask that fits the new image [48]. See Fig. 7.

4. Create a Minimal Deformation Atlas (MDA). After skull stripping, the images are ready to undergo spatial and intensity normalization. Again, because of the hyperintense Mn (II) signal concentrated at the injection site, care must be taken to align the images in a manner that ignores that signal. We found masking the injection site to be less effective than deploying a two-step alignment. Pre-injection images that have no Mn(II) intensity to worry about can thus be aligned into a minimal deformation atlas (MDA) that includes the anatomy of all subjects in the cohort. This MDA provides a target image for subsequent alignments (see Fig. 8).
5. Spatial normalization: After rigid body rotations to orient all injected and non-injected images for linear alignment of all images, the pre-injection image for each mouse is affine aligned to the MDA and its warp field applied to the same mouse's post-injection images for all time points. This protocol is given in detail in Medina et al. [49] See Fig. 8.
6. Intensity normalization: It is critical to preserve the Mn (II) signal while bringing the rest of the image into the intensity spectrum of the non-enhanced brain regions. We developed a method based on MATLAB that aligns the voxel/intensity histogram for all images using a curve-fitting approach. The method and code are provided in Medina et al. [49]. Assuming the peak of the histogram represents the vast number of non-enhanced voxels, this method preserves the higher intensity of the enhanced voxels and sets all voxels into the same gray scale. Whether intensity scaling should be performed before alignments or afterwards should be explored. This probably depends on which circuit is being analyzed, how intense the Mn(II) accumulation signal is, and location of the projections across the brain relative to other structures. To control for this step, review the intensity histograms before and after applying the code. Sometimes the best normalization can be obtained when modal scaling is done before alignment and in other cases, it should be done after alignment. See Fig. 9.
7. Computational analysis: Once all images are normalized, a variety of analyses can be performed. The Statistical Parametric Mapping (SPM) suite (https://www.fil.ion.ucl.ac.uk/spm/doc/) is a free program that runs on the proprietary platform of MATLAB [39, 40, 42]. It performs unbiased voxel-wise statistical comparisons of whole brain image intensity values.

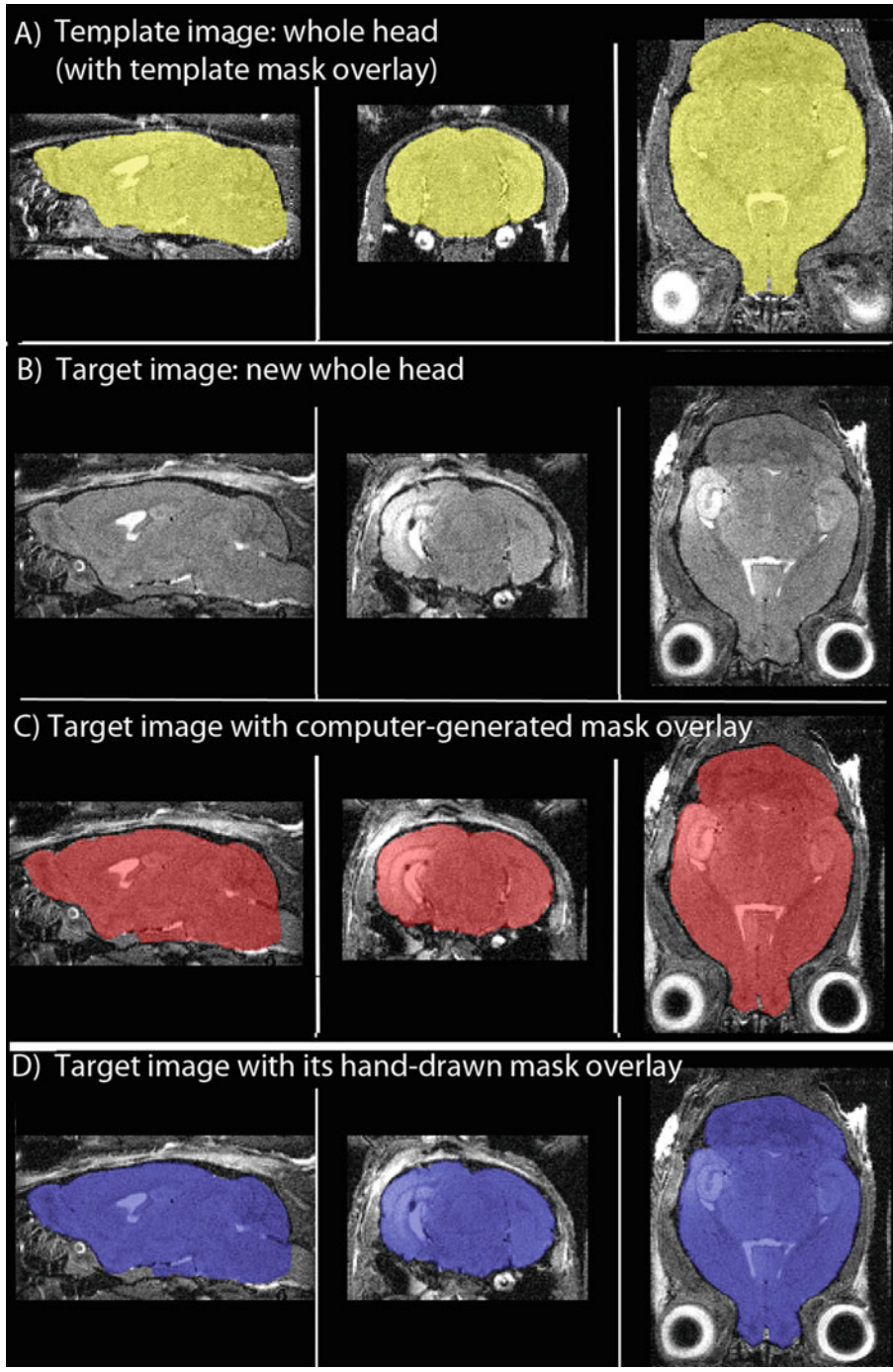

Fig. 7 Skull stripping. Examples of a template image (a) and a target image (b) with their respective masks. Orthogonal slices in sagittal, coronal, and axial projections of the 3D datasets for each condition are shown, with the whole head MR image in gray scale and extracted brain overlays color-coded. (**a**) The template whole head image, a pre-injection image with no Mn(II) signal, overlaid with its hand-drawn mask showing extracted brain in yellow. (**b**) The target image, a new whole head image for which a mask is needed, from the same cohort, imaged by the same protocol, but after $MnCl_2$ injection in CA3 of the hippocampus due to stereotactic $MnCl_2$ injection in the right hippocampus [25]. (**c)** The same target image as in (**B**) with its computer-

SPM may perform paired or unpaired *t*-tests or ANOVA. We have typically used paired *t*-tests to compare progress of Mn (II) between time points, since our data is longitudinally collected of the same subject at successive times after $MnCl_2$ injection (see Fig. 10). Other methods to explore the aligned dataset include region of interest (ROIs) analysis, where a small area is propagated across all images and the intensities measured and compared with other statistical models. ROIs are the best method to compare between cohorts of mice with differing anatomy [29]. Fitting a digital atlas to the dataset can be used as a method to automate the extraction of segment-wise intensity values, which can be useful for tracking the neuroanatomy of the projection/Mn(II) accumulation [53]. Examples of these analyses are shown in Fig. 11.

7 Notes

1. These measurements are for manganese dichloride tetrahydrate ($MnCl_2$-$4H_2O$), not for manganese chloride salt ($MnCl_2$). Do not use azide as a preservative. Sterilize all $MnCl_2$ stock solutions and store frozen. Filter with a 5-μm filter before use.

   We do not use a buffer with our tiny volume of injectate (3–5 nL), although this may decrease any tissue injury with larger volumes or continuous infusions of Mn(II) solutions [34]. At higher volumes, the osmolarity may also cause tissue damage. For injection of a 50 mM Mn(II) solution, adjust osmolarity by bringing Mn(II) solution to 75 mM NaCl.
2. MR scanning parameters are dependent on the scanner. Our work was done in the 89 mm vertical bore Bruker BioSpin Advance DRX500 scanner using a 20 mm birdcage RF coil. For optic nerve tracing, slab images of the optic tract were 0.45 cm thick with 32 axial slices and 6 min capture times [10]. Other scanners also work, including the 2.35T Magnex Scientific scanner, MRBR 4.7/400 mm magnet with DBX system equipped with B-GA20 gradients (200 mm internal diameter 100 mT/m maximum gradient strength) [11] or a 7T Avance imaging spectrometer with a 4-cm microimaging

Fig. 7 (continued) generated mask derived from the template mask, as shown in (**a**). Extracted brain shown in red. Note the slight differences in orientation and intensities between the two brains, (**a**) template and (**c**), target. (**d**) The same target image as in (**b**) but with a hand-drawn mask overlay. Brain shown in blue. Compare morphology of the masks between (**c**) computer-generated and (**d**) hand drawn. A Jacquard similarity index comparing the mask in Image (**c**) with the one in (D) gives a similarity of 0.92, and a Dicer index of 0.96, indicating highly precise correspondence between manually stripping, the gold standard which takes several hours, and our new automated stripping procedure, which takes less than a few minutes and can be iteratively applied to the entire dataset. Modified from DeLora et al. [48]

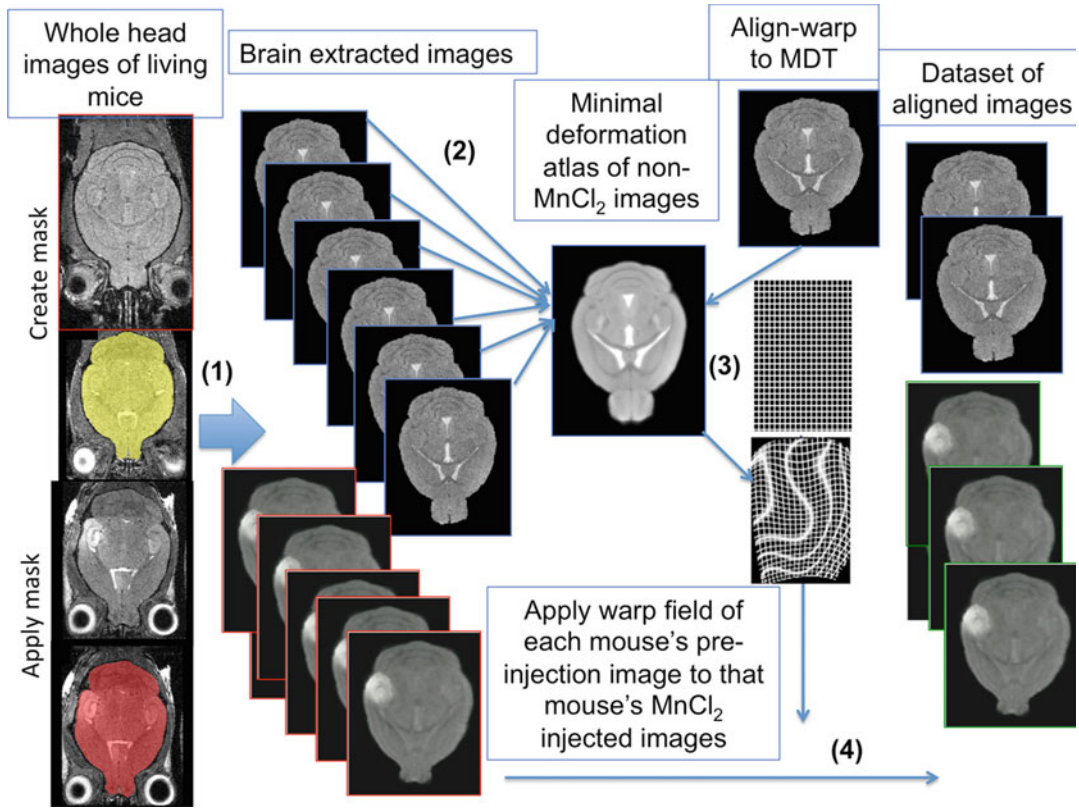

Fig. 8 Alignments. Steps in the preprocessing alignment procedure: (1) Whole head images are skull stripped; (2) pre-injection, non-contrast enhanced, images for each animal are aligned to create a minimal deformation atlas (MDA). Typically, this involves selecting a random image from the pre-injection set and aligning all brains to it to produce the first MDA, then re-aligning all brains to the first MDA to produce a final MDA. (3) Each animal's pre-injection image is aligned to the MDA generating a control-point grid/warp field. (4) The control-point grid is applied to that animal's post-injection images. Specific instructions for these steps can be found in Medina et al. [49]

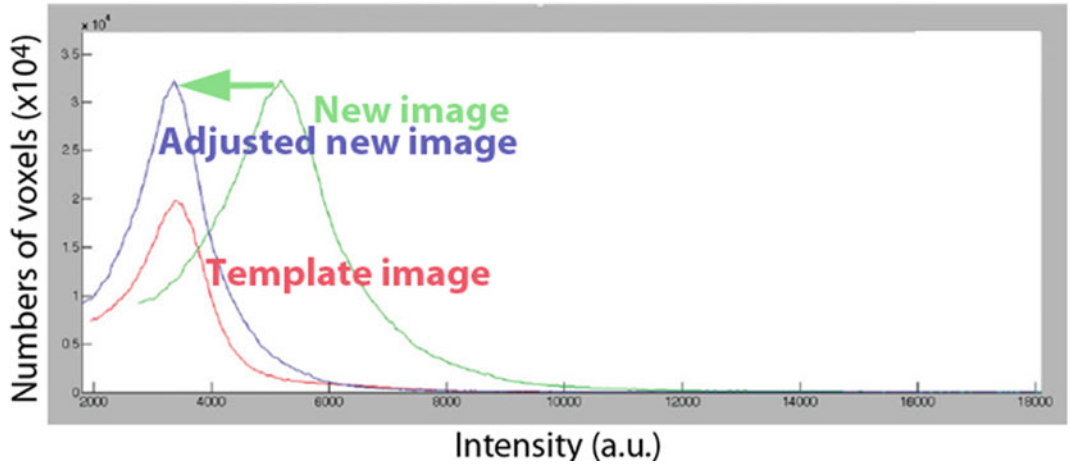

Fig. 9 Modal scaling. Histograms before (green) and after modal scaling (blue) to a template image (red). Horizontal axis: intensity values; vertical axis: number of voxels. Note that these are unsigned images (all intensity values are positive), and that histogram peaks for the template image (blue) and modal-scaled (red) images are similar, whereas prior to modal scaling (green), the peak of the intensity histogram for the new image was not coincident with the template histogram. The graph is generated in MATLAB as described in Medina et al. [49]

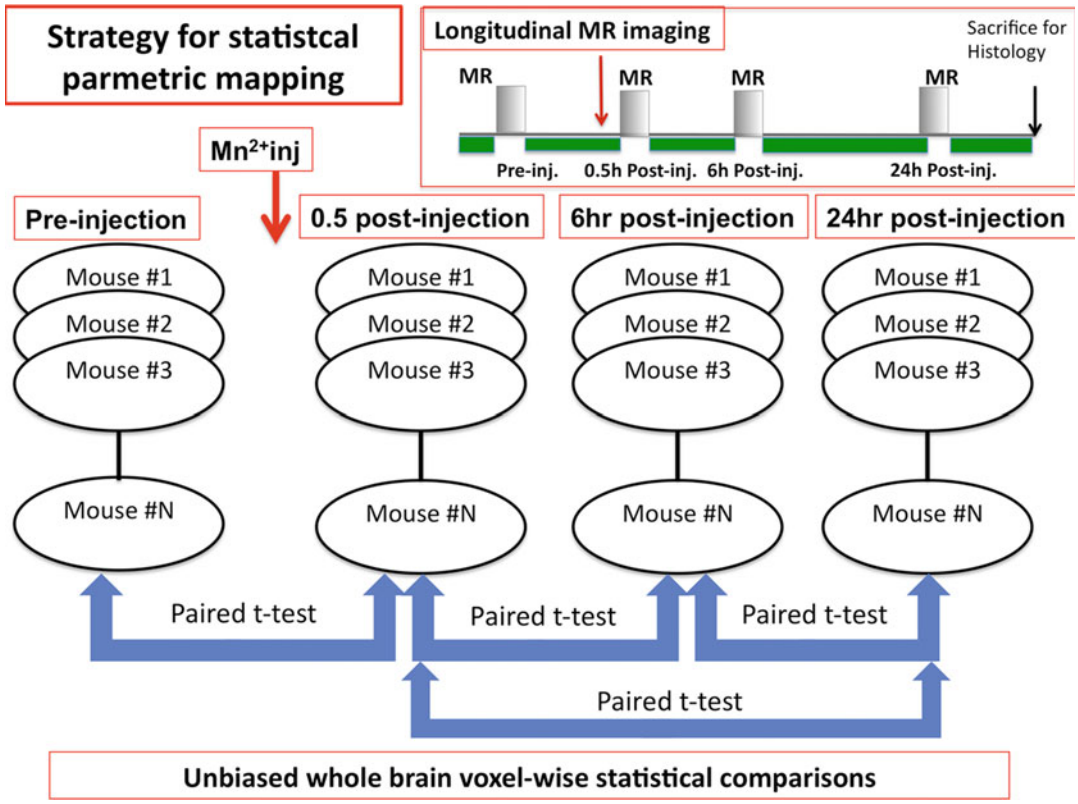

Fig. 10 Statistical parametric mapping schematic. Longitudinal MR imaging is performed before at successive times after stereotactic intracerebral injection. The green bars indicate time the mouse spends in the home cage freely moving. To detect the injection site by MR, a 0.5 h image, immediately after injection, is acquired. To validate injection site histologically, mice can be sacrificed either immediately or at 24 h after co-injection of rhodamine-dextran-amine (RDA). Alternatively, to capture both injection and tracings from the RDA, it is often necessary to wait 3 weeks before sacrifice for sufficient RDA to reach distal projections. Multiple individuals, numbers as predicted by the power analysis, are imaged with the identical parameters. Skull-stripped normalized images are compared on a voxel-wise basis with a paired *t*-test. This comparison can be between any two time points, although we found the identification of the injection site may best be done by comparing 0.5 h images with pre-injection. For projection tracing, compare each time point with the previous time point, or with the 0.5 h image, which has not achieved much transport. This comparison will eliminate the majority of the high intensity remaining in the injection site from the statistical map

gradient insert [5]. Other scanner types are possible. Determining the best pulse sequence is beyond the scope of this article (for more assistance in scanning parameters, see Uselman et al. [35]).

3. We co-inject RDA when performing intracerebral tracing. The RDA is a traditional tract tracer used in fluorescence microscopy to map projections. We use RDA to confirm placement of the injection site by post-mortem fluorescence microscopy of histologic sections [22, 24–26, 29]. At 3 weeks after injection,

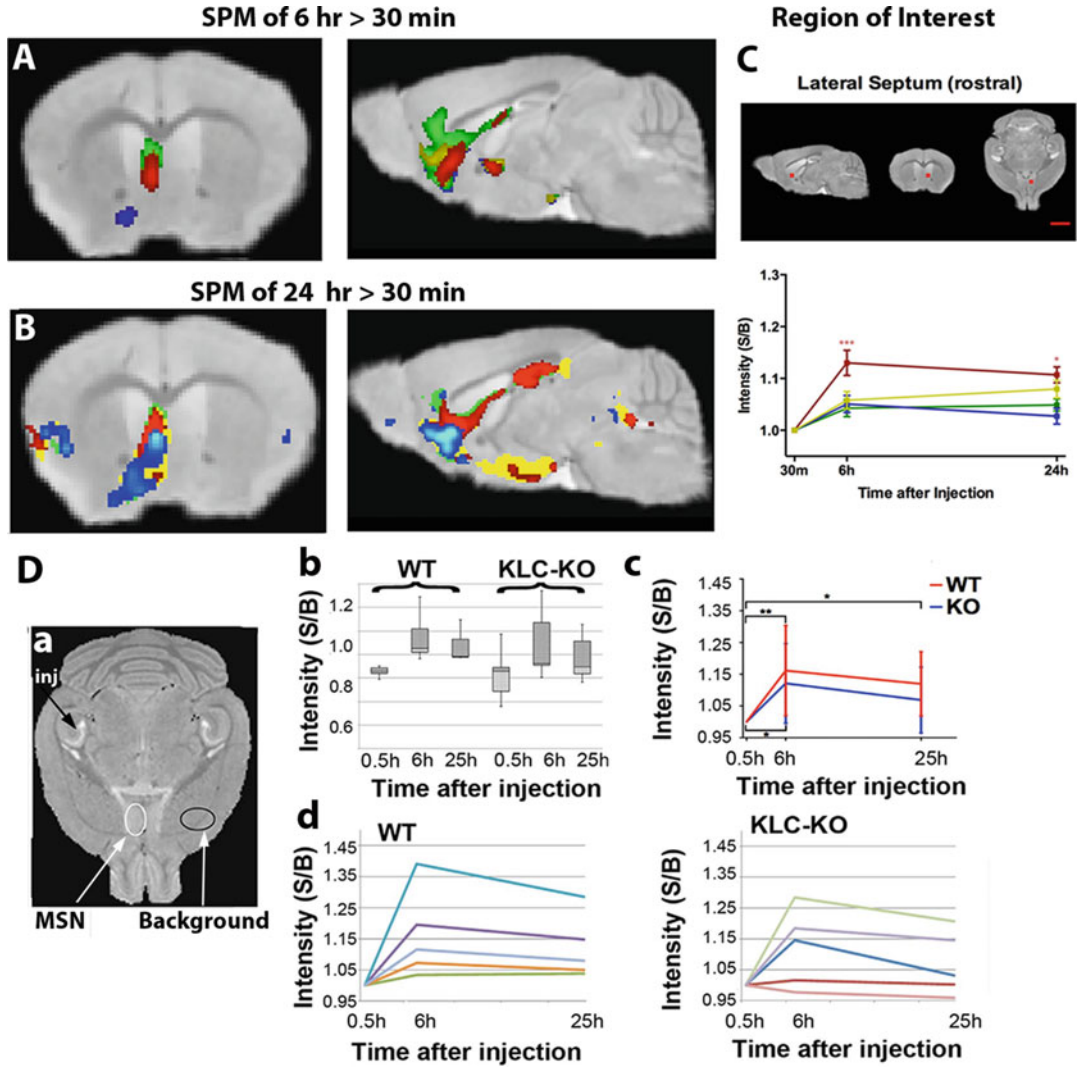

Fig. 11 Examples of analysis. (**a–b**) SPM t-maps of four treatmentgroups captured at each time point and projected onto a high-contrast MR atlas. Coronal and sagittal slices from the 3D dataset of four different treatment cohorts, injected in CA3 of the hippocampus and imaged according to the timeline in Fig. 10 as indicated. Color-coded for cohorts, green (WT); blue, yellow, and red are double transgenics APP^{Swlnd}/tTA with different doxycycline treatment schedules. Yellow have both plaques and mutated protein, blue have only mutated protein, and red has only plaques. Progression of Mn(II) intensity along the fornix to the forebrain at 6 h (**a**) and at 24 h (**b**). Note the differences in extent and location detected by this method, $p < 0.01$ FDR for each color. Projections are for anatomical correlations and are not statistical comparisons. Adapted from Medina et al. [47]. (**c**) ROI measuring the degree of intensity change in regions detected as having significant increases by SPM, color-coded as in (**a**) and (**b**). Shown is an example of intensity measurements in a region of interest (top panel) within the lateral septum, confirming the red signal in the SPM in A & B. Note that intensity increased more than 10% over the 0.5 h (30 min) time point. ROI allows statistics between datasets to be performed with unpaired ANOVAS. Adapted from Medina et al. [47]. (**d**) Comparison between different genotypes when one has altered morphology. Within group ROI measurements, taken as indicated in (**a**), inj, injection site; MSN, medial septal nuclei; Background, non-enhanced brain region not in the expected projection field used to normalize measurements. (**b**) Box and whisker plot of intensity at each time point for the two cohorts, WT and KLC-knockout. (**c**) Graph showing average intensity of each cohort $*p < 0.01$, $**p < 0.001$. (**d**) Graphs showing individual animals intensity values at each time point for wild-type littermates (WT) and kinesin-light-chain 1 knock-outs (KLC-KO, KO). Adapted from Medina et al. [47]

we reported that RDA traces the expected projections after either hippocampal or prefrontal cortex injections [23–26]. While 3K anionic dextran was thought to be transported preferentially retrograde [6, 7] and Mn(II) preferentially anterograde, we did not find this to be the case, as both tracers reach similar destinations. We have also injected 10 K fluorescein-labeled dextran amine (FDA), previously thought to be an anterograde tracer, and found little difference in distal distribution between 3 and 10 K dextrans 3 weeks post-injection (not published). The 10 K dextran is very sticky and may clog the micropipette and is thus less useful.

4. For mice we use 1–1.5% isoflurane in room air as higher doses may alter brain activity, and O_2 can also have deleterious effects.
5. We have not had to suppress movements with neuromuscular blockers, which can be deployed if needed, such a pancuronium bromide (2.5 mg.kg) or gallamine triethiodide (80 mg.kg), deliver IP just before inserting into the scanner providing the airway is secured and ventilation mechanically supported.

Acknowledgments

We are grateful to many people in our labs who contributed to this protocol over more than 15 years. We thank Taylor Uselman and Chris Medina for assistance with our computational image analysis pipeline, and for critical reading of this MS. We are grateful to Sharon Wu Lin for animal husbandry. Development of this protocol was supported by the Beckman Institute at Caltech (R.E.J. and X.Z.), the Moore Foundation (E.L.B.), the Harvey Family Foundation (E.L.B.), and a series of NIH grants: NIDA RO1-DA018184 (R.E.J.); NINDS RO1 NS062184 (E.L.B.); and NIMH RO1 MH096093 (E.L.B.).

References

1. Lauterbur PC, Mendonca MH, Rudin AM (1978) Augmentation of tissue water proton spin-lattice relaxation rates by in vivo addition of paramagnetic ions. In: Frontiers of Biological Energetics, vol 1. Academic Press, pp 752–759
2. Mendoca-Dias MH, Gaggelli E, Lauterbur PC (1983) Paramagnetic contrast agents in nuclear magnetic resonance medical imaging. Semin Nuclear Med 13(4):364–376
3. Lin YJ (1997) An approach to direct imaging of brain activation with MRI by activity-induced manganese dependent, "AIM," Contrast. Carnegie Mellon University, Pittsburgh
4. Lin YJ, Koretsky AP (1997) Manganese ion enhances T1-weighted MRI during brain activation: an approach to direct imaging of brain function. Magn Reson Med 38(3):378–388. https://doi.org/10.1002/mrm.1910380305
5. Pautler RG, Silva AC, Koretsky AP (1998) In vivo neuronal tract tracing using manganese-enhanced magnetic resonance imaging. Magn Reson Med 40(5):740–748. https://doi.org/10.1002/mrm.1910400515
6. Reiner A, Veenman CL, Medina L, Jiao Y, Del Mar N, Honig MG (2000) Pathway tracing using biotinylated dextran amines. J Neurosci Methods 103(1):23–37

7. Van Haeften T, Wouterlood FG (2000) Neuroanatomical tracing at high resolution. J Neurosci Methods 103(1):107–116
8. Inoue T, Majid T, Pautler RG (2011) Manganese enhanced MRI (MEMRI): neurophysiological applications. Rev Neurosci 22(6): 675–694. https://doi.org/10.1515/RNS.2011.048
9. Pautler RG, Koretsky AP (2002) Tracing odor-induced activation in the olfactory bulbs of mice using manganese-enhanced magnetic resonance imaging. Neuroimage 16(2):441–448. https://doi.org/10.1006/nimg.2002.1075
10. Bearer EL, Falzone TL, Zhang X, Biris O, Rasin A, Jacobs RE (2007) Role of neuronal activity and kinesin on tract tracing by manganese-enhanced MRI (MEMRI). Neuroimage 37(Suppl 1):S37–S46. https://doi.org/10.1016/j.neuroimage.2007.04.053
11. Watanabe T, Michaelis T, Frahm J (2001) Mapping of retinal projections in the living rat using high-resolution 3D gradient-echo MRI with Mn2+-induced contrast. Magn Reson Med 46(3):424–429. https://doi.org/10.1002/mrm.1209
12. Pautler RG (2004) In vivo, trans-synaptic tract-tracing utilizing manganese-enhanced magnetic resonance imaging (MEMRI). NMR Biomed 17(8):595–601. https://doi.org/10.1002/nbm.942
13. Pautler RG, Mongeau R, Jacobs RE (2003) In vivo trans-synaptic tract tracing from the murine striatum and amygdala utilizing manganese enhanced MRI (MEMRI). Magn Reson Med 50(1):33–39. https://doi.org/10.1002/mrm.10498
14. Tindemans I, Boumans T, Verhoye M, Van der Linden A (2006) IR-SE and IR-MEMRI allow in vivo visualization of oscine neuroarchitecture including the main forebrain regions of the song control system. NMR Biomed 19(1):18–29. https://doi.org/10.1002/nbm.989
15. Tindemans I, Verhoye M, Balthazart J, Van Der Linden A (2003) In vivo dynamic ME-MRI reveals differential functional responses of RA- and area X-projecting neurons in the HVC of canaries exposed to conspecific song. Euro J Neurosci 18(12): 3352–3360. https://doi.org/10.1111/j.1460-9568.2003.03056.x
16. Van der Linden A, Van Meir V, Boumans T, Poirier C, Balthazart J (2009) MRI in small brains displaying extensive plasticity. Trends Neurosci 32(5):257–266. https://doi.org/10.1016/j.tins.2009.01.005
17. Van der Linden A, Van Meir V, Tindemans I, Verhoye M, Balthazar J (2004) Applications of manganese-enhanced magnetic resonance imaging (MEMRI) to image brain plasticity in song birds. NMR Biomed 17(8):602–612
18. Van der Linden A, Van Meir V, Tindemans I, Verhoye M, Balthazart J (2004) Applications of manganese-enhanced magnetic resonance imaging (MEMRI) to image brain plasticity in song birds. NMR Biomed 17(8):602–612. https://doi.org/10.1002/nbm.936
19. Van der Linden A, Verhoye M, Van Meir V, Tindemans I, Eens M, Absil P, Balthazart J (2002) In vivo manganese-enhanced magnetic resonance imaging reveals connections and functional properties of the songbird vocal control system. Neuroscience 112(2): 467–474. https://doi.org/10.1016/s0306-4522(02)00070-2
20. Van Meir V, Pavlova D, Verhoye M, Pinxten R, Balthazart J, Eens M, Van der Linden A (2006) In vivo MR imaging of the seasonal volumetric and functional plasticity of song control nuclei in relation to song output in a female songbird. Neuroimage 31(3):981–992. https://doi.org/10.1016/j.neuroimage.2006.01.005
21. Van Meir V, Verhoye M, Absil P, Eens M, Balthazart J, Van der Linden A (2004) Differential effects of testosterone on neuronal populations and their connections in a sensorimotor brain nucleus controlling song production in songbirds: a manganese enhanced-magnetic resonance imaging study. Neuroimage 21(3): 914–923. https://doi.org/10.1016/j.neuroimage.2003.10.007
22. Bearer EL, Zhang X, Janvelyan D, Boulat B, Jacobs RE (2009) Reward circuitry is perturbed in the absence of the serotonin transporter. Neuroimage 46(4):1091–1104. https://doi.org/10.1016/j.neuroimage.2009.03.026
23. Gallagher JJ, Zhang X, Hall FS, Uhl GR, Bearer EL, Jacobs RE (2013) Altered reward circuitry in the norepinephrine transporter knockout mouse. PLoS One 8(3):e57597. https://doi.org/10.1371/journal.pone.0057597
24. Zhang X, Bearer EL, Boulat B, Hall FS, Uhl GR, Jacobs RE (2010) Altered neurocircuitry in the dopamine transporter knockout mouse brain. PLoS One 5(7):e11506. https://doi.org/10.1371/journal.pone.0011506
25. Bearer EL, Zhang X, Jacobs RE (2007) Live imaging of neuronal connections by magnetic resonance: robust transport in the hippocampal–septal memory circuit in a mouse model of Down syndrome. Neuroimage 37(1):

230–242. https://doi.org/10.1016/j.neuroimage.2007.05.010

26. Gallagher JJ, Zhang X, Ziomek GJ, Jacobs RE, Bearer EL (2012) Deficits in axonal transport in hippocampal-based circuitry and the visual pathway in APP knock-out animals witnessed by manganese enhanced MRI. Neuroimage 60(3):1856–1866. https://doi.org/10.1016/j.neuroimage.2012.01.132
27. Vale RD, Reese TS, Sheetz MP (1985) Identification of a novel force-generating protein, kinesin, involved in microtubule-based motility. Cell 42(1):39–50. https://doi.org/10.1016/S0092-8674(85)80099-4
28. Hirokawa N, Noda Y (2008) Intracellular transport and kinesin superfamily proteins, KIFs: structure, function, and dynamics. Physiol Rev 88(3):1089–1118. https://doi.org/10.1152/physrev.00023.2007
29. Medina CS, Biris O, Falzone TL, Zhang X, Zimmerman AJ, Bearer EL (2017) Hippocampal to basal forebrain transport of Mn(2+) is impaired by deletion of KLC1, a subunit of the conventional kinesin microtubule-based motor. Neuroimage 145(Pt A):44–57. https://doi.org/10.1016/j.neuroimage.2016.09.035
30. Black MM (2016) Chapter 1—Axonal transport: the orderly motion of axonal structures. In: Pfister KK (ed) Methods in Cell Biology, vol 131. Academic Press, San Diego, CA, pp 1–19. https://doi.org/10.1016/bs.mcb.2015.06.001
31. Grafstein B (1967) Transport of protein by goldfish optic nerve fibers. Science 157:196–199. https://doi.org/10.1126/science.157.3785.196
32. Lasek RJ (1980) Axonal transport: a dynamic view of neuronal structures. Trends Neurosci 3(4):87–91. https://doi.org/10.1016/0166-2236(80)90034-X
33. Yuan A, Lumar A, Petethof C, Duff K, Nixon RA (2008) Axonal transport rates in vivo are unaffected by tau deletion or overexpression in mice. J Neurosci 28(7):1682–1687. https://doi.org/10.1523/JNEUROSCI.5242-07.2008
34. Canals S, Beyerlein M, Keller AL, Murayama Y, Logothetis NK (2008) Magnetic resonance imaging of cortical connectivity in vivo. Neuroimage 40(2):458–472. https://doi.org/10.1016/j.neuroimage.2007.12.007
35. Uselman TW, Medina CS, Gray HB, Jacobs RE, Bearer EL (2021) Longitudinal manganese-enhanced magnetic resonance imaging of neural circuitry and activity. Neuroimage submitted
36. Bearer EL, Manifold-Wheeler BC, Medina CS, Gonzales AG, Chaves FL, Jacobs RE (2018) Alterations of functional circuitry in aging brain and the impact of mutated APP expression. Neurobiol Aging 70:276–290. https://doi.org/10.1016/j.neurobiolaging.2018.06.018
37. Medina CS, Uselman TW, Barto DR, Chaves F, Jacobs RE, Bearer EL (2019) Decoupling the effects of the amyloid precursor protein from amyloid-beta plaques on axonal transport dynamics in the living brain. Front Cell Neurosci 13:501. https://doi.org/10.3389/fncel.2019.00501
38. Medina CS, Uselman TW, Jacobs RE, Bearer EL (2021) Medial prefrontal cortical projections are altered by a single acute fear experience: evidence for biological mechanisms of anxiety and substance abuse disorders. Paper presented at the Society for Neuroscience Global Connect Virtual meeting, Virtual, January 12, 2021
39. Ashburner J, Barnes G, Chen C-C, Daunizeau J, Flandin G, Friston K, Jafarian A, Kiebel S, Kilner J, Litvak V, Moran R, Penny W, Razi A, Stephan K, Tak S, Zeidman P, Gitelman D, Henson R, Hutton C, Glauche V, Mattout J, Phillips C (2020) SPM12 Manual. Functional Imaging Laboratory Wellcome Centre for Human Neuroimaging, London, UK
40. Ashburner J, Friston KJ (2001) Why voxel-based morphometry should be used. Neuroimage 14(6):1238–1243
41. Friston KJ (1996) Statistical parametric mapping and other analysis of functional imaging data. In: Toga AW, Mazziotta JC (eds) Brain Mapping: The Methods. Academic Press, San Diego, CA, p 471
42. Penny W, Friston K, Ashburner J, Kiebel S, Nichols T (2007) Statistical parametric mapping: the analysis of functional brain images. Academic Press, San Diego, CA. https://doi.org/10.1016/B978-0-12-372560-8.X5000-1
43. Delcroix JD, Valletta J, Wu C, Howe CL, Lai CF, Cooper JD, Belichenko PV, Salehi A, Mobley WC (2004) Trafficking the NGF signal: implications for normal and degenerating neurons. Prog Brain Res 146:3–23
44. Connor RJ (1987 Sample size for testing differences in proportions for the paired-sample design. Biometrics 43(1):207–211.
45. Lachin JM (1981) Introduction to sample size determination and power analysis for clinical

trials. Control Clin Trials 2(2):93–113. https://doi.org/10.1016/0197-2456(81)90001-5

46. Medina CS, Manifold-Wheeler B, Gonzales A, Bearer EL (2018) Automated computational processing of 3-D MR images of mouse brain for phenotyping of living animals. Curr Protoc Mol Biol 119(1). https://doi.org/10.1002/cpmb.40
47. Medina CS, Uselman TW, Barto DR, Cháves F, Jacobs RE, Bearer EL (2019) Decoupling the effects of the amyloid precursor protein from amyloid-β plaques on axonal transport dynamics in the living brain. Front Cell Neurosci 13. https://doi.org/10.3389/fncel.2019.00501
48. Delora A, Gonzales A, Medina CS, Mitchell A, Mohed AF, Jacobs RE, Bearer EL (2016) A simple rapid process for semi-automated brain extraction from magnetic resonance images of the whole mouse head. J Neurosci Methods 257:185–193. https://doi.org/10.1016/j.jneumeth.2015.09.031
49. Medina CS, Manifold-Wheeler B, Gonzales A, Bearer EL (2017) Automated computational processing of 3-D MR images of mouse brain for phenotyping of living animals. Curr Protoc Mol Biol 119:29A 25 21–29A 25 38. https://doi.org/10.1002/cpmb.40
50. Sled JG, Zijdenbos AP, Evans AC (1998) A nonparametric method for automatic correction of intensity nonuniformity in MRI data. IEEE Trans Med Imaging 17(1):87–97. https://doi.org/10.1109/42.668698
51. Larsen CT, Iglesias JE, Van Leemput K (2014) N3 bias field correction explained as a bayesian modeling method, Bayesian and grAphical models for biomedical imaging. Springer, Cham, Switzerland, pp 1–12
52. Tustison NJ, Avants BB, Cook PA, Yuanjie Z, Egan A, Yushkevich PA, Gee JC (2010) N4ITK: improved N3 bias correction. IEEE Trans Med Imag 29(6):1310–1320. https://doi.org/10.1109/tmi.2010.2046908
53. Uselman TW, Barto DR, Jacobs RE, Bearer EL (2020) Evolution of brain-wide activity in the awake behaving mouse after acute fear by longitudinal manganese-enhanced MRI. Neuroimage 222(116975):1–22. https://doi.org/10.1016/j.neuroimage.2020.116975
54. Bearer EL, Barto D, Reviere ARH, Jacobs RE (2018, 2018) Neural activation imaged by MEMRI in mouse models of PTSD: early life stress and role of the serotonergic system in prolonged response to fear. Pro Int Soc Magn Reson Med Sci Meet Exhib Int Soc Magn Reson Med

Part III

Rodent Primary Neurons

Chapter 7

Microfluidic Neuromuscular Co-culture System for Tracking Cell-to-Cell Transfer and Axonal Transport of Labeled Proteins

Ariel Ionescu and Eran Perlson

Abstract

The molecular communication mechanisms within the Motor Neurons (MN) distant axon and its soma, as well as between MN and their neighboring cells and extracellular environment are of keen interest for our understanding of neurodevelopment and neurodegenerative diseases. One tool that has significantly improved our ability to study such processes with high spatiotemporal resolution is microfluidic devices. Here we describe a step-by-step guide to the neuromuscular co-culturing procedure and demonstrate how to track trophic factors transmission from muscle-to-neuron and their transport along the axons.

Key words Axonal transport, Motor neurons, Neuromuscular junction, Skeletal muscles, Microfluidic chambers, BDNF, GDNF

1 Introduction

The process of axonal transport has been thoroughly described and is fundamental for the function and survival of various neuronal cells [1–4]. Accumulating evidence have made it clear that defects in axonal transport are the cause for several neurodegenerative diseases [5–7] and are implicated in other [8–10]. Due to several limitations, the basic research of axonal transport was mainly performed on immature, developing axons, leaving the open questions of what is the nature and importance of axonal transport to mature motor neurons and their synapses with skeletal muscles [3]. As well as, whether and how is this process regulated by target-innervation e.g., muscle cells. Here we describe the method of co-culturing primary embryonic motor neurons with primary muscle cells in microfluidic chambers. We supply detailed protocols for the isolation of both primary motor neurons and primary satellite cells, as well as for the transfection of myoblasts. Using this method, we explore intercellular transmission of hBDNF-mCherry, and

Alessio Vagnoni (ed.), *Axonal Transport: Methods and Protocols*,
Methods in Molecular Biology, vol. 2431, https://doi.org/10.1007/978-1-0716-1990-2_7,
© The Author(s), under exclusive license to Springer Science+Business Media, LLC, part of Springer Nature 2022

hGDNF-GFP from muscle into motor neurons in co-culture. We demonstrate how these muscle-derived trophic factors are internalized and transport inside motor neuron axons and supply a set of tools to analyze these interactions. Thus, we introduce a simple, yet robust method that opens new avenues towards a better understanding of neuromuscular communication, and its contribution to neurodegenerative diseases, as well as for development of novel therapeutic approaches.

2 Materials

Solution preparation must be performed in a laminar hood and according to tissue culture-grade standards. All solutions should be passed through a 0.22 μm filter unless mentioned otherwise.

2.1 Motor Neuron Culture

1. Poly-L-ornithine (PLO) coating solution: 1.5 mg/mL stock Poly-L-ornithine (Sigma; P8638) dissolved in PBS, aliquoted and stored at −20 °C for up to 6 months. For coating, dilute PLO 1:100 in PBS to a final 150 μg/mL.
2. Laminin coating solution: 1 mg/mL stock Laminin (Sigma; L2020) diluted to 3 μg/mL working concentration in filtered double-distilled water (ddH_2O).
3. Matrigel® coating solution: Prepare Matrigel® (Corning; 356234) coating solution by diluting the stock 1:50 in filtered-DMEM containing 3 μg/mL Laminin. Thaw stock Matrigel® at 4 °C. While working on ice and using pre-cooled pipette tips, prepare 100 μL aliquots and store at −20°C for up to 6 months. Avoid rapid thawing of aliquots.
4. Hank's buffered saline solution (HBSS) + 1% penicillin-streptomycin: Dilute 50 mL of stock 10× HBSS (Gibco; 14185052) with 445 mL of ddH_2O, and 5 mL of 100× penicillin-streptomycin (P/S) solution (Biological Industries). Filter the mix through 0.22 μm vacuum filter bottle. Store at 4 °C.
5. 4% BSA solution: Dissolve 4 g of tissue culture-grade Bovine Serum Albumin (BSA, Sigma cat. A3311) in 100 mL of Leibowitz-15 medium (L-15; Gibco). Once solution becomes clear, sterilize by passing through 0.22 syringe filter, prepare 5 mL aliquots, and store at −20 °C for up to 6 months. Avoid rapid thawing or heating the BSA solution.
6. DNase solution: Dissolve 1 mg/mL DNase powder (Sigma, DN-25) in Neurobasal medium (Gibco; 21103049). Prepare 200 μL aliquot and store at −20 °C of up to 6 months. Avoid rapid thawing and preserve DNase tube on ice during the culture procedure.

7. Trypsin solution: Dissolve 25 mg/mL Trypsin powder (Sigma; T1426) in sterile PBS. Prepare 12 μL aliquots and store at −20 °C for up to 6 months.
8. Complete Neurobasal (CNB) medium (50 mL final volume): Mix 500 μL P/S, 500 μL Glutamax (Gibco), 1 mL of B27 supplement mix (Gibco), 1 mL of Horse Serum (Biological Industries), 25 μM of 2-mercaptoethanol, and 47 mL of Neurobasal medium. Sterilize by passing through a 0.22 μm syringe filter. After filtration, add the following neurotrophic factors: 1 ng/mL hBDNF, 1 ng/mL hGDNF, 0.5 ng/mL hCNTF (All three trophic factors are acquired from Alamone labs). The CNB medium should be prepared freshly and allowed to equilibrate in a CO_2 incubator for 1 h prior use.
9. Rich Neurobasal (RNB) medium: The RNB medium is used for plating MN inside microfluidic chambers, and for the first days of their culturing. For 10 mL of medium: Use 9.8 mL of trophic-factor free CNB medium prepared in **item 8**, add extra 200 μL of B-27 supplement, and filter using a syringe filter. After filtration, supplement the medium with the following neurotrophic factors: 25 ng/mL hBDNF, 1 ng/mL hBDNF, 0.5 ng/mL hCNTF. Equilibrate the medium in a CO_2 incubator for 1 h prior use.
10. Poor neurobasal medium: for 20 mL medium: Mix 200 μL P/S with 19.8 mL neurobasal medium. Sterilize by passing through a 0.22 μm syringe filter and store at 4°C for up to 2 weeks.
11. OptiPrep Density Gradient Medium: for 10 mL medium: Mix 5.27 mL of filtered-ddH_2O, with 2 mL of filtered 20% Glucose, 1 mL of filtered 100 mM Tricine, and 1.73 mL of sterile 60% OptiPrep medium. Protect solution from light and store at 4 °C for up to 6 months. This protocol uses a 17.3% V/V equal to 10.4 W/V OptiPrep concentration which gives higher neuronal yield over high MN purity. For enhancing MN fraction, reduce the OptiPrep concentration to 10.4% V/V equal to 6.24% W/V and adjust the filtered-ddH_2O volume, respectively.
12. Cytarabine (Ara-C): Prepare 2 mM stock solution by dissolving the appropriate amount in ultra-pure ddH_2O. Aliquot and store at −20 °C.
13. Alexa-647 conjugated Cholera toxin B (Thermo; C-347777): Prepare a stock solution of 1 μg/mL by dissolving the appropriate amount in PBS. Aliquot and store at −80 °C.

2.2 Primary Skeletal Muscle Culture

1. 5% BSA solution: Dissolve 5 g of tissue culture-grade BSA in 100 mL ddH_2O. Once solution becomes clear, sterilize by passing through 0.22 μm filter bottle. Store at 4 °C for up to 3 months.
2. DMEM Penicillin-Streptomycin-Nystatin 2.5% medium: for 100 mL: Mix 2.5 mL of 100× Penicillin-Streptomycin-Nystatin (PSN; Biological Industries; 03-032-1B). Sterilize by passing through 0.22 μm filter bottle. Store at 4 °C for up to 1 month.
3. Bioamf 2.0 medium: During the satellite cell isolation, Bioamf 2.0 medium (Biological Industries; 01-194-1A) should be supplemented with 1% of PSN, and filter sterilized. For later applications, such as the co-culturing procedures, Bioamf 2.0 medium is supplemented with 1% of P/S, and filter sterilized. For transfection of muscles, use filtered sterilized antibiotic-free Bioamf 2.0 medium. Bioamf 2.0 solutions may be stored at 4 °C for up to 1 week.
4. Trypsin-C EDTA: Thaw stock Trypsin EDTA Solution C solution (Biological Industries; 03-053-1B), aliquot to 5 mL vials and store at −20 °C.

3 Methods

The co-culture procedure uses both primary muscle cultures and motor neuron cultures. The protocols for each of those are described below, as well as their co-culturing. To achieve proper innervation, timing these procedures together is a key component of the success of this protocol. A timeline overview of key steps in the procedure is available in Fig. 1b.

3.1 Primary Muscle Culture

1. Prepare culture dishware:
   (a) Plate A**:** Wash a 10 cm tissue culture plate with 5% BSA solution and remove residual liquid. Then fill this plate with 12 mL of DMEM 2.5% PSN medium.
   (b) Plate B**:** Wash all wells of a 6-well plate similarly and fill each well with 2 mL of DMEM 2.5% PSN medium.
   (c) Plate C**:** Thaw a 100 μL Matrigel® aliquot in 4 °C, then add 900 μL of cold DMEM 2.5% PSN medium and mix well. Using a 1 mL pipette, wash all wells of a 6-well plate with the diluted Matrigel® by moving the solution from one well to another. Remove residual Matrigel® and incubate the empty 6-well plate inside a CO_2 incubator at 37 °C for 20–30 min, and not more. Following incubation, fill every well with 2 mL of Bioamf 1% PSN.

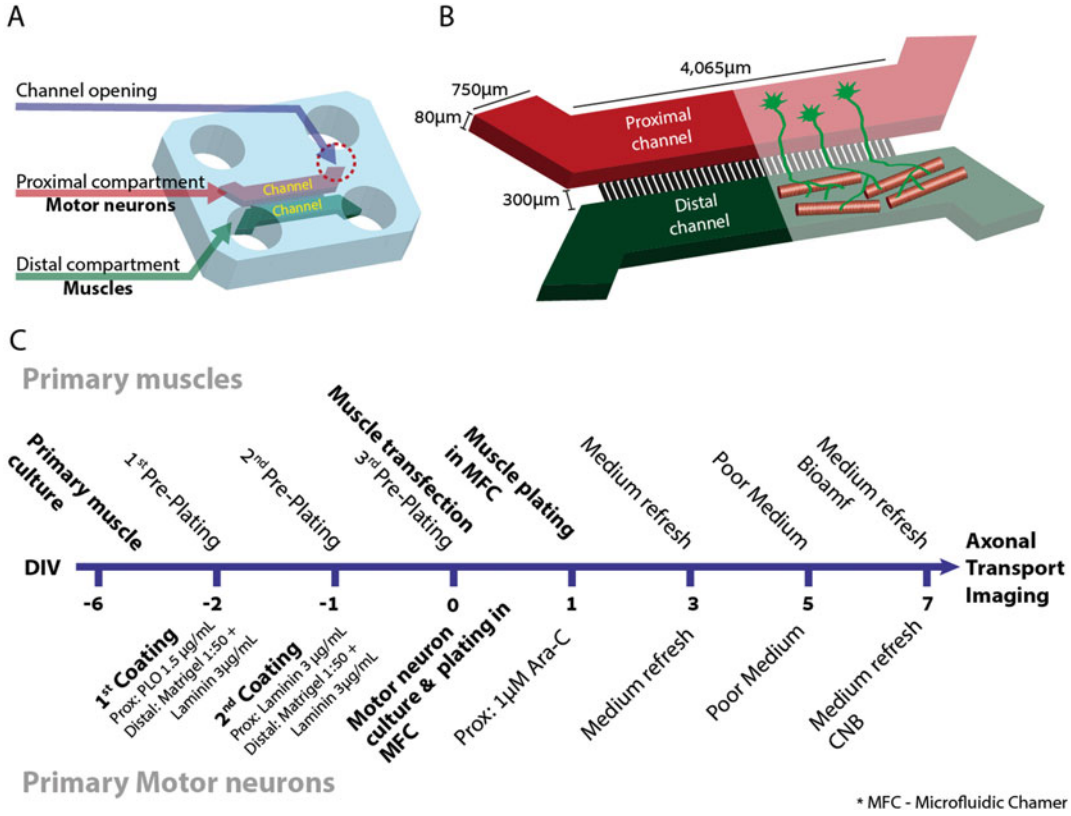

Fig. 1 Microfluidic chambers and experimental timeline. (**a**) Illustration of a microfluidic chamber indicating the (1) neuronal compartment (proximal), (2) Muscle/NMJ compartment (distal), and (3) the channel opening (red circle) where the pipette tip should be pointed to when passing coating solutions from through the channels or when plating motor neurons/muscles. (**b**) Magnified illustration of the microfluidic design and dimensions (left), along with illustrations of cellular and subcellular compartmentalization. (**c**) Experimental timeline highlighting the key procedures described in this method

2. Store Plates A–C in a CO_2 incubator at 37 °C until use.
3. Dissolve Collagenase-I powder in DMEM 2.5% PSN medium. Use 2 mg of Collagenase-I, and 1 mL of medium per muscle (*see* **Note 1**).
4. Euthanize a mature (P60 and older) mouse and remove both gastrocnemius muscles as previously illustrated [10].
5. Insert every muscle into its own flat-bottom 2 mL Eppendorf tube containing 1 mL of Collagenase-I solution, and incubate for 3 h in a CO_2 incubator at 37 °C.
6. After incubation, unite both muscle into Plate A, and incubate for an additional 30 min inside a CO_2 incubator at 37 °C.
7. Prepare a trituration pipette by removing the thin end of a 1 mL filter tip. Prepare a fiber collection pipette by fire-polishing one glass Pasteur pipette. Wash both pipettes with 5% BSA before use.

8. Gently triturate the muscles inside Plate A using the blunted 1 mL filter tip. After muscles begin dissociating, shift to a stronger trituration by pipetting the muscles back and forth through the blunt tip.
9. Under a stereoscope, use the fire-polished Pasteur pipette to collect single muscle fibers from Plate A into the wells of Plate B. Aim for collecting ~200 muscle fibers into every well of Plate B (*see* **Note 2**).
10. Place Plate B under the stereoscope and collect only long and intact fibers from each well into the parallel well of Plate C (*see* **Note 3**).
11. Incubate Plate C for 4 days in a CO_2 incubator at 37°C. After the 4-day incubation, begin with pre-plating phase (*see* **Notes 4** and **5**).
12. Discard the medium and fiber debris from all wells and wash every well with 1 mL (♀ 4 mL, *see* **Note 6**) of pre-warmed 1× PBS. Pipette forcefully to remove mature fibers that got adhered to the plate.
13. Discard the PBS and add 300 μL (♀ 1.5 mL) of room-temperature Trypsin EDTA Solution C solution into every well. Incubate the plate for 10–15 min in the CO_2 incubator, and examine every 5 min. Once cells have detached, proceed to the next step.
14. Neutralize the Trypsin with 1 mL (♀ 4 mL) of pre-warmed Bioamf 1% P/S into each well and collect the cells into a new-uncoated 10 cm plate—Plate D (*see* **Note 7**). Repeat this **step** twice for retrieving maximal number of cells (*see* **Note 8**).
15. Incubate Plate D for 1 h in CO_2 incubator at 37 °C.
16. During this incubation, prepare Plate E: Thaw a 100 μL Matrigel® in 4 °C, add 900 μL of DMEM 2.5% PSN medium, and coat one (or more; see **step 12**) 10 cm plate. Incubate the coated plate in CO_2 incubator for 20–30 min and then add 4 mL of Bioamf 1% P/S medium (*see* **Note 9**).
17. After 1 h, inspect Plate D under the microscope in order to assess the extent of contamination by fibroblast (which should be the only cells adhered to the surface at this phase).
18. Collect the supernatant from Plate D and transfer it into the Matrigel®-coated Plate E (*see* **Note 10**).
19. Incubate Plate E overnight in a CO_2 incubator at 37 °C.
20. Repeat **step 12–19** for the second and third days of pre-plating (for ♀: *see* **Note 6**).
21. After the third day of pre-plating, myoblasts count the cells and determine the yield of the culture.

22. For transduction of plasmids into muscles, coat wells in a 24-well plate with diluted Matrigel® as done previously in **step 1** (Plate C) (*see* **Note 11**).
23. After 20–30 min of coating, plate 150,000 myoblasts in every well in a total volume of 400 µL of filtered and antibiotic-free (no P/S) Bioamf 2.0 medium.
24. Remaining muscles can be cryopreserved in 95% FBS, 5% DMSO medium. Use 1 mL and 1–2 × 10^6/mL in each freezing vial (*see* **Notes 12** and **13**).

3.2 Muscle Transfection

In order to track the retrograde muscle-to-neuron delivery of proteins, muscle need to be transduced for expressing a fluorescently labeled target protein, or an empty backbone expressing only the fluorophore as a control. This can be achieved either by virally infecting the myoblast culture with lentiviral particles, or by lipofection. This protocol describes the use of a lipofection reagent. Muscle can be transfected 4 h after their plating into the coated wells in the 24-well plate prepared in Subheading 3.1, **step 23**.

1. Prepare a Turbofect® (Thermo; R0533) reaction in a 1.7 mL Eppendorf tube by mixing 1 µg of plasmid DNA with filtered Opti-MEM (Gibco; 31985-047). Complete to 100 µL per well.
2. Add Turbofect® transfection reagent 1.5 µL per well, and immediately vortex vigorously.
3. Incubate the reaction tube at room temperature for 15 min. Avoid agitation of the tube.
4. After 15 min, add 100 µL of transfection mix dropwise into every well, shake the plate for a few seconds, and incubate for 8–12 h in CO_2 incubator at 37 °C.
5. After incubation, discard the medium from each well, and add fresh, pre-warmed antibiotic-free Bioamf® medium.
6. Let the cells recover for 2–4 h and then prepare for their transfer into microfluidic chambers (in Subheading 3.5.2).

3.3 Microfluidic Chamber Preparation

Microfluidic chambers that fit the application of this protocol are commercially available, e.g., Xona microfluidics SND450 model. Alternatively molds for microfluidic devices can be fabricated in specialized nanofabrication facilities [11]. Within this method we describe the co-culturing in microfluidic chambers made in our institute's facilities (Fig. 1) [11].

3.3.1 Cleaning and Sterilizing Microfluidic Chambers

1. Use a thick industrial scotch tape to remove gross dirt from both sides of the PDMS microfluidic chambers. Avoid pressing hard over the microfluidic elements.

2. Move microfluidic chambers into a tissue culture-grade 10 cm plate, fill the plate with analytical grade 70% Ethanol, and place on an orbital shaker for 5 min.
3. In a laminar hood, dispose the Ethanol, leave the plate open and allow it also to evaporate from the microfluidic chambers.
4. Adhere the microfluidic devices to a 35 mm or 50 mm Fluorodish® glass bottom plate by pressing the chambers with your finger against the dish (*see* **Note 14**).
5. Move plates into a 70 °C oven for 20 min, and then inside a laminar hood press again the chambers against the plate (*see* **Note 15**).
6. To finalize sterilization, expose the plates to UV light for 10 min.

3.3.2 Coating Microfluidic Chambers for Neuromuscular Co-cultures

While coating follow the "proximal"/"distal" terminology as appeared in Fig. 1.

Be aware that coating procedure includes two overnight incubations, and time the coating according to motor neuron culture day.

1. Add 80 μL of PLO solution per each well of the proximal compartment. In order to confirm the flow of the PLO through growth channel, use a 200 μL pipette and point it to the opening of the channel (red circle in Fig. 1a) and pipette the PLO back and forth until it exits into the opposite proximal well.
2. Similarly, add the Matrigel®-Laminin coating solution to the distal compartment well. Again, verify that the coating flows through the growth channels.
3. Incubate overnight in a CO_2 incubator at 37 °C.
4. On the following day, remove coating from both compartments, wash the proximal wells once with 1× PBS, and allow the microfluidic chambers to dry for 15 min at room temperature inside the laminar hood.
5. In a similar fashion to **step 1**, add 80 μL of Laminin solution per each well in the proximal compartment, and 80 μL or 1× PBS to the wells in the distal compartment.
6. Incubate overnight in a CO_2 incubator at 37 °C.
7. The next day remove the Laminin solution and wash twice with CNB medium eventually leaving the wells in the proximal compartment with 80 μL of CNB. Replace the PBS in the distal compartment with 80 μL of Bioamf® 1% P/S medium per well.

3.4 Primary Motor Neuron Culture

1. Prepare one 10 cm plate and a 24-well plate with 10 mL and 1 mL/well of HBSS 1% P/S solution, respectively.
2. Prepare a 50 mL falcon tube and a 1.7 mL Eppendorf tube with 50 mL and 1 mL of HBSS 1% P/S, respectively. Mark the Eppendorf tube as *Tube 1*.
3. Euthanize an E12.5 pregnant mouse, sterilize the abdomen surface with 70% Ethanol, cut open the lower abdomen and reveal the uterus and embryo sacs. Remove uterus and embryonic sacs into the 10 cm plate with HBSS 1% P/S.
4. Separate the embryonic sacs from each other, and extract each embryo into a well within the 24-well plate with HBSS 1% P/S (*see* **Note 16**).
5. While working under a stereoscope, isolate the embryonic spinal cord, clear the meninges off, and remove the dorsal horns as illustrated previously [10]. Collect the 4-6 ventral-horn spinal cords into *Tube 1* (*see* **Notes 17** and **18**).
6. Continue the culture procedure inside a tissue culture-grade laminar hood.
7. Use sterile small surgery scissors to cut the spinal cords inside *Tube 1* into small ~1 mm fragments.
8. Add 10 μL of Trypsin solution to the bottom of *Tube 1*, mix well and incubate for 10 min in a 37 °C water bath. After 5 min tap forcefully on the tube to resuspend the spinal cord fragments. After 10 min you should notice that the fragments have formed a tall helical structure inside the tube.
9. During the incubation of the previous step, prepare a 15 mL falcon tube (*Tube 2*) containing 800 μL of pre-warmed filtered L-15 medium, 100 μL of BSA 4% solution, and 100 μL of DNase solution. Additionally, mark another empty 15 mL tube as *Tube 3*.
10. Using a 1 mL pipette tip, collect the digested spinal cord fragments from *Tube 1* into *Tube 2*. The fragments should be viscous and should pull together when they are pipetted into the tip, avoid collecting excess HBSS solution from *Tube 1*.
11. Inside *Tube 2* triturate the spinal cord fragments three times using a 1 mL pipette and let the undissolved fragments to sink for 2 min.
12. Collect only the supernatant from *Tube 2* into *Tube 3*. Make sure not to leave the undissolved fragments in *Tube 2*.
13. Return to *Tube 2* and add 100 μL of BSA 4% solution, 20 μL of DNase solution, and 900 μL of CNB medium in that order.
14. Triturate the spinal cord fragment six times. If any undissolved fragments persist, let those sink down for 2 min and only then collect the supernatant from *Tube 2* into *Tube 3*.

15. If there is still a large portion of undissolved spinal cord fragment in *Tube 2*, repeat **steps 13–14**.
16. Form a BSA-Cushion inside *Tube 3* by slowly adding 1 mL of BSA 4% solution to the bottom of the tube.
17. Centrifuge *Tube 3* at 400 × *g* for 5 min at room temperature.
18. Carefully discard the supernatant, tap on the tube several times to resuspend the cell pellet, and then add 1 mL of CNB medium.
19. Add 20 μL of DNase solution into *Tube 3*. And then triturate six times using a 1 mL pipette to dissolve the pellet completely.
20. Add 5 mL of CNB medium into *Tube 3*, mix well and then move 3 mL into a new empty 15 mL falcon tube—*Tube 4*.
21. Slowly add 1 mL of OptiPrep gradient solution into the bottoms of *Tubes 3 and 4* (*see* **Note 19**).
22. Centrifuge *Tubes 3 and4* at 770 × *g* for 20 min at room temperature. Reduce the acceleration and deceleration to minimum for avoiding distortion of the phase separation.
23. During centrifugation, prepare a new 15 mL falcon tube—*Tube 5* with 2 mL of warm CNB medium.
24. After centrifugation, motor neurons should be concentrated in the interphase between the top CNB solution and the bottom OptiPrep solution and appear as a white turbid fraction. Using a 1 mL pipette, collect the entire cell content within the interphase of *Tubes 3 and 4* and move them into *Tube 5*. Do that while collecting of any minimal OptiPrep solution as possible.
25. Add 4 mL of CNB medium to *Tube 5* and form a 1 mL BSA 4% solution cushion in the bottom of the tube.
26. Centrifuge at 400 × *g* for 5 min at room temperature.
27. Carefully discard the supernatant, tap on the tube several times to resuspend the cell pellet, and then add 1 mL of CNB medium. Mix gently until pellet is completely dissolved.
28. Determine the cell concentration and the total yield of the culture.

3.5 Plating Motor Neurons and Muscles Inside Microfluidic Chambers

The plating of motor neurons inside microfluidic chambers is performed by injecting highly concentrated cells directly into the proximal channel.

3.5.1 Plating Motor Neurons in the Proximal Compartment

1. In a 1.7 mL Eppendorf tube, concentrate 150,000 motor neurons per chamber at 400 × *g* for 5 min at room temperature.
2. Carefully and manually discard the supernatant, and then resuspend the pellet with RNB medium. Use 4 μL of RNB medium per microfluidic chamber (*see* **Note 20**).

3. Remove all medium from both proximal wells. Do not remove the remaining medium within the channel itself. Remove 95% of the medium from both distal wells leaving a minimal volume (~8 μL per well) of medium inside the wells to prevent unwanted cell flow from proximal to distal compartment.
4. Collect 4 μL of concentrated motor neurons in a 20 μL pipette tip, lift and tilt the microfluidic chamber so that the proximal channel becomes perpendicular, and inject the cells directly into the proximal channel opening of the top well, wait 5 s and then reorient the plate.
5. Pull the cells into the channel by aspirating them from the opposite channel opening, and then pushing them back in (*see* **Note 21**).
6. Incubate the microfluidic chambers in a CO_2 incubator at 37°C for 35 min for enabling the adherence of motor neurons within the channel.
7. After 35 min, slowly add 15 μL of RNB medium to both proximal wells, and 15 μL of Bioamf® 1% P/S medium to both distal wells. Place back inside the incubator for an additional 20 min.
8. Add 65–75 μL of RNB/Bioamf® 1% P/S to each proximal/distal well, respectively.

3.5.2 Plating the Transfected Muscles

Muscles can be added to the microfluidic chamber 3–16 h after neuronal plating.

1. Discard the medium in the 24-well plate containing the transfected muscles and wash the wells once with 500 μL pre-warmed 1× PBS.
2. Discard the PBS and add 100 μL of room-temperature Trypsin-C solution. Incubate the plate in CO_2 incubator at 37 °C for 10 min and inspect the cells after 5–7 min. If the cells have already detached, proceed to the next step.
3. Neutralize the trypsin by adding 200 μL of pre-warmed Bioamf® 1% P/S medium and collect the cells from all wells into a 15 mL falcon tube.
4. Repeat again with another 200 μL of Bioamf® 1% P/S.
5. Centrifuge at 400 × *g* for 5 min at room temperature.
6. Discard the supernatant and resuspend the cells in 1 mL of Bioamf® 1% P/S.
7. Determine the cell concentration.
8. Prepare myoblasts for plating: Dilute 75,000 myoblasts in a total volume of 160 μL Bioamf® 1% P/S per chamber.

9. Discard the medium from both distal wells of a microfluidic chamber and plate the myoblasts by pipetting the diluted cell solution from one well to another through the distal growth channel, add the remaining volume of cells to the second distal well.

3.6 Co-culture Maintenance

Days In Vitro (DIV) terminology refers neuronal culturing day as DIV 1.

1. At DIV 2, in order to prevent glial contamination, replace the medium in the proximal wells with RNB supplemented with 1 μM Cytarabine (Ara-C).
2. At DIV 4 discard all medium in proximal wells and add pre-warmed CNB medium. Discard 60 μL of medium from each well in the distal compartment and add 65 μL of pre-warmed Bioamf® 1% P/S.
3. Inspect the microfluidic chambers every day. When first axons cross into the distal compartment, replace the medium in both compartment to PNB for 2 days (*see* **Note 22**).
4. After 2 days with PNB medium, replace the mediums in proximal and distal compartments to CNB/Bioamf® 1% P/S, respectively.
5. At DIV 7, prior to imaging of axonal transport, and in the case that neurons are not fluorescently labeled, add 500 ng/mL of Alexa-647 conjugated Cholera toxin B to the medium in the proximal compartment. Maintain a higher volume of medium in the wells of the distal compartment for preventing unwanted diffusion of Cholera toxin. Incubate culture with Cholera toxin overnight in CO_2 incubator at 37 °C.
6. At DIV 8 onward, co-culture should be ready for imaging of axonal transport (Fig. 2a–b).

3.7 Axonal Transport Imaging

Aside from the genetic reporters used to visualize the axonal transport of specific proteins, general organelle dyes, e.g., MitoTracker, LysoTracker, as well as Qdot-labeled Neurotrophins can be used for counterstain, colocalization, and normalization [11, 12]. This sort of labeling can be performed immediately before imaging axonal transport. Follow manufacturer protocols and protocol publication for more specific applications.

1. Live axonal transport imaging should be performed in a 37 °C heated chamber with 5% CO_2 atmosphere conditions.
2. Image axonal transport using an oil 60× objective.
3. In order to prevent oxidative damage to the cultured cells, avoid using strong light/laser power. (*see* **Note 23**)
4. Focus on axons with proximity to a muscle expressing your fluorescent protein of interest in the distal compartment. For

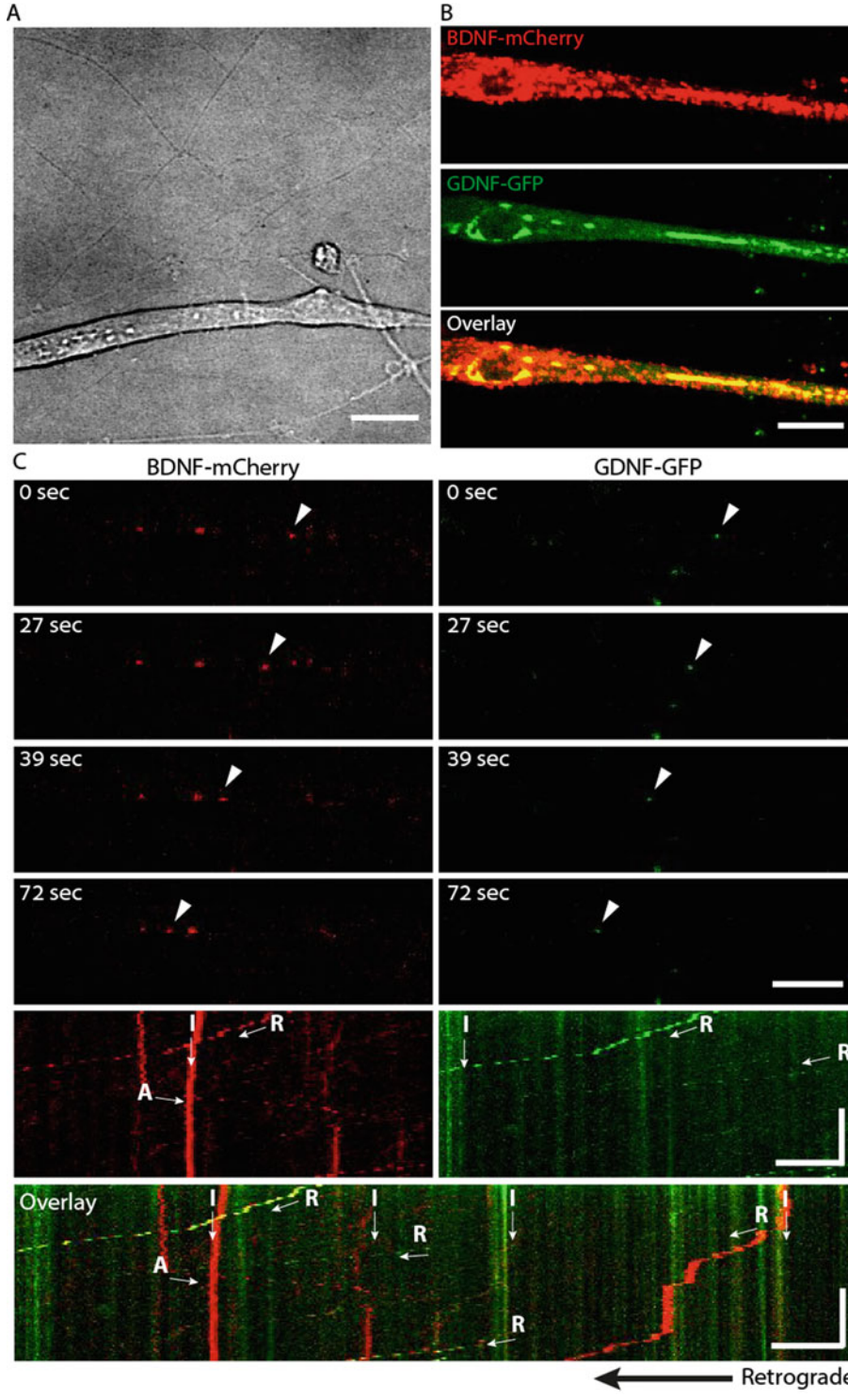

Fig. 2 Muscle-derived BDNF and GDNF are co-transported in motor axons. (**a**) Phase contrast representative images of axon-muscle interactions at the distal compartment after 1 week of co-culturing, at the day of axonal transport imaging. Scale bar: 20 μm. (**b**) Representative images of a GDNF-GFP (green) and BDNF-mCherry (red)-expressing muscle in the distal compartment of a microfluidic chamber. Scale bar: 10 μm. (**c**)

convenience, axons can be tracked back and imaged at a more proximal region within the aligned microgrooves.

5. Acquire 5-min movies at a frame interval of 3 s (100 frames) of all fluorescently labeled proteins. If available, use an autofocus/perfect focus/focus clamp function.

3.8 Image Analysis

Analysis of axonal transport can be performed to extract the following parameters: fraction of particles that are immobile or traveling anterogradely/retrogradely (extrapolated from kymographs; Fig. 2), average speed, instantaneous velocity, run length, pause duration (extrapolated from single particle tracking) [12].

3.8.1 Kymograph Analysis

1. Download the "Kymo_ToolBox.jar" plugin for FIJI/ImageJ.
2. Open the axonal transport image sequence with FIJI.
3. Set the image properties: Insert the correct micro/pixel ratio, time interval, and verify that the "Slices (z)" parameter is set to 100 (in case of 100 frames), while the "Frames (*t*)" parameter is set to 1.
4. Use the "Deinterleave" function to split the hyperstack into discrete channels images.
5. To identify the axonal trajectories, use the "Z Project" max intensity projection function on either one of the channels.
6. Set the width of the line tool to fit the width of the trajectory (usually 5–8).
7. Use the segmented line tool to draw a Region Of Interest (ROI) over an axon trajectory. Mind that the horizontal direction (left-to-right/right-to-left) of the line you are drawing will impact the orientation of the kymograph and is important for determining anterograde/retrograde directionality.
8. Save the ROI to the ROI manager.
9. Go to "Plugins/KymoToolBox/Draw Kymo," fill in the correct line width you used, check the "Get Kymo" checkbox and press ok (Fig. 2c).
10. Begin analyzing the kymograph to determine the fraction of particles traveling anterogradely/retrogradely or remain immobile throughout the movie.

Fig. 2 (continued) Representative time-lapse images of axonal transport and kymographs of muscle-derived GDNF-GFP (green) and BDNF-mCherry (red). Lower panel shows uncropped and overlaid kymographs of both channels indicating that a portion of GDNF and BDNF particles are co-transported in motor axons along with their discrete transport. Kymographs illustrate particles trafficking anterogradely (A), retrogradely (R), and particles that are immobile (I), as well as their vectors (white arrows). Scale bars: time-lapse images, 10 μm; kymographs: horizontal 10 μm; vertical, 100 s

11. In order to analyze particle mean velocity, run length, etc., draw a segmented line ROI over the particle trajectory in the kymograph and go to "Plugins/KymoToolBox/Analyse Kymo." Define parameters such as speed limitation of particles, line width, etc., and press ok.
12. Copy the data in the output (time, XY coordinates, frame-frame distance) into an excel spreadsheet where further analyses can be done to extrapolate the data listed in **step 11**.
13. Repeat **steps 5–12** for other channels as well.
14. Alternatively, use a semi-automated single particle tracking using Bitplane Imaris [12].

4 Notes

1. Prepare Collagenase-I solution freshly before use and bring to room temperature.
2. Attempt to collect only the longest and intact muscle fibers, and avoid from collecting any unidentified tissues, e.g., nerves, blood vessels, connective tissue.
3. This step is meant for avoiding contamination of unspecific cells and to further washout collagenase remains.
4. The pre-plating is a repetitive process performed over 3 consecutive days intended to purify myoblast fraction and minimize fibroblast contamination (Fig. 1).
5. Before beginning the pre-plating, examine the *Plate C* under a microscope and determine the confluency of adhered satellite cells on the bottom of the culture dish. It should range between ±30% and 70%. In case of high confluency in all wells, at Subheading 3.1, **step 17** consider splitting the cells into two 10 cm plates.
6. ♀—symbol indicates the reaction volume for the second and third pre-plating days.
7. Collect the cells rapidly as the cells tend to re-adhere rapidly to the matrigel® coated wells after the trypsin neutralization.
8. After collecting the cells in suspension, inspect the wells under a microscope to verify collection of all cells. In the case that many cells remained adhered, trypsinization process can be repeated.
9. Use a sterile cell scraper to evenly distribute the Matrigel® solution on the plate surface and collect the remainder liquid which can be used to coat additional plates. Diluted Matrigel® solution can be stored at 4 °C for use in the consecutive days.

10. Inspect *Plate D* again to verify only fibroblasts remained. If needed, *Plate D* may be washed again with additional 4 mL of Bioamf 1% P/S.
11. Coat the number of wells in a 24-well plate that correspond with the number of microfluidic chambers you intend plate muscles in.
12. Follow the standard cryopreservation procedure by gradually freezing the vials within an isopropanol container at −80 °C for 12–24 h prior to their deposition in liquid nitrogen.
13. Thawing of cryopreserved vials should be done rapidly in a 37 °C water bath. Then move the cells into 5 mL of pre-warmed filtered Bioamf® medium (no antibiotics), centrifuge 400 × *g* for 5 min at room temperature, and resuspend the cells in 1 mL of Bioamf® 1% P/S medium. Verify the cell concentration and then plate the cells. Myoblast will then begin to differentiate and cannot be cryopreserved for a second time.
14. Make sure that the microfluidic elements are facing the glass. While pressing, place the plate on a steady and hard surface to avoid the thin glass bottom from shuttering.
15. In order to verify that the chambers adhered properly, invert the plates and examine the reflection from the glass bottom. Where proper PDMS-glass contact is achieved you should be able to notice a different reflection from the glass.
16. Extraction of the embryos from the yolk sacs can be done by holding the placenta with one pair of forceps and pinching the yolk sac with another pair of forceps.
17. The neuronal yield is ~ 800,000 cells per ventral spinal cord. Adjust the number of spinal cords according to the total number of cells required.
18. To avoid damaging the fine forceps while dissecting, prepare a 35 mm culture dish layered with a thin 2–4 mm baked PDMS film. These plates are reusable.
19. Avoid from agitating the tubes after OptiPrep cushion formation, as this will break the phase separation.
20. Example for plating motor neurons at high concentration in microfluidic chambers: for 4 microfluidic chambers: Concentrate 600,000 cells in 16 μL of RNB medium.
21. This will equalize the volumes in both proximal wells and should trap the cells inside the channel. Assess the success of this procedure under a microscope while keeping the plates leveled.
22. Starvation with PNB enhances the axonal cross into the distal compartment and facilitates NMJ formation.

23. When attempting to image axonal transport in the proximity of a fluorescent muscle, image parameters should be set for visualizing the particles within the axons on the cost of acquiring a saturated image of the muscle. A shorter exposure image showing the unsaturated muscle for representative figures can be acquired prior to time-lapse imaging.

References

1. Ibáñez CF (2007) Message in a bottle: long-range retrograde signaling in the nervous system. Trends Cell Biol. 17:519–528
2. Harrington AW, Ginty DD (2013) Long-distance retrograde neurotrophic factor signalling in neurons. Nat Rev Neurosci 14: 177–187. https://doi.org/10.1038/nrn3253
3. Guedes-Dias P, Holzbaur ELF (2019) Axonal transport: driving synaptic function. Science 366(6462):eaaw9997. https://doi.org/10.1126/science.aaw9997. PMID: 31601744; PMCID: PMC6996143
4. Surana S, Villarroel-Campos D, Lazo OM et al (2020) The evolution of the axonal transport toolkit. Traffic 21(1):13–33. https://doi.org/10.1111/tra.12710. Epub 2019 Nov 28. PMID: 31670447
5. Brenner D, Yilmaz R, Müller K et al (2018) Hot-spot KIF5A mutations cause familial ALS. Brain 141:688–697. https://doi.org/10.1093/brain/awx370
6. Gunawardena S, Her L-S, Brusch RG et al (2003) Disruption of axonal transport by loss of huntingtin or expression of pathogenic polyQ proteins in Drosophila. Neuron 40: 25–40
7. Bilsland LG, Sahai E, Kelly G et al (2010) Deficits in axonal transport precede ALS symptoms in vivo. Proc Natl Acad Sci U S A 107: 20523–20528. https://doi.org/10.1073/pnas.1006869107
8. Ionescu A, Gradus T, Altman T et al (2019) Targeting the sigma-1 receptor via pridopidine ameliorates central features of ALS pathology in a SOD1 G93A model. Cell Death Dis 10. https://doi.org/10.1038/s41419-019-1451-2
9. Perlson E, Jeong G-B, Ross JL et al (2009) A switch in retrograde signaling from survival to stress in rapid-onset neurodegeneration. J Neurosci 29:9903–9917. https://doi.org/10.1523/JNEUROSCI.0813-09.2009
10. Ionescu A, Zahavi EE, Gradus T et al (2016) Compartmental microfluidic system for studying muscle-neuron communication and neuromuscular junction maintenance. Eur J Cell Biol 95:69–88. https://doi.org/10.1016/j.ejcb.2015.11.004
11. Gluska S, Chein M, Rotem N et al (2015) Tracking Quantum-Dot labeled neurotropic factors transport along primary neuronal axons in compartmental microfluidic chambers. Methods Cell Biol. https://doi.org/10.1016/bs.mcb.2015.06.016
12. Altman T, Maimon R, Ionescu A et al (2020) Axonal transport of organelles in motor neuron cultures using microfluidic chambers system. J Vis Exp 2020:60993. https://doi.org/10.3791/60993

Chapter 8

Imaging Diversity in Slow Axonal Transport

Archan Ganguly and Subhojit Roy

Abstract

The polarized morphology of neurons necessitates the delivery of proteins synthesized in the soma along the length of the axon to distal synapses; critical for sustaining communication between neurons. This constitutive and dynamic process of protein transport along axons termed "axonal transport" was initially characterized by classic pulse-chase radiolabeling studies which identified two major rate components: a fast component and a slow component. Early radiolabeling studies indicated "cohesive co-transport" of slow transport cargos. However, this approach could not be used to visualize or provide mechanistic insights on this highly dynamic process. The advent of fluorescent and photoactivatable imaging probes have now enabled real-time imaging of axonal transport. Conventional fluorescent probes have helped visualize and characterize the molecular mechanisms of transport of vesicular proteins. These proteins typically move in the fast component of axonal transport and appear as "punctate structures" along axons. However, a large majority of transported proteins that move in the slow component of transport, typically show a "uniform diffusive glow" along axons when tagged to conventional fluorescent probes. This makes it challenging to unequivocally track them in real time. Our lab has used photoactivatable fluorescent probes to tag three individual cytosolic proteins moving in the slow component of axonal transport, and identified three distinct modes of transport along axons. Our data from these experiments argue against the prevailing hypothesis based on classic radiolabeling studies, which suggested that all slow-transport proteins may move along the axon as one large macromolecular protein complex. Although other labs have started using photoactivation to study axonal transport of cytosolic proteins, this technique remains largely underutilized. Here, we describe the detailed protocols to image and analyze axonal transport of three typical slow-component cargoes along axons of cultured hippocampal neurons.

Key words Cytosolic proteins, Soluble proteins, Slow axonal transport, Photoactivation, PAGFP, Synapsin, Actin, Clathrin

1 Introduction

Neurons are polarized cells with morphologically and functionally distinct somato-dendritic and axonal domains. The axons of neurons typically connect the cell body of neurons with morphologically specialized structures called synapses, which form along distal end of axons. Observations from the early nineteenth century showing that axons disconnected from their cell bodies degenerate,

Alessio Vagnoni (ed.), *Axonal Transport: Methods and Protocols*,
Methods in Molecular Biology, vol. 2431, https://doi.org/10.1007/978-1-0716-1990-2_8,
© The Author(s), under exclusive license to Springer Science+Business Media, LLC, part of Springer Nature 2022

support the notion that the axons depend on the cell body for its survival [1]. Axon constriction experiments from the 1940s showing the accumulation of axoplasm and its subsequent proximal to distal flow upon the release of constriction, provided some of the first evidence for axonal transport [2]. However, it was not until the advent of radiolabeling in the 1960s that the phenomenon of axonal transport was characterized and defined. In classic pulse-chase radiolabeling experiments, radiolabeled amino acids were injected in the vicinity of neuronal cell bodies in vivo, and the radiolabeled amino acids were subsequently incorporated into newly synthesized proteins in the neuronal perikarya. These radiolabeled proteins were then transported into axons by the cell's innate transport machinery. Isolation of axons and examination of the profile of radiolabeled proteins along the length of the axon at various time points after injection led to the identification of two overall "waves" of movement along axons that were termed fast and slow axonal transport. The faster population moved at overall rates of ~ 50–200 mm/day and was composed of membranous proteins while the slower population moved only at overall rates of ~ 2–10 mm/day which consists of two distinct subsets of proteins: cytoskeletal (SCa) and cytosolic (SCb or soluble) proteins [3–6]. This distinction between slow and fast axonal transport is evolutionarily conserved across model organisms [7–17], highlighting its significance as a critical biological process in neurons. Early observations from radiolabeling experiments suggested the cohesive co-transport of both slow and fast proteins along axons as a unitary macromolecular complex [12, 18]. However, these radiolabeling studies could only identify static snapshots over time and were unable to capture the dynamics or provide molecular and mechanistic insights on the nature of slow axonal transport of proteins.

With the advent of fluorescence probes in the early 1990s, several fast-transport proteins were tagged with fluorescent probes and their movement along axons was tracked in real time by fluorescence microscopy. Fast-transport proteins appeared as punctate structures (due to their association with vesicles) along microtubule tracts and moved in association with kinesin motors in a proximal to distal (anterograde) direction, or with dynein motors moving in a distal to proximal (retrograde) direction along axons [19–23]. Tagging of cytoskeletal slow-transport cargos, such as neurofilaments, led to the identification of the intermittent, kinesin dependent movement along axons between long pauses (the "stop and go" model) [4, 24–27]. Similar studies with another cytoskeletal protein tubulin, suggested the sliding movement of short tubulin polymers in a motor protein dependent manner along axons [28, 29]. While these studies provide some support for the cohesive movement of fast- and slow-transport cargos, fluorescent tagging of cytosolic SCb cargoes results in a uniform diffusive glow along

axons [30] unlike the distinct punctate profile of fast-transport cargoes. This makes it challenging to visualize the transport of SCb cargos by conventional live-microscopy. Since many proteins transported in the SCb fraction are deposited at the synapse and have critical roles in regulating synaptic physiology (e.g., synapsin, synuclein, clathrin)[5], the inability to visualize their transport and to define the molecular mechanism essential for their transport to synapses remains a limitation in determining the role of their transport on neuronal physiology.

To address this shortcoming, we tagged synapsin, a typical SCb cargo protein, to a photoactivatable fluorescent probe (PAGFP). PAGFP is a modified form of the GFP protein which shows a 100-fold increase in fluorescence (compared to its low background fluorescence) upon activation by violet light (405 nm)[30, 31]. By tagging synapsin with PAGFP and tracking the movement of small segments of photoactivated synapsin along axons over time, our work has shown the presence of a macromolecular synapsin transport complex which moves along axons by "transient association" with fast-transport vesicles moving in a kinesin dependent manner [30, 32]. We also found that the heat-shock proteins like Hsc70 was critical for the transport and stability of the synapsin transport complex along axons [33]. Using similar photoactivation techniques, other research groups have suggested a variation of the "transient association" model, where they show direct interaction of SCb cargoes with molecular motors (kinesins) for their transport along axons [34, 35]. Interestingly, recent work from our lab has identified distinct modalities of slow axonal transport for individual SCb proteins. For example, when we tagged F-actin (cytoskeletal cargo known to move in slow transport) to PAFGP and tracked its movement along axons, we observed a slow anterograde movement of photoactivated F-actin, dependent on a biased assembly of F-actin without any involvement of microtubules (MTs) or MT-based motors [36]. On the other hand, our experiments with clathrin tagged to PAGFP showed punctate dedicated clathrin-transport vesicle like structures, which move intermittently at fast-transport rates between long pauses [37]. These are reminiscent of the "stop and go model" proposed for neurofilaments [4, 26].

In summary, our work on slow axonal transport along with recent discoveries from other laboratories indicate existence of diverse modes of transport for individual SCb cargos. This is in contrast to the hypothesis based on radiolabeling studies that suggested cohesive co-transport of all SCb proteins as a macromolecular complex along axons. These discoveries have only been possible due to the availability of photoactivatable fluorescent probes and their use in studying slow axonal transport. In this chapter we provide detailed protocols used in our laboratory to study the slow axonal transport of three individual SCb cargoes. We anticipate that the imaging and analysis protocols described in this

chapter will help scientists study the slow axonal transport of other cytosolic proteins. This may lead to identification of new modalities and mechanisms underlying this intriguing cellular phenomenon.

2 Materials

2.1 Reagents for Mouse Hippocampal Neuronal Cultures and Transfection

2.1.1 Reagents

1. CD1 mouse strain pups (ideally P0-early P1). Timed pregnant females can be ordered from Charles River Laboratories (https://www.criver.com/) under approved IACUC protocols.
2. Glass-bottom dishes, uncoated (e.g., from vendors such as Mattek, Catalog# P35G-1.5-10-C; ibidi, Catalog# 81218-200 or Cellvis, Catalog# D35-10-1.5-N).
3. Poly-D-lysine.
4. 0.25% Trypsin-EDTA.
5. HBSS.
6. D-Glucose.
7. HEPES.
8. Pen-Strep.
9. NaCl.
10. Boric acid.
11. Sodium Tetraborate anhydrous.
12. B27.
13. GlutaMAX-1 (100X).
14. Fetal bovine serum, $\leq$10 EU/mL endotoxin (FBS, Hyclone).
15. 10× PBS.
16. Opti-MEM.
17. Lipofectamine 2000.
18. Laminar flow hood for sterile tissue culture conditions.
19. 5% CO_2 incubator.
20. 70 μm cell strainer.
21. Hemocytometer.
22. 1.5 in. coverslips.
23. Constructs for protein of interest tagged to PAGFP
    (a) PAGFP:Synapsin—a gift from George Augustine (Nanyang Technological University, Seoul, South Korea).
    (b) PAGFP:Utrophin-CH (a construct which labels F-actin)—gift from W. Bement (University of Wisconsin, Madison, WI).

(c) PAGFP:Clathrin-light-chain (PAGFP:CLC)—available on request from the Roy lab. PAGFP:CLC subcloned from the GFP:Clathrin light chain construct, a gift from James Keen (Thomas Jefferson University, Philadelphia, PA).

2.1.2 Solutions and Buffers for Mouse Hippocampal Neuronal Cultures

1. *Borax Buffer*: Add 51.4 mM boric acid and 23.6 mM sodium tetraborate decahydrate to 40–50 mL dd H_2O. Ensure that both salts dissolve completely. Adjust pH to 8.5 and sterilize using a 0.22 μm syringe filter. Store at 4 °C for long-term use.
2. *HBSS (Dissection buffer)*: Dissolve 400 mg D-Glucose, 832 mg HEPES, 5 mL Pen-Strep to 500 mL HBSS. Adjust pH-7.3 and filter sterilize. Store at 4 °C for long-term use.
3. *Neurobasal/B27 (NB/B27—neuronal culture media)*: Dissolve 10 mL B27, 5 mL GlutaMAX (100×) in 500 mL Neurobasal and filter sterilize using a 0.22 μm filter. Aliquots of NB/B27 are kept frozen at −20 °C for long-term use and at 4 °C for short-term use.
4. *Blocking buffer*: Add 3 mL FBS to 7 mL 1× PBS, filter sterilize using 0.22 μm syringe filter.
5. *Plating media*: Add 1 mL FBS to 9 mL of NB/B27, filter sterilize using 0.22 μm syringe filter.

2.2 Equipment and Reagents Essential for Photoactivation

2.2.1 Microscope Setup (Olympus)

Typically photoactivation experiments are performed using an inverted epifluorescence microscope (Olympus) with 40× and 100× oil immersion objectives along with a dual light source fluorescence illuminator IX2-RFAW (Olympus), a CCD camera (CoolSnap HQ2 or similar), shutters IX2-SHA, a filter wheel, and a pinhole. The details of our microscope setup have been described in Roy et al. [31], and are not elaborated here.

1. Mercury lamp.
2. Violet excitation filter (D405/40, Chroma).
3. Smart Shutter (Sutter Instruments).
4. GFP cube set (Chroma, cat. no. U-N41001).
5. Dichroic mirror (T495pxr, Chroma).
6. Emission filter (HQ535/50).

2.2.2 Microscope Setup (Nikon)

1. More recently, we have also used a Nikon microscope setup for photoactivation experiments [36]. This setup consists of an inverted epifluorescence microscope (Eclipse Ti-E; Nikon) equipped with CFI Plan Apochromat 40× and VC 100× 1.40 NA oil (Nikon) objectives.

2. A QuantEM:512SC (Photometrics) electron-multiplying charge-coupled device camera or a Scientific CMOS camera (Prime95B; Photometrics).
3. A LED illuminator (SPECTRA X; Lumencor) as a light source.
4. A dual-emission filter cube (Chroma Technology Corp) was used to collect GFP/RFP emission with subpixel registration.
5. Photoactivation is carried out using a Mosaic3 device (Andor Technology) attached to the Nikon Ti-E microscope.

In addition to the two setups described above, a range of other photoactivation devices are also commercially available (e.g., Andor).

2.2.3 Live Imaging Setup and Solutions

1. Hibernate-E low fluorescence medium (Brainbits, Catalog# HE-lf).
2. Weather station (Precision control) air stream incubator or a heated stage chamber; model STEV (World Precision Instrument, Inc).
3. Vibration-isolation table (TMC).
4. Nitrogen tank.
5. *Live imaging buffer*: 485 mL of Hibernate-E medium is mixed with 5 mL GlutaMAX (2 mM), 2 g D-Glucose (0.4%), 1.1 g NaCl (37.5 mM), and 10 mL (2%) B27. Ensure that the components are thoroughly mixed. Once prepared, this can be stored as 40 mL aliquots at −20 °C. Once thawed, an aliquot can be stored at 4 °C for up to 1 week.

2.2.4 Image Acquisition and Analysis Tools

1. MetaMorph imaging software (acquisition module and offline module; Molecular Devices).
2. MATLAB software, basic package (MathWorks) or Python Software.

3 Methods

The overall experimental objective is to obtain hippocampal neurons in culture from mouse brain, allow the neurons to mature, transfect these neurons with photoactivatable vectors tagged to the protein of interest, and then determine the kinetics of the photoactivated protein pools over time.

3.1 Hippocampal Neuronal Culture

1. On the morning of dissection, at least a couple of hours before the procedure, prepare dishes by adding 100 μL of 1 mg/mL Poly-D-Lysine dissolved in borate buffer on the glass coverslip of each Mattek dish (inner well). Spread evenly and allow the dishes to coat for 2 h at room temperature in a laminar flow

hood. After 2 h, wash the dishes 3× with ddH_2O. Dry the dishes thoroughly using an aspirator and set aside in the hood until neurons are ready to be plated (*see* **Note 1**).

2. Dissect the hippocampus from P0-P1 mice pups after rapid decapitation using a standard hippocampus dissection protocol. A typical hippocampal dissection is demonstrated in a video at this link: https://www.youtube.com/watch?v=Upf15CB29V4&t=6s
3. After dissection, place the dissected hippocampi in ice cold HBSS buffer until enzymatic treatment (*see* **Notes 2** and **3**). Two hippocampi from each brain yield approximately 60,000 cells after dissociation. Typically, about 25,000 cells are plated per dish (10 mm inner well diameter). However, the number of hippocampi to be dissected for the desired plating density need to be determined empirically. All dissections are carried out in ice cold HBSS buffer. Ideally, dissected hippocampi should not be placed in ice cold HBSS for more than 45–50 min.

   Caution: Follow all relevant governmental and institutional ethics guidelines on the use of animals in research.
4. Once the desired number of hippocampi have been dissociated and collected in ice cold HBSS, transfer them to 10 mL of pre-warmed 0.25% Trypsin-EDTA at 37 °C. Incubate the hippocampi for 15 min at 37 °C in a water bath. After 15 min, stop enzymatic digestion by transferring the hippocampi to 10 mL blocking buffer containing 30% FBS.
5. Subsequently transfer hippocampi from the blocking solution to 5 mL of 1× PBS. Transfer the hippocampi to a vial containing 1 mL of plating media for dissociation (*see* **Note 4**).
6. Dissociate hippocampi in 1 mL plating media by triturating 5–8 times with a P1000 pipette tip or flame polished glass pipettes of appropriate thickness. The plating media should turn slightly turbid during the dissociation process. Once this is achieved and no large chunks of tissue are seen floating in the media, pass the cell suspension through a 70 μm cell strainer. Use 10 μL of the sterile cell suspension to count cells on a standard hemocytometer.

   Caution: Do not triturate more than 8–9 times. Please be aware that excessive trituration may lead to poor cell viability and cell death. It is acceptable to leave small chunks if necessary. Additionally, **steps 2–4** are strictly carried out in a laminar flow fume hood to maintain sterile cultures.
7. Plate 25,000 cells/100 μL of the cell suspension on to center well of each poly-D-lysine coated dish.
8. Incubate the cells in a 5% CO_2 incubator for an hour to allow recovery. Then add 1–1.5 mL of neurobasal/B27 (NB/B27) media to the culture dish and place the dish back in the CO_2

incubator (*see* **Note 5**). The health of the neurons is monitored for the next 7–8 days (days in vitro; DIV7–DIV8) and 0.5 mL of fresh NB/B27 is added to each dish every 48 h (*see* **Note 6**). We typically use DIV7-10 neurons for our experiments. At this time, they exhibit well-defined axons and dendrites.

3.2 Transfection and Live-Cell Imaging

1. A day before the imaging, transfect the neurons with the desired PAGFP construct (e.g., PAGFP:Synapsin, PAGFP: Utr-CH or PAGFP:CLC), and a soluble red fluorescent protein (typically soluble mCherry) to identify axons. Since the PAGFP constructs have minimal fluorescence before photoactivation, co-transfection with soluble markers such as monomeric red fluorescent protein (mRFP) or mCherry is essential to identify axons suitable for photoactivation. As an example, to transfect five dishes:
   (a) Aliquot 125 μL of OPTI-MEM in two 1.5 mL Eppendorf tubes.
   (b) To the first tube, add 7.5 μL of Lipofectamine 2000 and mix well by pipetting.
   (c) To the second tube, add 1.2 μg DNA of the desired PAGFP and soluble mRFP construct and mix well. As a negative control for imaging soluble proteins by photoactivation, one can co-transfect neurons with the PAGFP backbone alone with soluble mRFP or mCherry constructs.
   (d) Mix the contents of the two tubes and incubate at room temperature for 15 min.
   (e) In the meantime, warm NB/B27 in the water bath to 37 °C. After 15 min, add 5 mL of warmed NB/B27 to the OPTI-MEM mixture.
   (f) Once this is done, take out the conditioned media from each culture dish and save it for addition post-transfection. Add 1 mL of the NB/B27 OPTI-MEM mix to each culture dish to be transfected.
   (g) Incubate the dishes at 37 °C, 5% CO_2 in the incubator for 3 h with the transfection mix.
   (h) Following this, remove the transfection media from each dish and wash the cells with 1 mL fresh pre-warmed NB/B27. Remove the NB/B27 and replace with the conditioned media from the respective dishes collected before transfection.
   (i) Keep the dishes back in incubator. Allow at least 4–6 h post-transfection before imaging the cells; for most experiments, we typically image neurons 16–24 h post-transfection (*see* **Notes 7** and **8**).

2. Before imaging, turn on the stage incubator and let it equilibrate to 37 °C (this may take up to an hour or longer). Warm the live imaging buffer to 37 °C in a water bath. Now remove the NB/B27 in each transfected dish and rinse three times with 1 mL of pre-warmed HELF buffer. After the fourth rinse, move the dishes to the weather station and begin imaging (*see* **Note 9**).

   Caution: The HELF medium maintains the pH similar to NB/B27 at atmospheric CO_2 levels, eliminating the need for a CO_2 delivery system during live imaging for several hours. Neurons in HELF survive and axons continue to grow for at least 24–48 h.

3. Identify a transfected neuron based on the soluble mRFP signal using the 40× oil immersion objective. DIV8 neurons should have several dendrites and one single axon emanating from the soma. Avoid neurons which have an overtly complex morphology, especially ones in which the morphologic distinction between axons and dendrites is not clear. Usually, a long straight axon with minimal morphological variations is selected as indicated in Fig. 1a. Axons are identified based on their morphology alone, and this requires some practice (*see* **Note 10**).

4. Once an axon is selected, move to the 100× oil immersion objective and first determine the axonal region of interest (ROI) to be photoactivated based on the soluble mRFP signal. Select a suitable axon for the experiment (*see* **Notes 11** and **12**), and take an RFP image (Fig. 1a, upper panel). The exact method of photoactivation will depend on the instrument used. In our Olympus setup (described in [31]), we have a fixed pinhole that needs to be centered in the ROI. However, in our Nikon setup with the Mosaic3 device (Andor Technology)[36], any desired shape in any part of the ROI can be selected for photoactivation. Once this is done, the ROI in the axon is ready for photoactivation.

5. For PAGFP, photoactivation is done with violet (405 nm excitation wavelength) light. The goal here is to photoactivate a population of molecules so that they can be visualized reliably over time. The time for which a sample is photoactivated is important as less than optimal activation would give a poor signal, and excessive exposure of the sample to incident light may cause bleaching, or even toxicity. Thus, the exact time for which a sample needs to be activated has to be empirically determined (*see* **Note 13**). In our setup, we typically use 1 s of photoactivation and capture a 10-bit GFP image with PAGFP-synapsin (Fig. 1a, lower panel). Following this, we acquire a movie which demonstrates the movement of the activated protein over time. To track PAGFP-synapsin

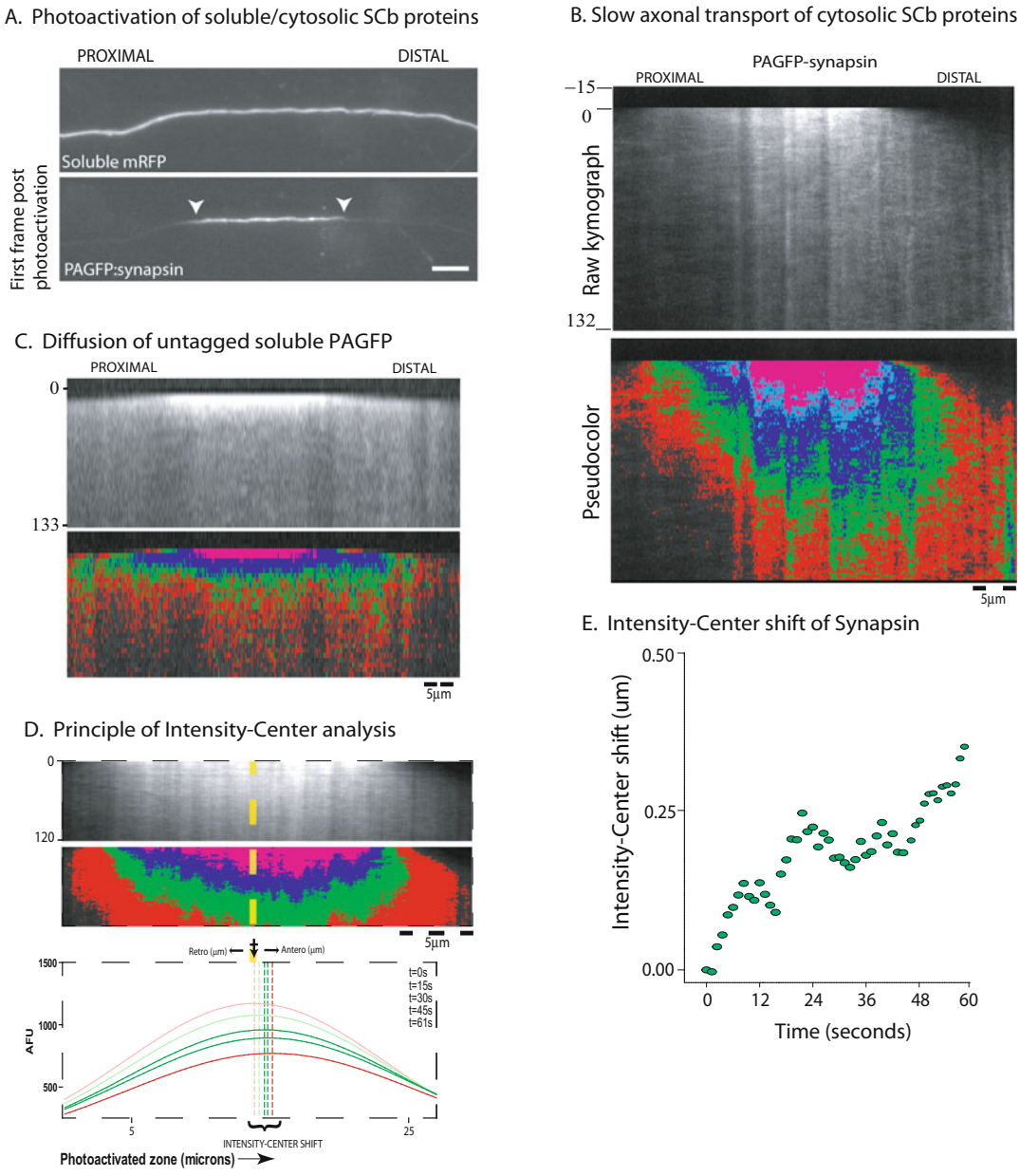

Fig. 1 Photoactivation strategy to visualize a typical slow-transport protein in axons. (**a**) Representative images of an axon co-transfected with soluble mRFP and PAGFP-Synapsin where the mRFP signal is used to identify the area of axon to be photoactivated. Synapsin, a stereotypic slow-transport protein shows a uniform diffusive glow in the photoactivated zone (marked by arrowheads) of the axon after photoactivation. (**b**) Kymographs of photoactivated PAGFP:synapsin showing bidirectional dispersion of photoactivated synapsin with a distinct anterograde (proximal to distal) bias. Pseudo color image of the kymograph clearly shows the anterogradely biased plume of fluorescence. Intensity ranges are represented by colors (red: lowest intensity bin, pink: highest intensity bin above background). Total number of exposure frames shown on left, scale bar is 5 µm. (**c**) When compared to PAGFP:synapsin, untagged PAGFP shows an unbiased and very rapid diffusion of fluorescence over time with no clear anterograde bias. Total number of exposure frames shown on left, scale bar is 5 µm. (**d**) Depiction of the primary principle of intensity-center shift assay used to analyze axonal transport of soluble (SCb) proteins. PAGFP:synapsin kymographs (above), and its quantification (below). The

movement, we typically collect ~30–60 s movies containing 65 frames at an interval of 500 ms at 2 x 2 camera binning. The movies are then used to generate a line scan kymograph for the photoactivated region using an in-built function in Metamorph software. A greyscale PAGFP-synapsin kymograph and corresponding pseudocolor heat map are shown in Fig. 1b. Note the anterograde bias in the PAGFP-synapsin fluorescence over time. In contrast, soluble PAGFP disperses bi-directionally, without any bias (Fig. 1c). The overall rate of movement of the synapsin population (Fig. 1e) is strikingly similar to rates seen with radiolabeling experiments [9].

Caution: The parameters above are specific to our settings and should be used only as a general guideline.

6. To photoactivate F-actin, a photoactivation region of interest (ROI) was selected based on the fluorescent intensity of mCherry. A region of interest with fairly uniform and bright mCherry fluorescence (Fig. 2a, top panel) between 150 and 250 μm from the soma was selected along the axon. The PAGFP:Utr-CH was photoactivated for 250 ms using a 405-nm diode laser light with the subsequent GFP fluorescence (Fig. 2a, lower panel) being imaged at one frame per second (with the 100× oil objective). For the control soluble PAGFP photoactivation, neurons were photoactivated for 30 ms, and GFP fluorescence was imaged every 600 ms. Kymographs depicting the movement of photoactivated F-actin over time post-photoactivation show fluorescent plumes moving away distally from the soma in an anterograde manner (Fig. 2b). The intensity shift of photoactivated F-actin from all axons imaged (Fig. 2c) and its combined average intensity shift (Fig. 2d) shows a distinct proximal to distal anterograde transport of F-actin over time. This slow anterograde movement of F-actin is dependent on the biased assembly and movement of the population without the involvement of microtubules (MTs) or MT-based motors [36]. Collectively, the biased polymerization of F-actin represents a model distinct from the "stop and go model" observed in neurofilaments.
7. Photoactivation of clathrin (PAGFP:CLC) was carried out using the Olympus microscope setup with a photoactivation

Fig. 1 (continued) curves below are overlays of selected line scan intensities from successive frames in the PAGFP:synapsin movie that was used to generate the kymograph above. The dashed vertical lines mark the center of mass (centroid or "intensity center") of the line scan fluorescence. Note the clear anterograde shift in the intensity center over time. Gaussian curves are shown for clarity, but raw data are used for actual calculations. (**e**) Graph depicting the "intensity-center shift" curve of PAGFP:Synapsin for the example in (**d**). A clear anterograde bias is seen in the numerical intensity-center value of each frame over time. Images adapted with permission from Scott et al. [30]

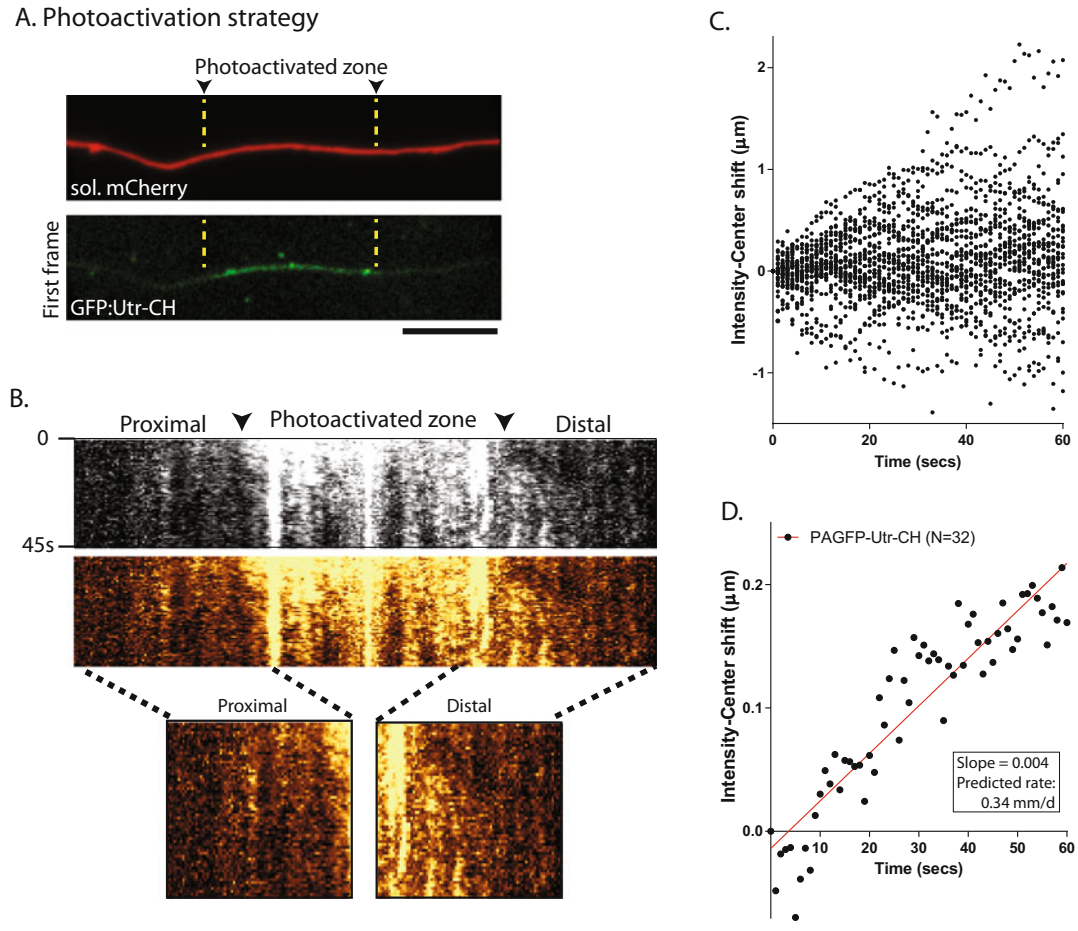

Fig. 2 Visualizing the biased anterograde transport of photoactivated F-actin along axons. (**a**) Representative images from an axon co-transfected with PAGFP:Utr-CH and soluble mCherry. The soluble mCherry signal is used to define the region of the axon to be photoactivated (arrowheads mark boundaries of photoactivated zone). Image in lower panel depicts the fluorescence of photoactivated PAGFP:Utr-CH immediately after photoactivation. (**b**) Kymograph depicting the movement of photoactivated F-actin (PAGFP:Utr-CH) over time along axons. The photoactivated zone is marked by arrowheads, and elapsed time in seconds is shown on left. Pseudo colored kymograph (middle panel) and zoomed insets from the proximal and distal regions of axons highlight the clear anterogradely biased dispersion of axonal actin with higher signal in distal axon segment. (**c**) The raw intensity-center shift of PAGFP:Utr-CH from all 32 axons imaged show a clear anterograde bias in intensity shift over time. (**d**) The mean intensity-center shift of all axons averaged over time shows a slow anterograde bias to the movement of photoactivated F-actin. Scale bars, 10 µm. Images adapted with permission from Chakrabarty et al. [36]

strategy similar to that used for PAGFP:synapsin. Axons were identified based on morphology, and only neurons with unambiguous morphology were selected for imaging. Axon ROI about 200–350 µm from the soma with moderate mCherry expression were selected for photoactivation. PAGFP:CLC was photoactivated with 405 nm light for 1 s and imaged every

1.2 s. Images were captured for a total of 100 frames. Unlike the dynamics of other SCb proteins described above, photoactivated PAGFP:CLC shows a punctate distribution in axons, instead of appearing as soluble pool like many other slow-transport proteins. Analysis of PAGFP:CLC particles over time revealed a slow anterogradely biased movement (see Fig. 1f–h in [37]). In addition to the photoactivation of slow component proteins, vesicular proteins that typically move in fast transport can also be visualized along axons using this photoactivation strategy (see Fig. 2a–c in [38]).

3.3 Image Analysis

1. For photoactivated proteins where individual PAGFP-tagged particles are seen post-photoactivation (PAGFP:CLC), a simple line scan kymograph can be generated using the built-in function in Metamorph, or Kymograph Builder plugin in Image J. Although such kymographs provide sufficient information about the movement of labeled particles along axons, we feel the intensity-center shift assay described below is more efficient at recapitulating the overall anterograde bias of photoactivated slow-component protein particles along axons.
2. For soluble proteins like synapsin where fluorescent molecules disperse as a plume of fluorescence, a combination of imaging functions in Metamorph and custom written code in Matlab are used to determine the overall bias along an axon. The main goal here is to measure the position of the fluorescence intensity-peak (centroid) along the axon, for every frame of a given movie. If there is bulk movement of fluorescence, then there would also be a corresponding shift in the centroid (see [31] for more details). To measure the centroid, first determine the boundaries of the photoactivated zone by thresholding the first frame of the time-lapse image series. Use a standard drop-down function in Metamorph to generate average intensity kymographs. This kymograph has information about each successive X axis and Y axis co-ordinates which carry information about the time points of imaging and successive distance from the proximal region of the axon. This generates a time distance plot which compresses the movie into a series of 2D images, facilitating further quantification [30].
3. Using custom written code in Matlab basic package, the change in the center of fluorescence mass is calculated for each time point in the movie. Briefly, the center of mass of each individual horizontal line scan of a kymograph is calculated. Then the center of mass of the photoactivated region (first frame) is subtracted from the center of mass for each subsequent frame. A shift in the center of mass with each subsequent frame in either direction represents a directional bias (Fig. 1d). When line scans are drawn from the proximal to

the distal direction, a net anterograde bias is seen from a sample PAGFP-synapsin kymograph (Fig. 1c). For a detailed description of the analysis and videos, refer to [30, 31]. We can provide Matlab codes upon request. More recently, we have used custom code written in Python software [36] based on a formula described in [30] to analyze intensity-center shift of photoactivated molecules over time.

4 Notes

1. Be sure to use sodium tetraborate decahydrate and not sodium decahydrate alone. The decahydrate salt dissolves readily in water and does not lead to poor coating resulting in cell death 2–3 days after plating.
2. To obtain consistent hippocampal neurons with good cell viability and transfection efficiency, we prefer using early P0-early P1 mice pups. Older pups result in higher cell death and poor viability. An alternative is to use neurons from embryonic (E18) pups.
3. During the hippocampi dissection, care should be taken to remove the fimbriae attached to the hippocampi. If not removed properly, these result in hippocampi aggregating during dissociation and lead to a lower cell yield.
4. We recommend dissociating not more than 8 hippocampi from 4 brains in 1–1.5 mL of plating media for best cell yields. If more hippocampi are dissected, the dissociation should be carried out in 2 mL of plating media.
5. Remember that the plating media has 10% FBS which allows the neurons to adhere to the glass coverslip after plating. The media used for feeding the neurons after plating has no FBS in it. Presence of FBS in the media used to feed the neurons will result in enrichment of non-neuronal cells.
6. Neuronal cultures are fed with 0.5 mL of fresh NB/B27 per dish every 2–3 days. This is essential to maintain neurons in optimal health. Allowing the neurons to stay in the incubator for long periods without adding fresh media leads to evaporation and change in the pH of the media.
7. The amount of DNA to be transfected needs to be determined empirically for each PAGFP-tagged protein and soluble marker. Too much PAGFP-tagged protein leads to high basal levels of GFP expression pre-photoactivation in the axons which may lead to inconsistent results with the intensity-center shift analysis.
8. Care should be taken to keep the imaging to between 16 and 24 h post-transfection for consistent results.

9. The weather station (on-stage incubator) should be equilibrated to 37°C before performing experiments and sudden changes in the temperature of the station should be avoided during the imaging session to prevent focal drift.
10. Rigorous selection criteria should be implemented before axons are selected for photoactivation, especially for imaging cytosolic proteins that also invariably have diffusible components. Since the axon selection is carried out based on the soluble mRFP signal, it is important to select axons showing an optimal amount of RFP (in the 12–14 bit range, using our camera). It is also of essence to avoid neurons expressing very high or very low levels of RFP. One can get better at axon selection by practice and by observing the entire range of RFP signal from the transfected neurons in each dish and selecting axons with moderate fluorescence falling within that range.
11. We recommend selecting a region of the axon at least 150–350 μm from the soma of the cell body for consistency. The length of axon from the soma to be photoactivated seems particularly important for F-actin since axons regions more distal than 200–250 μm show very little PAGFP:Utr-CH after photoactivation.
12. Neurons with complex morphology and axons with several bends along the primary axon should be avoided. Although movement can still be seen in those axons, analysis will be difficult—particularly in the case of soluble proteins. Ideally, linear axons with a uniform diameter should be selected. The region of axon to be photoactivated should be in uniform focus under the 100× objective during imaging. Low amount of post-photoactivation signal should be avoided and if needed photoactivation time can be increased. In case of soluble proteins, even very small defocused areas will render the time-lapse movie useless for analysis.
13. (Intensity of photoactivated zone) v/s (time of 405 nm light exposure) curves can be generated for each PAGFP-tagged protein, to empirically determine the time required for photoactivation.

Acknowledgments

Past and ongoing work on slow axonal transport in the Roy lab is supported by NIH grants R01NS075233, R01NS11978, and the March of Dimes (Basil O' Connor) grant. The authors thank the many researchers who have generously shared constructs with us.

Conflict of Interest

The authors declare no conflict of interest.

References

1. Ramon y Cajal S (1928) Degeneration and regeneration of the nervous system (trans: May RM). Oxford University Press, London
2. Weiss P, Hiscoe HB (1948) Experiments on the mechanism of nerve growth. J Exp Zool 107(3):315–395. https://doi.org/10.1002/jez.1401070302
3. Black MM (2016) Axonal transport: the orderly motion of axonal structures. Methods Cell Biol 131:1–19. https://doi.org/10.1016/bs.mcb.2015.06.001
4. Brown A (2003) Axonal transport of membranous and nonmembranous cargoes: a unified perspective. J Cell Biol 160(6):817–821. https://doi.org/10.1083/jcb.200212017
5. Roy S (2014) Seeing the unseen: the hidden world of slow axonal transport. Neuroscientist 20(1):71–81. https://doi.org/10.1177/1073858413498306
6. Roy S (2020) Finding order in slow axonal transport. Curr Opin Neurobiol 63:87–94. https://doi.org/10.1016/j.conb.2020.03.015
7. Baitinger C, Willard M (1987) Axonal transport of synapsin I-like proteins in rabbit retinal ganglion cells. J Neurosci 7(11):3723–3735
8. Black MM, Lasek RJ (1979) Axonal transport of actin: slow component b is the principal source of actin for the axon. Brain Res 171(3):401–413. https://doi.org/10.1016/0006-8993(79)91045-x
9. Brady ST, Lasek RJ (1982) Axonal transport: a cell-biological method for studying proteins that associate with the cytoskeleton. Methods Cell Biol 25(Pt B):365–398. https://doi.org/10.1016/s0091-679x(08)61434-x
10. Brady ST, Tytell M, Heriot K, Lasek RJ (1981) Axonal transport of calmodulin: a physiologic approach to identification of long-term associations between proteins. J Cell Biol 89(3):607–614. https://doi.org/10.1083/jcb.89.3.607
11. Dillman JF 3rd, Dabney LP, Pfister KK (1996) Cytoplasmic dynein is associated with slow axonal transport. Proc Natl Acad Sci U S A 93(1):141–144. https://doi.org/10.1073/pnas.93.1.141
12. Garner JA, Lasek RJ (1982) Cohesive axonal transport of the slow component b complex of polypeptides. J Neurosci 2(12):1824–1835
13. Koike H, Matsumoto H (1985) Fast axonal transport of membrane protein and intra-axonal diffusion of free leucine in a neuron of Aplysia. Neurosci Res 2(4):281–285. https://doi.org/10.1016/0168-0102(85)90006-9
14. Mills RG, Minamide LS, Yuan A, Bamburg JR, Bray JJ (1996) Slow axonal transport of soluble actin with actin depolymerizing factor, cofilin, and profilin suggests actin moves in an unassembled form. J Neurochem 67(3):1225–1234. https://doi.org/10.1046/j.1471-4159.1996.67031225.x
15. Sekimoto S, Tashiro T, Komiya Y (1991) Two 68-kDa proteins in slow axonal transport belong to the 70-kDa heat shock protein family and the annexin family. J Neurochem 56(5):1774–1782. https://doi.org/10.1111/j.1471-4159.1991.tb02080.x
16. Tytell M, Black MM, Garner JA, Lasek RJ (1981) Axonal transport: each major rate component reflects the movement of distinct macromolecular complexes. Science 214(4517):179–181. https://doi.org/10.1126/science.6169148
17. Yuan A, Mills RG, Bamburg JR, Bray JJ (1999) Cotransport of glyceraldehyde-3-phosphate dehydrogenase and actin in axons of chicken motoneurons. Cell Mol Neurobiol 19(6):733–744. https://doi.org/10.1023/a:1006953022763
18. Bray D (1997) The riddle of slow transport—an introduction. Trends Cell Biol 7(10):379. https://doi.org/10.1016/S0962-8924(97)01134-3
19. Bentley M, Banker G (2016) The cellular mechanisms that maintain neuronal polarity. Nat Rev Neurosci 17(10):611–622. https://doi.org/10.1038/nrn.2016.100
20. Maday S, Twelvetrees AE, Moughamian AJ, Holzbaur EL (2014) Axonal transport: cargo-specific mechanisms of motility and regulation. Neuron 84(2):292–309. https://doi.org/10.1016/j.neuron.2014.10.019
21. Misgeld T, Schwarz TL (2017) Mitostasis in neurons: maintaining mitochondria in an extended cellular architecture. Neuron 96(3):

651–666. https://doi.org/10.1016/j.neuron.2017.09.055

22. Nirschl JJ, Ghiretti AE, Holzbaur ELF (2017) The impact of cytoskeletal organization on the local regulation of neuronal transport. Nat Rev Neurosci 18(10):585–597. https://doi.org/10.1038/nrn.2017.100
23. Tas RP, Kapitein LC (2018) Exploring cytoskeletal diversity in neurons. Science 361(6399):231–232. https://doi.org/10.1126/science.aat5992
24. Roy S, Coffee P, Smith G, Liem RK, Brady ST, Black MM (2000) Neurofilaments are transported rapidly but intermittently in axons: implications for slow axonal transport. J Neurosci 20(18):6849–6861
25. Uchida A, Alami NH, Brown A (2009) Tight functional coupling of kinesin-1A and dynein motors in the bidirectional transport of neurofilaments. Mol Biol Cell 20(23):4997–5006. https://doi.org/10.1091/mbc.E09-04-0304
26. Wang L, Ho CL, Sun D, Liem RK, Brown A (2000) Rapid movement of axonal neurofilaments interrupted by prolonged pauses. Nat Cell Biol 2(3):137–141. https://doi.org/10.1038/35004008
27. Yan Y, Brown A (2005) Neurofilament polymer transport in axons. J Neurosci 25(30):7014–7021. https://doi.org/10.1523/JNEUROSCI.2001-05.2005
28. Rao AN, Patil A, Black MM, Craig EM, Myers KA, Yeung HT, Baas PW (2017) Cytoplasmic dynein transports axonal microtubules in a polarity-sorting manner. Cell Rep 19(11):2210–2219. https://doi.org/10.1016/j.celrep.2017.05.064
29. Wang L, Brown A (2002) Rapid movement of microtubules in axons. Curr Biol 12(17):1496–1501. https://doi.org/10.1016/s0960-9822(02)01078-3
30. Scott DA, Das U, Tang Y, Roy S (2011) Mechanistic logic underlying the axonal transport of cytosolic proteins. Neuron 70(3):441–454. https://doi.org/10.1016/j.neuron.2011.03.022
31. Roy S, Yang G, Tang Y, Scott DA (2012) A simple photoactivation and image analysis module for visualizing and analyzing axonal transport with high temporal resolution. Nat Protoc 7(1):62–68. https://doi.org/10.1038/nprot.2011.428
32. Tang Y, Scott D, Das U, Gitler D, Ganguly A, Roy S (2013) Fast vesicle transport is required for the slow axonal transport of synapsin. J Neurosci 33(39):15362–15375. https://doi.org/10.1523/JNEUROSCI.1148-13.2013
33. Ganguly A, Han X, Das U, Wang L, Loi J, Sun J, Gitler D, Caillol G, Leterrier C, Yates JR 3rd, Roy S (2017) Hsc70 chaperone activity is required for the cytosolic slow axonal transport of synapsin. J Cell Biol 216(7):2059–2074. https://doi.org/10.1083/jcb.201604028
34. Sadananda A, Hamid R, Doodhi H, Ghosal D, Girotra M, Jana SC, Ray K (2012) Interaction with a kinesin-2 tail propels choline acetyltransferase flow towards synapse. Traffic 13(7):979–991. https://doi.org/10.1111/j.1600-0854.2012.01361.x
35. Twelvetrees AE, Pernigo S, Sanger A, Guedes-Dias P, Schiavo G, Steiner RA, Dodding MP, Holzbaur EL (2016) The dynamic localization of cytoplasmic dynein in neurons is driven by kinesin-1. Neuron 90(5):1000–1015. https://doi.org/10.1016/j.neuron.2016.04.046
36. Chakrabarty N, Dubey P, Tang Y, Ganguly A, Ladt K, Leterrier C, Jung P, Roy S (2019) Processive flow by biased polymerization mediates the slow axonal transport of actin. J Cell Biol 218(1):112–124. https://doi.org/10.1083/jcb.201711022
37. Ganguly A, Sharma R, Boyer N, Wernert F, Phan S, Boassa D, Parra L, Das U, Caillol G, Han X, Yates JR, Ellisman MH, Leterrier C, Roy S (2021) Clathrin packets move in slow axonal transport and deliver functional payloads to synapses. Neuron 109(18):2884–2901. https://doi.org/10.1016/j.neuron.2021.08.016
38. Ganguly A, Roy S (2014) Using photoactivatable GFP to track axonal transport kinetics. Methods Mol Biol 1148:203–215. https://doi.org/10.1007/978-1-4939-0470-9_13

Chapter 9

Methods and Applications of Campenot Trichamber Neuronal Cultures for the Study of Neuroinvasive Viruses

Wesley M. Tierney, Ian A. Vicino, Stella Y. Sun, Wah Chiu, Esteban A. Engel, Matthew P. Taylor, and Ian B. Hogue

Abstract

The development of compartmentalized neuron culture systems has been invaluable in the study of neuroinvasive viruses, including the alpha herpesviruses Herpes Simplex Virus 1 (HSV-1) and Pseudorabies Virus (PRV). This chapter provides updated protocols for assembling and culturing rodent embryonic superior cervical ganglion (SCG) and dorsal root ganglion (DRG) neurons in Campenot trichamber cultures. In addition, we provide several illustrative examples of the types of experiments that are enabled by Campenot cultures: (1) Using fluorescence microscopy to investigate axonal outgrowth/extension through the chambers, and alpha herpesvirus infection, intracellular trafficking, and cell-cell spread via axons. (2) Using correlative fluorescence microscopy and cryo electron tomography to investigate the ultrastructure of virus particles trafficking in axons.

Key words Campenot, Neurons, Superior cervical ganglia, Dorsal root ganglia, Virus, Alphaherpesvirus, Herpes simplex virus, Pseudorabies virus, Fluorescence microscopy, Cryo electron tomography

1 Introduction

Neuroinvasive viruses are capable of infecting both the peripheral and central nervous systems. Natural or nosocomial neuroinvasive virus infections are often acutely severe, causing a variety of neuropathies, demyelinating disease, meningitis, and encephalitis [1, 2]. It is also clear that some viruses like the alpha herpesviruses (e.g., herpes simplex viruses, and varicella-zoster virus) can also spread to the central nervous system asymptomatically or sub-clinically, where they may cause chronic or recurrent neuroinflammation and trigger the development of neurodegenerative diseases like Alzheimer's [3]. While the spread of these viruses within the nervous system is not entirely understood, researchers have

Wesley Tierney and Ian A. Vicino contributed equally to this work.

Alessio Vagnoni (ed.), *Axonal Transport: Methods and Protocols*,
Methods in Molecular Biology, vol. 2431, https://doi.org/10.1007/978-1-0716-1990-2_9,
© The Author(s), under exclusive license to Springer Science+Business Media, LLC, part of Springer Nature 2022

taken advantage of their neuroinvasive properties as neuroanatomical circuit tracing tools [2, 4, 5].

Culturing peripheral neurons in vitro is an important aspect of studying neuroinvasive viral infections. Two well-established culture systems frequently implemented for viral research are embryonic rodent Superior Cervical Ganglia (SCG) and Dorsal Root Ganglia (DRG). These ganglia innervate the head, or much of the rest of the body, respectively. SCGs are part of the sympathetic nervous system, innervating areas such as the eyes, pineal gland, salivary glands, and some thoracic targets, including the heart. The SCG was one of the first model systems to study neurotransmission [6]. SCG neurons are relatively homogenous in culture (compared to primary CNS cultures or neurons differentiated in vitro from stem cells), and while they are mostly noradrenergic in vivo, they often undergo a phenotypic change and become cholinergic in vitro [7]. SCG neurons are strictly dependent on nerve growth factor (NGF) trophic support, but do not require co-culture with support cells, and can be maintained in culture for weeks. DRGs are part of the sensory system and consist of many subpopulations of neurons, such as proprioceptors, mechanoreceptors, thermoreceptors, and nociceptors. Mammalian DRG neurons are typically pseudounipolar in vivo, with one axonal process that innervates peripheral tissues, and another that conveys sensory information to the central nervous system. However, DRG neurons in vitro often exhibit variable numbers of axons, and it is unclear whether these axons maintain central vs. peripheral specializations. Different subpopulations of DRG neurons can be selected based on which neurotrophic factors are provided. DRG neurons do not require co-culture with support cells; however, it can be difficult to eliminate non-neuronal cells (such as Schwann cells) in DRG cultures [8, 9].

Studying the molecular and cell biology of virus infection in neurons has been greatly enhanced with novel live-cell imaging methods and fluorescent protein fusions. Recombinant viruses containing fluorescent protein fusions to viral structural proteins have been used to address viral entry, intracellular transport, and egress in neurons (e.g., [10–14]). However, a major difficulty is that the virus inoculum used to initiate the infection remains in typical dissociated neuron cultures, even for many hours post-infection. In strongly adherent non-neuronal cell lines, depending on the virus, excess inoculum that has not yet entered cells can be reduced or eliminated by briefly treating cells with an acidic buffer, neutralizing antibodies, or extensive washes/medium changes. However, neuronal cultures typically do not tolerate such perturbation to remove or neutralize viral inoculum. When tracking individual fluorescently labeled virus particles, it can be difficult to distinguish particles in the inoculum from progeny particles produced during infection. Given the very long distances virus particles

may need to traffic in axons, progeny particles may be exiting while, simultaneously, inoculum particles are still entering infected cells [15]. In the alpha herpesvirus literature, this problem has led to great confusion over the relationship between final-assembly/envelopment and axonal transport of virus particles [16]: do non-enveloped particles in axons represent progeny particles that are not yet enveloped, or inoculum particles that have already shed their envelopes during entry?

Campenot trichambers, like related microfluidics devices [17–19], are an important tool to clarify this problem of distinguishing virus inoculum and viral progeny (*see* **Note 1**). These compartmented neuron culture devices allow SCG and DRG neurons to extend axons between chambers, while maintaining fluidic separation between the chambers [20]. The "trichamber" version separates the culture volume into three compartments. Dissociated neurons can be seeded in one chamber, and over the course of approximately 2 weeks in vitro, axons can extend underneath two chamber walls into the opposite chamber [21, 22]. Using a lipophilic dye to measure axonal penetrance, anywhere from ~15–50% of neurons extend axons under both chamber walls [13, 23] (*see* **Note 2**). At this point, a virus infection experiment can be performed. For example, virus inoculum can be added to the cell body compartment to initiate infection, and following virus replication, progeny particles can be studied in the fluidically isolated axons in the opposite chamber. Because the chambers are fluidically separated, only progeny particles can reach the axon chamber via anterograde axonal transport processes. This ability to observe viral progeny without interference from the inoculum is important to better understand the intracellular transport, egress, and spread of neuroinvasive viruses.

2 Materials

2.1 Full List of Materials

1. 35-mm plastic tissue culture dishes.
2. Ibidi μ-dish, 35 mm, high (81156, Ibidi) (*see* Subheading 3.2.1).
3. Boric acid.
4. Sodium tetraborate.
5. Poly-DL-ornithine hydrobromide (*see* Subheading 2.2, **item 2**).
6. 0.2 μm filters, vacuum-driven and/or syringe-driven.
7. HBSS (-Ca, -Mg, +phenol red) (*see* **Note 3**).
8. Laminin, natural mouse (23017015, Invitrogen) (*see* Subheading 2.2, **item 3**).

9. Neurobasal medium (21103049, Invitrogen) (*see* Subheading 2.2, **items 4** and **6**).
10. B27 supplement (50×), serum free (1750444, Invitrogen).
11. Penicillin-streptomycin-glutamine (100×).
12. NGF mouse 2.5S native protein.
13. Water, tissue culture grade or ultrapure deionized.
14. DMEM, powder.
15. Methocel E4M (Hydroxypropylmethylcellulose, Hypromellose 2910 USP, viscosity 4000 cP at 2% in H_2O, H7509 Millipore-Sigma) (*see* Subheading 2.2, **items 5** and **6**).
16. Pin rake (Tyler Research).
17. Campenot trichambers (CAMP320, Tyler Research).
18. Reagents and equipment for cleaning Campenot chambers (*see* Subheading 3.4).
19. Hemostat forceps, 90° curved tip.
20. Silicone high-vacuum grease, Dow Corning (59344−055, VWR) (*see* Subheading 2.2, **item 1**).
21. Syringe, 10 mL disposable.
22. Syringe, 3 mL disposable Luer-lock (*see* Subheading 2.2, **item 1**).
23. Sawed-off 18G hypodermic needle (*see* **Note 4**) or blunt-fill needle (305181, BD) (*see* Subheading 3.2.2).
24. Rat, Sprague-Dawley, E15-E18 timed pregnant.
25. Forceps, fine tip Dumont #5.
26. Knives, microdissection.
27. Hibernate-E Medium (A1247601, ThermoFisher).
28. Trypsin (no EDTA, specific activity ≥10,000 BAEE units/mg) (*see* Subheading 2.2, **item 7**).
29. Pasteur pipets, 14.6 cm (*see* Subheading 2.2, **item 8**).
30. AraC (cytosine β-D-arabinofuranoside hydrochloride) (*see* Subheading 2.2, **item 9**).

2.2 Materials Prepared in Advance

1. *Silicone vacuum grease loaded into 3 mL Luer-lock syringes*: Initially load the silicone vacuum grease into a 10 mL syringe. Remove the plunger from the 10 mL syringe, align the opening of the silicone vacuum grease tube to the back of the 10 mL syringe, fill the syringe, and replace the plunger. Next, use the 10 mL syringe to fill the 3 mL syringe. Remove the 3 mL syringe plunger and fill the barrel with grease. Replace the plunger of the 3 mL syringe and squeeze out any excess air and grease so that the plunger is correctly seated. Wrap the grease-filled 3 mL syringe in aluminum foil and autoclave on a

liquid cycle. While only one syringe is sufficient to assemble trichambers, it is recommended to prepare multiple grease-filled 3 mL syringes in advance and store them at room temperature until use.

2. *Poly-ornithine solution (500 μg/mL in borate buffer)*: Make a 0.1 M sodium borate solution: Dissolve 19.1 g sodium tetraborate to 500 mL ddH_2O. Make a 0.1 M boric acid solution: Dissolve 6.2 g boric acid in 1 L ddH_2O. Make boric acid buffer: Beginning with 460 mL of boric acid solution, titrate in approximately 40 mL of sodium borate solution to pH 8.3. Make poly-ornithine solution: Dissolve 100 mg poly-DL-ornithine hydrobromide into 200 mL of borate buffer. Filter sterilize, aliquot into 50 mL conical tubes, store frozen at −20 °C, and thaw prior to use. Leftover poly-ornithine solution can be re-frozen and used for up to two freeze-thaw cycles.
3. *Laminin solution (10 μg/mL in HBSS)*: Thaw an aliquot of laminin and dilute 1:100 in HBSS, to a final concentration of 10 μg/mL. Make fresh each time and make the minimal amount required to coat dishes.
4. *Complete neuronal medium*: It is recommended to make complete neuronal medium in 50 mL batches. In a 50 mL conical tube, mix 48 mL of Neurobasal medium, 1 mL of 50× B-27 supplement, and 0.5 mL of 100× glutamine/penicillin/streptomycin solution. Filter sterilize using a 0.2 μm syringe-driven filter fitted to a 60 mL syringe. Add 30–50 μL of NGF after filter sterilizing (60–100 ng/mL final concentration). Use immediately, or store up to 2 weeks at 4 °C.
5. *1% or 2% methocel in DMEM*: DMEM thickened with methocel is required in two different concentrations: 1% methocel in DMEM is used during the process of assembling Campenot trichambers (*see* Subheading 3.2, **step 6**); 2% methocel in DMEM is used to make methocel-thickened neuronal medium (*see* **item 6** below). Make a 2% or 4% (w/v) solution of methocel in water: In a 500 mL autoclavable bottle, add a magnetic stir bar, 2 g or 4 g methocel, and 100 mL of tissue culture grade or ultrapure ddH_2O. Autoclave on liquid setting. Methocel is insoluble at high temperatures and is very slow to rehydrate and dissolve after autoclaving. Stir at room temperature or 4 °C until dissolved, which may take several days. Make a 7.5% (w/v) solution of sodium bicarbonate: Dissolve 7.5 g sodium bicarbonate in 100 mL of tissue culture grade or ultrapure ddH_2O.-Filter sterilize. Make a 2× DMEM solution: Follow manufacturer's instructions to measure the appropriate amount of DMEM powder to make 1 L of medium 1× DMEM, but dissolve in 500 mL to make a 2× DMEM solution. Autoclave or filter sterilize. Add 15 mL of 7.5% sodium

bicarbonate solution. Phenol red pH indicator in the solution should show a bright red color. Make methocel in DMEM: Mix 25 mL of the methocel in water solution with 25 mL of 2× DMEM, for a final concentration of 1% or 2% methocel in 1× DMEM (*see* **Note 5**). When making 1% methocel in DMEM for assembling Campenot chambers, adding penicillin/streptomycin is optional. Store at 4 °C for months.

6. *Neuronal medium containing 1% methocel*: Prepare an appropriate volume of neuronal medium (*see* Subheading 2.2, **item 4**, above), except with double the typical concentration of B-27 and glutamine/penicillin/streptomycin supplements. Filter sterilize. Add double the typical concentration of NGF, 200 ng/mL. Combine this Neurobasal medium with 2X supplements with an equal volume of 2% methocel in DMEM (*see* Subheading 2.2, **item 5**, above). Mix by pipette or inverting tube several times. The resulting medium is a 1:1 mixture of Neurobasal and DMEM medium, containing 1% methocel, and the typical concentration of supplements as in complete neuronal medium (*see* **Note 5**). Store up to 10 days at 4 °C.
7. *2X Trypsin solution*: Dissolve lyophilized trypsin in HBSS at a concentration of 0.5 mg/mL. Filter sterilize. Divide into 500 μL single-use aliquots and store at −20 °C (*see* **Note 6**).
8. *Flame-polished Pasteur pipets*: Partially close the air intake of a Bunsen burner for a cooler yellow/orange flame, which will provide more control over the flame-polishing process (optional). Pass the tip of the Pasteur pipet through the flame until the glass just begins to melt. As the glass melts, the opening of the pipet will become constricted. Continue to melt the tip slowly until the opening of the pipet tip is approximately half of its original diameter. Make flame-polished Pasteur pipets in batches and autoclave.
9. *AraC antimitotic solution*: Prepare a 1 mM stock solution in DMEM: Dissolve 25 mg of cytosine β-D-arabinofuranoside HCl into 89.4 mL DMEM (*see* **Note 7**).

3 Methods

The assembly of Campenot trichambers onto cell culture dishes requires finesse, and there are several common defects that can occur: Typically, a fraction of trichambers leak, or alternatively, trichambers can be too tightly sealed, preventing axonal penetration. Neuronal cultures can also fail over the course of 2–3 weeks required for robust axonal penetration. With these difficulties in mind, it is important to assemble more trichambers than required for planned experiments.

See **Note 8** for a summary schedule of the following procedures.

3.1 Preparation of 35 mm Cell Culture Dishes

1. Two days before trichamber assembly, begin coating the culture dishes. Add enough poly-ornithine solution to cover the cell culture area of each 35 mm dish, and incubate overnight in a cell culture incubator (37 °C, 5% CO_2, humidified).
2. The next day, remove the poly-ornithine solution, rinse once with tissue grade/ultrapure water or HBSS, and replace with enough laminin solution to cover the cell culture area, and incubate overnight in a cell culture incubator. If necessary, the laminin incubation can be reduced to 6 h.
3. The next day, gently remove the laminin solution and gently rinse dishes 3 times with HBSS. After the last rinse, leave the dishes open in the biological safety cabinet ~10 min until dry. Look for a splotch of dried salt residue on the plastic surface (visible in Fig. 1c, d) to be sure dishes are completely dry.

3.2 Assembling Campenot Trichambers

1. Sanitize the pin rake with 70% ethanol and dry, then scratch across the cell culture area in the middle of the dish, forming an array of parallel grooves, approximately 1.2 cm long (Fig. 1). The grooves must be long enough to pass under both inner chamber walls. Be firm! If the scratches are too shallow, the vacuum grease will form too tight of a seal, and axon penetration will be blocked or reduced. Figure 1c, d shows correctly scratched dishes.
2. Sanitize a hemostat or blunt forceps with 70% ethanol, and attach the blunt 18G needle to the autoclaved 3 mL grease-filled syringe, and depress plunger until a bead of grease is expelled.
3. Clamp the hemostat onto one of the inner trichamber walls, and lock the hemostat on the first notch (do not lock the hemostat any tighter because this can damage the trichamber wall). Lay the hemostat on the benchtop so the trichamber ring is facing up (Fig. 2a). Using a sterile p1000 pipette tip, push the trichamber so that it is level, parallel to the benchtop. Leveling the trichamber is important for subsequent greasing and assembly steps.
4. Using the grease-filled syringe, apply a bead of grease along the trichamber inner walls (Fig. 2b, c). Hold the syringe at a 45° angle to the trichamber walls, and dispense the grease slowly and evenly. Do not use pressure to stick the grease to the chamber walls; rather, dispense a bead of grease and allow it to lay onto the chamber wall under its own weight. It is important to dispense the grease evenly, so that there is a uniform unbroken bead of grease along the inner chamber

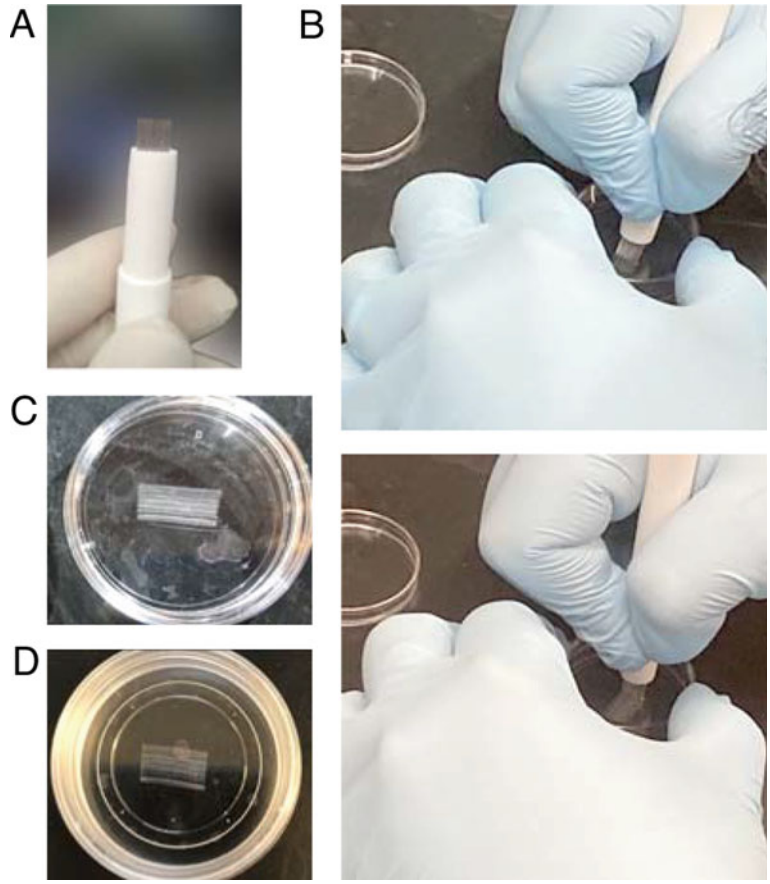

Fig. 1 Preparing cell culture dishes. (**a**) Commercially available pin rake (Tyler Research). (**b**) Using the pin rake to scratch an array of parallel grooves on the dish. Hold the pin rake at an angle and firmly press the pins into the plastic surface so the grooves are etched deeply. (**c**) Example of resulting grooves on a standard 35 mm culture dish. (**d**) Example of resulting grooves on an Ibidi μ-Dish. (**c**, **d**) Note the length and position of the grooves in the center of the culture area, particularly their position within the optical plastic inset of the Ibidi μ-Dish. Also, note the presence of a splotch of dried HBSS on each dish, indicating that the dish is fully dried

walls. If the bead of grease has imperfections, it can be gently scraped off with the blunt needle tip or a sterile pipette tip to try again. The quality of the grease barrier on the inner chamber walls is critical to avoid leaks while still allowing axonal penetration.

5. Next, apply a bead of grease around the outer circular chamber wall (Fig. 2d). More grease can be used on the outer wall, as this does not affect axonal penetration. Overlap the ends of the bead of grease to make a closed loop with no gaps. If necessary,

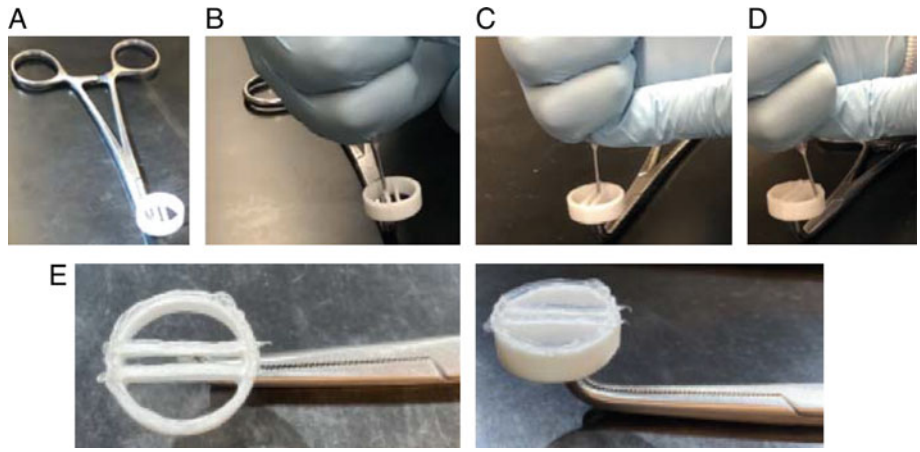

Fig. 2 Greasing the Campenot trichamber ring. (**a**) A trichamber ring held level in a hemostat. (**b**, **c**) Applying a bead of silicone grease to the two inner chamber walls. Note the sawed-off or blunt needle used to dispense the grease. (**d**) After applying grease to the inner chamber walls, apply grease to the outer chamber ring. (**e**) Example of resulting greased trichamber

apply two beads of grease to ensure the outer wall does not leak. Figure 2e shows a correctly greased trichamber ring.

6. Retrieve a prepared culture dish, and pipette a long drop (approximately 200 μL) of 1% methocel DMEM onto the array of grooves (Fig. 3a). The drop of methocel medium must be big enough to span the two inner chamber walls. This layer of methocel medium is critical to allow the axons to penetrate under the chamber walls. Proceed with the next steps immediately so the methocel does not dry.
7. Flip the dish over and place it gently on top of the trichamber (Fig. 3b), with the grooves arranged perpendicular to the inner walls of the trichamber. Do not apply any pressure; just let the dish lay onto the trichamber under its own weight. Lightly tap the hemostat 3–4 times on the work surface to attach the greased trichamber to the dish. Flip the hemostat over, unlock it, and allow the trichamber and culture dish to fall approximately 1–2 cm onto the benchtop. This tapping and dropping procedure applies enough force to allow the grease on the outer wall to seal against bare plastic, but does not cause the inner walls to be too tightly sealed.
8. Closely inspect the dish to ensure the grease between the dish and outer trichamber walls is completely attached with no gaps. If the outer walls are incompletely sealed to the dish, drop the dish 1–2 cm a few more times or apply very light pressure using a sterile pipette tip.
9. To check for leaks and prevent the methocel medium from drying, add complete neuronal medium (~250 μL) to the

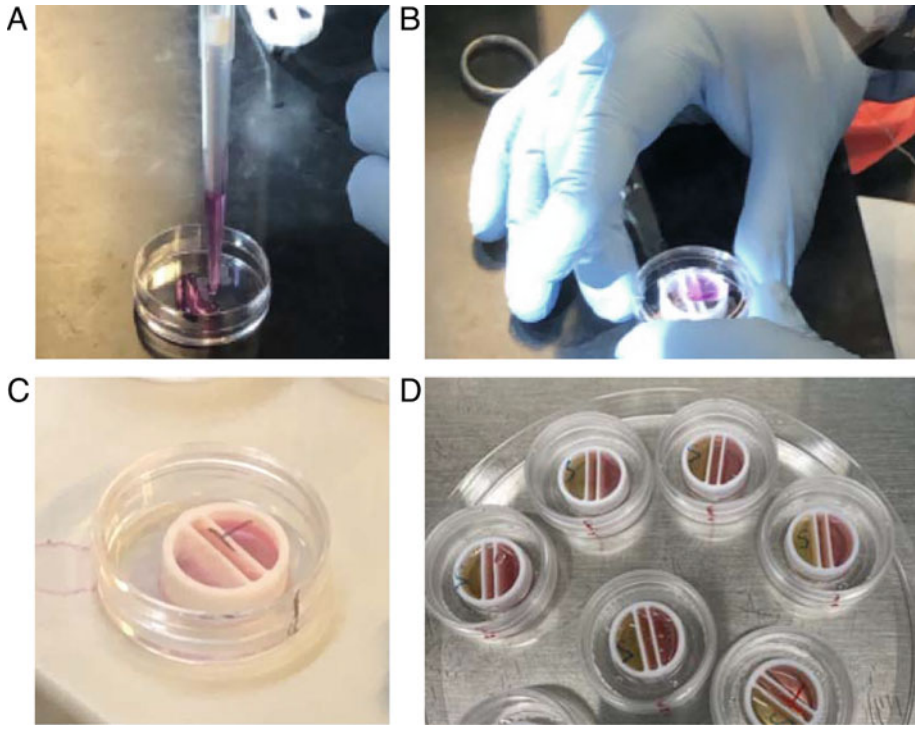

Fig. 3 Mounting the greased trichamber ring in the prepared cell culture dish. (**a**) Pipetting methocel-thickened DMEM to cover the etched grooves on the culture dish. (**b**) Placing the culture dish gently onto the greased trichamber held in the hemostat. (**c**) Example of assembled Campenot trichamber with neuronal medium added to the middle compartment to check for leaks. Note the mark on the side of the dish, which indicates orientation, and the T mark on the lid, which indicates a leak under one of the inner chamber walls. (**d**) Example of multiple Campenot trichamber cultures. Note the S mark of the lids, which indicates the cell body (soma) compartment, and the yellower color of the medium in the cell body compartment, which indicates no leaks have developed

middle compartment, cover, and set aside while assembling the remaining trichambers. If the medium leaks under both inner chamber walls, the assembled trichamber cannot be used. If the medium leaks under only one of the two inner walls, the trichamber might still be used, depending on experimental demands. It is helpful to mark the dishes to keep track of which of the two inner barriers is compromised.

10. Once assembled and checked for leaks, fill all three compartments with complete neuronal medium. Dissociated neurons can be plated immediately, if available, or the trichambers can be stored overnight, at room temperature or in a cell culture incubator. Figure 3c shows a correctly assembled Campenot trichamber containing neuronal medium.

3.2.1 Variation: Optical Plastic Campenot Trichambers

To facilitate microscopy using high-magnification oil-immersion objectives, it is possible to assemble Campenot trichambers in tissue culture dishes with optical plastic coverslips (Ibidi μ-Dish). It is important to use the Ibidi μ-Dish with high side walls, to accommodate the height of the Campenot chambers. Assembly of optical plastic trichambers is the same as for standard 35 mm dishes, with two major exceptions: First, when scratching parallel grooves with the pin rake, the optical plastic coverslip will flex under the pressure of the pin rake, so greater force is required to scratch the plastic surface deeply enough. Second, when mounting the greased trichamber onto the Ibidi μ-Dish, the trichamber must be carefully centered within the recessed area containing the optical plastic coverslip. Placement outside the recessed optical plastic area will compromise the grease barriers and cause leaks. Figure 1d shows a correctly scratched Ibidi μ-Dish.

3.2.2 Variation: 3D Printed Campenot Trichambers on Glass-Bottom Dishes

Another option is to use a 3D printer to fabricate the trichamber onto the tissue culture dish [24]. This method used a custom-designed 3D printer capable of extruding a wide variety of materials, including polymers to form grooves and the trichamber walls, silicone vacuum grease, and even cells suspended in culture medium. Importantly, this 3D printing method allowed the authors to fabricate trichambers on cell culture dishes with glass coverslips (e.g., MatTek dishes), which cannot be scratched with the pin rake (as in Subheading 3.2, **step 1**, above).

Assembling trichambers by hand requires experience, it is laborious and time-consuming, and trichambers vary in axonal penetration. 3D printing mitigates each of these limitations by automating the process. However, this method currently requires specialized 3D printing expertise, custom 3D printer devices that are capable of extruding a variety of materials, and is limited to using particular materials that are biocompatible and can be sterilized for cell culture applications, limiting its wider use.

3.3 Primary Superior Cervical Ganglia (SCG) and Dorsal Root Ganglia (DRG)

1. Euthanize an E15-18 timed-pregnant rat in accordance with all applicable animal care and use regulations. Euthanasia via CO_2 inhalation is preferred to maintain viability of peripheral ganglia.
2. Wet the abdominal fur with 70% ethanol.
3. Using sterile surgical scissors, open the abdomen and remove the uterus.
4. Using surgical knives and forceps, open the uterus and remove individual embryos. A detailed protocol for dissecting SCGs can be found in Ch'ng et al. 2005 [25] and a detailed protocol for dissecting DRGs can be found in Fenstermacher et al. [18].

5. For convenience and flexibility, dissected ganglia can be stored in Hibernate-E medium at 4 °C for 1–2 weeks; however, neuron viability gradually decreases during storage. As an added benefit, storing ganglia in this way also strongly reduces the viability of non-neuronal cells that would otherwise proliferate until antimitotic AraC treatment (*see* Subheading 3.5, **step 1**).

3.4 Dissociation of Peripheral Ganglia

1. Protein-coat the inside of a flame-polished Pasteur pipet, otherwise ganglia and dissociated neurons will stick to the glass. Fill the pipet with a protein-rich solution, and set aside during subsequent steps. This protein-rich solution can be 2–10% bovine serum albumin (BSA) in a saline buffer, fetal bovine or calf serum (FBS/FCS), cell culture medium containing 10% serum, or the HBSS containing blood and tissue debris from dissecting the ganglia.
2. At this point, ganglia will be in either HBSS containing some blood and tissue debris from dissection, or stored in Hibernate-E medium (*see* Subheading 3.3, **step 5**). In either case, wash the ganglia by adding HBSS to fill, centrifuge at 1200 × *g* for 1 min to pellet the ganglia, and then remove most of the HBSS, leaving approximately 0.5 mL. Gently flick and swirl the tube to dislodge the ganglia from the bottom of the tube.
3. Add 500 μL of trypsin, swirl to mix, and incubate 15 min at 37 °C.
4. Wash by adding HBSS to fill, centrifuge at 1200 × *g* for 1 min to pellet, and gently remove HBSS, being careful to not aspirate the ganglia. Repeat a total of three times to remove residual trypsin.
5. After removing the final HBSS wash, add 100 μL of complete neuronal medium per ganglion, but not less than 500 μL.
6. Using the protein-coated flame-polished Pasteur pipet, vigorously pipet up and down so that the ganglia break up into a uniform cell suspension. Try to minimize bubbling/foaming while pipetting. Triturating the ganglia too much will reduce neuron viability. Compared to SCGs, thicker DRG roots (the pre- and post-ganglionic nerves) do not break apart easily, so DRG suspensions are typically less homogenous.
7. Plate the resulting cell suspension into one compartment of the assembled Campenot trichambers. For rat SCGs, two-thirds of a ganglion per trichamber is sufficient. For mouse SCGs, use 1–1.5 ganglia per trichamber. For rat DRGs, use 1–2 ganglia per trichamber.

3.5 Maintaining Campenot Trichamber Cultures

1. SCG and DRG cultures must be treated with an antimitotic drug to suppress the proliferation of non-neuronal cell types. Add 1 μL of AraC solution to the cell body compartment. AraC can be added immediately to DRG cultures; however, embryonic SCG neurons sometimes undergo one round of cell division in vitro, so it is recommended to add AraC to SCG cultures after 2 days in vitro. Depending on the density of non-neuronal cells, cultures may need to be treated with AraC during subsequent media changes as well.
2. Change medium every 3–5 days. Using a P1000 pipette tip, gently remove about two-thirds of the media volume from all three compartments. To avoid disturbing the neurons, be sure to leave the culture area completely covered with medium. Gently fill the compartments with fresh pre-warmed complete neuronal medium. Allow the medium to drip gently down the chamber walls, but do not touch the trichamber walls with the pipette tip.
3. Before each medium change, observe the color of the phenol red pH indicator in the neuronal medium. The medium in the cell body compartment will acidify due to cell metabolism, resulting in a yellower color, whereas the compartments that do not contain cell bodies will remain a redder color (Fig. 3d). This color difference between compartments is a helpful indication that no leaks have developed.
4. Axons will begin to extend from neuronal cell bodies within 24 h, and will penetrate under both inner walls by 2 weeks in vitro. Axonal extension can be monitored by standard phase contrast cell culture microscope (Fig. 4).
5. Experiments can be performed between approximately 2–4 weeks in vitro. Prior to performing a virus infection experiment, be sure the medium has been changed several times without adding AraC, because residual AraC can inhibit viral DNA replication. The medium in the middle compartment can be replaced with neuronal medium containing 1% methocel to further reduce the risk of leaks (optional).

3.6 Cleaning the Trichambers

1. Campenot trichamber rings are made from Teflon, which can be cleaned and reused for years. Observe all applicable biosafety procedures, particularly if the trichambers have been used with hazardous viruses or neurotoxins.
2. First, remove trichamber rings from cell culture dishes using blunt forceps or hemostat.
3. Drop the trichamber rings into a bottle containing a 70% ethanol. If biohazardous agents are not effectively inactivated by ethanol, a 10% bleach solution can be used instead. Ensure sufficient contact time to inactivate biohazardous agents.

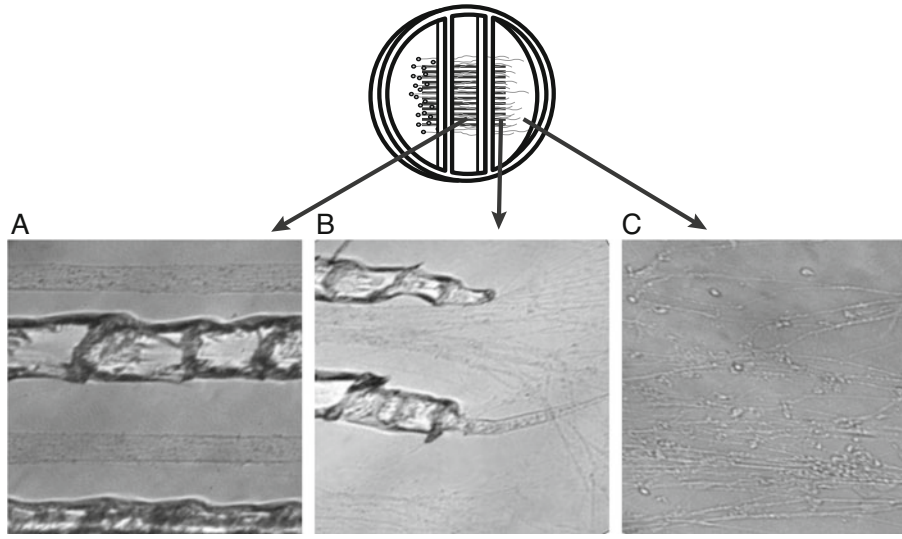

Fig. 4 Axons that have penetrated the inner chamber walls are visible by phase contrast microscopy. Axons of DRG neurons shown here, but axons of SCG neurons appear essentially the same. (**a**) Axons in the middle chamber tend to form a tight bundle (fascicle) between the grooves. (**b**, **c**) Where the grooves end in the axon compartment, axons fan out over the culture surface, no longer forming a tight bundle. Experiments are typically performed at this stage of axonal outgrowth, after about 2–3 weeks in culture

4. Drain the ethanol solution and manually wipe trichamber rings with low-lint paper towels/tissues to remove excess silicone grease.
5. Place the trichamber rings in a clean bottle with deionized water and bring to a boil in a microwave. Carefully shake the bottle. Depending on how much grease residue remains on the trichamber rings, grease droplets may make the water cloudy. Replace the deionized water and repeat, if necessary, until the water remains clear.
6. Drain the water and spread the trichamber rings on a low-lint paper towel to dry.
7. Autoclave the clean trichamber rings prior to re-use.

4 Notes

1. In classic studies investigating the infection and spread of neurotropic alpha herpesviruses, such as HSV-1 and pseudorabies virus, Campenot trichamber cultures were used to separate virus inoculum that initiated infection in one compartment, from progeny virus released in another compartment. To study post-entry retrograde axonal transport and subsequent establishment of infection, virus inoculum can be added to the axon compartment, and after a full replication cycle, progeny virus

can be titered from the cell body compartment. Alternatively, to study post-replication axonal sorting and transport, as described in the introduction, viral infection can be initiated in the cell body compartment and progeny virus titered in the axonal compartment. Typically, a monolayer of non-neuronal cells is added to the axonal compartment to amplify virus to more easily detectable amounts. Detailed procedures for these types of experiments, infecting and measuring virus spread through neurons via titering, are available from Curanović et al. [22].

In addition, Campenot trichamber cultures have allowed the compartmentalization not only of viral inoculum, but also compartmentalization of various experimental manipulations, such as drugs or signaling molecules. For example, cytokines and drugs can have dramatically different effects on entry, axonal transport, and establishment of infection depending on whether they are applied to the cell bodies or axons. These types of experiments have been important to better mimic the spatial and fluidic separation between axons and cell bodies that occurs in vivo, leading to a better understanding of infection and establishment of viral latency in neurons [13, 26–28].

2. Retrograde labeling of neurons using fluorescent lipophilic dyes is a powerful method to quantify axonal penetration and identify particular neuron cell bodies that have extended their axons through the trichamber [13, 22, 29]. To illustrate the key factors that govern how axons extend through the Campenot trichambers, we performed two-color fluorescent lipophilic dye experiments, comparing the standard Campenot trichamber (Fig. 7a) to an alternative chamber format (Fig. 7b–d). In the standard Campenot trichamber format, we added the fluorescent lipophilic dyes DiO or DiI (V22885 or V22886, Invitrogen) to the middle or right axonal chambers, respectively. Neuronal cell bodies were then imaged by phase contrast and fluorescence microscopy to identify DiO-labeled (green) and DiI-labeled (red) cells. Neurons that extended axons under both inner chamber walls exhibited a combination of red and green fluorescence; however, many neurons showed only green fluorescence, indicating that their axons had penetrated only as far as the middle chamber (Fig. 7a). This result shows that the chamber walls are a significant barrier to axonal penetration.

   In the alternative trichamber design, instead of a single array of grooves that span both inner chamber walls, we produced two separate, shorter sets of grooves, each spanning only one of the inner chamber walls (Fig. 7). We then plated dissociated SCG neurons in the middle compartment, so that these cells can extend axons into either the right or left chamber by extending under only one chamber wall. DiO or DiI

were added to the left or right axonal chambers, respectively. Over four independent replicates, 76.4 ± 14.1% (mean ± s.d.) of neurons were dye-labeled, indicating that their axons penetrated one chamber wall into either the left or right chamber. By comparison, typically 15–25% [22, 29], up to a maximum of 50% [13], of neurons extend axons under both chamber walls in the conventional trichamber format.

Importantly, whether the cell bodies were DiO- or DiI-labeled depended strongly on the proximity to the grooves extending under the middle chamber walls. Cell bodies between the grooves extending to the left were almost exclusively DiO-labeled (green, Fig. 7b), whereas cell bodies between the grooves extending to the right were almost exclusively DiI-labeled (red, Fig. 7d). Neurons in the middle, between the two sets of grooves, were roughly divided with some DiO-labeled and some DiI-labeled cell bodies (Fig. 7c). These data show that the pin rake-scratched grooves are critical for guiding axons towards the chamber walls and allowing them to penetrate under the chamber walls.

3. It is important to use a HBSS formulation that does not contain calcium or magnesium, because these ions will inhibit enzymatic dissociation of the ganglia and may cause excitotoxicity in neurons.
4. We use sawed-off 18 gauge needles to dispense silicone vacuum grease. To cut the needle, we use a Dremel rotary tool fitted with a metal cutting/grinding disc. The needles cannot be cut with scissors, metal shears, or wire-cutters, because these tools will crimp the needle. It is important that the cut opening is smooth, without any remaining metal burrs. We store the cut/blunt needles in 70% ethanol when not in use.
5. If it is more convenient, 2% methocel in DMEM can be diluted with standard (1×) liquid DMEM to make 1% methocel in DMEM for chamber assembly. To make neuronal medium with 1% methocel, it is also possible to make 4% methocel in DMEM and then dilute it 1:3 with neurobasal medium. When diluting any methocel-thickened medium, be sure to mix well to ensure a uniform viscosity.
6. It is possible to make the trypsin solution at other stock concentrations, such as 10× (2.5 mg/mL) or 1× (0.25 mg/mL), as long as the final working concentration on the ganglia is 0.25 mg/mL. Trypsin from other manufacturers may have a different specific activity, so concentrations may need to be adjusted. Do not use common cell dissociation solutions that contain EDTA.
7. Cytosine β-D-arabinofuranoside in the form of HCl salt is preferred because it is available in smaller 25 mg quantities

from Millipore-Sigma. It is possible to use cytosine β-D-arabinofuranoside that is not an HCl salt, but you will need to adjust molarity calculations to account for the slightly different molecular weight.

8. Summary of procedures with suggested schedule. Ensure that materials and reagents listed in Subheading 2.2 are prepared in advance. Clean and autoclave Campenot trichamber rings, dissection tools, etc.

   Day 1: Sacrifice pregnant rat and dissect embryos. Store peripheral ganglia in Hibernate-E at 4 °C. Based on number of ganglia available, plan experiments to determine how many trichamber dishes to assemble (plan to assemble more than needed). Add poly-ornithine solution to 35 mm dishes and incubate overnight.

   Day 2: Replace poly-ornithine solution with laminin solution, and incubate overnight. If necessary, laminin coating time can be reduced to 6 h. Once coating is completed, proceed immediately with next steps.

   Day 3: Rinse dishes, air-dry, and scratch with pin rake. Assemble trichambers on dishes by greasing a trichamber, apply a drop of 1% methocel DMEM, mount the trichamber, add complete neuronal medium to middle compartment to check for leaks. Once all trichambers are assembled and filled with complete neuronal medium, store overnight or proceed immediately with next steps.

   Day 4: Dissociate ganglia and plate in the assembled trichambers. If using DRG neurons, AraC can be added to the culture medium immediately.

   Day 6: Observe cultures by phase contrast microscopy to assess neuronal viability, axonal outgrowth, and proliferation of non-neuronal cells. Two days after plating SCG neurons, add AraC to the culture medium.

   Day 8: Observe cultures by phase contrast microscopy and change medium. Add AraC to the culture medium again if non-neuronal cells remain. Observe cultures and change medium every 3–5 days thereafter.

   Day 18–25: Observe cultures by phase contrast microscopy to assess axonal penetration through the chamber barriers. Campenot trichamber cultures are now ready for experiments.

9. While the classic approach of measuring virus spread in the Campenot trichamber by titering progeny virus output has provided many insights into virus infection and spread in neurons, this approach is cumbersome. Titering by serial dilution plaque assay takes days, and only a single timepoint post-

infection can be measured per trichamber culture. For basic molecular and cell biological studies, using recombinant viruses expressing genetically encoded fluorescent proteins allows virus infection and spread to be assessed over time by fluorescence microscopy. Detailed approaches and design considerations for making recombinant alpha herpesviruses expressing fluorescent proteins can be found in Hogue et al. 2015 [10].

Figure 5 illustrates an example of this approach. HSV-1 recombinants expressing a red fluorescent protein fused to the small capsid protein (mRFP-VP26) [30] were generated by viral homologous recombination, as previously described [10, 14]. HSV-1 17syn(+) mRFP-VP26 (also known as HSV-OK14) was generated using the common laboratory strain, 17syn(+), that exhibits wild-type anterograde axonal trafficking and spread. HSV-1 MacIntyre mRFP-VP26 (also known as HSV-425) contains mutations in viral membrane proteins gI (US7) and US9 [31], which are required for anterograde axonal trafficking and spread in neurons. SCG neurons were cultured in Campenot trichambers for 2–3 weeks, until axons were observed extending into the right axonal chamber by phase contrast microscopy. One day before infection, ~10^4 Vero cells (CCL-81, ATCC) were plated into the axonal chamber. The cell body compartments were then infected with HSV-1 recombinants at a high multiplicity of infection, and virus replication and spread was monitored over 48 h by fluorescence microscopy. Both recombinants efficiently infected neuronal cell bodies (Fig. 5, left images). Consistent with their expected phenotypes, HSV-1 17syn(+) mRFP-VP26 exhibited robust anterograde axonal spread to the axonal compartment, whereas the mutant HSV-1 MacIntyre mRFP-VP26 was not able to spread to the axon compartment (Fig. 5, right images). Importantly, axons are generally unable to cross the grooves etched by the pin rake (*see also* Fig. 4 and **Note 2**); therefore, virus spread was also restricted to particular "lanes" between the etched grooves (Fig. 5, top-right image). Altogether, these results illustrate the usefulness of genetically encoded fluorescent proteins and fluorescence microscopy to assess viral spread in Campenot trichamber cultures.

10. The ability to construct Campenot trichambers on optical plastic (*see* Subheading 3.2.1) or glass (*see* Subheading 3.2.2) allows for high-magnification live-cell fluorescence microscopy to track individual fluorescently labeled virus particles in axons. These types of experiments allow the visualization and quantification of viral transport and individual cell-cell transmission events. For example, carefully quantifying the anterograde, retrograde, and bidirectional motility of virus particles can

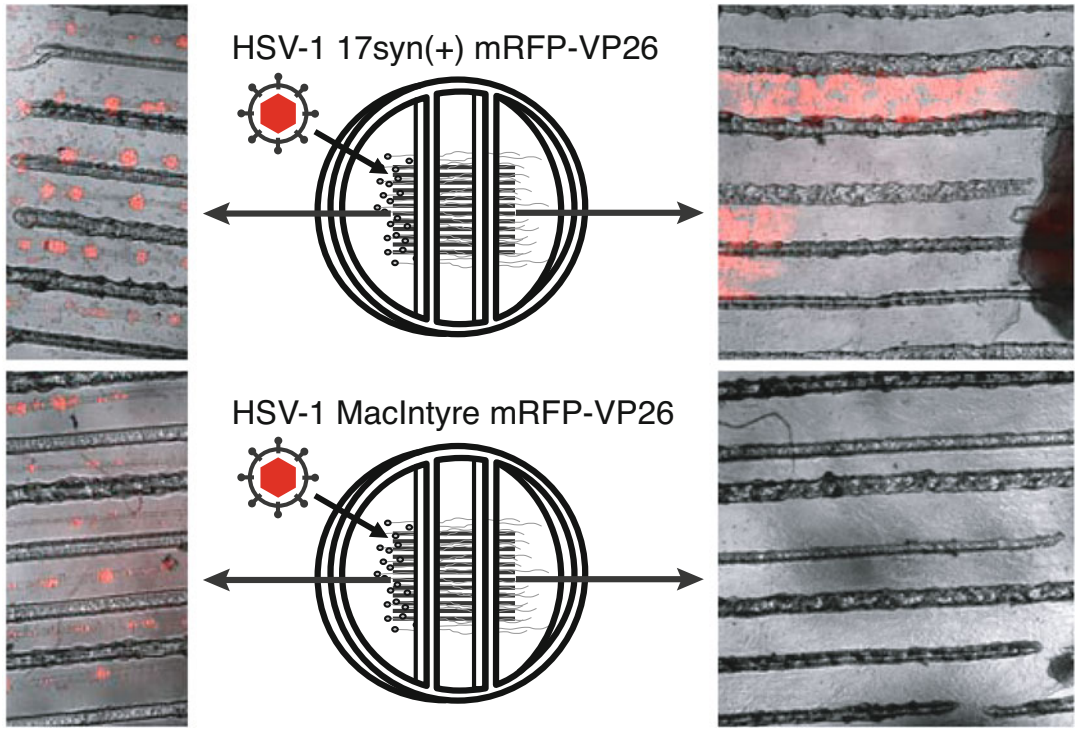

Fig. 5 Monitoring virus spread in the Campenot trichamber using genetically encoded fluorescent proteins (*see* **Note 9**). SCG neurons were cultured in Campenot trichambers for 2–3 weeks, and a monolayer of amplifying Vero cells was plated in the axon compartment. The cell body compartment was then infected with HSV-1 recombinants expressing a red fluorescent protein fusion to the small capsid protein, VP26 (mRFP-VP26). The HSV-1 17syn(+) parental strain exhibits wild-type anterograde axonal spread in trichamber cultures (top row), whereas the mutant, HSV-1 MacIntyre, is unable to traffic progeny particles via the axons, and cannot spread through the trichamber (bottom row)

shed light on the ensembles of microtubule motors that mediate axonal transport of virus particles, and multicolor fluorescence microscopy allows the visualization of co-transport between virus particles and fluorescently labeled cellular factors (e.g., [32–34]). Finally, it is possible to directly visualize cell-cell spread events, from axons to non-neuronal cells, mimicking the transmission of alpha herpesviruses from the peripheral nervous system following reactivation from latency [11]. Without the separation of inoculum and progeny virions provided by compartmentalized neuronal cultures, it would be very difficult to interpret the results of these types of experiments [16], because inoculum virus particles continue to enter and traffic in the retrograde direction in axons, even at very late times post-infection [15]. Unfortunately, even with the benefits provided by Campenot trichamber cultures, determining the direction of virus particle transport can be difficult because axons can take very circuitous paths while extending through

the trichambers. For example, while the axons in the Campenot trichamber are mostly oriented with their termini towards the axon compartment, axons can sometimes make a U-turn and run in an antiparallel direction, complicating the interpretation of anterograde vs. retrograde movements.

Tracking individual virus particles in optical Campenot trichambers requires relatively high-end fluorescence microscopy equipment. Because axonal transport is very sensitive to temperature, an objective warmer and heated stage-top incubator or microscope enclosure are essential to maintain the cultures at 36–37 °C during imaging. For longer-term imaging (>1 h), the stage-top incubator should also have a humidified 5% CO_2 atmosphere, or use a CO_2-independent pH-buffered cell culture medium.

Because virus particles labeled with fluorescent protein fusions are relatively dim and particles can transport in axons at velocities exceeding 1 or 2 μm/s, optical components must be optimized for fast and high-sensitivity image acquisition. Ideally, the fluorescence microscope should be equipped with a 60–100× magnification, high-numerical aperture, oil-immersion objective and a high-sensitivity camera (≥95% quantum efficiency preferred, e.g., Oxford Instruments Andor EMCCD or Teledyne Photometrics Prime sCMOS cameras).

For multicolor particle tracking, switching fluorescence filters is often a severely rate-limiting process. For example, on a typical inverted fluorescence microscope (as previously described [35]) equipped with an arc lamp and motorized filter wheels, it took about 625 ms to acquire sequential green and red fluorescence channels with an exposure time of 50 ms each (i.e., 525 ms of filter-switching overhead), limiting the acquisition framerate to 1.6 dual-color frames/s [36]. To illustrate the impact of this filter-switching lag time, we infected SCG neurons in Campenot trichambers with a pseudorabies virus recombinant (PRV-137 [37]) expressing red (mRFP-VP26) and green (gM-EGFP) fluorescent structural proteins, and imaged two-color virus particles transporting in axons (Fig. 6). The lag time between fluorescence channels results in the particle moving noticeably during acquisition, leading to offset red and green puncta in still images (Fig. 6a) and in kymographs projected over time (Fig. 6b). To overcome this limitation, we now use a single quad-band dichroic mirror and emission filter with a multi-band laser or LED light source (e.g., Lumencor Spectra X or [36]) capable of fast triggered switching of excitation light. In our test case, using triggered LED illumination on the same microscope took 106 ms to acquire sequential fluorescence channels with the same 50 ms exposure time (i.e., 6 ms of overhead), allowing an acquisition framerate of 9.5 dual-color frames/s [36]. This framerate is

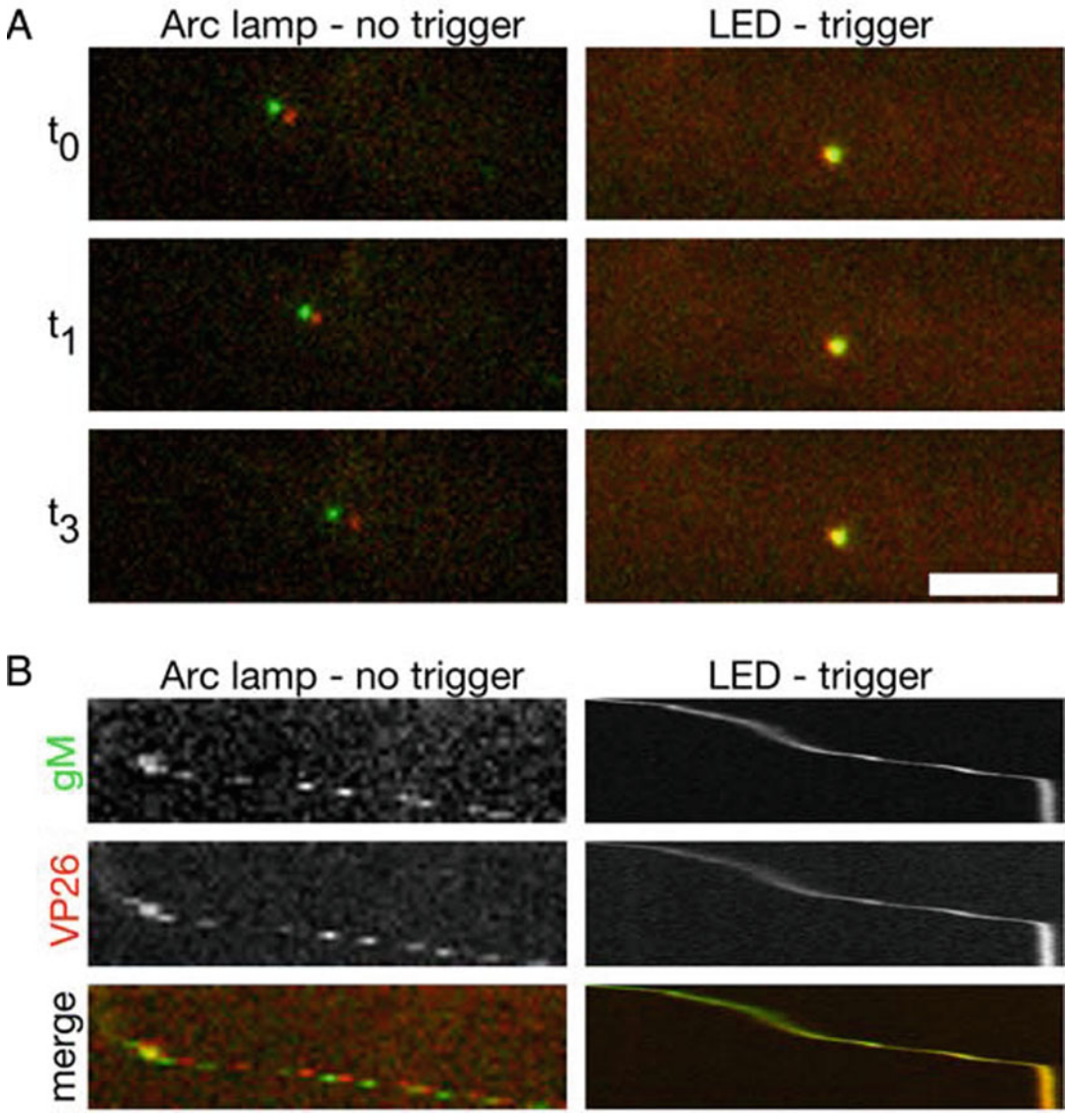

Fig. 6 Two-color fluorescence microscopy tracking individual virus particles in axons (*see* **Note 10**). SCG neurons were cultured in Campenot trichambers and infected in the cell body compartment with pseudorabies virus expressing gM-EGFP (gM, green) and mRFP-VP26 (VP26, red). 10 h post-infection, viral particles trafficking in axons were imaged in the axon compartments using mechanical filter wheel (Arc lamp—no trigger) or triggered LED illumination (LED—trigger). (**a**) Three consecutive still images taken from movies of representative virus particles transporting at ~1.5 μm/s for ~14 s. Scale bar indicates 5 μm. (**b**) The same microscopy datasets displayed as kymographs (projection of X-axis movement over time). This figure was originally published by Bosse et al. [36], and is reproduced here under the terms of the Creative Commons Attribution License

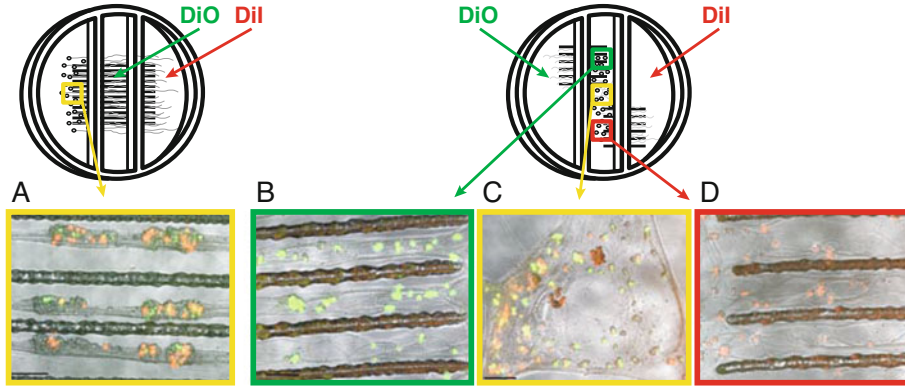

Fig. 7 Investigating axonal penetration (*see* **Note 2**). Schematics represent either the standard or an alternative trichamber format. Alternative trichambers have two separate sets of grooves, extending under the left or right inner chamber walls, with SCG neurons plated in the middle compartment. Axonal penetration is assessed using fluorescent lipophilic dyes, DiO (green) and DiI (red). (**a**) Merged fluorescent and phase contrast images of cell bodies in the standard trichamber, labeled by DiO in the middle compartment and DiI in the right axonal compartment. (**b-d**) Merged fluorescent and phase contrast images of cell bodies in the middle compartment of the alternative trichamber. Image areas are indicated in the trichamber schematics above

fast enough that there is very little noticeable particle movement between fluorescence channels, so co-localization and co-transport of the green and red fluorescent markers is much clearer (Fig. 6).

11. Compared to most microfluidics devices, the relatively large and open culture area of Campenot chambers facilitates their use in preparing samples for electron microscopy. For standard transmission electron microscopy, neurons can be fixed with glutaraldehyde, the trichamber ring can be carefully removed, and the sample can be stained, dehydrated, embedded in resin, and sectioned. Detailed procedures for preparing samples in Campenot trichambers for standard transmission electron microscopy are available from Curanović et al. [22].

    Alternatively, to image axons by cryo electron microscopy (cryoEM), we have developed a method to grow axons directly on electron microscopy grids using Campenot trichamber cultures (Fig. 8). In this method, SCG neurons were cultured in trichambers, as described in this chapter. Quantifoil gold NH2 finder grids with R2/2 or R1/4 amorphous carbon or SiO_2 support films were plasma-treated by glow discharge, sterilized, coated with poly-ornithine and laminin (as described in Subheading 3.1), and placed in the axon compartment (Fig. 8). After approximately 3 weeks in culture, axons penetrated through the trichamber, and began to extend onto the support film of the Quantifoil grids, visible by phase contrast light microscopy. Neuron cell bodies were then infected with a

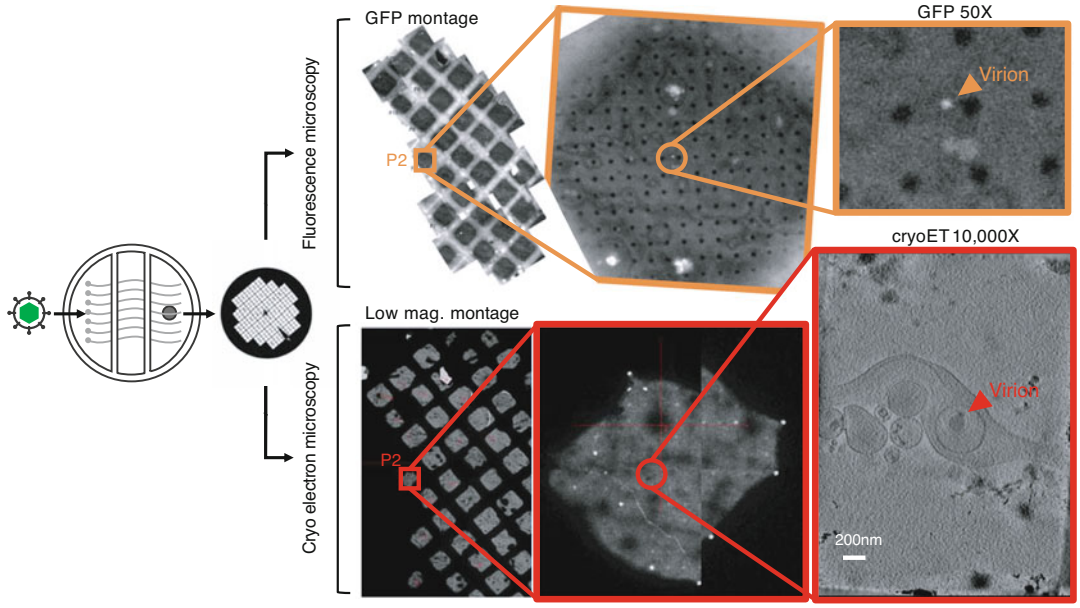

Fig. 8 Correlative fluorescence microscopy and cryo electron tomography (*see* **Note 11**). SCG neurons were cultured in Campenot trichambers, and Quantifoil gold cryoEM grids were placed in the axon compartment so that axons extend up and onto the grid. Neurons were infected in the cell body compartment with a pseudorabies virus recombinant expressing a green fluorescent protein (GFP) fusion to the small capsid protein. After plunge-freezing, grids were imaged by fluorescence microscopy to find fluorescent virus particles (top row). Regions of interest were then imaged by cryoEM and tomography to structurally characterize virus particles trafficking in axons

pseudorabies virus recombinant (PRV-959) expressing a green fluorescent protein-tagged small capsid protein (mNeonGreen-VP26) [10]. At approximately 15 h post-infection, grids were removed from the trichamber cultures, and loaded into a Leica EM GP2 plunge freezing apparatus. 1 μl of a 10 nm gold nanoparticle suspension was applied to the grids, grids were blotted with filter paper and plunged into liquid nitrogen-cooled liquid ethane. Following vitrification, we performed fluorescence microscopy using a Nikon Eclipse 90i upright fluorescent microscope equipped with a 50× long working distance objective and a Linkam CMS196 cryo-stage, to locate fluorescent virus particles in axons (Fig. 8, top row of images). We then performed cryo electron microscopy using a JEOL JEM2200FS electron microscope operated at 200 kV, with the objective aperture and an in-column omega energy filter set to a width of 20 eV (Fig. 8, bottom row of images). After acquiring a low magnification montage, we manually aligned the fluorescence microscopy and cryoEM images based on the gold grid and holes in the support film, which were visible in both fluorescence and cryoEM images. We then collected cryoEM tomography tilt series of the regions of

interest at 10,000× magnification, 6.63 Å/pixel, using a DE-20 direct electron detector recording 24 raw frames/s for a total exposure time of 0.6 s per image. Tilt series were acquired semi-automatically using SerialEM software [38] in low-dose mode with a target defocus of -6 μm or -8 μm. For each tilt series dataset, the images were acquired from a target range of −60° to +60° in increments of 2°. Total cumulative dose was 60 to 70 e/Å^2. Tomographic data were reconstructed using the Etomo package in IMOD [39], using the 10 nm gold beads as fiducial markers.

Most previous cryoEM tomography studies of alpha herpesviruses in axons (e.g., [40]) did not use any type of chambered or microfluidics neuron culture system; thus, it can be difficult to distinguish virus particles that are entering from those that are exiting axons. Many typical microfluidics devices have closed cell culture chambers, making them unsuitable to integrate a cryoEM grid. Thus, our example correlative fluorescence/cryoEM tomography workflow (Fig. 8) illustrates the utility of Campenot trichambers for this type of experiment.

Acknowledgments

We would like to especially thank Dr. Lynn Enquist, Princeton University, for his ongoing mentorship. Much of this work would not have been possible without his generosity, guidance, and patience, which directly contributed to the development of these methods. This work was supported by NIH grants K22 AI123159 (I.B.H.), R21 AI146952 (M.P.T.), P40 OD010996 (E.A.E.), and P41 GM103832 (W.C.).

References

1. Koyuncu OO, Hogue IB, Enquist LW (2013) Virus infections in the nervous system. Cell Host Microbe 13:379–393
2. Koyuncu OO, Enquist LW, Engel EA (2021) Invasion of the nervous system. Curr Issues Mol Biol 41:1–62
3. Itzhaki RF, Lathe R, Balin BJ, Ball MJ, Bearer EL, Braak H et al (2016) Microbes and Alzheimer's disease. J Alzheimers Dis 51:979–984
4. Card JP, Enquist LW (2012) Use and visualization of neuroanatomical viral transneuronal tracers. In: Visualization techniques. Humana Press, Totowa, NJ, pp 225–268
5. Ugolini G (2010) Advances in viral transneuronal tracing. J Neurosci Methods 194:2–20
6. Feldberg W, Gaddum JH (1934) The chemical transmitter at synapses in a sympathetic ganglion. J Physiol 81:305–319
7. Amendola J, Boumedine N, Sangiardi M, El Far O (2015) Optimization of neuronal cultures from rat superior cervical ganglia for dual patch recording. Sci Rep 5:14455
8. Nascimento AI, Mar FM, Sousa MM (2018) The intriguing nature of dorsal root ganglion neurons: linking structure with polarity and function. Prog Neurobiol 168:86–103
9. He Y, Baas PW (2003) Growing and working with peripheral neurons. Methods Cell Biol 71:17–35
10. Hogue IB, Bosse JB, Engel EA, Scherer J, Hu J-R, Del Rio T et al (2015) Fluorescent protein

approaches in alpha herpesvirus research. Viruses 7:5933–5961

11. Taylor MP, Kobiler O, Enquist LW (2012) Alphaherpesvirus axon-to-cell spread involves limited virion transmission. Proc Natl Acad Sci U S A 109:17046–17051
12. Smith GA, Gross SP, Enquist LW (2001) Herpesviruses use bidirectional fast-axonal transport to spread in sensory neurons. Proc Natl Acad Sci U S A 98:3466–3470
13. Koyuncu OO, MacGibeny MA, Hogue IB, Enquist LW (2017) Compartmented neuronal cultures reveal two distinct mechanisms for alpha herpesvirus escape from genome silencing. PLoS Pathog 13:e1006608
14. Wojaczynski GJ, Engel EA, Steren KE, Enquist LW, Patrick Card J (2014) The neuroinvasive profiles of H129 (herpes simplex virus type 1) recombinants with putative anterograde-only transneuronal spread properties. Brain Struct Funct 220(3):1395–1420
15. Scherer J, Yaffe ZA, Vershinin M, Enquist LW (2016) Dual-color herpesvirus capsids discriminate inoculum from progeny and reveal axonal transport dynamics. J Virol 90:9997–10006
16. Kratchmarov R, Taylor MP, Enquist LW (2012) Making the case: married versus separate models of alphaherpes virus anterograde transport in axons. Rev Med Virol 22:378–391
17. Danastas K, Cunningham AL, Miranda-Saksena M (2020) The use of microfluidic neuronal devices to study the anterograde axonal transport of herpes simplex Virus-1. Methods Mol Biol 2060:409–418
18. Fenstermacher SJ, Pazyra-Murphy MF, Segal RA (2015) Campenot cultures and microfluidics provide complementary platforms for spatial study of dorsal root ganglia neurons. In: Biffi E (ed) Microfluidic and compartmentalized platforms for neurobiological research. Humana Press, New York, pp 105–124
19. Wang Y, Wang S, Wu H, Liu X, Ma J, Khan MA et al (2020) Compartmentalized neuronal culture for viral transport research. Front Microbiol 11:1470
20. Campenot RB (1977) Local control of neurite development by nerve growth factor. Proc Natl Acad Sci U S A 74:4516–4519
21. Ch'ng TH, Enquist LW (2005) Neuron-to-cell spread of pseudorabies virus in a compartmented neuronal culture system. J Virol 79:10875–10889
22. Curanović D, Ch'ng TH, Szpara M, Enquist LW (2009) Compartmented neuron cultures for directional infection by alpha herpesviruses. Curr Protoc Cell Biol 43(1):26–24
23. Curanovic D, Lyman MG, Bou-Abboud C, Card JP, Enquist LW (2009) Repair of the UL21 locus in pseudorabies virus Bartha enhances the kinetics of retrograde, transneuronal infection in vitro and in vivo. J Virol 83:1173–1183
24. Johnson BN, Lancaster KZ, Hogue IB, Meng F, Kong YL, Enquist LW et al (2015) 3D printed nervous system on a chip. Lab Chip 16:1393–1400
25. Ch'ng TH, Flood EA, Enquist LW (2005) Culturing primary and transformed neuronal cells for studying pseudorabies virus infection. Methods Mol Biol 292:299–316
26. Song R, Koyuncu OO, Greco TM, Diner BA, Cristea IM, Enquist LW (2016) Two modes of the axonal interferon response limit Alphaherpesvirus neuroinvasion. MBio 7: e02145–e02115
27. Koyuncu OO, Perlman DH, Enquist LW (2013) Efficient retrograde transport of pseudorabies virus within neurons requires local protein synthesis in axons. Cell Host Microbe 13:54–66
28. Koyuncu OO, Song R, Greco TM, Cristea IM, Enquist LW (2015) The number of alphaherpesvirus particles infecting axons and the axonal protein repertoire determines the outcome of neuronal infection. MBio 6:e00276–e00215
29. Wu BW, Engel EA, Enquist LW (2014) Characterization of a replication-incompetent pseudorabies virus mutant lacking the sole immediate early gene IE180. MBio 5:e01850
30. Nagel C-H, Döhner K, Binz A, Bauerfeind R, Sodeik B (2012) Improper tagging of the non-essential small capsid protein VP26 impairs nuclear capsid egress of herpes simplex virus. PLoS One 7:e44177
31. Szpara ML, Tafuri YR, Parsons L, Shreve JT, Engel EA, Enquist LW (2014) Genome sequence of the anterograde-spread-defective herpes simplex virus 1 strain MacIntyre. Genome Announc 2:e01161–e01114
32. Kramer T, Greco TM, Taylor MP, Ambrosini AE, Cristea IM, Enquist LW (2012) Kinesin-3 mediates axonal sorting and directional transport of alphaherpesvirus particles in neurons. Cell Host Microbe 12:806–814
33. Scherer J, Hogue IB, Yaffe ZA, Tanneti NS, Winer BY, Vershinin M et al (2020) A kinesin-3 recruitment complex facilitates axonal sorting of enveloped alpha herpesvirus capsids. PLoS Pathog 16(1):e1007985
34. Antinone SE, Zaichick SV, Smith GA (2010) Resolving the assembly state of herpes simplex virus during axon transport by live-cell imaging. J Virol 84:13019–13030

35. Taylor MP, Kratchmarov R, Enquist LW (2013) Live cell imaging of alphaherpes virus anterograde transport and spread. J Vis Exp (78):e50723
36. Bosse JB, Tanneti NS, Hogue IB, Enquist LW (2015) Open LED illuminator: a simple and inexpensive LED illuminator for fast multicolor particle tracking in neurons. PLoS One 10:e0143547
37. Hogue IB, Bosse JB, Hu J-R, Thiberge SY, Enquist LW (2014) Cellular mechanisms of alpha herpesvirus egress: live cell fluorescence microscopy of pseudorabies virus exocytosis. PLoS Pathog 10:e1004535
38. Mastronarde DN (2005) Automated electron microscope tomography using robust prediction of specimen movements. J Struct Biol 152:36–51
39. Kremer JR, Mastronarde DN, McIntosh JR (1996) Computer visualization of three-dimensional image data using IMOD. J Struct Biol 116:71–76
40. Ibiricu I, Huiskonen JT, Döhner K, Bradke F, Sodeik B, Grünewald K (2011) Cryo electron tomography of herpes simplex virus during axonal transport and secondary envelopment in primary neurons. PLoS Pathog 7:e1002406

Chapter 10

Molecular Analysis of Axonal Transport Dynamics upon Modulation of Microtubule Acetylation

Silvia Turchetto, Romain Le Bail, Loïc Broix, and Laurent Nguyen

Abstract

Axonal transport is used by neurons to distribute mRNAs, proteins, and organelles to their peripheral compartments in order to sustain their structural and functional integrity. Cargoes are transported along the microtubule (MT) network whose post-translational modifications influence transport dynamics. Here, we describe methods to modulate MT acetylation and record its impact on axonal transport in cultured mouse cortical projection neurons as well as in motoneurons of *Drosophila melanogaster* third-instar larvae. Specifically, we provide a step-by step procedure to reduce the level of MT acetylation and to record and analyze the transport of dye-labeled organelles in projection neuron axons cultured in microfluidic chambers. In addition, we describe the method to record and analyze GFP-tagged mitochondria transport along the motoneuron axons of transgenic *Drosophila melanogaster* third-instar larvae.

Key words Axonal transport, MT acetylation, Cargo, Organelles, ATAT1, HDAC6

1 Introduction

Neurons are highly polarized cells that transport cargoes along their protracted axons to supply mRNAs, proteins, and organelles to the axoplasm. Intracellular trafficking of cargoes along axons is essential for neuron maturation and homeostasis as well as for their functional integration into neuronal network via synaptic activity. Cargoes are transported along MTs whose structure, properties, and dynamics rely on its constitutive tubulin subtypes as well as their post-translational modifications (PTMs) that can fine-tune the trafficking of cargoes (reviewed in [1]).

While most PTMs, such as glutamylation, glycylation, and detyrosination, occur on the C-terminal tails of α/β-tubulins, acetylation of α-tubulin takes place on intralumenal Lys40 (K40) of MTs. This PTM is catalyzed by the α-tubulin N-acetyltransferase

Silvia Turchetto and Romain Le Bail are Co-first authors. Loïc Broix and Laurent Nguyen are co-senior authors.

Alessio Vagnoni (ed.), *Axonal Transport: Methods and Protocols*,
Methods in Molecular Biology, vol. 2431, https://doi.org/10.1007/978-1-0716-1990-2_10,
© The Author(s), under exclusive license to Springer Science+Business Media, LLC, part of Springer Nature 2022

1 (ATAT1) and removed by the histone deacetylase 6 (HDAC6) [2]. The acetylation of α-tubulin modulates the mechanical properties of MTs by enhancing their flexibility, thereby protecting them from stress-induced mechanical aging [3]. Additionally, α-tubulin acetylation has been reported to increase the recruitment and processivity of molecular motors on MTs, pinpointing a functional correlation between MT acetylation and axonal transport dynamics [4, 5]. Accordingly, some neurodegenerative diseases exhibit transport defects which correlate with decreased MT acetylation levels. Restoring the balance of K40 acetylation using overexpression of ATAT1 or inhibitors of HDAC6 subsequently rescues axonal transport, therefore strengthening the link between this PTM and the regulation of axonal transport [4, 6, 7]. In accordance with the role that MTs play in neuronal development and activity, mice lacking ATAT1 display dentate gyrus deformation, hypoplasia of the septum and striatum and enlarged lateral ventricles. Moreover, their somatosensory cortical neurons suffer from axon overgrowth and overbranching, further suggesting an important role for MT acetylation during cortical maturation [8–10].

To investigate the role of ATAT1 on axonal transport dynamics and further untangle its regulatory molecular mechanisms, we assessed axonal transport dynamics in mouse cortical neurons and in third-instar larva motoneurons of *Drosophila melanogaster* upon RNA interference (RNAi)-induced knock-down (KD) of ATAT1 and ATAT2 (the *D. melanogaster* orthologs of mouse Atat1) [11]. We reported comparable axonal transport defects of membrane-bound organelles across species upon knock-down of ATAT1 that were rescued by the expression of a mutant α-tubulin (K40Q) mimicking K40 acetylation in mice or by pharmacological inhibition of HDAC6 in third-instar larvae [11].

Here, we provide an experimental paradigm to analyze the axonal transport of organelles in mouse cortical projection neurons cultured in microfluidics chambers as well as in motoneurons of live anaesthetized *D. melanogaster* third-instar larvae. These models are suitable to study the contribution of MTs acetylation to the transport dynamics of organelles and allow a comparison of these molecular parameters across species. More specifically, we provide a step-by-step method to knock down ATAT1 in mouse cortical neurons by in utero electroporation of short hairpin RNA (shRNA) and to record axonal transport dynamics of dye-labeled organelles in neurons cultured in microfluidic devices. As a culturing platform, microfluidics devices enable the physical isolation of axons from cell bodies and dendrites, thus allowing the study of axon biology and its transport dynamics. Moreover, we describe the experimental protocol to record axonal transport of mitochondria along the motoneuron axons from anesthetized third-instar larvae as well as the genetic strategies used to generate simple or compound conditional Atat1/2 and/or Hdac6 knock-down. We

further emphasize the pharmacological strategy used to rescue MT acetylation levels in larvae upon Atat1/2 KD and ultimately provide the detailed procedure to quantify the axonal transport parameters extracted from the time-lapse recordings.

2 Materials

2.1 Axonal Transport Recordings in Mouse Cortical Neurons

2.1.1 In Utero Electroporation

1. Micropipette puller (Sutter Instrument, #P-97).
2. Electroporator (BTX, #ECM 830).
3. Micro-injector (Eppendorf, #5252000013).
4. Isoflurane anesthesia vaporizer (Harvard Apparatus, #34-1041).
5. Heating pad (Beurer, HK 35 Heat pad).
6. Surgical lamp with flexible arm.
7. Endo-free plasmid maxi kit (Macherey-Nagel, #740420).
8. Sterile PBS.
9. Fast green.
10. Isoflurane.
11. Analgesic: Buprecare 0.3 mg/mL injection (Animalcare).
12. Ophthalmic lubrificant: Fucithalmic Vet 10 mg/g (Aventix).
13. 3 mm φ platinum electrodes (Sonidel, # CUY650P3).
14. Borosilicate Glass capillaries (Harvard Apparatus, #30-0016).
15. Syringe 1 mL.
16. Needle 26GA (0.45 × 10 mm).
17. Microloader tips (Eppendorf, #5242956003).
18. Scissors.
19. Spring scissors.
20. Ring forceps.
21. Vicryl suture 4–0.
22. Plasmids: pEGFP α-tubulin WT (Clontech) and pEGFP α-tubulin K40Q (Addgene, #105302).
23. Atat1 short hairpin RNA (shRNA); sequence: 5'- GCAG CAAATCATGACTATTGT -3′ [12]. Scrambled-shRNA; sequence: 5'-TACGCGCATAAGATTAGGG-3′.

2.1.2 Culturing and Plating Mouse Cortical Neurons in Microfluidic Devices

1. Vacuum desiccator.
2. Glass-bottom dish (*Mattek Life Science, #P50G-0-30-F).*
3. Microfluidic chambers, 450μm microgroove barrier (XONA microfluidics, # SND450).

4. 0,1 mg/mL Poly-D-Lysine, resuspended in sterile water, ready to use. Solution can be stored at 4 °C for up to 2 years.
5. Neurobasal medium (ThermoFisher, #21103049), to be supplemented with 1% Penicillin-Streptomycin, 1% Glutamine, and 2% B27 to prepare the culturing medium.
6. 200 mM Glutamine
7. 10,000 units/mL Penicillin-Streptomycin (P/S)
8. B27 (Gibco, Invitrogen, #15140122).
9. Forceps.
10. Perforated spoon.
11. 20μm/mL BDNF, resuspended in culturing medium and aliquoted for long-term storage at −20 °C (Peprotech, #450-02).
12. Mitotracker Red (ThermoFisher, # M7514).
13. Lysotracker Deep red (ThermoFisher, # L12492).
14. Ethanol 70%.
15. 40μm cell strainer.
16. 30% Glucose.
17. HBSS.

2.2 Axonal Transport Recordings *in* Drosophila melanogaster

2.2.1 Fly Lines and Husbandry

1. Drosophila culture tubes 25 × 95 mm (MLS, # QD789008).
2. Foam plug, Ø 36 × 40 mm (MLS, # QD330070).
3. Homemade cornmeal medium based on BDSC standard recipe (https://bdsc.indiana.edu/information/recipes/bloomfood.html).
4. Incubators.
5. Fly lines of the appropriate genotype (Table 1).

2.2.2 Recording of Axonal Transport

1. Ether.
2. 80% glycerol solution in water.
3. 10% Sucrose solution in water.
4. 50 mL conical centrifuge tubes.
5. 12-well plate.
6. Beaker.
7. Parafilm.
8. Forceps.
9. Tissue paper.
10. Standard microscope slides.
11. 32 × 32 mm microscope coverslips.

Table 1
Fly lines used in this protocol with their origin and purpose

Fly line	Origin	Purpose
D42-GAL4 > UAS-*mito*GFP	Bloomington drosophila stock center (BDSC) #42737	Expression of Gal4 in motor neurons [11]
UAS-RNAi HDAC6	BDSC #34072	UAS-dependent expression of interfering RNA (RNAi) against the HDAC6 enzyme to increase acetylation levels [11]
UAS-RNAi ATAT1	VDRC #106247	UAS-dependent expression of RNAi against the ATAT1 enzyme to decrease acetylation levels [11]
UAS-RNAi ATAT2	VDRC #101273	UAS-dependent expression of RNAi against the ATAT2 enzyme to decrease acetylation levels [11]
UAS-RNAi ZPG	VDRC #33277	Control line using UAS-dependent expression of RNAi against ZPG, a protein expressed in gonads [11]

12. Dissection microscope equipped with fluorescent lamp.
13. Confocal microscope.

2.2.3 Treating Third-instar Larvae with Tubastatin A

1. 24-well plates.
2. 10% sucrose solution in water.
3. Tubastatin A powder (Sigma, # SML0044).
4. DMSO.
5. Heating bath.
6. Vortex.

3 Methods

3.1 Axonal Transport Recording of Mouse Cortical Neurons Seeded in Microfluidic Devices

3.1.1 Preparation of the Microfluidic Chambers

1. Coat glass-bottom dishes with 0.1 mg/mL Poly-D-lysine (2 mL/dish) and incubate overnight at 4 °C. Rinse 3 times with sterile water and allow to air dry under a laminar flow hood for 30 min. Dried coated dishes can be stored at 4 °C until use for up to 1 month.
2. Sterilize microfluidics chambers with 70% ethanol for 30 min, making sure microgrooves are facing up. Remove ethanol and allow to dry under laminar flow hood (*see* **Note 1**).
3. Assemble the microfluidic chambers with the microgrooves facing downward on the coated dishes and press gently, either with your fingers or a pipette tip; be gentle on the grooves, to prevent their clogging that would hamper the media flow from somal to axonal compartments. To remove air bubbles that might have formed within the grooves, place microfluidics in a desiccator under vacuum for 30 min.

3.1.2 Irrigation of the Microfluidics

1. Irrigate the main channel of the somal compartment by adding into one of the two adjacent wells 200μL of Neurobasal medium complemented with 1% Glutamine, 1% P/S, and 2% B27 (culturing medium). Wait 5 min for the media to flow through the channel and equilibrate with the other somal well. Fill up both somal wells with further 100μL of media.
2. Wait up to 1 h to allow the media in the somal channel to flow through the microgrooves into the axonal channel, thus filling the adjacent axonal wells. Keep the microfluidics in the incubator until ready to use (*see* **Note 2**).

3.1.3 In Utero Electroporation of Cortical Projection Neurons

1. Prepare a mix of endotoxin-free plasmids in sterile nuclease-free water in a total volume of 10μL by diluting each plasmid at 1μg/μL with 0.1% (w/v) Fast green at 1/10 volume to visualize the injection site. To downregulate Atat1 and decrease MT acetylation level, you can use conditional sh-Atat1-expressing plasmid or sh-scrambled-expressing plasmid, as control, combined with a cre recombinase-expressing plasmid to drive their respective expression. To restore MT acetylation levels, use a plasmid encoding for α-tubulin K40Q which mimics MT acetylation or a WT tubulin-expressing plasmid, as control (*see* **Notes 3** and **4** for details of the plasmids).
2. By using a Needle Pipette Puller, pull glass microcapillaries tubing with inner diameter of 0.58 mm under the following conditions: heat: 634; pull: 92; velocity: 115; time: 210.
3. By using microloader tips, fill pulled microcapillaries with the plasmid mix. Use spring scissors to make progressively deeper diagonal cuts at the microcapillary tip, thus enlarging its diameter, until the plasmid solution passes through. To prevent air drying of the solution, cut the tip of microcapillaries only at the start of the surgery.
4. Anesthetize a pregnant mouse at E14.5 with a flow of 4% isoflurane; once sedated transfer it on a heating pad to quickly apply ophthalmic lubricant (Fucithalmic Vet® 5 mg/g) and inject the analgesic (Buprecare 0.1 mg/kg injection) subcutaneously.
5. Reduce the anesthetic flow to 2% and turn the mouse on its back. Shave the abdomen with depilatory cream and disinfect afterwards with 70% ethanol solution. Place the surgical field with rhomboidal aperture on the shaved area and wet it with warm phosphate-buffered saline (PBS) before performing a first incision of about 1.5 cm along the skin and a second along the midline of the abdominal muscles.
6. Use ring forceps to pull one uterine horn at a time out of the abdomen cavity by holding it at the junction between embryos. Expose the horn on the surgical field and make sure to apply

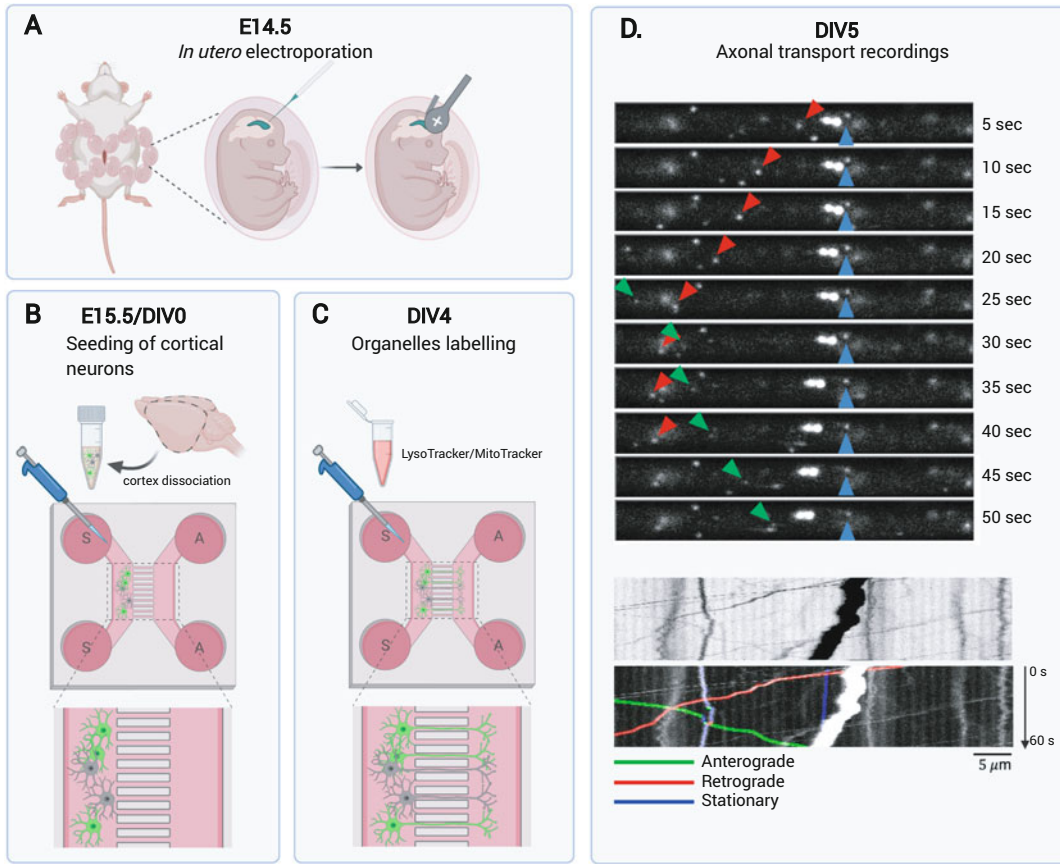

Fig. 1 Axonal transport recordings of mouse cortical neurons seeded in microfluidics chambers. (**a**) In utero electroporation of E14.5 mouse embryos with a solution of DNA plasmids to modulate MT acetylation level. Inject one lateral ventricle with the plasmid mix until the injection site is decorated by the fast green. Electroporate the injected plasmids into the neocortex by positioning the cathode (positively charged electrode) towards the target area and the anode (negatively charged electrode) at the opposite side of the brain. (**b**) Seeding of E15.5 cortical neurons dissociated from electroporated brains. Dissect and dissociate the electroporated hemisphere to prepare a cell suspension to be plated in the somal compartment (S) of the microfluidic chambers. Note that the seeded culture encompass also non-electroporated neuron. (**c**) Labeling of membrane-bound organelles. At DIV4, label seeded neurons with organelle-labeling dyes (e.g., LysoTracker for lysosomes and MitoTracker for mitochondria) for overnight incubation. (**d**) Recording of the axonal transport at DIV5 to follow the movements of labeled organelles. Wash somal (S) and axonal (A) wells with fresh medium and use a confocal microscope to record axonal transport dynamics of labeled organelles along the lower microgrooves segment lining the axonal channel

further warm saline solution during the entire procedure to prevent its drying.

7. Gently, hold an embryo steadily and by using a prepared micro-capillary connected to a mouth-controlled tube or micro-injector, inject 0.1–0.2μL of DNA plasmid mix through the placenta into one of the lateral ventricles. The filling of the ventricles with the Fast-Green dye indicates the success of the injection (*see* **Note 5**) (Fig. 1a).

8. Hold the embryo with electrode-type forceps, placing the anode at the injection site and the cathode at the opposite side of the brain and deliver 5 electric pulses of 40 V at 50-ms intervals for 950 ms (*see* **Note 6**) (Fig. 1a).
9. After performing ventricle injection and electroporation of the remaining embryos, wet the uterine horn before placing it back into the abdominal cavity. Perform the same procedure on the second uterine horn.
10. Suture first the abdominal muscles and then the skin before placing the operated mouse into a cage kept under a warming light. Monitor closely the recovery of the mouse (*see* **Note 7**).

3.1.4 Culture of Electroporated Cortical Projection Neurons in Microfluidic Chambers

1. Prepare primary mouse cortical neurons isolated from electroporated E14.5 mouse embryos. Briefly, 1 day after performing in utero electroporation (E15.5), dissect the brains and check for fluorescence of the co-electroporated reporter plasmid under a binocular fluorescent microscope. Dissect the electroporated cerebral hemisphere in ice-cold Hank's balanced salt solution (HBSS) supplemented with 1.5% glucose. In the case of embryos electroporated with the same plasmid mix, collect the micro-dissected electroporated cortexes in the same tube. Dissociate mechanically in culturing medium by using a P1000 pipette and pipetting up and down very gently for approximately 15–20 times. Filter the cellular suspension through a 40μm strainer, concentrate it by centrifugation at $150 \times g$ for 5 min, and finally resuspend the cells in culturing medium at 40×10^3 cells/μL (*see* **Note 8**).
2. Aspirate the medium from all the four wells to leave a thin layer of medium covering the well surface (*see* **Note 9**).
3. Load slowly, by keeping the pipette tip at the entrance of the somal channel, 5μL of cell suspension. To favor high seeding density within the channel, quickly after adding the cells, remove 5μL of media from the opposite somal well and slowly load it back in the same well. This practice allows first the cell transit along the channel and then it's slowing down. Quickly, observe under a microscope the cell flow through the channel until cell positioning; cells should have attached also along microgrooves entrance (*see* **Note 10**) (Fig. 1b).
4. Without adding any additional media to the wells, incubate in a humidifier incubator for 2 h until cells have attached.
5. Fill somal and axonal wells with fresh culture medium supplemented with 20 ng/mL BDNF and 50 ng/mL BDNF, respectively, to promote axon outgrowth. In order to establish a fluidically isolated system ensuring compartment-specific BDNF concentrations, keep a 50μL media volume difference between somal and axonal compartment, with the higher

volume in the somal well. This practice prevents diffusion of the higher BDNF concentrated solution from the axonal to the somal well.

6. Keep the devices in a humidified incubator at 37 °C, 5% CO_2.
7. Check the media volume in the wells every day, and fill up if evaporation occurred. Every 2 days, replace half of the media with fresh BDNF-enriched media.

3.1.5 Labeling of Membrane-Bound Organelles

1. At DIV4, label mitochondria or lysosomes by replacing half of each reservoir media with fresh culturing media containing 200 nM Mitotracker® or Lysotracker®, to reach a final concentration of 100 nM (*see* **Note 11**) (Fig. 1c).
2. Incubate for 60 min at 37 °C.
3. Wash twice the wells with fresh culturing media and incubate overnight. Acquisitions are performed the following day.

3.1.6 Recording and Axonal Transport Analysis

After overnight incubation of the culture upon labeling with organelle-specific dies, the transport dynamics of lysosomes and/or mitochondria can be recorded. Position the glass-bottom dish within a recording chamber controlled at 37 °C and 5% CO_2 of a confocal microscope (for Even et al. [11], we used a Zeiss LSM 880) and use a 63× oil objective with a working distance of 0.14 mm to acquire time-lapse movies. Given the shorter lengths of dendrites, image at the bottom of the microgrooves (approximately 450μm from the somal channel) lining the axonal channel to unambiguously focus on axons. The MitoTracker and LysoTracker label the organelles of all cultured neurons, including the non-electroporated ones. Focus only on the electroporated neurons identified by the fluorescent reporter gene of choice. We recommend to acquire three frames per second for 60 s in total, as mitochondria and lysosomes trafficking follows the dynamics of the fast axonal transport (*see* **Note 12**) (Fig. 1d).

3.2 Axonal Transport Recording upon Modification of MT Acetylation *in* Drosophila Melanogaster

3.2.1 Generation of Third-Instar Larvae

1. The D42-Gal4 > UAS *mito*GFP line is maintained at 20 °C and passed every 15–20 days.
2. To generate third-instar larvae for axonal transport, transfer stock vials in a 25 °C incubator to hasten the life cycle. Adult flies can be passed every 2 days to maximize the amount of eggs that are laid.
3. Transfer the vials with eggs in a 29 °C incubator to maximize the expression of Gal4 and check regularly to monitor the growth of larvae.

3.2.2 Anesthesia and Recording of Axonal Transport in Motoneurons from D42-Gal4 > UAS mito*GFP Larvae*

1. Prepare the anesthesia setup by perforating the lid of a 50 mL Falcon to allow ether fumes to penetrate. Place absorbing paper at the bottom of a glass beaker and add 5 mL of ether on the paper. Close the beaker hermetically with parafilm to prevent the evaporation of ether fumes (*see* **Note 13**).
2. When third-instar larvae from the D42-GAL4 > UAS-*mito*GFP line are abundant, collect and place 10 larvae in a 12-well plate filled with 10% sucrose solution (*see* **Note 14**). Larvae should only be kept in sucrose solution for a maximum of 1 h. Proceed immediately with the rest of the protocol.
3. Select the larvae with the brightest GFP expression in motoneurons using a dissection microscope equipped with a fluorescent lamp and discard the other larvae (*see* **Note 15**).
4. Select 3 larvae and place them on absorbing paper to dry them (*see* **Note 16**). Transfer the larvae on the inside of the perforated 50 mL falcon lid and close the falcon, making sure that the larvae rest on the inside of the falcon against the lid. Place the falcon with the lid against the paper soaked with ether to position the larvae directly on top of the ether fumes and seal with parafilm for 8 min (Fig. 2a).
5. Prepare 3 microscope slides and add 300μL glycerol in the center. All the following steps should be performed quickly since the anesthesia lasts about 30 min. After 8 min incubation, transfer one anesthetized larva per microscope slide. The larvae should always be placed with the same orientation (e.g., with the head facing the side of the slide reserved for annotation) to ensure that the orientation of the movies will be consistent. Use a dissection microscope and a pair of forceps to rotate the tracheas against the microscope slide so that the brain is facing up, as shown in Fig. 2b. Place a 32 × 32 mm coverslip on top of the larvae and adjust the position of the larvae by gently moving the coverslip with your finger until the brain and motoneurons are clearly visible on the dissection microscope (*see* **Note 17**).
6. Place the microscope slide with the coverslip facing the objective of the confocal microscope. The slide should be placed consistently so that the head of the larvae is always on the right (Fig. 2c).This will allow the discrimination between anterograde and retrograde transport during the analysis of the movies.
7. Find the brain and the motoneurons emerging from the ventral nerve cord using a small magnification objective and epifluorescent illumination (*see* **Note 18**). Focus on the proximal segment of motor neurons emerging from the ventral nerve cord with a 60× objective, as shown in the red square representing the field of view in Fig. 2c.

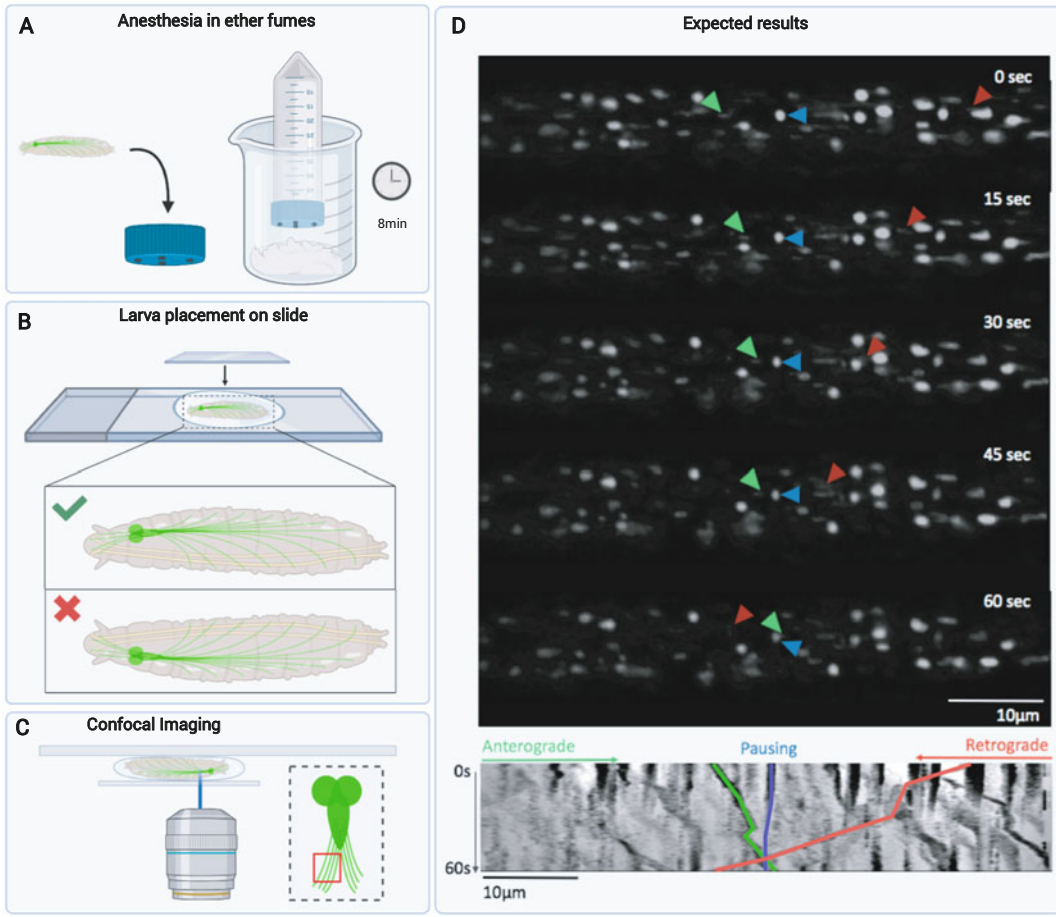

Fig. 2 Axonal transport recording in third-instar larvae. (**a**) The fly larvae are placed on the inside of a perforated 50 mL falcon lid. The falcon is then closed with the larvae on the inside and placed in a beaker with ether-soaker tissue paper for 8 min**.** (**b**) The anesthetized larva is placed in a drop of 80% glycerol on a microscope slide with the ventral side facing up and is then covered by a 32 × 32 mm glass coverslip. (**c**) A confocal microscope is used to record motile mitochondria in the proximal segment of the axon in motoneurons emerging from the ventral nerve cord, as shown in the red square depicting the field of view. (**d**) Motile mitochondria can be visualized as shown in the expected results and the corresponding kymograph. Arrows track moving mitochondria which are highlighted on the kymograph below. (Panel D is adapted from Le Bail et al. with permission [13])

8. Acquire 1-min movies with a maximum of 600 ms between frames. Settings of the laser, gain, and offset should be adjusted based on the setup (*see* **Note 19**). Multiple movies can be acquired in different motoneurons of the same larva to maximize the number of mitochondria that can be tracked. Multiple larvae should also be used for a single experiment to accurately represent inter-individual variability. Expected results and their corresponding kymograph for recordings of GFP-tagged mitochondria are shown in Fig. 2d (*see* **Note 20**).

3.2.3 Treatment with Tubastatin A to Increase MTs Acetylation

1. Prepare the stock solution of Tubastatin A by diluting the powder in DMSO at a concentration of 100 mM (*see* **Note 21**).
2. Select third-instar larvae as in Subheading 3.2.2 and maintain them in 10% sucrose solution.
3. Fill a 24-well plate with 500μL 10% sucrose solution per well and divide it in two halves for the control and treated conditions. For the control group add 5μL of DMSO (*see* **Note 22**) and for the treated group add 5μL of the tubastatin A stock solution to reach a final concentration of 1 mM.
4. Add larvae to the wells of the desired condition for 30 min. The larvae should move and absorb the drug through the feeding reflex. After treatment, immediately prepare the larvae for axonal transport recording, starting from drying the larvae on absorbing paper and following the steps as previously described in Subheading 3.2.2 (*see* **Note 23**).

3.2.4 Transgenic Fly Lines to Modulate MT Acetylation Levels

1. Transgenic fly lines expressing RNAi directed against the main regulators of MT acetylation can be used to modulate MT acetylation levels. To decrease MT acetylation, use a double transgenic line expressing both RNAi ATAT1 and RNAi ATAT2 (*see* **Note 24**), conversely, to increase MT acetylation, use RNAi against HDAC6. To record axonal transport and knock down ATAT1, ATAT2, or HDAC6, cross the D42-GAL4 > UAS-*mito*GFP with either of the RNAi expressing line. The steps to carry out the crossings are detailed below.
2. The flies used to carry out the crossings should be homozygous to ensure that the F1 larvae will all be heterozygous for the transgenic alleles. To generate homozygote flies, make sure that all flies have lost their balancer and the corresponding phenotypic marker (*see* **Note 25**). Males from one line should then be crossed with females from the other line.
3. Segregate males and virgin females based on their morphological characteristics (*see* **Note 26**).
4. Cross males from line 1 (e.g., D42-GAL4 > UAS-*mito*GFP) with females from line 2 (e.g., any RNAi line) to generate larvae expressing mitochondrial GFP and RNAi against the desired target in motoneurons (*see* **Note 27**). As in Subheading 3.2.1, carry out crossings at 25 °C and transfer adult flies every 2 days to a new vial. Transfer the vials with eggs at 29 °C to maximize the expression of mitochondrial GFP and RNAi before recording axonal transport. From this step, follow the protocol as described in Subheading 3.2.2.

3.3 Analysis of Axonal Transport Recordings

1. Open an image series in FIJI/ImageJ provided with the plugin KymoToolBox [14].
2. If necessary, separate stacked channels [Image | Color | Split channels].
3. Invert the values of Slices and Frames in the image properties [Image | Properties] (e.g., if the value in Slices is 1 and the value in Frames is 50, change the value of Slices to 50 and the value of Frames to 1). This step is necessary for the Kymotoolbox plugin.
4. Use the Segmented Line Tool [right-click on the Line icon | Segmented Line] to manually trace the shape of the axon. Make sure to always trace the line following the directionality of anterograde transport (starting from the soma to the tip of the axon) to ensure that the anterograde and retrograde directionality will be maintained in the kymograph.
5. Double-click on the Segmented Line Icon to select a width that encompasses all moving particles within the axon. Take note of the width and change the value back to 1. Click [t] to add the trace to the Region of Interest (ROI) Manager. Export the data set into excel to keep a trace of the axons that were tracked (*see* **Note 28**).
6. Use the KymoToolBox plugin to generate a kymograph [Plugin | KymoToolBox | Draw Kymo], tick [Get Kymo] and set the width to the value determined previously in **step 5**.
7. On the kymograph, draw a segmented line along the length of the particle's trajectories, and, as described in **step 5**, define their ROI and add it to the ROI Manager.
8. Analyze the displacement over time of the particles tracked by the segmented lines [Plugin | KymoToolBox | Analyse Kymo]. Set the directionality of the movement [Outward is... From left to Right] to ensure that the directionality of anterograde and retrograde transport is preserved. Set the minimum speed for movement to 0,10μm/s. Choose [Show colored kymo] to generate a color-coded kymograph for representative purposes where stationary particles are shown in blue, whereas motile particles moving with anterograde or retrograde directionality are shown in green and red, respectively (*see* **Note 2**).
9. Export the Summary data set from the Result panel into Excel. [Mean_speed_Out] is the average velocity in the anterograde direction for a given particle, conversely [Mean_speed_in] is the average velocity in the retrograde direction. A particle moving in the anterograde direction, then changing its course and moving in the retrograde direction would have a value for both these parameters. [Mean_speed] represents the average speed considering both retrograde and anterograde

movements of a given particle. [%_Time_Pause] is the percentage of time during which a given particle has a velocity lower than the threshold set in the previous step (0.10μm/s).

4 Notes

1. For the success of the bonding it is important that the device surface is debris-free. Surface contaminants may favor the formation of suboptimal hydrophobic bonds with the glass dish surface, leading to media leaking and axons growing outside the microgrooves. Before sterilization, tape can be used to gently remove debris and cell contaminants accumulated on the chamber surface from previous usages.
2. We recommend to prepare and irrigate the microfluidic platforms a few days before the plating day. If excessive pressure was exerted on the microgrooves during the bonding procedure, a longer time would be needed for the media to flow through the microgrooves. To improve the flow through the microgrooves, pipette up and down very gently at the entrance of the somal channel, making sure of not exerting an excess of pressure that could induce the detachment of the device from the dish. In case of incomplete filling of the microgrooves, ensure that the axonal wells are irrigated with a lower volume compared to the somal ones, to create a hydrostatic pressure that would force the media to pass through the microgrooves. Keep the microfluidic chamber in the incubator for 24–48 h until microgrooves are filled.
3. In Even et al. (2019) [11] we used a pCX-cre expressing plasmid to drive the expression of the sh-Atat1/scrambled-expressing plasmids. Alternatively, a conditional Cre recombinase, e.g., a CreERT2 Tamoxifen-driven expression plasmid, can be used to modulate in a time-controlled manner the downregulation of the protein of interest, e.g., downregulation of a protein of interest at post-mitotic stages by injecting tamoxifen to drive cre recombination after the neurogenesis window.
4. If possible, use plasmids expressing a fluorescent reporter. For example, in Even et al. (2019) we co-expressed the pair sh-Atat1/scrambled- and Cre-expressing plasmids with a plasmid expressing either pEGFP α-tubulin WT or pEGFP α-tubulin K40Q, to assess the Atat1-driven contribution of tubulin acetylation on axonal transport dynamics. If, on the other hand, the plasmids of interest do not express a fluorescent reporter, we recommend to co-inject a reporter plasmid expressing a fluorescent protein to allow the visualization of the electroporated neurons. Make sure that the fluorophore of the reporter

plasmid does not overlap with the channel of the MitoTracker/LysoTracker as this would interfere with the transport dynamics recording of the fluorescently labeled organelles.

5. A microcapillary tip optimally cut enables a precise and harmless injection into the ventricle. A suboptimal cut could prevent a sharp tissue perforation hampering its integrity and may allow the leakage of amniotic fluid.
6. Electroporation parameters should be adapted to the experimental design, in accordance with the developmental stage of the embryos to electroporate. The parameters described here were used in Even et al. (2019) [11]. The correct position of the positively and negatively charged electrodes with respect to the electroporated area, and their steady placement on the uterus wall are critical for the success of the electroporation. When delivering the electric pulses, pay attention not to touch the heart or the placenta with the electrodes, to prevent administering a shock to the dam. For more practical information, check Turchetto et al. (2020) [15].
7. To increase the survival rate of the operated mouse and electroporated embryos, it is crucial to perform the surgery within 45–50 min.
8. To increase cell survival rates, reduce the time required to prepare the cell suspension by dissociating the tissue mechanically without previous enzymatic digestion. This reduces the risk of cell damage that would induce cell aggregation and heterogeneous seeding along the axonal channel.
9. It is very important that both somal wells contain the same volume of media. As follows, the addition of cells into a somal well would generate a hydrostatic pressure between the two somal wells driving the cell to transit along the axonal channel.
10. If 5μL cell suspension does not ensure 60–70% cell confluency along the somal channel, repeat the loading a second time. Be careful to not load more than three times, as high confluency in the somal compartments would compromise survival of the cells in the channels.
11. Multiple fluorescent organelle dyes can be simultaneously added to a given culture.
12. To prevent neuron photodamages and loss of the fluorescent signal over time, set the lasers of the microscope at a low power to enable the visualization of the labeled cargos for the entire acquisition time.
13. This step should be performed inside a fume hood to prevent the inhalation of ether fumes.
14. Third instar is the last stage of larval growth. At this stage, larvae wander on the edge of the vials before starting pupation.

To collect third-instar larvae, use a pair of forceps to grab motile wandering larvae on the edge of a vial.

15. The D42 driver allows the expression of Gal4 in motoneurons but also in salivary glands. The GFP signal can be strong in the salivary glands bordering the brain but should not be taken into consideration when selecting the larvae. Focus instead on the brightness of the motoneurons emerging form the ventral nerve cord of the brain.
16. Incomplete drying of larvae will result in inconsistent anesthesia by the ether fumes.
17. If the coverslip is moving during transport or imaging, use nail polish on the sides of the coverslip to seal it.
18. The brightest mitochondria tend to remain stationary, whereas the motile mitochondria tend to be smaller and dimmer in fluorescent signal. The settings of the microscope should be adjusted accordingly in order to capture most motile mitochondria.
19. Axonal transport should always be recorded in the same region to ensure consistent results. We typically record in the proximal portion of the motoneurons, close to the ventral nerve cord.
20. We typically use a Nikon A1R confocal microscope in resonant mode.
21. Tubastatin A is a specific HDAC6 inhibitor which can be used to increase MT acetylation in models with reduced MT acetylation [16]. The Tubastatin solution should be clear in DMSO. If some precipitate can be observed, incubate the solution at 37 °C and vortex intermittently until it turns clear.
22. We have observed a slight effect of 1% DMSO solution on axonal transport velocity which explains why when treating with tubastatin A, the control group must be treated with DMSO as well.
23. We usually treat 3 larvae at a time with either the DMSO vehicle or the tubastatin A and anesthetize all 3 after the end of the treatment to record axonal transport. The timing of the experiment has to be followed rigorously and the anesthesia and recording of axonal transport should be carried out as quickly as possible following treatmen,t to minimize experimental variability.
24. ATAT1 is the major enzyme responsible for promoting the acetylation of Lysine 40 of MTs in mammals [17]. In consequence, its loss results in strong reduction of MT acetylation. *Drosophila Melanogaster* has two orthologs of the ATAT1 gene, ATAT1 and ATAT2 which have a redundant function, meaning that downregulation of one or the other will result in partial loss of MT acetylation, whereas combined downregulation will result in an almost complete loss of MT acetylation.

25. Balancer chromosomes are modified chromosomes which prevent homologous recombination, carry a dominant phenotype marker mutation and are recessive lethal. Based on these properties, flies can be identified based on the phenotypic marker associated to their balancer chromosome and cannot carry two copies of the same balancer chromosome. For instance, flies carrying the CyO balancer will exhibit curled wings (Cy marker) while flies carrying the TM6B balancer will be shorter and thicker than wild-type flies at both the larval and pupal stages (Tubby marker).
26. Males have a thin abdomen, slightly curved inwards with visible genitals appearing as a large brown mass in the postero-ventral part of the abdomen, whereas females are bigger than males and their abdomen is round and white. Virgin females are slightly translucent and can be recognized by the meconium, a dark spot in the upper left abdomen persisting up to 3 h after eclosion. The presence of the meconium guarantees that the female is a virgin since female flies are only fertile 8 h after eclosion.
27. Both sexes can be taken from each line for the crossing if the genes of interest are carried on the somatic chromosomes (1, 2, or 3). If a transgenic allele is carried by the X chromosome, only virgin females should be used to ensure that all the progeny will receive one transgenic allele.
28. If an axon harbors a high number of static cargoes which are cluttering the kymograph, it is possible to choose a smaller width which would allow to exclude some static cargoes to focus only on motile ones. We also recommend to trace segmented lines of the same length along all the axons/motoneurons considered for the analysis, for standardized calculations of vesicles run length.
29. By convention, anterograde transport is represented from left to right on representative kymographs and has a positive value for velocity, whereas retrograde transport is represented from right to left and has a negative value for velocity.

Acknowledgments

S.T. and R.L.B are PhD students from F.R.S-F.N.R.S.; L.B. and L.N. are respectively Postdoctoral Researcher and Director from F.R.S-F.N.R.S. The work in the Nguyen laboratory is supported by the F.R.S.-F.N.R.S. (Synet; EOS 0019118F-RG36), the Fonds Leon Fredericq, the Fondation Médicale Reine Elisabeth, the Fondation Simone et Pierre Clerdent, the Belgian Science Policy (IAP-VII network P7/20), and the ERANET Neuron STEM-MCD and NeuroTalk. The figures were made with Biorender (https://biorender.com/).

References

1. Janke C, Magiera MM (2020) The tubulin code and its role in controlling microtubule properties and functions. Nat Rev Mol Cell Biol 21(6):307–326. https://doi.org/10.1038/s41580-020-0214-3
2. Hubbert C, Guardiola A, Shao R et al (2002) HDAC6 is a microtubule-associated deacetylase. Nature 417:455–458. https://doi.org/10.1038/417455a
3. Portran D, Schaedel L, Xu Z et al (2017) Tubulin acetylation protects long-lived microtubules against mechanical ageing. Nat Cell Biol 19:391–398. https://doi.org/10.1038/ncb3481
4. Dompierre JP, Godin JD, Charrin BC et al (2007) Histone deacetylase 6 inhibition compensates for the transport deficit in Huntington's disease by increasing tubulin acetylation. J Neurosci 27:3571–3583. https://doi.org/10.1523/JNEUROSCI.0037-07.2007
5. Reed NA, Cai D, Blasius TL et al (2006) Microtubule acetylation promotes Kinesin-1 binding and transport. Curr Biol 16:2166–2172. https://doi.org/10.1016/j.cub.2006.09.014
6. Godena VK, Brookes-Hocking N, Moller A et al (2014) Increasing microtubule acetylation rescues axonal transport and locomotor deficits caused by LRRK2 Roc-COR domain mutations. Nat Commun 5:5245. https://doi.org/10.1038/ncomms6245
7. D'Ydewalle C, Krishnan J, Chiheb DM et al (2011) HDAC6 inhibitors reverse axonal loss in a mouse model of mutant HSPB1-induced Charcot-Marie-tooth disease. Nat Med 17:968–974. https://doi.org/10.1038/nm.2396
8. Kim GW, Li L, Gorbani M et al (2013) Mice lacking α-tubulin acetyltransferase 1 are viable but display α-tubulin acetylation deficiency and dentate gyrus distortion. J Biol Chem 288:20334–20350. https://doi.org/10.1074/jbc.M113.464792
9. Li L, Jayabal S, Ghorbani M et al (2019) ATAT1 regulates forebrain development and stress-induced tubulin hyperacetylation. Cell Mol Life Sci 76:3621–3640. https://doi.org/10.1007/s00018-019-03088-3
10. Wei D, Gao N, Li L et al (2018) α-Tubulin acetylation restricts axon overbranching by dampening microtubule plus-end dynamics in neurons. Cereb Cortex 28:3332–3346. https://doi.org/10.1093/cercor/bhx225
11. Even A, Morelli G, Broix L et al (2019) ATAT1-enriched vesicles promote microtubule acetylation via axonal transport. Sci Adv 5:eaax2705. https://doi.org/10.1126/sciadv.aax2705
12. Li L, Wei D, Wang Q et al (2012) MEC-17 deficiency leads to reduced α-tubulin acetylation and impaired migration of cortical neurons. J Neurosci 32:12673–12683. https://doi.org/10.1523/JNEUROSCI.0016-12.2012
13. Le Bail R, Morelli G, Gladwyn-ng I (2017) Dacapo regulates axonal transport through the modulation of microtubule acetylation. Master's Thesis, University of Liege, Belgium. https://orbi.uliege.be/handle/2268/235914
14. Zala D, Hinckelmann M-V, Yu H et al (2013) Vesicular glycolysis provides on-board energy for fast axonal transport. Cell 152:479–491. https://doi.org/10.1016/j.cell.2012.12.029
15. Turchetto S, Broix L, Nguyen L (2020) Ex vivo recording of axonal transport dynamics on postnatal organotypic cortical slices. STAR Protoc 1:100131. https://doi.org/10.1016/j.xpro.2020.100131
16. Butler KV, Kalin J, Brochier C, Vistoli G, Langley B, Kozikowski AP (2005) Rational design and simple chemistry yield a superior, neuroprotective HDAC6 inhibitor, tubastatin A. Bone 23:1–7. https://doi.org/10.1021/ja102758v.Rational
17. Kalebic N, Sorrentino S, Perlas E et al (2013) αTAT1 is the major α-tubulin acetyltransferase in mice. Nat Commun 4:1962. https://doi.org/10.1038/ncomms2962

Chapter 11

Live-Cell Imaging of RNA Transport in Axons of Cultured Primary Neurons

J. Tabitha Hees and Angelika B. Harbauer

Abstract

The use of fluorescent proteins has revolutionized the study of protein localization and transport. However, the visualization of other molecules and specifically RNA during live-cell imaging remains challenging. In this chapter, we provide guidance to the available methods, their advantages and drawbacks as well as provide a detailed protocol for the detection of RNA transport using the MS2/PP7-split-Venus system for background-free RNA imaging.

Key words RNA transport, MS2, PP7, Split-Venus, Transient transfection, Cultured primary neurons, Imaging

1 Introduction

RNA localization is an important process by which a cell transports and targets mRNA to predetermined areas, where the respective proteins are required [1]. In this way, protein translation can be regulated locally, thereby allowing the cell to respond rapidly to intra- and extracellular cues. Neurons are particularly challenged in regulating RNA transport due to their complex morphology. Most mRNAs have to travel long distances from the nucleus, where they are synthesized, to their subcellular destinations, where they can be locally translated [2]. In recent years, several microscopy methods have been developed to visualize (transport of) RNA in living cells including injection of fluorescently labeled RNAs or molecular beacons as well as the use of programmable RNA binding proteins (RBPs), a CRISPR/Cas9-based method or tagging the RNA with sequences recognized by RBPs like the phage-derived MS2 and PP7 proteins or with fluorescent RNA aptamers [3, 4]. Some of these methods exist more at a conceptual level, while others are more easily adapted in the lab. Advantages and disadvantages are summarized in Table 1.

Alessio Vagnoni (ed.), *Axonal Transport: Methods and Protocols*,
Methods in Molecular Biology, vol. 2431, https://doi.org/10.1007/978-1-0716-1990-2_11,
© The Author(s), under exclusive license to Springer Science+Business Media, LLC, part of Springer Nature 2022

Table 1
Live cell RNA imaging methods: advantages and disadvantages

	Advantages	Disadvantages
Molecular beacons	• Detection of endogenous, nonmodified RNA	• Challenging design of antisense sequence of molecular beacon • Accessibility of the target sequence can be restrictive • Ratio of fluorophore to target is 1:1; therefore, low abundance transcripts are hard to visualize • Microinjection as delivery method (harmful to neurons)
Engineered Pumilio homology domains	• Detection of endogenous transcript • Common transfection methods for delivery into the cells	• Lengthy cloning procedure • Accessibility of the target sequence can be restrictive • Has not been established in neurons yet
CRISPR/Cas9	• Detection of endogenous, nonmodified RNA • No influence on RNA abundance • Common transfection methods for delivery into the cells	• Has not been established in neurons yet
Fluorescently labeled RNAs	• High signal-to-noise ratio • High sensitivity • Allows simultaneous imaging of two or more RNAs	• Detection of labeled RNA • Microinjection as delivery method (harmful to neurons)
RNA aptamers	• Very low background fluorescence • No influence on dynamics of tagged RNA • Common transfection methods for delivery into the cells	• Detection of tagged RNA • Inability to detect single transcripts and low abundance RNAs • Low photostability of RNA-DFHBI complex
MS2 or PP7	• Common transfection methods for delivery into the cells • Successful use in neurons	• High background • Overexpression of tagged RNA • Potential influence on trafficking of RNA
MS2/PP7-split-Venus	• Background-free • Common transfection methods for delivery into the cells • Successful use in neurons	• Overexpression of tagged RNA • Potential influence on trafficking of RNA

A major consideration when choosing a suitable RNA imaging method is whether detection of the endogenous transcript is necessary or if overexpression of a tagged version can be employed.

In order to visualize the endogenous transcript during live cell imaging, the most elegant version is the use of "molecular beacons" [5]. Molecular beacons are oligonucleotides that form a stem loop structure. The loop part of the oligonucleotide is complementary to a sequence in the RNA of interest, while the stem contains two complementary sequences on either side of the probe sequence. Furthermore, one end of the probe is attached to a fluorescent molecule and the other end to a quenching molecule. The stem holds the fluorophore and the quencher in close proximity, resulting in a quenched fluorescent signal. However, when the RNA of interest is present, the probe binds to its target sequence within the RNA leading to a conformational change of the probe, which removes the fluorophore from the quencher. This results in a fluorescent signal visualizing the RNA of interest [5] (Fig. 1a). The major advantage of this approach is the ability to visualize endogenous, nonmodified RNAs. However, the design of the antisense sequence of the molecular beacon is very challenging. One requirement is the accessibility of the target sequence. It needs to be considered that parts of the target RNA can form higher order structures or can be hidden by proteins. Furthermore, it is important that molecular beacons do not interfere with the localization of the RNA of interest by disturbing its conformation upon binding. As a last requirement, the antisense sequences need to be very specific and should not recognize other RNAs in the cell. The major limitation of this approach is the necessity to use microinjection for probe delivery into the cells [6]. While molecular beacons have been successfully used in *Drosophila* oocytes, the use in neurons is more difficult since microinjection is very harmful to neurons [7]. Despite these limitations, molecular beacons have been successfully applied to neurons in a few studies [8–10].

Two other approaches that detect the endogenous transcript and may be suitable for live cell imaging in neurons have been reported. The RNA binding domain of the RBP Pumilio (Pum) can be engineered to allow the combinatorial recognition of any nucleotide sequence [11, 12]. This artificial RBP then binds in a sequence specific manner to the mRNA target and would allow the targeting of a fluorescent protein (FP) to the target (Fig. 1b). In one example, this approach was combined with split-green FP (GFP) complementation by designing two Pum homology domains that bind adjacent regions within a mitochondrially encoded transcript [13]. The use of this method for cytoplasmic RNAs still needs to be tested, as the highly conserved nature of the Pumilio family of proteins may lead to interference by endogenous Pum proteins and their binding partners with RNA localization, transport or stability [14].

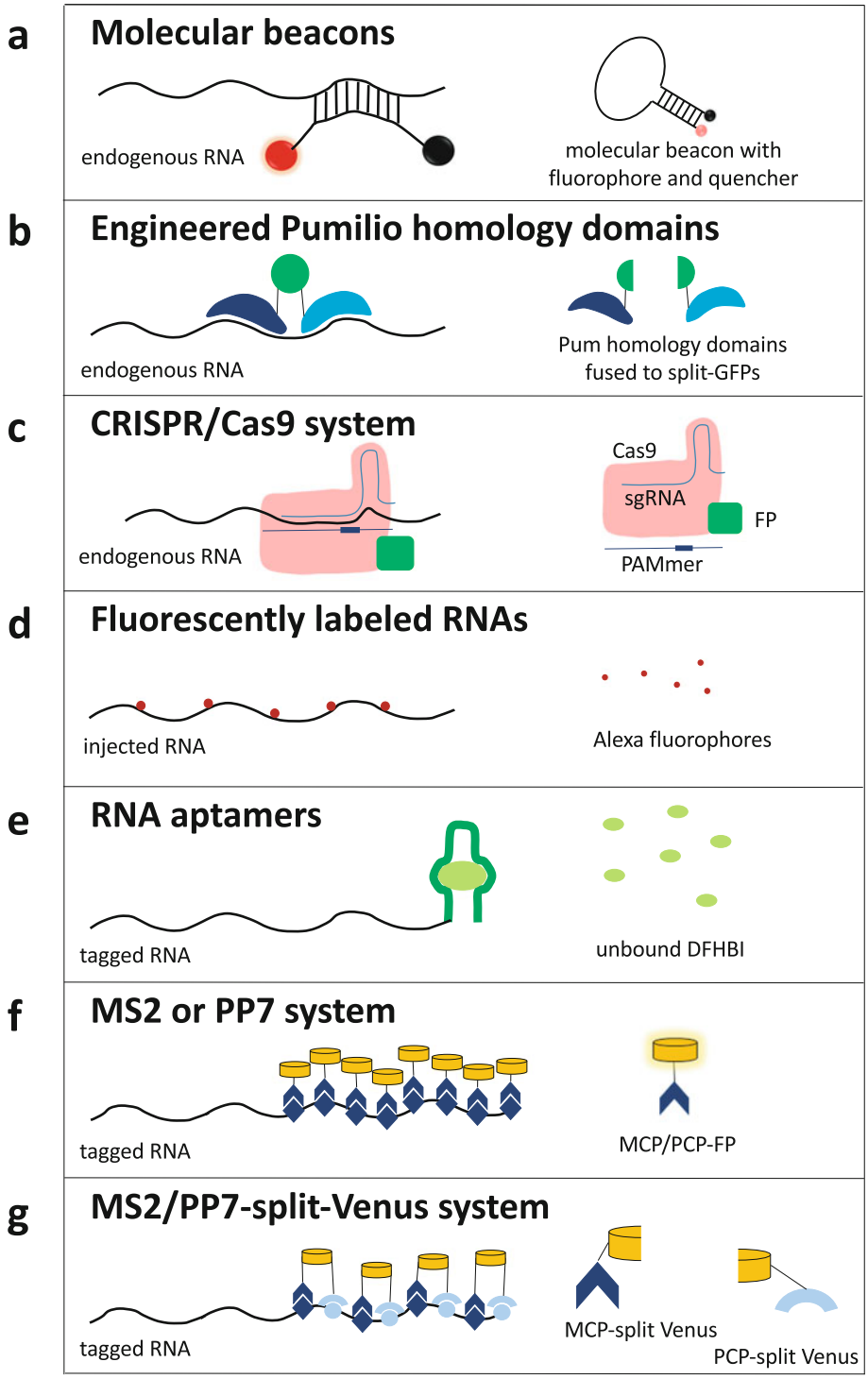

Fig. 1 Overview of RNA detection methods. (**a**) Molecular beacons are antisense RNA molecules that form a stem loop structure in the absence of target binding thereby positioning the attached fluorophore next to a quencher. Target recognition spreads the molecule and thereby unquenches the fluorophore. (**b**) Pumilio homology domains engineered to be sequence-specific to two adjacent regions of the target RNA are fused with split GFP halves. Upon target binding, the GFP molecule is reconstituted and becomes fluorescent. (**c**) An

Similarly, the CRISPR/Cas9 system can also be modulated to detect RNA instead of DNA. This system requires a single-guide RNA (sgRNA), which binds to the target sequence, and the endonuclease Cas. Furthermore, a short sequence downstream of the target sequence, called PAM (protospacer adjacent motif) is necessary for Cas and its associated sgRNA to recognize the target sequence. The CRISPR/Cas9 system has evolved to detect double-stranded DNA. However, it has been shown that also targeting of RNA is possible if the PAM sequence is part of an oligonucleotide that binds to the target RNA (PAMmer) [15]. Therefore, a nuclease-dead version of Cas9 that is fused to a FP could be guided to the endogenous RNA (Fig. 1c), allowing live cell imaging [16]. Unlike Pum, Cas9 does not have a mammalian counterpart and unlike molecular beacons, common transfection methods for delivering the constructs into the cells can be employed. However, so far this approach has not been established in living neurons yet.

Alternatively, exogenous RNA labeled with fluorescent dyes can be injected to visualize its transport and localization in living cells (Fig. 1d). For this approach, the RNA of interest is transcribed in vitro using Alexa-labeled UTP [17]. Major advantages of this approach are the high signal-to-noise ratio and the high sensitivity, which allows tracking of fast moving transcripts. Moreover, by using different Alexa dyes for labeling several RNAs can be imaged simultaneously. However, similar to the molecular beacons, the labeled RNAs are also delivered into the cells via microinjection. This method of delivery is necessary because very high amounts of the fluorescently labeled RNAs are required. Consequently, this approach has not been straightforward in neurons. Nevertheless, there are a few studies where Alexa-labeled RNAs have been successfully used in rat hippocampal neurons [18–20].

Other methods employ tagging of the RNA of interest to achieve efficient labeling in living cells. Comparative localization of the tagged with the endogenous RNA using in situ hybridization methods is a mandatory requirement in this case to ensure no artefacts are introduced by overexpression and/or by addition of a tag to the RNA of interest. On the bright side, tagging allows to introduce multiple binding sites within one molecule, greatly enhancing the signal-to-noise ratio.

Fig. 1 (continued) antisense guide-RNA targets a nuclease-dead Cas9-FP construct to the RNA of interest. (**d**) In vitro transcribed, fluorescent RNAs can be directly injected. (**e**) RNA aptamers such as Broccoli or Spinach become fluorescent upon binding of the small molecule DFHBI. (**f**) The RNA of interest is tagged with multiple binding sites of the MCP or PCP. Simultaneous expression of FP-fused respective coat proteins allows visualization of the RNA in living cells. (**g**) Expression of the RNA of interest with a tag consisting of alternating MCP and PCP binding sites and coexpression of MCP and PCP fused to the respective halves of split-Venus combines the strength of the MS2-system with fluorophore reconstitution for background-free RNA imaging

One tag-based approach utilizes RNA aptamers, such as Spinach or Broccoli, and the fluorophore DFHBI (3,5-difluoro-4-hydroxybenzylidene imidazolinone) [21]. For this approach, the RNA of interest is coupled to the RNA aptamer and expressed in cells. Upon addition of DFHBI to the cells, the RNA of interest can be visualized due to binding of DFHBI to the RNA aptamer. DFHBI is a mimic of the GFP fluorophore (Fig. 1e), which is nonfluorescent in solution but becomes highly fluorescent upon binding to Spinach or Broccoli [22]. Importantly, due to the small size of the Spinach/Broccoli-DFHBI complex the dynamics of the tagged RNA are basically not affected. Furthermore, the background fluorescence is very low and common transfection methods can be used for delivering the tagged RNA into the cells. The major drawbacks, however, are the low photostability of the RNA-DFHBI fluorescent complexes and the inability to visualize low-abundance or single RNAs, which can partially be solved by adding several RNA aptamer molecules to the transcript of interest [22]. Overall, RNA imaging using RNA aptamers and DFHBI works very well in live bacterial cells, while the fluorescent signal in live mammalian cells is usually dim and requires a lot of optimization [22].

The most widely used approach to live cell RNA imaging makes use of tagging the RNA of interest with a sequence known to bind specifically and selectively to an RBP, which is then coexpressed coupled to a FP. The use of a phage-derived RNA/RBP sequence has the advantage that no endogenous sequences would be recognized by these proteins. This approach has been first used in yeast, using the MS2 stem loop/MS2 coat protein (MCP) pair from the MS2 phage [23]. For this method, several repeats of RNA stem loops that are derived from the MS2 phage are integrated into the target RNA. This integration usually happens before or after the three prime untranslated region (3' UTR). The MCP specifically recognizes the MS2 stem loop with high validity. By tagging the MCP with a FP (MCP-FP), the target RNA carrying the stem loops can be visualized in live cells (Fig. 1f). Since its first use several improvements have been applied to the MS2-MCP system. The main issue was the high fluorescent background caused by unbound MCP-FP in the cytosol. This problem has been tackled using two strategies. First, multiple repeats of the MS2 stem loops were integrated into the target RNA sequence. It has been shown that 24 repeats are required to visualize single RNA molecules [24]. Second, a nuclear localization signal has been added to the MCP-FP, which keeps the protein within the nucleus when not bound to a target RNA molecule [25]. While these strategies reduced the background, only the recent introduction of a split-FP approach completely eliminated the background signal. In this optimized approach, a MS2/PP7 hybrid system is used [26]. Similar to MCP, the PP7 bacteriophage coat protein (PCP) is also an

RBP, which specifically binds to the PP7 stem loop derived from the PP7 phage. Both MCP and PCP are fused with one half of the yellow FP Venus. Furthermore, the target RNA is tagged with alternating MS2 and PP7 stem loops. Accordingly, the split-Venus parts only form a functional fluorescence protein when the MCP and PCP are bound to the respective stem loops, thereby allowing background-free RNA imaging in living cells (Fig. 1g). In this chapter, we provide a detailed protocol for imaging mRNA in living neurons using the MS2/PP7-split-Venus approach including construct design, neuron preparation and seeding, transient transfection using Lipofectamine and imaging at a spinning disk or confocal scanning microscope.

2 Materials

2.1 Constructs

1. MS2/PP7-tagged RNA of interest (stem loops can be amplified from Addgene construct #52984, deposited by Robert Singer).
2. MCP/PCP-split-Venus (Addgene construct #52985, deposited by Robert Singer).
3. Optional: Fluorescent marker for axon initial segment (AIS, e.g., AnkyrinG-mCherry, Addgene construct #42566, deposited by Benedicte Dargent).

2.2 Neuron Culture and Transfection Reagents

1. Primary mouse hippocampal neurons.
2. 35 mm dishes with coverslip bottom or 24 well glass bottom plates.
3. Neuronal growth medium: Neurobasal medium supplemented with B27 (2%) and L-glutamine–penicillin–streptomycin (1%).
4. Plain neurobasal medium: Neurobasal medium containing L-glutamine–penicillin–streptomycin (1%).
5. L-glutamine–penicillin–streptomycin solution (29.2 mg/ml L-glutamine, 10,000 units/ml penicillin, and 10,000 μg/ml streptomycin).
6. Poly-L-lysine (1 mg/ml in H_2O).
7. Laminin (0.5–2 mg/ml in 50 mM Tris–HCl (pH 7.4), 0.15 M NaCl).
8. Lipofectamine 2000 transfection reagent.
9. Incubator, 37 °C, 5% CO_2.
10. Water bath, 37 °C.
11. Sterile cell culture hood.

2.3 Microscopy

1. Spinning disk or confocal scanning microscope,
   (a) equipped with filters/lasers for YFP detection,
   (b) equipped with temperature control chamber (no CO_2 required).
2. Hibernate E medium.

3 Methods

3.1 Cloning of the MS2/PP7-Tagged RNA of Interest

1. Select a suitable expression vector. We have had good experiences with the pHAGE vectors that are also employed for expression of the MCP/PCP constructs and use the comparatively weak Ubiquitin C (UBC) promoter. However, strong viral promoters, such as CMV, might also work.
2. Select the placement of the MS2/PP7-stem loops. Traditionally the stem loops are placed just after the stop codon or after the 3'UTR. It is recommended to try both options since placement in either spot could interfere with putative RNA targeting signals.
3. Use standard cloning procedures to insert your RNA of interest (*see* **Note 1**).

3.2 Neuron Preparation and Seeding

1. Plate primary mouse hippocampal neurons (obtained from E16.5 mouse embryos) in poly-L-lysine (20 μg/ml) and laminin (3.5 μg/ml) coated coverslip bottom dishes (35 mm) at a density of 5×10^5 neurons per dish. Add 2 ml neuronal growth medium per dish. For 24 well glass bottom plates seed $1–2 \times 10^5$ neurons in 500 μl neuronal growth medium per well (*see* **Note 2**).
2. For maintenance, replace 50% of the neuronal growth medium every 2–3 days with fresh medium.

3.3 Lipofectamine Transfection

1. Carry out all procedures in a sterile cell culture hood, unless stated otherwise.
2. Transfect the primary mouse neurons 5–7 days after plating (DIV5–7).
3. Prewarm neuronal growth medium and plain neurobasal medium in a water bath to 37 °C and thaw DNA constructs on ice.
4. Add 48 μl plain neurobasal medium and 2 μl Lipofectamine 2000 transfection reagent into a sterile 1.5 ml microcentrifuge tube (total volume per dish/well: 50 μl). Mix by pipetting and do not vortex or centrifuge.
5. In a separate microcentrifuge tube, mix plain neurobasal medium with the DNA constructs to reach a total volume of

50 µl. Take 45 µl plain neurobasal medium, 4 µl of the MS2/PP7-tagged RNA of interest (1 µg/µl; DNA amount per dish/well: 4 µg) and 1 µl of the MCP/PCP-split-Venus construct (1 µg/µl; DNA amount per dish/well: 1 µg). Mix by pipetting (*see* **Notes 3–5**). If cotransfection of an AIS maker is desired, include 0.3 µg per dish/well of AnkyrinG-mCherry (*see* **Note 6**).

6. Incubate the Lipofectamine mix and the DNA mix separately at room temperature for 5 min. Afterward, add all 50 µl of the lipofectamine mix dropwise to the DNA mix. Perform dropwise pipetting for mixing.
7. Incubate the Lipofectamine–DNA mix for at least 20 min at room temperature. During that time, DNA-liposome complexes will form.
8. Take the primary mouse neurons out from the incubator. Remove the neuronal growth medium and keep it in the water bath at 37 °C (conditioned medium). Wash the neurons three times with plain neurobasal medium (1 ml per dish; 250 µl per well). After the last wash, leave just enough medium in the dish/well to cover the cells (about 300 µl per dish; 150 µl per well) (*see* **Note 7**).
9. Mix again the Lipofectamine–DNA mixture dropwise and add the mixture dropwise onto the cells. Swirl the medium in the dish/well slowly to ensure proper distribution.
10. Incubate the neurons for 20 min in the incubator at 37 °C (*see* **Note 8**).
11. After incubation, remove the Lipofectamine–DNA mixture and wash the neurons three times with plain neurobasal medium (1 ml per dish; 250 µl per well).
12. After the last wash step, add conditioned and fresh neuronal growth medium to the neurons in a 1:1 ratio (total volume per dish: 2 ml; total volume per well: 500 µl).
13. Place neurons back into the incubator and allow expression for 48 h.

3.4 Imaging

1. On the day of imaging prewarm the appropriate amount of Hibernate E (2 ml per dish or 500 µl per well) in a water bath to 37 °C.
2. Replace neuronal growth medium with Hibernate E.

   Optional: This can also be done a few hours before imaging to give the neurons time to equilibrate in Hibernate E (*see* **Note 9**).
3. Prewarm your microscope set-up to 37 °C.

4. Place cells onto the imaging platform of an inverted microscope. We recommend a spinning disk set-up over a confocal due to the increased temporal resolution provided by the spinning disk. We also have found that the signal-to-noise ratio in the GFP/YFP channel of most wide-field instruments is insufficient to effectively visualize the weak Venus signal especially in neuronal processes.
5. Find your cells using a 10 or 20× objective and then switch to a 40× or 60/63× oil-immersion objective.
6. Scan the field of view for cells showing a clear Venus signal over background. This can take some time as the fluorophore complementation does not happen in every transfected cell and in general, Lipofectamine transfection of primary neurons only transfects up to 10% of the culture even under optimal conditions (*see* **Note 10**).
7. Once you have focused on a cell, identify your region of interest. If cotransfection with Ankyrin G-mCherry was performed, the identification of the axon is facilitated (Fig. 2a, *see* **Note 11**).
8. Image your region of interest using time-lapse microscopy. For most transport dynamics, an imaging frequency of 1 Hz and a movie duration of 2–3 min will be sufficient (Fig. 2b).

4 Notes

1. The Addgene construct #52984 has an optimized sequence to avoid repetitive sequences within the stem loops. However, during cloning, especially when using Gibson assembly or similar techniques that amplify the whole vector, some repeats may be lost. Validation of the final construct by sequencing is therefore highly recommended.
2. Neuron dissection and plating are very critical steps and will influence the transfection efficiency. Furthermore, the density plays an important role since it can directly affect the health of the neurons and transfection efficiency. Plating the neurons at a too low cell density will cause cell death, while a very high density decreases DNA uptake due to contact inhibition.
3. For the transfection, it is very important to use high quality DNA that is free of RNA and proteins. The $A_{260/280}$ ratio should be between 1.8 and 2.0.
4. The ratio of the MCP/PCP-split-Venus construct and the MS2/PP7-tagged RNA of interest needs to be optimized for each target RNA. A ratio of approximately 1:4 is recommended as a starting point. Furthermore, the amount of DNA added to the cells is very important. In this case, a very high amount of

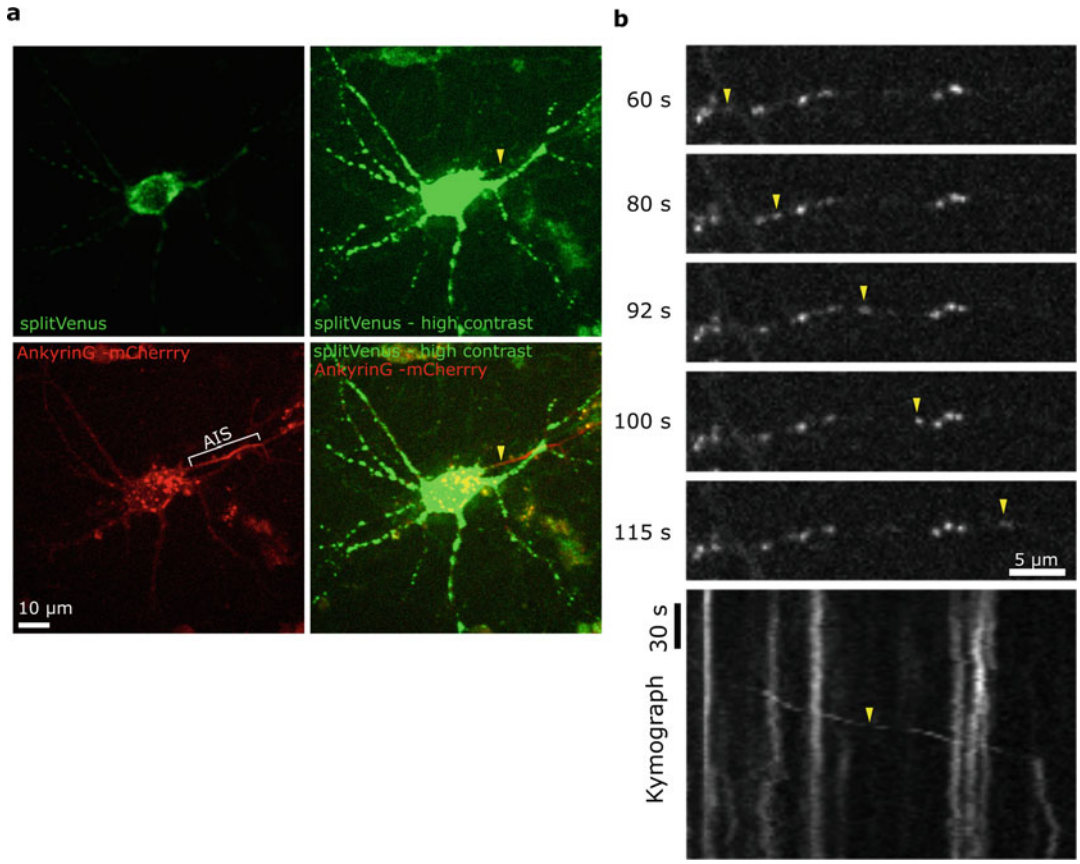

Fig. 2 MS2/PP7-split-Venus system for background-free RNA imaging. (**a**) Inclusion of an axon initial segment (AIS) marker greatly enhances the identification of the usually dim axonal signal. A yellow arrowhead marks an RNA particle within the axon. (**b**) Representative time points of a 3 min long movie taken at 1 Hz. A yellow arrowhead marks the position of a moving RNA particle over time. In the kymograph, movement is represented by a diagonal line, again marked by a yellow arrowhead

the MS2/PP7-tagged RNA of interest (4 µg) is necessary. We have observed that lower amounts lead to retention of the RNA inside the nucleus by unknown mechanisms, which can be overcome by transfection of higher amounts of DNA.

5. The DNA-to-Lipofectamine ratio used here differs from the manufacturer's instructions. Usually a ratio of 1:2 or 1:3 is recommended. In this case, however, a high amount of DNA is required as mentioned above, while the Lipofectamine amount remains constant. Increasing the Lipofectamine amount accordingly would lead to increased cell death due to toxicity of Lipofectamine.
6. Cotransfection of an AIS marker greatly facilitates the identification of the axon in cultured neurons, especially as the efficiency of axonal RNA labeling is stronger in the proximal axon.

Overexpression of AIS components, however, may alter AIS structure and trafficking through this region; therefore post-imaging staining with antibodies against AIS proteins would be a suitable alternative.

7. The neurons need to be washed three times with plain neurobasal medium to remove the B27 supplement. B27 supplement interferes with the DNA–liposome complexes. Always keep a minimal amount of medium on the cells (e.g., do not use an aspirator) to avoid dryness.
8. Similar to the amount of Lipofectamine, also the incubation time with Lipofectamine needs to be optimized. While a longer incubation time improves transfection efficiency, it also leads to increased cell death due to toxicity of Lipofectamine.
9. We do not recommend leaving the cells in Hibernate E for several days as we have observed a drop in cellular viability. Equilibration for about 1 h, however, greatly helps RNA mobility, but this may be specific to your RNA of interest and its mode of transport.
10. Transfection efficiency is crucial for a successful experience, since a highly transfected culture increases the chances of successful fluorophore complementation. For troubleshooting, refer to **Notes 3–5** and **7–8**.
11. The amount of RNA in the somatodendritic region usually outshines the dim axonal signals.

References

1. St Johnston D (2005) Moving messages: the intracellular localization of mRNAs. Nat Rev Mol Cell Biol 6:363–375
2. Buxbaum AR, Yoon YJ, Singer RH, Park HY (2015) Single-molecule insights into mRNA dynamics in neurons. Trends Cell Biol 25: 468–475
3. Bauer KE, Kiebler MA, Segura I (2017) Visualizing RNA granule transport and translation in living neurons. Methods 126:177–185
4. Mikl M, Vendra G, Doyle M, Kiebler MA (2010) RNA localization in neurite morphogenesis and synaptic regulation: current evidence and novel approaches. J Comp Physiol A 196:321–334
5. Tyagi S, Kramer FR (1996) Molecular beacons: probes that fluoresce upon hybridization. Nat Biotechnol 14:303–308
6. Santangelo PJ, Alonas E, Jung J, Lifland AW, Zurla C (2012) Probes for intracellular RNA imaging in live cells. Methods Enzymol 505: 383–399
7. Lappe-Siefke C, Maas C, Kneussel M (2008) Microinjection into cultured hippocampal neurons: a straightforward approach for controlled cellular delivery of nucleic acids, peptides and antibodies. J Neurosci Methods 175:88–95
8. Alami NH, Smith RB, Carrasco MA, Williams LA, Winborn CS, Han SSW et al (2014) Axonal transport of TDP-43 mRNA granules is impaired by ALS-causing mutations. Neuron 81:536–543
9. Simon B, Sandhu M, Myhr KL (2010) Live FISH: imaging mRNA in living neurons. J Neurosci Res 88:55–63
10. Zepeda A, Arias C, Flores-Jasso F, Vaca L (2013) RNA imaging: tracking in real-time RNA transport in neurons using molecular beacons and confocal microscopy. Methods Cell Biol 113:361–389
11. Cheong C-G, Hall TMT (2006) Engineering RNA sequence specificity of Pumilio repeats. Proc Natl Acad Sci U S A 103:13635–13639
12. Adamala KP, Martin-Alarcon DA, Boyden ES (2016) Programmable RNA-binding protein

composed of repeats of a single modular unit. Proc Natl Acad Sci U S A 113:E2579–E2588

13. Ozawa T, Natori Y, Sato M, Umezawa Y (2007) Imaging dynamics of endogenous mitochondrial RNA in single living cells. Nat Methods 4:413–419
14. Dictenberg J (2012) Genetic encoding of fluorescent RNA ensures a bright future for visualizing nucleic acid dynamics. Trends Biotechnol 30:621–626
15. O'Connell MR, Oakes BL, Sternberg SH, East-Seletsky A, Kaplan M, Doudna JA (2014) Programmable RNA recognition and cleavage by CRISPR/Cas9. Nature 516: 263–266
16. Nelles DA, Fang MY, O'Connell MR, Xu JL, Markmiller SJ, Doudna JA, Yeo GW (2016) Programmable RNA tracking in live cells with CRISPR/Cas9. Cell 165:488–496
17. Wilkie GS, Davis I (2001) Drosophila wingless and pair-rule transcripts localize apically by dynein-mediated transport of RNA particles. Cell 105:209–219
18. Gao Y, Tatavarty V, Korza G, Levin MK, Carson JH (2008) Multiplexed dendritic targeting of alpha calcium calmodulin-dependent protein kinase II, neurogranin, and activity-regulated cytoskeleton-associated protein RNAs by the A2 pathway. Mol Biol Cell 19: 2311–2327
19. Shan J, Munro TP, Barbarese E, Carson JH, Smith R (2003) A molecular mechanism for mRNA trafficking in neuronal dendrites. J Neurosci 23:8859–8866
20. Tübing F, Vendra G, Mikl M, Macchi P, Thomas S, Kiebler MA (2010) Dendritically localized transcripts are sorted into distinct ribonucleoprotein particles that display fast directional motility along dendrites of hippocampal neurons. J Neurosci 30:4160–4170
21. Paige JS, Wu KY, Jaffrey SR (2011) RNA mimics of green fluorescent protein. Science 333:642–646
22. Filonov GS, Jaffrey SR (2016) RNA imaging with dimeric broccoli in live bacterial and mammalian cells. Curr Protoc Chem Biol 8:1–28
23. Bertrand E, Chartrand P, Schaefer M, Shenoy SM, Singer RH, Long RM (1998) Localization of ASH1 mRNA particles in living yeast. Mol Cell 2:437–445
24. Fusco D, Accornero N, Lavoie B, Shenoy SM, Blanchard J-M, Singer RH, Bertrand E (2003) Single mRNA molecules demonstrate probabilistic movement in living mammalian cells. Curr Biol 13:161–167
25. Wells AL, Condeelis JS, Singer RH, Zenklusen D (2007) Imaging real-time gene expression in Mammalian cells with single-transcript resolution. CSH Protoc 2007:pdb.prot4869
26. Wu B, Chen J, Singer RH (2014) Background free imaging of single mRNAs in live cells using split fluorescent proteins. Sci Rep 4:3615

Chapter 12

Visualizing Vesicle-Bound Kinesins in Cultured Hippocampal Neurons

Andrew Montgomery, Alex Garbouchian, and Marvin Bentley

Abstract

Eukaryotic cells use microtubule-based vesicle transport to exchange molecules between compartments. Kinesin family members mediate all microtubule plus end-directed vesicle transport. Of the 45 kinesins expressed in humans, some 20 mediate microtubule plus-end directed vesicle transport. Here we describe a technique to visualize vesicle-bound kinesins in cultured hippocampal neurons. The method involves the expression of the vesicle-binding tail domain while minimizing the cytoplasmic pool. Using this approach drastically improves vesicle labeling compared to full-length kinesins. This tool is useful for systematically comparing the localization of different kinesins in the same cell type and for identifying cargo proteins that reside in vesicles moved by a specific kinesin family member. While we describe the assay in cultured hippocampal neurons, we expect it to be easily transferable to other eukaryotic cell types.

Key words Kinesin, Myosin V, Vesicle transport, Membrane trafficking, Live-cell imaging, Cultured hippocampal neurons

1 Introduction

Kinesin motor proteins mediate long-range vesicle transport in eukaryotic cells [1, 2]. Kinesins operate as dimers with two functional domains: a dimerized motor domain that uses ATP to generate locomotive force along microtubules and a tail domain that binds vesicles and other cargoes [3]. Because it facilitates movement, much attention has been paid to the motor domain, both in purified single-molecule systems [4–8] and in cells [9–19]. Much less is known about how kinesin tails interact with vesicles. In contrast to the conserved motor domains, kinesin tails are highly variable in the ~20 members of the Kinesin-1, −2, −3, and − 4 families that are thought to mediate vesicle transport [1]. One important function of this diversity is for each individual kinesin

Andrew Montgomery and Alex Garbouchian contributed equally to this work.

Alessio Vagnoni (ed.), *Axonal Transport: Methods and Protocols*,
Methods in Molecular Biology, vol. 2431, https://doi.org/10.1007/978-1-0716-1990-2_12,
© The Author(s), under exclusive license to Springer Science+Business Media, LLC, part of Springer Nature 2022

family member to bind a specific subset of the many cellular vesicle populations. Furthermore, interactions between kinesin tails and adaptors can regulate the transport behavior of kinesins once they are bound to vesicles [20–23]. Recently, there has been increased attention toward defining interactions between kinesin tails and the vesicles they bind. However, such experiments largely relied on detecting interactions indirectly [20, 24, 25], as visualizing vesicle-bound kinesins in cells has proved challenging.

Visualizing the vesicle population that a specific kinesin binds is valuable for understanding each kinesin's transport function. Patterns in the subcellular distribution and transport parameters of these vesicles (e.g., velocity and run length) can give insight into the function of a specific kinesin family member. For example, vesicles labeled by closely related members of the Kinesin-3 family display a range of different localization and transport patterns in multipolar neurons: KIF1A-labeled vesicles traffic equally in axon and dendrites, KIF13B-labeled vesicles preferentially enter the axon, KIF13A-labeled vesicles are restricted to the somatodendritic region, and KIF1C-labeled vesicles are mostly stationary and localized to the soma and proximal dendrites [26]. Another benefit of labeling vesicles with kinesins is to identify the cargoes they carry. Colocalization of kinesin-labeled vesicles with fluorescent candidate cargo proteins is evidence of vesicle identity. Even better, cotransport—the coincident movement of two fluorescently tagged proteins—is perhaps the strongest evidence of two proteins residing on or in the same vesicle. Finally, changes in the transport parameters of kinesin-labeled vesicles can provide a direct readout for any manipulations that are made to kinesin regulation.

Labeling vesicles with fluorescent kinesins is challenging. In most cases, expression of fluorescently tagged full-length kinesins results in diffuse cellular labeling, comparable to expression of a cytoplasmic GFP (Fig. 1a) [2, 26, 27]. When not bound to vesicles, most (if not all) transport kinesins can assume an autoinhibited state in which the kinesin tail binds the motor domain [27]. The majority of kinesins assume this cytosolic state, and only a small fraction is bound to vesicles at any given moment [28]. When expressing fluorescent kinesins, the unbound cytoplasmic pool obscures the vesicle-bound fraction. Reducing the cytoplasmic pool is therefore a key requirement to visualize the vesicle-bound kinesin fraction.

Here we describe an approach we developed to improve vesicle labeling by expressing fluorescently tagged kinesins in cultured hippocampal neurons (Fig. 1b). This approach uses a combination of strategies. First, expression of only the vesicle-binding kinesin tail markedly reduces the cytoplasmic pool and enhances vesicle labeling. This is likely because the tail alone cannot assume an autoinhibited conformation, which makes the tail more available for binding vesicles. Second, smaller kinesins with tails small

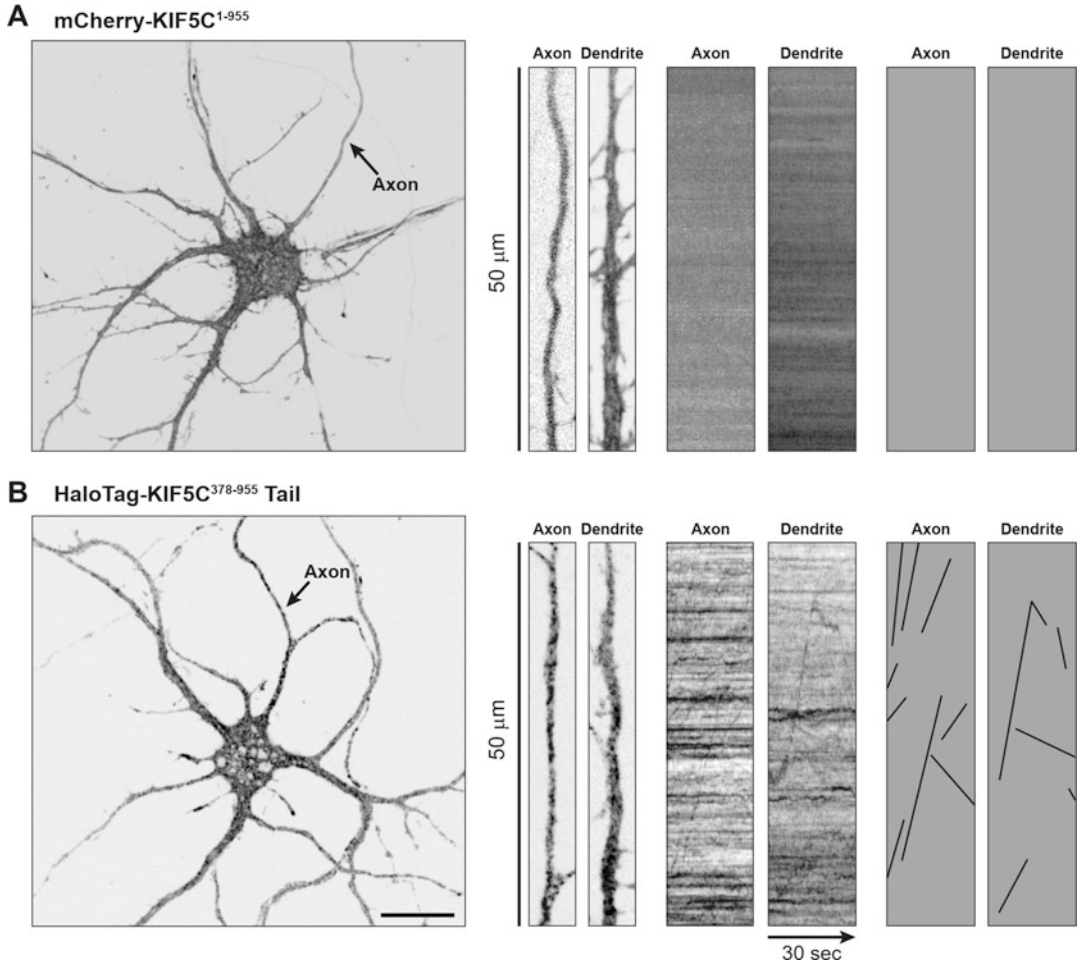

Fig. 1 7 DIV cultured hippocampal neurons expressing full-length mCherry-KIF5C (**a**) or Halotag-KIF5C$^{378–955}$ tail visualized with JF549 (**b**) for 4–6 h, each coexpressing KLC1a. High magnification images and kymographs were taken from representative stretches of the axon and a dendrite. For clarity, transport events from kymographs were redrawn as solid black lines. Kymograph lines with a positive slope indicate anterograde transport, and those with a negative slope indicate retrograde transport. Scale bar = 20 µm

enough to fit through nuclear pores [29]) (i.e., Kinesin-1 family members), are designed with a transcription control system developed by the Arnold lab [30]. Here, the kinesin tail is fused to a nuclear localization signal that targets unbound kinesins to the nucleus. In the nucleus, a DNA-binding zinc finger domain represses transcription of the kinesin expression vector. Combining these strategies with short expression times results in vesicle labeling with most transport kinesins. We describe this method in cultured hippocampal neurons. Due to the extreme scale and geometry of neurons, these cells are particularly reliant on efficient and accurate vesicle transport [31]. Consequently, neurons express a large number of kinesins involved in vesicle transport [32].

Using kinesin tails to label vesicles allows for the systematic comparison of kinesins in the same cell type or model system. The localization and transport parameters of individual kinesins can give insight into the specific transport behavior they confer in cells. We applied this approach to analyze the distribution and transport parameters of Kinesin-1, -2, and -3 family members in cultured hippocampal neurons [26]. A second use for labeling kinesins is to identify the subpopulations of vesicles specific kinesins bind. Colabeling with a kinesin tail and a candidate cargo protein, followed by the evaluation of colocalization or cotransport, can definitively determine whether a particular cargo is moved by a specific kinesin. Finally, the tail labeling strategy also improves labeling of myosin V family members, motor proteins that mediate actin-based vesicle transport [33]. Therefore, the tail labeling strategy has broad applications and is a useful addition to the toolkit for analyzing the cellular function of cytoskeletal motors.

2 Materials

1. Isolated hippocampal neurons [34] or other cultured cells.
2. 18 mm glass coverslips (Fisher Scientific, cat. no. 12-545-84-1D) coated with poly-L-lysine [34].
3. DNA constructs encoding fluorophore-tagged kinesin tails. A library of GFP- and Halo-tagged kinesin tails we designed is available on Addgene (https://www.addgene.org/Marvin_Bentley). For considerations about tail construct design, *see* **Note 1**.
4. Lipofectamine 2000 (Life Technologies, cat. no. 11668027) or another transfection reagent.
5. Imaging medium (Hibernate E low fluorescence; BrainBits, SKU: HELF).
6. Imaging chamber for 18 mm coverslips (Chamlide CMB, Quorum Technologies, cat. no. CM B18-1).
7. Fluorescence microscope with a high-NA objective and sCMOS or EMCCD camera suitable for live-cell imaging. We use an Andor Dragonfly built on a Nikon Ti2 with a CFI Apo 60× 1.49 objective with a Zyla 4.2+ sCMOS camera.
8. JF549 or JF646 dyes for visualizing Halo-tagged kinesins (Promega, GA1110 and GA1120) (*see* **Note 2**).

3 Methods

1. Prepare hippocampal neuron cultures on glass coverslips. We plate neurons at a density of 150,000–250,000 cells per 6 cm dish (~7000–12,000 cells/cm^2) onto poly-L-lysine–treated 18 mm coverslips.
2. Transfect 5–10 DIV neurons with DNA expression constructs encoding the kinesin tail of interest (*see* **Notes 3–5**). Use 0.5–1.0 μg of DNA for the fluorescently tagged kinesin tail. For coexpression of multiple constructs, adjust the molar ratio of DNA constructs to tune relative expression levels.
3. Return cells to an incubator that maintains a humidified 37 °C 5% CO_2 environment. For optimal results with kinesin tails, short expression times are desirable to minimize cytoplasmic background. Imaging as early as 3.5–5 h post-transfection is a good starting point, although some kinesin tails continue to label vesicles after overnight expression (*see* **Note 3** and Table 1).
4. Equilibrate imaging medium, coverslip chamber, and the environmental enclosure of the microscope to 37 °C.
5. If using Halo-tagged kinesins, incubate coverslips with 50 nM substrate (i.e., JF549 or JF646) for 15 min. Rinse twice with medium and incubate for at least 10 min in conditioned medium to wash out unbound dye.
6. Mount a coverslip in the imaging chamber for live-cell imaging. Maintain cells in phenol red-free imaging medium (i.e., Hibernate E) for imaging.
7. Place the imaging chamber on the microscope and locate a transfected cell. Dim cells typically exhibit the most labeled vesicles. Increasing the light intensity for scanning the coverslip can make finding dim cells (i.e., low expressing cells) easier. Scanning coverslips rapidly is crucial to minimize photobleaching. Because transfected cells vary in their expression time and the window for tail labeling is relatively short, expect to find fewer imageable cells per coverslip than with a typical transfection.
8. Record movies of transfected cells. Optimizing the proper imaging conditions will require some amount of trial and error (*see* **Note 6**).
9. Continuously image new coverslips. Kinesin-labeled vesicles are visible only during a limited time frame which varies between individual cells. We recommend imaging many coverslips over a 3–5 h period to maximize the number of usable cells.

Table 1
Confirmed vesicle labeling in cultured hippocampal neurons

Kinesin family	Kinesin tail	Short-term labeling[a]	Long-term labeling[b]	Accessory subunit[c]
Kinesin-1	KIF5A			
	KIF5B	Yes		Kinesin light chain
	KIF5C	Yes		Kinesin light chain
Kinesin-2	KIF3A	Yes		KIF3B or KIF3C
	KIF3B	Yes		KIF3A
	KIF3C	Yes		KIF3A
	KIF17			
Kinesin-3	KIF1A	Yes	Yes	
	KIF1Bα	Yes	Yes	
	KIF1Bβ	Yes		
	KIF1C	Yes		
	KIF13A	Yes	Yes	
	KIF13B	Yes	Yes	
	KIF16B	Yes		

[a]Indicated kinesin tails label vesicles 3.5–8 h after transfection
[b]Indicated kinesin tails label vesicles 12–18 h after transfection
[c]Indicated accessory subunits improve vesicle labeling

4 Notes

1. We designed kinesin expression constructs to include as much of the tail region as possible. Only the motor domain and the first predicted coiled coil were excluded, and each tail was fused to an N-terminal fluorophore. The first coiled coil is required for kinesin dimerization, and its removal decreases the likelihood of exogenous tails dimerizing with native endogenous kinesins. Dimerization of motorless tails with endogenous full-length kinesins could result in "single-footed" kinesins unable to processively move along microtubules. Expression of tails without the first coiled coil, combined with the fact that endogenous kinesin dimers are relatively stable, make a dominant negative effect unlikely during short expression times.

   For members of the Kinesin-1 family, we implemented a transcription control system [30]. In addition to the fluorescent tag, these tails have a nuclear localization signal and a DNA-binding zinc finger motif. Tails that do not bind to vesicles are targeted to the nucleus where the zinc finger motif recognizes the plasmid and inhibits transcription. Because proteins larger than ~100 kDa cannot pass through nuclear pores [29], this strategy is predominantly helpful for members of the Kinesin-1 family, which have shorter tails than most other transport kinesins.

2. Even when labeling is successful, kinesin tail-labeled vesicles are dim when compared to fluorescently tagged luminal or transmembrane cargo proteins. Use of sensitive sCMOS or EMCCD cameras and bright fluorophores improve detection of kinesin-labeled vesicles. For optimal labeling, we recommend HaloTag with Janelia dyes JF549 or JF646 [35] although eGFP is a suitable alternative.
3. Imaging early after transfection maximizes vesicle labeling, especially for difficult-to-image kinesins. Because low expressing cells exhibit the best labeling, scanning the coverslip to find transfected cells may require brighter illumination than typical vesicle labels. Transfected cells vary in their expression levels and at any given point, only a subset of transfected cells will display vesicle labeling. Members of the Kinesin-3 family consistently label vesicles at longer expression times. Table 1 shows which tail constructs consistently label vesicles at early (3.5–8 h) and late (12–18 h) expression times.
4. In some cases, coexpression of accessory or adaptor proteins may be necessary for vesicle labeling. Most kinesins are thought to bind multiple vesicle types [1], which is likely mediated by different adaptor proteins [20]. If exogenous kinesin expression exceeds that of a specific endogenous adaptor protein, that particular vesicle population will not be visualized. Table 1 lists adaptor proteins that improve labeling. Coexpression of other proposed adaptors may reveal additional vesicle populations bound by specific kinesins.
5. Managing light and minimizing phototoxicity is essential for live-cell imaging. This is particularly important for recording kinesin-labeled vesicles because such dim samples require high-intensity excitation light. Others have extensively described best practices for live imaging, and we refer the reader to their publications [36–38].
6. One concern when overexpressing motorless kinesins is a potential dominant-negative effect on vesicle transport. In principle, kinesin tails could saturate binding sites on transport vesicles and displace the endogenous full-length motors. We have not detected any change in the transport parameters or localization of vesicles when expressing the tails of kinesins that bind them for short time periods [26, 33, 39–41]. For example, expression of the KIF5B tail does not impair axonal movement of vesicles labeled with neuron–glia cell adhesion molecule, which is mediated by this kinesin [26]. Similarly, expression of KIF13A or KIF13B tail does not affect the transport of their vesicle cargoes in dendrites [39]. While expression of kinesin tails for multiple days may result in dominant negative effects, focusing on low expressing cells and short expression times appears to avoid that risk.

Acknowledgments

We thank members of the Bentley lab for their feedback on the manuscript. This work was supported by NIH grant R01MH066179 and an NIH-funded predoctoral fellowship to A.G. (T32GM067545).

References

1. Hirokawa N, Noda Y, Tanaka Y, Niwa S (2009) Kinesin superfamily motor proteins and intracellular transport. Nat Rev Mol Cell Biol 10: 682–696. https://doi.org/10.1038/nrm2774
2. Verhey KJ, Hammond JW (2009) Traffic control: regulation of kinesin motors. Nat Rev Mol Cell Biol 10:765–777. https://doi.org/10.1038/nrm2782
3. Vale RD (2003) The molecular motor toolbox for intracellular transport. Cell 112:467–480. https://doi.org/10.1016/S0092-8674(03)00111-9
4. Hancock WO (2016) The kinesin-1 chemomechanical cycle: stepping toward a consensus. Biophys J 110:1216–1225. https://doi.org/10.1016/j.bpj.2016.02.025
5. Gilbert SP, Guzik-Lendrum S, Rayment I (2018) Kinesin-2 motors: kinetics and biophysics. J Biol Chem 293:4510–4518. https://doi.org/10.1074/jbc.R117.001324
6. Belyy V, Yildiz A (2014) Processive cytoskeletal motors studied with single-molecule fluorescence techniques. FEBS Lett 588:3520–3525. https://doi.org/10.1016/j.febslet.2014.05.040
7. Yildiz A, Tomishige M, Vale RD, Selvin PR (2004) Kinesin walks hand-over-hand. Science 303:676–678. https://doi.org/10.1126/science.1093753
8. Tomishige M, Stuurman N, Vale RD (2006) Single-molecule observations of neck linker conformational changes in the kinesin motor protein. Nat Struct Mol Biol 13:887–894. https://doi.org/10.1038/nsmb1151
9. Kapitein LC, Schlager MA, Kuijpers M et al (2010) Mixed microtubules steer dynein-driven cargo transport into dendrites. Curr Biol 20:290–299. https://doi.org/10.1016/j.cub.2009.12.052
10. Yang R, Bentley M, Huang CF, Banker G (2016) Analyzing kinesin motor domain translocation in cultured hippocampal neurons. Methods Cell Biol 131:217–232. https://doi.org/10.1016/bs.mcb.2015.06.021
11. van Bergeijk P, Adrian M, Hoogenraad CC, Kapitein LC (2015) Optogenetic control of organelle transport and positioning. Nature 518(7537):111–114. https://doi.org/10.1038/nature14128
12. Huang C-F, Banker G (2012) The translocation selectivity of the kinesins that mediate neuronal organelle transport. Traffic 13: 549–564. https://doi.org/10.1111/j.1600-0854.2011.01325.x
13. Jacobson C, Schnapp B, Banker GA (2006) A change in the selective translocation of the kinesin-1 motor domain marks the initial specification of the axon. Neuron 49:797–804. https://doi.org/10.1016/j.neuron.2006.02.005
14. Lipka J, Kapitein LC, Jaworski J, Hoogenraad CC (2016) Microtubule-binding protein doublecortin-like kinase 1 (DCLK1) guides kinesin-3-mediated cargo transport to dendrites. EMBO J 35:302–318. https://doi.org/10.15252/embj.201592929
15. Nakata T, Hirokawa N (2003) Microtubules provide directional cues for polarized axonal transport through interaction with kinesin motor head. J Cell Biol 162:1045–1055. https://doi.org/10.1083/jcb.200302175
16. Cai D, Verhey KJ, Meyhofer E (2007) Tracking single kinesin molecules in the cytoplasm of mammalian cells. Biophys J 92:4137–4144. https://doi.org/10.1529/biophysj.106.100206
17. Cai D, McEwen DP, Martens JR et al (2009) Single molecule imaging reveals differences in microtubule track selection between kinesin motors. PLoS Biol 7:e1000216. https://doi.org/10.1371/journal.pbio.1000216
18. Karasmanis EP, Phan C-T, Angelis D et al (2018) Polarity of neuronal membrane traffic requires sorting of kinesin motor cargo during entry into dendrites by a microtubule-associated septin. Dev Cell 46:518–524. https://doi.org/10.1016/J.DEVCEL.2018.08.004
19. Schimert KI, Budaitis BG, Reinemann DN et al (2019) Intracellular cargo transport by single-

headed kinesin motors. Proc Natl Acad Sci U S A 116:6152–6161. https://doi.org/10.1073/pnas.1817924116

20. Nabb AT, Frank M, Bentley M (2020) Smart motors and cargo steering drive kinesin-mediated selective transport. Mol Cell Neurosci 103:103464. https://doi.org/10.1016/j.mcn.2019.103464
21. Keren-Kaplan T, Bonifacino JS (2021) ARL8 relieves SKIP autoinhibition to enable coupling of lysosomes to kinesin-1. Curr Biol 31(3): 540–554.e5. https://doi.org/10.1016/j.cub.2020.10.071
22. Fu MM, Holzbaur ELF (2013) JIP1 regulates the directionality of APP axonal transport by coordinating kinesin and dynein motors. J Cell Biol 202:495–508. https://doi.org/10.1083/jcb.201302078
23. Wang X, Schwarz TL (2009) The mechanism of Ca2+ −dependent regulation of kinesin-mediated mitochondrial motility. Cell 136: 163–174. https://doi.org/10.1016/j.cell.2008.11.046
24. Lu W, Gelfand VI (2017) Moonlighting motors: kinesin, dynein, and cell polarity. Trends Cell Biol 27(7):505–514. https://doi.org/10.1016/j.tcb.2017.02.005
25. Siddiqui N, Straube A (2017) Intracellular cargo transport by kinesin-3 motors. Biochemist 82:803–815. https://doi.org/10.1134/S0006297917070057
26. Yang R, Bostick Z, Garbouchian A et al (2019) A novel strategy to visualize vesicle-bound kinesins reveals the diversity of kinesin-mediated transport. Traffic 20(11):851–866. https://doi.org/10.1111/tra.12692
27. Verhey KJ, Kaul N, Soppina V (2011) Kinesin assembly and movement in cells. Annu Rev Biophys 40:267–288. https://doi.org/10.1146/annurev-biophys-042910-155310
28. Lorenzo DN, Badea A, Zhou R et al (2019) βII-spectrin promotes mouse brain connectivity through stabilizing axonal plasma membranes and enabling axonal organelle transport. Proc Natl Acad Sci 116(31): 15686–15695. https://doi.org/10.1073/pnas.1820649116
29. Wang R, Brattain MG (2007) The maximal size of protein to diffuse through the nuclear pore is larger than 60 kDa. FEBS Lett 581: 3164–3170. https://doi.org/10.1016/j.febslet.2007.05.082
30. Gross GG, Junge JA, Mora RJ et al (2013) Recombinant probes for visualizing endogenous synaptic proteins in living neurons. Neuron 78:971–985. https://doi.org/10.1016/j.neuron.2013.04.017
31. Bentley M, Banker G (2016) The cellular mechanisms that maintain neuronal polarity. Nat Rev Neurosci 17:611–622. https://doi.org/10.1038/nrn.2016.100
32. Silverman MA, Kaech S, Ramser EM et al (2010) Expression of kinesin superfamily genes in cultured hippocampal neurons. Cytoskeleton 67:784–795. https://doi.org/10.1002/cm.20487
33. Frank M, Citarella CG, Quinones GB, Bentley M (2020) A novel labeling strategy reveals that myosin Va and myosin Vb bind the same dendritically polarized vesicle population. Traffic 21:689–701. https://doi.org/10.1111/tra.12764
34. Kaech S, Banker G (2006) Culturing hippocampal neurons. Nat Protoc 1:2406–2415. https://doi.org/10.1038/nprot.2006.356
35. Grimm JB, English BP, Chen J et al (2015) A general method to improve fluorophores for live-cell and single-molecule microscopy. Nat Methods 12:244–250. https://doi.org/10.1038/nmeth.3256
36. Magidson V, Khodjakov A (2013) Circumventing photodamage in live-cell microscopy, 4th edn. Elsevier Inc.
37. Kiepas A, Voorand E, Mubaid F et al (2020) Optimizing live-cell fluorescence imaging conditions to minimize phototoxicity. J Cell Sci 133:jcs.242834. https://doi.org/10.1242/jcs.242834
38. Icha J, Weber M, Waters JC, Norden C (2017) Phototoxicity in live fluorescence microscopy, and how to avoid it. BioEssays 39:1–15. https://doi.org/10.1002/bies.201700003
39. Jenkins B, Decker H, Bentley M et al (2012) A novel split kinesin assay identifies motor proteins that interact with distinct vesicle populations. J Cell Biol 198:749–761. https://doi.org/10.1083/jcb.201205070
40. Bentley M, Banker G (2015) A novel assay to identify the trafficking proteins that bind to specific vesicle populations. Curr Protoc Cell Biol 69:13.8.1–13.8.12. https://doi.org/10.1002/0471143030.cb1308s69
41. Bentley M, Decker H, Luisi J, Banker G (2015) A novel assay reveals preferential binding between Rabs, kinesins, and specific endosomal subpopulations. J Cell Biol 93:4604. https://doi.org/10.1083/jcb.201408056

Chapter 13

Retrograde Axonal Transport of Neurotrophins in Basal Forebrain Cholinergic Neurons

Arman Shekari and Margaret Fahnestock

Abstract

Axonal transport is key for the survival and function of all neurons. This process is especially important in basal forebrain cholinergic neurons due to their extremely long and diffuse axonal projections. These neurons are critical for learning and memory and degenerate rapidly in age-related neurodegenerative disorders like Alzheimer's and Parkinson's disease. The vulnerability of these neurons to age-related neurodegeneration may be partially attributed to their reliance on retrograde axonal transport for neurotrophic support. Unfortunately, little is known about the molecular biology underlying the retrograde transport dynamics of these neurons due to the difficulty associated with their maintenance in vitro. Here, we outline a protocol for culturing primary rodent basal forebrain cholinergic neurons in microfluidic chambers, devices designed specifically for the study of axonal transport in vitro. We outline protocols for labeling neurotrophins and tracking neurotrophin transport in these neurons. Our protocols can also be used to study axonal transport in other types of primary neurons such as cortical and hippocampal neurons.

Key words Neurotrophins, Cholinergic, Microfluidic chambers, Aging, BDNF, NGF, proNGF, Axonal transport, Basal forebrain, Retrograde

1 Introduction

Intracellular trafficking is critical for the survival and proper function of all neurons due to their extreme structural and biochemical polarity. Neurons orchestrate the bidirectional transport of a wide variety of cellular cargo, from proteins and RNA to entire organelles, along their lengthy axonal projections in a tightly regulated manner via a process termed axonal transport [1]. Axonal transport occurs along microtubules, cytoskeletal elements composed of polarized tubulin polymers that span the entirety of the axon [2]. These polymers are organized in parallel radial arrays, forming unipolar filaments with plus ends proximal to the axon tip and minus ends proximal to the cell body [2, 3]. The transport of cargo toward the axon tip is referred to as anterograde or "plus-

Alessio Vagnoni (ed.), *Axonal Transport: Methods and Protocols*,
Methods in Molecular Biology, vol. 2431, https://doi.org/10.1007/978-1-0716-1990-2_13,
© The Author(s) 2022

end directed" while transport toward the cell body is referred to as retrograde or "minus-end directed."

Anterograde and retrograde transport occur via the procession of two classes of ATP-dependent molecular motors along microtubules: kinesin and dynein. Kinesin family motor proteins are responsible for carrying out anterograde transport, while the cytoplasmic dynein motor protein is responsible for carrying out retrograde transport [2, 4]. Both kinesin family and dynein motors are large and complex proteins consisting of multiple polypeptide chains classified as either heavy, light, or intermediate chains, depending on their molecular weight [5]. The association of these chains via their N-terminal tail domains creates binding domains for cargo adapter proteins [2]. A wide variety of adapter proteins exist and facilitate critical functions of both kinesin family and dynein motors, including the binding of cargo to the motors themselves and the binding of motors to microtubule tracks [2, 6–9].

While the motor proteins underlying retrograde and anterograde transport share some similarities, they, like the transport processes they govern, are distinct from one another. This chapter will focus largely on retrograde axonal transport, specifically within the basal forebrain, a brain area where deficits in retrograde transport have been heavily implicated in the development of age-related neurodegenerative disorders [10, 11].

The basal forebrain is located at the ventral rostrocaudal extent of the brain and consists of multiple structures including the diagonal band of Broca, nucleus basalis of Meynert, and the medial septal nucleus [12, 13]. Most neurons within these structures produce the neurotransmitter acetylcholine, making the basal forebrain the major cholinergic output of the central nervous system (CNS). Basal forebrain projections are extremely lengthy and diffuse, projecting upward and terminating widely throughout the hippocampus and neocortex [12, 13]. These projections are critical for learning, memory, and attention, making the basal forebrain a vital cognitive center [13].

The degeneration of ascending basal forebrain cholinergic projections occurs both in normal aging and with increased severity in age-related neurodegenerative disorders like Alzheimer's and Parkinson's disease [14–16]. Loss of cholinergic innervation correlates strongly with cognitive decline and is considered a hallmark of Alzheimer's disease (AD) [13, 15, 17, 18]. Basal forebrain cholinergic neurons (BFCNs) demonstrate a striking selective vulnerability in AD, as they are among the first neurons in the brain to degenerate in the disorder [15, 18–22]. This vulnerability results in up to 95% of BFCNs degenerating by the end stages of AD [23, 24].

One factor that may explain the selective vulnerability of BFCNs to age-related neurodegenerative disorders is their inability

to produce a family of growth factors termed neurotrophins. Neurotrophins are a family of extracellular signaling proteins that are critical for neuronal development, survival, and plasticity [25]. BFCNs are dependent upon the neurotrophins nerve growth factor (NGF) and brain derived neurotrophic factor (BDNF) for their survival and function [26–32]. NGF and BDNF, like all neurotrophins, are initially synthesized as proproteins that can be processed to their mature forms [33]. However, proneurotrophins are capable of facilitating intracellular signaling independently of their mature counterparts [34–37]. Additionally, while pro and mature BDNF and proNGF are detectable in the mammalian CNS, mature NGF is not, further highlighting the importance of studying proneurotrophins in the context of CNS neurons like BFCNs [38–40].

BFCNs are reliant on their synaptic targets in the hippocampus and cortex for their supply of BDNF and proNGF [41–43]. Upon release, these neurotrophins bind to either tropomyosin-related kinase (Trk) or $p75^{NTR}$ receptors at BFCN axon terminals and are retrogradely transported to BFCN cell bodies [10, 11, 25, 41, 44, 45]. In AD and in animal models of AD, NGF-immunoreactive material accumulates in BFCN target areas and is decreased in the basal forebrain itself, suggesting impaired retrograde neurotrophin axonal transport [46, 47]. Additionally, both BDNF and proNGF retrograde transport are reduced in aged BFCNs, further implicating dysfunctional retrograde transport in the selective vulnerability of these neurons to age-related neurodegeneration [10]. Unfortunately, the mechanisms underlying these observed transport deficits are currently unknown. In fact, very little is known about the mechanisms governing retrograde neurotrophin transport in this highly vulnerable neuron population.

The mechanistic study of retrograde neurotrophin transport is complicated by the diffuse and highly arborized projections primary neurons develop in vitro. Organizing and separating neuronal cell bodies and axon terminals facilitates the accurate assessment and quantification of axonal transport in vitro. Recently, microfluidic chambers have been developed to achieve this organization and to advance the direction-specific assay of axonal transport in CNS neurons [48, 49]. These chambers contain microgrooves that are connected to a main channel that houses neuronal cell bodies. Axons grow through these microgrooves and emerge into another channel that maintains fluidic isolation from the channel that houses the cell bodies, permitting the independent manipulation of neuronal cell bodies and axons. This fluidic isolation allows neurotrophins to be administered exclusively to the axon terminals of neurons. The microgrooves also linearize axons and enable anterograde and retrograde transport to be accurately quantified. While BFCNs seem like ideal candidates for study using

microfluidic chambers due to their unique reliance on retrograde transport, they are difficult to maintain in vitro.

Here we describe a protocol for the culture and maintenance of embryonic rodent BFCNs in microfluidic culture, as well as a protocol for the tracking of retrograde transport of biotinylated neurotrophins conjugated to streptavidin-labeled quantum dot fluorophores. We provide a protocol for the purification of biotinylated proNGF from the medium of human embryonic kidney (HEK) cells transfected with a plasmid coding for Avi-tagged, cleavage-resistant proNGF [10, 50]. We also provide a protocol for the immunocytochemical analysis of these neurons to validate cholinergic phenotype. These protocols may be used in conjunction with other primary neuron types such as cortical neurons, however with some minor modifications that are mentioned below.

2 Materials

2.1 Preparation of Microfluidic Chambers

1. XC450 Microfluidic devices (Xona Microfluidics, Research Triangle Park, NC, USA).
2. Precoat ethanol solution (Xona Microfluidics, included with XC450 devices).
3. Humidity-controlled ChipTrays™ (Recommended only, *see* **Note 1**) (Xona Microfluidics).
4. 1× phosphate buffered saline (PBS): 137 mM NaCl, 2.7 mM KCl, 10 mM Na_2HPO_4, and 1.8 mM KH_2PO_4. Adjust solution to pH 7.4.
5. 0.01% sterile-filtered poly-L-lysine (PLL) solution.

2.2 Dissection and Processing of Basal Forebrain Tissue

1. Dissection tools suitable for embryonic murine dissection (fine-tip Dumont forceps and scissors, tweezers, petri dishes).
2. Dissection microscope.
3. Clinical centrifuge capable of reaching 250 × *g*.
4. Hemocytometer.
5. 100× penicillin–streptomycin (P/S) (10,000 units/mL of penicillin and 10,000 μg/mL of streptomycin).
6. 1× Hanks's Balanced Salt Solution (HBSS): Dilute 10× HBSS stock solution using sterile double-distilled water, add 1% P/S and pH to 7.4 before sterile filtering.
7. Fine fire-polished glass Pasteur Pipettes: Expose the tip of a glass Pasteur pipette to the flame of a Bunsen burner for a few seconds while rotating the base of the pipette. Repeat until the tip has become smooth and the opening has shrunk to about 1 mm in diameter (*see* **Note 2**). Autoclave and keep sterile before use.

8. DNase I solution (1 mg/mL).
9. 10× trypsin–EDTA solution.
10. BFCN Plating Medium: Neurobasal medium, 1% P/S, 2% B27 serum-free supplement, 1% GlutaMAX, 10% fetal bovine serum (FBS), 50 ng/mL recombinant murine BDNF (Peprotech, Rocky Hill, NJ, USA), 50 ng/mL recombinant human β-NGF (Peprotech).

2.3 Plating and Maintenance of BFCNs in Microfluidic Chambers

1. BFCN Plating Medium: Neurobasal medium, 1% P/S, 2% B27 serum-free supplement. 1% GlutaMAX, 10% fetal bovine serum (FBS), 50 ng/mL recombinant murine BDNF, 50 ng/mL recombinant human β-NGF.
2. BFCN Maintenance Medium: Neurobasal medium, 1% P/S, 2% B27 serum-free supplement, 1% GlutaMAX, 50 ng/mL recombinant murine BDNF, 50 ng/mL recombinant human β-NGF (*see* **Note 3**).

2.4 Immunocytochemical Staining of BFCNs in Microfluidic Chambers

1. Widefield or confocal microscope capable of fluorescence microscopy.
2. 4% paraformaldehyde (PFA) sterile solution: Dilute 1 g of PFA powder per 15 mL of sterile water. Water should be heated to 60 °C before addition of PFA. Add 1 N NaOH until powder has fully dissolved, then add 10 mL of 3× PBS for every 15 mL of water. Adjust the pH of the solution to 7.2 and sterile filter before use.
3. 10% Triton X-100 Solution.
4. PBS-A: 0.01% Triton X-100 diluted in 1× PBS.
5. PBS-B: Dissolve 300 mg bovine serum albumin in ~8 mL of 1× PBS and add 500μL of FBS. Bring the solution to a final volume of 10 mL, and sterile filter before use.
6. Primary antibodies: Any primary antibody compatible with immunocytochemistry can be used. To confirm cholinergic phenotype, vesicular acetylcholine transporter (VAChT, Santa Cruz Biotechnology, Dallas, TX, USA) antibodies can be used. TrkA antibodies (Alomone Labs, Jerusalem BioPark, Israel) can also be used to confirm cholinergic phenotype, as BFCNs express TrkA [51, 52].
7. Secondary antibodies: Any secondary antibodies compatible with immunocytochemistry can be used. Our lab uses Alexa-Fluor antibodies.
8. DAPI nuclear counterstain.
9. Silicone immersion oil (Ibidi, Fitchburg, WI, USA) (*see* **Note 4**).

2.5 Purification of Biotinylated proNGF

1. HEK293-FT cells (ATCC, Manassas, VA, USA).
2. Centrifuge capable of reaching speeds of 300 × *g*.
3. 10 kDa centrifugal concentrators.
4. Cold room or large refrigerator.
5. HEK Plating Medium: Dulbecco's Modified Eagle Medium (DMEM), 10% FBS, 1% GlutaMAX, 1% P/S, 1% sodium pyruvate, 1% nonessential amino acids.
6. HEK Transfection Medium: Dulbecco's Modified Eagle Medium (DMEM), 1% GlutaMAX, 1% P/S, 1% sodium pyruvate, 1% nonessential amino acids, 1 mg/mL d-biotin.
7. Turbofect™ transfection reagent (ThermoFisher Scientific).
8. Nickel nitrilotriacetic acid (Ni-NTA) resin.
9. Reusable nickel purification columns.
10. proNGF-R-1G-Avi-His and Bir-A biotin ligase pcDNA-3.1 plasmids [10, 50] (Bir-A biotin ligase plasmid also available from Addgene, Watertown, MA, USA).
11. Ni-NTA wash buffer: 1× PBS, 20 mM imidazole, 1 mM phenylmethylsulfonyl fluoride (PMSF). Adjust to a final pH of 8.0.
12. Ni-NTA elution buffer (50 mL): 1× PBS, 300 mM imidazole, phosSTOP, and ULTRA tablets (Roche, Basel, Switzerland). Adjusted to a final pH of 8.0.

2.6 Tracking and Analysis of Neurotrophin Axonal Transport

1. Widefield or confocal microscope equipped with an on-stage incubator capable of maintaining 37 °C, 5% CO_2 and capable of fluorescence microscopy.
2. Quantum dot (Qdot) 625-streptavidin conjugate (ThermoFisher Scientific) (*see* **Note 5**).
3. Qdot625 or Texas Red fluorescence filter cube set (*see* **Note 6**).
4. DAPI and Cy5 fluorescence filter cube set.
5. Biotinylated neurotrophins (Alomone or via Ni-NTA chromatography).
6. TubulinTracker™ Deep Red (ThermoFisher Scientific), optional (*see* **Note 7**).
7. Axonal Imaging Medium: Neurobasal medium minus phenol red, 1× P/S, 1× B27 serum-free supplement, 1× GlutaMAX.
8. Somal Imaging Medium: Neurobasal medium minus phenol red, 1% P/S, 2% B27 serum-free supplement, 1% GlutaMAX, 50 ng/mL recombinant BDNF, 50 ng/mL recombinant β-NGF.
9. NucBlue™ LiveReadyProbes™ Hoechst nuclear counterstain (ThermoFisher Scientific).

10. ImageJ 1.53c equipped with the "ImageScience" plugin set (included with ImageJ) and the KymoToolBox plugin (available from: https://github.com/fabricecordelieres/IJ-Plugin_KymoToolBox).

3 Methods

3.1 Preparation of Microfluidic Chambers (To Be Done 24 h Before Dissection)

XC450 devices must be sterilized using the included precoat solution before use. The devices must also be coated with an adhesion substrate, in this case poly-L-lysine (PLL), to improve the adherence of primary neurons to the channels of the device. Working with microfluidic chambers requires a great deal of patience and care. The fluidic isolation and neuronal organization these devices provide is only possible if the devices are handled optimally, which we outline below (Figs. 1 and 2).

1. Within a biosafety cabinet, add 100 μL of precoat solution to the top left well of each chamber (Fig. 1) and let stand for 1 min (*see* **Note 8**).
2. Add 100 μL of precoat solution to the bottom left well of each chamber and let stand for 5 min.
3. Add 100 μL of precoat solution to the top right well of each chamber and let stand for 1 min.
4. Add 100 μL of precoat solution to the bottom right well of each chamber and let stand for 5 min.
5. Aspirate the precoat solution from every well, making sure to leave ~20 μL of residual solution within each well, and immediately add 150 μL of PBS to the top left well of each chamber. Let stand for 1 min (*see* **Notes 9** and **10**).
6. Repeat **steps 2–5** with 150 μL of PBS (Fig. 1).
7. Add 150 μL of PBS to both top wells of the device. Immediately repeat for both bottom wells (Fig. 2).
8. Aspirate the PBS solution from all wells and then repeat steps 1–4 using 120 μL of 0.01% PLL solution (warmed to 37 °C) (Fig. 1).
9. Place chambers in a 37 °C, 5% CO_2 incubator for 24 h.
10. Inspect all chambers to ensure no bubbles have formed within the main channels (*see* **Note 11**).
11. Aspirate the PLL from all wells and repeat **steps 1–4** with 150 μL of PBS.
12. Aspirate the PBS from all wells and add 150 μL of plating medium that has been warmed to 37 °C to both top wells of the device (Fig. 2). Immediately repeat for both bottom wells.
13. Store chambers in a 37 °C, 5% CO_2 incubator until plating.

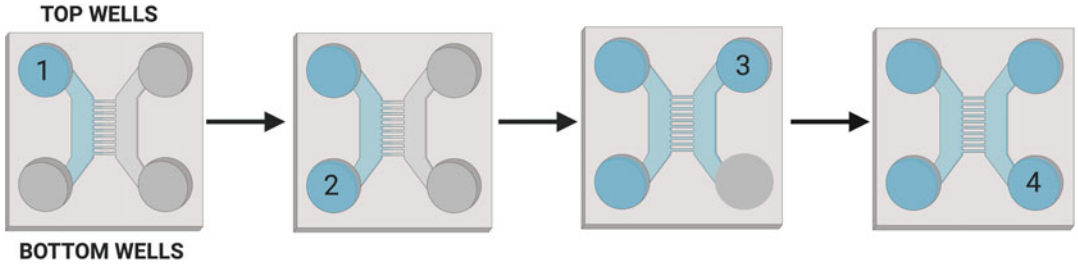

Fig. 1 Microfluidic device schematic depicting the well order to be followed during device preparation

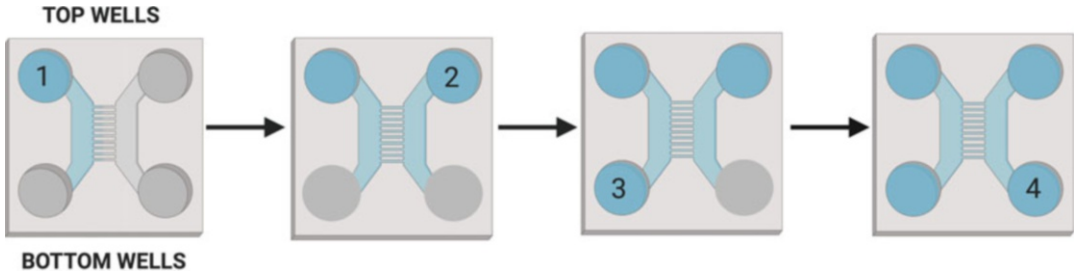

Fig. 2 Microfluidic device schematic depicting the well order to be followed during media changes and washes. This well order is also used once during device preparation for the second PBS incubation

3.2 Dissection and Processing of Embryonic Basal Forebrain Tissue (Fig. 3)

The basal forebrain is relatively small compared to commonly dissected neural structures like the cortex and hippocampus. Thankfully, its structure is very distinct and can be easily distinguished from neighboring brain areas. The small working volumes afforded by microfluidic culture allow many chambers to be prepared using a minimal amount of tissue.

The following protocol can also be used for preparing cortical and hippocampal neuronal cultures. These neurons are far more robust in culture and can be plated at higher densities than basal forebrain (within the 10^5 cells/mL range). The plating medium for cortical and hippocampal neurons does not need to contain any neurotrophins.

1. Sacrifice a pregnant rat or mouse at embryonic day (E)18 using CO_2 euthanasia or cervical dislocation and remove all embryos (*see* **Note 12**). Place embryos on ice.
2. Remove embryos from the embryonic sac using fine Dumont forceps, and separate the head from the body using a small pair of scissors. Place the head in a petri dish containing a small amount of cold HBSS solution and remove the brain from the skull using fine Dumont forceps.
3. Place the brain in a separate petri dish containing a small amount of HBSS. Under a dissection microscope, remove the meninges from the brain using fine Dumont forceps.

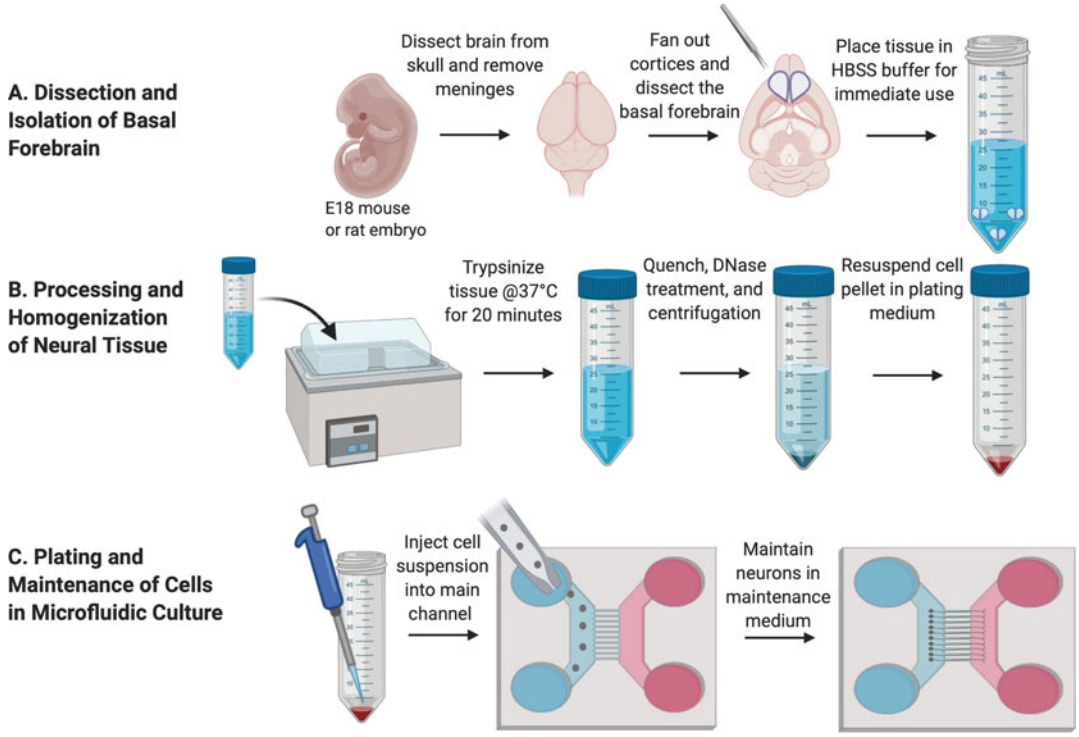

Fig. 3 Graphical depiction of the dissection and processing procedure outlined in Subheading 3.2

4. Remove the olfactory bulbs using a small pair of scissors. Place two medial cuts at the front of each cortical lobe. Fan out each lobe to expose the basal forebrain (*see* **Note 13**). Remove the basal forebrain from the brain using a pair of small scissors. Aspirate the tissue into a tube filled with a small amount of cold HBSS, and place on ice.
5. Repeat **steps 2–4** for each embryo (*see* **Note 14**).
6. In a biosafety cabinet, aspirate as much HBSS solution as possible from the collection tube without disturbing the tissue. Add 1 mL of fresh, cold HBSS to the tube. Repeat 5 times to wash.
7. Aspirate as much HBSS solution from the collection tube as possible without disturbing the tissue. Add 450 μL of fresh, cold HBSS to the tube. Immediately add 50 μL of 10× trypsin-EDTA to the tub and incubate in a 37 °C water bath for 20 min, gently agitating the tube every 5 min.
8. Add 50 μL of 10× DNase I to the collection tube. Triturate the tissue using a fire-polished glass Pasteur pipette until the solution becomes cloudy and no visible chunks of tissue remain. Add 1 mL of plating medium warmed to 37 °C to quench the trypsin.

9. Centrifuge the solution at 250 × *g* for 4 min and remove the supernatant. Resuspend the cell pellet using warm plating medium to a final density of 1×10^6 cells/mL using a hemocytometer. Repeatedly triturate this cell mixture to ensure homogeneity.

3.3 Plating and Maintenance of BFCNs in Microfluidic Chambers

BFCNs are difficult to maintain in culture and require consistent medium changes using neurotrophin-rich medium. These neurons must be plated at high densities (in the range of 10^6 cells/mL) to be viable in microfluidic culture. BFCNs produce axonal projections in vitro that cross the microgrooves in a matter of days if properly maintained (Fig. 4).

Cortical and hippocampal neurons can also be maintained using this protocol. However, like the plating medium, the maintenance medium used for these neurons does not need to contain any neurotrophins.

1. In a biosafety cabinet, aspirate the plating medium from all wells (*see* **Note 9**).
2. Inject 10 μL of the previously prepared cell solution into the top left well of the chamber by placing the tip of the pipette directly adjacent to the opening of the main channel to ensure the cell solution flows from the well into the main channel (*see* **Note 15**). Repeat for the bottom left well and place the chambers in a 37 °C, 5% CO_2 incubator for 5 min to allow neuronal adherence to the substratum.
3. Add 150 μL of plating medium to both top wells. Immediately repeat for both bottom wells. Incubate the chambers at 37 °C, 5% CO_2 for 24 h.
4. Replace the plating medium with maintenance medium after 24 h (Fig. 2). Repeat every 48–72 h (*see* **Notes 9** and **10**). Axonal projections usually take 5–7 days to cross the microgrooves (Fig. 3). Basal forebrain neurons maintain transport for 2 weeks [10] (*see* **Note 16**).

3.4 Immunocytochemical Staining of BFCNs in Microfluidic Chambers

Immunostaining neurons cultured in microfluidic chambers requires many incubations and washes. This is mainly due to the restrictive opening joining the wells of the device to the main channels. High quality images comparable to those obtained using cells cultured in standard well plates on glass coverslips can be obtained from microfluidic chambers using this protocol (Fig. 5).

1. In a biosafety cabinet, perform a PBS wash by replacing the maintenance medium in all wells with 150 μL of PBS. Immediately replace the PBS with a 4% PFA solution (*see* **Notes 9** and **10**). Incubate at room temperature for 30 min in a light-proof

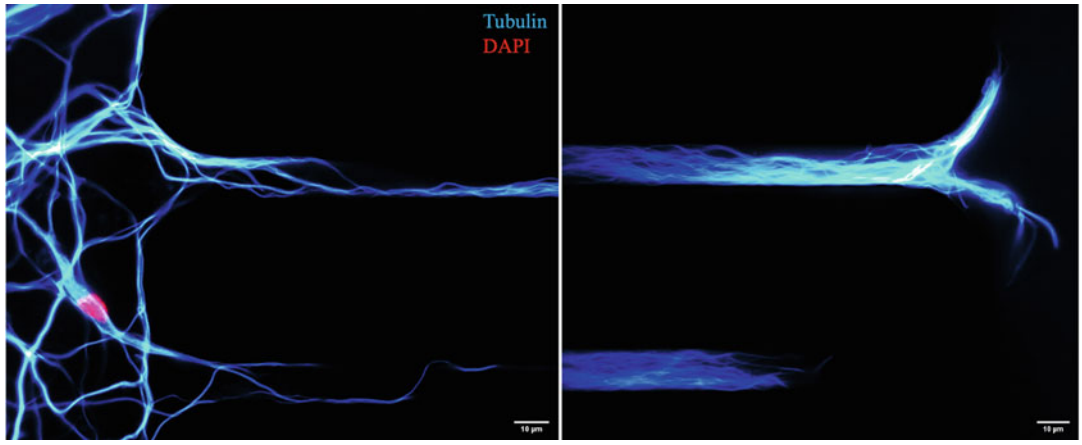

Fig. 4 Basal forebrain cholinergic neurons (BFCNs) stained for tubulin (cyan) and DAPI (red) at day in vitro (DIV) 5. The left panel depicts BFCN cell bodies extending their axons into the microgrooves. The right panel depicts BFCN axons extending across the entire length of the 450 μM microgroove barrier and beginning to enter the axonal main channel

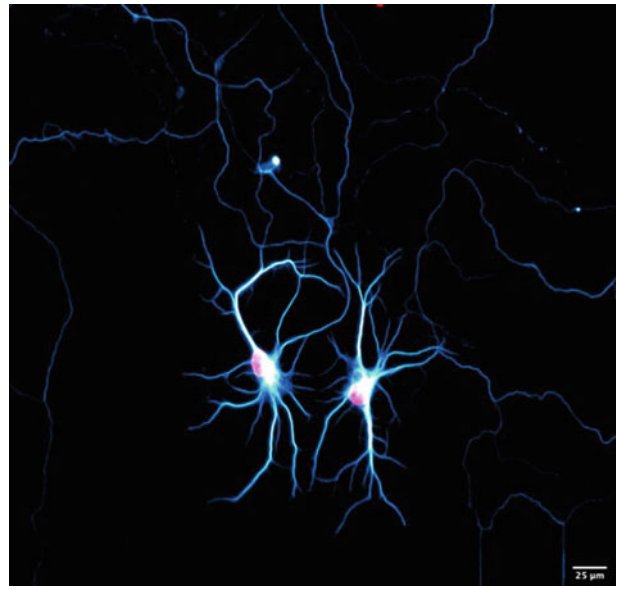

Fig. 5 Basal forebrain cholinergic neurons (BFCNs) cultured in microfluidic chambers stained for tubulin (cyan) and DAPI (red) at day in vitro (DIV) 7 following the immunocytochemical staining protocol outlined in Subheading 3.4

box. The chambers must be protected from light during all subsequent incubations.

2. Perform a PBS wash with 150 μL of PBS and then immediately add 150 μL of PBS-A to all wells (*see* **Notes 9** and **10**). Incubate at room temperature for 30 min.

3. Replace the PBS-A solution with 150 μL of PBS-B per well (*see* **Notes 9** and **10**). Incubate at room temperature for 30 min. During this time, prepare the primary antibody solution using PBS-B as the diluent.
4. Replace the PBS-B solution with 150 μL of the primary antibody solution per well (*see* **Notes 9** and **10**). Incubate at 4 °C overnight.
5. Perform 3 washes using 150 μL of PBS-B per well (*see* **Notes 9** and **10**). Incubate at room temperature for 10 min in between each wash. During the last wash, prepare the secondary antibody solution using PSB-B as the diluent.
6. Replace the PBS-B solution with 150 μL of the secondary antibody solution per well (*see* **Notes 9** and **10**). Incubate at room temperature for 2 h. During this time, prepare a DAPI nuclear counterstain using PBS as the diluent.
7. Aspirate the secondary antibody solution from all wells and add 150 μL of the DAPI counterstain solution to the top left well, followed by 150 μL of PBS to the top right well. Repeat this for the bottom two wells and incubate at room temperature for 10 min.
8. Perform two 150 μL PBS washes. Incubate at room temperature and wait 5 min between each wash. Perform two additional 150 μL PBS washes in immediate succession (*see* **Notes 9** and **10**).
9. Image the cells using either wide field or confocal fluorescence microscopy (*see* **Note 17**).

3.5 Purification of Biotinylated proNGF

Our lab uses a slightly modified version of the protocol outlined in Sung et al. (2011) to obtain monobiotinylated proNGF from transfected HEK cell medium [50]. HEK cells are grown in a biotin-containing transfection medium and are cotransfected with the biotin-ligase coding construct BirA and our custom proNGF construct. Biotinylation of proNGF occurs due to the inclusion of a biotin-accepting AviTag™ region within our construct. This process can be skipped when studying BDNF, proBDNF, and NGF, as biotinylated versions of these neurotrophins are available commercially (Alomone). Due to the lack of mature NGF in the CNS, we recommend the use of proNGF over mature NGF when studying transport in CNS neurons [10, 38].

1. Plate HEK293 cells at an initial density of $1.5x10^6$ cells/ml. Grow to ~50% confluence in 30 ml growth medium in a 30 cm petri dish.
2. In a biosafety cabinet, replace the growth medium with transfection medium and incubate cells for 72 h at 37 °C, 5% CO_2.

3. Dilute 20 μg of proNGF-R-1G-Avi-His and Bir-A biotin ligase pcDNA-3.1 plasmids into 1 mL of DMEM. Add 60 μL of Turbofect™ to this solution, mix via inversion, and incubate at room temperature for 15 min.
4. Add the transfection solution dropwise and incubate cells for 72 h in a 37 °C, 5% CO_2 incubator (*see* **Note 18**).
5. Harvest the medium from the cells and adjust to 50 mL (per 30 mm dish) using Ni-NTA wash buffer. Let stand on ice for 5 min.
6. Centrifuge the harvested medium at 300 × *g* for 20 min at 4 °C. Collect the supernatant and adjust to 300 mL (per 30 cm dish) using Ni-NTA wash buffer.
7. Add 300 μL (per 30 cm dish) of Ni-NTA resin (suspended in wash buffer) to the harvested medium and incubate at 4 °C with gentle stirring overnight.
8. In a cold room or large refrigerator, load the solution into a reusable nickel chromatography column. Let stand for 5 min to allow the Ni-NTA resin to settle. Purify using 2 column volumes of wash buffer (discard) followed by 1/10 column volumes of elution buffer.
9. Load eluate onto a 10kD centrifugal concentrator and centrifuge at 300 × *g* for 20 min at 4 °C, discarding the flow through. Aliquot the reserved solution and store at −80 °C.

3.6 Tracking and Analysis of Neurotrophin Axonal Transport

The brightness of quantum dots allows visualization of single particle neurotrophin transport without the need for expensive confocal microscopy. However, confocal microscopy is recommended for maximum visual fidelity. Biotinylated BDNF and proNGF are both easily conjugated to streptavidin-conjugated quantum dots. However, the conditions required to promote the transport of BDNF and proNGF are different and are discussed below.

3.6.1 Conjugation of Quantum Dots and Administration of Labeled BDNF to Axon Terminals

1. 24 h prior to the transport assay, view the neurons under a widefield microscope using bright-field light to confirm that the axonal compartment is populated with axonal projections. If axons are present, replace the axonal medium with neurotrophin-free axonal imaging medium. Incubate the neurons for 24 h at 37 °C, 5% CO_2. BFCN axons usually populate the axonal compartment by days in vitro (DIV) 5–7.
2. In a biosafety cabinet, add 1 μL of Qdot625 streptavidin conjugate stock solution to 20 μL of 300 nM biotinylated BDNF solution. Mix via brief centrifugation, and incubate on ice, protected from light, for 1 h (*see* **Note 19**).
3. Dilute the QD-BDNF solution to 1 nM using axonal imaging medium.

4. (Optional) Dilute TubulinTracker™ Deep Red 1:1000 into both the somal and axonal imaging medium.
5. Administer 80 μL of the dilute QD-BDNF solution to the top right well, wait 30 s, and repeat with the bottom right well (*see* **Note 20**). Incubate for 1 h at 37 °C, 5% CO_2. During this time, equilibrate the microscope stage to 37 °C, 5% CO_2 (*see* **Note 21**).
6. Wash the axonal side 3 times with 120 μL of axonal imaging medium before imaging.

3.6.2 Conjugation of Quantum Dots and Administration of Labeled proNGF to Axon Terminals

1. Observe neurons under a widefield microscope using bright-field light to confirm that the axonal compartment is populated with axonal projections. Return the chambers to the incubator.
2. In a biosafety cabinet, add 1 μL of QD625 streptavidin conjugate stock solution to 20 μL of 400pM biotinylated proNGF solution. Mix via brief centrifugation, and incubate on ice, protected from light, for 1 h (*see* **Note 19**).
3. Dilute the QD-proNGF solution to a final concentration of 50pM using axonal imaging medium.
4. (Optional) Dilute TubulinTracker™ Deep Red 1:1000 into both the somal and axonal imaging medium.
5. Aspirate the medium from all wells and replace the medium in the top left well with 150 μL of somal imaging medium. Immediately replace the medium in the top left well with 80 μL of the dilute QD-proNGF solution. Repeat for the bottom two wells (*see* **Note 22**).
6. Incubate for at least 15 min at 37 °C, 5% CO_2. During this time, equilibrate the microscope stage to 37 °C, 5% CO_2 (*see* **Note 22**).

3.6.3 Image Acquisition

1. Stage neurons in either a widefield or confocal microscope equipped with an on-stage incubator, 60–100× oil immersion objective (N.A 1.40), and requisite fluorescent filter cubes (*see* **Notes 5** and **6**).
2. Focus on the neurons using bright-field light. Translate the stage toward the middle of the device so that the microgrooves are visible.
3. Switch to either the Qdot625 or Texas Red channels and search for labeled neurotrophins traversing the microgrooves (*see* **Note 23**). Quantum dots exhibit a blinking behavior and are very sensitive to focus changes, making them difficult to locate at first.
4. Once the labeled neurotrophins have been located, create a time lapse by acquiring images at a single location at fixed intervals. Our lab uses intervals of 2–5 s for time lapses lasting

2–5 min. If TubulinTracker™ is being used, acquire a single image of the axon projections at the desired site using the Cy5 channel before beginning the time-lapse (*see* **Note 24**).

5. Repeat **step 4** on as many QD-positive microgrooves as possible. A minimum of 5 microgrooves containing at least 20 QD particles in total is recommended for statistical analysis. When using a 60× objective, microgrooves can be divided into approximately 3 nonoverlapping sections: retrograde (proximal to the axonal channel), middle, and anterograde (proximal to the somal channel). Ensure time-lapses are taken at all locations (*see* **Note 25**). Distal projections within the axonal compartment can also be imaged for the purposes of determining axonal uptake (*see* **Note 26**).

3.6.4 Image Analysis

1. Import time-lapse images into ImageJ by selecting "File > Import > Image Sequence…" and selecting the first image within the sequence, ensuring that all the images from the time-lapse are within a single folder and are in chronological order based on file name.
2. Open the "Properties" window by pressing "Control + Shift + P" and ensure that the "Pixel width" unit is in μM and not inches. If inches are selected by default, simply type "um" in its place. Set the "Frame interval" to the time interval between each of the images within the time-lapse.
3. Select "MTrackJ" under the "Plugins" tab of the ImageJ toolbar. The efficiency of retrograde transport can be determined in multiple ways using this plugin, the simplest of which compares how many particles are present in the section of the microgrooves closest to the cell body compartment between conditions. To do this, select "Tracking" on the MTrackJ pop-up menu and uncheck the "move to next time index after adding point" option. Individual particles can then be indexed by simply pressing "add" on the MTrackJ menu and clicking on the dots. This can be done using the "Multi point tool" (without MTrackJ, present on the ImageJ toolbar by default) if there are a small number of dots present.
4. Retrograde transport can also be assessed by quantifying the speed and pause duration of individual neurotrophin particles using MTrackJ. To do this, select "Tracking" on the MTrackJ pop-up menu and check the "move to next time index after adding point" option. Select "Add" on the MTrackJ popup menu and continually click on the particle to trace its path (*see* **Note 27**). Repeat this process with all visible particles in the time-lapse and select "Measure" on the MTrackJ popup menu. Particle speed can be calculated by taking the average value of the "v (μm/s)" column per particle. Pause duration can be

calculated by multiplying the number of instances where the speed of a particle is 0 μm/s by the frame duration of the time-lapse. Approximately 60–100 particles per group are recommended for statistical analysis.

5. Finally, retrograde transport can also be assessed by generating kymographs from the time-lapse images to trace the overall path of the particles. To do this, first repeat **step 2** and then draw a single, straight line across a single microgroove using the "Single segmented line tool" found on the ImageJ toolbar. Open the KymoToolBox plugin by navigating to "Plugins > KymoToolBox> Draw Kymo" from the ImageJ menu bar and set the width value to 100. Particle speed can also be calculated from kymographs by calculating the slope of the path traced by the particles. However, we recommend determining particle speed using single particle analysis via MTrackJ. The clarity of the kymograph can be improved by pressing "Control + Shift + C" and adjusting the brightness and contrast sliders. If images were saved as greyscale, we recommend inverting the lookup table (LUT) for better clarity by pressing the "LUT" button on the ImageJ toolbar and selecting "Invert LUT."

4 Notes

1. Each of the 4 wells of the microfluidic chamber holds only ~150 μL of media. Because of this small volume, significant evaporation occurs during handling. We recommend that chambers be handled in humidity-controlled containers (Proprietary ChipTrays™ from Xona Microfluidics, or any suitable holder with a small water reservoir) and in an incubator that is seldom opened, if possible, to avoid any confounding effects linked to excess evaporation.
2. Ensure that the opening of the pipette is not bent or sealed during the fire polishing process. An opening of <1 mm will result in reduced cell yield due to excessive shearing force during trituration.
3. We do not recommend using maintenance medium older than 1 week to ensure the health of BFCNs in culture. Preparing multiple aliquots of medium components for the quick and convenient preparation of small volumes of maintenance medium is recommended.
4. XC450 devices are made of an optically neutral plastic that is not compatible with most mineral-based immersion oils.
5. While quantum-dot streptavidin conjugates are available in a variety of wavelengths, we do not recommend the use of conjugates in the yellow-green spectrum due to their relatively

weak fluorescence compared to conjugates in the orange-red spectrum. We recommend the 625 variant, as its emission spectrum aligns very well with the commonly used Texas Red filter set.

6. Quantum dots exhibit a very large stokes shift in their excitation–emission properties. Qdot filter cube sets account for this shift and are recommended for optimal imaging. However, the brightness of quantum dots allows nonproprietary filter cube sets to be used, albeit with higher background noise due to the increased light intensities required to excite quantum dots using nonoptimal wavelengths.
7. The fluorescent labeling of tubulin using TubulinTracker™ in live cells is helpful, but not required, for imaging axonal projections within microgrooves (standard brightfield microscopy can also be used to image axonal projections, but with less clarity). While our lab has not observed significant differences in neurotrophin uptake and transport between labeled and unlabeled conditions, we recommend running pilot experiments using both labeled and unlabeled neurons to ensure that the labeling does not interfere with axonal transport in your specific experimental paradigm.
8. It is *critical* to adhere to the listed standing times during microfluidic chamber preparation. These standing times allow liquid to fully penetrate throughout all compartments of the device, reducing the risk of air bubble formation within the main channels. Refer to Fig. 6 for an example of an improperly prepared chamber containing an air bubble.
9. It is *critical* to never completely aspirate liquid from the wells of the devices. A residual volume of approximately 20 μL remaining within each well is recommended to avoid forming air bubbles and drying out the cells in the main channel.
10. Solutions should be aspirated from the top 2 wells of all devices first, followed by the bottom 2 (Fig. 2). This creates a transient volume difference across the top and bottom of the device, ensuring adequate liquid flow within the main channel.
11. Air bubbles within the main channel must be removed before plating cells. This can be done by placing the tip of a micropipette against the opening of the main channel and gently depressing and releasing the plunger.
12. Our protocol is compatible with both rat and mouse embryonic tissue. Please be sure to follow all institutional guidelines regarding proper animal care and safety during the euthanasia and dissection process.
13. A helpful video of this procedure is included in Schnitzler et al. 2008 [53].

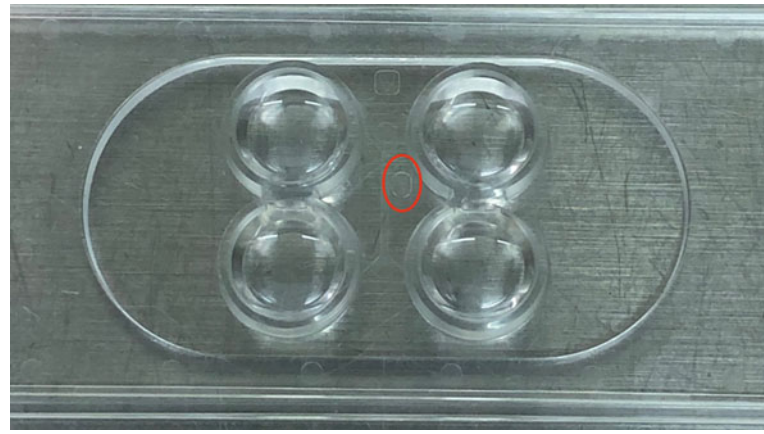

Fig. 6 A microfluidic device with an air bubble (marked with a red oval) present within one of the 2 main channels

14. The tissue from three Sprague-Dawley rat embryos is usually sufficient to prepare 8 microfluidic chambers.
15. The devices are symmetrical, and any side can be used to house the cell bodies.
16. The axonal transport of BDNF and proNGF is reduced in BFCNs after 18 days in vitro [10].
17. XC450 devices are designed to fit into most standard slide holders.
18. HEK293 cells should be plated in petri dishes as opposed to flasks to facilitate the dropwise addition of the transfection solution.
19. The neurotrophin concentration can be increased or decreased depending on the experimental paradigm. However, the ratio of neurotrophin to quantum dots should remain constant.
20. Maintaining an 80 μL volume difference between the somal and axonal sides of the chambers creates a small anterograde liquid flux, ensuring that any retrograde transport is due to axonal uptake and not incidental retrograde liquid flux.
21. BDNF uptake is significantly more rapid in BFCNs compared to cortical neurons [10]. If cortical neurons are being used, incubate the QD-BDNF solution for 4 h before imaging.
22. proNGF uptake is significantly more efficient compared to BDNF uptake in BFCNs and can be visualized using concentrations within the picomolar range [10]. The uptake also occurs much more rapidly, with QD-proNGF particles appearing in axons within 15 min [10]. Unlike BDNF, proNGF uptake is significantly inhibited upon axonal neurotrophin starvation [10].

23. Excessive exposure of neurons to light from the QD625 filter cube set is damaging due to its use of high-energy 445 nm light to maximally excite the quantum dots. We recommend minimizing both the light intensity and duration neurons are exposed to this light to avoid damaging cells.
24. We recommend staggering the incubation of individual chambers with labeled neurotrophins by between 30 min to 1 h to account for the time it takes to image a single chamber.
25. Ensure that time-lapses at each of the three sections of the microgrooves are taken at identical time intervals after neurotrophin addition to avoid the passage of time as a confound when comparing chambers.
26. Time-lapses are not necessary when imaging axonal projections for the purposes of assessing neurotrophin uptake. Uptake can simply be quantified by counting labeled particles present within a predefined length of distal axon (our lab uses 100 μm). Length can be measured using the "Straight segmented line tool" in ImageJ.
27. Neurotrophin particles can exhibit bidirectional movement during transport within the span of a single time lapse. It is recommended to analyze the retrograde and anterograde components of a given particle's transport separately. This can be done by selecting "Add" in the MTrackJ popup window following the completion of the retrograde movement of a particle and treating the anterograde component of its movement as a separate particle.

Acknowledgments

We thank Dr. Chengbiao Wu (Department of Neurosciences, University of California at San Diego, La Jolla, CA, USA) for providing us with an NGF-Avi-His plasmid and for his assistance in the development of our monobiotinylated neurotrophin purification protocols. Supported by grant #PJT-159493 from the Canadian Institutes of Health Research to MF.

References

1. Terenzio M, Schiavo G, Fainzilber M (2017) Compartmentalized signaling in neurons: from cell biology to neuroscience. Neuron 96:667–679. https://doi.org/10.1016/j.neuron.2017.10.015
2. Maday S, Twelvetrees AE, Moughamian AJ, Holzbaur ELF (2014) Axonal transport: cargo-specific mechanisms of motility and regulation. Neuron 84:292–309. https://doi.org/10.1016/j.neuron.2014.10.019
3. Rao AN, Baas PW (2018) Polarity sorting of microtubules in the axon. Trends Neurosci 41:77–88. https://doi.org/10.1016/j.tins.2017.11.002
4. Roberts AJ, Kon T, Knight PJ et al (2013) Functions and mechanics of dynein motor

proteins. Nat Rev Mol Cell Biol 14:713–726. https://doi.org/10.1038/nrm3667
5. Hirokawa N (1998) Kinesin and dynein superfamily proteins and the mechanism of organelle transport. Science 279:519–526. https://doi.org/10.1126/science.279.5350.519
6. van Spronsen M, Mikhaylova M, Lipka J et al (2013) TRAK/Milton motor-adaptor proteins steer mitochondrial trafficking to axons and dendrites. Neuron 77:485–502. https://doi.org/10.1016/j.neuron.2012.11.027
7. Lin MY, Sheng ZH (2015) Regulation of mitochondrial transport in neurons. Exp Cell Res 334:35–44
8. Debattisti V, Gerencser AA, Saotome M et al (2017) ROS control mitochondrial motility through p38 and the motor adaptor Miro/Trak. Cell Rep 21:1667–1680. https://doi.org/10.1016/j.celrep.2017.10.060
9. Moughamian AJ, Osborn GE, Lazarus JE et al (2013) Ordered recruitment of dynactin to the microtubule plus-end is required for efficient initiation of retrograde axonal transport. J Neurosci 33:13190–13203. https://doi.org/10.1523/JNEUROSCI.0935-13.2013
10. Shekari A, Fahnestock M (2019) Retrograde axonal transport of BDNF and proNGF diminishes with age in basal forebrain cholinergic neurons. Neurobiol Aging 84:131–140. https://doi.org/10.1016/j.neurobiolaging.2019.07.018
11. Fahnestock M, Shekari A (2019) ProNGF and neurodegeneration in Alzheimer's disease. Front Neurosci 13:129. https://doi.org/10.3389/fnins.2019.00129
12. Woolf NJ (1991) Cholinergic systems in mammalian brain and spinal cord. Prog Neurobiol 37:475–524. https://doi.org/10.1016/0301-0082(91)90006-m
13. Ballinger EC, Ananth M, Talmage DA, Role LW (2016) Basal forebrain cholinergic circuits and signaling in cognition and cognitive decline. Neuron 91:1199–1218. https://doi.org/10.1016/j.neuron.2016.09.006
14. Köppen JR, Stuebing SL, Sieg ML et al (2016) Cholinergic deafferentation of the hippocampus causes non-temporally graded retrograde amnesia in an odor discrimination task. Behav Brain Res 299:97–104. https://doi.org/10.1016/j.bbr.2015.11.021
15. Ypsilanti AR, Girão da Cruz MT, Burgess A, Aubert I (2008) The length of hippocampal cholinergic fibers is reduced in the aging brain. Neurobiol Aging 29:1666–1679. https://doi.org/10.1016/j.neurobiolaging.2007.04.001
16. Whitehouse PJ, Hedreen JC, White CL, Price DL (1983) Basal forebrain neurons in the dementia of Parkinson disease. Ann Neurol 13:243–248. https://doi.org/10.1002/ana.410130304
17. Ferreira-Vieira TH, Guimaraes IM, Silva FR, Ribeiro FM (2016) Alzheimer's disease: targeting the cholinergic system. Curr Neuropharmacol 14:101–115. https://doi.org/10.2174/1570159X13666150716165726
18. Whitehouse P, Price D, Struble R et al (1982) Alzheimer's disease and senile dementia: loss of neurons in the basal forebrain. Science 215:1237–1239. https://doi.org/10.1126/science.7058341
19. Ginsberg SD, Mufson EJ, Alldred MJ et al (2011) Upregulation of select rab GTPases in cholinergic basal forebrain neurons in mild cognitive impairment and Alzheimer's disease. J Chem Neuroanat 42:102–110. https://doi.org/10.1016/j.jchemneu.2011.05.012
20. Schmitz TW, Nathan Spreng R (2016) Basal forebrain degeneration precedes and predicts the cortical spread of Alzheimer's pathology. Nat Commun 7:13249. https://doi.org/10.1038/ncomms13249
21. Whitehouse PJ (1998) The cholinergic deficit in Alzheimer's disease. J Clin Psychiatry 59 (Suppl 1):19–22
22. Hyman B, Van Hoesen G, Damasio A, Barnes C (1984) Alzheimer's disease: cell-specific pathology isolates the hippocampal formation. Science 225:1168–1170. https://doi.org/10.1126/science.6474172
23. Baker-Nigh A, Vahedi S, Davis EG et al (2015) Neuronal amyloid-β accumulation within cholinergic basal forebrain in ageing and Alzheimer's disease. Brain 138:1722–1737. https://doi.org/10.1093/brain/awv024
24. Schmitz TW, Nathan Spreng R, Weiner MWM et al (2016) Basal forebrain degeneration precedes and predicts the cortical spread of Alzheimer's pathology. Nat Commun 7:13249. https://doi.org/10.1038/ncomms13249
25. Bothwell M (2014) NGF, BDNF, NT3, and NT4. In: Lewin G, Carter B (eds) Neurotrophic factors, Handbook of experimental pharmacology, vol 220. Springer, Berlin, pp 3–15
26. Alderson RF, Alterman AL, Barde YA, Lindsay RM (1990) Brain-derived neurotrophic factor increases survival and differentiated functions of rat septal cholinergic neurons in culture. Neuron 5:297–306. https://doi.org/10.1016/0896-6273(90)90166-d
27. Sanchez-Ortiz E, Yui D, Song D et al (2012) TrkA gene ablation in basal forebrain results in

dysfunction of the cholinergic circuitry. J Neurosci 32:4065–4079. https://doi.org/10.1523/JNEUROSCI.6314-11.2012

28. Latina V, Caioli S, Zona C et al (2017) Impaired NGF/TrkA signaling causes early AD-linked presynaptic dysfunction in cholinergic primary neurons. Front Cell Neurosci 11:68. https://doi.org/10.3389/fncel.2017.00068
29. Hartikka J, Hefti F (1988) Development of septal cholinergic neurons in culture: plating density and glial cells modulate effects of NGF on survival, fiber growth, and expression of transmitter-specific enzymes. J Neurosci 8:2967–2985
30. Hatanaka H, Tsukui H, Nihonmatsu I (1988) Developmental change in the nerve growth factor action from induction of choline acetyltransferase to promotion of cell survival in cultured basal forebrain cholinergic neurons from postnatal rats. Dev Brain Res 39:85–95. https://doi.org/10.1016/0165-3806(88)90069-7
31. Rylett RJ, Williams LR (1994) Role of neurotrophins in cholinergic-neurone function in the adult and aged CNS. Trends Neurosci 17:486–490. https://doi.org/10.1016/0166-2236(94)90138-4
32. Hefti F (1986) Nerve growth factor promotes survival of septal cholinergic neurons after fimbrial transections. J Neurosci 6:2155–2162. https://doi.org/10.1523/JNEUROSCI.06-08-02155.1986
33. Sun CB-Y, Xia Y et al (2013) Functional switch from pro-neurotrophins to mature neurotrophins. Curr Protein Pept Sci 14:617–625. https://doi.org/10.2174/1389203711209070658
34. Clewes O, Fahey MS, Tyler SJ et al (2008) Human ProNGF: biological effects and binding profiles at TrkA, P75NTRand sortilin. J Neurochem 107:1124–1135. https://doi.org/10.1111/j.1471-4159.2008.05698.x
35. Fahnestock YG, Michalski B et al (2004) The nerve growth factor precursor proNGF exhibits neurotrophic activity but is less active than mature nerve growth factor. J Neurochem 89:581–592. https://doi.org/10.1111/j.1471-4159.2004.02360.x
36. Ioannou M, Fahnestock M (2017) ProNGF, but not NGF, switches from neurotrophic to apoptotic activity in response to reductions in TrkA receptor levels. Int J Mol Sci 18:599. https://doi.org/10.3390/ijms18030599
37. Koshimizu H, Kiyosue K, Hara T et al (2009) Multiple functions of precursor BDNF to CNS neurons: negative regulation of neurite growth, spine formation and cell survival. Mol Brain 2:27. https://doi.org/10.1186/1756-6606-2-27
38. Fahnestock MB, Xu B, Coughlin M (2001) The precursor pro-nerve growth factor is the predominant form of nerve growth factor in brain and is increased in Alzheimer's disease. Mol Cell Neurosci 18:210–220. https://doi.org/10.1006/mcne.2001.1016
39. Garcia KLP, Yu G, Nicolini C et al (2012) Altered balance of proteolytic isoforms of pro-brain-derived neurotrophic factor in autism. J Neuropathol Exp Neurol 71(4):289–297. https://doi.org/10.1097/NEN.0b013e31824b27e4
40. Michalski B, Fahnestock M (2003) Pro-brain-derived neurotrophic factor is decreased in parietal cortex in Alzheimer's disease. Mol Brain Res 111:148–154. https://doi.org/10.1016/S0169-328X(03)00003-2
41. Seiler M, Schwab ME (1984) Specific retrograde transport of nerve growth factor (NGF) from neocortex to nucleus basalis in the rat. Brain Res 300:33–39. https://doi.org/10.1016/0006-8993(84)91338-6
42. Lu B, Nagappan G, Lu Y (2014) BDNF and synaptic plasticity, cognitive function, and dysfunction. In: Lewin G, Carter B (eds) Neurotrophic factors, Handbook of experimental pharmacology, vol 220. Springer, Berlin, pp 223–250
43. Lauterborn JC, Bizon JL, Tran TMD, Gall CM (1995) NGF mRNA is expressed by GABAergic but not cholinergic neurons in rat basal forebrain. J Comp Neurol 360:454–462. https://doi.org/10.1002/cne.903600307
44. Ha DH, Robertson RT, Roshanaei M, Weiss JH (1999) Enhanced survival and morphological features of basal forebrain cholinergic neurons in vitro: Role of neurotrophins and other potential cortically derived cholinergic trophic factors. J Comp Neurol 406:156–170. https://doi.org/10.1002/(SICI)1096-9861(19990405)406:2<156::AID-CNE2>3.0.CO;2-K
45. DiStefano PS, Friedman B, Radziejewski C et al (1992) The neurotrophins BDNF, NT-3, and NGF display distinct patterns of retrograde axonal transport in peripheral and central neurons. Neuron 8:983–993. https://doi.org/10.1016/0896-6273(92)90213-W
46. Scott SA, Mufson EJ, Weingartner JA et al (1995) Nerve growth factor in Alzheimer's disease: increased levels throughout the brain coupled with declines in nucleus basalis. J Neurosci 15:6213–6221. https://doi.org/10.1523/JNEUROSCI.15-09-06213.1995

47. Salehi A, Delcroix J-D, Belichenko PV et al (2006) Increased app expression in a mouse model of Down's syndrome disrupts NGF transport and causes cholinergic neuron degeneration. Neuron 51:29–42. https://doi.org/10.1016/j.neuron.2006.05.022
48. Taylor AM, Blurton-Jones M, Rhee SW et al (2005) A microfluidic culture platform for CNS axonal injury, regeneration and transport. Nat Methods 2:599–605. https://doi.org/10.1038/nmeth777
49. Taylor AM, Rhee SW, Jeon NL (2006) Microfluidic chambers for cell migration and neuroscience research. Methods Mol Biol 321:167–178
50. Sung K, Maloney MT, Yang J, Wu C (2011) A novel method for producing monobiotinylated, biologically active neurotrophic factors: an essential reagent for single molecule study of axonal transport. J Neurosci Methods 200:121–128. https://doi.org/10.1016/j.jneumeth.2011.06.020
51. Sobreviela T, Clary DO, Reichardt LF, Brandabur MM, Kordower JH, Mufson EJ. (1994) TrkA-immunoreactive profiles in the central nervous system: colocalization with neurons containing p75 nerve growth factor receptor, choline acetyltransferase, and serotonin. J Comp Neurol 350(4):587–611. https://doi.org/10.1002/cne.903500407
52. Holtzman DM, Li Y, Parada LF et al (1992) p140trk mRNA marks NGF-responsive forebrain neurons: evidence that trk gene expression is induced by NGF. Neuron 9:465–478. https://doi.org/10.1016/0896-6273(92)90184-F
53. Schnitzler AC, Lopez-Coviella I, Blusztajn JK (2008) Purification and culture of nerve growth factor receptor (p75)-expressing basal forebrain cholinergic neurons. Nat Protoc 3:34–40. https://doi.org/10.1038/nprot.2007.477

Open Access This chapter is licensed under the terms of the Creative Commons Attribution 4.0 International License (http://creativecommons.org/licenses/by/4.0/), which permits use, sharing, adaptation, distribution and reproduction in any medium or format, as long as you give appropriate credit to the original author(s) and the source, provide a link to the Creative Commons license and indicate if changes were made.

The images or other third party material in this chapter are included in the chapter's Creative Commons license, unless indicated otherwise in a credit line to the material. If material is not included in the chapter's Creative Commons license and your intended use is not permitted by statutory regulation or exceeds the permitted use, you will need to obtain permission directly from the copyright holder.

Chapter 14

Use of Microfluidics Chambers to Image Axonal transport in Adult Sensory Neurons

Maria Fransiska Emily, Lokesh Agrawal, Paolo Barzaghi, Miki Otsuki, and Marco Terenzio

Abstract

Transport of cargoes along axons is crucial for ensuring effective neuronal function and survival. Lysosomes, which are membrane-bound organelles responsible for the degradation of macromolecules, are among the many cargoes being transported. Compartmentalized systems that allow for the separation of the somatic compartment from the axonal network, are widely used in the field of neurobiology and in the study of axonal transport in particular. Among the various solutions available, microfluidics chambers that take advantage of fluidic separation between different compartments, have seen widespread adoption. Said chambers are made of polydimethylsiloxane (PDMS), a transparent, gas permeable compound, which is compatible with fluorescence microscopy, and have significantly positively impacted cellular neuroscience, drastically increasing our understanding of axonal peripheral signaling. Here we describe a two-layered microfluidics chamber, engineered to allow for the culture of adult sensory neurons. This device was designed to promote the proper placement of adult sensory neurons in the somatic chamber in proximity of the microgrooves. We detail the production of the master mold, how to fabricate and assemble the device and how to disaggregate and load the cells in it. In addition, we provide details on how to conduct and analyze an axonal transport experiment using a custom made script in MATLAB designed by our laboratory.

Key words Lysosomes, Microfluidics Chambers, Intracellular Transport, Axons, Adult Sensory Neurons

1 Introduction

Since the first observation of intracellular movement in algae in the eighteenth century, our understanding of the quantity and types of cargoes that are being transported intracellularly has tremendously broadened. In eukaryotes, effective intracellular transport is made possible by molecular motor proteins that carry cargoes such as organelles, mRNA, proteins, and cytoskeletal filaments along a cytoskeletal track [1, 2]. In neurons, intracellular transport is critical due to the highly asymmetric organization and complex

Alessio Vagnoni (ed.), *Axonal Transport: Methods and Protocols*,
Methods in Molecular Biology, vol. 2431, https://doi.org/10.1007/978-1-0716-1990-2_14,
© The Author(s), under exclusive license to Springer Science+Business Media, LLC, part of Springer Nature 2022

morphology of axons and dendrites. In axons, anterograde and retrograde transport are mediated by coupling of organelles to kinesin and dynein–dynactin microtubule motors [3]. Indeed, mutations of genes involved in intracellular trafficking have been shown to lead to neurodegeneration [4, 5], while both anterograde and retrograde axonal transport deficits have been linked to neurological disorders such as amyotrophic lateral sclerosis (ALS), Alzheimer's disease, and Charcot–Marie–Tooth disease (CMT) [6, 7]. Thus, investigation of the features of the movement of axonal carriers is critical to the understanding of the role of axonal transport in the pathogenesis of neuronal disorders [6–8].

It is possible to take advantage of natural occurring anatomical compartmentalization of nerves compared to their respective cell bodies in in vivo studies. For instance, models such as sciatic nerve transection, optic nerve crush and lateral fluid percussion, have been used to investigate axonal morphological and biochemical changes after injury [9–11]. In order to perform comparable studies in vitro and achieve segregation between neuronal cell bodies and their neurite network, several devices have been tested by the community. The first compartmentalized platform to allow for local treatment of axons and somas, was the Campenot chamber, consisting of a reusable Teflon piece with three individual chambers glued to a petri dish through a thin layer of silicon vacuum grease. This device has been widely utilized to study signaling within axons and synthesis of structural protein [12, 13]. While this device has greatly contributed to our understanding of long-distance signaling, such as retrograde endosomal trafficking, it suffers from severe limitations linked to its design [12]. (1) Campenot chambers have a high rate of failure connected to their labor-intensive assembly and possible leakages. There is also variability in the extent and timing of axons crossing the barrier. (2) Axons needs to be strong enough to pass through the silicon grease, thus, most central nervous system (CNS) neurons are not suitable for this device. (3) Since Campenot chambers are opaque and generally assembled on plastic, they are ill-suited for high resolution microscopy [9, 14].

For these reasons, the design of the Campenot chamber has been integrated into the use of Polydimethylsiloxane (PDMS)-based microfluidic chambers (MFC), which are easier to assemble, cheaper to produce, and allow for the use of a small number of cells and a reduced amount of medium [15]. MFCs rely on very small channels, or microgrooves (dimension in the range of micrometers), connecting two bigger chambers. The neurons are seeded in one chamber and their axons grow through the microgrooves into the other chamber (Fig. 1a, b). Separation is achieved fluidically by virtue of the size of the microgrooves [16]. Such devices have been extensively used to study neuronal injury and degeneration [17–19], with a variety of neurons, from both from the peripheral nervous system (PNS) and the CNS, including

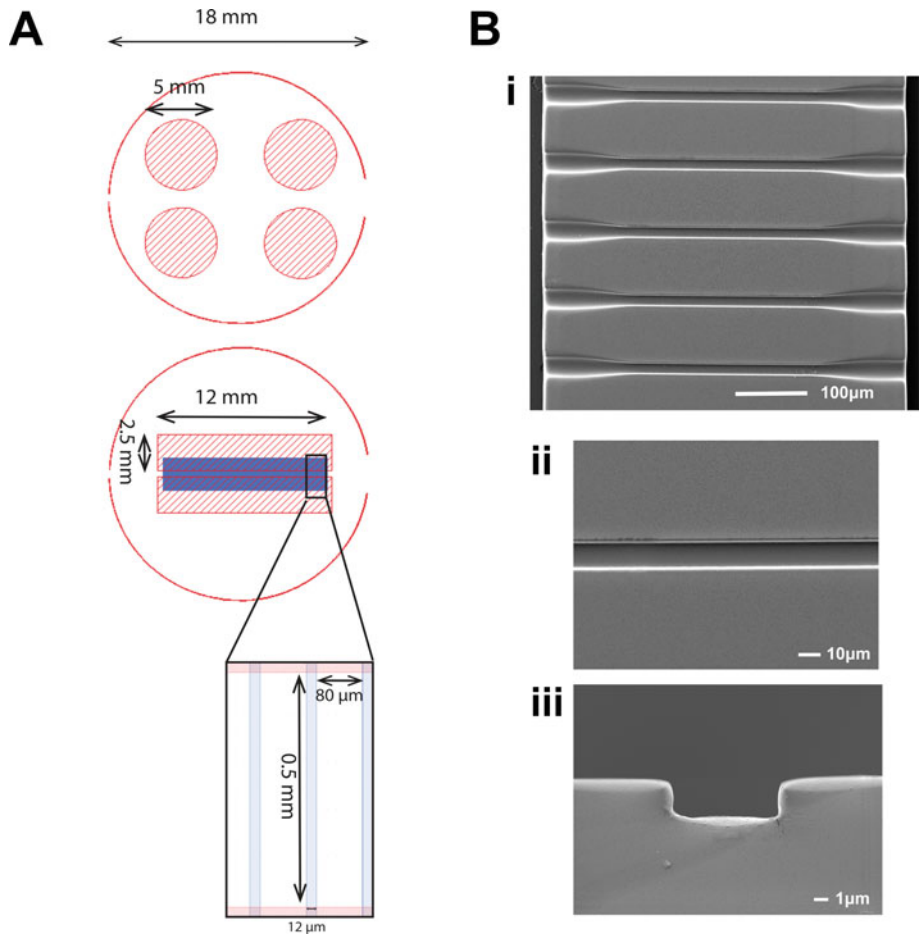

Fig. 1 Features of the MFC for adult DRG neuron culture. (**a**) Schematic representation of the first (top) and second layer (bottom) of the MFC. The first layer consists of four reservoirs of 5 mm in diameter, while the second layer consists of a microchamber with the dimension of 12 mm (l), 2.5 mm (w) and 100 µm (h), and microgrooves with the dimension of 0.55 mm (l), 12 µm (w) and 5 µm (h). (**b**) Scanning electron microscope (SEM) images of the microgrooves of the MFC. (**i**) horizontal view of the microchannels that are located 80 µm apart from each other, (**ii**) horizontal view of a single microgroove, (**iii**) vertical view of the microgroove. Scale bars: 100 µm (l), 10 µm (ii), 1 µm (iii)

embryonic sensory (PNS) and hippocampal (CNS) neurons. In addition, since PDMS is transparent, biocompatible and can be bonded to glass surfaces, MFCs have the distinct advantage of being compatible with high-resolution microscopy and other critical neuroscience techniques, such as electrophysiology [9, 20].

Sensory neurons, which relay important environmental cues to the central nervous system (CNS), are located in the dorsal root ganglia (DRG) [21]. While embryonic DRG neurons can be easily cultured in MFCs, it is more difficult to culture primary DRG neurons from adult mice in MFCs, though not impossible [22]. Indeed, the larger size of adult DRG neurons combined

with a slow kinetics of attachment to a laminin substrate, makes them vulnerable to the flow of liquid created when injecting the cells into the main chamber, causing them to accumulate to one side, far from the microgrooves. We also noticed that adult DRG neurons are very sensitive to medium acidification, requiring constant refreshing of the medium, causing the neurons to detach due to their relatively poor adhesion properties. This can pose a problem for long experiments, requiring constant changes of the culture medium. In this protocol, we describe a 2 layered MFC design, which can accommodate between 5000–10,000 DRG neurons per device (Figs. 1a and 3a). The MFC features two main chambers on the first layer which are directly connected to the microgrooves, ensuring most of the DRG neurons will settle near the microgrooves. The reservoirs are instead located on the second layer, which is bonded on top of the first one (Figs. 1 and 2). This setup can prevent detaching of DRG neurons while changing the medium. We have also observed that the MFC was able to establish fluidic isolation of the somal side for more than 24 h (Fig. 2b). Using these MFCs we were able to culture adult DRG neurons in absence of growth factors. Under these conditions, neurons were able to extend their axons through the microgrooves in 12–15 days (Fig. 3b). If needed, axon crossing can be greatly enhanced by adding 50 ng/ml NGF to the axonal side of the chamber (Fig. 3b). Being able to culture adult DRG neurons in absence of growth factors could prove advantageous in studies where specific peripheral signaling or intrinsic mechanisms are assessed.

Among the many cargoes transported, lysosomes are particularly important due to their degradative housekeeping functions in support to axonal metabolism and longevity (reviewed in [6, 23, 24]). Lysosomal anterograde transport is mediated by the Arl8 effector that can directly interact with kinesin light chain [25]. Impairment of lysosomes is associated with axonal dystrophy characterized by axonal swellings due to accumulation of nondegraded cargoes. Indeed, axonal lysosomal deficits have been described in neurodegenerative diseases such as Alzheimer [23, 24, 26–28]. Autophagy-lysosomal deficits has also been described in a mouse model for amyotrophic lateral sclerosis (ALS) and frontotemporal dementia (FTD) [29], while lysosomal impairment is a hallmark of neurological lysosomal storage disorder (LSDs) [30]. As a testament to a growing set of axonal functions for late endosomes/lysosomes, late endosomes have recently been described as platform for axonal local translation [31]. This chapter focuses on the imaging and analysis of lysosomal axonal transport using custom made MFCs suitable for the culture of adult DRG neurons and a MATLAB script for the quantification of carriers instantaneous speed. While axonal transport can be tracked manually or automatically by tracking the carries movements directly in a time-lapse image sequence, this approach is fairly labor intensive

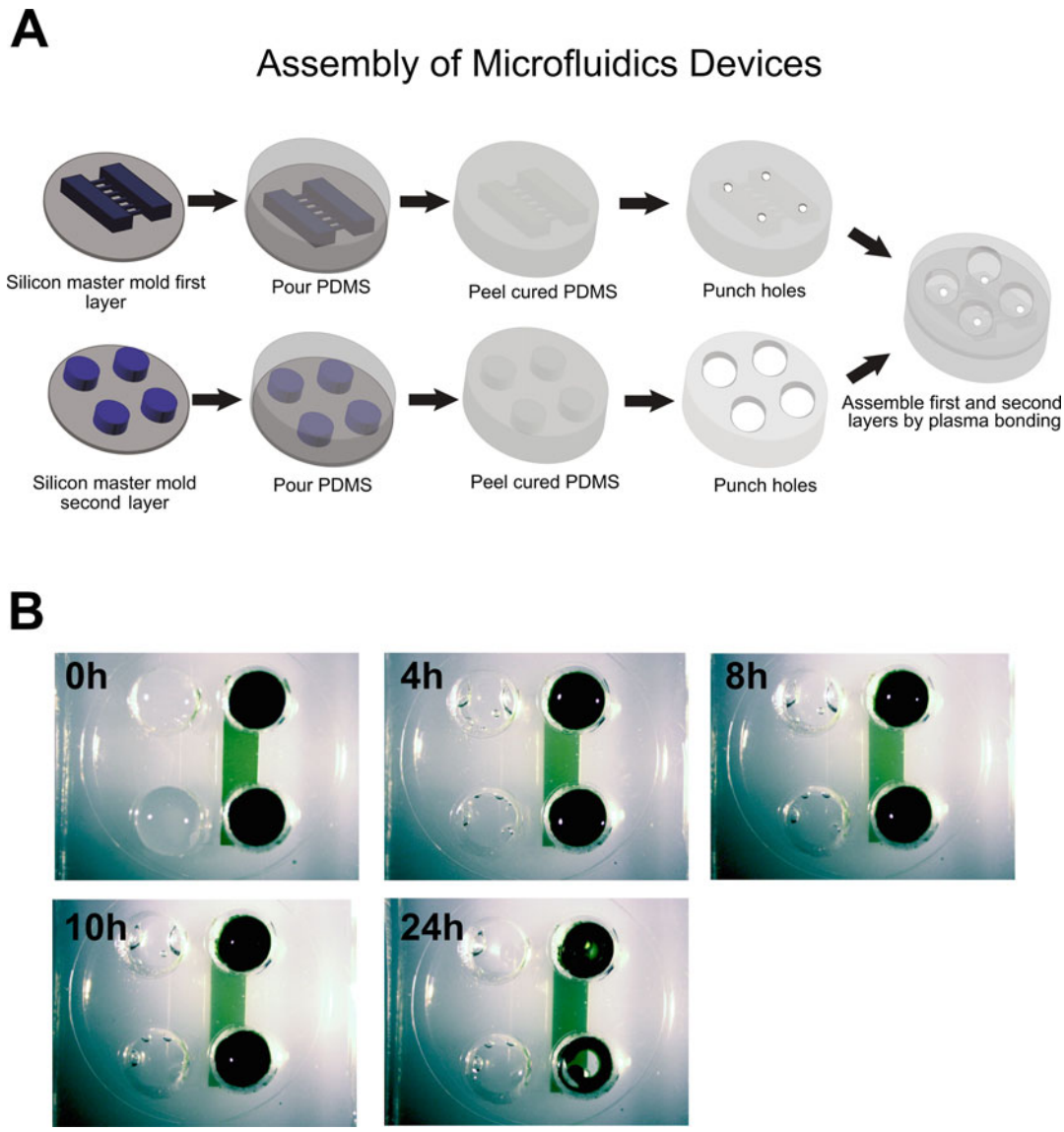

Fig. 2 MFC fabrication and assembly. (**a**) Workflow of the fabrication of a MFC. MFCs are fabricated using soft lithography, where PDMS is poured on top of a silicon master mold. After the PDMS is cured by baking it in an oven, it can be peeled off from the master mold and holes are punched in the cured PDMS. The first and second layer are then assembled using plasma bonding. (**b**) Food coloring was added to one side of the MFC, while water was added to the other. Pictures were taken every 4 h up to 24 h. the MFC was able to maintain compartmentalization throughout the time series

and can be prone to errors due to the change in morphology of the carries between frames of the transport movie [32]. Thus, we decided to take advantage of a kymograph representation, in which each frame of the transport movie is flattened in a 2D image, making the visualization of the transported carriers easier [33] (Fig. 4a). From the kymograph, retrograde and anterograde

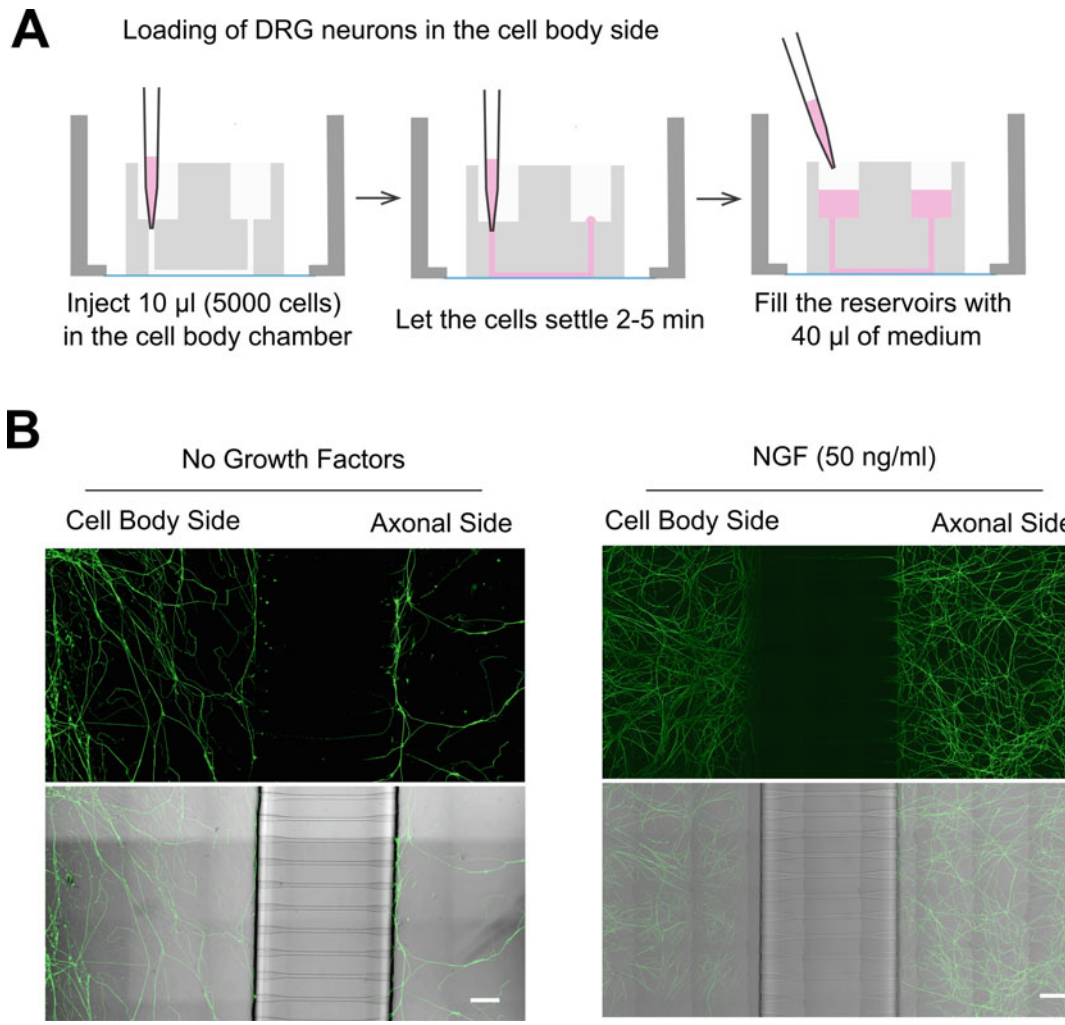

Fig. 3 Culturing adult DRG neurons in our MFC design. (**a**) Schematic representation of the loading of adult DRG neurons in our MFC chip. DRG neurons are loaded in the microfluidic device in the somal chamber by injection using a 10 µl pipette tip. After waiting a few minutes for the cells to settle, 40 µl of medium is added to both reservoirs. The axonal chamber and reservoirs can then be filled. (**b**) Images of adult DRG cultures in a MFC, 15 days after plating. No growth factors were added to the chamber on the left, while 50 ng/ml of NGF was added to the axonal side of the chamber of the right. NGF addition clearly stimulates growth as well as axons passing through the grooves. Tuj1 staining in green. The images are maximum intensity projections of large field of view stitched 3D images acquired using a Nikon A1R laser confocal system equipped with a 20× PlanApo objective (NA 0.75). Scale bar: 100 µm

transport, pause, velocity and displacement can be measured. In this current protocol, we describe an analysis paradigm utilizing the kymograph of the time-lapse acquired to analyze the instantaneous speed of different carriers by using a script that we have developed. Our script is able to recognize pixel by pixel movement of the carriers in a time and distance-based manner to calculate the

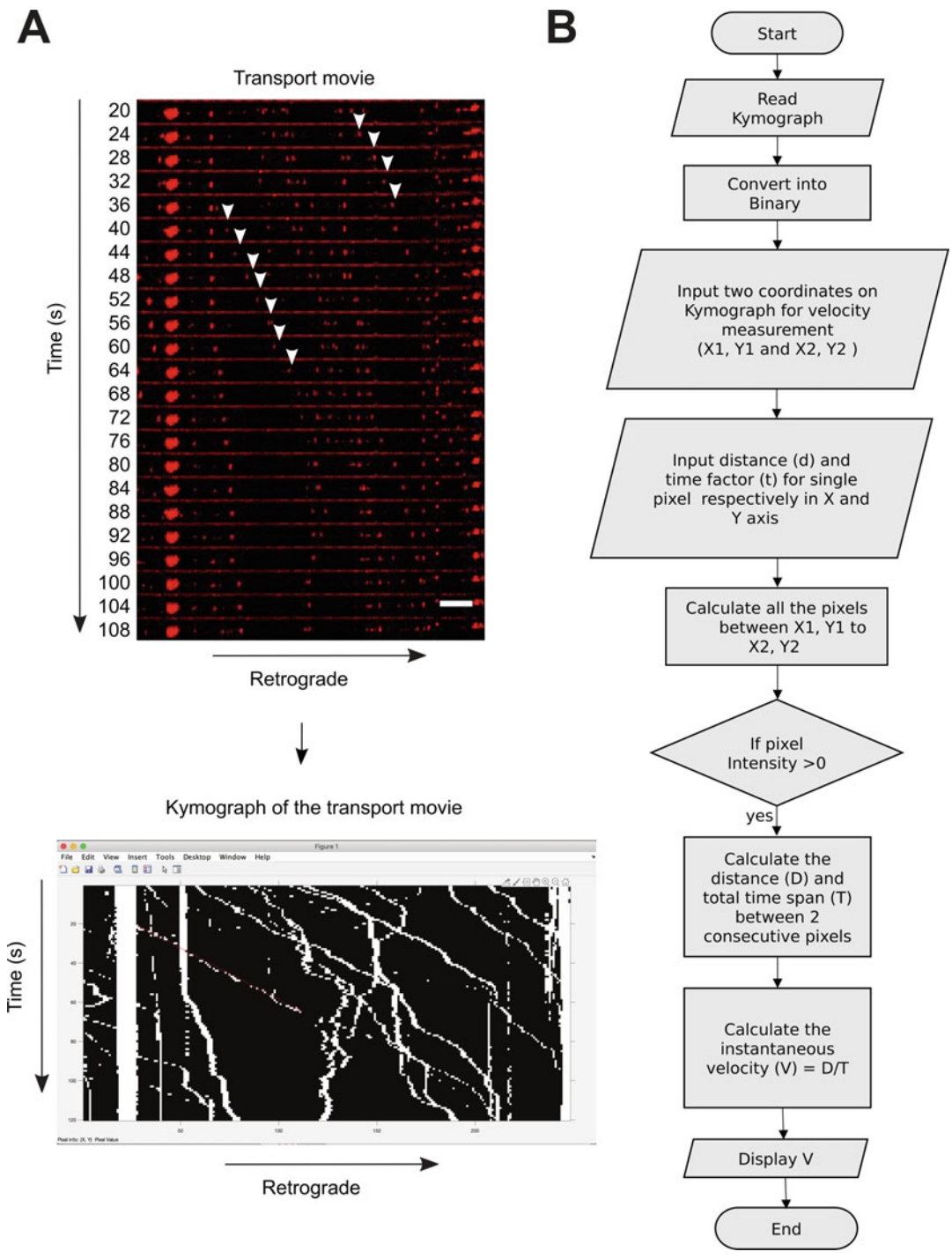

Fig. 4 Outline of the axonal transport analysis. (**a**) Adult DRG neurons at DIV 13 in a MFC were incubated with LysoTracker™ (in red) for 1 h at 37 °C before being imaged in an Olympus FV10i-LV laser scanning confocal microscope with a 60× water immersion objective (NA 1.2). Frames from an axonal transport movie from the previously described experiment taken 4 s apart from each other and the kymograph generated from the movie using the software Fiji. Examples of moving individual lysosomes highlighted by white arrows. Scale bar: 20 μm. (**b**) Schematics workflow of the algorithm underlying our MATLAB script for instantaneous speed quantification

instantaneous speed and displacement of a single carrier for each frame (Fig. 4b, c). We have observed that most lysosomal carriers speed ranges from 0.2 μm/s to 0.5 μm/s (Fig. 5a, b), while the average instantaneous lysosomal speed was around 0.4 μm/s (Fig. 5c, d).

2 Materials

2.1 Microfluidic Chamber Fabrication

1. Hot plate.
2. Spin coating device.
3. Photoresists (mr_DWL_5, mr_DWL_40).
4. Photoresist developer (propylene glycol monomethyl ether acetate, PGMEA).
5. Isopropanol (IPA).
6. Maskless lithography apparatus (Nano System solution, model Dlight DL-1000).
7. PDMS (cat. no. Sylgard™ 184, Dow Corning).
8. Razor blades.
9. Stir rods (or metal spoons).
10. Digital scale.
11. Disposable plastic cup for mixing PDMS.
12. Vacuum desiccator for degassing PDMS.
13. Oven for curing PDMS.
14. Stainless steel punchers with 1.5 mm and 5 mm diameter.
15. Scotch Tape (3 M Magic™ Tape).
16. Plasma cleaner (Harrick Plasma PCD-001-HP or equivalent).

2.2 DRG Neuron Culture

1. HBSS solution: 440 ml of double-distilled water (DDW), 50 ml of 10× HBSS, 2.5 ml of 1 M Hepes, 2.5 ml of 2 M D-glucose, and 1 ml of Primocin™ (Invivogen). Titrate with 1 M NaOH until a pH of 7.35 is reached. Filter and keep in 50 ml tubes at 4 °C.
2. Poly-L-lysine (PLL), MW 150,000-300,000.
3. 10 cm Teflon Silicone Mold Holder or Petri Dish that fits the silicon wafer.
4. 0.5–2.0 mg/ml Laminin. Thaw 1 mg of Laminin on ice and dilute with ice cold HBSS to make a final volume of 5 ml. Make 100 μl aliquots and freeze at −80 °C.
5. F12 medium: mix 445 ml of F-12 media, 50 ml of fetal calf serum, and 1 ml of Primocin™ (Invivogen). Keep the medium at 4 °C.

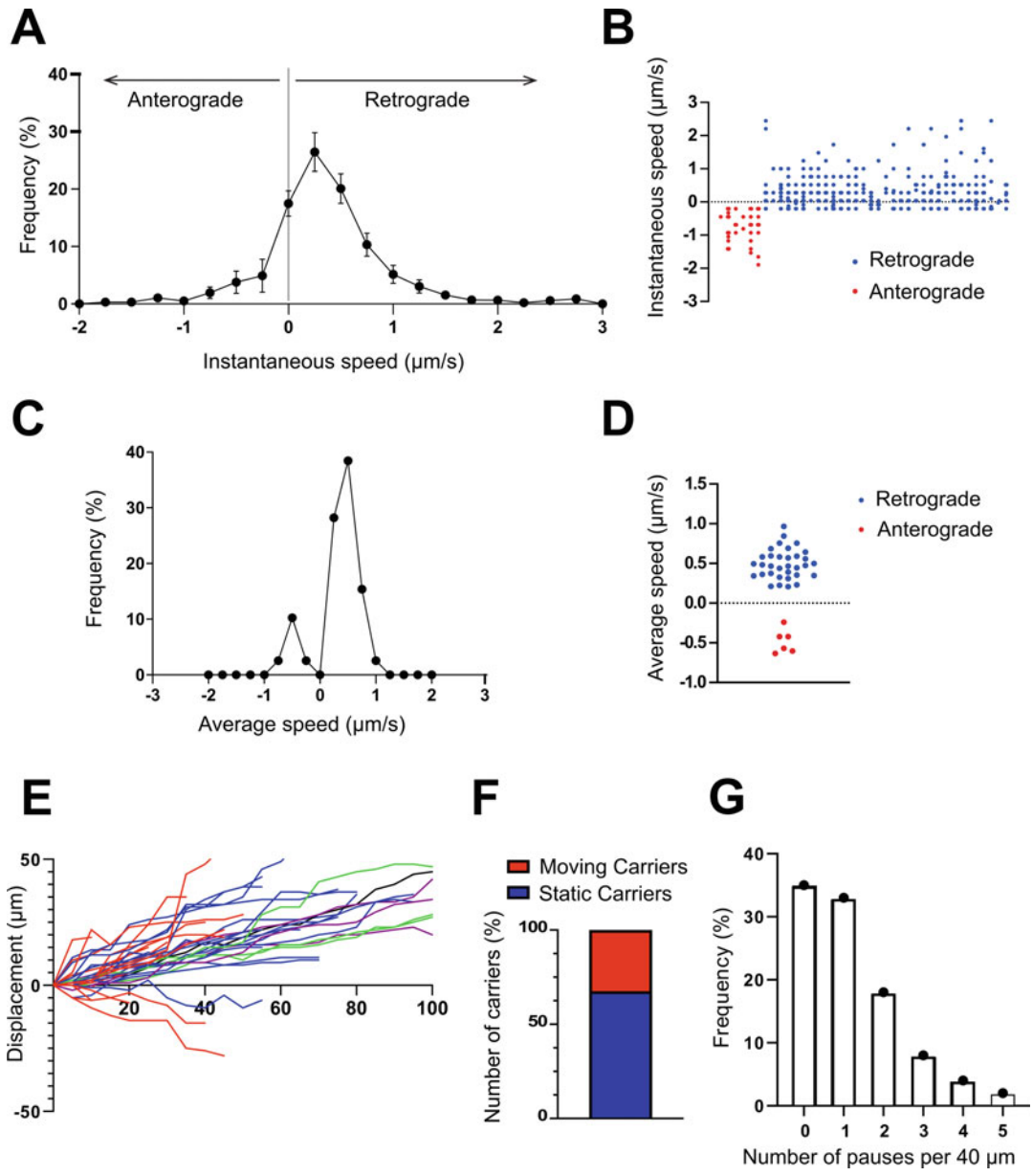

Fig. 5 Analysis of axonal lysosomal transport marked with LysoTracker™. (**a**) Frequency of retrograde and anterograde carriers associated with their instantaneous speed from 3 biological independent replicates. N = 3, ± s.e.m. (**b**) Instantaneous speed distribution of 39 carriers; both retrograde (blue) and anterograde (red) carriers. (**c**) Frequency of anterograde and retrograde carriers associated with their respective average speed. (**d**) Average speed distribution of each carrier; both retrograde (blue) and anterograde (red). (**e**) Displacement of each carrier within a 100 s time-frame. The different colors represent individual carriers moving for 50 (red), 100 (blue), 200 (green), 300 (purple) and more than 300 s (black). (**f**) Percentages of moving carriers (red) and static carriers (blue). (**g**) Frequency of carriers plotted against with their number of pause every 40 μm traveled

6. L15 medium: mix 445 ml of L15 media, 50 ml of fetal calf serum, 2.5 ml from 1 M Hepes stock, and 1 ml of Primocin™ (Invivogen). Keep the medium at 4 °C.
7. Percoll.
8. Papain stock solution (200 U/ml): 5 ml HBSS, 1000 units (100 mg) papain. Keep at 4 °C.
9. Collagenase–Dispase stock solution (10 mg/ml Collagenase and 12 mg/ml Dispase): 10 ml HBSS, 100 mg Collagenase II, 120 mg Dispase II. Aliquot to 1 ml and freeze at −20 °C.
10. 3.5 mm glass bottom dishes.
11. Nerve growth factor (NGF). Optional, to be applied to the axonal side at a concentration of 50 ng/ml.

2.3 Imaging of Axonal Transport

1. DRG neurons, 13 days in vitro (DIV) or longer after plating in MFCs.
2. LysoTracker™ Red DND-99.
3. HBSS solution: 440 ml of DDW, 50 ml of 10× HBSS, 2.5 ml of 1 M Hepes, 2.5 ml of 2 M D-Glucose, and 1 ml of Primocin™ (Invivogen). Titrate with 1 M NaOH until a pH of 7.35 is reached. Filter and keep in 50 ml tubes at 4 °C.

2.4 Analysis of Axonal Transport

1. ImageJ 1.53a (or later) with "Stack Builder" and "KymoToolBox™" plug-ins or Fiji.
2. Instantaneous speed MATLAB script (*see* **Note 1**).
3. Microsoft Excel and GraphPad Prism or equivalent software to open .csv files and perform statistical analysis/plotting of data.

3 Methods

3.1 Preparation of a Master Mold

This procedure requires a clean room and specialized costly equipment. We suggest to commission the fabrication of the master mold to a dedicated facility and/or a company. Our MFC design is detailed in Fig. 1a with the relevant dimensions of the chambers and microgrooves.

1. Clean the surface of a 10-in. silicon wafer was using a plasma cleaner for 3 min and place it on top of a hot plate at 150 °C for 10 min.
2. Place the clean wafer on top of a spin-coater, and pour the photoresist (mr_DWL_5) on it.
3. Spin the silicon wafer at 1400 × *g* for 45 s, to achieve a height of 7.8 μm.

4. Soft bake the wafer on top of a hot plate at 50 °C. Increase the temperature 10 °C every minute until it reaches 90 °C, and keep it there for 10 min.
5. Place the wafer inside a maskless lithography apparatus (Nano System solution, model Dlight DL-1000), and expose the wafer.
6. Put the wafer back on the hot plate at 50 °C, and increase the temperature 10 °C every minute until it reaches 70 °C. Keep said temperature for additional 10 min.
7. Develop the mold by submersion in PGMEA for 10 min. Wash the mold with IPA.
8. Clean the surface of the wafer with a plasma cleaner for 3 min and hard bake the master mold at 120 °C for 30 min.
9. To develop the main chamber structure, place the clean wafer in a spin-coater, and pour the photoresist (mr_DWL_40) on it.
10. Spin the silicon wafer at 68 × *g* for 45 s.
11. Soft bake the wafer on top of a hot plate at 50 °C, increasing the temperature 10 °C every minute until it reaches 90 °C. Keep the temperature at 90 °C for 10 min.
12. Put the wafer back in the spin-coater and pour a second layer of mr_DWL_40.
13. Spin the silicon wafer at 95 × *g* for 45 s to achieve a final height of 103 μm and soft bake as described in **step 11**.
14. Repeat **step 5** and **6**.
15. Develop the mold by submersion in PGMEA for 10 min. Wash the mold with IPA.
16. Clean the surface of the wafer with a plasma cleaner for 3 min and hard bake the master mold at 120 °C for 30 min. Plasma exposure might shorten the structure of the mold. The final height we achieved using the described protocol was 4.5 μm for the microchannels and 97 μm for the main channels.

3.2 Fabrication of a PDMS Device Using a Master Mold

1. Mix PDMS prepolymer and catalyst thoroughly with a 10:1 ratio, or according to the manufacturer instruction, in a disposable plastic cup. The mixture needs then to be degassed inside a vacuum desiccator for 20 min (*see* **Note 2**).
2. Once fully degassed, pour the PDMS mixture on top of the master mold that has been taped to a 10 cm silicone mold holder. Degas again for 10 min to make sure there are no microbubbles around the chambers (*see* **Note 3**).
3. Remove the silicone mold holder containing the PDMS from the desiccator chamber and transfer it inside a leveled laboratory oven for at least 3 h at 60 °C (*see* **Note 4**).

4. Once the PDMS is cured, cut out the MFCs individually using a razor blade following the 18 mm pattern guide and peel them off carefully from the mold. Be careful not to scratch the mold, as it will reduce its lifetime. When cutting the PDMS, do not touch the bottom side of the PDMS as it might disturb the delicate structure of the microgrooves (*see* **Note 5**).
5. Punch holes with a 5 mm and 1.5 mm stainless steel puncher on the second and first layer consecutively according to the schematic provided (Fig. 2a). It is advised to punch from the chamber side of the MFC. Use Scotch tape to remove any dust particles, as small particles might cause incomplete sealing and leakage of the chamber when assembled (*see* **Note 6**).

3.3 Assembly of a 2 Layered Microfluidic Chamber

In this protocol, we bond the MFC to a 3.5 glass bottom dish using plasma bonding (Fig. 2a). Plasma bonding increases surface energy and makes the attachment of the MFC to glass stronger. The increase of surface energy will stay for approximately 48 h, so it is advised that the assembly of the MFC should be done at most 2 days before cell culture. If a plasma cleaner is not available, reversible bonding using manual attachment is also possible. Reversible bonding, however, presents a higher risk of leakage and the MFC detaching from the glass bottom dish. Hence, we recommend using plasma bonding if possible.

1. Transfer the first MFC layer and the glass bottom dish inside the plasma cleaner. Turn the RF power and the vacuum pump on according to the manufacturer's instructions. After the pressure drops below 400 mTorr, set the plasma setting to high in order to ignite the plasma.
2. Leave the plasma on high for 30 s before turning it off and slowly opening the vacuum chamber. Once the pressure is back to 760 Torr, take out the MFC and the 3.5 mm glass bottom dish from the plasma cleaner, and carefully place the first layer of the MFC in the center of the glass bottom dish.
3. To make sure that the device is attached properly on the glass surface, push gently on the structure, especially on the microgrooves.
4. Add the second layer on top of the first layer by repeating **steps 6** and **7**. It is important to make sure that the 1.5 mm inlet on the first layer is accessible and located inside the 5 mm reservoir on the second layer.

3.4 Coating the Microfluidics Chamber for Cell Culture

In order to prevent contamination, it is important to perform the following steps inside a laminar flow hood.

1. Inject 100% EtOH into the main channels as well as the reservoirs to sterilize the MFC. Leave the chamber in EtOH for at least 10 min.
2. Wash the device with filtered milliQ water and let it dry for 30 min under the laminar flow.
3. Once the MFC has completely dried, inject 20 µl and 40 µl of PLL into the main chamber, as well as the reservoirs respectively. Leave the PLL in the device for at least 1 h at room temperature or overnight at 4 °C.
4. Aspirate the PLL and wash the device with filtered water as described in 2.
5. Thaw 100 µl of aliquoted laminin solution and add 1 ml of HBSS. Inject 20 µl and 40 µl of the diluted laminin into the main chamber and the reservoir respectively. Place the laminin coated device at 4 °C for 1 h, before aspirating all the laminin from the chamber.

3.5 DRG Neurons Preparation and Loading Inside the MFC

DRG neurons are collected from adult mice following the protocol described in [34]. Briefly (volumes are adjusted to total DRG dissection of 1 mouse):

1. While dissecting the DRG ganglia, prepare a solution of 0.5 ml of Papain added to 4.5 ml of HBSS. The Papain thus prepared needs to be activated at 37 °C for 30 min.
2. Spin the dissected DRG ganglia at 160 × *g* for 4 min and resuspend them in the activated Papain solution (previously filtered with a 0.22 µm syringe filter).
3. Digest the DRG ganglia at 37 °C for 30 min (*see* **Note 7**). During this time, prepare a Collagenase–Dispase solution for a second round of enzymatic digestion (1 ml Collagenase–Dispase stock solution added to 4 ml HBSS solution).
4. Spin the DRG ganglia at 160 × *g* for 4 min and resuspend them in the Collagenase–Dispase solution. Leave them at 37 °C for 30 min (*see* **Note 7**).
5. Spin the DRG ganglia at 160 × *g* for 4 min, resuspend them in 1 ml of HBSS solution and triturated mechanically using a 1 ml pipette (*see* **Note 8**).
6. Carefully layer the disaggregated DRG neurons on top of a Percoll cushion (1 ml of Percoll mixed in 4 ml of L15 medium).
7. Spin the cells at 160 × *g* for 8 min with the breaks removed to allow for a gentle deceleration.
8. Discarded the Percoll solution and add 2 ml of F12 medium to the neuronal pellet.
9. Spin the cells again for 5 min at 160 × *g* (leave the brakes on).

10. Dilute 5000 cells in 10 μl of F12 medium and inject them into the somal side of the MFC (Fig. 3a).
11. Leave the MFC inside the laminar hood for 2–5 min to allow the cells settle. Add 10 μl of additional F12 medium in the axonal chamber, and use 40 μl of F12 medium to fill each reservoir to prevent evaporation (*see* **Note 9**).
12. Place the MFC was placed inside an incubator at 37 °C and replace the medium daily by removing the F12 medium in the reservoirs and replacing it with 40 μl of fresh F12.

3.6 Axonal Transport Imaging

At 13 DIV, most of the axons should have passed the microgrooves and started to settle at the axonal side of the chamber (Fig. 3b). If NGF was added to the axonal side at a concentration of 50 ng/ml, the axonal network should be more pronounced. Adding growth factors, though, might affect axonal transport.

1. Thaw 0.1 μl of LysoTracker™ and dilute it with 200 μl of F12 medium.
2. Remove the F12 medium from the reservoirs on the axonal side. Fill one of the reservoirs with the diluted LysoTracker™ and let it flow into the other.
3. Remove the diluted LysoTracker™ from the reservoirs and repeat **step 3** before incubating the MFC at 37 °C for 1 h. This is done to assure that the axonal chamber is properly flashed and loaded with the dye.
4. Before imaging axonal transport, remove the medium for the axonal and somal side and replace it with 10 μl of HBSS per chamber. Add 40 μl of HBSS into each reservoir to prevent evaporation.
5. We used an Olympus FV10i-LV laser scanning confocal microscope with a 60× water immersion objective (NA 1.2) for the imaging. Any equivalent microscope equipped with an environmental chamber can be used. The cells should remain viable for imaging up to 30 min -1 h after replacing the medium with HBSS.
6. Allow a few minutes for the focus to stabilize. Select axons passing through the microgrooves. We recommend selecting a region of interest and use frame imaging (faster).
7. Depending on how stable the focus of the imaging setup is, the settings will be different. We use Z-stacks to prevent loss of focus during the acquisition of the video. In order to prevent laser damage to the axons, we acquire 1 stack every 5 s for 10 min. Depending on the microscope and laser settings, this time interval can be changed.
8. The movie files should be saved in a format that is readable by ImageJ. In our case, we used ".oif".

3.7 Axonal Transport Analysis

1. Open the movie files individually in ImageJ or Fiji. A menu-bar titled "Bio-Formats import Options" should appear. Make sure that "Hyperstack," "Open files individually," "Autoscale," and "Split channels" options are selected.
2. If needed, adjust brightness and contrast by selecting "Image > Adjust > Brightness and Contrast" from the menu.
3. Create a Z-stack projection by selecting "Image > Stack > Z project". Use the options "Average Intensity" and "All time frames" when generating the projection.
4. Select the "line selection tools" in ImageJ toolbar and set it to a segmented line. Draw a line along the entire length of the axon.
5. Build a Kymograph by selecting "Analyze > Multi Kymograph > Multi Kymograph". Set the width of the segmented line to be analyzed appropriately.
6. Save the Kymograph as a ".tiff" or ".jpeg" file (*see* **Note 10**).
7. Download the "Instantaneous Speed" script (*see* **Note 1**) and decompress it using WinRAR or WinZip.
8. The images that are to be processed can be saved in the same folder as the folder containing the software.
9. Open the file "Main_program_software_file.mat" in MATLAB. Set the name of the kymograph file to be processed accordingly in "line 11" of the script (or refer to the "how to use" file on the website in case the script is updated).
10. In Mac OS, the directory where the files are to be saved need to be the "Current Working Directory" in the MATLAB software. In Windows, the file will be saved in the C directory in the folder "C/Instantaneous_vel/".
11. Run the script by selecting "Editor > Run" on the menu bar of MATLAB, and an image of the kymograph will appear. The program works by calculating the pixels representing the time (y coordinate) and distance (x coordinate) traveled by a single carrier per frame. Follow the instructions of the "how to use"file in order to perform the quantification.
12. The analyzed data will be shown in the "Command Window" of MATLAB, and will be saved in a ".csv" file in the directory discussed in **step 10**.
13. Repeat **steps 11** and **12** for each carrier track.
14. Copy the instantaneous speed from all of the ".csv" files in one Excel file and use Prism or equivalent software to plot the desired parameters (instantaneous speed distribution, average instantaneous speed, displacement, and frequency) (Fig. 5).

4 Notes

1. We archived the MATLAB script, together with a brief instruction document on how to use it at this link: https://groups.oist.jp/mnu/productalgorithmsoftware. Updated versions of the software and instructions will be uploaded there.
2. The amount of PDMS needed depends on the desired height of the PDMS mold. This will also affect the height of the reservoirs. In this protocol, we use a 10 cm Teflon silicon mold holder, which has the height of 2 mm. The amount of the PDMS needed for this size is 18 grams of PDMS with 1.8 grams of curing agent.
3. If a silicon mold holder cannot be obtained, a petri dish can be used as an alternative. Make sure that the PDMS can fit inside the petri dish, and that the petri dish is not too big as it would consume a large amount of PDMS. We recommend taping the silicon master mold onto the petri dish to prevent it from lifting when the PDMS is poured, causing the surface to be uneven.
4. The surface of the oven where the PDMS is placed should be even. The amount of time required to bake the PDMS depends on the amount of PDMS to be baked. For 20 grams of PDMS, 3 h should be enough. Nevertheless, we recommend baking the PDMS for at least 4 h to ensure the PDMS is cured.
5. When cutting the PDMS, make sure that the PDMS is cut all the way to the surface of the master mold. Do not put too much pressure when cutting the PDMS mold as the master mold is delicate and can break easily.
6. Scotch tape can be placed on the chamber side of the PDMS to make punching holes easier. In order to ensure that the inlet is located inside the reservoir, the second layer should be punched first and aligned on top of the first layer when the inlet is punched.
7. Both digestions with Papain and Collagenase–Dispase can be performed in the incubator. The digestion time can be increased to 40–45 min to make the mechanical disaggregation easier.
8. Make sure to coat the pipette's tip with L15 medium containing serum. This is critical to avoid loss of cells due to their attachment to the pipette's tip.
9. In this protocol we use around 5000 cells for a single MFC. If a higher number of cells is needed, cells can be diluted with a lower volume of F12 medium. It is also possible to inject additional cells (5 μl volume) from the opposite inlet from the first injection in the somal side. We advise to inject the cells slowly not to flush away the cells that already settled in.

10. It is important to make sure that the kymographs are saved correctly as a .tiff file. If the image on MATLAB fails to load properly, it might have not been saved correctly in ImageJ.

Acknowledgments

We thank the OIST Imaging Section for providing access to Nikon A1R laser confocal system and a scanning electron microscope, and the Mechanical Engineering and Microfabrication Support Section for their support in the MFC generation. We thank Prof. Amy Shen for fruitful discussion about the MFC design. M.F.E. and M.T. participated in the design and writing of this method paper. M.F.E., M.O., P.B., and M.T. collected and analyzed the experimental data. L.A. designed and implemented the script for axonal transport quantification. This work was generously funded by JSPS/Kakenhi #20K07458 to M.T. The authors declare not to have any conflict of interests.

References

1. Vale RD (2003) The molecular motor toolbox for intracellular transport. Cell 112:467–480
2. Sweeney HL, Holzbaur ELF (2018) Motor proteins. Cold Spring Harb Perspect Biol 10: a021931
3. De Pace R, Britt DJ, Mercurio J, Foster AM, Djavaherian L, Hoffmann V, Abebe D, Bonifacino JS (2020) Synaptic vesicle precursors and lysosomes are transported by different mechanisms in the axon of mammalian neurons. Cell Rep 31:107775
4. Schiavo G, Greensmith L, Hafezparast M, Fisher EMC (2013) Cytoplasmic dynein heavy chain: the servant of many masters. Trends Neurosci 36:641–651
5. Maday S, Twelvetrees AE, Moughamian AJ, Holzbaur ELF (2014) Axonal transport: cargo-specific mechanisms of motility and regulation. Neuron 84:292–309
6. Sleigh JN, Rossor AM, Fellows AD, Tosolini AP, Schiavo G (2019) Axonal transport and neurological disease. Nat Rev Neurol 15: 691–703
7. Guillaud L, El-Agamy SE, Otsuki M, Terenzio M (2020) Anterograde axonal transport in neuronal homeostasis and disease. Front Mol Neurosci 13:556175
8. Kim HJ, Park JW, Byun JH, Poon WW, Cotman CW, Fowlkes CC, Jeon NL (2012) Quantitative analysis of axonal transport by using compartmentalized and surface micropatterned culture of neurons. ACS Chem Neurosci 3:433–438
9. Yong Y, Hughes C, Deppmann C (2020) A microfluidic culture platform to assess axon degeneration. Methods Mol Biol 2143:83–96
10. Cheriyan T, Ryan DJ, Weinreb JH, Cheriyan J, Paul JC, Lafage V, Kirsch T, Errico TJ (2014) Spinal cord injury models: a review. Spinal Cord 52:588–595
11. Xiong Y, Mahmood A, Chopp M (2013) Animal models of traumatic brain injury. Nat Rev Neurosci 14:128–142
12. Jadhav AD, Wei L, Shi P (2016) Compartmentalized platforms for neuro-pharmacological research. Curr Neuropharmacol 14:72–86
13. Campenot RB (1977) Local control of neurite development by nerve growth factor. Proc Natl Acad Sci U S A 74:4516–4519
14. Park JW, Kim HJ, Byun JH, Ryu HR, Jeon NL (2009) Novel microfluidic platform for culturing neurons: culturing and biochemical analysis of neuronal components. Biotechnol J 4: 1573–1577
15. Wang J, Ren L, Li L, Liu W, Zhou J, Yu W, Tong D, Chen S (2009) Microfluidics: a new cosset for neurobiology. Lab Chip 9:644–652
16. Whitesides GM (2006) The origins and the future of microfluidics. Nature 442:368–373
17. Taylor AM, Blurton-Jones M, Rhee SW, Cribbs DH, Cotman CW, Jeon NL (2005) A microfluidic culture platform for CNS axonal injury,

regeneration and transport. Nat Methods 2: 599–605

18. Park JW, Vahidi B, Taylor AM, Rhee SW, Jeon NL (2006) Microfluidic culture platform for neuroscience research. Nat Protoc 1: 2128–2136
19. Gamage KK, Cheng I, Park RE, Karim MS, Edamura K, Hughes C, Spano AJ, Erisir A, Deppmann CD (2017) Death receptor 6 promotes Wallerian degeneration in peripheral axons. Curr Biol 27:890–896
20. Millet LJ, Gillette MU (2012) New perspectives on neuronal development via microfluidic environments. Trends Neurosci 35:752–761
21. Haberberger RV, Barry C, Dominguez N, Matusica D (2019) Human dorsal root ganglia. Front Cell Neurosci 13:271
22. Jocher G, Mannschatz SH, Offterdinger M, Schweigreiter R (2018) Microfluidics of small-population neurons allows for a precise quantification of the peripheral axonal growth state. Front Cell Neurosci 12:166
23. Ferguson SM (2018) Axonal transport and maturation of lysosomes. Curr Opin Neurobiol 51:45–51
24. Lie PPY, Nixon RA (2019) Lysosome trafficking and signaling in health and neurodegenerative diseases. Neurobiol Dis 122:94–105
25. Rosa-Ferreira C, Munro S (2011) Arl8 and SKIP act together to link lysosomes to kinesin-1. Dev Cell 21:1171–1178
26. Gowrishankar S, Yuan P, Wu Y, Schrag M, Paradise S, Grutzendler J, Camilli PD, Ferguson SM (2015) Massive accumulation of luminal protease-deficient axonal lysosomes at Alzheimer's disease amyloid plaques. Proc Natl Acad Sci U S A 112:E3699–E3708
27. Torres M, Jimenez S, Sanchez-Varo R, Navarro V, Trujillo-Estrada L, Sanchez-Mejias-E, Carmona I, Davila JC, Vizuete M, Gutierrez A, Vitorica J (2012) Defective lysosomal proteolysis and axonal transport are early pathogenic events that worsen with age leading to increased APP metabolism and synaptic Abeta in transgenic APP/PS1 hippocampus. Mol Neurodegener 7:59
28. Lee S, Sato Y, Nixon RA (2011) Lysosomal proteolysis inhibition selectively disrupts axonal transport of degradative organelles and causes an Alzheimer's-like axonal dystrophy. J Neurosci 31:7817–7830
29. Liang C, Shao Q, Zhang W, Yang M, Chang Q, Chen R, Chen J-F (2019) Smcr8 deficiency disrupts axonal transport-dependent lysosomal function and promotes axonal swellings and gain of toxicity in C9ALS/FTD mouse models. Hum Mol Genet 28:3940–3953
30. Farfel-Becker T, Roney JC, Cheng X-T, Li S, Cuddy SR, Sheng Z-H (2019) Neuronal soma-derived degradative lysosomes are continuously delivered to distal axons to maintain local degradation capacity. Cell Reports 28:51–64.e4
31. Cioni J-M, Lin JQ, Holtermann AV, Koppers M, Jakobs MAH, Azizi A, Turner-Bridger B, Shigeoka T, Franze K, Harris WA, Holt CE (2019) Late endosomes act as mRNA translation platforms and sustain mitochondria in axons. Cell 176:56–72.e15
32. Zhang K, Osakada Y, Xie W, Cui B (2011) Automated image analysis for tracking cargo transport in axons. Microsc Res Tech 74: 605–613
33. Neumann S, Chassefeyre R, Campbell GE, Encalada SE (2017) KymoAnalyzer: a software tool for the quantitative analysis of intracellular transport in neurons. Traffic 18:71–88
34. Melli G, Höke A (2009) Dorsal root ganglia sensory neuronal cultures: a tool for drug discovery for peripheral neuropathies. Expert Opin Drug Discov 4:1035–1045

Part IV

Human-Derived Neurons

Chapter 15

High-Resolution Imaging of Mitochondria and Mitochondrial Nucleoids in Differentiated SH-SY5Y Cells

Emily Annuario, Kristal Ng, and Alessio Vagnoni

Abstract

Mitochondria are highly dynamic organelles which form intricate networks with complex dynamics. Mitochondrial transport and distribution are essential to ensure proper cell function, especially in cells with an extremely polarised morphology such as neurons. A layer of complexity is added when considering mitochondria have their own genome, packaged into nucleoids. Major mitochondrial morphological transitions, for example mitochondrial division, often occur in conjunction with mitochondrial DNA (mtDNA) replication and changes in the dynamic behaviour of the nucleoids. However, the relationship between mtDNA dynamics and mitochondrial motility in the processes of neurons has been largely overlooked. In this chapter, we describe a method for live imaging of mitochondria and nucleoids in differentiated SH-SY5Y cells by instant structured illumination microscopy (iSIM). We also include a detailed protocol for the differentiation of SH-SY5Y cells into cells with a pronounced neuronal-like morphology and show examples of coordinated mitochondrial and nucleoid motility in the long processes of these cells.

Key words SH-SY5Y cells, Mitochondria, Nucleoids, Mitochondrial DNA, Axonal transport, Mitochondrial fission, Neuronal differentiation, Instant structured illumination microscopy (iSIM), Superresolution

1 Introduction

Neurons are highly polarised cells with long axons and dendrites. Due to their peculiar architecture, neurons are particularly reliant on long-range intracellular transport mechanisms to efficiently distribute organelles, proteins, and other cargoes with spatiotemporal precision [1, 2]. This process is crucial to maintain neuronal

Emily Annuario and Kristal Ng contributed equally to this work.

Supplementary Information The online version of this chapter (https://doi.org/10.1007/978-1-0716-1990-2_15) contains supplementary material, which is available to authorized users.

Alessio Vagnoni (ed.), *Axonal Transport: Methods and Protocols*,
Methods in Molecular Biology, vol. 2431, https://doi.org/10.1007/978-1-0716-1990-2_15,
© The Author(s) 2022

function, and transport defects have been shown to be involved in several neurodegenerative disorders [3].

Mitochondria are essential neuronal cargoes, whose efficient transport is crucial for maintaining neuronal homeostasis through calcium buffering, metabolite synthesis and provision of ATP at sites with high energy demand, such as synapses [4, 5]. Not surprisingly, disruption of mitochondrial transport has been shown to alter neuronal functionality and prime neurons for degeneration [6]. Mitochondria are unique axonal transport cargoes as the majority of them can remain stationary for significant amounts of time, which is unusual for most axonal cargoes [7]. Despite the fact that only a fraction of mitochondria are motile in neurons, the importance of their transport is underscored by the increasing evidence that reduced axonal motility of these organelles can be considered a hallmark of ageing and neurodegeneration [8].

Mitochondria are the only organelles harbouring their own genome, a trace of their prokaryotic origin and symbiotic incorporation into eukaryotic cells [9, 10]. The mitochondrial genome is distinct from that stored in the nucleus of the cell and encodes 13 essential subunits of respiratory chain complexes, 22 tRNAs and 2 rRNAs necessary for their translation [11, 12]. The mitochondrial DNA (mtDNA) is located in the mitochondrial matrix and is condensed in small ~100-nm [13] nucleoprotein complexes called nucleoids, by the mtDNA binding protein mitochondrial transcription factor A (TFAM), a key regulator of mtDNA replication and transcription [14, 15].

Live-imaging experiments have shown nucleoids to be highly dynamic structures that are able to redistribute through the mitochondrial network via mitochondrial fission and fusion [11, 16, 17]. Repositioning and/or redistribution of the nucleoids during mitochondrial morphological transitions are intimately linked to the replication of mtDNA. Thus, mtDNA replication marks the site of ER-mediated mitochondrial constriction and subsequent DRP1-dependent fission, thus priming the organelles for division [18, 19]. On the other hand, mitochondrial fusion aids in the redistribution of mtDNA throughout the mitochondrial network, ensuring mitochondrial integrity and functionality are retained throughout the network [20].

To date, many models for the study of mitochondrial dynamics in neurons have been established in cultured cells and in model organisms. Model organisms are extremely beneficial for in vivo studies of axonal transport in a physiological context [21–31], with the potential added advantage of observing changes that occur during organismal ageing [32–36]. On the other hand, in vitro models for trafficking studies, such as primary neuronal cultures and iPSCs, can be more easily manipulated and afford greater flexibility for pharmacological and genetic manipulation [21, 37–46]. These models, however, have not yet been used

extensively to study nucleoid dynamics, except in some instances [47]. Axonal trafficking of nucleoids has rarely been investigated and how mitochondrial dynamics affects the distribution of nucleoids in neuronal cells of human origin is currently unknown.

In this chapter, we describe a protocol to image mitochondrial and nucleoid dynamics in differentiated SH-SY5Y cells. This cell line is a clone of the SK-N-SH neuroblastoma cell line originally isolated from a human metastatic bone marrow [48] and can be differentiated to produce cells that express neuronal markers and have mature neuronal morphology [49, 50]. The simplicity and efficiency of the differentiation protocol, combined with the human origin of this cell line, the ease of maintenance and mass expansion at relative low cost, make SH-SY5Y cells an advantageous alternative to iPSCs and primary neuronal cultures for routine studies of intracellular trafficking. This system can be easily established in most laboratories and the findings obtained with this system could then be validated in primary neuronal cultures or in model organisms.

We detail how to obtain differentiated SH-SY5Y cultures exhibiting extended neuronal-like processes which facilitate the visualization of long-range mitochondrial and nucleoid transport in this compartment. Additionally, we show examples of the coordinated movements of instant structured illumination microscopy (iSIM)-resolved mitochondria and nucleoids structures, including different modes of nucleoid partitioning during mitochondrial fission in the neurites of these cells.

2 Materials

2.1 Culture and Differentiation of SH-SY5Y Cells

1. SH-SY5Y neuroblastoma cell line (ATCC CRL-2266) routinely cultured in T75 flasks and plated on Ibidi μ-Slide 8 Well Glass Bottom slides (Ibidi, #80827) coated with 5 μg/cm^2 poly-D-lysine (PDL) for differentiation.
2. SH-SY5Y standard culture medium: add 45 mL of Heat Inactivated FBS (10% v/v, ThermoFisher #10500064) and 5 mL of 200 mM L-Glutamine, to 450 mL of DMEM (ThermoFisher, supplemented with 4.5 g/L D-Glucose and 0.11 g/L pyruvate).
3. 0.25% Trypsin–EDTA
4. Phosphate buffered saline (PBS).
5. Hemocytometer for counting cells.
6. *Phase I medium*: to 47 mL of DMEM F12 (ThermoFisher, supplemented with 542 mg/L GlutaMAX) add 500 μL penicillin–streptomycin (10,000 U/mL, 100×), 2.5 mL of FBS (5% v/v), and 50 μL of EC23 at a final concentration of 10 μM.

7. *Phase II medium*: to 48.5 mL of Neurobasal-A (ThermoFisher) add 500 µL of 200 mM L-glutamine, 500 µL of N2 Supplement (100×, ThermoFisher), 500 µL penicillin–streptomycin (10,000 U/mL, 100×), and 2.5 µL of BDNF at a final concentration of 50 ng/mL.

2.2 Transfection of SH-SY5Y Cells

1. NeuroMag transfection reagent (OzBiosciences, #NM50500).
2. Magnetic plate.

2.3 Imaging of Cell Morphology, Mitochondrial and Nucleoid Transport in Differentiated SH-SY5Y Cells

1. Confocal microscope. We use the following settings.
   (a) For recording cell morphology during differentiation using phase contrast imaging.
   Nikon A1R equipped with a PMT detector, a 40× Plan Fluor ELWD Ph2 ADM dry objective (0.6NA) using a Ph2 condenser. Images were acquired upon sample excitation at 513 nm (*see* **Note 1**). For immunofluorescence images, the same microscope is used with 60 × CFI Apo oil-immersion objective (1.4 NA).
   (b) For high-resolution imaging of nucleoid and mitochondrial motility.
   Nikon inverted Ti-E equipped with Vt-iSIM head (Vistech), Hamamatsu Orca Flash 4.0sCMOS camera fitted with a 100× CFI TIRF oil-immersion objective (1.49 NA).
   For both (a) and (b), imaging was performed at constant temperature of 37 °C and 5% CO_2 using a microscope enclosure with temperature and CO_2 control (Okolab).
2. 1 mM MitoTracker Deep Red (ThermoFisher): add 91.98 µL of DMSO to the 50 µg of lyophilized MitoTracker. Divide into aliquots and store at −20 ° C.
3. 1:100 dilution of SYBR Gold: 1 µL of the commercial stock of SYBR Gold (10′000×, ThermoFisher, #S11494) is diluted in 99 µL DMSO to create the working stock.
4. 1× CellMask Green staining solution: 1 µL of the commercial stock of CellMask Green (1′000×, ThermoFisher, #C37608) is diluted 1:1′000 in culture media to be used to perform CellMask staining.
5. Imaging chambers.

2.4 Analysis of Mitochondrial and Nucleoid Transport

1. Fiji/Image J (https://fiji.sc/ or http://rsbweb.nih.gov/ij/).
2. ImageJ software featuring the following plugins: Stack Reg (Philippe Thevenaz, EPFL, Switzerland), Straighten (Eva Kocsis, NIH, USA), and Velocity Measurement Tool (http://dev.mri.cnrs.fr/projects/imagej-macros/wiki/Velocity_Measurement_Tool).

3 Methods

The SH-SY5Y cell line was shown to be composed of two cellular subpopulations: substrate adherent epithelial-like (S-type) and neuroblastic (N-type) cells, with the latter undergoing differentiation to produce neuronal-like cells [49, 51]. Currently, a number of differentiation protocols exist which utilize various neutralizing agents that can drive differentiation toward a more cholinergic, adrenergic, or dopaminergic phenotypes [52, 53]. Due to the versatility of the differentiation protocols, SH-SY5Y cells have been extensively used as disease models for different neurological disorders. They have been largely employed to model several aspects of Parkinson's disease biology [52, 54, 55], but they were also exploited to study Alzheimer's disease-related insults [56] and neurodevelopment in the context of psychiatric disorders [57].

Retinoic Acid (RA)-mediated differentiation protocols have been shown to induce differentiation into cells with higher choline acetyltransferase activity [58–60], while other studies have focused on a more dopaminergic phenotype [61]. RA has also been often used in combination with other agents, such as 12-O-tetradecanoylphorbol-13-acetate (TPA), for a more efficient induction of cells with a dopaminergic phenotype, for example increased expression of tyrosine hydroxylase (TH), the dopamine transporter (DAT), and dopamine receptor subtypes 2 and 3 [62–64]. If desirable, treating SH-SY5Y cells with siRNA targeting the splicing factor PTBP1 prior to differentiation could be used to potentiate neurite outgrowth, as reported for SH-SY5Y cybrids [65].

For the purpose of studying trafficking, the combination of RA treatment with decreasing amounts of serum, followed by the addition of neurotrophic factors such as BDNF, has been shown to be particularly effective in promoting neurite extension during neuronal differentiation [66–68], with the end point of differentiation defined as commitment to a neuronal phenotype with long extended processes [69]. SH-SY5Y cells expressing a truncated form of spastin have been used to study the trafficking of synaptophysin-positive vesicles [70]. Furthermore, mitochondrial trafficking was found to be perturbed in SH-SY5Y cells differentiated with RA and BDNF for 8 days in vitro and overexpressing the A53T α-synuclein mutant [67], indicating the suitability of the differentiation protocol to study trafficking in neuronal processes.

We differentiated SH-SY5Y cells by adapting a protocol published by Forster et al. [68], which requires the addition of neutralizing agents such as EC23 (a synthetic analog of all-trans retinoic acid [71–73]) and BDNF to sustain neurite outgrowth (Fig. 1a). Coating matrices, seeding densities and time in vitro were optimised to ensure the morphology of the cells was suitable for neurite tracking, that is, cultures sparse enough to visualise long

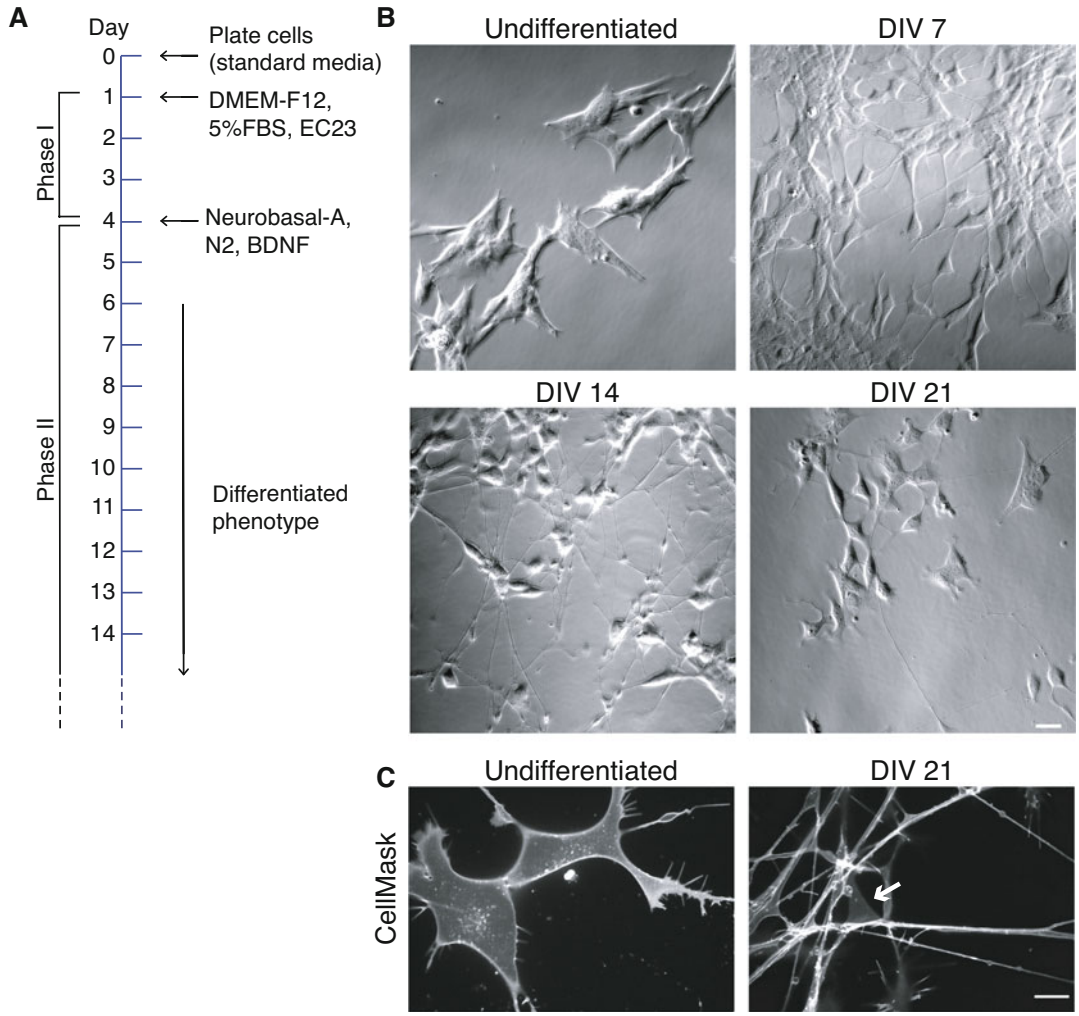

Fig. 1 SH-SY5Y differentiation protocol. (**a**) Timeline of the SH-SY5Y differentiation protocol outlining the media changes and the different supplements provided. After 1 week in culture, the cells start displaying a clear neuronal-like phenotype ('Differentiated phenotype'). (**b**) Representative images of live SH-SY5Y cultures before the start of the differentiation protocol ('Undifferentiated') and during the first (DIV 7), second (DIV 14) and third (DIV 21) week of differentiation. Scale bar: 25 μm. (**c**) Higher magnification images of live SH-SY5Y cells stained with the vital dye CellMask Green (CellMask) to mark plasma membrane compartments. Cells at DIV 21 of differentiation display a dramatic change in cellular morphology compared to undifferentiated cells, including the extension of long processes and reduced somal volume. Arrow indicates a cell body. Scale bar: 10 μm

processes derived from a specific cell body but without compromising their survival. Morphological assessments via phase contrast image acquisition (Fig. 1b) and staining of plasma membrane compartments (Fig. 1c), immunocytochemistry (ICC) and biochemical analysis (Fig. 2) validate our differentiation protocol. Figure 1b shows the progression of typical SH-SY5Y cultures throughout

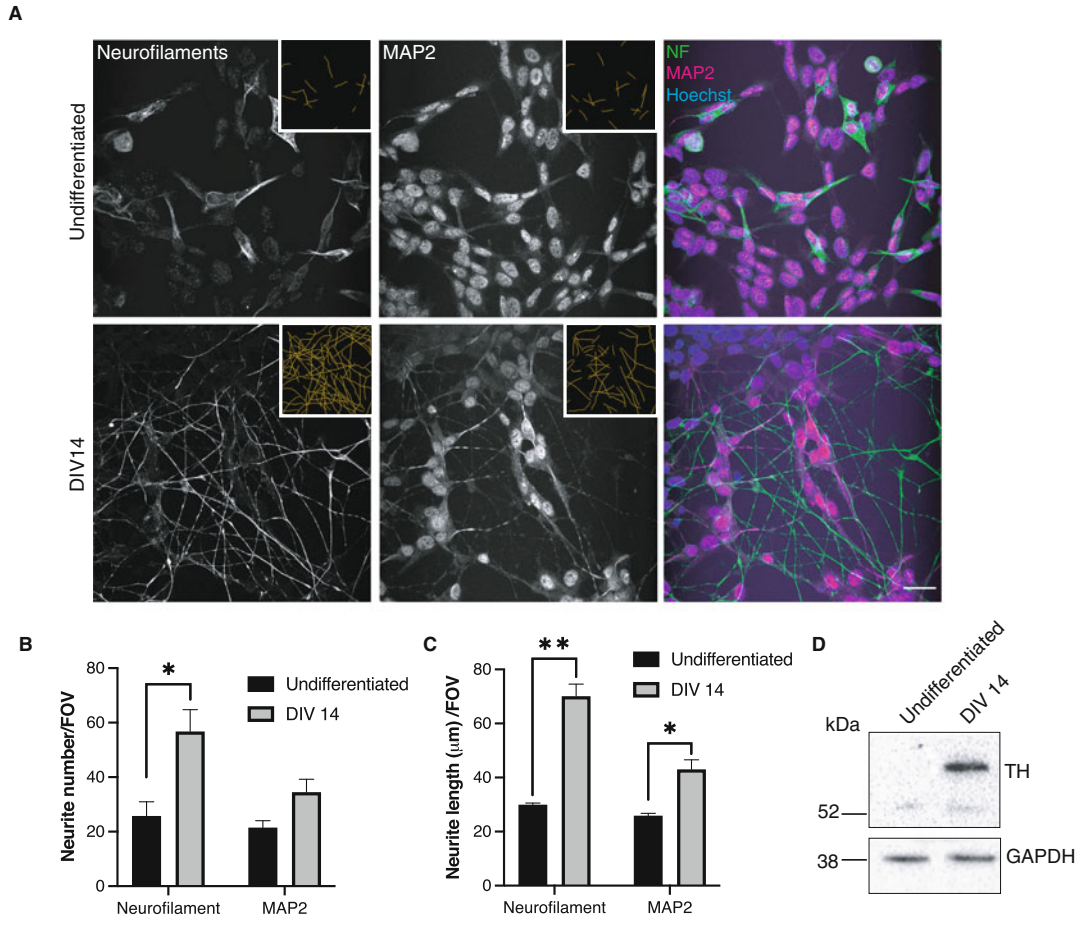

Fig. 2 Neuronal markers in differentiated SH-SY5Y cells. (**a**) Representative images of undifferentiated and DIV 14 cultures stained for neurofilaments and MAP 2. Panels on the right show the markers merged with the Hoechst nuclear staining. Inserts show the neurites traced with NeuronJ for each channel. Each image represents a Z-stack projection of 40 and 30 planes for the undifferentiated and DIV 14 images, respectively. Scale bars: 25 μm. (**b**) Quantification of neurite number and length indicates a higher number of neurites positive for the neurofilament and MAP 2 staining in differentiated cells. (**c**) Neurofilament and MAP 2-positive neurites are significantly longer in DIV 14 cells. In (**b**) and (**c**), quantifications were done on 8 fields of view (FOV) of 212.13 μm by 212.13 μm. Data are presented as mean ± s.e.m. $*P \leq 0.05$; $**P \leq 0.01$, Multiple *t*-tests. (**d**) Western blot showing upregulation of tyrosine hydroxylase (TH) in differentiated SH-SY5Ys compared to undifferentiated cultures. GAPDH is used as loading control

the differentiation protocol, with a noticeable increase in neurite extension, accompanied by clustering of cellular somata, already visible around DIV7 and with a clear network of neuronal-like processes around DIV14 (*see* **Note 2**). Figure 2 shows substantial upregulation of neuronal markers (neurofilaments, MAP 2, Fig. 2a–c), including markers for catecholaminergic neurons (tyrosine hydroxylase, Fig. 2d) in differentiated cells compared to undifferentiated SH-SY5Y. A significant increase in the number of

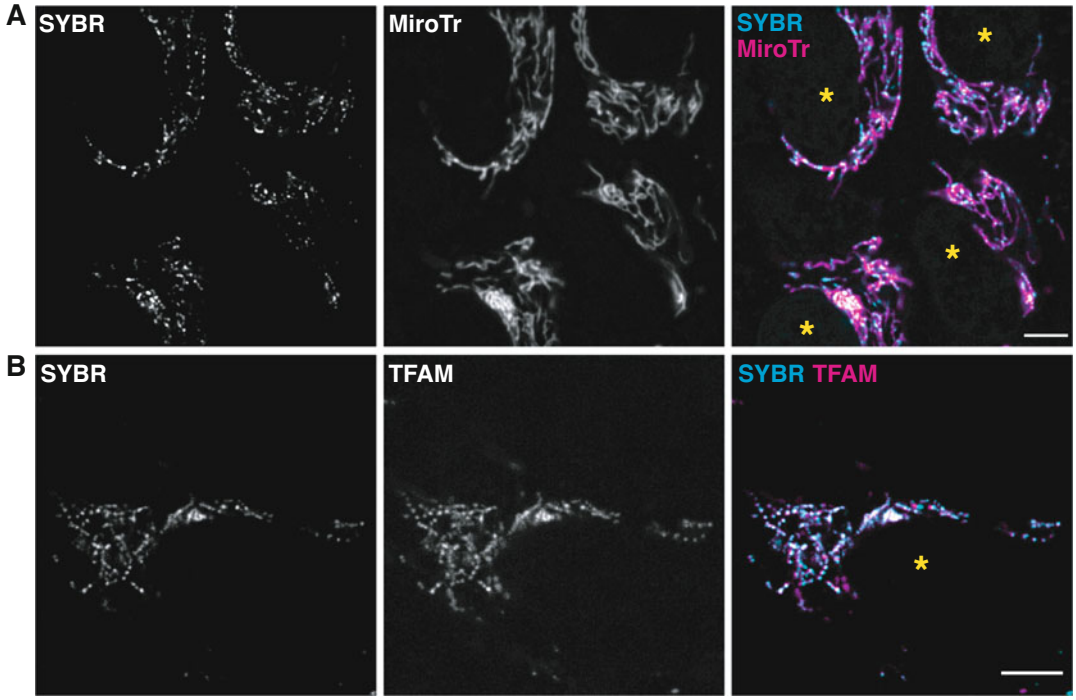

Fig. 3 Visualisation of mitochondria and nucleoids in live undifferentiated SH-SY5Y cells. (**a**) SH-SY5Y cells were stained with SYBR Gold (SYBR) and MitoTracker Deep Red (MitoTr) to visualise the mtDNA and the mitochondria, respectively. The merge pseudocolored image shows the distribution of mtDNA puncta (SYBR, cyan) within the mitochondrial network (MitoTr, magenta). (**b**) Cells were transfected with TFAM m-Scarlet to mark nucleoids and stained with SYBR Gold to visualise the mtDNA. Right panel: merge image showing extensive colocalization between TFAM (magenta) and mtDNA (SYBR, cyan). Yellow asterisks indicate the position of the nuclei. Scale bars: 5 μm

axonal-like, neurofilament positive neurites can be observed, which were also significantly longer than the sparser processes extended by undifferentiated cells (Fig. 2b, c).

SH-SY5Y cells stained with the SYBR Gold nucleotide dye at low concentration [74] display a discrete punctuated pattern that colocalises with the mitochondrial network (Fig. 3a), indicative of specific nucleoid staining. Overexpression of the fluorescently tagged nucleoid protein TFAM, a major component of mammalian nucleoids and routinely used as nucleoid marker, results in extensive colocalization between TFAM and the SYBR signals (Fig. 3b), thus confirming SYBR Gold as a suitable dye for the visualisation of nucleoids in these cells. In the neurites of differentiated cells, mitochondria and nucleoids exhibit robust motility with most mitochondria containing at least one nucleoid when observed by live-cell iSIM imaging (Figs. 4 and 5 and Movies 1 and 2). Differentiated SH-SY5Y cells have been recently used for imaging the movement of synaptic vesicles by single-molecule localization microscopy [75]. Our protocol shows the suitability of this system

for studying long-range cotransport of mitochondria and nucleoids by live super-resolution imaging. The method also lends itself to studying the partitioning and distribution of nucleoids during mitochondrial dynamics in the neurites of the cells. Figures 4 and 5 show that nucleoids can be distributed differently into daughter mitochondria during fission in the processes, and mitochondria devoid of nucleoids can arise after mitochondrial division, as recently shown in Cos-7 cells and mouse cardiomyocytes [76].

3.1 Differentiation of SH-SY5Y cells into Neuronal-like Cells

1. On the first day of the differentiation protocol, coat the wells of an 8 well Ibidi chamber with PDL matrix by adding 4 µL of 10 mg/mL PDL to 2 mL autoclaved MilliQ water and incubate at 37 °C for at least 2 h. We coat each Ibidi well (1 cm^2) with 250 µL of matrix solution (*see* **Note 3**).
2. Wash the wells 3× times with PBS and allow them to dry out prior to seeding cells. Ensuring the PDL has dried out will improve cell adhesion.
3. Add 1 mL of Trypsin-EDTA (approximately 0.014 mL/cm^2) to a T75 flask of undifferentiated SH-SY5Y cells and leave for 3 min to detach the cells.
4. Add 4 mL of standard media to detached cells (total 5 mL), collect the cell suspension in a falcon tube, spin at 300 × *g* for 3 min, and resuspend the pellet in 3 mL.
5. Make a 1:5 dilution of cells in Trypan blue (50 µL cells plus 200 µL Trypan Blue) and count cells with an hemocytometer.
6. Seed SH-SY5Y cells at a density of 15′000 cells/cm^2 and keep them in their standard culture medium overnight (300 µL/well) (*see* **Note 4**).
7. The following day change the standard medium to 300 µL of Phase I medium containing the retinoic acid receptor agonist EC23. This starts the differentiation process and is referred to as DIV 1 (Fig. 1a).
8. After 72 h, on DIV 4, change medium to 300 µL Phase II containing BDNF to sustain neurite outgrowth. This is the medium used throughout the rest of the experiment and is changed every 3–4 days (*see* **Note 5**).
9. Assess cell differentiation daily by brightfield or phase contrast microscopy (Fig. 1b). At key timepoints (Fig. 1a), markers of cell differentiation can be verified by ICC, western blotting and CellMask staining (Fig. 2 and *see* **Note 6**).

3.2 Transfection of SH-SY5Y Cells

If transfection is required to visualise fluorescent organelles or proteins, we suggest performing it 48 h before imaging (e.g., DIV 12 for imaging DIV 14). For each well of an Ibidi µ-Slide 8-well Glass Bottom slide:

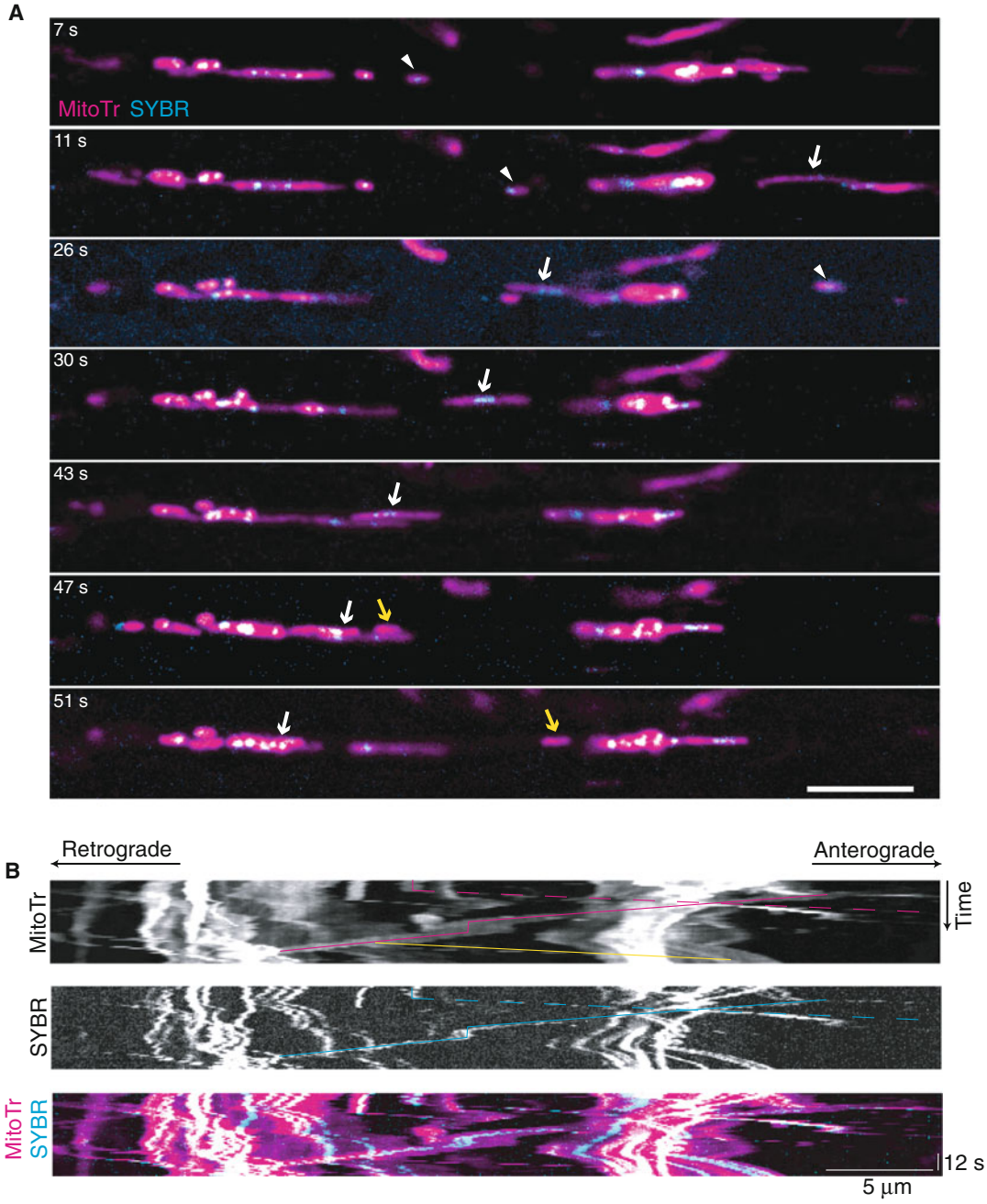

Fig. 4 Visualisation of mitochondria and nucleoids dynamics in neurites of differentiated SH-SY5Y (relative to Movie 1). Cells were stained with SYBR Gold (SYBR) and MitoTracker Deep Red (MitoTr) to visualise the mtDNA and the mitochondria, respectively. (**a**) Still frames showing mitochondria moving in a neurite of DIV 14 cells. The arrowhead indicates a unidirectional movement of a mitochondrion (magenta) containing a nucleoid punctum (cyan). The white arrow shows an example of a mitochondrion that undergoes fission during transport (47 s), with the two resulting mitochondria (white and yellow arrows) moving in opposite directions. The nucleoid puncta are partitioned within the same mitochondrion after fission, with one mitochondrion seemingly devoid of mtDNA (yellow arrow). Scale bar: 5 µm. (**b**) Kymographs of mitochondrial (MitoTr) and mtDNA (SYBR) dynamics. The dashed lines in magenta (MitoTr) and cyan (SYBR) highlight the mitochondrial

1. Seed the cells as described in Subheading 3.1 for the transfection of differentiated cells. For transfection of undifferentiated cells, cells are plated the day before at a density of 55′000/cm^2.
2. Tube 1: Mix 0.6 μL of NeuroMag in 24.4 μL 1× PBS.
3. Tube 2: Mix 0.3 μg of DNA in a final volume of 25 μL 1× PBS and flick tube to mix DNA.
4. Add the contents of the tubes together, mix well by flicking and leave to incubate for 20 min in the hood. The ratio of NeuroMag to DNA is 2:1 in a volume of 50 μL (*see* **Note 7**). This ratio should be maintained if scaling experiments into different vessels.
5. Remove enough conditioned media from cells to leave a volume of 200 μL in each well.
6. Add the transfection solution dropwise onto cells, ensuring it spreads evenly within the well and incubate at 37 °C for 30 min on the magnetic plate.
7. Remove the magnetic plate and leave the transfection mix to incubate for 48 h, until imaging or subsequent experiments.

3.3 Imaging Transport of Mitochondria and Nucleoids in Differentiated SH-SY5Y Cells

1. One hour before imaging, prepare the medium containing dyes by thawing the aliquots and diluting as follows (we recommend preparing serial dilutions):
   (a) 1:5′000 of the 1 mM MitoTracker Deep Red, for a final solution of 200 nM in imaging media
   (b) 1:2′000 of the previously made 1:100 SYBR Gold stock.
2. Remove media from wells and gently add 300 μL/well of media containing dyes per well. Leave the cells with dyes in the incubator for 30 min.
3. During incubation, set the microscope temperature to 37 °C and CO_2 to 5% (*see* **Note 8**).
4. After incubation, remove the dyes and wash wells 3× with PBS to remove excess dye, which might otherwise aspecifically stain other nonmitochondrial compartments (*see* **Note 9**).
5. Once finished with the washes, add fresh Phase II media to the cells.
6. Go to the microscope and image the cells.

Fig. 4 (continued) and mtDNA movements, respectively, as indicated by the arrowhead in (**a**), while the continuous lines of the same colours highlight the mitochondrial and mtDNA movements as indicated by the white arrow in (**a**). The yellow line in the MitoTr kymograph marks the formation and the movement of a mitochondrion generated after a fission event (yellow arrow in (**a**)). The same track is not present in the SYBR kymograph, suggesting that no mtDNA is partitioned in this mitochondrion

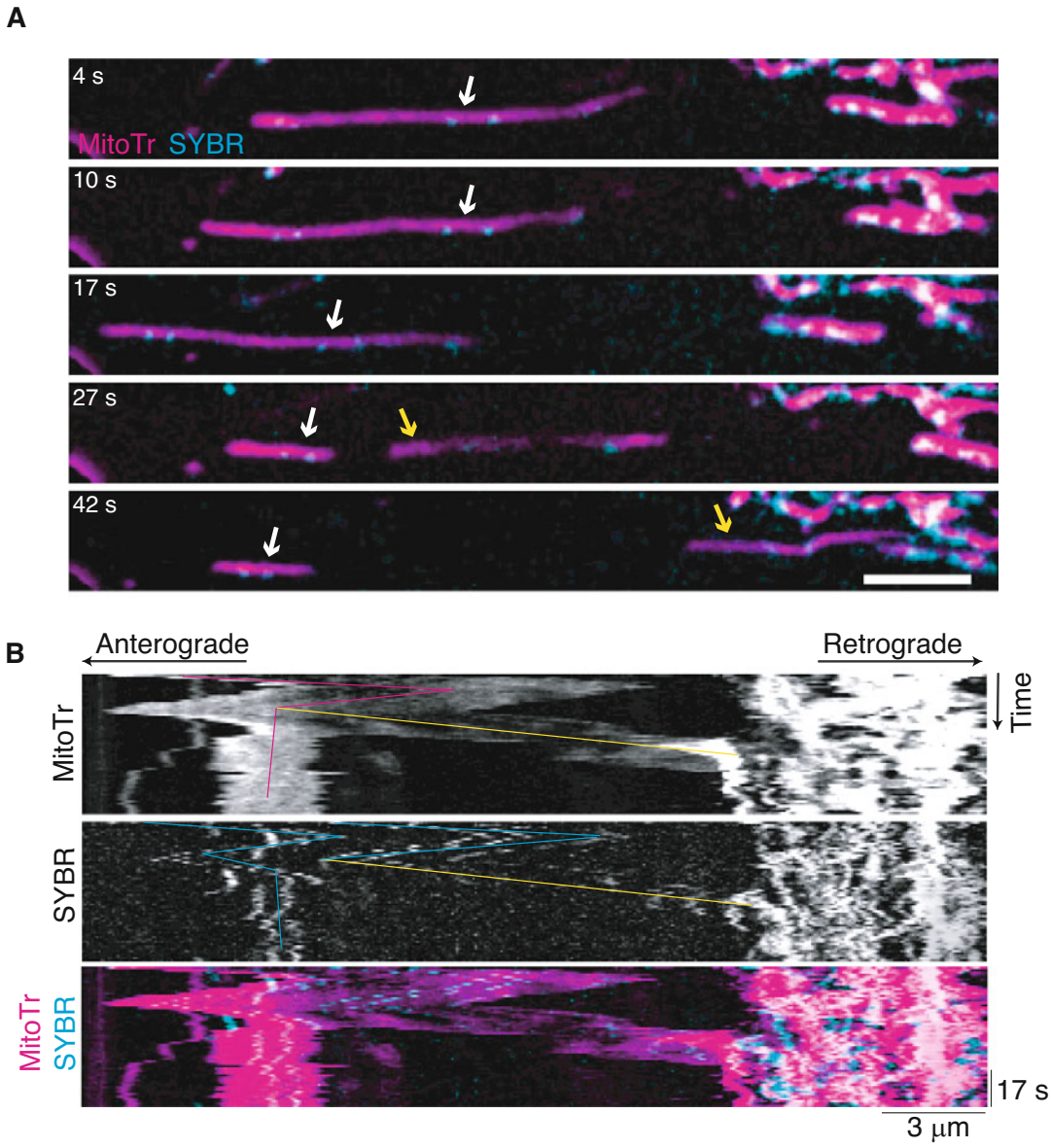

Fig. 5 Visualisation of mitochondria and nucleoids dynamics in neurites of differentiated SH-SY5Y cells (relative to Movie 2). Cells were stained with SYBR Gold (SYBR) and MitoTracker Deep Red (MitoTr) to visualise the mtDNA and the mitochondria, respectively. (**a**) Still frames showing a mitochondrion undergoing fission (27 s) in a neurite of DIV 14 cells, with the two resulting mitochondria (white and yellow arrows) displaying different dynamics. Contrarily to what showed in Fig. 4, the nucleoid puncta are partitioned within both mitochondria after fission. Scale bar: 3 μm. (**b**) Kymographs of mitochondrial (MitoTr) and mtDNA (SYBR) dynamics. The magenta (MitoTr) and cyan (SYBR) lines highlight the coordinated mitochondrial and mtDNA movements, respectively, as indicated by the white arrow in (**a**). The yellow lines mark the formation and the movement of a mitochondrion (MitoTr) generated after a fission (yellow arrow in (**a**)), which includes a subset of nucleoids (SYBR) deriving from the original mitochondrion

7. Focus on the cells by using the transmitted light (through eyepiece) and scan the well to find an appropriate area which contains a good number of processes that can be traced back to their cell bodies (*see* **Note 10**).
8. Switch to confocal mode (through microscope software) and observe the MitoTracker Deep Red signal on the computer via the 640 nm laser. Fine tune the focus and laser settings so that the mitochondria are clearly visible in the region of interest. Do the same for the SYBR Gold signal with the 488 nm laser (*see* **Notes 11** and **12**).
9. Image the region of interest at a rate of 1fps for 1 min (*see* **Note 13**). This will be saved as a ".nd2" file that contains two channels and 61 timeframes.

3.4 Analysis of Mitochondria and Nucleoids Transport

1. Open the ".nd2" file with Fiji/ImageJ. Adjust the intensity settings with the "Brightness/Contrast" tool, if needed (Image> Adjust> Brightness/Contrast).
2. Inspect the images for any potential sample drifts that may have occurred during imaging. Align image frames using the StackReg plugin to correct the drift, if necessary.
3. Identify process you wish to analyse, select it with the "Segmented" or "Freehand" (right click to change in Line Selection Tool) and use the Straighten plugin to straighten it. When the pop-up window appears, adjust the "Line width" to ensure it includes the whole width of your process and select "Process Entire Stack." This will open a new window which shows the whole movie of the straightened process; the direction from which you select the process will result in its orientation in this window.
4. The straightened segment can now be used to create a kymograph with the Velocity Measurement Tool. Once the plugin has been launched, retrace the straightened process ("Straight line," press Shift while selecting to keep line straight) and press the "k" button which will have appeared on the toolbar (*see* **Note 14**).

4 Notes

1. Phase contrast imaging was performed on live samples at a constant temperature of 37 °C and 5% CO_2. We feel the use of live cells rather than fixed sample gives a more accurate representation of the culture as a whole, especially in preparation for the trafficking experiments in live cells.
2. Formation of clear neuronal-like neurites was observed between DIV 10 and DIV 17, without a discernible difference

in neurite length between DIV 14 and DIV 21. With this protocol, we found that cultures at DIV 21 started to appear less healthy, with a reduced number of processes and clusters of somata. They also tended to detach more easily from the glass surface during media changes. Thus, DIV 10–17 was determined to be the best interval for imaging experiments. Within this interval, we recommend using cells at the same DIV throughout an experimental series. We did not observe a decrease in the differentiation efficiency of SH-SY5Y cells cultured for many passages (>40 passages in vitro).

3. We also tested coating the wells with 10 μg/mL laminin [77] but no significant differences in cell morphology and neurite extension were noticed when compared to PDL.
4. We use Ibidi μ-Slide 8-well Glass Bottom slides for live imaging experiments. In these chambers, the area of a well is 1 cm^2, therefore the seeding density will be 15′000 cells/well. We tested a range of seeding densities to obtain cultures where the cells are sparse enough for the purpose of mitochondria and nucleoid tracking within single processes and to be able to unequivocally assign a process to the cell body it emanates from. At the same time, the cells need to be seeded at a sufficient density as to not compromise cell survival. In 8-well Ibidi slides, densities lower than 10′000 cells/cm^2 lead to poor growth and occasional cell death after few days of culture, while densities above 20′000 cells/cm^2 result in cultures that are too compact for clear imaging of single processes. We recommend testing a range of seeding concentrations to find the optimal density for imaging studies.
5. Because retinoic acid is used to reduce cell proliferation and induce neuronal differentiation, we tested leaving the cells in Phase I media for an additional 72 h (i.e., throughout DIV 1–6) to prolong the incubation in EC23. Only at this point (DIV 7), we changed to Phase II. We expected this alternative protocol to bring forward the point of optimal differentiation. Surprisingly, we found that the culture reached full confluency by DIV 6 with many cells detaching during media changes. As a result, these cultures badly withstood transfection, with the majority of cells detaching prior to imaging.

   It is worth noting that two cellular subtypes exist within the SH-SY5Y population: a predominant N-type cell population which becomes nonproliferative upon differentiation, and a small S-type subpopulation that continues to proliferate. Different differentiation methods can result in a different balance of proliferative and nonproliferative cell types [49, 51].
6. For ICC analysis, cells were grown on coverslips, fixed in ice-cold methanol for 3 min, permeabilized in 0.2% Triton

X-100 for 10 min and blocked in 5% goat serum for 30 min. Cells were then stained with anti-neurofilament (1:100, BioLegend, #837904) and anti-MAP 2 (1:250, GeneTex, GTX82661) primary antibodies for 1.5 h at room temperature. After washing 3× times with PBS, the coverslips were incubated with Alexa Fluor secondary antibodies (1:2′000) for 45 min at room temperature, followed by a 5-min wash in Hoechst (1:5′000) and three more PBS washes. Coverslips were mounted with Prolong Gold Antifade mounting solution. Neurite analysis was performed in Fiji using the NeuronJ plugin (ttp://imagescience.org/meijering/software/neuronj/).

For western blotting analysis, 5 μg of protein were run on 4–12% Bis-Tris acrylamide gels and transferred on PVDF membranes for 1–1.5 h at 35 V. The membranes were incubated with anti-GAPDH (1:5′000, ThermoFisher) and anti-TH (1:200, Abcam) primary antibodies overnight at 4 °C. Membranes were then incubated with HRP-conjugated secondary antibodies (1:5′000, Amersham) for 1.5 h at room temperature, before being imaged with a Bio-Rad ChemiDoc Imager. Exposure times to detect specific immunoreactive protein bands were set between 5 and 10 min.

For plasma membrane staining with CellMask, cells were incubated with 300 μL/well of culture media supplemented with a 1:1′000 dilution of the commercial CellMask Green stock for 30 min. Prior to imaging, the dye was removed, wells were washed 3× times with PBS to remove excess dye, and kept in Phase II media post-wash and during imaging.

7. PEI and Lipofectamine were also tested during the optimisation of the transfection protocol but using NeuroMag resulted in higher transfection rate and healthier cell cultures. The transfection rate is significantly reduced in differentiated cells with all reagents, which is a further confirmation of the neuronal identity of these cells. We recommend using lentiviral transduction of differentiated cells for high expression of exogenous genes.
8. It is advisable to turn on the temperature and CO_2 control with enough time before the start of the imaging session to allow the system to reach the desired temperature (37 °C) and CO_2 (5%).
9. Be gentle while washing off the excess dye with PBS by pipetting into the side of the well as to not mechanically detach the cells from the bottom of the well, especially at higher DIV. From DIV 16–17, the cells appear to come off more easily during media changes.
10. Finding a field of view where neurites can be traced back to their cell body with ease is essential for analysing anterograde and retrograde trafficking (i.e., away from and toward the cell

soma, respectively). Using a cell membrane dye such as CellMask (Fig. 1c) could aid in doing so (*see* **Note 6**).

11. In time-lapse iSIM experiments in HeLa cells, SYBR Gold was used at a 1:10′000 dilution of the commercial stock (i.e., 1×) [74]. In our setup, we found that the range of SYBR dilution that yielded specific and visible puncta varied between 1:100′000 and 1:1′000’000 of the commercial stock (i.e., 0.1–0.01×). With further dilutions, the SYBR stain was barely detectable, while higher concentrations often produced bright and nonspecific aggregates. We recommend optimisation of the working dilution prior to live imaging experiments.
12. SYBR Green [17] and PicoGreen [78] have been previously used as mtDNA dye. We therefore tested PicoGreen (Invitrogen, P7581) in addition to SYBR Gold. We observed colocalization between overexpressed TFAM and PicoGreen-positive puncta at concentrations as low as 1.5 μL/mL, which confirms the suitability of this dye to stain nucleoids in SH-SY5Y cells. SYBR Gold was preferred for quantification of trafficking and dynamics due to the higher resolution and more defined puncta observed. As with SYRB Gold, the DIV of the cells affects the quality of PicoGreen staining, with cultures at higher DIV more commonly showing nonspecific staining in the form of larger extracellular accumulations of dye.
13. To avoid bleaching, find the lower exposure time and laser power at which the mitochondria and the nucleoids are clearly detectable. We observe minimal phototoxicity with our settings of 30% laser power, 100 ms exposure time for both channels and 1 fps acquisition rate. A high acquisition rate captures more detailed movements which is beneficial when observing the dynamics of small structures such as nucleoids, although it comes at the expense of phototoxicity.
14. Other plugins and kymograph analysis bundles are suitable to produce Kymographs, for instance, KymographBuilder (http://imagej.net/KymoResliceWide), KymoToolBox (https://github.com/fabricecordelieres/IJ-Plugin_KymoToolBox), KymoClear and KymoDirect [79], KymoAnalyzer [80], or KymoButler [81].

Acknowledgments

This work was funded through a NC3Rs David Sainsbury Fellowship and SKT grants (NC/N001753/2 and NC/T001224/1), a van Geest Fellowship in Dementia and Neurodegeneration from King’s College London, a Royal Society Research Grant (RGS\R2\180450), an Academy of Medical Sciences Springboard Award

(SBF004\1088) and a BBSRC CTP Studentship (BB/T508597/1) to AV.
We would like to thank the Wohl Cellular Imaging Centre at King's College London for help with light microscopy and Ricky Patel (King's College London) for sharing an early adapted version of the differentiation protocol from Forster et al. [68].

References

1. Guedes-Dias P, Holzbaur ELF (2019) Axonal transport: driving synaptic function. Science 366:eaaw9997. https://doi.org/10.1126/science.aaw9997
2. Surana S, Villarroel-Campos D, Lazo OM et al (2020) The evolution of the axonal transport toolkit. Traffic 21:13–33. https://doi.org/10.1111/tra.12710
3. Sleigh JN, Rossor AM, Fellows AD et al (2019) Axonal transport and neurological disease. Nat Rev Neurol 15:691–703. https://doi.org/10.1038/s41582-019-0257-2
4. Chamberlain KA, Sheng ZH (2019) Mechanisms for the maintenance and regulation of axonal energy supply. J Neurosci Res 97:897–913. https://doi.org/10.1002/jnr.24411
5. Misgeld T, Schwarz TL (2017) Mitostasis in neurons: maintaining mitochondria in an extended cellular architecture. Neuron 96:651–666. https://doi.org/10.1016/j.neuron.2017.09.055
6. Sheng Z-H, Cai Q (2012) Mitochondrial transport in neurons: impact on synaptic homeostasis and neurodegeneration. Nat Rev Neurosci 13:77–93. https://doi.org/10.1038/nrn3156
7. Hollenbeck PJ, Saxton WM (2005) The axonal transport of mitochondria. J Cell Sci 118:5411–5419. https://doi.org/10.1242/jcs.02745
8. Mattedi F, Vagnoni A (2019) Temporal control of axonal transport: the extreme case of organismal ageing. Front Cell Neurosci 13:393. https://doi.org/10.3389/fncel.2019.00393
9. Sagan L (1967) On the origin of mitosing cells. J Theor Biol 14:255–274. https://doi.org/10.1016/0022-5193(67)90079-3
10. Gray MW (2017) Lynn Margulis and the endosymbiont hypothesis: 50 years later. Mol Biol Cell 28:1285–1287. https://doi.org/10.1091/mbc.E16-07-0509
11. Nicholls TJ, Gustafsson CM (2018) Separating and segregating the human mitochondrial genome. Trends Biochem Sci 43:869–881. https://doi.org/10.1016/j.tibs.2018.08.007
12. Taanman JW (1999) The mitochondrial genome: structure, transcription, translation and replication. Biochim Biophys Acta Bioenerg 1410:103–123. https://doi.org/10.1016/S0005-2728(98)00161-3
13. Kukat C, Wurm CA, Spåhr H et al (2011) Super-resolution microscopy reveals that mammalian mitochondrial nucleoids have a uniform size and frequently contain a single copy of mtDNA. Proc Natl Acad Sci U S A 108:13534–13539. https://doi.org/10.1073/pnas.1109263108
14. Farge GÉR, Falkenberg M (2019) Organization of DNA in mammalian mitochondria. Int J Mol Sci 20:2770. https://doi.org/10.3390/ijms20112770
15. Chapman J, Ng YS, Nicholls TJ (2020) The maintenance of mitochondrial DNA integrity and dynamics by mitochondrial membranes. Life (Basel) 10:1–42. https://doi.org/10.3390/life10090164
16. Chen Z, Wang ZH, Zhang G et al (2020) Mitochondrial DNA segregation and replication restrict the transmission of detrimental mutation. J Cell Biol 219:e201905160. https://doi.org/10.1083/JCB.201905160
17. Ban-Ishihara R, Ishihara T, Sasaki N et al (2013) Dynamics of nucleoid structure regulated by mitochondrial fission contributes to cristae reformation and release of cytochrome c. Proc Natl Acad Sci U S A 110:11863–11868. https://doi.org/10.1073/pnas.1301951110
18. Garrido N, Griparic L, Jokitalo E et al (2003) Composition and dynamics of human mitochondrial nucleoids. Mol Biol Cell 14:1583–1596. https://doi.org/10.1091/mbc.E02-07-0399
19. Lewis SC, Uchiyama LF, Nunnari J (2016) ER-mitochondria contacts couple mtDNA synthesis with mitochondrial division in human cells. Science 353:aaf5549. https://doi.org/10.1126/science.aaf5549

20. Ramos ES, Motori E, Brüser C et al (2019) Mitochondrial fusion is required for regulation of mitochondrial DNA replication. PLoS Genet 15:e1008085. https://doi.org/10.1371/journal.pgen.1008085
21. Turchetto S, Le Bail R, Broix L, Nguyen L (2021) Molecular analysis of axonal transport dynamics upon modulation of microtubule acetylation. Methods Mol Biol; This volume
22. Sleigh JN, Vagnoni A, Twelvetrees AE, Schiavo G (2017) Methodological advances in imaging intravital axonal transport. F1000Res 6:200. https://doi.org/10.12688/f1000research.10433.1
23. Mattedi F, Chennell G, Vagnoni A (2021) Detailed imaging of mitochondrial transport and precise manipulation of mitochondrial function with genetically-encoded photosensitizers in adult Drosophila neurons. Methods Mol Biol; This volume
24. Huang R, Xu Y, Chen M et al (2021) Visualizing the intracellular trafficking in zebrafish Mauthner cells. Methods Mol Biol; This volume
25. Atkins M, Hazan J, Fassier C (2021) In vivo live imaging of axonal transport in developing zebrafish axons. Methods Mol Biol; This volume
26. Barmaver SN, Shanmugam MM, Wagner OI (2021) Methods to quantify and relate axonal transport defects to changes in C. elegans behavior. Methods Mol Biol; This volume
27. Knabbe J, Protzmann J, Kuner T (2021) In vivo imaging of axonal organelle transport in the mouse brain. Methods Mol Biol; This volume
28. Anazawa Y, Niwa S (2021) Analyzing the impact of gene mutations on axonal transport in Caenorhabditis elegans. Methods Mol Biol; This volume
29. Robinson W, Godenschwege TA (2021) Live imaging of axonal transport in the adult drosophila central nervous system. Methods Mol Biol; This volume
30. Nadiminti SSP, Koushika SP (2021) Imaging intracellular trafficking in neurons of C. elegans. Methods Mol Biol; This volume
31. Bearer E, Zhang X, Jacobs R (2021) Studying axonal transport in the brain by manganese-enhanced magnetic resonance imaging (MEMRI). Methods Mol Biol This volume
32. Vagnoni A, Hoffmann PC, Bullock SL (2016) Reducing Lissencephaly-1 levels augments mitochondrial transport and has a protective effect in adult Drosophila neurons. J Cell Sci 129:178–190. https://doi.org/10.1242/jcs.179184
33. Vagnoni A, Bullock SL (2018) A cAMP/PKA/Kinesin-1 Axis promotes the axonal transport of mitochondria in aging drosophila neurons. Curr Biol 28:1265–1272.e4. https://doi.org/10.1016/j.cub.2018.02.048
34. Morsci NS, Hall DH, Driscoll M, Sheng Z-H (2016) Age-related phasic patterns of mitochondrial maintenance in adult Caenorhabditis elegans neurons. J Neurosci 36:1373–1385. https://doi.org/10.1523/JNEUROSCI.2799-15.2016
35. Takihara Y, Inatani M, Eto K et al (2015) In vivo imaging of axonal transport of mitochondria in the diseased and aged mammalian CNS. Proc Natl Acad Sci U S A 112:10515–10520. https://doi.org/10.1073/pnas.1509879112
36. Sleigh JN, Tosolini AP, Gordon D et al (2020) Mice carrying ALS mutant TDP-43, but not mutant FUS, display in vivo defects in axonal transport of signaling endosomes. Cell Rep 30:3655–3662.e2. https://doi.org/10.1016/j.celrep.2020.02.078
37. Tierney W, Vicino I, Sun S et al (2021) Methods and applications of Campenot trichamber neuronal cultures for the study of Neuroinvasive viruses. Methods Mol Biol; This volume
38. Voelzmann A, Sanchez-Soriano N (2021) Drosophila primary neuronal cultures as a useful cellular model to study and image axonal transport. Methods Mol Biol; This volume
39. Ganguly A, Roy S (2021) Imaging diversity in slow axonal transport. Methods Mol Biol; This volume
40. Badal K, Zhao Y, Miller K, Puthanveettil S (2021) Live imaging and quantitative analysis of organelle transport in sensory neurons of Aplysia Californica. Methods Mol Biol; This volume
41. Hees TJ, Harbauer AB (2021) Live-cell imaging of RNA transport in axons of cultured primary neurons. Methods Mol Biol; This volume
42. Shekari A, Fahnestock M (2021) Retrograde axonal transport of neurotrophins in basal forebrain cholinergic neurons. Methods Mol Biol; This volume
43. Ionescu A, Perlson E (2021) Microfluidic neuromuscular co-culture system for tracking cell-to-cell transfer and axonal transport of labeled proteins. Methods Mol Biol; This volume
44. Montgomery A, Garbouchian A, Bentley M (2021) Visualizing vesicle-bound kinesins in cultured hippocampal neurons. Methods Mol Biol; This volume
45. Emily MF, Agrawal L, Barzaghi P et al (2021) Use of microfluidics chambers to image axonal transport in adult sensory neurons. Methods Mol Biol; This volume

46. Mehta AR, Chandran S, Selvaraj BT (2021) Assessment of mitochondrial trafficking as a surrogate of fast axonal transport in human induced pluripotent stem cell derived spinal motor neurons. Methods Mol Biol; This volume
47. Bateman JM (2021) Mitochondrial DNA transport in Drosophila neurons. Methods Mol Biol; This volume
48. Biedler JL, Helson L, Spengler BA (1973) Morphology and growth, tumorigenicity, and cytogenetics of human neuroblastoma cells in continuous culture. Cancer Res 33:2643–2652
49. Encinas M, Iglesias M, Liu Y et al (2000) Sequential treatment of SH-SY5Y cells with retinoic acid and brain-derived neurotrophic factor gives rise to fully differentiated, neurotrophic factor-dependent, human neuron-like cells. J Neurochem 75:991–1003. https://doi.org/10.1046/j.1471-4159.2000.0750991.x
50. Shipley MM, Mangold CA, Szpara ML (2016) Differentiation of the SH-SY5Y human neuroblastoma cell line. J Vis Exp 108:53193. https://doi.org/10.3791/53193
51. Ross RA, Spengler BA, Biedler JL (1983) Coordinate morphological and biochemical interconversion of human neuroblastoma cells. J Natl Cancer Inst 71:741–747. https://doi.org/10.1093/jnci/71.4.741
52. Xicoy H, Wieringa B, Martens GJM (2017) The SH-SY5Y cell line in Parkinson's disease research: a systematic review. Mol Neurodegener 12:1–11
53. Kovalevich J, Langford D (2013) Considerations for the use of SH-SY5Y neuroblastoma cells in neurobiology. Methods Mol Biol 1078: 9–21. https://doi.org/10.1007/978-1-62703-640-5_2
54. Xie W, Chung KKK (2012) Alpha-synuclein impairs normal dynamics of mitochondria in cell and animal models of Parkinson's disease. J Neurochem 122:404–414. https://doi.org/10.1111/j.1471-4159.2012.07769.x
55. Ito K, Eguchi Y, Imagawa Y et al (2017) MPP+ induces necrostatin-1-and ferrostatin-1-sensitive necrotic death of neuronal SH-SY5Y cells. Cell Death Discov 3:17013. https://doi.org/10.1038/cddiscovery.2017.13
56. de Medeiros LM, De Bastiani MA, Rico EP et al (2019) Cholinergic differentiation of human neuroblastoma SH-SY5Y cell line and its potential use as an in vitro model for Alzheimer's disease studies. Mol Neurobiol 56: 7355–7367. https://doi.org/10.1007/s12035-019-1605-3
57. Chiocchetti AG, Haslinger D, Stein JL et al (2016) Transcriptomic signatures of neuronal differentiation and their association with risk genes for autism spectrum and related neuropsychiatric disorders. Transl Psychiatry 6:e864. https://doi.org/10.1038/tp.2016.119
58. Påhlman S, Ruusala AI, Abrahamsson L et al (1984) Retinoic acid-induced differentiation of cultured human neuroblastoma cells: a comparison with phorbolester-induced differentiation. Cell Differ 14:135–144. https://doi.org/10.1016/0045-6039(84)90038-1
59. Adem A, Mattsson MEK, Nordberg A, Påhlman S (1987) Muscarinic receptors in human SH-SY5Y neuroblastoma cell line: regulation by phorbol ester and retinoic acid-induced differentiation. Dev Brain Res 33:235–242. https://doi.org/10.1016/0165-3806(87)90156-8
60. Hashemi SH, Li JY, Ahlman H, Dahlström A (2003) SSR2(a) receptor expression and adrenergic/cholinergic characteristics in differentiated SH-SY5Y cells. Neurochem Res 28: 449–460. https://doi.org/10.1023/A:1022848718109
61. Korecka JA, van Kesteren RE, Blaas E et al (2013) Phenotypic characterization of retinoic acid differentiated SH-SY5Y cells by transcriptional profiling. PLoS One 8:e63862. https://doi.org/10.1371/journal.pone.0063862
62. Presgraves SP, Ahmed T, Borwege S, Joyce JN (2003) Terminally differentiated SH-SY5Y cells provide a model system for studying neuroprotective effects of dopamine agonists. Neurotox Res 5:579–598. https://doi.org/10.1007/BF03033178
63. Constantinescu R, Constantinescu AT, Reichmann H, Janetzky B (2007) Neuronal differentiation and long-term culture of the human neuroblastoma line SH-SY5Y. In: Neuropsychiatric disorders an integrative approach. Springer, Vienna, pp 17–28
64. Lopes FM, Schröder R, da Frota MLC Jr et al (2010) Comparison between proliferative and neuron-like SH-SY5Y cells as an in vitro model for Parkinson disease studies. Brain Res 1337: 85–94. https://doi.org/10.1016/j.brainres.2010.03.102
65. Pignataro D, Francia S, Zanetta F et al (2017) A missense MT-ND5 mutation in differentiated Parkinson disease cytoplasmic hybrid induces ROS-dependent DNA damage response amplified by DROSHA. Sci Rep 7: 9528. https://doi.org/10.1038/s41598-017-09910-x
66. Mastroeni D, Grover A, Leonard B et al (2009) Microglial responses to dopamine in a cell culture model of Parkinson's disease. Neurobiol Aging 30:1805–1817. https://doi.org/10.1016/j.neurobiolaging.2008.01.001

67. Melo TQ, van Zomeren KC, Ferrari MFR et al (2017) Impairment of mitochondria dynamics by human A53T α-synuclein and rescue by NAP (davunetide) in a cell model for Parkinson's disease. Exp Brain Res 235:731–742. https://doi.org/10.1007/s00221-016-4836-9
68. Forster JI, Köglsberger S, Trefois C et al (2016) Characterization of differentiated SH-SY5Y as neuronal screening model reveals increased oxidative vulnerability. J Biomol Screen 21:496–509. https://doi.org/10.1177/1087057115625190
69. Shipley MM, Mangold CA, Kuny CV, Szpara ML (2017) Differentiated human SH-SY5Y cells provide a reductionist model of herpes simplex virus 1 neurotropism. J Virol 91: e00958-17. https://doi.org/10.1128/jvi.00958-17
70. Leo L, Weissmann C, Burns M et al (2017) Mutant spastin proteins promote deficits in axonal transport through an isoform-specific mechanism involving casein kinase 2 activation. Hum Mol Genet 26:2321–2334. https://doi.org/10.1093/hmg/ddx125
71. Clemens G, Flower KR, Henderson AP et al (2013) The action of all-trans-retinoic acid (ATRA) and synthetic retinoid analogues (EC19 and EC23) on human pluripotent stem cells differentiation investigated using single cell infrared microspectroscopy. Mol BioSyst 9:677–692. https://doi.org/10.1039/c3mb25505k
72. Christie VB, Barnard JH, Batsanov AS et al (2008) Synthesis and evaluation of synthetic retinoid derivatives as inducers of stem cell differentiation. Org Biomol Chem 6:3497–3507. https://doi.org/10.1039/b808574a
73. Palomares T, Cordero M, Bruzos-Cidon C et al (2018) The neuroprotective effect of conditioned medium from human adipose-derived mesenchymal stem cells is impaired by N-acetyl cysteine supplementation. Mol Neurobiol 55:13–25. https://doi.org/10.1007/s12035-017-0714-0
74. Jevtic V, Kindle P, Avilov SV (2018) SYBR Gold dye enables preferential labelling of mitochondrial nucleoids and their time-lapse imaging by structured illumination microscopy. PLoS One 13:e0203956. https://doi.org/10.1371/journal.pone.0203956
75. Halabi EA, Pinotsi D, Rivera-Fuentes P (2019) Photoregulated fluxional fluorophores for live-cell super-resolution microscopy with no apparent photobleaching. Nat Commun 10: 1232. https://doi.org/10.1038/s41467-019-09217-7
76. Kleele T, Rey T, Winter J et al (2021) Distinct fission signatures predict mitochondrial degradation or biogenesis. Nature 593(7859): 435–439. https://doi.org/10.1038/s41586-021-03510-6
77. Dwane S, Durack E, Kiely PA (2013) Optimising parameters for the differentiation of SH-SY5Y cells to study cell adhesion and cell migration. BMC Res Notes 6:366. https://doi.org/10.1186/1756-0500-6-366
78. Ashley N, Harris D, Poulton J (2005) Detection of mitochondrial DNA depletion in living human cells using PicoGreen staining. Exp Cell Res 303:432–446. https://doi.org/10.1016/j.yexcr.2004.10.013
79. Mangeol P, Prevo B, Peterman EJG (2016) KymographClear and KymographDirect: two tools for the automated quantitative analysis of molecular and cellular dynamics using kymographs. Mol Biol Cell 27:1948–1957. https://doi.org/10.1091/mbc.E15-06-0404
80. Neumann S, Chassefeyre R, Campbell GE, Encalada SE (2017) KymoAnalyzer: a software tool for the quantitative analysis of intracellular transport in neurons. Traffic 18:71–88. https://doi.org/10.1111/tra.12456
81. Jakobs MA, Dimitracopoulos A, Franze K (2019) Kymobutler, a deep learning software for automated kymograph analysis. Elife 8: e42288. https://doi.org/10.7554/eLife.42288

Open Access This chapter is licensed under the terms of the Creative Commons Attribution 4.0 International License (http://creativecommons.org/licenses/by/4.0/), which permits use, sharing, adaptation, distribution and reproduction in any medium or format, as long as you give appropriate credit to the original author(s) and the source, provide a link to the Creative Commons license and indicate if changes were made.

The images or other third party material in this chapter are included in the chapter's Creative Commons license, unless indicated otherwise in a credit line to the material. If material is not included in the chapter's Creative Commons license and your intended use is not permitted by statutory regulation or exceeds the permitted use, you will need to obtain permission directly from the copyright holder.

Chapter 16

Assessment of Mitochondrial Trafficking as a Surrogate for Fast Axonal Transport in Human Induced Pluripotent Stem Cell–Derived Spinal Motor Neurons

Arpan R. Mehta, Siddharthan Chandran, and Bhuvaneish T. Selvaraj

Abstract

Axonal transport is essential for the development, function, and survival of the nervous system. In an energy-demanding process, motor proteins act in concert with microtubules to deliver cargoes, such as organelles, from one end of the axon to the other. Perturbations in axonal transport are a prominent phenotype of many neurodegenerative diseases, including amyotrophic lateral sclerosis. Here, we describe a simple method to fluorescently label mitochondrial cargo, a surrogate for fast axonal transport, in human induced pluripotent stem cell–derived motor neurons. This method enables the sparse labeling of axons to track directionality of movement and can be adapted to assess not only the cell autonomous effects of a genetic mutation on axonal transport but also the cell non-autonomous effects, through the use of conditioned medium and/or co-culture systems.

Key words Axonal transport, Mitochondria, Motor neuron, Human induced pluripotent stem cell

1 Introduction

Axonal transport is a critical energy demanding cellular process describing the movement of organelles, vesicles, and macromolecules toward (retrograde) or away from (anterograde) the soma. Neurons, by virtue of their extraordinarily elongated polarization, are especially dependent on long-range cytoskeletal transport, and defective axonal transport has been implicated in the pathogenesis of a myriad age-related neurodegenerative diseases, including amyotrophic lateral sclerosis [1].

Here, we describe a simple method to fluorescently label mitochondrial cargo, a surrogate for fast axonal transport, in human induced pluripotent stem cell–derived motor neurons [2]. This method allows for sparse labeling of axons to track directionality of movement and can be adapted to assess not only the cell autonomous effects of a genetic mutation on axonal transport but also

Alessio Vagnoni (ed.), *Axonal Transport: Methods and Protocols*,
Methods in Molecular Biology, vol. 2431, https://doi.org/10.1007/978-1-0716-1990-2_16,
© The Author(s) 2022

the cell non-autonomous effects, through the use of conditioned medium and/or co-culture systems.

We first describe a method for the generation of spinal (lower) motor neurons (MNs) from human induced pluripotent stem cells (iPSCs) using an established protocol [3] with minor modifications, yielding a highly enriched and electrophysiologically active neuronal culture, devoid of glia, with circa 60% of cells being positive for islet-1 and islet-2 homeobox MN markers 1 week post platedown [4]. We then describe a method for sparse labeling of neuronal mitochondria [2], allowing for the quantification of various parameters such as pausing, and speed, but also directionality of movement. It is thus advantageous over dye-based methods, which label all cells, such as MitoTracker [5].

2 Materials

Prepare all solutions using sterile technique in a tissue culture hood.

2.1 Maintenance of Human Induced Pluripotent Stem Cells (iPSCs)

1. Matrigel Growth Factor Reduced Basement Membrane Matrix-coated plastic dishes (*see* **Note 1**).
2. Essential 8 medium (Gibco; A1517001) at 37 °C and 5% CO_2.
3. iPSCs are passaged weekly using a 1:1 mixture of 1 mg/ml dispase and 2 mg/ml collagenase.

2.2 Motor Neuron (MN) Differentiation

1. Incubator set at 37 °C, 5% CO_2 with a mini orbital shaker (cat-code: 10309644)(*see* **Note 2**).
2. 9-cm nonadherent Petri dishes.
3. Accutase for single-cell dissociation of iPSCs.
4. Recommended stock concentrations of critical factors for aliquoting and storing at −20 °C, with freeze–thaw cycles minimized (*see* **Note 3**): 10 mM Activin inhibitor SB-431542 (AI) in DMSO, 50 mM ascorbic acid (light sensitive), 10 μg/ml recombinant human brain-derived neurotrophic factor (BDNF; we recommend cat code: 248-BDB) diluted in PBS + 0.1% BSA (carrier protein), 3 mM CHIR-99021 in DMSO, 10 μg/ml recombinant human ciliary neurotrophic factor (CNTF; we recommend cat code: 257-NT) diluted in PBS + 0.1% BSA (carrier protein), 10 mM DAPT in DMSO, 5 mg/ml DNase in 0.15 M NaCl (we recommend cat code: DN25, Sigma), 20 μg/ml FGF-2 (basic) diluted in PBS + 0.1% BSA (carrier protein), 10 μg/ml recombinant human glial-derived neurotrophic factor (GDNF; we recommend cat code: 212-GD) diluted in PBS + 0.1% BSA (carrier protein), 20 μg/ml recombinant human insulin-like growth factor-1 (IGF-1) diluted in PBS + 0.1% BSA (carrier protein), 100 μM

LDN-193189 in DMSO (light sensitive), 1 mM retinoic acid (RA; all trans) in DMSO (light sensitive), 1 mM smoothened agonist (SAG, light sensitive), 10 mM Y-27632 (ROCK inhibitor, RI).

5. MN Differentiation medium ("MN-Diff-Base"): 0.5× Advanced DMEM/F12, 0.5× Neurobasal medium, 1× Antibiotic–Antimycotic, 1× Glutamax, 100 μM beta-mercaptoethanol, 1× N-2 supplement, 1× B-27 supplement, 10 μM ascorbic acid. Filter units should be used and volumes adjusted accordingly to last no more than 7–10 days. Protect from light by covering with aluminum foil. Store at 4 °C and allow medium to naturally warm up toward ambient room temperature before using to feed cells.
6. Day 0 medium: MN-Diff-Base + 3i + 10 ng/ml FGF-2 + 10 μM RI, where "3i" refers to 20 μM SB-431542, 0.1 μM LDN-193189, and 3 μM CHIR-99021 (*see* **Note 4**).
7. Day 2/4 medium: MN-Diff-Base + 3i + 0.1 μM RA + 500 nM SAG (*see* **Note 5**).
8. Day 7 medium: MN-Diff-Base + 0.1 μM RA + 500 nM SAG + 10 ng/ml BDNF.
9. Day 9/11 medium: Day 7 medium + 10 μM DAPT.
10. Day 14 medium: MN-Diff-Base + 0.1 μM RA + 10 ng/ml BDNF + 10 μM DAPT +10 ng/ml GDNF.

2.3 Motor Neuron Plating and Maintenance

1. Cell strainers (40 μm).
2. μ-slide 8-well ibidi dishes (*see* **Note 6**).
3. Coating (store at −20 °C): poly-L-ornithine bromide, laminin from Engelbreth-Holm-Swarm murine sarcoma basement membrane, fibronectin human plasma, and Matrigel.
4. Wash buffer: 1× DPBS (calcium and magnesium free), 0.45% glucose, 0.1% BSA, 2 mM $MgCl_2$, 0.8 mM EDTA, 2.5% fetal bovine serum (FBS), 50 μg/ml DNase, 1× B-27 supplement, 1× N-2 supplement. Store at 4 °C and it can be prepared up to 1 week prior to MN dissociation (with DNase, B-27 and N-2 supplements being added to the buffer immediately prior to its use in the MN dissociation procedure).
5. Trypsin + DNase solution: 3 ml of 0.05% trypsin-EDTA (*see* **Note 7**) + 200 μl DNAse (5 mg/ml stock; *see* **Note 8**) per 9-cm Petri dish.
6. "Stop" solution: FBS + DNase (3 ml per plate): 3 ml FBS + 60 μl DNase per 9-cm Petri dish.
7. MN Neurotrophic Factor medium ('MN-NF'): 1× Neurobasal medium, 1× anti-anti/PSF, 1× MEM Non-Essential Amino Acids Solution, 1× Glutamax, 1× B-27 supplement, 1× N-2

supplement, 100 μM beta-mercaptoethanol, 2.5 μM ascorbic acid, 1 μM retinoic acid, 10 ng/ml recombinant human BDNF, 10 ng/ml recombinant human CNTF, 10 ng/ml recombinant human GDNF, and 10 ng/ml recombinant human IGF-1. Filter units should be used and volumes adjusted accordingly to last no more than 7–10 days. Protect from light by covering with aluminum foil. Store at 4 °C and allow medium to naturally warm toward ambient room temperature before using to feed cells.

8. 25 μM L-glutamic acid (GluE) and 1 μM uridine/5-fluoro-2′-deoxyuridine (U/FDU), stored at −20 °C, are added to MN-NF in the initial phases of MN culture (L-glutamic acid just at platedown).

2.4 Mitochondrial Labeling with Mito-DsRed2

1. To label individual mitochondria in a variable proportion of MNs, a lentivirus expressing a mitochondrial targeting sequence fused to the N-terminal region of DsRed2 protein under CMV promoter should be generated. Lentiviral titers for each batch should be empirically calculated.
2. Phenol red-free Neurobasal medium to address the high visible light absorption extinction coefficient of phenol red and thus increase the signal-to-noise ratio by minimizing the source of autofluorescence (although this is not essential for imaging DsRed2 when compared to imaging GFP/cyan spectrum, as phenol red is particularly fluorescent when excited at 440 nm).
3. A live-imaging compatible widefield microscope with Cy3 filter set, a 63× oil 1.4 N.A. objective, and an incubation chamber maintained at 37 °C and 5% CO_2.
4. Fiji software [6] for image analysis.

3 Methods

3.1 Motor Neuron Differentiation from Human iPSCs (Summarized Workflow in Table 1)

1. Dissociate iPSCs into single cells using Accutase, and neuralize as a suspension culture using "3i" providing dual-SMAD inhibition (via SB-431542 and LDN-193189) and potentiation with the Wnt-agonist (CHIR-99021) in "Day 0" medium.
   (a) Add 1 ml of Accutase per well (iPSCs at ~80% confluency) and incubate at 37 °C for no longer than 5–10 min. Keep checking until condensed iPSC colonies start to loosen. Pipette up and down to remove difficult areas.
   (b) During the incubation time, prepare 15 ml Falcon tubes by labeling tubes and adding 2–3 ml of PBS.
   (c) Add 1 ml of PBS to each well (to dilute Accutase 1:1) and pipette cells up and down to break up the colonies into

Table 1
Summary timeline and feeding schedule from iPSC to MN. "3i" refers to SB-431542, LDN-193189, and CHIR-99021. OCT4 is an iPSC marker; OLIG2 is a marker of the pMN domain that gives rise to MNs (and oligodendrocytes); and HB9 is a marker of spinal motor neurons

Day	Medium for feeding	Marker		
Day 0	MN-diff-base +3i+FGF+RI (single-cell iPSC dissociation with Accutase)	OCT4	3i + FGF+RI	Day 0–1
Day 1	No feeding			
Day 2	MN-diff-base +3i +RA+SAG		3i+ RA+SAG	Day 2–6
Day 3	No feeding			
Day 4	MN-diff-base +3i +RA+SAG			
Day 5	No feeding			
Day 6	No feeding			
Day 7	MN-Diff Base +RA+SAG+BDNF		RA+SAG+BDNF	Day 7–8
Day 8	No feeding			
Day 9	MN-Diff Base +RA+SAG+BDNF+DAPT	OLIG2	RA + SAG + BDNF +DAPT	Day 9–13
Day 10	No feeding			
Day 11	MN-Diff Base +RA+SAG+BDNF+DAPT	HB9		
Day 12	No feeding			
Day 13	No feeding			
Day 14	MN-Diff Base +RA+BDNF+DAPT+GDNF		RA+BDNF+DAPT +GDNF	Day 14–16
Day 15	No feeding			
Day 16	Dissociation and platedown			

single cells (N.B. cells that form thread-like structures are dying).

(d) Add the cells to the prepared 15-ml Falcon tubes.

(e) Centrifuge at 400 rcf for 4 min.

(f) Aspirate supernatant and add 5 ml of PBS, resuspend and centrifuge again at 400 rcf for 4 min.

(g) Aspirate supernatant and add an appropriate volume of "Day 0" medium depending on the size of the pellet (1–3 ml).

(h) Count cells and plate 2×10^6 cells per 9-cm Petri dish in "Day 0" medium.

(i) Place labeled Petri dish on a mini orbital shaker set at 50 rpm within an incubator set at 37 °C, 5% CO_2.

2. On day 1, check plate to see if small embryoid bodies (EBs) have formed. If there are only single cells, then there is likely a problem. If EBs are already forming big clusters visible by eye, then decrease the starting cell number (from 2×10^6 cells) or make sure you spread the cells in the dish when you place the dish back on the shaker in the incubator.

3. On day 2, neural spheres are simultaneously patterned to spinal cord identity by treating with RA and SAG, promoting

caudalization and ventralization, respectively, along with 3i for an additional 5 days.

(a) Gently swirl Petri dish to collect EBs (spheres) into the middle of the plate.

(b) Transfer spheres into 15-ml Falcon tube (*see* **Note 9**).

(c) Re-use plates by washing petri dish with PBS, aspirate PBS from the Petri dish and lid if any condensation has formed (*see* **Note 10**).

(d) Centrifuge at 200 rcf for 4 min (*see* **Note 11**).

(e) Add 10 ml of "Day 2/4" medium using a 10-ml pipette to gently dislodge the pellet and add to Petri dish. Care should be taken not to dissociate into single cells.

(f) Re-place the Petri dish on the mini orbital shaker set at 50 rpm within the incubator (*see* **Note 12**).

(g) On day 4, repeat the above, but it may now be possible to swirl the plate so as to move the spheres into the center of the plate and then aspirate the surrounding medium without the need for collecting the cells in a Falcon and centrifuging (which is more disruptive).

4. On day 7, spheres are maintained in culture with "Day 7" medium containing RA and SAG, with the addition of BDNF, to generate MN progenitors. By this stage, all feeding should be done by swirling the plate and aspirating the surrounding medium and replacing with 10 ml of fresh medium.
5. From day 9, MN progenitors are cultured in "Day 9/11" medium, which has DAPT, an inhibitor of Notch signaling (*see* **Note 13**), for an additional two feeds (day 9 and day 11). If the medium in the plates is yellowing prior to the day of feeding, we recommend splitting the plate into two plates (each fed with 10 ml of medium).
6. At day 14, the spheres should be fed with "Day 14" medium, which has GDNF, but lacks SAG (which is now no longer needed).

3.2 Motor Neuron Dissociation and Platedown (from Day 16 Onwards, See *Note 14)*

1. At day 14, pre-treat μ-slide eight-well ibidi dishes with 100 μg/ml poly-L-ornithine bromide by overnight coating at room temperature, followed by washing with tissue-culture grade water three times and then air drying and UV treatment inside a tissue culture hood.
2. Next, on day 15, coat the plate with laminin from 5 μg/ml Engelbreth-Holm-Swarm murine sarcoma basement membrane, 10 μg/ml fibronectin human plasma, and Matrigel (1:20) ("LMF" coating) (*see* **Note 15**) and leave overnight at 4 °C (*see* **Note 16**).

3. Between days 14 and 16, MN spheres are dissociated using 0.05% trypsin–EDTA as follows (*see* **Note 17**):
   (a) Take LMF plates out of the fridge and place in incubator.
   (b) Collect spheres in a 15-ml Falcon tube. Discard Petri dishes.
   (c) Wash twice with 5 ml of calcium/magnesium-free DPBS (*see* **Note 18**).
   (d) Aspirate DPBS.
   (e) Add 3 ml of pre-warmed 0.05% trypsin/DNase per 15-ml tube.
   (f) Incubate for 10–15 min, occasionally inverting a few times to separate the EBs.
   (g) Stop the trypsin enzymatic reaction by adding 1 volume (3 ml) of "Stop" solution and then add 4 ml of cold Wash Buffer.
   (h) Allow spheres to settle to the bottom of the Falcon tube.
   (i) Aspirate the supernatant.
   (j) Add 1 ml of cold Wash Buffer.
   (k) Dissociate spheres with P1000 pipette, pipetting up and down 10–12 times, avoiding the generation of air bubbles.
   (l) Add 2 ml of cold Wash Buffer, shake the tube and let non-dissociated spheres settle down over 4–5 min.
   (m) Collect supernatant (approximately 2.5 ml) and transfer to a new 15-ml tube containing 2 ml of cold Wash Buffer.
   (n) Add 0.5 ml of cold Wash Buffer and dissociate for a second time. Add a further 2 ml of cold Wash Buffer. Leave to settle and take off supernatant and pool.
   (o) Repeat **Step n** one more time.
   (p) Filter pooled supernatants through 40 μm cell strainer filter into a new 50-ml Falcon tube that already contains 2–4 ml of cold Wash Buffer.
   (q) Once filtered, transfer this to a new, labeled 15-ml Falcon tube.
   (r) Centrifuge at 400 rcf for 5 min.
   (s) Aspirate supernatant.
   (t) Resuspend in 3–4 ml of MN-NF, supplemented with GluE & U/FDU, depending on the size of the pellet (aiming for 1–5 million cells/ml) (*see* **Note 19**).
   (u) Aspirate the LMF coating from μ-slide 8-well ibidi dishes.

(v) Plate cells at a density of 50,000–70,000 cells per well. 50% of the MN-NF medium should be replaced every 2–3 days. The medium should be supplemented with 1 μM U/FDU for at least 1 week post platedown to remove residual proliferating progenitor cells. If cell non-autonomous effects on axonal transport are to be assessed, one can use conditioned medium (from, for example, astrocyte monocultures) or plate the MNs in direct contact with different cell types.

3.3 Labeling of Mitochondria

1. Sparsely transduce the cells at platedown with lentivirus expressing mitoDsRed2. Lentivirus stored at −80 °C should be thawed on ice and the appropriate volume of lentivirus (*see* **Note 20**) should be added to the cell suspension (total volume: 300 μl) for 10 min prior to platedown onto a μ-slide 8-well ibidi dish. The virus is washed off at the next routine replacement of the cell culture medium after 2–3 days.
2. At the chosen time point for imaging, such as 21 days post platedown, change the medium 30 min prior to imaging to phenol red-free Neurobasal supplemented with 1× Glutamax (*see* **Note 21**).
3. Heat the microscope stage for at least 30–60 min prior to experimentation to minimize focal drift.
4. Perform fluorescence live-cell imaging of mitochondrial axonal transport. Typical settings to capture mitochondrial motility are a 0.2 Hz capture of a ~100 μm stretch of axon and a small z-stack (because the axons are not homogeneously in the same plane) for a 5 min time lapse. Guard against unnecessary excitation/laser power to minimize bleaching.
5. Image at least 4 axons (n) per line per differentiation (N, where $N = 3$). "Proximal" axon measurements are acquired from the axon immediately adjoining the cell body, and "distal" were measured from the distal tip. Notably, this method sparsely labels only a few neurons in a highly dense culture, thus permitting the assessment of the directionality of mitochondrial movement (and hence velocity) within the axon. Maximum intensity projections can be computed in Fiji [6].
6. Generate kymographs (space–time plots) to determine the numbers of stationary (≤0.1 μm/s) versus bidirectionally motile mitochondria (either predominantly toward or away from the soma). Kymographs can be generated and analyzed using a number of softwares, including KymoToolBox (*see* **Note 22**) [7, 8] in Fiji.

4 Notes

1. Matrigel is thawed at 4 °C for 1–2 h. While thawing, chill a 10-ml stripette, 1.5-ml tubes, and 1-ml pipette tips. Once thawed, dilute 1:2 with cold Advanced DMEM/F12 using a cold stripette. Create 1-ml aliquots using cold tips and tubes for storage at −20 °C. For coating iPSC plates, use aliquots at 1:30 (i.e., 1:60 final concentration) Matrigel, leaving plates overnight at 4 °C, or 30 min at 37 °C, or room temperature for 2 h. Plates can be kept for up to 7 days at 4 °C.
2. We recommend the shakers to be on a backup battery power supply.
3. Light-sensitive components should be wrapped with aluminum foil when exposed to light. Aliquots once thawed can be kept at 4 °C for 7–10 days before discarding. N.B. for LDN-193189, the solubility on the specification sheet should be checked for each batch, since it differs.
4. ROCK (rho kinase) inhibitor (10 μM) is added to the initial feed (days 0 medium) to improve iPSC survival following Accutase dissociation to single cells, together with basic fibroblast growth factor (FGF-2) (10 ng/ml) to promote proliferation.
5. The original analysis by Maury et al. [3] showed no statistical difference in the proportion of OLIG2-positive cells between use of either 1 μM or 0.1 μM RA.
6. We recommend the use of μ-slide 8-well ibidi dishes (80826, ibidi GmbH) because of their high optical quality. The volume of media per well for this plate is 300 μl.
7. 0.25% Trypsin–EDTA is diluted in calcium- and magnesium-free Earle's Balanced Salt Solution (EBSS).
8. Since DNase may lose <10% of its activity when stored for a week in aliquots at −20 °C, we recommend using the stocks up in 4–5 weeks, otherwise consider doubling the volume added in dissociation buffers. In any event, one may need to adjust the DNase concentration, since some lines tend to be more difficult to dissociate than others. In general, this protocol generates large, sticky EBs; thus, it is better to start out with a higher concentration of DNase and optimize accordingly.
9. Check the volume, since some evaporation can occur; if there is less than 8 ml of medium present, then ensure that the incubator has enough water in the RH pan.
10. Avoid cross-contamination by using a different aspirator pipette for each plate.

11. This is a lower rcf centrifugation than for day 0, so that single cells remain in the supernatant (to be aspirated).
12. Always mark on the lid of the Petri dish the details of the date of feeding and composition of the medium.
13. Inhibition of the Notch pathway reduces progenitor cell proliferation and differentiates OLIG2 positive progenitors to neuronal, i.e., MN, fate.
14. We recommend dissociation at day 16 (but it can be done from day 14 onwards; the earlier dissociation will have more MN progenitors and fewer post-mitotic MNs); however, half of the spheres can be dissociated and half kept back and fed with "day 14" medium every other day, with a second platedown procedure planned 5–7 days later (in case the dissociation process fails the first time).
15. Make up in fresh cold Advanced DMEM/F12. From the working stock aliquots as described in **Note 1**, Matrigel is used at 1:10 (i.e., 1:20 final concentration).
16. Plates are best left overnight at 4 °C, or, if they are needed sooner, leave them at 37 °C for 30–60 min prior to platedown. Plates can be kept for up to 10 days at 4 °C.
17. Speed of platedown is critical to success. As such, we do not recommend handling more than six different cell lines at ones.
18. Invert the Falcon tubes several times and let the spheres settle for 2 min.
19. Adding too little MN-NF will lead to clumping of cells. Ensure that the pellet is resuspended fully and invert the tubes regularly and be vigilant for clumping. Plate cells as quickly as possible.
20. We recommend that the transduction multiplicity of infection (MOI) is optimized to visualize 1–10% of cells labeled with mito-dsRed2. Such sparse labeling permits the visualization of labeled mitochondria in single axons without distraction from the visualization of overlapping axons from neighboring cells.
21. Supplements such as B-27 are phototoxic.
22. Refer to https://github.com/fabricecordelieres/IJ_KymoToolBox for a detailed description of the plugin.

Acknowledgments

The authors thank Dr. Emily R. Lowry for her optimized protocol of motor neuron generation from human iPSCs, which has been adapted here. A.R.M. is a Lady Edith Wolfson Clinical Fellow, jointly funded by the Medical Research Council (MRC) and the

Motor Neurone Disease Association (MR/R001162/1). He also acknowledges support from the Rowling Scholars scheme, administered by the University of Edinburgh. The authors also acknowledge funding from the Anne Rowling Regenerative Neurology Clinic, Euan MacDonald Centre for Motor Neuron Disease Research, and the UK Dementia Research Institute (DRI), which receives its funding from UK DRI Ltd., funded by the MRC, Alzheimer's Society and Alzheimer's Research UK.

References

1. Sleigh JN, Rossor AM, Fellows AD, Tosolini AP, Schiavo G (2019) Axonal transport and neurological disease. Nat Rev Neurol 15(12): 691–703. https://doi.org/10.1038/s41582-019-0257-2
2. Mehta AR, Gregory JM, Dando O, Carter RN, Burr K, Nanda J, Story D, McDade K, Smith C, Morton NM, Mahad DJ, Hardingham GE, Chandran S, Selvaraj BT (2021) Mitochondrial bioenergetic deficits in C9orf72 amyotrophic lateral sclerosis motor neurons cause dysfunctional axonal homeostasis. Acta Neuropathol 141(2):257–279. https://doi.org/10.1007/s00401-020-02252-5
3. Maury Y, Come J, Piskorowski RA, Salah-Mohellibi N, Chevaleyre V, Peschanski M, Martinat C, Nedelec S (2015) Combinatorial analysis of developmental cues efficiently converts human pluripotent stem cells into multiple neuronal subtypes. Nat Biotechnol 33(1): 89–96. https://doi.org/10.1038/nbt.3049
4. Selvaraj BT, Livesey MR, Zhao C, Gregory JM, James OT, Cleary EM, Chouhan AK, Gane AB, Perkins EM, Dando O, Lillico SG, Lee YB, Nishimura AL, Poreci U, Thankamony S, Pray M, Vasistha NA, Magnani D, Borooah S, Burr K, Story D, McCampbell A, Shaw CE, Kind PC, Aitman TJ, Whitelaw CBA, Wilmut I, Smith C, Miles GB, Hardingham GE, Wyllie DJA, Chandran S (2018) C9ORF72 repeat expansion causes vulnerability of motor neurons to Ca(2+)-permeable AMPA receptor-mediated excitotoxicity. Nat Commun 9(1):347. https://doi.org/10.1038/s41467-017-02729-0
5. Fumagalli L, Young FL, Boeynaems S, De Decker M, Mehta AR, Swijsen A, Fazal R, Guo W, Moisse M, Beckers J, Dedeene L, Selvaraj BT, Vandoorne T, Madan V, van Blitterswijk M, Raitcheva D, McCampbell A, Poesen K, Gitler AD, Koch P, Berghe PV, Thal DR, Verfaillie C, Chandran S, Van Den Bosch L, Bullock SL, Van Damme P (2021) C9orf72-derived arginine-containing dipeptide repeats associate with axonal transport machinery and impede microtubule-based motility. Sci Adv. 7(15):eabg3013. https://doi.org/10.1126/sciadv.abg3013. PMID: 33837088; PMCID: PMC8034861.
6. Schindelin J, Arganda-Carreras I, Frise E, Kaynig V, Longair M, Pietzsch T, Preibisch S, Rueden C, Saalfeld S, Schmid B, Tinevez JY, White DJ, Hartenstein V, Eliceiri K, Tomancak P, Cardona A (2012) Fiji: an open-source platform for biological-image analysis. Nat Methods 9(7):676–682. https://doi.org/10.1038/nmeth.2019
7. Zala D, Hinckelmann MV, Yu H, Lyra da Cunha MM, Liot G, Cordelieres FP, Marco S, Saudou F (2013) Vesicular glycolysis provides on-board energy for fast axonal transport. Cell 152(3): 479–491. https://doi.org/10.1016/j.cell.2012.12.029
8. Bodakuntla S, Magiera MM, Janke C (2020) Measuring the impact of tubulin posttranslational modifications on axonal transport. Methods Mol Biol 2101:353–370. https://doi.org/10.1007/978-1-0716-0219-5_20

Open Access This chapter is licensed under the terms of the Creative Commons Attribution 4.0 International License (http://creativecommons.org/licenses/by/4.0/), which permits use, sharing, adaptation, distribution and reproduction in any medium or format, as long as you give appropriate credit to the original author(s) and the source, provide a link to the Creative Commons license and indicate if changes were made.

The images or other third party material in this chapter are included in the chapter's Creative Commons license, unless indicated otherwise in a credit line to the material. If material is not included in the chapter's Creative Commons license and your intended use is not permitted by statutory regulation or exceeds the permitted use, you will need to obtain permission directly from the copyright holder.

Part V

Zebrafish

Chapter 17

In Vivo Live Imaging of Axonal Transport in Developing Zebrafish Axons

Melody Atkins, Jamilé Hazan, and Coralie Fassier

Abstract

Axonal transport is crucial for neuronal homeostasis, survival, and development. Indeed, axonal transport needs to be precisely regulated for developing axons to swiftly and accurately respond to their complex and evolving environment in space and time. A growing number of studies have started to unravel the diversity of regulatory and adaptor proteins required to orchestrate the axonal transport machinery. Despite some discrepancies between in vitro and in vivo axonal transport studies, most analyses aiming at deciphering these regulatory complexes, as well as their mode of action, were carried out in vitro in primary cultures of neurons, and mainly focused on their impact on axon specification and elongation, but rarely on axon navigation per se. Given the clear influence of the in vivo environment on axonal transport, including chemical and physical interactions with neighboring cells, it is essential to develop in vivo models to identify and characterize the molecular complexes involved in this key process. Here, we describe an experimental system to monitor axonal transport in vivo in developing axons of live zebrafish embryos with high spatial and temporal resolution. Due to its optical transparency and easy genetic manipulation, the zebrafish embryo is ideally suited to study such cellular dynamics at a single axon scale. Using this approach, we were able to unravel the key role of Fidgetin-like 1 in the regulation of bidirectional axonal transport required for motor axon targeting. Moreover, this protocol can be easily adapted to characterize a wide range of axonal transport regulators and components in physiological conditions and may additionally be used to screen new therapeutic compounds based on their ability to recue axonal transport defects in pathological conditions.

Key words Axonal transport, Zebrafish, Axon guidance, Molecular motors, Fidgetin-like 1, KIF1Bβ

1 Introduction

One of the unique characteristics of neurons stems from their highly polarized morphology with axons that can extend up to 1 m. Constant communication between the soma and the axon tip at the other end of the neuron is therefore crucial to ensure correct neuronal functions and survival. Anterograde axonal transport is required to forward newly synthesized cargoes to the axon tip, such as RNAs, proteins/receptors, lipids and organelles.

Alessio Vagnoni (ed.), *Axonal Transport: Methods and Protocols*,
Methods in Molecular Biology, vol. 2431, https://doi.org/10.1007/978-1-0716-1990-2_17,
© The Author(s), under exclusive license to Springer Science+Business Media, LLC, part of Springer Nature 2022

Conversely, retrograde axonal transport ensures proper neuronal homeostasis and responses to environmental changes by transporting toxic/misfolded proteins or damaged organelles and bringing cell signaling molecules from the periphery back to the soma [1–3].

This long-range active transport relies on a complex and tightly regulated machinery. The major components of this machinery are the ATPase-dependent molecular motors—namely kinesins and dynein—which use microtubules (MTs) as rails to transport cargoes from the soma to the axon terminal and reciprocally. In axons, unlike in dendrites, microtubules are organized in a highly polarized manner with a fast-growing end (plus-end) pointed toward the synapse and a slow-growing end (minus-end) oriented toward the soma. While kinesins are mostly responsible for the anterograde axonal transport (toward MT plus-ends), dynein is a minus-end directed motor that mediates retrograde transport back to the soma [3–5]. However, a number of cargoes (RNA granules, mitochondria, late endosomes, lysosomes) are found to move bidirectionally along axons, displaying back-and-forth movements with an overall net directionality toward one or the other end of the axon. In the case of bidirectional transport, opposite polarity-directed motors are found together on a same cargo, where they act in a cooperative or competitive manner to ensure accurate cargo delivery [6]. In addition to molecular motors, adaptors and regulatory proteins are crucial players of the axonal transport machinery, respectively promoting molecular motor recruitment on appropriate cargoes or modulating molecular motor directionality, processivity and/or speed to fine tune cargo delivery in space and time [7–11]. Importantly, alterations of either of these components can be deleterious to axonal transport and have been extensively involved in a wide range of neurodegenerative disorders [1, 4, 5, 12–14].

While mostly studied in a neurodegenerative context so far, axonal transport deficit has also been reported in neurodevelopmental disorders [1, 4, 5, 12, 14], implying a role for axonal transport in neuronal circuit wiring in addition to neuron homeostasis and survival. Such evidence is consistent with the need of the growth cone (i.e., the tip of growing axons) to be provided with the building and navigational material required for its accurate probing and responsiveness to environmental changes. Indeed, a few studies suggest a role for molecular motors in the establishment of neuronal connectivity, and more precisely during the axon navigation steps before synaptogenesis [15, 16]. However, most analyses aiming at deciphering the role of molecular motors and their regulatory complexes in developing axons were carried out in vitro, in primary cultures of neurons, and mainly focused on neuronal polarity establishment/maintenance [17] or axon elongation, but rarely on axon navigation per se [18–25]. This is mainly due to the technical challenge represented by the imaging of axonal transport within a developing axon, elongating in a 3D environment and

sometimes deeply beneath the embryo surface. In this context, the zebrafish embryo provides an excellent in vivo system to study axonal transport in developing axons. Indeed, the rapid and external development of the zebrafish embryo as well as its optical transparency and straightforward genetic manipulations are ideally suited for in vivo live imaging of cellular dynamics at a single axon scale. Furthermore, the zebrafish has been extensively used as a powerful vertebrate model for several neurodevelopmental or neurodegenerative disorders [26–31], strengthening its relevance to study axonal transport in vivo in physiological and pathological conditions.

For example, we have recently identified the MT-associated ATPase Fidgetin-like 1 (Fignl1) as a novel key player in motor circuit wiring [32] and direct binding partner of the kinesin-3 family member KIF1bβ and the dynein adaptor Bicd1 [33], supporting a functional link between axonal transport and motor axon navigation. For the aforementioned reasons, we took advantage of the zebrafish to explore the role of this tripartite complex in axonal transport and its contribution to motor axon targeting. We therefore developed a protocol to monitor the transport of different cargoes (including known Kif1bβ cargoes such as Rab3 vesicles or the Neurotrophin receptor TrkB) along individual growing axons en route for their muscle targets in live control, Fignl1- or Kif1bβ-deficient larvae. We here describe the protocol that we used to (1) trigger the mosaic expression of axonal transport markers in vivo in spinal motor neurons, (2) monitor their trafficking in navigating axons using spinning-disk microscopy, as well as (3) to extract and analyze several axonal transport dynamic parameters from these in vivo time-lapse movies (Fig. 1). For this latter step, we used kymograph analysis to track single Fignl1 or Rab3-positive vesicles and characterize their dynamic behaviors, such as anterograde and retrograde speeds, run lengths (i.e., the covered distance between two pauses or directional shifts), as well as the number of static vesicles. Using this experimental workflow, we showed that Fignl1 localized to vesicles that exhibited bidirectional axonal transport in zebrafish navigating motor axons at speeds consistent with molecular motor-based fast axonal transport. Furthermore, we showed that Fignl1 depletion increased Rab3 vesicle retrograde speed—as Kif1bβ depletion did—and decreased their anterograde run lengths [33]. These live imaging results suggested a key role for Fignl1 in bidirectional vesicular axonal transport through dynein speed limitation and improvement of kinesin processivity. Notably, reducing Dynein-based transport through bath application of the Dynein inhibitor ciliobrevin D partially rescued the axon targeting defects of Fignl1-deficient larvae [33], highlighting the robustness of our protocol in generating physiologically relevant and reliable axonal transport data.

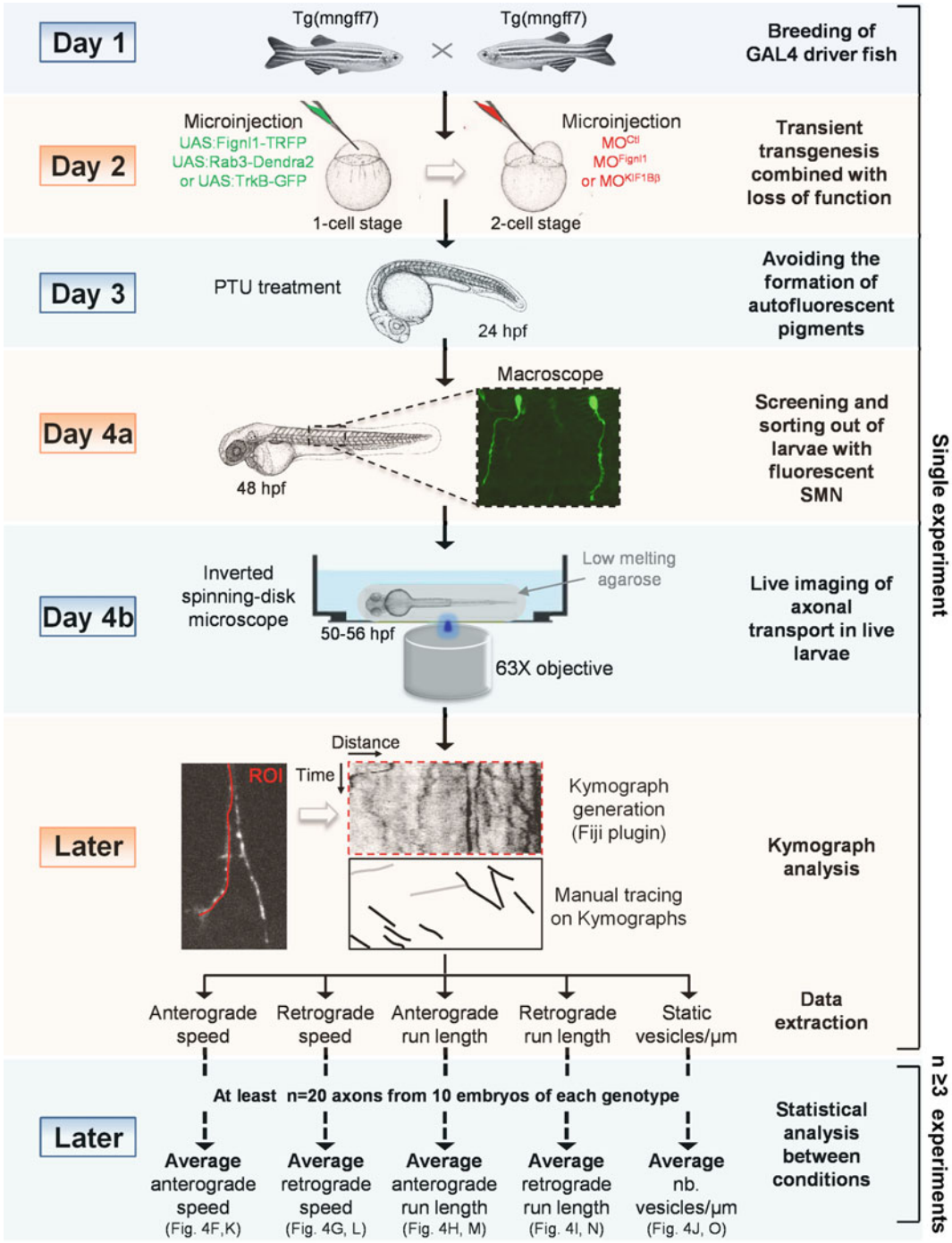

Figure 1

Fig. 1 Schematic representation of the successive steps used to investigate and compare axonal transport in vivo between different experimental conditions. Embryos obtained from natural spawning of SMN GAL4 driver zebrafish Tg(mnGFF7) (Day 1) were sequentially injected with Tol1 or Tol2 DNA constructs expressing fluorescently labeled axonal transport markers under a *UAS* promoter (at the 1-cell stage) and *Fignl1* or *KIF1Bβ* morpholinos (at the two-cell stage; Day 2). Injected embryos were treated at 24 h post-fertilization (hpf) (Day 3) with PTU to block the formation of autofluorescent pigments that represent a major source of

This is particularly important in view of contrasting data reporting discrepancies between in vivo and in vitro axonal transport modalities [34–39]. These findings are not surprising given the number of parameters shown to influence axonal transport and which cannot be fully reproduced in vitro, such as physical and chemical interactions between axons and surrounded cells/tissues (e.g., axon ensheathment by glial cells, neurotrophic factors, guidance molecules [40–43]), neuronal activity and connectivity [23, 44] as well as several physiological parameters (e.g., the glycolytic machinery, oxygen metabolism) [45–48]. These data therefore emphasize the importance of developing methods to monitor axonal transport in vivo to better understand the modalities of long-range transport in a physiological context and define novel strategies to restore it in pathological conditions. In this context, we believe that the present protocol offers a broad spectrum of possible applications, from fundamental studies to identify novel key players/regulators of the transport machinery in developing axons, to more translational studies aiming at assessing the efficiency of specific genetic/pharmacological approaches to rescue axonal transport deficit in zebrafish models of neurodevelopmental/degenerative disorders, thereby defining novel therapeutic avenues (*see* **Note 1**).

2 Materials

2.1 Targeted Expression of Axonal Transport Markers in a Subset of Zebrafish Neurons Using Transient Transgenesis

1. Adult zebrafish GAL4 driver: the Tg(mnGFF7) [49, 50] or Tg (*HuC*:GAL4) [51] transgenic fish respectively expressing the GAL4 transactivator in spinal motor neurons (SMN) or in all neurons.
2. Tol2 or Tol1 DNA plasmids expressing fluorescently labeled axonal transport markers (e.g., molecular motors, cargoes, or adaptor proteins) under the control of a *UAS* promoter: Tol2_*UAS*:Rab3-Dendra2, Tol1_14*UAS*: Fignl1-TRFP [33], and Tol2_10*UAS*:TrkB-GFP (kindly provided by F. Del Bene's lab).
3. *Tol1* or *Tol2* mRNA, in vitro transcribed from linearized pCS2-Tol1 (#61388; Addgene) or pT3TS-Tol2 (#31831; Addgene)

Fig. 1 (continued) background in live imaging experiments. Injected embryos with isolated fluorescent SMN were selected (Day 4a) and embedded in low melting agarose in a glass bottom dish. Axonal transport of specific markers was recorded using an inverted spinning disk microscope for 5 min (1 Z-stack every 4 s; Day 4b). Z-stack movies were analyzed using the KymographClear2.0 plugin of the Fiji software. Anterograde and retrograde vesicle speeds or run lengths as well as the number of static vesicles/100 μm were extracted from kymographs, averaged for each axon, and statistically compared between each experimental condition using the GraphPad Prism software

plasmids using the mMESSAGE mMACHINE Transcription Kit (Ambion) (*see* **Note 2**).

4. DNA solution for transgenesis of axonal transport markers: mix 20–50 ng of the *UAS* DNA plasmid, 25–50 ng of *Tol1* or *Tol2* mRNA, 1 μL of phenol red (to assess the injected volume), and DNAse-/RNAse-free water to 10 μL.
5. Morpholino solution: dilute 2 nM Fignl1 or KIF1bβ morpholino stock solution at 1/10 in DNAse-/RNAse-free water (*see* **Note 3**).
6. 100-mm petri dishes to collect and raise zebrafish embryos.
7. Programmable microinjector with the integrated pressure supply.
8. Stereomicroscope (Leica M80).
9. Clark Borosilicate Standard Wall with Filament, model GC100F-10.
10. Micropipette Puller for the preparation of microinjection glass capillaries.
11. 100-mm petri dish filled with agarose. Make linear furrows on the agarose to maintain eggs during injection.
12. E3 medium to raise injected embryos: 5 mM NaCl, 0.17 mM KCl, 0.33 mM $CaCl_2$, 0.33 mM $MgSO_4$, 10^{-5}% Methylene Blue.
13. 50× Phenyl-2-thiourea solution (PTU; 0.15% (w/v)) to avoid pigmentation.
14. Chilling/heating incubator to raise injected zebrafish embryos.

2.2 In Vivo Imaging of Axonal Transport

1. Macroscope Axio Zoom V 16 (Carl Zeiss, Jena, Germany) to screen and sort transgenic larvae showing mosaic expression of the transgene.
2. Stereomicroscope (Leica M80) for embryo mounting.
3. 0.8% low-melting agarose solution for embryo embedding: dissolve 0.8 g of low-melting agarose in 100 mL of E3 medium and make 1.5 mL aliquots.
4. 35-mm glass-bottom dishes.
5. 1-mL syringe filled with silicone grease.
6. E3 videomedium: Add 200 μL of 50× PTU solution and 800 μL of 4% Tricaine solution to 19 mL of Methylene Blue-free E3 medium.
7. Leica DMI 6000B inverted spinning-disk microscope equipped with an incubation chamber set at 28 °C, a 63× oil immersion objective (NA 1.4), 491 nm and 561 nm 100 mW Cobolt calypso lasers, an EMCCD camera (Photometrics

Quantem 512 SC) controlled through the Metamorph software (Molecular Devices).

2.3 Analysis of Axonal Transport Movies

1. Fiji software equipped with the KymographClear 2.0 macro toolset (Fiji software; [52]) and/or The KymoTool plugin (ImageJ software).
2. Microsoft Excel and GraphPad Prism (GraphPad Software, San Diego, CA) or equivalent software to pool and statistically analyze the data extracted from kymographs.

3 Methods

The following protocol describes the different steps and general parameters used to conduct in vivo live imaging of axonal transport in developing axons of zebrafish embryos/larvae as well as the analysis paradigm that we used to investigate the role of the Fignl1/KIF1Bβ complex in the regulation of this process. Using this methodological approach, we first assessed whether Fignl1 is actively transported in zebrafish developing SMN axons. We next investigated how its loss of function impacts the axonal transport of a known Kif1bβ cargo—Rab3 vesicles—compared to Kif1bβ deficiency. To this aim, we first took advantage of the *UAS*/GAL4 and Tol1/2 transposition systems, which are commonly used in the zebrafish, to drive the mosaic expression of fluorescently labeled Fignl1 in SMN and monitored the motility of Fignl1-positive vesicles in individual navigating axons of live transgenic larvae. We then used the same genetic approach (i.e., targeted expression of a Rab3-Dendra2 fusion protein) in combination with transient loss-of-function experiments (i.e., morpholino-based knockdown strategy) to analyze the axonal transport of Rab3 vesicles in Fignl1- and Kif1bβ-deficient larvae at a single SMN axon scale. In these two sets of experiments, Fignl1 or Rab3 axonal transport was recorded in three dimensions under an inverted spinning-disk microscope over a 5-min period with a z-stack acquisition of 5 μm-thickness every 4 s. Maximum z-stack projection movies were converted into kymographs and analyzed using the KymoClear2.0 plugin [52]. This plugin uses a Fourier transformation-based algorithm to assign a color code to each type of motion (anterograde, retrograde, static), which facilitates the interpretation of the often noisy kymographs generated from in vivo recordings. Distinguishable particle movements were manually traced on each kymograph ($n = 20–50$). Slopes and covered distances between two pauses or change in directionality were extracted from these segmental manual traces and used to respectively determine the mean velocities and run lengths for both anterograde and retrograde transport. The mean number of static vesicles was determined by counting

the number of vertical lines per kymograph normalized to the length of the imaged axonal segment. Average values obtained for each individual axon were used for statistical analysis.

Using this experimental paradigm, we showed that the KIF1Bβ-binding partner Fignl1 was located on vesicles that were transported in both anterograde and retrograde directions within SMN axons at mean velocities consistent with molecular motor-based fast axonal transport (Fig. 4a–c). Our transport analysis further revealed that Fignl1 loss of function significantly increased retrograde transport velocities of Rab3 vesicles in navigating SMN axons as Kif1bβ deficiency did. Fignl1 depletion also led to a significant decrease in Rab3 vesicle anterograde run lengths, suggesting a dual role for Fignl1 in Kif1bβ processivity and dynein speed restriction (Fig. 4d–o). Overall, these live imaging results together with other pharmacological, genetic, and biochemical data allowed us to uncover Fignl1 as a regulator of bidirectional axonal transport required for motor circuit wiring [33].

3.1 Targeted Expression of Axonal Transport Markers in a Subset of Zebrafish Neurons Using Transient Transgenesis

1. Prepare the DNA and morpholino solutions required for transient transgenesis and loss-of-function experiments, respectively. Keep the solutions on ice until injection.
2. Collect the eggs obtained from natural spawning of pan-neuronal or SMN GAL4-driver fish in E3 medium (Fig. 1, Day 1 and 2).
3. Transfer the eggs in an agarose-filled petri dish with linear furrows. Place and orient one-cell-stage embryos quickly but gently along each furrow to keep them from turning during microinjection.
4. Use a filament-containing glass capillary pulled with a Flaming-Brown puller as a needle to microinject one-cell-stage embryos. Fill the capillary with 3 μL of the DNA solution and connect it to the FemtoJet®4i microinjector. Select the automatic mode of the microinjector. Adjust the pressure and delivery time to inject 1–1.5 nL of the DNA solution mix into the single cell of the embryo (*see* **Note 4**) and proceed to the injection of several GAL4 transgenic embryos (Fig. 1, Day 2).
5. For subsequent loss of function experiments, exchange the capillary for a new one filled with the morpholino solution. Wait for the injected embryos to reach the two-cell stage and re-inject them at the yolk/cell boundary with 0.4 or 1.4 pmol of *Fignl1* [32] or *KiF1bβ* [53] morpholinos, respectively (Fig. 1, Day 2; *see* **Note 3**).
6. Gently transfer the injected embryos in a petri dish containing E3 medium (30 mL) and raise them in a heating incubator calibrated at 28 °C.

7. The following day, clean the petri dish by discarding the embryos that were not fertilized or have failed to develop properly. Add 300 μL of 50× PTU solution in the petri dish to avoid pigmentation and place the embryos back in the incubator (Fig. 1, Day 3).

3.2 In Vivo Imaging of Axonal Transport

1. On the imaging day (Day 4), melt the 0.8% low-melting agarose solution and maintain it at 50 °C in a dry bain-marie placed close to your stereomicroscope.
2. Switch on the microscope device and set the imaging chamber temperature at 28 °C before sorting and mounting the embryos, so that the system has time to equilibrate in temperature prior to axonal transport recordings. All experiments and replicates must be conducted at the same temperature (*see* **Note 5**).
3. Use a fluorescent stereomicroscope to screen and sort 48-h post fertilization (hpf) transgenic embryos for normal gross morphology and mosaic expression of the transgene in SMN (Fig. 1, Day 4a; *see* **Note 6**).
4. Dechorionate the selected embryos under a stereomicroscope and transfer them in a 35-mm plastic petri dish containing 2 mL of E3 videomedium for anesthesia. Concomitantly, use a syringe filled with silicone grease to delimit two compartments at the center of the 35-mm glass bottom petri dishes in which transgenic embryos will be individually mounted for subsequent imaging.
5. Use a plastic pipet to suck a single anesthetized embryo in a minimum volume of E3 videomedium, rapidly embed it in pre-warmed 0.8% agarose solution and place it in lateral view against the bottom of the dish in the silicone grease-delineated compartment (Fig. 1, Day 4b). Proceed exactly the same way for at least five embryos per experimental condition.
6. Image transgenic fish using a Leica DMI 6000B inverted spinning-disk microscope equipped with a 63× immersion objective (NA 1.4), 491-nm and 561-nm 100-mW Cobolt calypso lasers and an EMCCD camera (Photometrics Quantem 512 SC) supported by the Metamorph software (Molecular Devices).
7. Place the petri dish containing the embryos under the microscope and wait for at least 5 min for the system to equilibrate in temperature. During this time, run the Metamorph software and enter all your acquisition parameters in the Multi-Dimensional Acquisition menu:
   (a) Time lapse: make an acquisition every 4 s for a period of 5 min (i.e., a total of 76 time points) (*see* **Note 7**).

(b) Wavelengths: select the appropriate wavelength and configure it as follows: gain: 1; digitizer: 10 MHz (EM gain); exposure time: 50–150 ms; acquire: every time point; auto expose: never; auto focus: never; binning: 1 × 1. The exposure time is limited by the high acquisition rate required for fast axonal transport recording and the z-stack thickness due to in vivo 3D imaging of a consequential axon segment (*see* **Note 8**).

(c) Z-stack: determine the focal plane in which the largest portion of the axon can be focused and select the "Center around Current" option. Use a step size of 0.8 μm and set the number of steps at 6 maximum. Note that Z-stack thickness and z-step size must be adapted to the time-lapse interval constraint.

(d) Stream: select the z-stream mode to collect the Z-stack image sequence as a continuous data stream to the random access memory (RAM) of the computer (*see* **Note 9**). The images will be saved on the local hard disk only after the entire imaging is completed. Choose a Z motor that supports streaming for the available option.

8. Use the bright-field light to position the objective on the spinal cord portion located around the yolk tube and switch to the appropriate fluorescent illumination to rapidly search for isolated fluorescent SMN. Limit fluorescent excitation of the focal plane to prevent photobleaching and phototoxicity. We here focused our analysis on rostrally projecting secondary motor neuron (RoP-like sMN) axons located around the yolk tube and used the specific topography of their axonal projection to identify them (*see* **Note 10**).
9. Once ready to image a selected axon, switch to laser illumination, adjust the laser power to get high dynamic range images (we recommend to keep the laser power under 35% to avoid rapid bleaching of the fluorescent marker during the acquisition time and to minimize phototoxicity/photodamage), bring the axonal transport marker in focus and run the acquisition.
10. Image at least two individual SMN per fish and at least five embryos per experimental condition and injection slot.
11. For each acquisition, Z-stack images of each individual time point are recorded as a TIFF (Tagged Image File Format) file and a global ".nd" file is generated.

3.3 Analysis of Axonal Transport Movies

In this section, we will extract quantitative parameters such as speed and run lengths from our in vivo axonal transport movies through the generation of kymographs. However, before describing the analysis workflow, a few issues that may complexify in vivo analyses with respect to in vitro studies need to be mentioned. For instance,

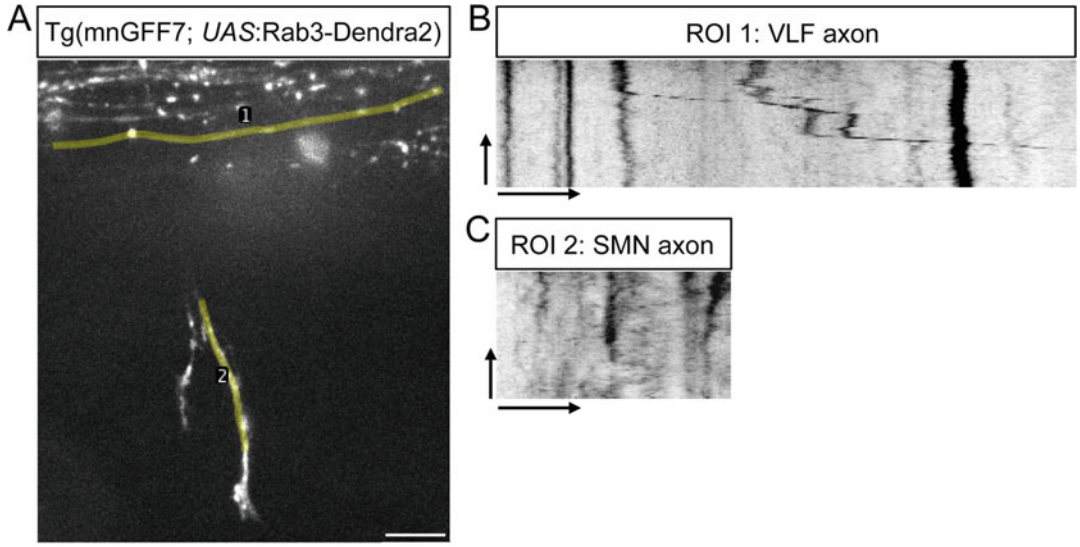

Fig. 2 The readability of kymographs generated from in vivo axonal transport movies may significantly vary with different axonal populations. (**a**) Still images extracted from time-lapse recordings of Rab3-Dendra2 vesicles in the spinal cord of 50-hpf Tg(mnGFF7) larvae injected with a *UAS*:Rab3-Dendra2 plasmid. Yellow lines represent the ROI (region of interest) used for kymograph analysis of Rab3-Dendra2 motility in an axon of the ventral longitudinal fasciculus (VLF; ROI 1) and a spinal motor neuron (SMN) axon (ROI 2). Scale bar: 10 μm. (**b**, **c**) Representative kymographs of Rab3-Dendra2 vesicular transport in a control VLF (**b**) or SMN (**c**) axon. Kymographs were generated using the Kymotool plugin (Image J software).Vertical black lines represent static vesicles. Vertical scale bars: 2 min and horizontal scale bars: 10 μm. Kymographs generated from VLF axons are less noisy and thus easier to read than those generated from SMN axons. This is mainly due to the difference in size and density of Rab3 vesicles in these two axonal populations

tissue samples scatter more light above and below the focal plane due to their thickness, which reduces the signal-to-noise ratio. As a result, still and time-lapse videos monitored in vivo from intact animals are often noisier by nature than acquisitions from their cell culture counterpart, which has a direct impact on kymograph quality. Moreover, the 3D trajectory of specific axonal populations will directly influence the size of the axon portion that can be imaged under the imaging constraints mentioned above (Z-stack thickness and temporal resolution) and thereby the size of the kymograph. Furthermore, as illustrated in Fig. 2, the quality and readability of kymographs generated from in vivo data can significantly vary according to the targeted neuronal population and subtype, although they are generated within the same embryo using the same plugin (*see* **Note 11**). This is mainly due to the fact that the size, density, and distribution of specific cargoes may differ from one population to the other (Fig. 2). As an example, kymographs generated from axonal transport movies of secondary motor neuron axons with standard KymoTool or KymoBuilder plugins were noisier than those obtained from reticulospinal

neurons (Fig. 2). To improve kymograph quality, we here used the "KymographClear" macro toolset of the Fiji software as an alternative. A special feature of this plugin is that it allows users to separate motion directions in the kymograph thanks to a Fourier transformation-based algorithm. Forward and backward motions as well as pauses are represented in different colors, which greatly eases kymograph interpretation. Notably, as highlighted below, KymographClear kymographs are of high quality, which enables the analysis of smaller particle movements than kymographs generated by KymoTool or KymoBuilder plugins (*see* Fig. 3e for comparison and **Note 12**). This is of particular importance given that the larger particles—that are systematically detected on kymographs, independently of the choice of the plugin—are often far less motile than smaller particles and are not necessarily representative of the global particle population, since they may be the direct result of excessive overexpression.

Before starting the analysis, we recommend to keep the raw data in a storage folder and create a new folder per experiment—named "Experiment 1" here—which will be dedicated to data analysis. In the "Experiment 1" folder, it is advisable to create a folder for each analyzed axon, in which all the files generated during the different steps of analysis will be saved. Here, we have named the corresponding folder "Axon1."

3.3.1 Kymograph Generation

1. Open the "Axon1.nd" Metamorph file in the Fiji software by drag-dropping the file on the Fiji toolbar. Generate a maximum intensity projection by using "Image > Stack > Z Project." Make sure to select "Max intensity" for the projection type.
2. Calibrate the stack by using the "Image > Properties" menu in Fiji. Units for defining pixel size and frame interval time are micrometers and seconds, respectively.
3. Save the stack as "Axon1_stack.tiff" in its dedicated folder.
4. Save the file as an image sequence in an "Axon1_ImageSequence" folder by using "File > Save as > Image sequence." This will be important to open the stack using the "KymographClear" plugin of Fiji.
5. Open the "KymographClear" macro toolset by clicking on the "More tools" button (Fig. 3a). Refer to https://sites.google.com/site/kymographanalysis/ for detailed description of the macro toolset.
6. Use the first button of the macro toolset to open the image sequence saved at the above **step 4**. Make sure to choose the "Open a sequence and compute max intensity image" option (Fig. 3a).
7. Select the segmented line (second button of the macro toolset) to manually trace a line along the axon in which cargo

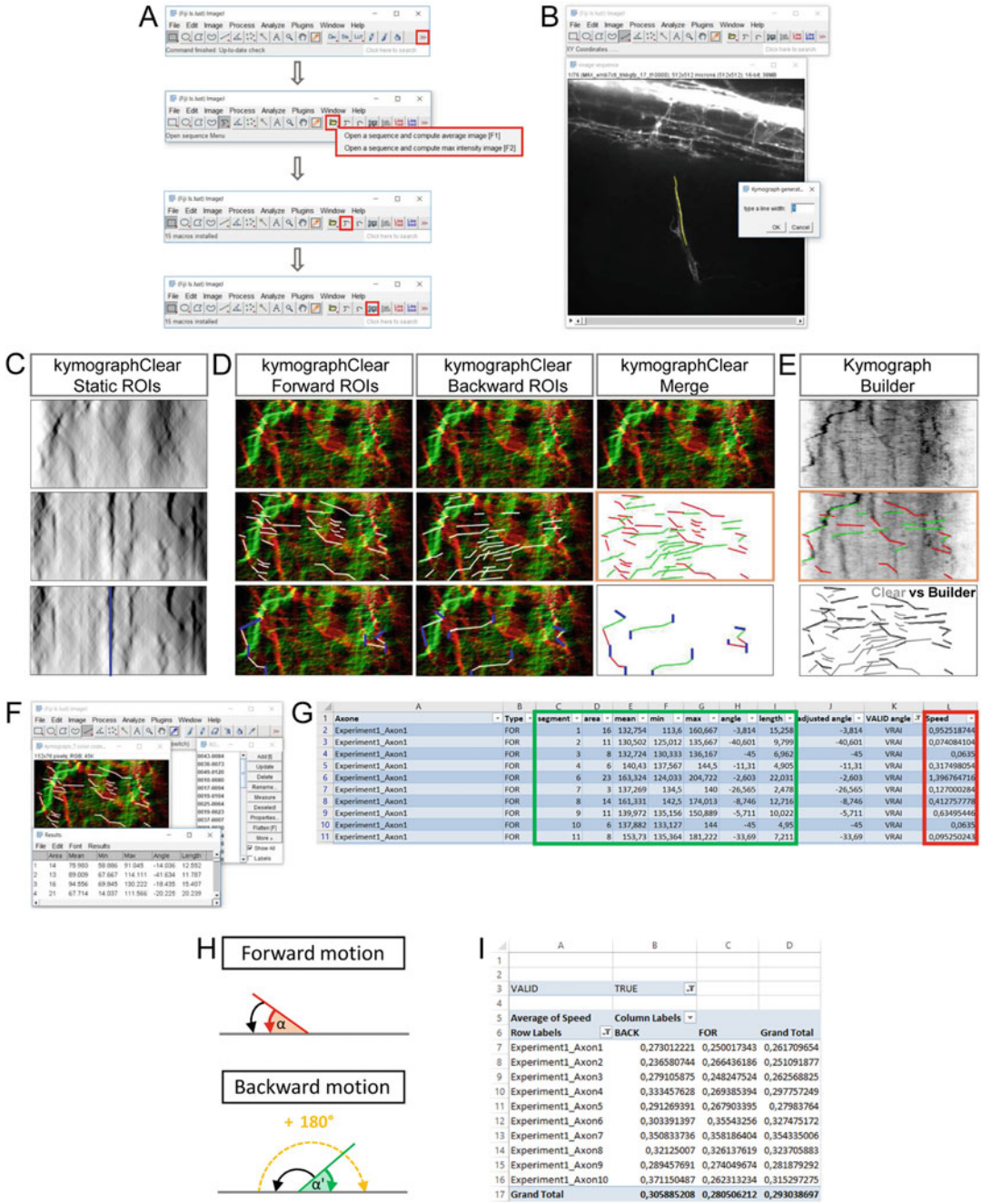

Axone	Type	segment	area	mean	min	max	angle	length	adjusted angle	VALID angle	Speed
Experiment1_Axon1	FOR	1	16	132,754	113,6	160,667	-3,814	15,258	-3,814	VRAI	0,952518744
Experiment1_Axon1	FOR	2	11	130,502	125,012	135,667	-40,601	9,799	-40,601	VRAI	0,074084104
Experiment1_Axon1	FOR	3	8	132,724	130,333	136,167	-45	6,962	-45	VRAI	0,0635
Experiment1_Axon1	FOR	4	6	140,43	137,567	144,5	-11,31	4,905	-11,31	VRAI	0,317498054
Experiment1_Axon1	FOR	6	23	163,324	124,033	204,722	-2,603	22,031	-2,603	VRAI	1,396764716
Experiment1_Axon1	FOR	7	3	137,269	134,5	140	-26,565	2,478	-26,565	VRAI	0,127000284
Experiment1_Axon1	FOR	8	14	161,331	142,5	174,013	-8,746	12,716	-8,746	VRAI	0,412757778
Experiment1_Axon1	FOR	9	11	139,972	135,156	150,889	-5,711	10,022	-5,711	VRAI	0,63495446
Experiment1_Axon1	FOR	10	6	137,882	133,127	144	-45	4,95	-45	VRAI	0,0635
Experiment1_Axon1	FOR	11	8	153,73	135,364	181,222	-33,69	7,211	-33,69	VRAI	0,095250243

	A	B	C	D
1				
2				
3	VALID	TRUE		
4				
5	Average of Speed	Column Labels		
6	Row Labels	BACK	FOR	Grand Total
7	Experiment1_Axon1	0,273012221	0,250017343	0,261709654
8	Experiment1_Axon2	0,236580744	0,266436186	0,251091877
9	Experiment1_Axon3	0,279105875	0,248247524	0,262568825
10	Experiment1_Axon4	0,333457628	0,269385394	0,297757249
11	Experiment1_Axon5	0,291269391	0,267903395	0,27983764
12	Experiment1_Axon6	0,303391397	0,35543256	0,327475172
13	Experiment1_Axon7	0,350833736	0,358186404	0,354335006
14	Experiment1_Axon8	0,32125007	0,326137619	0,323705883
15	Experiment1_Axon9	0,289457691	0,274049674	0,281879292
16	Experiment1_Axon10	0,371150487	0,262313234	0,315297275
17	Grand Total	0,305885208	0,280506212	0,293038697

Fig. 3 Workflow of the analysis paradigm used to generate kymographs from in vivo axonal transport movies and extract transport parameters. (**a**) Summary showing the sequential use of the different KymographClear macro toolset buttons for kymograph generation from in vivo axonal transport movies of a selected cargo. Recordings of TrkB-GFP axonal transport are here used as an example. (**b**) Line drawn manually at a chosen width along an individual axon (i.e., ROI) on the maximum intensity projection generated from the Metamorph ".nd" file. (**c**) Analysis of the kymograph filtered for static particles. No TrkB receptor presents a static trajectory (i.e., a vertical trajectory from start to finish; top panel). By contrast, middle kymograph generated

movement will be quantified. As a general rule, always start from the proximal part of the axon and move toward the distal end. If necessary, use "Image > Adjust > Brightness/Contrast" beforehand for a better visualization of the selected axon. At this step, it is important to make sure that you are selecting individual axons (*see* **Note 13**).

8. Add the traced line to the "ROI manager" using "Analyse > Tools > ROI Manager> Add" or by pressing the "Ctrl" and "t" buttons. Save the ROI by using the "More > save" option.
9. Press the "Kymograph" button (Fig. 3a) and choose the right line width (Fig. 3b, *see* **Notes 14** and **15**). Five kymographs are generated:
   (a) A kymograph filtered for forward motion (kymograph_1 filtered_forward.tif).
   (b) A kymograph filtered for backward motion (kymograph_1 filtered_backward.tif).
   (c) A kymograph filtered for static particles (kymograph_1 static.tif).
   (d) The resulting kymograph (kymograph1.tif).
   (e) The filtered kymographs combined in a color-coded image (kymograph_1 color coded direction.tif).

These kymographs are automatically saved within a "kymograph" folder generated by the macro toolset in your

Fig. 3 (continued) from a different movie shows one static vesicle, highlighted in blue in the bottom panel. (**d**) Analysis of the color-coded kymograph generated by the KymographClear plugin, in which forward (left panel, white ROIs), backward (middle panel, white ROIs), and overall motion (right panel, red and green ROIs for forward and backward motion, respectively) are represented. Static vesicles (in the blue channel) have deliberately been retrieved from this color-coded kymograph for better visualization of forward and backward motions. ROIs for segmental velocity and run length extraction are depicted in rows 2 and 3, respectively. For run length ROIs, blue segments show static trajectories (when vertical) or vesicular change of direction (when inclined) framing each run. (**e**) Comparison of the segmental velocity ROIs generated with the KymographBuilder plugin or with the KymographClear macro toolset. The ROI manually traced in (**b**) was used to generate a kymograph with the KymographBuilder plugin (top). Segmental velocity ROIs were traced (middle panel; red and green ROIs for forward and backward motions, respectively) and merged to the ROIs generated from the KymographClear color-coded kymograph on the bottom panel. Black and gray dotted lines indicate ROIs that overlap between the two plugins while gray traces are additional ROIs generated with the KymographClear plugin. (**f**) Screenshot of the color-coded kymograph with its forward segmental velocity ROIs in the "ROI Manager" as "Show all." The use of the "Measure" button enables to extract the "Angle" parameter. (**g**) Organization of all collected data in an Excel sheet for analysis. (**h**) Diagram depicting the evaluation of forward and backward speeds from adjusted angles. The forward (α) and backward (α') angles that need to be extracted for speed calculation are represented in red and green, respectively. The black arrows delineate the angles that are calculated by the "ROI manager." The angle adjustment required for backward motion appears in yellow. (**i**) Screenshot of a representative pivot generated from the Excel sheet

"Axon1_ImageSequence" folder (**step 4**). You can therefore have access to the kymographs by going through "Experiment1 > Axon1> Axon1_ImageSequence > kymograph > kymograph_1."

3.3.2 Analysis of Static Vesicles

1. Open the "kymograph_1 static.tif" file and count the number of vertical lines. Lines that are vertical only during part of the acquisition (Fig. 3c, top panel) are not taken into account. Indeed, trajectories must remain vertical from start to finish to be considered static (Fig. 3c, middle and bottom panels).
2. Extract the length of the analyzed axon from the ROI saved at **step 8** (Subheading 3.3.1) and use the following equation:

$$\text{Number of static vesicles per 100 µm} = \frac{\text{Number of static particles} \times 100}{\text{Length of analysed axon (µm)}}$$

3.3.3 Analysis of Run Lengths

1. To extract run lengths, which correspond to the distance covered by a vesicle between two pauses or changes in direction, open the "kymograph_1 color coded direction.tif" file.
2. Using "Image> Adjust> Brightness/Contrast," adjust the parameters so as to only visualize forward and backward motions (Fig. 3d, row 1). Identify runs (Fig. 3d, row 3, white ROIs) that are framed by vertical lines indicating pauses or by a switch in directions (Fig. 3d, row 3, blue ROIs).
3. Use the "Multipoint tool" to mark the initial (i) and final (f) points of each trajectory framed by two pauses/directional switch.
4. Add to the "ROI Manager" as in **step 8** (Subheading 3.3.1), then click on the "Measure" button to access their x-coordinates. We recommend identifying a minimum of four/five trajectories per axon. Save ROIs as "Axon1_ForwardRun."
5. Calculate the difference between each pair of x-coordinates to define the run lengths. For a setup in which a corresponds to the pixel size in micrometers:

$$\text{Run length (µm)} = |(Xf - Xi) \times a|$$

6. Repeat **steps 1–5** on the "kymograph_1 color coded direction.tif" file to identify retrograde run lengths and save the ROIs as "Axon1_BackwardRun."

3.3.4 Analysis of Segmental Velocity

1. On the same "kymograph_1 color coded direction.tif" file, generate a different set of ROIs dedicated to particle segmental anterograde velocity. Depending on the vesicle density in the target axonal population, kymograph interpretation may be

rendered more complicated by the fact that several particles keep crossing each other's paths. Thus, being absolutely certain that you are following the same vesicle from start to finish may become tricky.

2. Use the straight line to trace 20–50 individual segmental runs to avoid kymograph over-interpretation (Fig. 3d, row 2). If necessary, use the "kymograph_1 filtered_forward.tif" file to help identify trajectories. We recommend tracing each segment (i.e., ROI) on the "kymograph_1 color coded direction.tif" file to avoid taking background noise into account.
3. Add each tracing to the "ROI manager." Select "Show all" on the "ROI manager" to keep track of the traced trajectories.
4. Save all the ROIs as "Axon1_ForwardVelocity" in the "Experiment1 > Axon1> Axon1_ImageSequence > kymograph > kymograph_1" folder.
5. Close the "ROI Manager" and discard the displayed ROIs as an overlay.
6. Repeat **steps 1–5** on the "kymograph_1 color coded direction.tif" file to identify retrograde segmental velocities and save each set of ROIs as "Axon1_BackwardVelocity."

3.3.5 Data Extraction from ROIs

1. Repeat steps in Subheadings 3.3.1–3.3.4 for all imaged axons of a single experiment.
2. On the "kymograph_1 color coded direction.tif" kymograph, open the forward traces from **step 4** (Subheading 3.3.4) in the ROI Manager using "More> Open> Experiment1> Axon1> Axon1_ImageSequence> kymograph > kymograph_1 > Axon1_ForwardVelocity."
3. Click on the "Measure" button to extract the different parameters from the forward tracings (Fig. 3f). Here, we recommend copying and pasting the seven columns in the columns "C" to "I" of an Excel sheet. Use column "A" to identify each of these segmental runs as belonging to "Experiment1_Axon1," and column "B" to identify them as "FOR" for forward movement (Fig. 3g).
4. Open the "Axon1_BackwardVelocity." ROIs saved at **step 6** (Subheading 3.3.4) and repeat **step 3**. Here, use the "B" column of your Excel sheet to identify runs as "BACK" for backward movement (Fig. 3g).
5. Repeat the above **steps 2–4** for each pair of forward and backward kymographs corresponding to each analyzed axon (Axon1, Axon2, Axon3,. . .) and pool the data from all axons of a single experiment. Use different Excel sheets for the different experimental conditions of your setup.

6. Segmental speeds will be calculated based on the "angle" parameter (column H of your Excel sheet, Fig. 3g). As depicted in Fig. 3h, the angle measured by Fiji always corresponds to the angle between the segmented line you have drawn and a virtual horizontal line crossing your segmented line (black arrows in Fig. 3h). While this angle is correct in the case of forward motion, it requires adjustment in the case of backward motion by adding 180° (column J in Fig. 3g).
7. To eliminate possible aberrant traces that can sometimes be generated when manually tracing segmental runs, we recommend checking that all the adjusted angles are valid, that is that forward angles should be comprised between −90° and 0°, while backward angles should be comprised between 0° and 90° (column K in Fig. 3g).
8. Calculate segmental speeds. For an acquisition in which a and b respectively correspond to pixel size (μm) and time interval (s), use the equation:

$$\text{Particle velocity}\left(\frac{\mu m}{s}\right) = \left|\frac{-1}{\tan\left(\text{adjusted angle} \times \frac{\pi}{180}\right)} \times \frac{a}{b}\right|$$

9. Use a pivot table to generate the mean backward and forward motion speeds for each axon of a given condition (Fig. 3i). Generate such a pivot table for each experimental condition.
10. Repeat the experiments and analyze each set of data at least three times.
11. Finally, calculate the mean number of static vesicles per 100 μm, mean run length, and mean segmental speed by pooling the data of all experiments for each condition (*see* **Note 16**). Compare the means of each axon (taken from at least three experiments) between conditions using an unpaired two-tailed *t*-test or another appropriate statistical method and determine which differences are statistically significant (Fig. 4f–o).

4 Notes

1. We would like to highlight the fact that the zebrafish embryo is ideally suited for drug treatment and screening since water-soluble drugs can be directly added to the E3 medium. The present protocol can thus be readily expanded to investigate the consequences of specific pharmacological treatments on axonal transport modalities in vivo under physiological and pathological conditions. It could also be used to conduct drug screening aiming at identifying novel pharmacological modifiers of

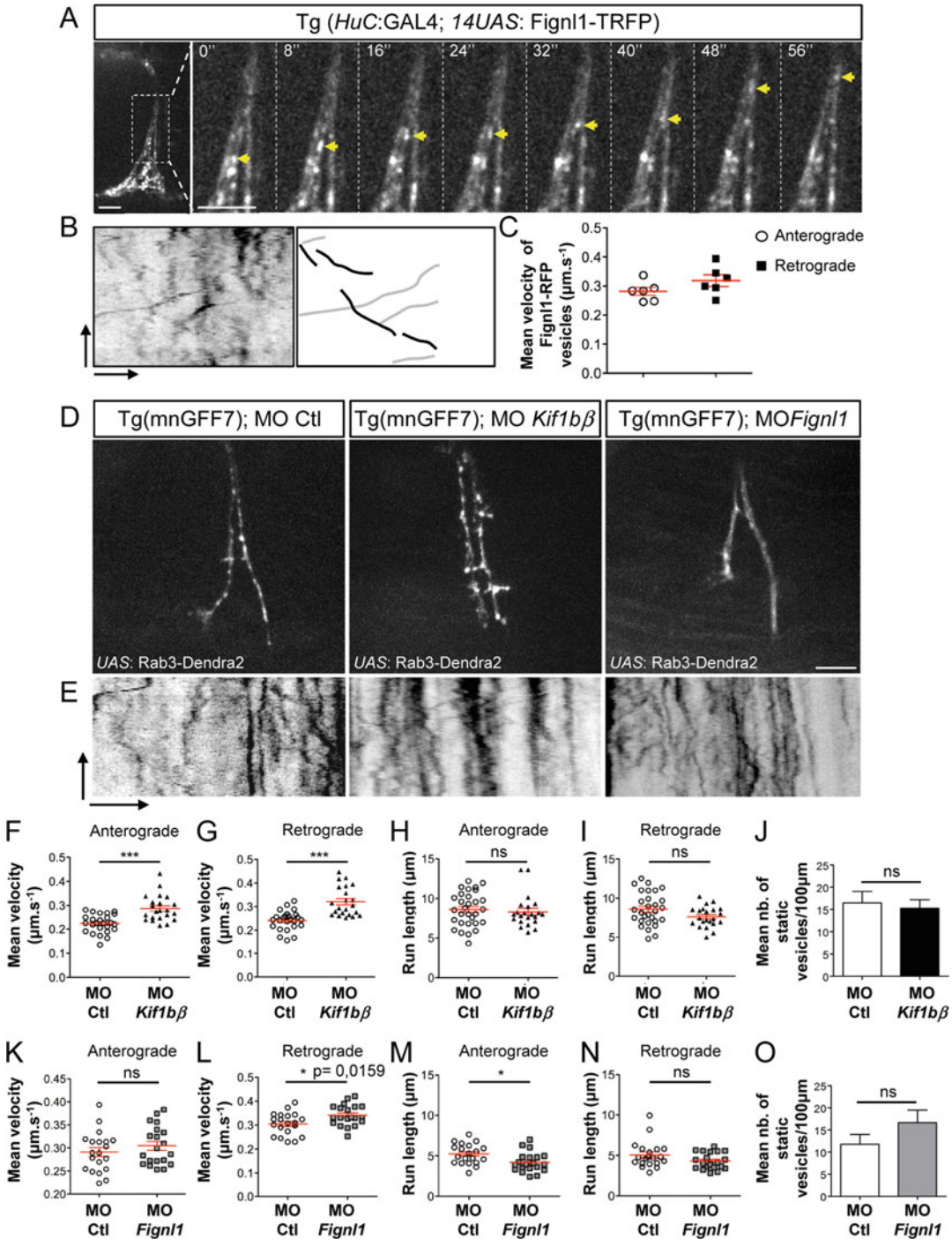

Fig. 4 Representative examples of data generated from in vivo recordings and kymograph analysis of FignI1-TRFP or Rab3-Dendra2 axonal transport (Adapted from Atkins et al. [33]). ©2019 Atkins et al. Originally published in *The Journal of Cell Biology*. https:/doi.org/10.1083/jcb.201805128. (**a**–**c**) Analysis of FignI1-TRFP motility in navigating zebrafish spinal motor neuron (SMN) axons. (**a**) Still images from time-lapse recordings of FignI1-TRFP in secondary motor neuron axons of 56-hpf Tg(*HuC*:GAL4;14*UAS*:FignI1-TRFP) transgenic larvae. Right-hand panels are higher magnifications of the axon boxed in the left-hand panel. Yellow arrowheads track a FignI1-TRFP-positive vesicle moving in the retrograde direction. Scale bars: 7.4 µm. (**b**)

axonal transport that may represent attractive therapeutic targets for neurological disorders associated with axonal transport defects.

2. *Tol1* and *Tol2* mRNA respectively encode the Tol 1 and Tol 2 transposases required for the genome insertion of the Tol1- or Tol2-UAS constructs.
3. One of the most important points we would like to mention regards the use of morpholinos to conduct loss-of-function experiments in zebrafish. Morpholinos must be validated according to the recently published guidelines for controlled use of morpholinos, which include—among others—the generation of mutants [54]. Once validated, morpholinos can be used to complement mutant analyses in tricky experiments such as live imaging (as in the present study) to circumvent the difficulties or time constraints associated with obtaining mutant embryos on a GAL4 genetic background or blind imaging embryos of the wrong genotype.
4. To get reproducible injection results, we advise you to use the automatic mode of the injection program and adjust the pressure and delivery time to inject 1–1.5 nL of the solution. Increasing the injection volume or concentration of Tol1/Tol2 mRNA or DNA plasmid beyond 50 ng in the solution will not improve transgenesis efficiency but on the contrary could be toxic and affect embryonic development and morphology.
5. Zebrafish development and its underlying cellular processes are influenced by temperature. Indeed, the development of this

Fig. 4 (continued) Left-hand panel: Representative kymograph of Fignl1-TRFP motility in SMN axons. Right-hand panel: schematic kymograph illustrating anterograde (black) and retrograde (gray) Fignl1-TRFP traces. Vertical scale bar: 85 s; horizontal scale bar: 5.6 μm. (**c**) Mean anterograde and retrograde velocities of Fignl1-TRFP-positive vesicles in SMN axons ($n = 6$) selected randomly from four transgenic fish. Mean velocities per axon were extracted from 50 kymograph traces and are coherent with fast molecular motor-based axonal transport (0.28 $\mu m/s^{-1}$ and 0.31 $\mu m/s^{-1}$, respectively). (**d–o**) Analysis of Rab3-Dendra2 axonal transport in SMN axons of Kif1bβ- or Fignl1-depleted larvae. (**d**) Still images extracted from time-lapse recordings of Rab3-Dendra2 vesicles in SMN axons of 50-hpf Tg(mnGFF7) larvae injected with a *UAS*:Rab3-Dendra2 plasmid and control (Ctl), *Kif1bβ* or *Fignl1* morpholinos. Scale bar: 10 μm. (**e**) Representative kymographs of Rab3-Dendra2 axonal transport in control, *Kif1bβ*- and *Fignl1*-depleted SMN axons. Vertical black lines represent static vesicles. Vertical scale bar: 2 min; horizontal scale bar: 10 μm. (**f–i** and **k–n**) Scatter dot plots of the mean anterograde and retrograde velocities or run lengths of Rab3-vesicles measured in at least 20 control, *Kif1bβ*- (**f–i**) *or Fignl1*-depleted (**k–n**) SMN axons. $*p \leq 0.05$, $***p \leq 0.001$, ns: nonsignificant ($p > 0.05$); unpaired two-tailed *t*-test with Welch's correction and Mann–Whitney test for velocity and run length comparisons, respectively. Error bars are SEM. Kif1bβ and Fignl1 loss of function similarly increase dynein-based Rab3 retrograde transport velocity. (**j**, **o**) Bar graphs of the mean number of static vesicles in a 100-μm axon portion. ns: non-significant ($p > 0.05$); Mann–Whitney test. Error bars are SEM. The number of static vesicles remained unchanged in Kif1bβ- or Fignl1-depleted SMN axons compared to control axons

teleost can be accelerated by increasing the incubator temperature and vice versa [55]. This phenomenon highlights the need to use a microscope equipped with a thermostatically controlled imaging chamber to precisely control the temperature during the acquisition time. This is essential to reduce the dispersion of the axonal transport values obtained from different embryos, experimental conditions, and replicates and therefore to improve the statistical significance of the results.

6. Macroscope devices allow wide-field observations at very high magnifications with depth and are thus ideally suited to screen and select injected embryos that show normal gross morphology and isolated fluorescent neurons in the brain or spinal cord.
7. Time-lapse parameters were estimated according to the speed of Kinesin-based axonal transport [56] and transport velocities previously described in zebrafish neurons [22, 57] and adjusted to fit with the Z-stack acquisition constraints required to image significant segments of axons. This will considerably depend on the axon morphology and trajectory, as well as on the developmental stage of the embryo. In our case, axonal transport recordings of Fignl1-, TrkB-, or Rab3-positive vesicles in secondary motor neuron axons of 56-hpf larvae were acquired every 4 s for 5 min, which represents a good compromise to reliably track these vesicles. Increasing the acquisition speed is possible if you work with linear axonal segments allowing single-plane time-lapse imaging. Note that your microscope setup will be critical for in vivo live imaging experiments since it has to reconcile large working distance—to image axon populations that grow deep beneath the embryo surface—high resolution (i.e., the numeric aperture of the objective) to image cargoes of nanometer-scale size and high time frequency to monitor highly dynamic cellular processes.
8. Time exposure is limited by time-lapse interval constraints (i.e., directly linked to the Z-stack thickness) and should thus not exceed 150 ms. If the fluorescence intensity of the axon is too low under this time exposure, adjust the laser power to get an optimal signal/noise ratio and a signal strong enough to allow cargo detection until the end of the imaging period. Note that the laser power should be kept within the same range from one embryo/experimental condition to another and should not exceed 35% to avoid artifacts associated with phototoxicity.
9. The z-stream mode enables to collect your Z-stack image sequence as a continuous data stream to the random access memory (RAM) of your computer. The images will be saved on the local hard disk only after the entire imaging is completed. This option is essential to (1) avoid any delays between each time-point acquisition (due to the extra time required to save

each Z-stack sequence before acquiring the next one) and (2) to acquire images with accurate temporal precision. Note that you must have a Z motor that supports streaming for this option to be available.

10. Two distinct populations of motor neurons have been described in the zebrafish spinal cord: the primary and the secondary motor neurons. Both populations are composed of three different subtypes that have their own functions, anatomical properties, and connectivity [58] and may thus have different axonal transport dynamic profiles. Accordingly, when performing live imaging experiments in motor neurons, it is recommended to focus on a specific motor neuron subtype to limit data heterogeneity. We here focused our analysis on rostrally projecting secondary motor neuron (RoP-like) axons, the axon population mainly affected by the depletion of either Fignl1 or Kif1bβ. To further reduce data heterogeneity, we repeatedly imaged the secondary motor neurons that are located around the yolk tube to avoid the rostro-caudal developmental delay. Moreover, motor axons located in the most rostral part of the embryo are often difficult to image. This is mainly due to the fact that the yolk is very thick in this anterior region and prevents the embryo from being well stuck against the culture dish bottom. As a consequence, a greater working distance is required to be in focus. Note that this region is also located close to the heart, whose beats can generate slight movements.
11. As mentioned in Subheading 3.3, the size, number, and distribution of vesicles can vary between different neuronal populations, which directly influences kymograph quality and readability. Accordingly, the plugin used to generate kymographs from axonal transport movies should be adapted to the neuronal population of interest in order to facilitate kymograph interpretation and optimize the amount of data that can be extracted from each kymograph.
12. It is important to highlight the fact that the KymographClear macro toolset generates kymographs that enable the visualization of more segmental runs—often corresponding to smaller particles—than kymographs generated by the Kymograph Builder plugin (Fig. 3e, gray ROIs). Nevertheless, a certain amount of ROIs generated with each plugin do overlap (Fig. 3e, black and gray dotted ROIs).
13. As described in Subheadings 3.1 and 3.2, mosaic expression of the constructs with the *UAS*/GAL4 system is crucial to ensure that subsequent imaging is occurring in individual axons. When screening for mosaic expression of the construct at the macroscope (Subheading 3.2), you might want to be over-

selective and make sure that you only keep the embryos with the highest mosaic expression of your construct. Bear in mind that imaging hemisegments in which mosaicism is poor will only make the data analysis and interpretation more complex.

14. When performing live imaging on a total embryo, it is important to bear in mind that the embryo is continuing its development during acquisition. Axons might therefore seem to have moved slightly between the beginning and the end of the movie. The laser may also locally induce the melting of the agarose embedding the embryo, which may partially free the embryo and enable movement. It is therefore necessary to check that the entire width of the axon is covered by the ROI traced at **step 8** throughout the whole movie, without overlapping other axons.
15. For reasons described in **Note 14**, it is possible for imaged axons to shift slightly during acquisition. It might therefore be cautious to stabilize movies, for example, by using "Plugins>Registration>Linear Stack Alignment with SIFT." This can be important to improve kymograph quality, as it will make it easier to follow an individual axon—with the ROI traced at step 8—throughout the whole length of the acquisition, without increasing the ROI width too much. Indeed, increasing ROI widths also increases the risk of including background noise on the resulting kymographs.
16. When pooling data generated in different experiments, it is essential to check that values do not differ significantly between control embryos from different set of experiments. Indeed, despite the thermostatic chamber that ensures the same imaging temperature, a certain variability (e.g., the age of the embryos, the heterogeneity in the imaged axonal segment, more or less proximal/distal) cannot always be excluded. If control values do change significantly between experiments, we recommend normalizing values before pooling.

Acknowledgments

We would like to warmly thank Valérie Bercier and Céline Revenu from Filippo Del Bene's lab for providing us with the *UAS*:Rab3-Dendra2, 14*UAS*:Fignl1-TRFP, and 10*UAS*:TrkB-GFP constructs as well as David Lyons and Marion Baraban for their kind gift of the *Kif1bβ* splice site morpholinos. We are grateful to Jean-François Gilles, France Lam, and Susanne Bolte from the imaging facility of the IBPS (Sorbonne University) for their support in microscopy and to Alex Bois, Stéphane Tronche, and Abdelkrim Mannioui from the IBPS aquatic animal facility for fish care. We are also obliged to Annie Andrieux for fruitful discussions and insightful comments on the

study. This work was supported by the INSERM integration grant and ASL-HSP France funding attributed to CF, the research grants from the ASL-HSP, Association Française contre les Myopathies (AFM), and the UPMC Emergence programme attributed to JH, and the MENRT PhD fellowship attributed to MA.

References

1. Millecamps S, Julien J-P (2013) Axonal transport deficits and neurodegenerative diseases. Nat Rev Neurosci 14:161–176. https://doi.org/10.1038/nrn3380
2. Hendricks AG, Perlson E, Ross JL, Schroeder HW, Tokito M, Holzbaur ELF (2010) Motor coordination via a tug-of-war mechanism drives bidirectional vesicle transport. Curr Biol 20:697–702. https://doi.org/10.1016/j.cub.2010.02.058
3. Guedes-Dias P, Holzbaur ELF (2019) Axonal transport: driving synaptic function. Science 366:eaaw9997. https://doi.org/10.1126/science.aaw9997
4. Hirokawa N, Niwa S, Tanaka Y (2010) Molecular motors in neurons: transport mechanisms and roles in brain function, development, and disease. Neuron 68:610–638. https://doi.org/10.1016/j.neuron.2010.09.039
5. Maday S, Twelvetrees AE, Moughamian AJ, Holzbaur ELF (2014) Axonal transport: cargo-specific mechanisms of motility and regulation. Neuron 84:292. https://doi.org/10.1016/j.neuron.2014.10.019
6. Hancock WO (2014) Bidirectional cargo transport: moving beyond tug of war. Nat Rev Mol Cell Biol 15:615–628. https://doi.org/10.1038/nrm3853
7. Akhmanova A, Hammer JA (2010) Linking molecular motors to membrane cargo. Curr Opin Cell Biol 22:479–487. https://doi.org/10.1016/j.ceb.2010.04.008
8. Fu M, Holzbaur ELF (2014) Integrated regulation of motor-driven organelle transport by scaffolding proteins. Trends Cell Biol 24:564–574. https://doi.org/10.1016/j.tcb.2014.05.002
9. Schlager MA, Serra-Marques A, Grigoriev I, Gumy LF, Esteves da Silva M, Wulf PS, Akhmanova A, Hoogenraad CC (2014) Bicaudal D family adaptor proteins control the velocity of dynein-based movements. Cell Rep 8:1248–1256. https://doi.org/10.1016/j.celrep.2014.07.052
10. Cross JA, Dodding MP (2019) Motor-cargo adaptors at the organelle-cytoskeleton interface. Curr Opin Cell Biol 59:16–23. https://doi.org/10.1016/j.ceb.2019.02.010
11. Olenick MA, Holzbaur ELF (2019) Dynein activators and adaptors at a glance. J Cell Sci 132:jcs227132. https://doi.org/10.1242/jcs.227132
12. Beijer D, Sisto A, Van Lent J, Baets J, Timmerman V (2019) Defects in axonal transport in inherited neuropathies. J Neuromuscul Dis 6:401–419. https://doi.org/10.3233/JND-190427
13. Guo W, Stoklund Dittlau K, Van Den Bosch L (2020) Axonal transport defects and neurodegeneration: molecular mechanisms and therapeutic implications. Semin Cell Dev Biol 99:133–150. https://doi.org/10.1016/j.semcdb.2019.07.010
14. Sleigh JN, Rossor AM, Fellows AD, Tosolini AP, Schiavo G (2019) Axonal transport and neurological disease. Nat Rev Neurol 15:691–703. https://doi.org/10.1038/s41582-019-0257-2
15. Phillis R, Statton D, Caruccio P, Murphey RK (1996) Mutations in the 8 kDa dynein light chain gene disrupt sensory axon projections in the drosophila imaginal CNS. Development 122:2955–2963
16. Tischfield MA, Baris HN, Wu C, Rudolph G, Van Maldergem L, He W, Chan W-M, Andrews C, Demer JL, Robertson RL, Mackey DA, Ruddle JB, Bird TD, Gottlob I, Pieh C, Traboulsi EI, Pomeroy SL, Hunter DG, Soul JS, Newlin A, Sabol LJ, Doherty EJ, de Uzcátegui CE, de Uzcátegui N, Collins MLZ, Sener EC, Wabbels B, Hellebrand H, Meitinger T, de Berardinis T, Magli A, Schiavi C, Pastore-Trossello M, Koc F, Wong AM, Levin AV, Geraghty MT, Descartes M, Flaherty M, Jamieson RV, Møller HU, Meuthen I, Callen DF, Kerwin J, Lindsay S, Meindl A, Gupta ML, Pellman D, Engle EC (2010) Human TUBB3 mutations perturb microtubule dynamics, kinesin interactions, and axon guidance. Cell 140:74–87. https://doi.org/10.1016/j.cell.2009.12.011
17. Kapitein LC, Hoogenraad CC (2011) Which way to go? Cytoskeletal organization and polarized transport in neurons. Mol Cell

Neurosci 46:9–20. https://doi.org/10.1016/j.mcn.2010.08.015

18. Schlager MA, Kapitein LC, Grigoriev I, Burzynski GM, Wulf PS, Keijzer N, de Graaff E, Fukuda M, Shepherd IT, Akhmanova A, Hoogenraad CC (2010) Pericentrosomal targeting of Rab6 secretory vesicles by Bicaudal-D-related protein 1 (BICDR-1) regulates neuritogenesis. EMBO J 29:1637–1651. https://doi.org/10.1038/emboj.2010.51
19. van Spronsen M, Mikhaylova M, Lipka J, Schlager MA, van den Heuvel DJ, Kuijpers M, Wulf PS, Keijzer N, Demmers J, Kapitein LC, Jaarsma D, Gerritsen HC, Akhmanova A, Hoogenraad CC (2013) TRAK/Milton motor-adaptor proteins steer mitochondrial trafficking to axons and dendrites. Neuron 77:485–502. https://doi.org/10.1016/j.neuron.2012.11.027
20. Deng C-Y, Lei W-L, Xu X-H, Ju X-C, Liu Y, Luo Z-G (2014) JIP1 mediates anterograde transport of Rab10 cargos during neuronal polarization. J Neurosci 34:1710–1723. https://doi.org/10.1523/JNEUROSCI.4496-13.2014
21. Lorenzo DN, Badea A, Davis J, Hostettler J, He J, Zhong G, Zhuang X, Bennett V (2014) A PIK3C3–Ankyrin-B–dynactin pathway promotes axonal growth and multiorganelle transport. J Cell Biol 207:735–752. https://doi.org/10.1083/jcb.201407063
22. Drerup CM, Lusk S, Nechiporuk A (2016) Kif1B interacts with KBP to promote axon elongation by localizing a microtubule regulator to growth cones. J Neurosci 36:7014. https://doi.org/10.1523/JNEUROSCI.0054-16.2016
23. Moutaux E, Christaller W, Scaramuzzino C, Genoux A, Charlot B, Cazorla M, Saudou F (2018) Neuronal network maturation differently affects secretory vesicles and mitochondria transport in axons. Sci Rep 8:13429. https://doi.org/10.1038/s41598-018-31759-x
24. Saez TMM, Bessone IF, Rodriguez MS, Alloatti M, Otero MG, Cromberg LE, Devoto VMP, Oubiña G, Sosa L, Buffone MG, Gelman DM, Falzone TL (2020) Kinesin-1-mediated axonal transport of CB1 receptors is required for cannabinoid-dependent axonal growth and guidance. Development 147:dev184069. https://doi.org/10.1242/dev.184069
25. Heintz TG, Heller JP, Zhao R, Caceres A, Eva R, Fawcett JW (2014) Kinesin KIF4A transports integrin β1 in developing axons of cortical neurons. Mol Cell Neurosci 63:60–71. https://doi.org/10.1016/j.mcn.2014.09.003
26. Bandmann O, Burton EA (2010) Genetic zebrafish models of neurodegenerative diseases. Neurobiol Dis 40:58–65. https://doi.org/10.1016/j.nbd.2010.05.017
27. Kabashi E, Lin L, Tradewell ML, Dion PA, Bercier V, Bourgouin P, Rochefort D, Bel Hadj S, Durham HD, Vande Velde C, Rouleau GA, Drapeau P (2010) Gain and loss of function of ALS-related mutations of TARDBP (TDP-43) cause motor deficits in vivo. Hum Mol Genet 19:671–683. https://doi.org/10.1093/hmg/ddp534
28. Santoriello C, Zon LI (2012) Hooked! Modeling human disease in zebrafish. J Clin Invest 122:2337–2343. https://doi.org/10.1172/JCI60434
29. Babin PJ, Goizet C, Raldúa D (2014) Zebrafish models of human motor neuron diseases: advantages and limitations. Prog Neurobiol 118:36–58. https://doi.org/10.1016/j.pneurobio.2014.03.001
30. Patten SA, Armstrong GAB, Lissouba A, Kabashi E, Parker JA, Drapeau P (2014) Fishing for causes and cures of motor neuron disorders. Dis Model Mech 7:799–809. https://doi.org/10.1242/dmm.015719
31. Fontana BD, Stefanello FV, Mezzomo NJ, Müller TE, Quadros VA, Parker MO, Rico EP, Rosemberg DB (2018) Taurine modulates acute ethanol-induced social behavioral deficits and fear responses in adult zebrafish. J Psychiatr Res 104:176–182. https://doi.org/10.1016/j.jpsychires.2018.08.008
32. Fassier C, Fréal A, Gasmi L, Delphin C, Ten Martin D, De Gois S, Tambalo M, Bosc C, Mailly P, Revenu C, Peris L, Bolte S, Schneider-Maunoury S, Houart C, Nothias F, Larcher J-C, Andrieux A, Hazan J (2018) Motor axon navigation relies on Fidgetin -like 1-driven microtubule plus end dynamics. J Cell Biol 217:1719–1738. https://doi.org/10.1083/jcb.201604108
33. Atkins M, Gasmi L, Bercier V, Revenu C, Del Bene F, Hazan J, Fassier C (2019) FIGNL1 associates with KIF1Bβ and BICD1 to restrict dynein transport velocity during axon navigation. J Cell Biol 218:3290–3306. https://doi.org/10.1083/jcb.201805128
34. Gibbs KL, Kalmar B, Sleigh JN, Greensmith L, Schiavo G (2016) In vivo imaging of axonal transport in murine motor and sensory neurons. J Neurosci Methods 257:26–33. https://doi.org/10.1016/j.jneumeth.2015.09.018
35. Klinman E, Holzbaur ELF (2016) Comparative analysis of axonal transport markers in primary mammalian neurons. Methods Cell Biol

131:409–424. https://doi.org/10.1016/bs.mcb.2015.06.011

36. Knabbe J, Nassal JP, Verhage M, Kuner T (2018) Secretory vesicle trafficking in awake and anaesthetized mice: differential speeds in axons versus synapses. J Physiol 596: 3759–3773. https://doi.org/10.1113/JP276022
37. Smit-Rigter L, Rajendran R, Silva CAP, Spierenburg L, Groeneweg F, Ruimschotel EM, van Versendaal D, van der Togt C, Eysel UT, Heimel JA, Lohmann C, Levelt CN (2016) Mitochondrial dynamics in visual cortex are limited in vivo and not affected by axonal structural plasticity. Curr Biol 26: 2609–2616. https://doi.org/10.1016/j.cub.2016.07.033
38. Sorbara CD, Wagner NE, Ladwig A, Nikić I, Merkler D, Kleele T, Marinković P, Naumann R, Godinho L, Bareyre FM, Bishop D, Misgeld T, Kerschensteiner M (2014) Pervasive axonal transport deficits in multiple sclerosis models. Neuron 84: 1183–1190. https://doi.org/10.1016/j.neuron.2014.11.006
39. Takihara Y, Inatani M, Eto K, Inoue T, Kreymerman A, Miyake S, Ueno S, Nagaya M, Nakanishi A, Iwao K, Takamura Y, Sakamoto H, Satoh K, Kondo M, Sakamoto T, Goldberg JL, Nabekura J, Tanihara H (2015) In vivo imaging of axonal transport of mitochondria in the diseased and aged mammalian CNS. Proc Natl Acad Sci U S A 112: 10515–10520. https://doi.org/10.1073/pnas.1509879112
40. Edgar JM, McLaughlin M, Yool D, Zhang S-C, Fowler JH, Montague P, Barrie JA, McCulloch MC, Duncan ID, Garbern J, Nave KA, Griffiths IR (2004) Oligodendroglial modulation of fast axonal transport in a mouse model of hereditary spastic paraplegia. J Cell Biol 166: 121–131. https://doi.org/10.1083/jcb.200312012
41. Chada SR, Hollenbeck PJ (2004) Nerve growth factor signaling regulates motility and docking of axonal mitochondria. Curr Biol 14: 1272–1276. https://doi.org/10.1016/j.cub.2004.07.027
42. Leung K-M, Lu B, Wong HH-W, Lin JQ, Turner-Bridger B, Holt CE (2018) Cue-polarized transport of β-actin mRNA depends on 3′UTR and microtubules in live growth cones. Front Cell Neurosci 12:300. https://doi.org/10.3389/fncel.2018.00300
43. Akiyama H, Fukuda T, Tojima T, Nikolaev VO, Kamiguchi H (2016) Cyclic nucleotide control of microtubule dynamics for axon guidance. J Neurosci 36:5636–5649. https://doi.org/10.1523/JNEUROSCI.3596-15.2016
44. Wang T, Martin S, Nguyen TH, Harper CB, Gormal RS, Martínez-Mármol R, Karunanithi S, Coulson EJ, Glass NR, Cooper-White JJ, van Swinderen B, Meunier FA (2016) Flux of signalling endosomes undergoing axonal retrograde transport is encoded by presynaptic activity and TrkB. Nat Commun 7:12976. https://doi.org/10.1038/ncomms12976
45. Zala D, Hinckelmann M-V, Saudou F (2013) Huntingtin's function in axonal transport is conserved in Drosophila melanogaster. PLoS One 8:e60162. https://doi.org/10.1371/journal.pone.0060162
46. Hinckelmann M-V, Virlogeux A, Niehage C, Poujol C, Choquet D, Hoflack B, Zala D, Saudou F (2016) Self-propelling vesicles define glycolysis as the minimal energy machinery for neuronal transport. Nat Commun 7:13233. https://doi.org/10.1038/ncomms13233
47. Liao P-C, Tandarich LC, Hollenbeck PJ (2017) ROS regulation of axonal mitochondrial transport is mediated by Ca2+ and JNK in drosophila. PLoS One 12:e0178105. https://doi.org/10.1371/journal.pone.0178105
48. Fang C, Bourdette D, Banker G (2012) Oxidative stress inhibits axonal transport: implications for neurodegenerative diseases. Mol Neurodegener 7:29. https://doi.org/10.1186/1750-1326-7-29
49. Asakawa K, Suster ML, Mizusawa K, Nagayoshi S, Kotani T, Urasaki A, Kishimoto Y, Hibi M, Kawakami K (2008) Genetic dissection of neural circuits by Tol2 transposon-mediated Gal4 gene and enhancer trapping in zebrafish. Proc Natl Acad Sci U S A 105:1255–1260. https://doi.org/10.1073/pnas.0704963105
50. Asakawa K, Abe G, Kawakami K (2013) Cellular dissection of the spinal cord motor column by BAC transgenesis and gene trapping in zebrafish. Front Neural Circuits 7:100. https://doi.org/10.3389/fncir.2013.00100
51. Akerboom J, Chen T-W, Wardill TJ, Tian L, Marvin JS, Mutlu S, Calderón NC, Esposti F, Borghuis BG, Sun XR, Gordus A, Orger MB, Portugues R, Engert F, Macklin JJ, Filosa A, Aggarwal A, Kerr RA, Takagi R, Kracun S, Shigetomi E, Khakh BS, Baier H, Lagnado L, Wang SS-H, Bargmann CI, Kimmel BE, Jayaraman V, Svoboda K, Kim DS, Schreiter ER, Looger LL (2012) Optimization of a GCaMP calcium indicator for neural activity imaging. J Neurosci 32:13819–13840.

https://doi.org/10.1523/JNEUROSCI.2601-12.2012

52. Mangeol P, Prevo B, Peterman EJG (2016) KymographClear and KymographDirect: two tools for the automated quantitative analysis of molecular and cellular dynamics using kymographs. Mol Biol Cell 27:1948–1957. https://doi.org/10.1091/mbc.E15-06-0404
53. Lyons DA, Naylor SG, Scholze A, Talbot WS (2009) Kif1b is essential for mRNA localization in oligodendrocytes and development of myelinated axons. Nat Genet 41:854–858. https://doi.org/10.1038/ng.376
54. Stainier DYR, Raz E, Lawson ND, Ekker SC, Burdine RD, Eisen JS, Ingham PW, Schulte-Merker S, Yelon D, Weinstein BM, Mullins MC, Wilson SW, Ramakrishnan L, Amacher SL, Neuhauss SCF, Meng A, Mochizuki N, Panula P, Moens CB (2017) Guidelines for morpholino use in zebrafish. PLoS Genet 13: e1007000. https://doi.org/10.1371/journal.pgen.1007000
55. Kimmel CB, Ballard WW, Kimmel SR, Ullmann B, Schilling TF (1995) Stages of embryonic development of the zebrafish. Dev Dyn 203:253–310. https://doi.org/10.1002/aja.1002030302
56. Arpağ G, Norris SR, Mousavi SI, Soppina V, Verhey KJ, Hancock WO, Tüzel E (2019) Motor dynamics underlying cargo transport by pairs of Kinesin-1 and Kinesin-3 motors. Biophys J 116:1115–1126. https://doi.org/10.1016/j.bpj.2019.01.036
57. Bercier V, Rosello M, Del Bene F, Revenu C (2019) Zebrafish as a model for the study of live in vivo Processive transport in neurons. Front Cell Dev Biol 7:17. https://doi.org/10.3389/fcell.2019.00017
58. Ott H, Diekmann H, Stuermer CA, Bastmeyer M (2001) Function of Neurolin (DM-GRASP/SC-1) in guidance of motor axons during zebrafish development. Dev Biol 235:86–97. https://doi.org/10.1006/dbio.2001.0278

Chapter 18

Visualizing the Intracellular Trafficking in Zebrafish Mauthner Cells

Rongchen Huang, Yang Xu, Min Chen, Leiqing Yang, Xinliang Wang, Yueru Shen, Yubin Huang, and Bing Hu

Abstract

Axonal transport is crucial for the development and survival of neurons and maintenance of neuronal function. Disruption in this active process causes diverse neurological diseases. Thus, study of the intracellular trafficking as one way to gain the knowledge of the kinetics of axonal transport is essential to understand the mechanisms underlying the neuropathology. A lot of studies have been completed in vitro with neuron cultures and tissues, which may not accurately replicate the in vivo situation. Therefore, intravital manipulations are essential to achieve this goal. Here we introduce a technique that has been widely used in our lab to study the cargo trafficking in zebrafish at single-cell resolution. We use mitochondria as a representative neuronal cargo and provide step-by-step instructions on how to label specific cargoes within zebrafish Mauthner cells. This method can also be expanded to study the kinetics of other cargoes as well as the role of molecular regulators in axonal transport.

Key words Axonal transport, Mitochondria, Single-cell electroporation, In vivo imaging; Mauthner cells

1 Introduction

Axonal transport is a vital process to neurons as it maintains neuronal metabolism in both axons and nerve terminals by supplying with proteins, RNA and ATP, and clearing misfolded proteins to avoid the build-up of toxic aggregates, and enables communication between these processes, allowing neurons to respond effectively to trophic signals or stress insults [1]. Impairment of axonal transport is sufficient to induce neurodegeneration and has emerged as a common factor in several neurodegenerative disorders, such as

Rongchen Huang and Yang Xu contributed equally to this work.

Supplementary Information The online version of this chapter (https://doi.org/10.1007/978-1-0716-1990-2_18) contains supplementary material, which is available to authorized users.

Alessio Vagnoni (ed.), *Axonal Transport: Methods and Protocols*,
Methods in Molecular Biology, vol. 2431, https://doi.org/10.1007/978-1-0716-1990-2_18,
© The Author(s), under exclusive license to Springer Science+Business Media, LLC, part of Springer Nature 2022

Amyotrophic Lateral Sclerosis (ALS), Huntington's, Parkinson's, and Alzheimer's disease. Therefore, the visualization and quantitative analysis of axonal transport are essential to improve our understanding of disease pathogenesis and the identification of novel therapeutics.

Many studies on axonal transport have been accomplished with primary neuron culture and ex vivo tissue neurons, where individual fluorescently labeled cargoes, such as mitochondria, were tracked [2, 3], partly contributing to our understanding of the mechanisms underlying defective axonal transport which eventually leads to neurological disease. However, in vitro systems and ex vivo tissue preparations do not always accurately recapitulate the in vivo environment, especially when modelling dynamic, tightly regulated processes such as axonal transport, which can be affected by endogenous signaling [4] and cell–cell interaction [5, 6]. A number of live imaging techniques have been established to study axonal transport in real-time with different live organisms and provided novel insight to this dynamic process. Although invertebrate systems such as *Drosophila* and *C. elegans* are evolutionary distant from humans compared to vertebrate models, studying axonal transport in these systems is advantageous due to the shorter generation times and lower maintenance cost. Mouse models, which maintain high genetic conservation when compared to humans, have been widely used. However, due to the lack of transparency, it usually requires additional surgeries prior to live imaging and only allows access to axonal transport in a restricted area of the targeted cell population. In addition, visualizing cargo in mouse requires the generation of a transgenic line to label specific axonal cargo, which is time-consuming and expensive. Moreover, the transgenic approach usually labels multiple neurons, precluding imaging at single-cell resolution.

As a promising vertebrate model, zebrafish possess many of the advantages of invertebrate species, such as short generation time and cost-effectiveness, while also have the properties that avoid the obstacles typical of mouse models, making them an ideal model to study axonal transport in an in vivo context [7, 8] (Fig. 1). Zebrafish larvae remain translucent throughout development, which eliminates the need for invasive imaging techniques and allows longitudinal in vivo measurement. Also, both transient and stable transgenic approaches are well-established in zebrafish. One of the most common systems to build a transient transgenic line is the GAL-UAS system, allowing expression of cargo protein fusion in a tissue- or cell-type-specific manner in a short time. More importantly, the mosaic nature of this transient expression allows visualization of cargo movement in a single axon. Zebrafish Mauthner cells (M-cells) are a pair of identifiable reticulospinal neurons with huge soma and large diameter, myelinated axons that project along a stereotyped path from the midline of rhombomere into the

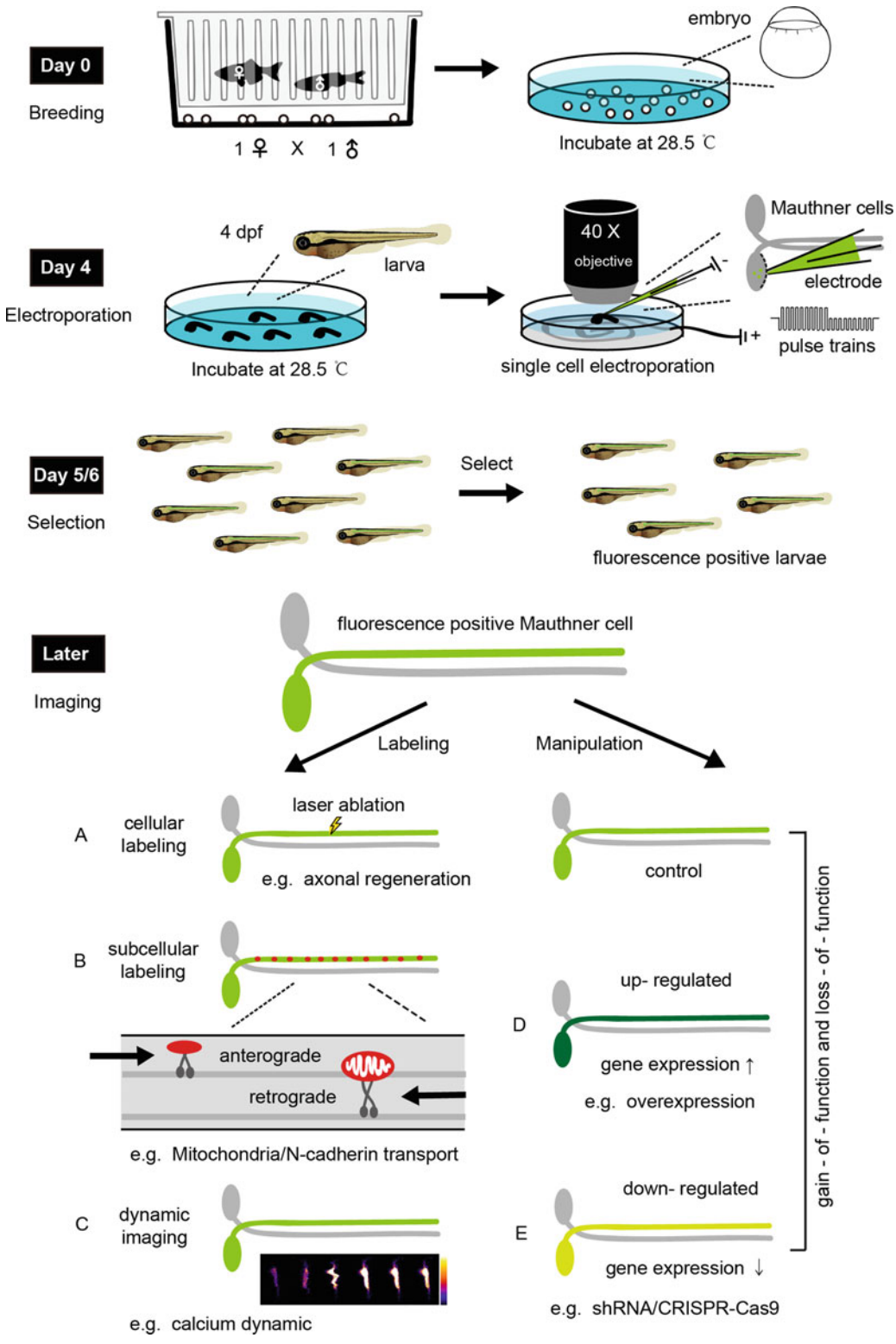

Fig. 1 Schematic diagram of the single-cell electroporation for all applications. After fertilization, zebrafish embryos were incubated at 28.5 °C. M-cells of larvae were single-cell electroporated at 4 dpf, and we can

ventral spinal cord [9, 10]. Their unique morphology enables them to be individually visualized in vivo and renders them a valuable model to study axonal transport at the single-cell level.

Microinjection is one of the most common and easiest ways to deliver plasmids into zebrafish embryos and larvae. Different plasmid constructions and combinations enable us to label different types of cells. However, this microinjection-based system often results in robust and widespread expression and thus increases background fluorescence, which complicates in vivo imaging, especially for subcellular imaging that requires higher spatial resolution. In addition, this technique does not always precisely label our specific target. Single-cell electroporation has been widely used for stable longitudinal imaging in vivo in different models [11–13]. For this method, DNA vectors are precisely electroporated into a single neuron using a glass pipette that is closely attached to the neuron's membrane [14]. Expression can usually be observed within 24 h post electroporation. Here we choose mitochondria as an example to describe our procedure for labeling and imaging subcellular trafficking in M-cells combined with single-cell electroporation, as well as our analysis paradigm to reflect any potential changes in axonal transport under different contexts.

This method not only can be applied to study the transport of other subcellular proteins, including cadherins [15], but also allows us to regulate gene expression [16] and monitor neural activity [17], providing a new way to understand the dynamics of axonal transport and mechanisms underlying different disease pathogenesis related with axonal transport deficits.

2 Materials

2.1 Labeling Subcellular Structures in Mauthner Cells (Mitochondria Labeling as a Representative)

1. Incubator maintained at 28.5 °C with a 14 h light/10 h dark cycle.
2. Electroporation electrode: borosilicate glass capillaries with filament (e.g., TW100F-4, World Precision Instruments) pulled by Micropipette Pullers (P97, Sutter Instrument Company). Empirically, use a two-step method to pull electrode with tip diameter < 1 μm and tip taper angle $>10°$ (e.g., Step 1: HEAT 484, PULL 0, VEL 60, TIME 255; Step 2: HEAT 484, PULL 0, VEL 46, TIME 255).
3. Electroporation solution: 100–200 ng/μl Endo-free plasmid DNA (Gal4-vp16 system, e.g., PCS2^{+}-CMV-Gal4-VP16 to

Fig. 1 (continued) screen successfully labeled M-cells at 5 dpf or 6 dpf. Then the labeled zebrafish larvae can be applied in various experimental conditions at a single-neuron level, including cellular labeling (**a**), subcellular tracking (**b**), dynamic imaging of biosensors (**c**), and gene regulation (**d**, **e**)

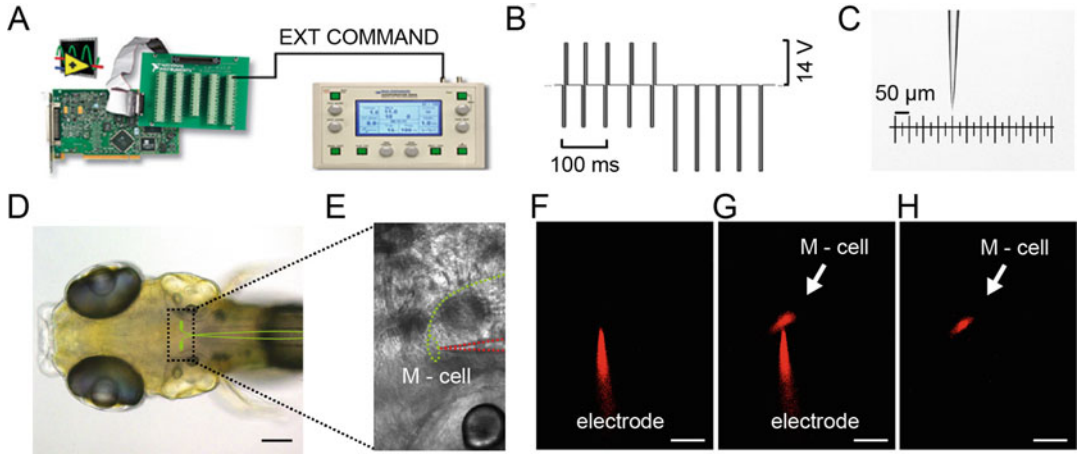

Fig. 2 Labeling mitochondria in M-cells using single-cell electroporation. (**a**) Major single-cell electroporation devices including a data acquisition card (left) and an Axoporator 800A (right). (**b**) A series of square waves followed by negative pulses were used to electroporate electroporation solution into target cells. (**c**) A representative electroporation electrode. Details of the zebrafish brain (**d**) and M-cells near an electrode (**e**) were demonstrated through an optical microscope. To illustrate them clearly, M-cells were drawn in green (**d**) or outlined in green (**e**), and the electrode was outlined in red (**e**). (**f–h**) Fluorescence images to indicate the electroporation procedure. (**f**) The electrode was attached the M-cell surface and filled with electroporation solution and fluorescent dyes. (**g**) After applying a series pulse train, the M-cell was labeled with electroporation solution. (**h**) The labeled M-cells could be observed after the electrode retraction. Scale bars: (**c**) 50 μm, (**d**) 100 μm, (**e–h**) 20 μm

drive expression of Gal4-VP16 under cytomegalovirus (CMV) promoter; PCS2^{+}-UAS-mito-EGFP (Enhanced Green Fluorescent Protein, EGFP) to label mitochondria with EGFP; PCS2^{+}-UAS-DsRed2/PCS2^{+}-UAS-mCherry to label cell morphology with DsRed2/ mCherry), 0.05–0.3 mM Dextran (Alexa Fluor 488; 3000 MW, Anionic). All substances are diluted in distilled H_2O.

4. Loading pipette (Microloader, 0.5–20 μl, Eppendorf).
5. Data acquisition card (e.g., NI PCI-6024E) with customized parameters programmed by LabView. During application, it will be connected to the EXT COMMAND port of the Axoporator 800A (Molecular Devices) to ten times amplify the output voltage (Fig. 2a).
6. Axoporator 800A Electroporation System containing electrode holder. It provides the required voltage for electroporation with inputs from NI PCI-6024E.
7. Micromanipulator.
8. Silver wire (diameter ~ 0.25 mm).
9. Zebrafish (*Danio rerio*) larvae from wild-type AB lines at 4 days post-fertilization (dpf), larvae were maintained in embryo

medium containing 0.2 mM *N*-phenylthiourea (PTU) since 1 dpf to prevent pigment formation.

10. Embryo medium (EM): 1.0 ml Stock#1, 0.1 ml Stock#2, 1.0 ml Stock#4, 95.9 ml ddH_2O, 1.0 ml Stock#5, 1.0 ml fresh Stock#6. Add around ten droplets of 1 M NaOH to adjust to pH 7.2 and add several droplets of 1‰ Methylene blue.
    (a) Stock#1: 8.0 g NaCl, 0.4 g KCl in 100 ml ddH_2O.
    (b) Stock#2: 0.358 g Na_2HPO_4, 0.6 g KH_2PO_4 in 100 ml ddH_2O.
    (c) Stock#4: 0.72 g $CaCl_2$ in 50 ml ddH_2O.
    (d) Stock#5: 1.23 g $MgSO_4{\cdot}7H_2O$ in 50 ml ddH_2O.
    (e) Stock#6: 0.35 g $NaHCO_3$ in 10 ml ddH_2O.
11. 0.2 mM PTU diluted with EM.
12. 0.02% (w/v) Tricaine methanesulfonate (MS222) diluted with EM.
13. Electroporation chamber: place the sliver wires on the bottom of a petri dish (diameter ~ 100 mm) covered with agarose. One side of the sliver wire will be connected to the Axoporator 800A to form a closed loop for electroporation.
14. Disposable transfer pipette.
15. #5 Tweezer (Dumont).
16. Low melting agarose: 1% (w/v) in EM, keep in a heating block at 40–42 °C.
17. Upright light microscope (Olympus BX61) with 10× and 40× water immersion objective (LUMPLFLN 40XW, N.A. = 0.8, Olympus) with fluorescent lighting sources.

2.2 Imaging of Axonal Transport in Mauthner Neurons

1. Customized mounting chamber for imaging of the zebrafish larvae: stick an acrylic ring (diameter ~ 1 cm, height ~ 3 mm) on the glass coverslip using nail polish or silicon grease.
2. Low melting agarose: 1% (w/v) in EM, keep in a heating block at 40–42 °C.
3. #5 Tweezer (Dumont).
4. Petri dish: diameter ~ 35 mm.
5. EM.
6. MS222: EM with 0.02% (w/v) MS222.

7. Upright Confocal Laser Microscope (FV1000/FV1200, Olympus) equipped with 60× water-immersion objectives (e.g., LUMFLN 60XW, N.A. = 1.1, Olympus) and camera (CoolSNAP) controlled by FV10-ASW 4.2/FV31S-SW software (Olympus).
8. Microscope stage micrometer (0.01 mm).

2.3 Analysis of Axonal Transport in Mauthner Cells

1. Fiji Image J equipped with "WalkingAverage" and "StackReg" plugins or equivalent plugins.
2. Microsoft and GraphPad Prism to statistically analyze and plot the acquired data.

3 Methods

In this protocol, we describe the general procedures to achieve intracellular trafficking in zebrafish Mauthner cells in vivo, including intracellular labeling, imaging, and data analysis (Fig. 1).

We selected mitochondria as a representative cargo for organelle labeling in Mauthner cells. We developed a single-cell electroporation system which allows to deliver different materials, including plasmids, miRNAs, and dextrans into Mauthner cells (Fig. 2). To label mitochondria specifically, plasmid with fluorescent proteins fused to mitochondrial localization tags was used, making mitochondria visible in Mauthner cells (Fig. 3 and Video 1).

Time-lapse imaging of the labeled mitochondria was recorded using a confocal laser microscope. Each T-series imaging was 2–3 min long. Raw data was analyzed with Fiji ImageJ equipped with several plugins that are described in detail below. Based on analysis paradigms, we obtained the mitochondrial motility, transport direction proportion, anterograde, and retrograde velocity (Fig. 4). We assume other events such as mitochondrial fission and fusion can be analyzed as well if higher spatial resolution is achieved.

This single-cell electroporation technique has potential to expand its applications (Fig. 1), including other subcellular labeling (e.g., N-Cadherin) [15], gene regulation (e.g., MicroRNA-133b) [16], and signal monitoring with biosensors (e.g., GCamp6f) [17], only by changing the types of materials we electroporated. Besides, single-cell labeling facilitates the observation and manipulation of cell morphology at a single-cell level as we showed in a previous study on the relationship between Mauthner axonal regeneration and mitochondrial transport [18].

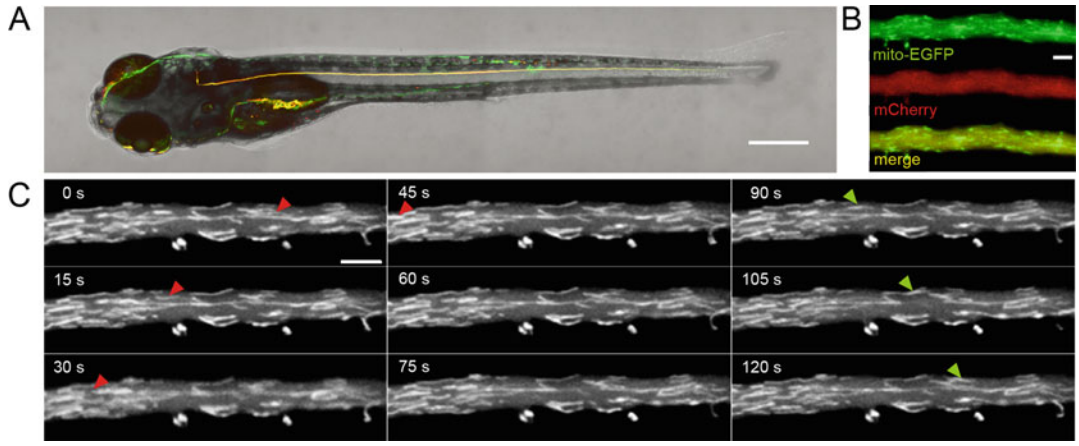

Fig. 3 Imaging mitochondrial trafficking in zebrafish M cells. (**a**) Representative of a successfully electroporated zebrafish larvae at 6 dpf. A Mauthner cell was labeled in yellow. (**b**) The interested area was enlarged by a confocal microscope, recording multichannel details about mitochondria (mito-EGFP, top) and axon (mCherry, middle). (**c**) Mitochondrial transport was imaged in the M axon with arrowheads to indicate moving mitochondria (anterograde mitochondria, green; retrograde mitochondria, red). 0 s indicates the onset time of imaging. Scale bars: (**a**) 300 μm, (**b**) 5 μm, (**c**) 5 μm

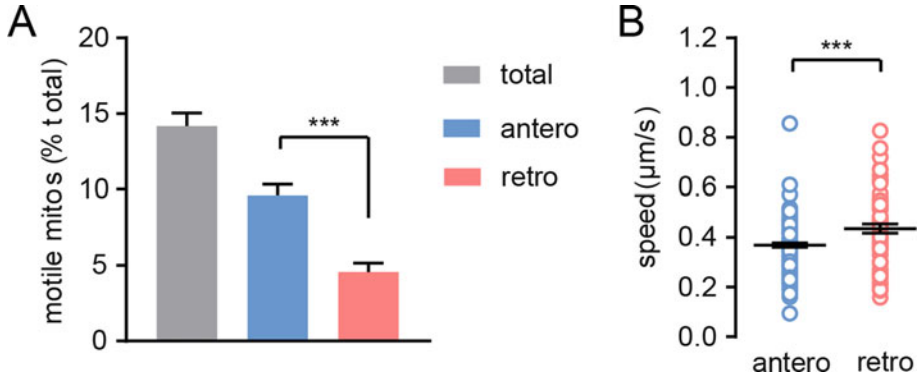

Fig. 4 Mitochondrial transport in zebrafish M cells. (**a**) A bar graph of mitochondrial motility at 8 dpf (total mitochondrial motility: 14.18 ± 0.87%, anterograde mitochondrial motility 9.62 ± 0.70%, retrograde mitochondrial motility 4.57 ± 0.58%, $n = 17$ fish, Student's *t*-test, $p < 0.001$). (**b**) A scatter dot plot of mitochondrial speed in axons (anterograde mitochondrial speed 0.369 ± 0.009 μm/s, $n = 141$ mitos from 17 fish, retrograde mitochondrial speed 0.435 ± 0.018 μm/s, $n = 71$ mitos from 17 fish, Student's *t*-test, $p < 0.001$). $***p < 0.001$. Bars and error bars represent the mean ± SEM

3.1 Labeling Subcellular Structures in Mauthner Cells

1. After centrifugation, load the electroporation solution into an electrode with a loading pipette (*see* **Notes 1–3**). Avoid bubbles in the electrode tip when loading (*see* **Note 4**). Empirically, 0.5–1 μl of the loading solution is sufficient.
2. Put the electrode into the electrode holder on the micromanipulator. Make sure the silver wire inside the electrode is contacted with the filling solution (*see* **Note 5**). Adjust the electrode holder at a 30–45-degree angle to the horizontal line.

3. Anesthetize the 4 dpf zebrafish larvae in EM containing 0.02% MS222 for 1 min or until entirely anesthetized (*see* **Notes 6** and **7**).
4. Put the anesthetized zebrafish larvae onto the customized electroporation chamber using a disposable transfer pipette, and carefully position the zebrafish larvae with a #5 tweezer until all the dorsal sides faced up. After removing residual solution on the surface of the chamber, embed anesthetized zebrafish larvae into the 1% low melting agarose and wait until agarose cools down naturally.
5. Connect the customized electroporation chamber to Axoporator 800A through cables. Add EM that contains 0.02% MS222 in the chamber to keep zebrafish larvae anesthetized and from drying out (*see* **Note 7**).
6. Find the field of view (FOV) under the 10× objective. Bring both the electrode tip and selected zebrafish larva to the field. Lower the electrode along with FOV by adjusting the *Z*-axis on the micromanipulator until the electrode is attached to the hindbrain surface of zebrafish larvae where the Mauthner soma are located.
7. Switch to the 40× objective and finely tune the position of the electrode tip above the target region in the zebrafish brain. Slowly lower the electrode tip until it dimples the skin, and then apply a brief, rapid forward force to puncture into the skin of zebrafish larvae and enter the superficial layer of the brain. Push the electrode tip against the Mauthner soma, which can be seen in the bright field (Fig. 2d, e).
8. Monitor the electrode resistance screening on the Axoporator 800A. The electrode resistance typically ranges from 40 to 70 MΩ (*see* **Note 8**).
9. Apply voltage pulse train (e.g., a series of square waves followed by negative pulses output from PCI-6024E). Frequency: 200 Hz; pulse width: 0.5 ms; voltage and train duration of square waves: 14 V, 0.5 s; voltage and train duration of negative pulses: 28 V, 0.5 s. A successfully electroporated soma will turn red immediately under epifluorescence due to the existence of dextrans (*see* **Notes 9** and **10**) (Fig. 2f, g).
10. Retract the electrode (Fig. 2h). The electrode can be reused if it does not clog.
11. Repeat **steps 6–10** to electroporate more Mauthner somas. Typically, we only electroporate the left Mauthner soma in each zebrafish larvae because of consistency (*see* **Note 11**).
12. Recover the zebrafish larvae by placing them into a petri dish containing EM.

13. Screen electroporated Mauthner cells with an epifluorescence microscope 24–48 h post single-cell electroporation. Select morphologically normal and healthy zebrafish larvae for further imaging (*see* **Note 12**) (Fig. 3a).

3.2 Imaging of Axonal Transport in Mauthner Cells

1. Anesthetize the zebrafish larvae after 6 dpf with fluorescence expressed in Mauthner cells in EM solution containing 0.02% MS222 for 1 min or until they are entirely anesthetized.
2. Mount the larvae onto the coverslip of the customized mounting chamber using 1% (wt/vol) low-melting agarose. Adjust the position of the zebrafish larvae with a #5 tweezer before the low-melting agarose solidifies. The embedded larvae's dorsal side is against the coverslip. Wait until low-melting agarose fully solidified.
3. Invert the customized mounting chamber and put it on a 35-mm petri dish filling with 0.02% MS222. Make sure that low-melting agarose can be fully immersed in the dish's EM so that the larvae are able to keep under anesthesia and from drying out.
4. Close field stop on the microscope to illuminate the field of view only, which avoids photobleaching areas out of focus.
5. Use 60× water-immersion objectives (N.A. = 1.1) to select an area of Mauthner axons. Activate the camera and inspect the chosen area in microscope software (*see* **Note 13**).
6. Set up imaging parameters to obtain the axon morphology. Scanning speed (20 μs/pixel), resolution (1024 pixel × 1024 pixel), ROI (205 pixel × 50 pixel), stepsize (1 μm/slice). Take images of all channels (excitation wavelength: 488 nm and 543 nm) before time-lapse imaging (Fig. 3b).
7. Set up imaging parameters to record the mitochondrial dynamics. Scanning speed (20 μs/pixel), resolution (1024 pixel × 1024 pixel), ROI (205 pixel × 50 pixel), stepsize (1.5–2 μm/slice, 3 slices total), frame rate (1.58 s/image, 100 images total). Take images of only 488 nm channel as time-lapse imaging (*see* **Note 14**) (Fig. 3c).
8. When imaging is completed, check the time-lapse imaging before saving them. Images with severe motion artifacts or overexposure are excluded and will be re-taken (*see* **Note 15**).
9. Return the zebrafish larvae to the EM and allow them to recover.

3.3 Analysis of Axonal Transport in Mauthner Neurons

We recommend using Fiji ImageJ, an open-source software providing many bundled plugins to process time-lapse imaging.

1. Open Fiji ImageJ and load the time-lapse file and use "Z-projection" to allow the 3D dataset to be visualized in 2D.

Click "Image/Stacks/Z-projection." Subsequently, select "Maximum Intensity" and "All time frames," and "start slice" and "stop slice" as 1 and 3, individually.

2. Apply "Plugins/Walking average" and set "number of frames to average" as 3 to optimize image quality of mitochondria time-lapse files.

   (WalkingAverage, http://www.embl.de/eamnet/html/body_kymograph.html).

3. Use the StackReg plugin for motion correction.

   (StackReg, http://bigwww.epfl.ch/thevenaz/stackreg/).

4. To determine mitochondrial motility, first manually count the number of mitochondria in the median frame of the time-lapse movie using "Plugins/Cell counter" as the number of total mitochondria.

   Mitochondrial motility is the percentage of moving mitochondria during a 2.5 min time-lapse movie in a given field of axonal segments (Fig. 4a).

   Individual mitochondria that move less than 2 μm during the whole imaging period is defined as **static mitochondria**. On the contrary, the individual mitochondrion that moves at least 2 μm during the imaging window is defined as a **moving mitochondrion**. Moving mitochondria can be then divided into anterograde movement that move away from soma and retrograde movement that move toward soma.

5. To trace movements of an individual mitochondrion, trace the position of the mitochondrion frame-by-frame manually in the time-lapse files to determine the start and end time-points with "plugins/Cell counter." The coordinates of the dots in the trajectory are exported to Office Excel using Fiji ImageJ and will be used to calculate an approximate moving speed. **Mitochondrial velocity** is defined as the total moving distance of a mitochondrion divided by its observed moving time (Fig. 4b).

4 Notes

1. It is essential to guarantee the quality of electrode, as it is the main factor to affect the success rate of electroporation. The diameter of electrode tip needs to be smaller than the soma size to minimize damage to the cell and enhance efficiency of electroporation. There is a tradeoff between a small tip and a rigid tip with an open end and more details can be found on the "Micropipette Puller Operation Manual" (Sutter Instrument Company). Especially, puller parameters are required to be adjusted based on different soma size.

2. To increase the success rate of electroporation, we recommend using endo-free plasmid DNA since excessive residues of endotoxins from plasmid extraction may have side effects on cell development.
3. It is important to centrifuge electroporation solution before loading since it minimizes the possibility of clogging the electrode.
4. Slightly flick the electrode to help release bubbles if exist.
5. The end of the silver wire might be adjusted to make sure it contacts the filling solution. Do not insert it too deep to avoid breaking the electrode tip.
6. To prevent pigment formation from interfering imaging, zebrafish larvae are maintained in EM with 0.2 mM PTU from 1 dpf till the end of the experiments.
7. The larvae should not be kept under anesthesia for more than 1 h.
8. When electrode tip approaches Mauthner soma, make sure that the tip is not too small or clogged as showed with a high electrode resistance on the monitor nor too large or broken (low resistance).
9. Addition of a train of biphasic pulses in front of a series of negative pulses provides higher efficiency of electroporation compared to negative pulses alone.
10. Determine the pulse voltage empirically and constantly observe the impedance on the electroporator's screen to make sure that the tip is not clogged or broken.
11. The success rate of labeling M-cells is 5–20%. Some successfully labeled M-cells may not show fluorescence due to necrosis, which could affect the other unlabeled M-cell. Therefore, to enhance the survival of labeled M-cells, we only electroporate one-sided Mauthner soma in each zebrafish larvae. Besides, it can simplify the operation process because of this operational consistency.
12. It is difficult to observe the expression of plasmids in Mauthner somas within 12 h. Prolonged time benefit expression of fluorescent proteins.
13. Block excitation laser when the larvae are not under imaging to avoid photobleaching.
14. Avoid touching the microscope or the stage of the microscope while imaging to reduce motion artifacts.
15. Severe motion artifacts can be caused by zebrafish waking up during imaging. When this happens, adjourn imaging and place zebrafish in another petri dish containing fresh EM with 0.02% MS222. Do not restart imaging until zebrafish is re-anesthetized.

Acknowledgments

This work was supported by NSFC 82071357, 31771183, and MOST 2019YFA0405600. We thank Dr. Jiulin Du from Institute of Neuroscience (Chinese Academy of Sciences) for the gift of some plasmids. We would like to thank our Core Facility Center for Life Sciences at the University of Science and Technology of China for Olympus FV1200 and ZEISS 710/880.

References

1. Perlson E, Maday S, Fu MM, Moughamian AJ, Holzbaur EL (2010) Retrograde axonal transport: pathways to cell death? Trends Neurosci 33(7):335–344. https://doi.org/10.1016/j.tins.2010.03.006
2. Plucinska G, Misgeld T (2016) Imaging of neuronal mitochondria in situ. Curr Opin Neurobiol 39:152–163. https://doi.org/10.1016/j.conb.2016.06.006
3. Xu CC, Denton KR, Wang ZB, Zhang X, Li XJ (2016) Abnormal mitochondrial transport and morphology as early pathological changes in human models of spinal muscular atrophy. Dis Model Mech 9(1):39–49. https://doi.org/10.1242/dmm.021766
4. Pathak A, Stanley EM, Hickman FE, Wallace N, Brewer B, Li D, Gluska S, Perlson E, Fuhrmann S, Akassoglou K, Bronfman F, Casaccia P, Burnette DT, Carter BD (2018) Retrograde degenerative signaling mediated by the p75 Neurotrophin receptor requires p150(glued) deacetylation by axonal HDAC1. Dev Cell 46(3):376–387. e377. https://doi.org/10.1016/j.devcel.2018.07.001
5. Kiryu-Seo S, Ohno N, Kidd GJ, Komuro H, Trapp BD (2010) Demyelination increases axonal stationary mitochondrial size and the speed of axonal mitochondrial transport. J Neurosci 30(19):6658–6666. https://doi.org/10.1523/JNEUROSCI.5265-09.2010
6. Badal KK, Akhmedov K, Lamoureux P, Liu XA, Reich A, Fallahi-Sichani M, Swarnkar S, Miller KE, Puthanveettil SV (2019) Synapse formation activates a transcriptional program for persistent enhancement in the bi-directional transport of mitochondria. Cell Rep 26(3):507–517. e503. https://doi.org/10.1016/j.celrep.2018.12.073
7. Plucinska G, Paquet D, Hruscha A, Godinho L, Haass C, Schmid B, Misgeld T (2012) In vivo imaging of disease-related mitochondrial dynamics in a vertebrate model system. J Neurosci 32(46):16203–16212. https://doi.org/10.1523/JNEUROSCI.1327-12.2012
8. Paquet D, Plucinska G, Misgeld T (2014) In vivo imaging of mitochondria in intact zebrafish larvae. Methods Enzymol 547:151–164. https://doi.org/10.1016/B978-0-12-801415-8.00009-6
9. Korn H, Faber DS (2005) The Mauthner cell half a century later: a neurobiological model for decision-making? Neuron 47(1):13–28. https://doi.org/10.1016/j.neuron.2005.05.019
10. Sillar KT (2009) Mauthner cells. Curr Biol 19(9):R353–R355. https://doi.org/10.1016/j.cub.2009.02.025
11. Bestman JE, Ewald RC, Chiu SL, Cline HT (2006) In vivo single-cell electroporation for transfer of DNA and macromolecules. Nat Protoc 1(3):1267–1272. https://doi.org/10.1038/nprot.2006.186
12. Haas K, Sin WC, Javaherian A, Li Z, Cline HT (2001) Single-cell electroporation for gene transfer in vivo. Neuron 29(3):583–591. https://doi.org/10.1016/s0896-6273(01)00235-5
13. Huang YB, Hu CR, Zhang L, Yin W, Hu B (2015) In vivo study of dynamics and stability of dendritic spines on olfactory bulb interneurons in Xenopus laevis tadpoles. PLoS One 10(10):e0140752. https://doi.org/10.1371/journal.pone.0140752
14. Judkewitz B, Rizzi M, Kitamura K, Hausser M (2009) Targeted single-cell electroporation of mammalian neurons in vivo. Nat Protoc 4(6):862–869. https://doi.org/10.1038/nprot.2009.56
15. Chen M, Xu Y, Huang R, Huang Y, Ge S, Hu B (2017) N-cadherin is involved in neuronal activity-dependent regulation of myelinating capacity of zebrafish individual oligodendrocytes in vivo. Mol Neurobiol 54(9):6917–6930. https://doi.org/10.1007/s12035-016-0233-4

16. Huang R, Chen M, Yang L, Wagle M, Guo S, Hu B (2017) MicroRNA-133b negatively regulates zebrafish single Mauthner-cell axon regeneration through targeting tppp3 in vivo. Front Mol Neurosci 10:375. https://doi.org/10.3389/fnmol.2017.00375
17. Chen M, Huang RC, Yang LQ, Ren DL, Hu B (2019) In vivo imaging of evoked calcium responses indicates the intrinsic axonal regenerative capacity of zebrafish. FASEB J 33(6):7721–7733. https://doi.org/10.1096/fj.201802649R
18. Xu Y, Chen M, Hu B, Huang R, Hu B (2017) In vivo imaging of mitochondrial transport in single-axon regeneration of zebrafish Mauthner cells. Front Cell Neurosci 11:4. https://doi.org/10.3389/fncel.2017.00004

Part VI

Drosophila In Vivo, *Ex Vivo*, and Primary Neurons

Chapter 19

Dissection and Direct Imaging of Axonal Transport in *Drosophila* Segmental Nerves

William M. Saxton, Angeline Lim, and Inna Djagaeva

Abstract

For neurons, especially those with long axons, the forceful transport of mitochondria, vesicles, and other cytoplasmic components by cytoskeletal motors is vital. Defects in cytoplasmic transport machinery cause a degradation of signaling capacity that is most severe for neurons with the longest axons. In humans, with motor axons up to a meter long, even a mild mutation in one copy of the gene that codes for kinesin-1, the primary anterograde axonal transport motor, can cause spastic paraplegia and other distal neuropathies.

To address questions about the molecular mechanisms of organelle movement, we turned to *Drosophila* as a model system, because it offered rigorous genetic and molecular approaches to the identification and inhibition of specific elements of transport machinery. However, methods for direct observation of organelle transport were largely lacking. We describe here an approach that we developed for imaging the transport behaviors of specific organelles in the long motor axons of larvae. It is straightforward, the equipment is commonly available, and it provides a powerful tool for studying the contributions of specific proteins to organelle transport mechanisms.

Key words Axonal organelles, Fast transport, Mitochondria, Neuropeptides, *Drosophila*

1 Introduction

Long-distance axonal transport of cytoplasmic components is especially important in motor neurons because of their long thin architecture. In humans, motor axons to the feet can extend a meter from their cell bodies, in which reside nuclei and the central biosynthetic/recycling machinery. Because of this length and functional asymmetry, even slight defects in fast transport mechanisms can cause a degradation of axon signaling that compromises muscle control in the extremities (spastic paraplegia, CMT, and ALS). Defective axonal transport is also an important contributing factor in the pathologies of other neurodegenerative diseases (e.g., Alzheimer's, Parkinson's, and Huntington's) [1, 2]. Thus the molecular mechanisms that underlie axonal transport are a critical focus area for basic biomedical research.

Alessio Vagnoni (ed.), *Axonal Transport: Methods and Protocols*,
Methods in Molecular Biology, vol. 2431, https://doi.org/10.1007/978-1-0716-1990-2_19,
© The Author(s), under exclusive license to Springer Science+Business Media, LLC, part of Springer Nature 2022

Direct imaging of organelle movements in living neurons offers a powerful means to answer questions about axonal transport mechanisms. Observations on the distribution and motion of mitochondria and other axonal organelles by brightfield microscopy with vital dyes were first reported over 100 years ago by Takasubure Matsumoto who was working in the laboratory of Margaret and Warren Lewis [3]. For the next six decades, investigations of the identities, directions, and flow rates of different axonal components focused largely on observing the effects of transport blockages and the migration of radioactive tracers [4–7]. Later, video-enhanced differential interference contrast microscopy (VE-DIC) provided a key advance in direct imaging of not only unstained organelles but also microtubules in axons and free axoplasm [8]. Insights from VE-DIC imaging, in conjunction with biochemical fractionation of axoplasm, led in short order to the identification of molecular motor proteins; ATPases that drive the processive transport of axonal organelles and other components along microtubules [9, 10].

Those decades of pioneering work produced many central insights, including that different axoplasmic components have unique transport behaviors, that those different behaviors must be central to maintaining proper asymmetric distributions of neuronal components, and that multiple types of molecular motor complexes, cytoskeletal filaments, and regulatory proteins must be responsible for controlling those behaviors. Many mechanistic questions emerged, such as: Which motors carry what cargoes? How are motors assigned to different cargoes? How is the velocity and direction of an individual cargo controlled? and What intracellular and extracellular biochemical signals initiate and terminate transport?

To address such questions, we turned to *Drosophila* as a model organism [11–13]. It offers deeply understood classical genetics and genetic engineering for pursuing the molecular mechanisms of transport through function disruption. It also offers paradigm setting research on developmental biology and neuroscience that provides a rich context for exploring the biological impacts of organelle transport mechanisms. However, at the outset, an approach for the direct observation of axonal organelle movements was lacking.

This chapter will detail a method that we developed for filling the axonal transport imaging gap. The foundation was laid by pioneering neurophysiology studies at Cal Tech by Lily and Yuh-Nung Jan in Seymour Benzer's group [14]. Mature third instar larvae were dissected in buffered saline to expose the ventral ganglion of the central nervous system and the long segmental nerves that connect it to the abdominal body wall muscles. Electrodes were used to stimulate axons in segmental nerves and to record responses in body wall muscles. Beginning with that larval

dissection method, we first developed approaches to image axons and their organelles in fixed specimens [15, 16]. In an initial attempt, we imaged live segmental nerves by VE-DIC. That failed, because of the complexity of the light path to the axonal organelles; through cuticle, muscle cells, nerve sheath, and glial cells. Organelles were not distinguishable even if segmental nerves were snipped out and imaged alone. Thankfully, the advent of engineered genes that encoded green fluorescent protein (GFP) offered a transformative solution to the imaging problem [17, 18]. GFP fusion proteins could be targeted to specific types of organelles in specific cell types. By adapting GFP (and now other FPs) for expression in motor neurons, but not glial or muscle cells, we were able to use fluorescence microscopy to image moving organelles in segmental nerve axons. Using this expressed fluorescent protein approach in *Drosophila*, studies of the mechanisms of axonal transport led to the discovery that microtubule motor defects cause distal neuropathies [16, 19] and ongoing mechanistic insights into how things move.

2 Materials

2.1 Drosophila Culture and Genetics

1. *Drosophila* culture medium: 3.8 g/l agar, 60 ml/l corn syrup, 53 g/l corn meal, 7.6 g/l soy flour, 13.5 g/l yeast, 3.8 ml/l propionic acid. Used in vials with cotton plugs (Bloomington *Drosophila* Stock Center cornmeal food, https://bdsc.indiana.edu/information/recipes/bloomfood.html).
2. *Drosophila* strains carrying transgenes for neuronal GAL4 "drivers" and GAL4-activated fluorescent protein "responders" (Table 1).
3. Stereo dissection microscope and epi-illumination white light source (e.g., Leica S4E with KL300LED).
4. CO_2 delivery system: compressed CO_2 gas tank, CO_2 regulator, hose system with Y at the dissection scope station, branch hoses with pinch valves ending in (a) an 18 gauge needle for gassing vials and (b) a *Drosophila* CO_2 gas pad.
5. Fly sorting tools: e.g., artist's paintbrushes and small spatulas.

2.2 Larval Neuromuscular Preparation

1. Dissection dishes containing Sylgard pads (*see* **Note 1**).
2. Sharp microdissection scissors (Roboz, RS-5620).
3. Two pairs of extra-fine forceps (Dumont #5).
4. A small oilstone (Norton Arkansas Stone)(*see* **Note 2**).
5. Cacti for dissection pins (*see* **Note 3**).
6. Schneiders tissue culture medium (*see* **Note 4**).

Table 1
Drosophila GAL4 driver and UAS responder strains. These are strains that we use for live imaging of axonal transport in *Drosophila* larvae. Note that expression is common in salivary gland cells. The RNAi column indicates whether or not we have obtained knockdown phenotypes with the specified driver combined with both *UAS-mito-GFP* and UAS-shRNAs specific for kinesin heavy chain mRNA. Fly strains can be obtained from the Bloomington Drosophila Stock Center or by inquiry to the authors of the listed references

GAL4 drivers				
Transgene (short name)	**Expression patterns**	**RNAi**	**Bloomington stock numbers**	**References**
D42-GAL4	Strong in larval motor neurons and some sensory neurons	Yes	8816, 9263, 42737	[37]
OK6-GAL4	Strong in larval motor neurons	Yes	64199	[38]
OK371-GAL4	Strong in glutamatergic motor neurons	Yes	26160	[39]
RRa-Gal4	Weak to moderate in motor neurons aCC, RP2, and A1-7 DA1	No	–	[40]
RN2-Gal4	Weak to moderate in motor neurons aCC, pCC and RP2	No	7470, 7473	[40]
CCAP-GAL4	Weak to moderate in a subset of peptidergic neurons (CCAP neurons)	No	25685, 25686	[41]
UAS responders				
Transgene (short name)	**Fusion protein and its localization**		**Bloomington stock number**	**References**
UAS-Mito-GFP	hCOX8A mitochondrial import sequence fused to HA epitope followed by GFP(S65T). Concentrates in mitochondrial matrix		8442, 8443	[30]
UAS-ANF-GFP	Human atrial natriuretic factor neuropeptide fused to GFP(emerald). Concentrates in lumens of dense core vesicles		7001	[42]

7. VaLaP: by weight 1:1:1 Vaseline, lanolin, and paraffin melted/mixed over low heat.
8. Cotton swab applicator sticks.
9. Pasteur pipettes.
10. Absorbent paper (Kimwipes, etc.).
11. Microscope slides, coverslips, and spacers (*see* **Note 5**).

2.3 Axonal Transport Imaging

1. Fluorescence microscope equipped for digital video imaging (*see* **Note 6**).
2. Low light digital video camera (*see* **Note 7**).

3. Computer to control the system and record images (*see* **Note 7**).
4. Image capture and analysis Software (*see* **Note 7**).

2.4 Tracking and Data Analysis

1. Software for organelle tracking and kymography (e.g., Fiji).
2. Statistical analysis software (e.g., IBM SPSS Statistics).

3 Methods

The approach detailed here will focus largely on how to dissect *Drosophila* larvae for direct imaging of fluorescence-tagged organelles in segmental nerve motor axons. The steps are conceptually straightforward (Fig. 1), but mastering some of the skills requires patience and practice. A benefit, as compared to imaging organelles in segmental nerve axons in non-dissected immobilized larvae [20–22], is that dissected larvae yield organelle images with brighter fluorescence and finer spatial resolution (Fig. 2). This is because organelle fluorescence from motor axons in a dissected specimen must pass through only glial cells and the nerve sheath to reach the coverslip, whereas in an intact larva, it must pass glial cells, nerve sheath, muscle cells, and cuticle. Intact immobilized larvae produce outstanding images of sensory neurons and motor neuron synaptic terminals that are close to the cuticle because of shorter and simpler light paths.

Another issue to consider is how the method of larva preparation and observation impacts the process of axonal transport in segmental nerves. One advantage with the dissection approach is that bright images of organelles can be obtained with less excitation illumination than with intact larva. This decreases fluorophore bleaching and photodamage to the specimen. On the other hand, transport behaviors in segmental nerves may be altered by the trauma of dissection and/or by exposing the nervous system to dissection medium [23]. While observing transport in the nerves of intact larvae immobilized by anesthetization avoids both of those insults, the anesthetic does have a powerful influence on nervous system function, so it too may alter axonal transport. We use both approaches. Table 2 compares neurosecretory vesicle transport behaviors in dissected vs intact wild-type larvae. It does not show major differences that cannot be explained by differences in fluorescence intensity and image quality. This indicates that dissection trauma and medium do not cause major changes in neurosecretory vesicle transport. Our conclusion is that while either approach may alter axonal transport in some fashion, using either (or better, both) to compare wild-type axonal transport with that in larvae with a single molecular variable (e.g., a genetic mutation or a specific RNAi knockdown) will give valid insights into how that gene product contributes to the transport mechanism.

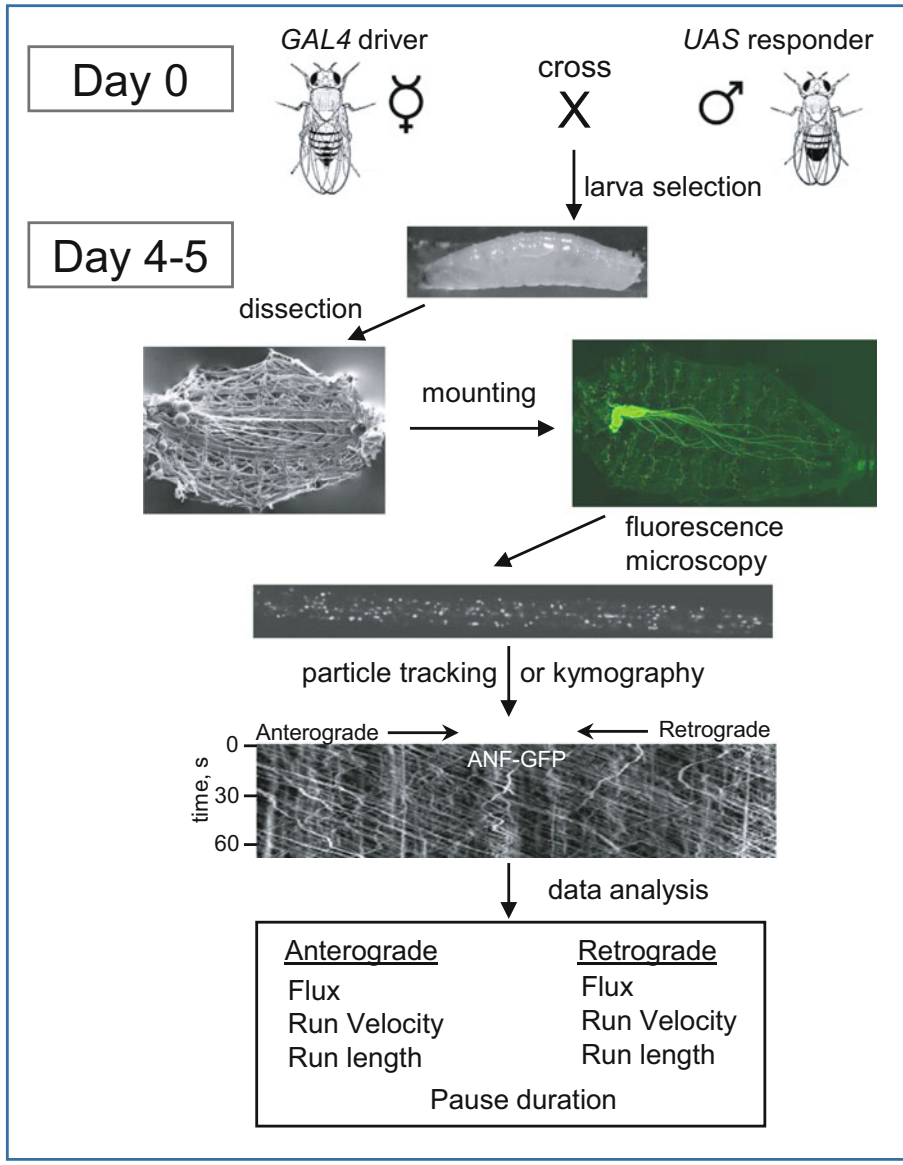

Fig. 1 Experimental Flow Diagram. At 4–5 days after mating, a third instar larva of the desired genotype is selected (lateral view), dissected, mounted on a slide, and observed by fluorescence microscopy. In the low-magnification image (green), the intensely fluorescent ventral ganglion on the left is by chance rotated to lie on its side. Long segmental nerves extend rightward from it to innervate different segments along the body wall. The high magnification image shows a portion of a single segmental nerve that contains many motor axons that contain neurosecretory vesicles loaded with GFP. The kymograph shows position on the *X*-axis relative to time (seconds) on the *Y*-axis. (The scanning electron micrograph is adapted from Hurd et al. [16], and the fluorescent low magnification image of the neuromuscular system is adapted from Pilling et al. [30])

To sum things up, to study transport mechanisms in the long axons of motor neurons that have normal synaptic connections and glial cell support in a functioning nervous system, the dissection method described here offers a fine approach. Learning dissection

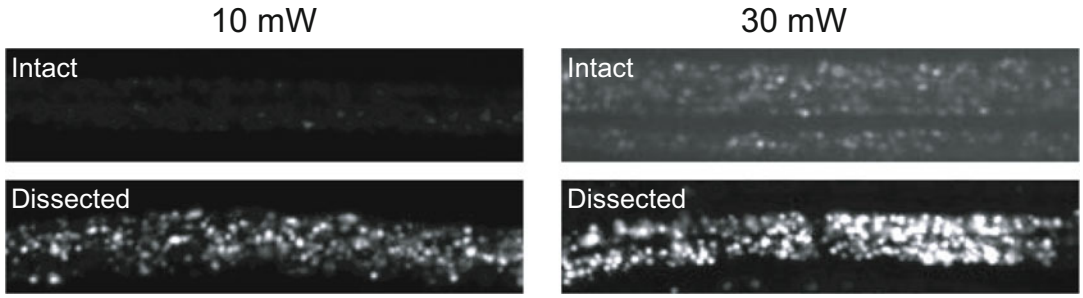

Fig. 2 Fluorescence Intensity Comparison: Intact vs Dissected Larvae. Intact third instar larvae carrying one copy of the D42-Gal4 driver and one of the ANF:GFP responder were immobilized by anesthesia with desflurane [21]. Dissected larvae were prepared by dissection as described here. Images were collected with fluorescence excitation at two different laser powers (10 mW or 30 mW) with otherwise identical imaging parameters

Table 2
Comparison of axonal transport behavior of neurosecretory vesicles in dissected and intact larvae analyzed by manual tracking. Flux reflects the number of vesicles that could be observed passing a fiduciary point in a segmental nerve per minute. Vel reflects the average forward run velocities of vesicles. Length reflects the average distances that vesicles could be tracked in continuous forward runs. % Time reflects forward run duty cycles; the fraction of time vesicles spent in forward runs as opposed to pauses and reverse runs. These data sets were excerpted from published studies of dissected and intact anesthetized larvae that had identical D42-GAL4 and UAS-ANF-GFP genotypes [21, 29]. Both were obtained by imaging with a Nikon E800 scope and a Perkin Elmer Ultraview spinning disk confocal fluorescence microscope system. The Barkus study used a Hamamatsu ORCA ER CCD camera. The Lim study used a more sensitive Hamamatsu C9100-50 EM CCD camera. Despite the more sensitive camera that Lim used for imaging the intact larvae, vesicle fluorescence was substantially dimmer (Fig. 2), because the fluorescence from axonal vesicles had to pass not only glial cells and nerve sheath but also body wall muscles and cuticle. This accounts for the threefold reduction of flux and the twofold decrease of observable run lengths in the intact larvae. The 10–25% reduction in forward duty cycle observed in the dissected specimens may reflect physiological changes caused by dissection. Variances in parentheses are ±SEM

	Anterograde				Retrograde			
	Flux	Vel	Length	% Time	Flux	Vel	Length	% Time
Dissected	104 (7.4)	1.1 (0.1)	41.8 (6.5)	85.1 (3.9)	38.8 (1.9)	1.0 (0.1)	17.4 (4.1)	67.8 (4.3)
Intact	35.7 (4.6)	1.0 (0.1)	19.1 (4.7)	94.0 (3.5)	10.1 (2.5)	1.0 (0.1)	8.0 (2.3)	87.0 (3.8)

and mounting of larval neuromuscular pelt preparations may require a couple of weeks for researchers with average dexterity, as opposed to a few days for learning immobilization approaches. However once mastered, it produces superior image quality that allows better organelle tracking, and the material requirements are relatively simple.

3.1 Drosophila Culture and Genetics

To obtain larvae with neurons that have fluorescent organelles, use standard genetic approaches to produce animals with a genotype that includes a neuronal GAL4 driver and a UAS fluorescence-tagged organelle-targeted protein responder (*see* **Note 8**). For example:

1. Collect newly enclosed female *D42-GAL4/D42-GAL4* flies, and age them 3 days in fresh culture vials.
2. Collect male *UAS-mito-GFP/TM6b Tb* flies and mate them with the aged females in fresh vials (five females and three males per vial).
3. 2 days after mating, transfer the adults to new vials to continue production of progeny.
4. 4–5 days after mating (at 25 °C), larvae that are *D42-GAL4/UAS-mito-GFP* will be recognized by their normal body shape (non-tubby) or by GFP fluorescence concentrated in their ventral ganglia and nerves.

3.2 Larval Neuromuscular Pelt Preparation

1. Place a Sylgard-coated dissection dish on a black/white striped platform on the stage of a stereo microscope (*see* **Note 9**).
2. Using forceps, snap spines from a cactus (*see* **Note 3**), check to be sure that their tips are sharp, push tips well into the Sylgard, and break them off at a length that is convenient for your dissection (~2 mm works for us). They should be positioned out of the way, either on the perimeter of the dissection pad or in another dish that is easily reached by your forceps during dissection.
3. Pick a third instar larva that is crawling along the wall of a culture vial with an artist's brush, clean it in a small dish of water or dissection medium with the brush, then place it ventral side down on the center of the dissection pad with its head pointing "north" (Fig. 3).
4. Use the sides of the tips of one pair of forceps to hold the larva in place and insert a spine held with a second pair of forceps to anchor its posterior end to the pad such that the butt of the spine is angled south. Ideally, the pin will pierce the larva between its protruding posterior spiracles. With another spine, pierce the head just in front of the mouth hooks and anchor it to the pad with the butt of the spine angled north. The larva should be slightly stretched such that it is held straight between the anterior and posterior anchor points.
5. After flooding the well with Schneider's medium, hold the microdissection scissors vertically with points oriented north-south, and snip a small incision on the dorsal midline in front of the posterior spine (Fig. 3). Fat body that extrudes can be removed gently with forceps to allow a clear view of the

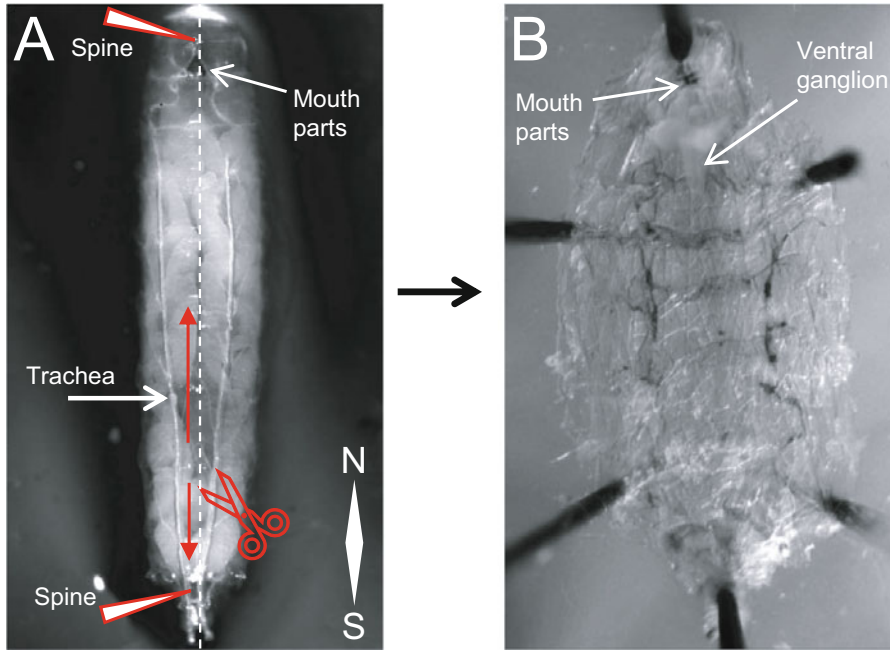

Fig. 3 Spine Placement and Incisions for Dissection. (**a**) A third instar larva on a dissection pad showing ideal locations for the initial placement of anterior and posterior cactus spines and two incisions (red arrows) along its dorsal midline (dashed white line). Anterior is up (North) and posterior is down (South). (**b**) A third instar larval neuromuscular preparation (pelt) after a completed dissection

incision. Angling the butt of the scissors south, insert the lower tip just under the cuticle at the north end of the incision and use small snips to extend it to the anterior spine (*see* **Note 10**). Angling the butt of the scissors north, use the tip to extend the incision to the posterior spine. Small diagonal snips from the ends of the main incision to make cuts that pass the sides of the spines will help with the cuticle spreading in **step 7**.

6. To uncover the neuromuscular system, grasp the main tracheal tubes near the posterior with forceps and gently lift toward the anterior. Much of the fat and gut will come away with them.
7. Spread the incision laterally. About 1/3 back from the head, insert a spine tip just under the lip of the incision, move it sideways to expose the segmental nerves and body wall muscles, then pierce the cuticle and Sylgard while angling the butt of the spine away from center. The next spine should be set in the same manner opposite the first. Set another spine pair 2/3 back from the head in the same fashion. The six pins should form an elongated hexagon (Fig. 3). With proper spine placement, the cuticle will be spread without diagonal wrinkles and the ventral midline will remain straight between the anterior and posterior spines.

8. Remove remaining bits of viscera that may get in the way of your subsequent nerve imaging, then exchange the medium to get rid of debris. Do not bother to remove the tightly attached imaginal discs in the head region, unless you need to image the ventral ganglion. Remove most of the dissection medium from the dish, leaving the specimen wet. Grasping the anterior tip of the cuticle with one pair of forceps, remove all the spines with a second pair, leaving the anterior spine for last. The pelt will relax and roll up toward your anterior forceps. Transfer it to a microscope slide such that the nerves and ventral ganglion will be away from the glass. Use the second pair of forceps tips to move the incision edges out to the sides (*see* **Note 11**).
9. Set spacers of appropriate thickness around the pelt, then gently lower a coverslip over it (*see* **Note 5**). Seal the coverslip's corners first and then its edges with a cotton swab dipped in molten VaLaP, leaving gaps above the anterior and below the posterior of the larva.
10. Using absorbent paper at the posterior gap and small drops of Schneider's medium at the anterior gap, flow medium under the coverslip from anterior to posterior.

3.3 Axonal Transport Imaging

1. Center the mounted pelt on a fluorescence microscope stage with a low magnification dry objective lens. Switch to a high magnification lens and focus on the portion of a segmental nerve to be observed (*see* **Note 12** and Fig. 4).
2. Collect an image series that can be used to create a time-lapse movie. Use the minimum intensity of fluorescence excitation light and the minimum frequency of images needed to track individual moving organelles from one frame to the next with confidence (*see* **Note 13**).

3.4 Data Analysis

1. Flux assessments can be done directly from time-lapse videos by simply counting the numbers of anterograde and retrograde organelles that pass a fiduciary mark per unit time. Reasonably accurate counts can also be obtained by counting diagonal tracks on kymographs of those videos (*see* **Note 14**).
2. Anterograde and retrograde motion parameters, such as run velocity, run length, pause frequency, and pause duration, can be determined by manual frame-by-frame tracking of single organelles or by kymograph analysis (Fig. 5) (*see* **Note 14**).
3. Statistical assessments of differences in transport behavior can be done using SPSS Statistics or other similar programs (*see* **Note 15**).

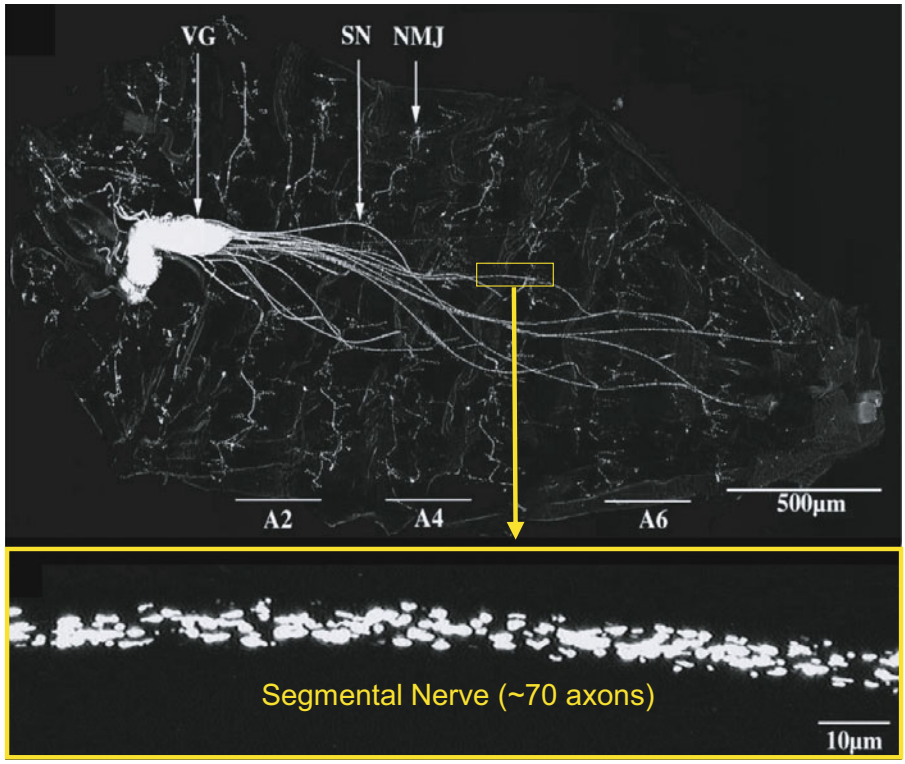

Fig. 4 Fluorescence imaging of GFP-mitochondria in a dissected third instar larva. The larva carried a D42-Gal4 driver and a UAS-mito-GFP responder. A tiled image is shown above with labels for VG—ventral ganglion, SN—segmental nerve, NMJ—neuromuscular junction, and A2, A4, A6—abdominal segments. The lower image shows a magnified view of the boxed portion of a segmental nerve that delivers motor axons to A6. (Adapted from Pilling et al. [30])

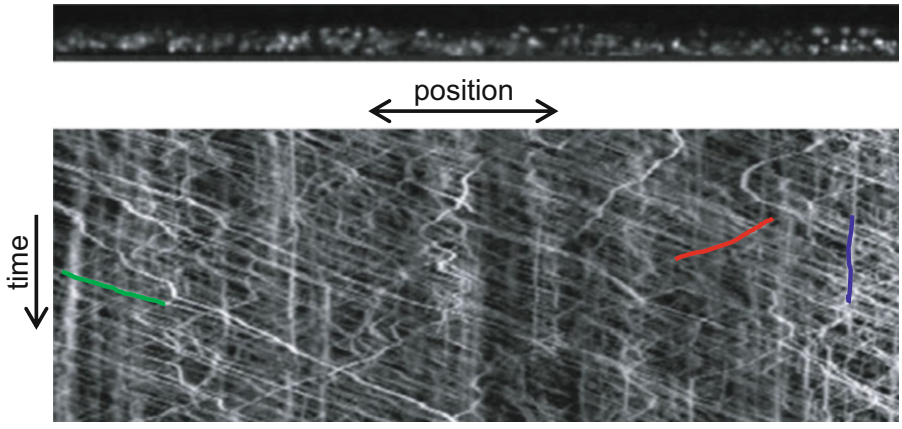

Fig. 5 Kymograph of GFP in neurosecretory vesicles. The top panel shows a single frame from a time-lapse image series of ANF::GFP in motor axons of a segmental nerve. A kymograph from the same image series is shown below. Examples are highlighted for anterograde (green), retrograde (red), and stationary (blue) particle tracks

4 Notes

1. We use thick glass slides with three depression wells; however, a single depression slide, a petri dish, or anything that can hold a pad of polymerized Sylgard, dissection medium, and allow free access by your tools will work. Sylgard (Dow: SYLGARD 184 elastomer) has two viscous liquid components that when mixed will polymerize into a transparent rubbery pad that provides an excellent base for dissection. Mix the components slowly to minimize air bubbles and use a pipette to apply a layer $\geq$2 mm deep to each dissection dish. It will polymerize slowly at room temperature and faster at elevated temperatures.
2. Fine tipped stainless steel spring handle microdissection scissors and extra fine forceps are important for rapid dissection of larvae. After each use, be sure to clean them with a stream of water while opening and closing the jaws and then dry them with a stream of ethanol. After drying, their tips should be shielded with a soft plastic cover (e.g., a micropipette tip) to prevent damage from contact with hard surfaces. When accidents do blunt the tips, they can usually be restored by careful honing on a super-fine oilstone that is set on a dissection scope stage. Use carefully directed light strokes along the lengths of the backs and sides of the jaws to re-sharpen symmetrically such that their points close perfectly. A steep taper to the points is best for their future durability.
3. We use sharp stiff spines from *Notocactus eugeniae* and *Mammillaria spinosissima*. They or similar species can be obtained from garden shops. A manufactured alternative is stainless steel Minutien dissection pins [24].
4. Dissection medium composition can influence the physiology of the specimen [23]. The calcium-free medium favored for electrophysiology prevents body wall muscle contraction. It is convenient for dissection and time-lapse imaging, but may alter calcium-dependent signaling pathways that influence the cytoskeleton and organelle transport processes. Schneider's culture medium has low enough calcium levels to diminish muscle contractions while allowing organelle transport that appears similar to that observed in non-dissected immobilized larvae (Table 2).
5. After spreading the pelt on a slide (Subheading 3.2.8 and **Note 11**), position 3 or 4 small fragments of broken coverslip where they will support the overlaid coverslip. The spacers should be thin enough to allow light contact between the coverslip and the pelt. Fragments from coverslips of different thicknesses can be tested to get the best level of contact. Ideally, the portions of the nerves to be imaged will be touching or close to the

overlying coverslip and will lie in the focal plane across the entire field of view when imaged at high magnification on the compound fluorescence microscope.

6. Various types of fluorescence microscopes can be used to observe axonal organelles loaded with fluorescent proteins. In the beginning (1998), we used an inverted widefield fluorescence microscope or an upright Biorad MRC600 scanning confocal. At present, we use a Solamere system with solid state lasers and a Nikon TE2000-E2 with a Yokagawa CSU10 spinning disk confocal head. Our most useful objectives are a CFI PLAN Fluor 10× (0.3NA), DIC PLAN Fluor 40× (0.17NA), a CFI PLAN Fluor 40× oil immersion (1.30NA), and a CFI PLAN APO 60× VC oil immersion (1.4NA).
7. For the sort of time-lapse imaging that allows detailed quantification of organelle behaviors, a high-speed low-light digital video camera is necessary. We currently use a Hamamatsu 9100c-23B EM-BT camera. It captures high-quality fluorescence images induced by excitation with brief low-level light exposures. The current imaging computer that we use is a Thinkmate Imaging Workstation with an i7 Core Processor 64 GB RAM, 2 TB SATA drive, 500 GB SSD RAID, and a Windows 7 (64 bit) operating system. The image capture/analysis software that we use, and highly recommend, is Micro-Manager [25].
8. Methods for rearing and genetic manipulation of *Drosophila* using the materials listed in Subheading 2.1 can be found online (BDSC-Fly Culture, https://bdsc.indiana.edu/information/fly-culture.html) and in publications [26, 27].

   Our standard genetic approach employs a transgenic GAL4-UAS system [28]. Screens for the random insertion of a yeast-derived GAL4 transcriptional activation gene into useful enhancer regions in *Drosophila* chromosomes have generated fly lines that express GAL4 in specific subsets of cells. When a neuronal GAL4 "driver" is present in a fly that carries a "responder" transgene that has GAL4 binding sites upstream of a gene for an organelle-targeted fluorescent protein, that protein will be synthesized in neurons of interest and will concentrate on or in the targeted organelles (Table 1). Well-characterized driver and responder fly strains can be obtained from the Bloomington *Drosophila* Stock Center (https://bdsc.indiana.edu/stocks/index.html) and from members of the *Drosophila* research community (Table 1).

   To study axonal organelles in neurons with alterations in known or suspected components of transport machinery, additional genetic manipulations will be necessary to combine the GAL4-UAS fluorescence transgenes with classical mutations or with additional UAS-responder transgenes that allow

overexpression or knockdown of the genes of interest. Such strain constructions can usually be accomplished in three generations [21].

Levels of fluorescence and knockdown RNAs expressed using the GAL4-UAS system can be increased in some cases by generating animals that are homozygous for both a driver and a responder [29, 30] and by elevating the temperature at which flies are cultured. High temperature (~29 °C) increases and low temperature (~18 °C) decreases expression by the GAL4-UAS system.

RNA interference is a convenient method of inhibiting the expression of specific genes in neurons. A large collection of transgenic fly strains has been generated by the TRiP Project (https://fgr.hms.harvard.edu/) that can be induced to express UAS-hairpin RNAs that are specific for most *Drosophila* genes [31]. Transgenes that express short hairpins usually are more effective than those that express long hairpins, unless *UAS-Dicer2* transgenes are added to the long hairpin genotypes. Both Valium20 and Valium22 TRiP transgenes are effective at reducing expression of their targeted genes in neurons.

9. Fine control of the small motions needed for microdissection is not difficult if one's arms hands and fingers are braced well. The dissection platform should be arranged to minimize the distance between the business end of an instrument and brace points for the fingers holding the instrument. Old textbooks, sandbags, rubber pads, etc. can be arranged such that forearms and the heels of one's hands are comfortable and motionless. The fingers that operate a forceps or scissors can rest on the edge of the dissection platform or on the dish itself. The platform can be a fly gas pad topped with a piece of paper with alternating black and white stripes. Positioning the larva over a black–white boundary will improve the visibility of body wall muscles and the nervous system during dissection.
10. Keep in mind the anatomy of the neuromuscular system; the segmental nerves and ventral ganglion are closer to the ventral body wall than to the dorsal. A dorsal incision can be made without damaging the nerves if the tips of the scissors are not inserted deeply. Similarly, tip insertion should be shallow for forceps and cactus spines.
11. The neuromuscular preparation will curl up during transfer from the dissection dish to the slide. Arranging it such that the nerves will be straight during imaging is challenging and frustrating for those new to the approach. A large part of the challenge is that while you will be manipulating the pelt to spread it such that the ventral ganglion and nerves are arranged well, a white light dissection microscope will not produce the contrast needed for a good view of the nervous system.

Learning this step in the procedure will be greatly facilitated by using a fluorescence dissection microscope with a filter set appropriate for the fluorophore that you are using. If the larval driver is robust (e.g., D42-GAL4), the fluorescence illumination will show ventral ganglion, nerves, motor axon terminals, and sensory neurons (e.g., Fig. 4). Switching back and forth between fluorescence and white light will allow one to see how particular manipulations with the forceps produce good alignment of the segmental nerves. To see outstanding views of what is possible, *see* Fig. 1 of Kohsaka et al. [32].

Maintaining the anterior hold with the pair of forceps that brought the pelt and its associated droplet of medium to the slide, use the sides of the tips of a second pair of forceps to gently stroke the mass away from that anterior hold point, "rolling" the posterior end of the pelt away from it. The posterior will remain in its new position if there is not too much medium present. One or both pairs of forceps can then be used to spread the pelt edges out laterally. The amount of dissection medium on the specimen and the amount of time you take to get through **steps 8–10** (spreading/mounting/medium application) quickly are critical. Too much liquid will allow the incision edges to roll back toward center, but too little (or too slow to get past **step 10**) will compromise the physiology of the specimen.

12. Axonal organelle behaviors can differ along the length of a nerve and between different nerves of the same animal. To help minimize experimental variation, image the same region of the same nerve throughout the generation of a data set. We usually image axonal organelles in the long segmental nerves that innervate segments A6, A7, or A8 as they pass through segments A4 and A5. Transport behavior will vary with time after dissection. Practice the procedure until your time from dissection start to image capture start is 5–10 min and limit imaging to an additional 10 min. Transport in well-mounted larval neuromuscular preparations kept supplied with fresh medium lasts more than 2 h, so 15–20 min from the first dissection step to the end of imaging is a conservative schedule.
13. Do not use more light than is needed for accurate observations. With our current spinning disc microscope system, axonal mitochondria that move at an average rate of ~0.25 μm/s can be tracked well in image series recorded at 1 frame per second (100 ms exposure/frame). Vesicles that carry neuropeptides move 3- to four-fold faster, so the minimum frame rate is 2–4 per second (100 ms exposure/frame). Increasing the frequency can allow finer assessments of run/pause behavior, but the enhanced illumination will increase both fluorescence photobleaching and photodamage to the specimen.

14. Axonal transport in segmental nerves is well suited to analysis by manual point-to-point tracking [30] (e.g., Fiji, Manual Tracking plugin, https://imagej.net/plugins/track/track.html) or by kymography (Fig. 5) [33, 34] (e.g., KymoToolBox plugin, https://github.com/fabricecordelieres/IJ-Plugin_KymoToolBox) [35]. We have tested various automated tracking approaches but were discouraged by frequent ambiguities caused by organelles passing one another and by fluorescence intensity changes. Improvements in automated tracking software are ongoing however, so such problems should diminish [36].
15. Reliable interpretation of tracking results requires careful statistical analysis. We routinely work with colleagues who have a deep practical understanding of how to apply statistics to biological problems. Tracking data in our experiments that compare organelle transport behaviors in mutant and control animals can be analyzed at different levels. For velocities, one can consider point-to-point velocities between individual tracked positions, aggregate those into average velocities for single continuous runs, aggregate those to get average run velocity for each organelle tracked, aggregate those to get average organelle run velocity for each animal, and finally, aggregate those to get an average organelle run velocity for each animal. At which of these nested levels, each with a progressively smaller sample size, should one do the statistical comparison to determine the influence of genotype? In our tests, point-to-point velocities and average run velocities by an organelle do not vary appreciably, so we usually compare mutant vs control at the level of average run velocity for each organelle using linear contrast [30].

Acknowledgments

We would like to acknowledge key contributions by Aaron Pilling, Rosemarie Barkus, and Curt Lively in developing the dissection, imaging, and analysis methods at Indiana University. Their work and ongoing development of the method were supported by grants from the National Institutes of Health to WMS (GM46295) and from the American Heart Association to AP, RVB, and WMS.

References

1. Sleigh JN, Rossor AM, Fellows AD et al (2019) Axonal transport and neurological disease. Nat Rev Neurol 15:691–703. https://doi.org/10.1038/s41582-019-0257-2
2. Vitet H, Brandt V, Saudou F (2020) Traffic signaling: new functions of huntingtin and axonal transport in neurological disease. Curr Opin Neurobiol 63:122–130. https://doi.org/10.1016/j.conb.2020.04.001

3. Matsumoto T (1920) The granules, vacuoles and mitochondria in the sympathetic nerve-fibers cultivated in vitro. Johns Hopkins Hosp Bull 31:91–93
4. Grafstein B, Forman DS (1980) Intracellular transport in neurons. Physiol Rev 60: 1167–1283. https://doi.org/10.1152/physrev.1980.60.4.1167
5. Lasek RJ (1970) Protein Transport in Neurons. Int Rev Neurobiol 13:289–324
6. Ochs S (1972) Fast transport of materials in mammalian nerve fibers. Science 176: 252–260. https://doi.org/10.1126/science.176.4032.252
7. Weiss P, Hiscoe HB (1948) Experiments on the mechanism of nerve growth. J Exp Zool 107:315–395. https://doi.org/10.1002/jez.1401070302
8. Allen R, Metuzals J, Tasaki I et al (1982) Fast axonal transport in squid giant axon. Science 218:1127–1129. https://doi.org/10.1126/science.6183744
9. Brady ST (1985) A novel brain ATPase with properties expected for the fast axonal transport motor. Nature 317:73–75. https://doi.org/10.1038/317073a0
10. Vale RD, Reese TS, Sheetz MP (1985) Identification of a novel force-generating protein, kinesin, involved in microtubule-based motility. Cell 42:39–50
11. Saxton WM, Porter ME, Cohn SA et al (1988) Drosophila kinesin: characterization of microtubule motility and ATPase. Proc Natl Acad Sci U S A 85:1109–1113. https://doi.org/10.1073/pnas.85.4.1109
12. Yang JT, Saxton WM, Goldstein LS (1988) Isolation and characterization of the gene encoding the heavy chain of *Drosophila* kinesin. Proc Natl Acad Sci U S A 85:1864–1868. https://doi.org/10.1073/pnas.85.6.1864
13. Saxton WM, Hicks J, Goldstein LS, Raff EC (1991) Kinesin heavy chain is essential for viability and neuromuscular functions in *Drosophila*, but mutants show no defects in mitosis. Cell 64:1093–1102. https://doi.org/10.1016/0092-8674(91)90264-y
14. Jan LY, Jan YN (1976) Properties of the larval neuromuscular junction in Drosophila melanogaster. J Physiol 262:189–214. https://doi.org/10.1113/jphysiol.1976.sp011592
15. Gho M, McDonald K, Ganetzky B, Saxton WM (1992) Effects of kinesin mutations on neuronal functions. Science 258:313–316. https://doi.org/10.1126/science.1384131
16. Hurd DD, Saxton WM (1996) Kinesin mutations cause motor neuron disease phenotypes by disrupting fast axonal transport in *Drosophila*. Genetics 144:1075–1085
17. Chalfie M, Tu Y, Euskirchen G et al (1994) Green fluorescent protein as a marker for gene expression. Science 263:802–805. https://doi.org/10.1126/science.8303295
18. Wang S, Hazelrigg T (1994) Implications for bcd mRNA localization from spatial distribution of Exu protein in *Drosophila* oogenesis. Nature 369:400–403. https://doi.org/10.1038/369400a0
19. Reid E, Kloos M, Ashley-Koch A et al (2002) A kinesin heavy chain (KIF5A) mutation in hereditary spastic paraplegia (SPG10). Am J Hum Genet 71:1189–1194. https://doi.org/10.1086/344210
20. Fuger P, Behrends LB, Mertel S et al (2007) Live imaging of synapse development and measuring protein dynamics using two-color fluorescence recovery after photo-bleaching at *Drosophila* synapses. Nat Protoc 2: 3285–3298. https://doi.org/10.1038/nprot.2007.472
21. Lim A, Rechtsteiner A, Saxton WM (2017) Two kinesins drive anterograde neuropeptide transport. Mol Biol Cell 28:3542–3553. https://doi.org/10.1091/mbc.E16-12-0820
22. Moua P, Fullerton D, Serbus LR et al (2011) Kinesin-1 tail autoregulation and microtubule-binding regions function in saltatory transport but not ooplasmic streaming. Development 138:1087–1092. https://doi.org/10.1242/dev.048645
23. Louie K, Russo GJ, Salkoff DB et al (2008) Effects of imaging conditions on mitochondrial transport and length in larval motor axons of *Drosophila*. Comp Biochem Physiol A Mol Integr Physiol 151:159–172. https://doi.org/10.1016/j.cbpa.2008.06.023
24. Kuznicki ML, Gunawardena S (2010) In vivo visualization of synaptic vesicles within *Drosophila* larval segmental axons. J Vis Exp 44: 2151. https://doi.org/10.3791/2151
25. Edelstein AD, Tsuchida MA, Amodaj N et al (2014) Advanced methods of microscope control using muManager software. J Biol Methods 1:e10. https://doi.org/10.14440/jbm.2014.36
26. Ashburner M (1989) Drosophila: a laboratory handbook. Cold Spring Harbor Laboratory Press, New York
27. Greenspan RJ (1997) Fly pushing: the theory and practice of drosophila genetics. Cold Spring Harbor Laboratory Press, New York
28. Brand AH, Perrimon N (1993) Targeted gene expression as a means of altering cell fates and generating dominant phenotypes.

Development 118:401–415. https://doi.org/10.1101/lm.1331809

29. Barkus RV, Klyachko O, Horiuchi D et al (2007) Identification of an axonal Kinesin-3 Motor for Fast Anterograde Vesicle Transport that facilitates retrograde transport of neuropeptides. Mol Biol Cell 19:274–283. https://doi.org/10.1091/mbc.E07-03-0261
30. Pilling AD, Horiuchi D, Lively CM, Saxton WM (2006) Kinesin-1 and dynein are the primary motors for fast transport of mitochondria in drosophila motor axons. Mol Biol Cell 17:2057–2068. https://doi.org/10.1091/mbc.E05-06-0526
31. Perkins LA, Holderbaum L, Tao R et al (2015) The transgenic RNAi project at Harvard Medical School: resources and validation. Genetics 201:843–852. https://doi.org/10.1534/genetics.115.180208
32. Kohsaka H, Guertin PA, Nose A (2017) Neural circuits underlying Fly larval locomotion. Curr Pharm Des 23:1722–1733. https://doi.org/10.2174/1381612822666161208120835
33. Bodakuntla S, Magiera MM, Janke C (2020) Measuring the impact of tubulin posttranslational modifications on axonal transport. Methods Mol Biol 2101:353–370. https://doi.org/10.1007/978-1-0716-0219-5_20
34. Zhang XM, Francois U, Silm K et al (2019) A proline-rich motif on VGLUT1 reduces synaptic vesicle super-pool and spontaneous release frequency. Elife 8:e50401. https://doi.org/10.7554/eLife.50401
35. Mattedi F, Chennell G, Vagnoni A (2021) Detailed imaging of mitochondrial transport and precise manipulation of mitochondrial function with genetically-encoded photosensitizers in adult *Drosophila* neurons. Methods Mol Biol; This volume.
36. Tinevez JY, Perry N, Schindelin J et al (2017) TrackMate: an open and extensible platform for single-particle tracking. Methods 115:80–90. https://doi.org/10.1016/j.ymeth.2016.09.016
37. Yeh E, Gustafson K, Boulianne GL (1995) Green fluorescent protein as a vital marker and reporter of gene expression in *Drosophila*. Proc Natl Acad Sci U S A 92(15):7036–7040. https://doi.org/10.1073/pnas.92.15.7036
38. Aberle H, Haghighi AP, Fetter RD et al (2002) Wishful thinking encodes a BMP type II receptor that regulates synaptic growth in *Drosophila*. Neuron 33(4):545–558. https://doi.org/10.1016/S0896-6273(02)00589-5
39. Meyer F, Aberle H (2006) At the next stop sign turn right: the metalloprotease Tolloid-related 1 controls defasciculation of motor axons in *Drosophila*. Development 133:4035–4044. https://doi.org/10.1242/dev.02580
40. Fujioka M, Lear BC, Landgraf M et al (2003) Even-skipped, acting as a repressor, regulates axonal projections in *Drosophila*. Development 130:5385–5400. https://doi.org/10.1242/dev.00770
41. Park JH, Schroeder AJ, Helfrich-Förster C et al (2003) Targeted ablation of CCAP neuropeptide-containing neurons of *Drosophila* causes specific defects in execution and circadian timing of ecdysis behavior. Development 130(12):2645–2656. https://doi.org/10.1242/dev.00503
42. Rao S, Lang C, Levitan ES, Deitcher DL (2001) Visualization of neuropeptide expression, transport, and exocytosis in Drosophila melanogaster. J Neurobiol 49:159–172. https://doi.org/10.1002/neu.1072

Chapter 20

Detailed Imaging of Mitochondrial Transport and Precise Manipulation of Mitochondrial Function with Genetically Encoded Photosensitizers in Adult *Drosophila* Neurons

Francesca Mattedi, George Chennell, and Alessio Vagnoni

Abstract

Precise distribution of mitochondria is essential for maintaining neuronal homeostasis. Although detailed mechanisms governing the transport of mitochondria have emerged, it is still poorly understood how the regulation of transport is coordinated in space and time within the physiological context of an organism. How alteration in mitochondrial functionality may trigger changes in organellar dynamics also remains unclear in this context. Therefore, the use of genetically encoded tools to perturb mitochondrial functionality in real time would be desirable. Here we describe methods to interfere with mitochondrial function with high spatiotemporal precision with the use of photosensitizers in vivo in the intact wing nerve of adult *Drosophila*. We also provide details on how to visualize the transport of mitochondria and to improve the quality of the imaging to attain super-resolution in this tissue.

Key words *Drosophila*, Mitochondria, Reactive oxygen species (ROS), KillerRed, SuperNova, Axonal transport, Neurons, Intravital imaging, Super-resolution radial fluctuations (SRRF)

1 Introduction

Mitochondria are highly dynamic organelles, and their correct distribution is crucial to support many cellular functions. The remarkably long processes of neurons mean that these cells are particularly dependent on mechanisms for long-range cytoskeletal transport of mitochondria. Due to their peculiar architecture, and the stereotypical directionality of the transport in the axons, neurons are a particularly good model to understand the logic of intracellular trafficking.

The fundamental importance of axonal transport for achieving maturation and maintaining the functionality of neurons is well

Supplementary Information The online version of this chapter (https://doi.org/10.1007/978-1-0716-1990-2_20) contains supplementary material, which is available to authorized users.

Alessio Vagnoni (ed.), *Axonal Transport: Methods and Protocols*,
Methods in Molecular Biology, vol. 2431, https://doi.org/10.1007/978-1-0716-1990-2_20,
© The Author(s) 2022

documented [1] and many models have been developed to visualize this process. High throughput, ease of gene manipulation, and accessibility to pharmacological treatments make cultured neuronal cells, for example, primary neurons or neurons derived from neuroblastoma and stem cells, arguably the mainstay of neuronal trafficking studies and have significantly contributed toward the mechanistic understanding of the transport process [2–13]. Ex vivo models, where a whole tissue is dissected and maintained in culture or imaged directly after dissection, are valid alternatives [14–21] with the advantage of potentially preserving a near-native environment while affording accessibility for pharmacological and electrophysiological studies.

In vivo animal models to study the transport process in neurons are now also widely used [6, 22–30]. A clear advantage of an in vivo system is the possibility of studying the transport process while retaining the full complexity of an organismal setting, which may be preferable when studying axonal transport during aging and in animal models of age-dependent neurodegenerative disorders [31]. However, because the neurons of interest are often buried deep into the tissue that is being imaged, this advantage tends to be offset by the need of complex surgery required to visualize the neurons of interests. This is the case, for example, for the implantation of cranial windows for the observation of thalamo-cortical projections in mice [32] or for the exposure of the mouse sciatic nerve for trafficking studies [33]. In addition, the resolution at which dynamic subcellular components are resolved during in vivo imaging is often modest compared to the quality that can be obtained from in vitro cultured cells. Despite the current rapid development of super-resolution techniques, only few in vitro studies have focused on long-range intracellular transport captured by live-cell super-resolution imaging [34, 35]. While challenging, achieving super-resolution of trafficked organelles in vivo would be desirable, and a tangible step forward, to better understand the intricacies of intracellular trafficking in this context.

Performing gene manipulations to interfere with the transport or function of specific cargoes might not be straightforward in vivo, especially in mammalian systems. Knockdown or knockout studies are time-consuming; acute modulation of transport, for instance, by the addition of drugs, also presents challenges in an in vivo setting, limiting the possibility of gaining in-depth mechanistic insight of this process. This is problematic when studying mitochondrial dynamics which often relies on pharmacological manipulation to interfere with different stages of the oxidative phosphorylation.

We developed a system for detailed imaging of organelle transport in adult *Drosophila* in vivo, which exploits the accessibility of the wing neurons for microscopic observation and does not require surgical procedures [36]. In this chapter, we describe methods to

image mitochondrial transport in different neuronal population of the wing using anesthetized adult animals. We have previously showed the suitability of this tissue for structured illumination microscopy (SIM) of neuronal membranes and nuclear markers [36]. With the aim of improving the resolution for in vivo imaging of mitochondrial trafficking, here we describe the application of Super-Resolution Radial Fluctuation (SRRF) microscopy [37, 38] to live imaging in the wing nerve of adult *Drosophila*. Finally, we report the generation of new transgenic flies encoding the photosensitizers KillerRed and SuperNova targeted to the mitochondria and describe photostimulation protocols to induce mitochondrial damage rapidly, coupled to the imaging of the redox state and motility of the organelles. We believe this will expand the utility of the wing nerve system and provide additional tools for the study of mitochondrial function and transport in vivo.

2 Materials

2.1 Generation of Plasmids for the Production of Transgenic Fly Lines

1. Plasmids containing the mitochondrial targeting sequence (MTS) of the human cytochrome *c* oxidase subunit VIII (Cox VIII), KillerRed, and SuperNova coding sequences. We used an 2x-MTS-mCherry (Vagnoni lab collection), #45761 and #53234 from Addgene for KillerRed and SuperNova, respectively.
2. PCR primers (underlined, sequences complementary to the coding sequences of interest; *italic*, overlapping sequences—*see* also Subheading 3.1):
   (a) 2×-MTS.
   Forward (FWD):
   5′-*GCGTTAGGTCCTGTTCATTG* gtac-cATGTCCGTCCTGACGCCGCTGCTGCTGCGG-3′.
   Reverse (RVS) with overlapping sequence to KillerRed:
   5′-*AGGGCGGGGCCGCCCTCGGA* ggatccCAAC-GAATGGATCTTGGCGCGCGGCACTGG-3′.
   RVS with overlapping sequence to SuperNova:
   5′-*GGGCCGACCTCTGAACCCAT* ggatccCAAC-GAATGGATCTTGGCGCGCGGCACTGG-3′.
   (b) KillerRed.
   FWD: 5′-*GCGCCAAGATCCATTCGTTG* ggatccTCC-GAGGGCGGCCCCGCCCTGTTCCAGAGC-3′.
   RVS: 5′-*ACTCTAGCCACCGCGGTGGC* ggccgcTTAATCCTCGTCGCTACC-GATGGCGCTGGTG-3′.

(c) SuperNova.

FWD: 5′-*GCGCCAAGATCCATTCGTTG* ggatcc ATGG GTTCAGAGGTCGGCCCCGCCCTGTTC-3′.

RVS: 5′-*ACTCTAGCCACCGCGGTGGC* ggccgc TTAATCCTCGTCGCTACC-GATGGCGCTGGTG-3′.

3. pUASP plasmid for P-element-mediated transgenesis.

2.2 Fly Maintenance

1. Fly food: 70 mg/ml yeast, 55 mg/ml glucose, 7.7 mg/ml agar, 35 mg/ml organic plain white flour, 1.2 mg/ml Tegosept, 0.4% propionic acid (*see* **Note 1**).
2. Adult flies: adult transgenic animals expressing a fluorescent reporter to mark the mitochondria in the wing marginal nerve. The stocks used in this study are described in Table 1.
3. Incubator equipped with temperature and humidity control, and 12 h light/12 h dark cycle (*see* **Note 2**).

2.3 Sample Preparation for Imaging

1. Coverslips no. 0, 1, or 1.5 (*see* **Note 3**).
2. 10S halocarbon oil (*see* **Note 4**).
3. Dumont forceps #5.
4. Round tip artist paintbrush for *Drosophila* work.
5. Masking tape and double-sided tape.
6. Stereo microscope for *Drosophila* work.

2.4 Imaging Axonal Transport in the Drosophila Wing and Photostimulation

1. Inverted confocal microscope equipped with 40×, 60×, or 100× oil immersion objective and with temperature control. For photostimulation experiments, the microscope should be equipped with a photostimulation module (*see* **Note 5**).
2. ImageJ or Fiji equipped with RatioProfiler plugin (https://imagej.net/Cookbook) and the "Velocity measurement tool" (http://dev.mri.cnrs.fr/projects/imagej-macros/wiki/Velocity_Measurement_Tool) for kymographs generation (*see* **Note 6**).
3. NIS-element software (Nikon) for image processing.
4. Microsoft Excel and GraphPad Prism to analyze and plot the data.

2.5 SRRF Analysis

ImageJ or Fiji equipped with NanoJ Core and NanoJ-SRRF plugins [39].

Table 1
***Drosophila* stocks used in this study**

Drivers and reporters	Purpose	Source
nSyb-Gal4	To express Gal4 pan-neuronally in the wing sensory neurons	BDSC (#68222) [59]
ChAT-Gal4	To express Gal4 in the cholinergic neurons of the wing	BDSC (#56500) [60]
UAS-mito::KillerRed	To mark mitochondria and trigger light-dependent ROS production	This study
UAS-mito::SuperNova	To mark mitochondria and trigger light-dependent ROS production	This study
UAS-mito::roGFP2-Grx1	To mark and measure the oxidation state of the mitochondria	BDSC (#67664) [43]
UAS-mito::GFP	To mark mitochondria	BDSC (#8442) [61]
UAS-mito::PA-GFP	To mark mitochondria after activation with the 405 nm laser line	R. Rikhy (Indian Institute of Science Education and Research, Pune, India) [62]

3 Methods

We use the GAL4-UAS binary system [40] to drive the expression of GFP in the mitochondria of the adult wing neurons. By using either a pan-neuronal driver, for example, *nSyb-Gal4*, or a more restricted driver such as the cholinergic neuronal driver *ChAT-Gal4*, mitochondria can be visualized clearly in the neurons of the adult *Drosophila* wing (Fig. 1b–d) (*see* **Note 7**). However, application of the SRRF algorithm to time series acquired by spinning disk microscopy allows to achieve a considerably improved resolution of both stationary and moving mitochondria (Fig. 1d and Movie 1), which is useful to appreciate finer details of mitochondrial dynamics.

In order to damage mitochondria with spatiotemporal precision, we produced novel transgenic *Drosophila* lines expressing the photosensitizers KillerRed (KR) [41] and SuperNova (SN) [42] targeted to the mitochondrial matrix (mito::KR and mito::SN, respectively) (Table 1, Figs. 2 and 5a). Upon irradiation with green light, KR and SN produce a large amount of reactive oxygen species (ROS). As direct readout of the efficacy of our stimulation protocol, we measured the mitochondrial redox state with the roGFP2-Grx1 ratiometric reporter (mito::roGFP2-Grx1). This reporter exhibits differential fluorescence intensity when excited with 488 nm and 405 nm light, with an increase in the

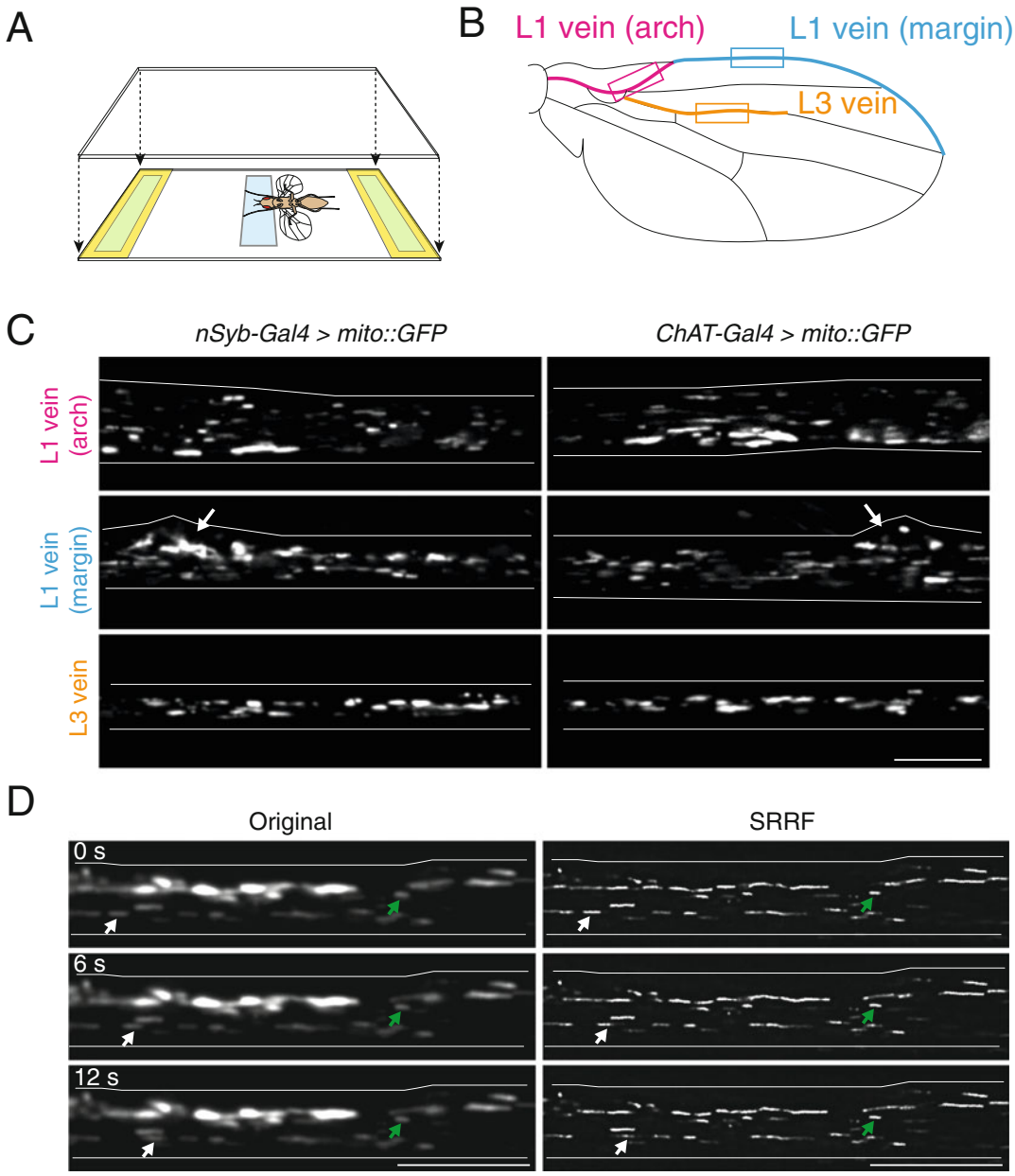

Fig. 1 Imaging mitochondria in vivo in the neurons of the adult *Drosophila* wing. (**a**) Schematic of the chamber where the flies are mounted for imaging. Each of the short sides of a bottom coverslip are occupied by three layers of masking tape (yellow). A layer of double-sided tape (light blue) is attached onto the masking tape and in the center of the coverslip. A second coverslip is used to seal the chamber. (**b**) Schematic of the wing with areas where live imaging is typically performed highlighted in colors. Rectangular selections represent the areas imaged in (**c**). The arch of the L1 vein (magenta) and the L3 vein (orange) are areas of high axonal density with relatively low number of cell bodies and ideal for imaging studies of axonal transport. (**c**) Mitochondria marked by GFP expressed pan-neuronally ($nSyb^{+}$ neurons, left panels) and in cholinergic neurons ($ChAT^{+}$ neurons, right panels). Arrows indicate neuronal cell bodies. Scale bar: 10μm. (**d**) Selected frames of a time-lapse movie (Movie 1) acquired from the wing arch before ("Original") and after ("SRRF") SRRF processing. The degree of resolution improvement was measured to range between 2.4- and 3.1-fold, with the average diameter of the mitochondria measured to be approximately 470 nm and 180 nm before and after SRRF analysis, respectively, which is in line with previous estimates [57, 58]. White arrow: moving mitochondrion. Green arrow: stationary mitochondrion. Genotype: *ChAT-Gal4* > *UAS-mito::GFP*. In (**c**) and (**d**): white lines, outline of the wing nerve. Scale bar: 10μm

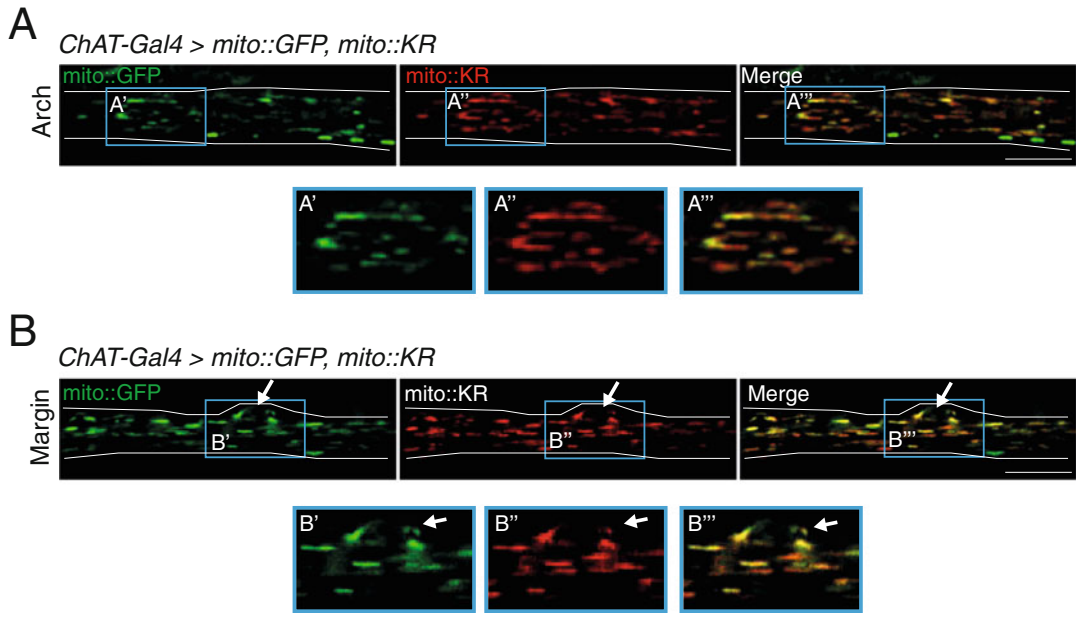

Fig. 2 Mito::KR is localized to mitochondria in the wing nerve. Representative images of a 50-μm-long region from the arch (**a**) and margin (**b**) of the adult *Drosophila* wing. The vast majority of mitochondria are double stained with GFP and KillerRed. (**a′**–**a″**) and (**b′**–**b″**) show magnified insets (blue rectangles) from (**a** and **b**), respectively. Arrows indicate neuronal cell bodies. In (**a**) and (**b**): white lines, outline of the wing nerve. Scale bars: 10μm

405/488 nm ratio reflecting augmented mitochondrial oxidation [43, 44]. Brief stimulations of mito::KR with a 561-nm laser light are sufficient to trigger a rapid and transient increase in mitochondrial oxidation (Fig. 3). Our protocol allows to stimulate areas covering a large portion of the nerve (Fig. 3) as well as achieving precise photostimulation of a single mitochondrion (Fig. 4). *Mito::KR*$^{-}$ neurons that do not express mito::KR do not show a detectable mitochondrial oxidative response when subjected to the same photostimulation regime, ruling out the possibility that the exposure to the 561-nm laser light alone is sufficient to strongly increase mitochondrial oxidation, at least for the brief irradiation times used here. No significant change in the mitochondrial redox state was observed after brief stimulation of mito::SN with a 561-nm laser light (Fig. 5b–d). This suggests heightened sensitivity to mito::KR in our system which we find advantageous to be able to probe the early consequences of mitochondrial oxidation while minimizing light-induced phototoxicity. SuperNova is a monomeric variant of KillerRed and was shown to generate a different proportion of singlet oxygen and superoxide species compared to KillerRed [42, 45]. This was not reported to diminish its phototoxic effect [42], although a robust effect of SuperNova stimulation might become clearer on longer timescales in vivo or after longer

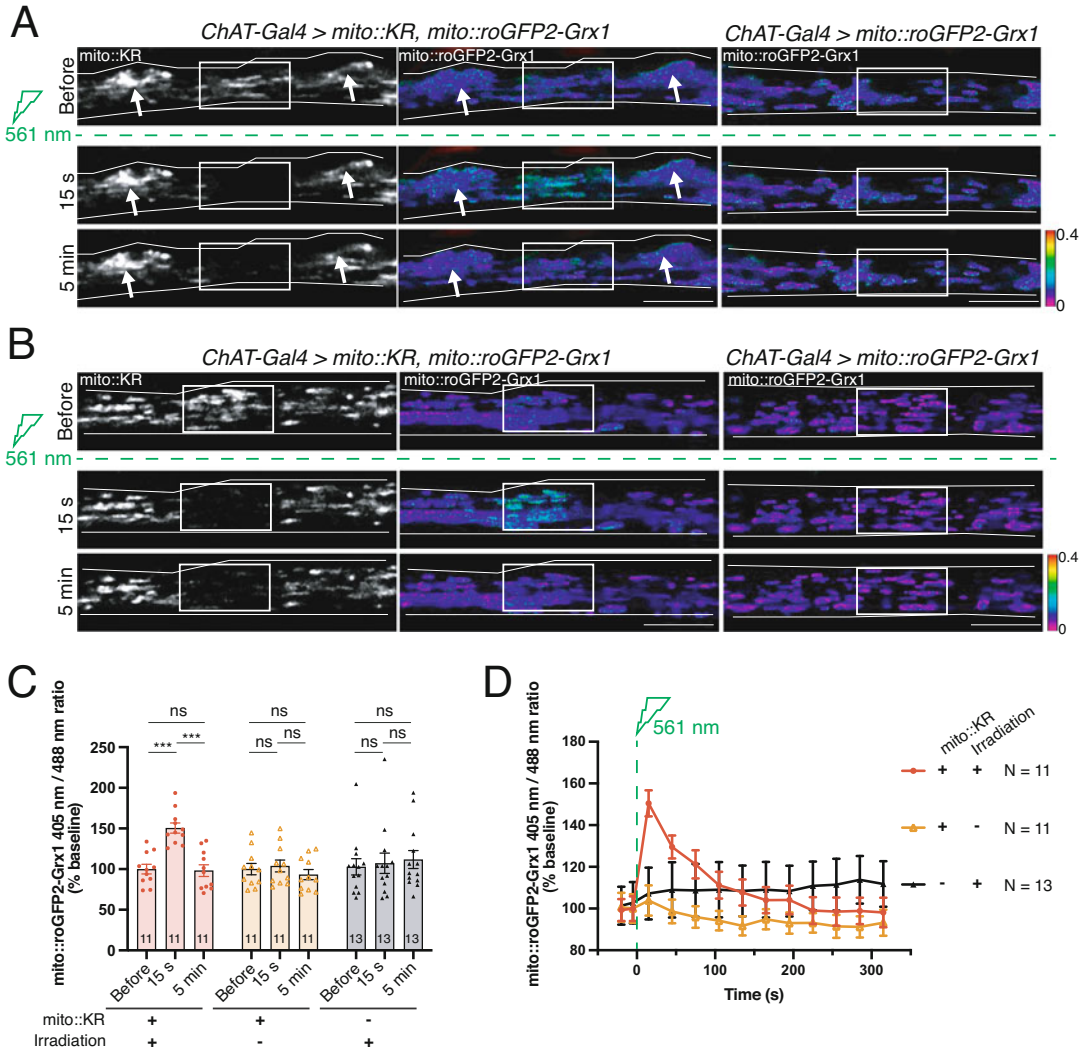

Fig. 3 Photostimulation of mito::KR results in a local increase in mitochondrial ROS. (**a**, **b**) Left panels: mito::KR signal before and after 561-nm irradiation (dashed green line) shows efficient bleaching of mito::KR in the axons of the marginal wing nerve (**a**) and arch region (**b**). Middle panels: ratiometric images reveal a rapid local increase in mitochondrial ROS shortly after irradiation. Mitochondrial oxidation returns to pre-bleach levels within 5 min. Right panels: control neurons lacking mito::KR do not display an increase in mitochondrial ROS. In all panels, the bleached area is marked by white rectangles and the white lines mark the outline of the wing nerve. Arrows indicate neuronal cell bodies. Scale bars: 10μm. (**c**) Quantification of the mitochondrial redox state in the wing arch before mito::KR bleaching, 15 s after bleaching and at the end of the experimental series, as shown in (**b**). Repeated Measures One-Way Anova with Tukey's post hoc test. ns = not significant ($p > 0.05$), ***$p < 0.001$. (**d**) Quantification of the mitochondrial redox state in the wing arch for the entire experimental series. The 405/488 nm ratio was measured at two timepoints before bleaching (dashed green line) and at 30-s intervals after that for 5 min. In (**c**) and (**d**), "baseline" is the mean 405/488 nm ratio prior to stimulation. Quantifications of non-irradiated areas ("−Irradiation") are performed on the same *UAS-mito::KR* flies that were subject to irradiation ("+Irradiation"), as described in Subheading 3.9. Error bars are mean ± SEM. N: number of wings, one ROI per wing was selected for bleaching

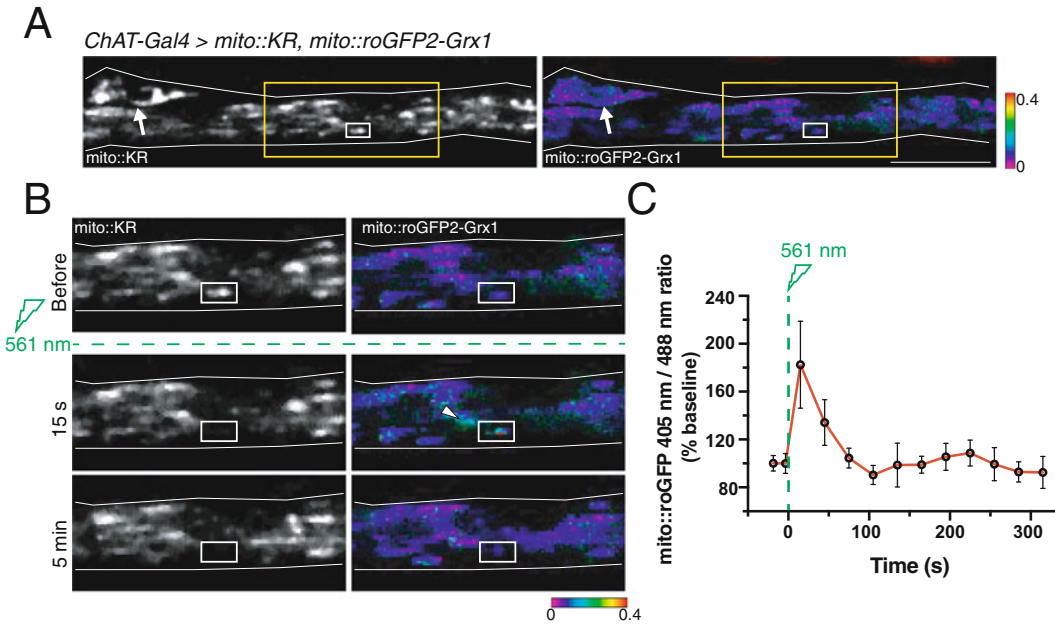

Fig. 4 Restricted photostimulation of mito::KR results in ROS increase in single mitochondria. (**a**) Representative images of the neurons in the wing margin before stimulation. White box: stimulation ROI, yellow box: magnified insets in (**b**). Arrows indicate neuronal cell bodies. Scale bar: 10μm. (**b**) Left panels: mito::KR signal before and after 561-nm irradiation (dashed green line) shows precise and efficient bleaching of mito::KR in a single mitochondrion of the marginal wing. Right panels: ratiometric images reveal a rapid local increase in mitochondrial ROS shortly after irradiation. Mitochondrial oxidation returns to pre-bleach levels within 5 min. In all panels, the bleached area is marked by white rectangles. Despite the precise bleaching of the mito::KR signal, a change in the 405/488 nm ratio in the immediate surrounding of the bleached area was also observed 15 s post-bleaching (white arrowhead). This might be due to light scattering during the bleaching protocol that could activate mito::KR in close proximity of the stimulated ROI (*see* **Note 21**). In (**a**) and (**b**): white lines, outline of the wing nerve. (**c**) Quantification of the redox state in single mitochondria of the wing margin. The 405/488 nm ratio was measured at two timepoints before bleaching (dashed green line) and at 30-s intervals after that for 5 min. Scale bars are mean ± SEM. $N = 3$ mitochondria

irradiation times [46]. SuperNova2, a variant of SuperNova with enhanced phototoxicity, has been recently engineered [47] and could be a valid alternative to enhance the phototoxicity of the protein in an in vivo setting.

To investigate the consequences of acute mitochondrial damage on the motility of the organelle, we present two specular approaches. In the first approach, KillerRed is bleached in *mito::KR mito::GFP* neurons and the damaged mitochondria undergo a yellow-to-green color switch (Fig. 6a and Movie 2). An alternative approach is to use mito::KR in combination with a mitochondrially targeted photoactivatable GFP (mito::PA-GFP). In this case, simultaneous stimulation with 405-nm and 561-nm lasers leads to quenching of the red signal and concomitant activation of the green fluorophore, with mitochondria undergoing a red to green

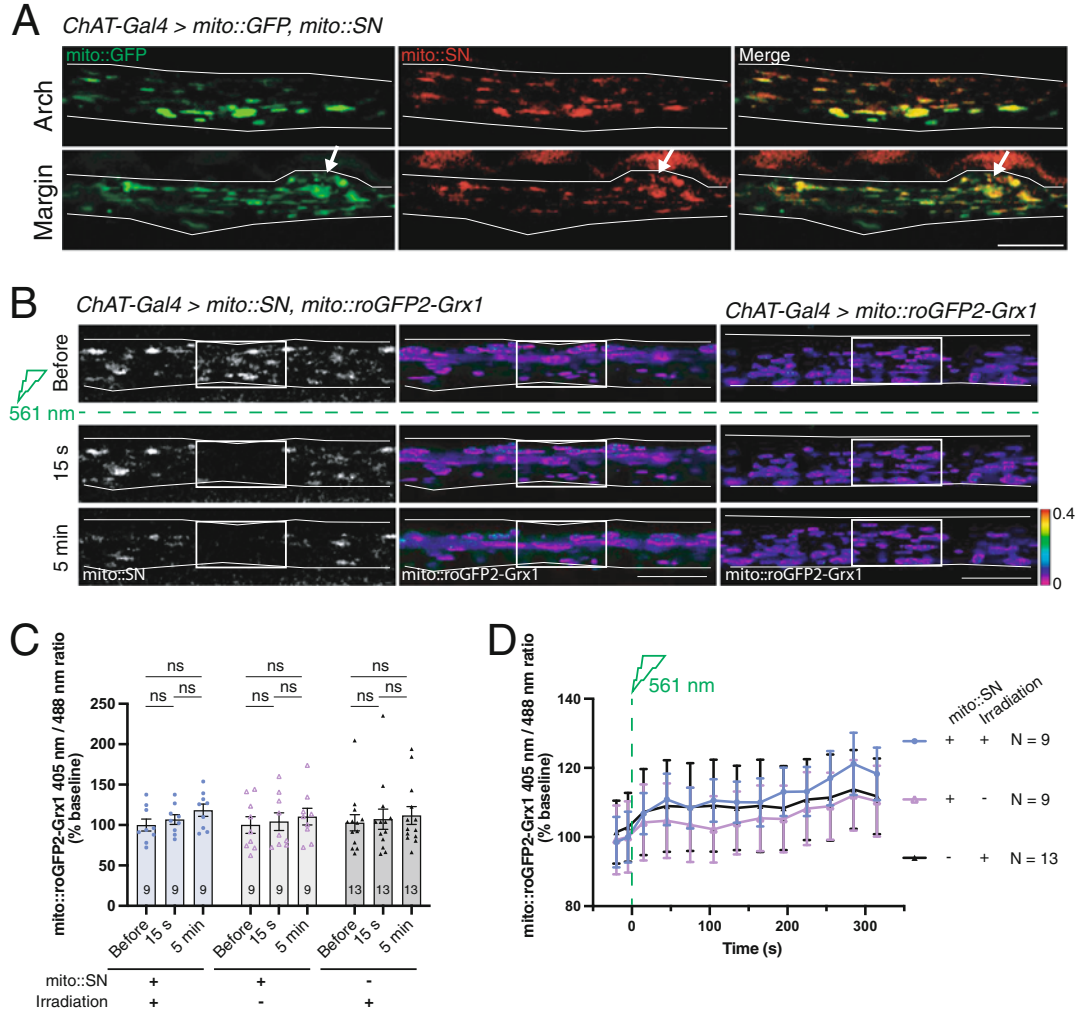

Fig. 5 Mito::SN is localized to mitochondria in the wing nerve. (**a**) Representative images of a 50-μm-long region from the arch (top panels) and margin (bottom panels) of the adult *Drosophila* wing. The vast majority of mitochondria are double stained with GFP and SuperNova. Arrows indicate neuronal cell bodies. Scale bar: 10μm. (**b**) Left panels: mito::SN signal before and after 561-nm irradiation (dashed green line) shows efficient bleaching of mito::SN in the axons of arch region. Middle panels: ratiometric images show no significant increase in mitochondrial ROS after irradiation. Right panels: control neurons lacking mito::SN do not display an increase in mitochondrial ROS. In all panels, the bleached area is marked by white rectangles and the white lines mark the outline of the wing nerve. Scale bars: 10μm. (**c**) Quantification of the mitochondrial redox state in the wing arch before mito::SN bleaching, 15 s after bleaching and at the end of the experimental series, as shown in (**b**). (**d**) Quantification of the mitochondrial redox state in the wing arch for the entire experimental series. The 405/488 nm ratio was measured at two timepoints before bleaching (dashed green line) and at 30-s intervals after that for 5 min. Error bars are mean ± SEM. N: number of wings, one ROI per wing was selected for bleaching. In (**c**) and (**d**), "baseline" is the mean 405/488 nm ratio prior to stimulation. Quantifications of non-irradiated areas ("−Irradiation") are performed on the same *UAS-mito::SN* flies that were subject to irradiation ("+Irradiation"), as described in Subheading 3.9. Repeated Measures One-Way Anova with Tukey's post hoc test. Ns = not significant ($p > 0.05$)

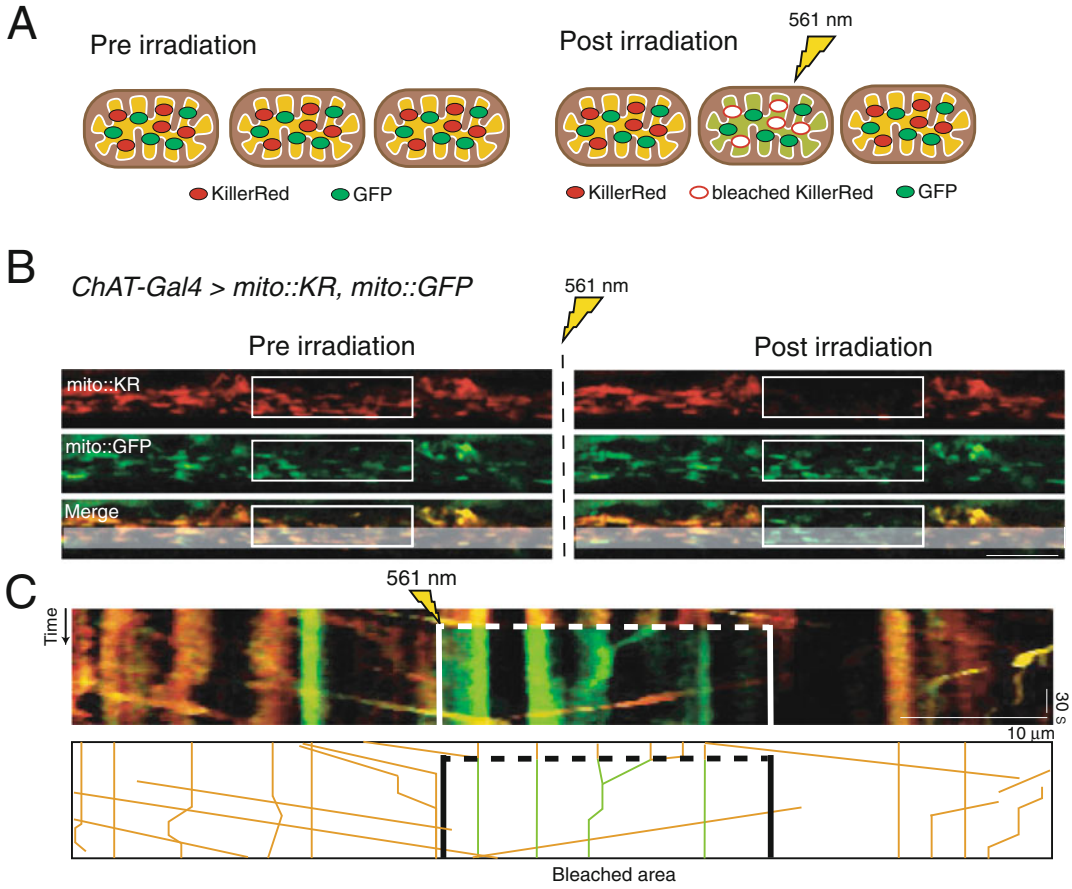

Fig. 6 Assessing mitochondrial motility after acute mitochondrial damage using mito::KR and mito::GFP. (**a**) The cartoon illustrates the experimental design. After bleaching KillerRed with the 561-nm laser, mitochondria undergo a yellow-to-green transition, indicated by the change in the color of the mitochondrial matrix in the cartoon: the red KillerRed signal is quenched and only the green GFP fluorescence is retained in the mitochondria. Bleached (i.e., dysfunctional) mitochondria can therefore be followed by illumination with both 488-nm and 561-nm lasers. (**b**) Neurons in the margin of the wing nerve before and after irradiation (dashed black line). The white rectangles indicate the photostimulated ROI. The area shaded in the bottom panels was used to generate the kymograph in (**c**). Scale bar: 10μm. (**c**) Kymograph indicating a representative portion of stationary and motile mitochondria before and after KillerRed bleaching. The white and black rectangles (top and bottom panels, respectively) delimit the bleached area, with the dashed line indicating the time of bleaching. Only mitochondria that intersect the dashed line were bleached. Bottom panel: orange-to-green tracks: bleached mitochondria, while in motion or stationary. Orange tracks: unbleached mitochondria

transition (Fig. 7a and Movie 3). Coexpression of the two mitochondrial markers does not affect the motility and morphology of the organelles, and, with both approaches, irradiated (i.e., dysfunctional) mitochondria can be tracked through color switch. However, the use of PA-GFP is preferable when the aim is to study the dynamics of the irradiated mitochondria, as only one laser line (488 nm) is required to directly follow the mitochondria after

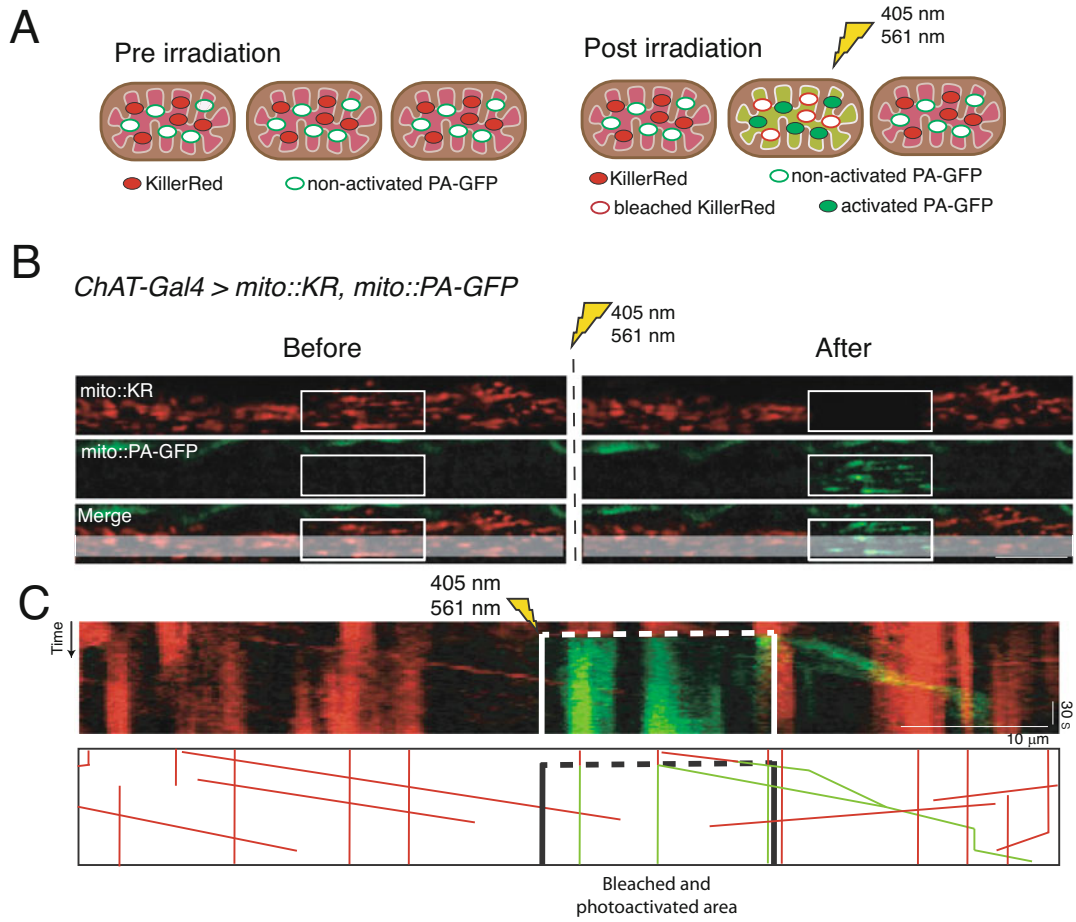

Fig. 7 Assessing mitochondrial motility after acute mitochondrial damage using mito::KR and mito::PA-GFP. (**a**) The cartoon illustrates the experimental design. After simultaneously bleaching KillerRed and photoactivating the GFP, mitochondria undergo a red-to-green transition, indicated by the change in the color of the mitochondrial matrix in the cartoon: the red KillerRed signal is quenched while the green GFP fluorescence appears in the mitochondria. Bleached (i.e., dysfunctional) mitochondria can therefore be followed by illumination with the 488 nm laser only. (**b**) Neurons in the margin of the wing nerve before and after irradiation with the 405 nm and 561 nm lasers (dashed black line). The white rectangles indicate the stimulated ROI. The area shaded in the bottom panels was used to generate the kymograph in (**c**). Scale bar: 10μm. (**c**) Kymograph indicating a representative portion of stationary and motile mitochondria before and after KillerRed bleaching and PA-GFP activation. The white and black rectangles (top and bottom panels, respectively) delimit the bleached area, with the dashed line indicating the time of bleaching. Only mitochondria that intersect the dashed line were bleached and photoactivated. Bottom panel: red-to-green tracks: bleached mitochondria, while in motion or stationary. Red tracks: unbleached mitochondria

photostimulation. To study the dynamics of both irradiated and non-irradiated mitochondria, the simultaneous use of both 488-nm and 561-nm laser lines for the whole duration of image acquisition is recommended.

3.1 Generation of Plasmids for the Production of Transgenic Lines

1. The Cox VIII MTS, KillerRed, and SuperNova are PCR amplified using the Q5® Hot-Start High-Fidelity 2× Master Mix (NEB) and FWD and RVS primers reported in Subheading 2.1, which include overlapping sequences complementary to adjacent fragments and necessary for the assembly as described in **step 3**.
2. The PCR products are purified through solid-phase purification using spin columns (we routinely use Monarch® PCR&DNA Cleanup kit, NEB).
3. The NEBuilder® HiFi DNA assembly method is used to introduce the KillerRed and SuperNova in the pUASP vector, downstream of two MTS from the human cytochrome *c* oxidase subunit VIII (*see* **Note 8**).

3.2 Fly Maintenance

1. Cross males and virgin females to obtain flies of the desired genotype. In our protocol, the Gal4 drivers and UAS responders are heterozygous in all genotypes.
2. Keep the crosses at 25 °C with a 12 h light/12 h dark cycle.
3. Remove the flies after 4–5 days and keep the vial with wandering larvae.
4. Collect newly emerged flies and select the desired genotype. Put the selected flies in new vials, maintain them at 25 °C with a 12 h light/12 h dark cycle and image them after 24–48 h, when approximately 30% of mitochondria are motile [48].

3.3 Sample Preparation

1. Anesthetize the flies on a CO_2 pad (*see* **Note 9**), while preparing the imaging chamber (Fig. 1a).
2. On each of the short sides of the coverslip, make a stack of three layers of masking tape.
3. Add a piece of double-sided tape in the middle of the coverslip and on each stack of masking tape.
4. Apply a thin layer of 10S halocarbon oil on one side of the double-sided tape in the middle of the coverslip.
5. Mount one fly on the coverslip. Pick the fly up by the legs and place it on the oil, with the ventral side up and with the head on the double-sided tape in the center of the coverslip.
6. Dip a fine paintbrush in oil and use it to spread out the wings. Make sure that the wings are flat on the coverslip and most air bubbles are removed (*see* **Note 10**).
7. Place a second coverslip on top to seal the chamber and image the fly immediately. To minimize delay, we recommend mounting the fly in proximity of the microscope used for live imaging.

3.4 Imaging Axonal Transport in the Drosophila Wing

1. Set the microscope temperature controller at 25 °C.
2. Mount the flies expressing a fluorescence marker (for instance, GFP) targeted to neuronal mitochondria.
3. Find the region of interest in the *Drosophila* wing by using the transmitted light (through eyepieces).
4. Inspect the whole wing for damage (for instance, small cuts). If the wing is damaged, discard the chamber and mount another fly.
5. Switch to fluorescence mode to check the fluorescent signal (through eyepieces) and then to confocal mode (through microscope software) to acquire the images.
6. Adjust exposure time and laser power to obtain a good signal, clearly visible above background. Here, we used exposure time 300–500 ms and 15–25% laser power.
7. Image mitochondrial transport at 1 fps (Fig. 1c) (*see* **Note 11**).

3.5 SRRF Imaging

1. Repeat **steps 1–5** reported in Subheading 3.4.
2. Adjust exposure time and laser power to obtain a good signal, clearly visible above background. Here, we used 30 ms exposure time and 50–60% laser power (*see* **Note 12**).
3. Change the size of the field of view so that the time to acquire a single frame is shorter than the chosen exposure time (*see* **Note 13**).
4. Acquire a series of 33 frames by continuous imaging, i.e., where the interval between each frame is limited by the exposure time, in this case 30 ms. Each series of 33 frames will be used to create a single SRRF timepoint (*see* Subheading 3.6).
5. Repeat the 33-frame acquisition with an interval of 1 or 2 s, depending on the desired time lapse between acquisitions (0.5 fps and 0.33 fps, respectively) (*see* **Note 14**).

3.6 SRRF Analysis

1. Open the raw data in Fiji having installed the Nano-SRRF plugin (Update > Manage Update Sites: add NanoJ-Core and NanoJ-SRRF and complete update process).
2. Calculate the dataset drift using the NanoJ-Core Drift estimation tool in Fiji which computes the sample drift and yields a table later applied to SRRF processing (Plugins > NanoJ-Core > Drift Correction > Estimate Drift). Set the time averaging for drift estimation to the number of frames taken per SRRF time point (in this case, 33 frames) with the reference frame set to "previous frame."
3. Configure SRRF Temporal Analysis setting to Temporal Radiality Pairwise Product Mean (TRPPM) (Plugins > NanoJ-SRRF > SRRF Configure Advanced Settings). Here, the

SRRF analysis settings were set as follows: Ring Radius = 0.3 and a Radiality Magnification = 2 (*see* **Note 15**).

4. For easier presentation, the results can be imported to NIS-Elements and converted from 32-bit float to 16-bit images. With our settings, the final result is an image sequence of 30 SRRF frames ("SRRF" in Movie 1).
5. To create a movie of the original data with the same frame number to the one obtained through SRRF analysis, generate the mean of 33 frames for each acquisition series, which corresponds to a single SRRF time point. With our settings, this results in a final image sequence composed of 30 frames ("Original" in Movie 1).

3.7 Photostimulation in the Drosophila Wing: Monitoring Mitochondrial Redox State Upon Acute Mitochondrial Damage

1. Repeat **steps 1–5** of Subheading 3.4. In this case, select *mito::KR mito::roGFP2-Grx1* or *mito::SN mito::roGFP2-Grx1* flies. Flies expressing only mito::roGFP2-Grx1 can be used to control for potential light-dependent, photosensitiser-independent, mitochondrial damage.
2. Set up two different optical configurations to image simultaneously roGFP2-Grx1 (A) and the photosensitizers (B):
   (A) Create two channels with different excitation lasers (405-nm laser and 488-nm laser) and same emission filter set (525/50 bandpass filter).
   (B) Use the 561-nm excitation laser and collect the emission signal with a 595/50 bandpass filter.
3. Define the stimulation area by drawing a stimulation ROI (Fig. 3a, b) and save it (*see* **Note 16**).
4. Set up an imaging protocol with three steps: "before stimulation", "stimulation", "after stimulation".
5. Before stimulation: acquire 2–5 frames using optical configurations (A) and (B) from **step 2**.
6. Stimulation: to efficiently and precisely bleach mito::KR and mito::SN, use a 561-nm laser with 95% (3.98 mW) laser power, 16 fps scan speed, and 31 loops of stimulation for the cell bodies and axons (ROI area: 65μm^2) or 15 loops for single mitochondria (ROI area: 2.9μm^2). With this configuration, the total duration of the stimulation step never exceeds 3 s (*see* **Notes 17** and **18**).
7. After stimulation: acquire 1 frame every 30 s for 5 min using optical configurations (A) and (B) from **step 2**.

3.8 Photostimulation in the Drosophila Wing: Assessing Mitochondria Motility Upon Acute Mitochondrial Damage

1. Repeat **steps 1–5** reported in Subheading 3.4. In this case, select *mito::KR mito::PA-GFP* or *mito::KR mito::GFP* flies.
2. Define the stimulation area by drawing a stimulation ROI and save it (*see* **Note 19**).
3. Set up an imaging protocol with three phases: "before stimulation", "stimulation", "after stimulation".
4. Before stimulation: acquire 1 frame every 2.5 s for 15–20 s.
5. Stimulation: set a scanning speed of 16 fps. Use 561-nm laser with 95% (3.98 mW) laser power and 62 loops to bleach mito::KR (ROI area: 141μm^2). For simultaneous mito::KR bleaching and mito::PA-GFP activation, use 561-nm laser with 80% (3.39 mW) power and 405-nm laser with 100% (0.388 mW) power and scan simultaneously with 79 loops (ROI area: 90μm^2). With these configurations, the total amount of time for the stimulation step never exceeded 8 s.
6. After stimulation: acquire a frame every 2.5 s for 2 min.

3.9 Analysis of Mitochondrial Redox State Upon Acute Mitochondrial Damage

1. Open the ".nd2" file in Fiji and split the channels.
2. Select the mito::roGFP2-Grx1 channels (Channel 1 and Channel 2) and run "Subtract background" (Process > Subtract background). Define the rolling radius according to the pixel size (in this case, it was set to 20 px). Channel 1 and Channel 2 represent the fluorescent signal after excitation with the 405-nm and the 488-nm laser, respectively.
3. Merge Channel 1 and 2, in this order, and save the file as ".tiff."
4. Open the stimulation ROI used to bleach the mito::KR signal (Subheading 3.7, **step 3**) in the ROI manager.
5. Overlay the stimulation ROI on the ".tiff" file from **step 3**.
6. Run "Ratio profiler" (Cookbook > Image Intensity Processing > Ratio Profiler). A "Results" tab will open and report the ratio between Channel 1 and Channel 2 for each frame. This value is the 405 nm/488 nm ratio for the mito::roGFP2-Grx1 probe, used to quantify the mitochondrial redox state.
7. Produce ratio images for the visualization of mitochondrial redox changes (Figs. 3a, b, 4a, b, and 5b) (*see* **Note 20**).
8. To control for the specificity of the irradiation to the region defined by the ROI, run "Ratio profiler" again on an area that has not been stimulated (Figs. 3c, d, and 5c, d) (*see* **Note 21**).
9. In order to obtain the fold change of mitochondrial redox state over time, normalize the 405 nm/488 nm ratio at each time point to the mean 405 nm/488 nm prior to stimulation (Figs. 3c, d, 4c, and 5c, d).

3.10 Analysis of Mitochondria Motility Upon Acute Mitochondrial Damage

1. Open the ".nd2" file in Fiji and split the channels.
2. Run "Subtract background" on each channel and apply a filter to reduce the noise, if needed. For instance, use "Despeckle" (Process > Noise > Despeckle) or "Smooth" (Process > Smooth) in Fiji.
3. Crop the image to analyze only the area of interest. Here we consider a nerve portion of 70μm in length (*see* **Note 22**).
4. Open the "Velocity measurement tool" (use the ≫ button on the Fiji/ImageJ launcher to select this toolset).
5. Draw a straight line along the axons of interest. Define the thickness of the line to include all the axons of interest for kymograph generation. Here, we used 20-px-thick line, running along the whole length of the selected portion of the nerve (Figs. 6b and 7b).
6. Press the "k" button to generate the kymograph for each channel.
7. Merge the two kymographs (Figs. 6c and 7c).

4 Notes

1. Flies were grown on "Iberian" food, although other recipes are also suitable for visualization of cargo transport in wing neurons. It is crucial, however, to be consistent with the recipe used as changes in the diet can influence the outcome of the experiments. We found that inconsistent use of the yeast and flour can be the source of experimental variability.
2. To minimize variability in the experimental outcome, it is important that temperature, humidity, and light–dark cycle are maintained constant.
3. The shorter working distance afforded by the coverslips no. 0 means that acquiring clear images is straightforward. However, these coverslips are thin and very flexible, which makes stabilizing the sample in the imaging chamber more difficult and might lead to drifting while imaging. We find coverslips no. 1 to be a good compromise between quality of images obtained, sample stability, and maintenance of an appropriate optical configuration. However, coverslips no. 1.5 are recommended for live super-resolution imaging (e.g., instant SIM).
4. We compared the 10S halocarbon oil from both VWR (cat. no. 24627.188) and the halocarbon oil 700 from Sigma Aldrich (cat. no H8898). We found the former to be more viscous and to better aid sample stabilization. However, using the Sigma oil does not prevent obtaining high-quality images.

5. Different microscopes can be used to this purpose. We find spinning disk confocal to be the best option for live imaging, as it is gentler on the sample (i.e., less phototoxicity) and affords both high-resolution and high-speed. We routinely use two types of confocal settings: a Nikon Ti-E inverted system equipped with a Yokogawa-CSU-X1 Spinning Disk head, Andor iXon Ultra DU-897 EMCCD Camera (for axonal transport studies and SRRF) and an inverted Nikon A1RHD confocal microscope equipped with both GaAsP, multi-alkali and spectral detectors equipped with a photostimulation unit (for light-induced activation of the photosensitizers). With both systems, imaging was performed with a Nikon 60×/1.4NA Plan Apochromatic oil immersion objective.
6. Other kymograph analysis bundles can also be used effectively in this system, for example, KymoClear and KymoDirect [49, 50], KymoAnalyzer [51], or KymoButler [52]. Alternatively, a kymograph of only motile mitochondria could be generated from manually annotated tracks. This would eliminate the background associated with the numerous stationary mitochondria in the wing neurons.
7. The *ChAT-Gal4* driver can be used effectively to visualize mitochondria in the wing neurons using different fluorophores. The mitochondria in *ChAT-Gal4*$^{+}$ neurons display robust motility and invariably good fluorescent signal in both the L1 and L3 wing veins. *ChAT-Gal4* is therefore an excellent alternative to pan-neuronal and more restricted drivers currently used in this system for live imaging of axonal transport [36, 53–56]. We do not recommend the use of ubiquitous drivers as the fluorescent signal from non-neuronal cells in the wing would mask the signal from the axons of the marginal nerve.
8. We found that fusing KillerRed and SuperNova to one MTS results in diffuse cytoplasmic distribution of the proteins in *Drosophila* S2R+ cells, while using two MTS is sufficient for efficient mitochondrial targeting.
9. Make sure that the selected fly does not carry markers that affect wings morphology (e.g., CyO). Carefully check the wings at the stereo microscope. If damaged, discard the fly.
10. Wings not being flat on the coverslip will decrease the precision of the photostimulation and the clarity of the signal. The wing arch region (which is closer to the body) might not be flat on the bottom coverslip as a result of head and the thorax of the fly becoming unstuck from the coverslip, for instance, if the head of the animal is not well attached on the double-sided tape. In this case, the application of little oil could be used to further

restrain the animal. We found that finer round tip paintbrushes (e.g., no. 1) are particularly suitable to carefully position the fly.

11. It is possible to image mitochondrial transport in the wing for up to 30 min [36]. However, when imaging for longer periods of time, we recommend using a slower frame rate (e.g., 0.5 or 0.33 fps) to reduce phototoxicity. On the other hand, if the study focuses on the analysis of instantaneous velocities, recording at higher frame rates for a shorter period is more appropriate.
12. For good quality SRRF movies, a strong fluorescent signal and acquisition at high fps are essential. Therefore, we recommend against using dim fluorophores.
13. To obtain a single SRRF image, a series of frames need to be acquired in a short time interval (e.g., 1 s) and exposure times between 10 ms and 100 ms are recommended [38].
14. The effective elapsed time between time series is defined by the combination of both the time needed to acquire 1 loop of 33 consecutive frames (1 s, with our settings) and the interval between each loop (2 s in our case). Our effective acquisition time is therefore of 0.33 fps. In an imaging period of 90 s, this equals to 30 acquisition loops for a total of 990 frames. These settings allow to follow mitochondria reliably without significant photobleaching.
15. The settings were chosen by adjustment and comparison of several images. Ring Radius, used to calculate the intensity gradients of nearby subpixels, was chosen by iterative trials of different radii, until an optimal response of the analysis was observed, typically judged by the best resolution improvement and minimal patterning. Radiality Magnification, which determines the number of subpixels each pixel is split into, was not increased to more than 2 as improvements were not evident at greater values.
16. The size of the stimulation ROI, the scan speed, and the laser intensity can influence the density of photons delivered per unit area. For each experiment, the stimulation ROI size, the number of loops, scan speed, and laser intensity should be empirically optimized and then the settings kept constant throughout the experiment. In our experience, keeping the scan speed and laser intensity constant while adjusting the number of iterations gives the most reliable results.
17. At constant laser power, high scanning speed and high number of loops result in more precise bleaching than a low scanning speed and low number of loops. For experimental design, it is useful to consider the time it takes to switch between optical configurations or stimulation loops, which may vary considerably depending on the microscope setup.

18. Our stimulation protocol is sufficient to trigger a rapid change in the redox state of the mitochondria. However, this recovers almost to pre-stimulation levels within 5 min (Fig. 3c, d). If desired, longer and more frequent stimulation loops can be used which may result in sustained oxidation of the irradiated area. In this case, however, it is important to carefully control for potential light-induced mitochondrial oxidation.
19. The size of the ROI can be chosen depending on the specific experimental aim. To bleach moving mitochondria, the bigger the stimulation ROI, the higher the probability that motile mitochondria will cross it at any given time. In the wing neurons, average mitochondria speed is approximately 0.2μm/s and 0.4μm/s for anterograde and retrograde transport, respectively [48]. With a stimulation step of 10–15 s, the displacement of irradiated motile mitochondria could be of up to approximately 2–6μm. We found that using a 15–25-μm-long ROI for stimulation is sufficient for reliable bleaching of mito::KR in motile mitochondria.
20. Ratiometric images were generated with the "RatioView" modality of NIS-element software. Alternatively, the Image Calculator command in Fiji can also be used.
21. Some areas immediately outside the bleached ROI are likely to be reached by the scattering of the excitation light and may respond to the stimulation protocol. This can be ascertained empirically and the extent of the irradiated sample outside the boundaries of the ROI minimized. When quantifying control regions (i.e., areas that have not been stimulated), it is therefore preferable to choose an area not adjacent to the irradiated ROI. Alternatively, using two-photon microscopy to perform the photostimulation experiments is likely to reduce the scattering of light in the tissue.
22. The wing nerve does not always appear in focus in the whole field of view when live flies are mounted. To reliably analyze mitochondria motility, select an area displaying minimal drifting where the nerve is flat on the coverslip.

Acknowledgments

This work was funded through a NC3Rs David Sainsbury Fellowship and SKT grants (NC/N001753/2 and NC/T001224/1), a van Geest Ph.D. Studentship and a van Geest Fellowship in Dementia and Neurodegeneration from King's College London, a Royal Society Research Grant (RGS\R2\180450) and an Academy of Medical Sciences Springboard Award (SBF004\1088) to AV.

We would like to thank the Wohl Cellular Imaging Centre at King's College London for help with light microscopy and the Fly Facility of the Department of Genetics, University of Cambridge for help with Drosophila embryo injections.

References

1. Sleigh JN, Rossor AM, Fellows AD et al (2019) Axonal transport and neurological disease. Nat Rev Neurol 15:691–703. https://doi.org/10.1038/s41582-019-0257-2
2. Badal K, Zhao Y, Miller K, Puthanveettil S (2021) Live imaging and quantitative analysis of organelle transport in sensory neurons of Aplysia Californica. Methods Mol Biol; This volume.
3. Hees TJ, Harbauer AB (2021) Live-cell imaging of RNA transport in axons of cultured primary neurons. Methods Mol Biol; This volume.
4. Tierney W, Vicino I, Sun S et al (2021) Methods and applications of Campenot Trichamber neuronal cultures for the study of Neuroinvasive viruses. Methods Mol Biol; This volume.
5. Ganguly A, Roy S (2021) Imaging diversity in slow axonal transport. Methods Mol Biol; This volume.
6. Turchetto S, Le Bail R, Broix L, Nguyen L (2021) Molecular analysis of axonal transport dynamics upon modulation of microtubule acetylation. Methods Mol Biol; This volume.
7. Shekari A, Fahnestock M (2021) Retrograde axonal transport of Neurotrophins in basal forebrain cholinergic neurons. Methods Mol Biol; This volume.
8. Ionescu A, Perlson E (2021) Microfluidic neuromuscular co-culture system for tracking cell-to-cell transfer and axonal transport of labeled proteins. Methods Mol Biol; This volume.
9. Montgomery A, Garbouchian A, Bentley M (2021) Visualizing vesicle-bound kinesins in cultured hippocampal neurons. Methods Mol Biol; This volume.
10. Emily MF, Agrawal L, Barzaghi P et al (2021) Use of microfluidics chambers to image axonal transport in adult sensory neurons. Methods Mol Biol; This volume.
11. Mehta AR, Chandran S, Selvaraj BT (2021) Assessment of mitochondrial trafficking as a surrogate of fast axonal transport in human induced pluripotent stem cell derived spinal motor neurons. Methods Mol Biol; This volume.
12. Voelzmann A, Sanchez-Soriano N (2021) Drosophila primary neuronal cultures as a useful cellular model to study and image axonal transport. Methods Mol Biol; This volume.
13. Annuario EA, Ng KY-W (2021) High-resolution live imaging of mitochondria and mitochondrial nucleoids in differentiated SH-SY5Y cells. Methods Mol Biol; This volume.
14. Smit-rigter L, Rajendran R, Silva CAP et al (2016) Mitochondrial dynamics in visual cortex are limited in vivo and not affected by axonal structural report mitochondrial dynamics in visual cortex are limited in vivo and not affected by axonal structural plasticity. Curr Biol 26: 2609–2616. https://doi.org/10.1016/j.cub.2016.07.033
15. Turchetto S, Broix L, Nguyen L (2020) Ex vivo recording of axonal transport dynamics on postnatal Organotypic cortical slices. STAR Protoc 1:100131. https://doi.org/10.1016/j.xpro.2020.100131
16. Lin JQ, Cioni J-M (2021) Live imaging of RNA transport and translation in Xenopus retinal axons. Methods Mol Biol; This volume.
17. Medioni C, Vijayakumar J, Ephrussi A, Besse F (2021) High-resolution live-imaging of axonal RNP granules in drosophila pupal brain explants. Methods Mol Biol; This volume.
18. Gould SA, Adalbert R, Milde S, Coleman M (2021) Imaging axonal transport in ex vivo central and peripheral nerves. Methods Mol Biol; This volume.
19. Bateman JM (2021) Mitochondrial DNA transport in drosophila neurons. Methods Mol Biol; This volume.
20. Saxton WM, Lim A, Djagaeva I (2021) Dissection and direct imaging of axonal transport in drosophila segmental nerves. Methods Mol Biol; This volume.
21. DeGiorgis J, Jang M, Bearer EL (2021) The giant axon of the squid: A simple system for axonal transport studies. Methods Mol Biol; This volume.
22. Sleigh JN, Vagnoni A, Twelvetrees AE, Schiavo G (2017) Methodological advances in imaging intravital axonal transport. F1000Res 6:200. https://doi.org/10.12688/f1000research.10433.1

23. Huang R, Xu Y, Chen M et al (2021) Visualizing the intracellular trafficking in zebrafish Mauthner cells. Methods Mol Biol; This volume.
24. Atkins M, Hazan J, Fassier C (2021) In vivo live imaging of axonal transport in developing zebrafish axons. Methods Mol Biol; This volume.
25. Barmaver SN, Shanmugam MM, Wagner OI (2021) Methods to quantify and relate axonal transport defects to changes in C. ele-gans behavior. Methods Mol Biol; This volume.
26. Knabbe J, Protzmann J, Kuner T (2021) In vivo imaging of axonal organelle transport in the mouse brain. Methods Mol Biol; This volume.
27. Anazawa Y, Niwa S (2021) Analyzing the impact of gene mutations on axonal transport in Caenorhabditis elegans. Methods Mol Biol; This volume.
28. Robinson W, Godenschwege TA (2021) Live imaging of axonal transport in the adult drosophila central nervous system. Methods Mol Biol; This volume.
29. Nadiminti SSP, Koushika SP (2021) Imaging intracellular trafficking in neurons of *C. elegans*. Methods Mol Biol; This volume.
30. Bearer E, Zhang X, Jacobs R (2021) Studying axonal transport in the brain by manganese-enhanced magnetic resonance imaging (MEMRI). Methods Mol Biol; This volume.
31. Mattedi F, Vagnoni A (2019) Temporal control of axonal transport: the extreme case of organismal ageing. Front Cell Neurosci 13: 393. https://doi.org/10.3389/fncel.2019.00393
32. Knabbe J, Nassal JP, Verhage M, Kuner T (2018) Secretory vesicle trafficking in awake and anaesthetized mice: differential speeds in axons *versus* synapses. J Physiol 596: 3759–3773. https://doi.org/10.1113/JP276022
33. Sleigh JN, Tosolini AP, Schiavo G (2020) In vivo imaging of anterograde and retrograde axonal transport in rodent peripheral nerves. Methods Mol Biol 2143:271–292. https://doi.org/10.1007/978-1-0716-0585-1_20
34. Halabi EA, Pinotsi D, Rivera-Fuentes P (2019) Photoregulated fluxional fluorophores for live-cell super-resolution microscopy with no apparent photobleaching. Nat Commun 10: 1232. https://doi.org/10.1038/s41467-019-09217-7
35. Wang T, Li W, Martin S et al (2020) Radial contractility of actomyosin rings facilitates axonal trafficking and structural stability. J Cell Biol 219:e201902001. https://doi.org/10.1083/jcb.201902001
36. Vagnoni A, Bullock SL (2016) A simple method for imaging axonal transport in aging neurons using the adult drosophila wing. Nat Protoc 11:1711–1723. https://doi.org/10.1038/nprot.2016.112
37. Gustafsson N, Culley S, Ashdown G et al (2016) Fast live-cell conventional fluorophore nanoscopy with ImageJ through super-resolution radial fluctuations. Nat Commun 7:1–9. https://doi.org/10.1038/ncomms12471
38. Culley S, Tosheva KL, Matos Pereira P, Henriques R (2018) SRRF: Universal live-cell super-resolution microscopy. Int J Biochem Cell Biol 101:74–79. https://doi.org/10.1016/j.biocel.2018.05.014
39. Laine RF, Tosheva KL, Gustafsson N et al (2019) NanoJ: a high-performance open-source super-resolution microscopy toolbox. J Phys D Appl Phys 52:163001. https://doi.org/10.1088/1361-6463/ab0261
40. Brand AH, Perrimon N (1993) Targeted gene expression as a means of altering cell fates and generating dominant phenotypes. Development 118:401–415
41. Bulina ME, Chudakov DM, Britanova OV et al (2006) A genetically encoded photosensitizer. Nat Biotechnol 24:95–99. https://doi.org/10.1038/nbt1175
42. Takemoto K, Matsuda T, Sakai N et al (2013) SuperNova, a monomeric photosensitizing fluorescent protein for chromophore-assisted light inactivation. Sci Rep 3:2629. https://doi.org/10.1038/srep02629
43. Albrecht SC, Barata AG, Grosshans J et al (2011) In vivo mapping of hydrogen peroxide and oxidized glutathione reveals chemical and regional specificity of redox homeostasis. Cell Metab 14:819–829. https://doi.org/10.1016/j.cmet.2011.10.010
44. Grimm A, Cummins N, Götz J (2018) Local oxidative damage in the Soma and Dendrites quarantines neuronal mitochondria at the site of insult. iScience 6:114–127. https://doi.org/10.1016/j.isci.2018.07.015
45. Onukwufor JO, Trewin AJ, Baran TM et al (2020) Quantification of reactive oxygen species production by the red fluorescent proteins KillerRed, SuperNova and mCherry. Free Radic Biol Med 147:1–7. https://doi.org/10.1016/j.freeradbiomed.2019.12.008
46. Trewin AJ, Bahr LL, Almast A et al (2019) Mitochondrial reactive oxygen species generated at the complex-II matrix or intermembrane space microdomain have distinct effects

on redox signaling and stress sensitivity in *Caenorhabditis elegans*. Antioxid Redox Signal 31: 594–607. https://doi.org/10.1089/ars.2018.7681

47. Gorbachev DA, Staroverov DB, Lukyanov KA, Sarkisyan KS (2020) Genetically encoded red photosensitizers with enhanced Phototoxicity. Int J Mol Sci 21:8800. https://doi.org/10.3390/ijms21228800
48. Vagnoni A, Hoffmann PC, Bullock SL (2016) Reducing Lissencephaly-1 levels augments mitochondrial transport and has a protective effect in adult drosophila neurons. J Cell Sci 129:178–190. https://doi.org/10.1242/jcs.179184
49. Mangeol P, Prevo B, Peterman EJG (2016) KymographClear and KymographDirect: two tools for the automated quantitative analysis of molecular and cellular dynamics using kymographs. Mol Biol Cell 27:1948–1957. https://doi.org/10.1091/mbc.E15-06-0404
50. Mórotz GM, Glennon EB, Greig J et al (2019) Kinesin light chain-1 serine-460 phosphorylation is altered in Alzheimer's disease and regulates axonal transport and processing of the amyloid precursor protein. Acta Neuropathol Commun 7:200. https://doi.org/10.1186/s40478-019-0857-5
51. Neumann S, Chassefeyre R, Campbell GE, Encalada SE (2017) KymoAnalyzer: a software tool for the quantitative analysis of intracellular transport in neurons. Traffic 18:71–88. https://doi.org/10.1111/tra.12456
52. Jakobs MA, Dimitracopoulos A, Franze K (2019) Kymobutler, a deep learning software for automated kymograph analysis. Elife 8: e42288. https://doi.org/10.7554/eLife.42288
53. Vagnoni A, Bullock SL (2018) A cAMP/PKA/Kinesin-1 Axis promotes the axonal transport of mitochondria in aging drosophila neurons. Curr Biol 28:1265–1272.e4. https://doi.org/10.1016/j.cub.2018.02.048
54. Neukomm LJ, Burdett TC, Gonzalez MA et al (2014) Rapid in vivo forward genetic approach for identifying axon death genes in drosophila. Proc Natl Acad Sci U S A 111:9965–9970. https://doi.org/10.1073/pnas.1406230111
55. Smith GA, Lin T-H, Sheehan AE et al (2019) Glutathione S-transferase regulates mitochondrial populations in axons through increased glutathione oxidation. Neuron 103:52–65.e6. https://doi.org/10.1016/j.neuron.2019.04.017
56. Fang Y, Soares L, Bonini NM (2013) Design and implementation of in vivo imaging of neural injury responses in the adult drosophila wing. Nat Protoc 8:810–819. https://doi.org/10.1038/nprot.2013.042
57. Kaasik A, Safiulina D, Zharkovsky A, Veksler V (2007) Regulation of mitochondrial matrix volume. Am J Physiol Physiol 292: C157–C163. https://doi.org/10.1152/ajpcell.00272.2006
58. Long Q, Zhao D, Fan W et al (2015) Article modeling of mitochondrial donut formation. Biophys J 109:892–899. https://doi.org/10.1016/j.bpj.2015.07.039
59. Verstreken P, Ohyama T, Haueter C et al (2009) Tweek, an evolutionarily conserved protein, is required for synaptic vesicle recycling. Neuron 63:203–215. https://doi.org/10.1016/j.neuron.2009.06.017
60. Salvaterra PM, Kitamoto T (2001) Drosophila cholinergic neurons and processes visualized with Gal4/UAS-GFP. Gene Expr Patterns 1: 73–82. https://doi.org/10.1016/S1567-133X(01)00011-4
61. Pilling AD, Horiuchi D, Lively CM, Saxton WM (2006) Kinesin-1 and dynein are the primary motors for fast transport of mitochondria in drosophila motor axons. Mol Biol Cell 17: 2057–2068. https://doi.org/10.1091/mbc.E05-06-0526
62. Chowdhary S, Tomer D, Dubal D et al (2017) Analysis of mitochondrial organization and function in the drosophila blastoderm embryo. Sci Rep 7:1–17. https://doi.org/10.1038/s41598-017-05679-1

Open Access This chapter is licensed under the terms of the Creative Commons Attribution 4.0 International License (http://creativecommons.org/licenses/by/4.0/), which permits use, sharing, adaptation, distribution and reproduction in any medium or format, as long as you give appropriate credit to the original author(s) and the source, provide a link to the Creative Commons license and indicate if changes were made.

The images or other third party material in this chapter are included in the chapter's Creative Commons license, unless indicated otherwise in a credit line to the material. If material is not included in the chapter's Creative Commons license and your intended use is not permitted by statutory regulation or exceeds the permitted use, you will need to obtain permission directly from the copyright holder.

Chapter 21

Mitochondrial DNA Transport in *Drosophila* Neurons

Joseph M. Bateman

Abstract

Mitochondria are essential organelles that generate energy and play vital roles in cellular metabolism. The small circular mitochondrial genome encodes key components of the mitochondrial respiratory apparatus. Depletion of, or mutations in mitochondrial DNA (mtDNA) cause mitochondrial dysfunction and disease. mtDNA is packaged into nucleoids, which are transported throughout the cell within mitochondria. Efficient transport of nucleoids is essential in neurons, where mitochondrial function is required locally at synapses. Here I describe methods for visualization of nucleoids in *Drosophila* neurons using a GFP fusion of the mitochondrial transcription factor TFAM. TFAM-GFP, together with mCherry-labeled mitochondria, was used to visualize nucleoids in fixed larval segmental nerves. I also describe how these tools can be used for live imaging of nucleoid dynamics. Using *Drosophila* as a model system, these methods will enable further characterization and analysis of nucleoid dynamics in neurons.

Key words Mitochondrial DNA, Nucleoid, TFAM, Live imaging, *Drosophila*

1 Introduction

Mitochondria are essential cellular organelles with vital conserved roles in the generation of ATP, amino acids, reactive oxygen species, nucleotides, heme, and cholesterol [1]. Mitochondrial function is paramount in the nervous system, and neurons are acutely dependent on mitochondria to maintain their membrane potential and for synaptic vesicle release and recycling [2]. At the synapse, mitochondria are also essential for maintaining local ATP levels, calcium buffering, and regulating local translation [2]. Compromised mitochondrial function is a common feature in neurological diseases including neurodegenerative conditions, autism spectrum disorders and schizophrenia [3–6].

Mitochondrial biogenesis occurs through the coordinated action of both the nuclear and mitochondrial genomes

Supplementary Information The online version of this chapter (https://doi.org/10.1007/978-1-0716-1990-2_21) contains supplementary material, which is available to authorized users.

Alessio Vagnoni (ed.), *Axonal Transport: Methods and Protocols*,
Methods in Molecular Biology, vol. 2431, https://doi.org/10.1007/978-1-0716-1990-2_21,
© The Author(s), under exclusive license to Springer Science+Business Media, LLC, part of Springer Nature 2022

[7, 8]. Mitochondrial DNA (mtDNA) encodes vital components of the mitochondrial respiratory machinery. mtDNA is maintained in multiple copies, which vary between 10 s and 1000 s of copies per cell depending on the cell and tissue type [9]. The mitochondrial genome is packaged and organized into nucleoprotein complexes called nucleoids by the mtDNA binding protein mitochondrial transcription factor A (TFAM) [10, 11]. TFAM is highly abundant, with around 1000 molecules per mitochondrial genome. In mammalian cell lines, each nucleoid contains around one copy of the mitochondrial genome [12, 13]. The mitochondrial replisome complex, consisting of the heterodimeric DNA polymerase gamma (formed from separate catalytic and processivity subunits), the DNA helicase Twinkle, and the mitochondrial single-stranded DNA binding protein, replicates the mitochondrial genome to maintain mtDNA copy number [14]. Mutations in TFAM, POLγ and Twinkle lead to reduced or complete loss of mtDNA and mitochondrial dysfunction.

Mitochondrial nucleoids can be visualized using dyes that intercalate into DNA, anti-DNA antibodies, or using fluorescently tagged mtDNA binding proteins [13]. Nucleoids are at or below the limit of resolution for standard confocal microscopy, but can be resolved using super-resolution microscopy [13, 15]. Mitochondrial nucleoid numbers and dynamics have been studied in budding yeast and cell culture models, and mtDNA replication has been observed in neurites in primary rodent neurons [16, 17]. However, very little is known about nucleoid localization and dynamics in the nervous system.

Mitochondrial function and mtDNA are highly conserved in *Drosophila*. *Drosophila* also have a complex nervous system, and the mechanisms regulating axonal transport are very similar to mammals [18], making flies an excellent model for studying mitochondrial and nucleoid dynamics. Here I have used a TFAM-GFP fusion protein and mCherry-labeled mitochondria to visualize mtDNA nucleoids and mitochondria in *Drosophila* neurons in fixed and living tissue. I used *Drosophila* carrying a BAC transgene including the TFAM genomic locus with GFP inserted at the C-terminus (P{TFAM-GFP}) [19, 20]. These flies ubiquitously express TFAM-GFP, which is fully functional as it rescues the lethality caused by the $TFAM^{c01716}$ loss-of-function mutation (this study). Using super resolution imaging, I show that TFAM-GFP can be used to visualize nucleoids in *Drosophila* larval segmental nerves (Fig. 1). I also generated flies carrying a UAS-TFAM-GFP transgene, which I expressed in neurons using the Gal4/UAS system. However, when expressed in motor neurons, UAS-TFAM-GFP is localized to the mitochondrial matrix and so does not allow visualization of nucleoids (data not shown). I therefore describe a method for simultaneous live imaging of mitochondria and nucleoid axonal transport using P{TFAM-GFP} (Fig. 2 and Movie 1).

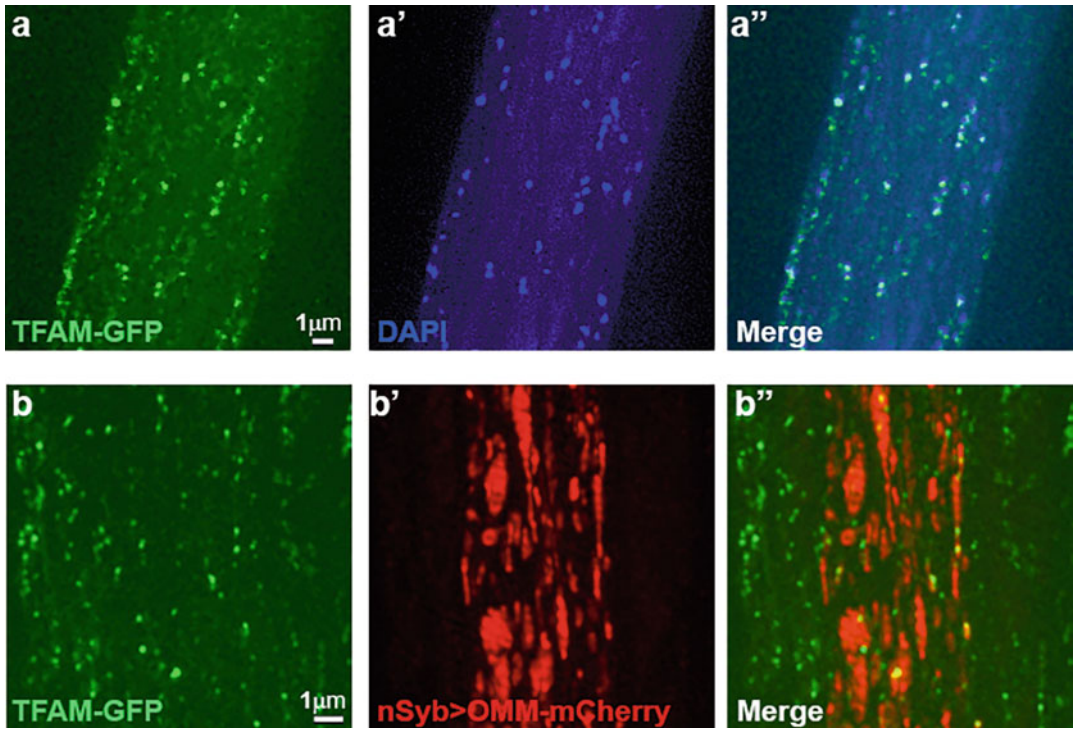

Fig. 1 *TFAM-GFP labels nucleoids in Drosophila neurons.* (**a**–**a**″) Late third instar larval segmental nerve showing TFAM-GFP (green) colocalization with DAPI stained nucleoids (blue). (**b**–**b**″) TFAM-GFP (green) flies expressing OMM-mCherry (red) in late third instar larval segmental neurons. Imaged using Nikon iSIM

2 Materials

2.1 Drosophila *Strains and Growth Conditions*

1. Standard fly food: 640 g glucose, 160 g cornmeal, 800 g yeast, 64 g agar, 8 L distilled water, which is autoclaved then cooled to 50 °C and 20 g nipagin (methyl 4-hydroxybenzoate; in 200 ml 70% ethanol), 40 ml propionic acid added.
2. Incubator equipped with temperature control (set at 25 °C) and 12-h light/dark cycle.
3. Fly stocks: *PBAC-TFAM-GFP* [19, 20], *UAS-TFAM-GFP* (this study), *OK371-Gal4* (BDSC 26160), *UAS-mCherry.mito.OMM* (BDSC 66532), *lexAop-mCherry.mito.OMM* (BDSC 66531), *nSyb-LexAp65* [21].

2.2 Generation of UAS-TFAM-GFP Flies

1. TFAM cDNA PCR amplified from clone LD40493 (DGRC).
2. Primers 5′-CACCATGATCTACACCACAACACTG-3′ and 5′-TATATCTTTGGAGGCCAGCGTCTTG-3′.
3. Plasmid pENTR/D-TOPO for cloning TFAM cDNA, plasmid pTWG (DGRC) for Gateway recombination (ThermoFisher). Transgenic flies were generated by BestGene.

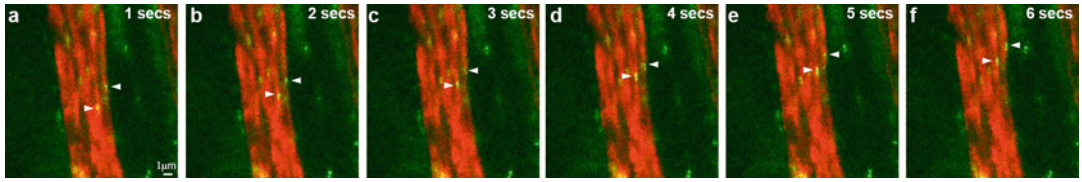

Fig. 2 *Nucleoid dynamics in Drosophila neurons.* (**a–f**) Late third instar larval segmental nerve expressing TFAM-GFP (green) to label nucleoids. Mitochondria are labeled with OMM-mCherry (red) expressed in neurons. 1 second interval still images from Movie 1. Arrowheads indicate two different dynamic nucleoids. Imaged using Nikon A1R

2.3 Fixed and Live Tissue Imaging

1. 4% formaldehyde/phosphate-buffered saline (PBS).
2. Tweezers (Dumont Biology Tweezers 5 Dumoxel, 0.05 × 0.01 mm tip).
3. Sylgard 184.
4. SuperFrost Plus slides.
5. 22 mm × 22 mm no. 1.5 coverslips.
6. Vectashield+DAPI (H-1200, Vectalabs).
7. Halocarbon oil.
8. Dental wax.

3 Methods

3.1 Dissection, Fixation, and Super Resolution Imaging of Nucleoids in Drosophila *Third Instar Larval Segmental Nerves*

1. Cross 6-10 *lexAop-mCherry.mito.OMM; nSyb-LexAp65* or *OK371-Gal4*, *UAS-mCherry.mito.OMM* virgin females to 3-5 P{TFAM-GFP} males at 25 °C (*see* **Note 1**). *Nb*, I have also used *OK371-Gal4* to express *UAS-TFAM-GFP*. However, *UAS-TFAM-GFP* is localized to the mitochondrial matrix in motor neurons so cannot be used to visualize nucleoids in this context (data not shown).
2. After 3 days, discard the adult flies or transfer the flies to a new vial if more larvae are required.
3. 7 days after the crosses were set up, use blunt tweezers to remove 10 late third instar larvae and place them in a drop of PBS on a Sylgard dish (*see* **Note 2**).
4. Briefly agitate the larvae to clean them, then transfer them to a new drop of PBS.
5. Using sharp tweezers pull a larva in two, approximately two thirds of the way toward the posterior (Fig. 3a).
6. Using one closed pair of tweezers, push the tip into the mouth-parts, then using the other pair pull the cuticle down over the first pair, akin to inverting a sock over your hand.

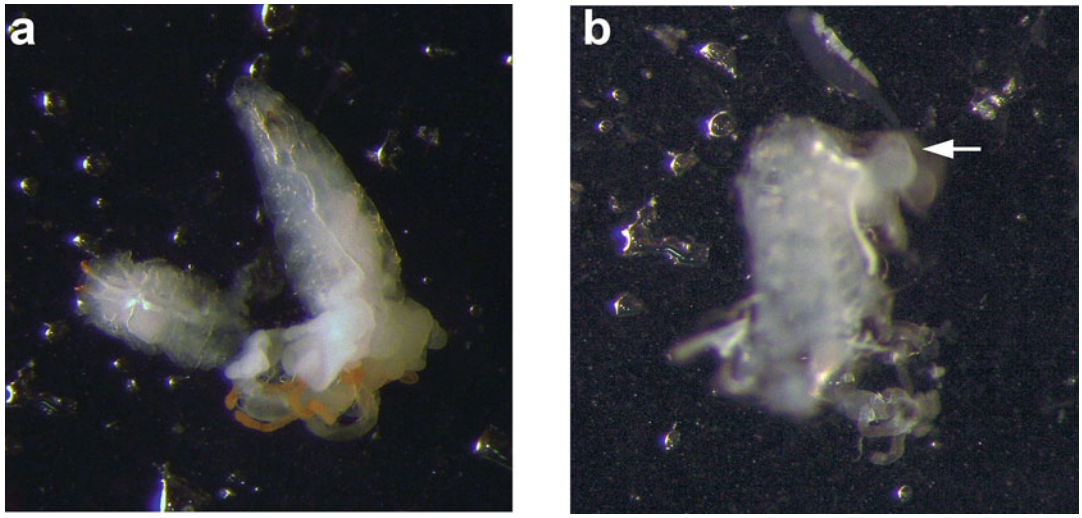

Fig. 3 *Larval CNS dissection*. (**a**) After the first stage of dissection where the larva is pulled in two. (**b**) After the second stage of dissection where the anterior of the larva has been inverted and the extraneous tissues removed, exposing the CNS (arrow) attached to the body wall

7. The larva is now inside out, and the CNS and imaginal tissues are easily visible (Fig. 3b). Remove the fat body and other extraneous tissue.
8. Place the tissue in 0.5 ml PBS on ice.
9. Repeat the dissection for the remaining larvae.
10. Carefully remove the PBS, replace with 4% PBS/formaldehyde and incubate on ice for 20 min.
11. Remove the fixative and wash carefully with PBS twice (*see* **Note 3**).
12. Transfer the tissue to a Superfrost slide under a dissecting microscope with a fiber optic cold light source (*see* **Note 4**).
13. Dissect the CNS away from the cuticle using tweezers, gently releasing the segmental nerves away from the body wall muscle, then discard the cuticle.
14. Repeat **step 13** for the remaining CNS tissue and arrange so that the segmental nerves are separate from adjacent tissue, such as the CNS or imaginal discs, so that neurons can be imaged without interference from other tissues.
15. Tilting the slide, gently dab off the excess PBS using a tissue and carefully add 14 μl Vectashield+DAPI, avoiding bubbles (*see* **Note 5**).
16. Carefully place a coverslip over the tissue and store a 4 °C in the dark.

17. Using a Nikon iSIM, or alternative super resolution microscope, find a segmental nerve using a low power lens (*see* **Note 6**).
18. Switch to a 100× oil immersion lens and image specimen (*see* Fig. 1).
19. Images can be deconvolved using Nikon NIS-Elements software.

3.2 Live Imaging of Nucleoids in Drosophila Third Instar Larval Segmental Nerves

1. Cross 6-10 *lexAop-mCherry.mito.OMM; nSyb-LexAp65* or *OK371-Gal4*, *UAS-mCherry.mito.OMM* virgin females to 3-5 P{TFAM-GFP} males at 25 °C.
2. After 3 days, discard the adult flies or transfer the flies to a new vial if more larvae are required.
3. 7 days after the crosses were set up, use blunt tweezers remove a white pre-pupa and transfer it to a slide under a dissecting microscope with a fiber optic cold light source (*see* **Note 7**).
4. Turn the pre-pupa ventral side up (*see* **Note 8**).
5. Using a P20 pipette, add a small drop of halocarbon oil onto the ventral surface of the pre-pupa.
6. Place four small pieces of dental wax on the slide and then place a coverslip on top of the pre-pupa and gently press down so the coverslip adheres to the dental wax and slightly compresses the pre-pupa.
7. Immediately image the pre-pupa using confocal microscopy. I used a Nikon A1R confocal (Fig. 2 and Movie 1 and *see* **Note 9**).

4 Notes

1. *nSyb-LexAp65* drives mCherry.mito.OMM expression in both motor neurons and sensory neurons in segmental nerves. *OK371-Gal4* drives mCherry.mito.OMM expression only in motor neurons.
2. Larvae expressing mCherry.mito.OMM can be selected using a dissecting microscope with fluorescence, if necessary.
3. Fixed tissue can be stored at 4 °C.
4. Use a fiber optic cold light source and illuminate the tissue from the side, which gives the tissue greater contrast.
5. Tissue slightly adheres to Superfrost slides so does not move when removing the PBS.
6. Nucleoids can be imaged using standard confocal microscopy but are below the limit of resolution using this technique, so super resolution imaging is required for accurate

quantification. I used a Nikon iSIM with Vt-iSIM scan head and Hamamatsu Flash4.0 sCMOS camera, oil immersion 100×/1.49 NA objective, 488 nm and 561 nm excitation lasers.

7. White pre-pupae are still relatively transparent, similar to larvae, but do not require anesthetizing to prevent movement. However, the white pre-pupal stage only lasts for ~1 h at 25 °C, so several vials may need to be set up to obtain enough white pre-pupae.
8. The dorsal side of the pre-pupa can be identified using the pair of dorsal trachea easily visible below the cuticle.
9. I used a Nikon A1R confocal system with 2× GaAsP Detectors, oil immersion 100×/1.4 NA objective, 488 nm and 561 nm excitation lasers.

Acknowledgments

Work in this area in my laboratory is currently funded by grants from Alzheimer's research UK (ARUK-IRG2017A-2), the NC3Rs (NC/V001884/1), and the MRC (MR/V013130/1). I thank the Wohl Cellular Imaging Centre at King's College London for help with light microscopy.

References

1. Spinelli JB, Haigis MC (2018) The multifaceted contributions of mitochondria to cellular metabolism. Nat Cell Biol 20(7):745–754. https://doi.org/10.1038/s41556-018-0124-1
2. Devine MJ, Kittler JT (2018) Mitochondria at the neuronal presynapse in health and disease. Nat Rev Neurosci 19(2):63–80. https://doi.org/10.1038/nrn.2017.170
3. Granat L, Hunt RJ, Bateman JM (2020) Mitochondrial retrograde signalling in neurological disease. Philos Trans R Soc Lond Ser B Biol Sci 375(1801):20190415. https://doi.org/10.1098/rstb.2019.0415
4. Khacho M, Harris R, Slack RS (2019) Mitochondria as central regulators of neural stem cell fate and cognitive function. Nat Rev Neurosci 20(1):34–48. https://doi.org/10.1038/s41583-018-0091-3
5. Hunt RJ, Granat L, McElroy GS, Ranganathan R, Chandel NS, Bateman JM (2019) Mitochondrial stress causes neuronal dysfunction via an ATF4-dependent increase in L-2-hydroxyglutarate. J Cell Biol 218(12): 4007–4016. https://doi.org/10.1083/jcb.201904148
6. Duncan OF, Granat L, Ranganathan R, Singh VK, Mazaud D, Fanto M, Chambers D, Ballard CG, Bateman JM (2018) Ras-ERK-ETS inhibition alleviates neuronal mitochondrial dysfunction by reprogramming mitochondrial retrograde signaling. PLoS Genet 14(7): e1007567. https://doi.org/10.1371/journal.pgen.1007567
7. Nunnari J, Suomalainen A (2012) Mitochondria: in sickness and in health. Cell 148(6): 1145–1159. https://doi.org/10.1016/j.cell.2012.02.035
8. Duncan OF, Bateman JM (2016) Mitochondrial retrograde signaling in the *Drosophila* nervous system and beyond. Fly (Austin) 10:1–6. https://doi.org/10.1080/19336934.2016.1174353
9. St John JC (2016) Mitochondrial DNA copy number and replication in reprogramming and differentiation. Semin Cell Dev Biol 52: 93–101. https://doi.org/10.1016/j.semcdb.2016.01.028

10. Kang I, Chu CT, Kaufman BA (2018) The mitochondrial transcription factor TFAM in neurodegeneration: emerging evidence and mechanisms. FEBS Lett 592(5):793–811. https://doi.org/10.1002/1873-3468.12989
11. Cagin U, Duncan OF, Gatt AP, Dionne MS, Sweeney ST, Bateman JM (2015) Mitochondrial retrograde signaling regulates neuronal function. Proc Natl Acad Sci U S A 112(44): E6000–E6009. https://doi.org/10.1073/pnas.1505036112
12. Kukat C, Davies KM, Wurm CA, Spahr H, Bonekamp NA, Kuhl I, Joos F, Polosa PL, Park CB, Posse V, Falkenberg M, Jakobs S, Kuhlbrandt W, Larsson NG (2015) Cross-strand binding of TFAM to a single mtDNA molecule forms the mitochondrial nucleoid. Proc Natl Acad Sci U S A 112(36): 11288–11293. https://doi.org/10.1073/pnas.1512131112
13. Kukat C, Wurm CA, Spahr H, Falkenberg M, Larsson NG, Jakobs S (2011) Super-resolution microscopy reveals that mammalian mitochondrial nucleoids have a uniform size and frequently contain a single copy of mtDNA. Proc Natl Acad Sci U S A 108(33): 13534–13539. https://doi.org/10.1073/pnas.1109263108
14. Falkenberg M, Larsson NG, Gustafsson CM (2007) DNA replication and transcription in mammalian mitochondria. Annu Rev Biochem 76:679–699. https://doi.org/10.1146/annurev.biochem.76.060305.152028
15. Brown TA, Tkachuk AN, Shtengel G, Kopek BG, Bogenhagen DF, Hess HF, Clayton DA (2011) Superresolution fluorescence imaging of mitochondrial nucleoids reveals their spatial range, limits, and membrane interaction. Mol Cell Biol 31(24):4994–5010. https://doi.org/10.1128/mcb.05694-11
16. Lewis SC, Uchiyama LF, Nunnari J (2016) ER-mitochondria contacts couple mtDNA synthesis with mitochondrial division in human cells. Science 353(6296):aaf5549. https://doi.org/10.1126/science.aaf5549
17. Van Laar VS, Arnold B, Howlett EH, Calderon MJ, St Croix CM, Greenamyre JT, Sanders LH, Berman SB (2018) Evidence for compartmentalized axonal mitochondrial biogenesis: mitochondrial DNA replication increases in distal axons as an early response to Parkinson's disease-relevant stress. J Neurosci 38(34): 7505–7515. https://doi.org/10.1523/jneurosci.0541-18.2018
18. Bellen HJ, Tong C, Tsuda H 100 years of Drosophila research and its impact on vertebrate neuroscience: a history lesson for the future. Nat Rev Neurosci 11(7):514–522. https://doi.org/10.1038/nrn2839
19. Zhang Y, Chen Y, Gucek M, Xu H (2016) The mitochondrial outer membrane protein MDI promotes local protein synthesis and mtDNA replication. Embo J 35(10):1045–1057. https://doi.org/10.15252/embj.201592994
20. Chen Z, Wang ZH, Zhang G, Bleck CKE, Chung DJ, Madison GP, Lindberg E, Combs C, Balaban RS, Xu H (2020) Mitochondrial DNA segregation and replication restrict the transmission of detrimental mutation. J Cell Biol 219(7):e201905160. https://doi.org/10.1083/jcb.201905160
21. Pfeiffer BD, Ngo TT, Hibbard KL, Murphy C, Jenett A, Truman JW, Rubin GM (2010) Refinement of tools for targeted gene expression in *Drosophila*. Genetics 186(2):735–755. https://doi.org/10.1534/genetics.110.119917

Chapter 22

Live Imaging of Axonal Transport in the Adult *Drosophila* Central Nervous System

Wayne Robinson and Tanja A. Godenschwege

Abstract

Live imaging of axons allows for the determination of motility and directionality of proteins or organelles. In *Drosophila*, axonal transport has been predominantly characterized in peripheral neurons, such as larval motor neurons and sensory neurons of the adult wing. As peripheral neurons and central nervous system (CNS) neurons are inherently different, we provide a method to live-image axonal transport of CNS neurons in the cervical connective using an upright or inverted microscope. The method involves dissecting and mounting an entire CNS in a glass bottom petri dish, which is suitable for imaging of nearly any axon in cervical connective. Here, we show an example for simultaneous imaging of both giant fiber axons, which are part of the fly's escape response circuitry, and due to their large diameter provide outstanding resolution.

Key words Axon transport, Organelle trafficking, Giant fiber, *Drosophila*, Central nervous system, Whole-mount dissection, Live imaging

1 Introduction

Live imaging has advanced the understanding of mechanisms involved in regulating protein and organelle trafficking. Due to the typically long distance between soma and synapse, neurons are particularly sensitive to transport defects, and dysfunction is a common cellular pathological phenotype of almost all neurodegenerative diseases [1, 2]. To properly understand age-related neuronal diseases associated with axonal transport defects, it is vital to be able to perform live imaging of adult neurons at different time points. A noninvasive method to live image trafficking in mechano- or chemisensory neurons in the *Drosophila* wing has been established [3]. However, expression, trafficking, and processing of many proteins are different in distinct types of neurons, such as reported for the invertebrate amyloid precursor protein (APP) [4–6]. Thus, it is

Alessio Vagnoni (ed.), *Axonal Transport: Methods and Protocols*,
Methods in Molecular Biology, vol. 2431, https://doi.org/10.1007/978-1-0716-1990-2_22,
© The Author(s), under exclusive license to Springer Science+Business Media, LLC, part of Springer Nature 2022

essential to assess axon trafficking with live imaging in various types of neurons.

A CNS whole-mount preparation to access the cervical connective (CC) and ventral nerve cord (VNC) to image the giant fiber (GF) axons and terminals in semi-intact animals has been previously described in detail [7]. While this preparation is suitable for live imaging as well, it is limited to imaging with a water immersion objective on an upright microscope. The method presented here was used successfully to assess trafficking of transmembrane proteins Neuroglian and APPL using a water immersion objective on an upright confocal or an inverted microscope equipped with an oil immersion objective by mounting the dissected CNS with either the dorsal side up or down in a glass bottom petri dish, respectively [4, 8]. Since Gal4-lines have been established that allow selective transgenic expression in numerous other identified neurons that descend from the brain into the ventral nerve cord, this approach is suitable to asses trafficking in other types of CNS neurons as well [9, 10].

2 Materials

2.1 CNS Dissection

1. Stainless Steel Minutien Pins, 0.1 mm diameter.
2. Dumont forceps, pattern #5, 0.05 × 0.01 mm tip size, 110 mm length. For effective dissection, an unaltered, sharp forceps and a modified more blunt-ended forceps should be used (*see* **Note 1**). Use a sharpening stone to file the tip of Dumont forceps as depicted in Fig. 1a.
3. Sylgard-coated petri dish, 27–35 mm diameter (*see* **Note 2**).
4. *Drosophila* saline: 128 mM NaCl, 2 mM KCl, 1.8 mM $CaCl_2$, 4 mM $MgCl_2$, HEPES 5 mM, 35.5 mM sucrose, pH = 7.1–7.3. Set up 1 M Stock solutions for NaCl (29.220 g in 500 ml dH_2O), KCl (1.491 g in 20 ml dH_2O), $CaCl_2$ (2.22 g in 20 ml), $MgCl_2$ (4.066 g in 20 ml), HEPES (4.766 g in 20 ml), and 1 M NaOH (4 g in 100 ml). Add 64 ml NaCl, 1 ml NaCl, 0.9 ml $CaCl_2$, 2 ml $MgCl_2$, 2.5 ml HEPES, and 6.08 g sucrose to 400 ml diH_2O. Adjust solution with NaOH to pH = 7.1–7.3 at room temperature, and add diH_2O to final volume of 500 ml (*see* **Note 3**).
5. 3.5–90× zoom stereo microscope with gooseneck light source (*see* **Note 4**).
6. Adult transgenic *Drosophila* expressing a fluorophore-tagged protein or organelle of interest selectively in the GFs or other descending neurons (*see* **Note 5**).

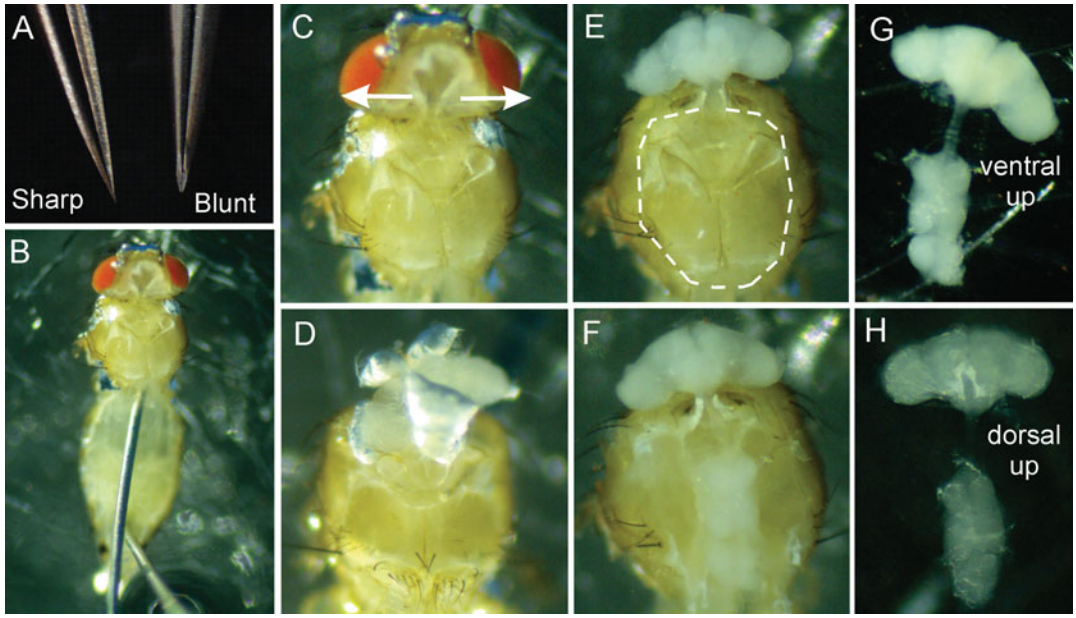

Fig. 1 *Drosophila* CNS dissection. (**a**) Unaltered (sharp) and modified Dumont forceps used for dissection. (**b**) Specimen stabilized with two pins and its proboscis, legs and wings removed. (**c**) Arrows display placement and directions of forceps movement to remove the head capsule. (**d**) Exposed brain with attached air sacks. (**e**) *Drosophila* brain after air sack removal. Perforated line surrounds the sternum plate. Removal of cuticular along the perforated line will allow to lift up the sternum plate from posterior side. (**f**) Exposed VNC after the removal of the sternum plate. (**g**) *Drosophila* CNS with view onto the ventral side. (**h**) *Drosophila* CNS with view onto the dorsal side

2.2 CNS Mounting for Imaging

1. Poly-L-Lysine or VECTABOND® solution for coating (*see* **Note 6**).
2. Glass bottom petri dishes 27–35 mm diameter or larger.
3. Dumont forceps.
4. *Drosophila* saline.
5. 3.5–90× zoom stereo microscope with gooseneck light source.

2.3 Live Imaging of the Giant Fiber Axons in the Cervical Connective

1. Inverted confocal microscope with any type of a 10–20× objective and a 60× oil immersion objective or an upright confocal microscope with any type of 10–20× objective and a 60× water immersion objective. In addition to the appropriate laser lines to excite the fluorophores, the confocal should have a high-resolution, high-speed scan head.

3 Methods

3.1 Drosophila *Whole-Mount Dissection*

1. Under a stereo microscope, pin the fly, anesthetized with CO_2, with two Minutien pins in a Sylgard-coated petri dish and submerge the fly in *Drosophila* saline solution (*see* Fig. 1b, **Note 8**).

2. Use blunt-end forceps to remove wings, legs, and proboscis (*see* Fig. 1b, **Note 9**).
3. Use two blunt-end forceps to grab both retina through the hole generated by the removal of the proboscis, and pull simultaneously in lateral but opposite direction and with equal force to remove the head capsule from the brain (*see* Fig. 1c, **Note 10**).
4. Remove air sacks and any other debris from the brain (*see* Fig. 1d, **Note 11**).
5. The ventral nerve cord (VNC) lies directly under the thoracic sternum. To expose it, tear off the cuticula around the sternum plate using sharp and blunt forceps. Then, slowly lift off the sternum plate from the posterior side (*see* Fig. 1e, **Note 12**).
6. Place a slightly open set of forceps under the CNS in an anterior to posterior manner to lift it up and out of the dissected fly. Do not grab or pull the CNS (*see* Fig. 1f, **Note 13**).
7. Remove any debris still attached to the CNS and ensure that the CC is undamaged (*see* Fig. 1g, h, **Note 14**).

3.2 Coating Glass Bottom Petri Dishes

3.2.1 Poly-L-Lysine Coating

1. Clean glass coverslip of the glass bottom petri dish thoroughly with 100% ethanol and subsequently rinse with deionized water (diH_2O).
2. Coat the glass coverslip for 5 min with a 0.01% Poly-L-Lysine solution (3 mg in 30 ml diH_2O) at room temperature.
3. Remove Poly-L-Lysine solution and wash glass coverslip three times with diH_2O.
4. Let coverslip of the glass bottom petri dish dry for 2 h or longer.

3.2.2 VECTABOND® Coating

1. Dilute VECTABOND® solution 1:50 in 100% acetone.
2. Coat glass coverslip of the glass bottom petri dish with 100% acetone for 5 min (*see* **Note 7**).
3. After acetone removal apply diluted VECTABOND® solution to glass coverslip for 5 min.
4. Wash glass coverslip with diH_2O and let dry for at least 30 min.

3.3 Mounting CNS in Glass Bottom Petri Dishes

1. Pipette a little drop (approximately 50 µl) of *Drosophila* saline onto the middle of the coated coverslip in the glass bottom petri dish (*see* Fig. 2a, **Note 15**).
2. Under a stereo microscope, place the closed tips of a set of forceps from the lateral side under the CC to lift the dissected CNS out of the dissection dish and transfer into the saline droplet of the glass bottom petri dish. The CNS will typically float on the surface of the saline and due to the convex shape of

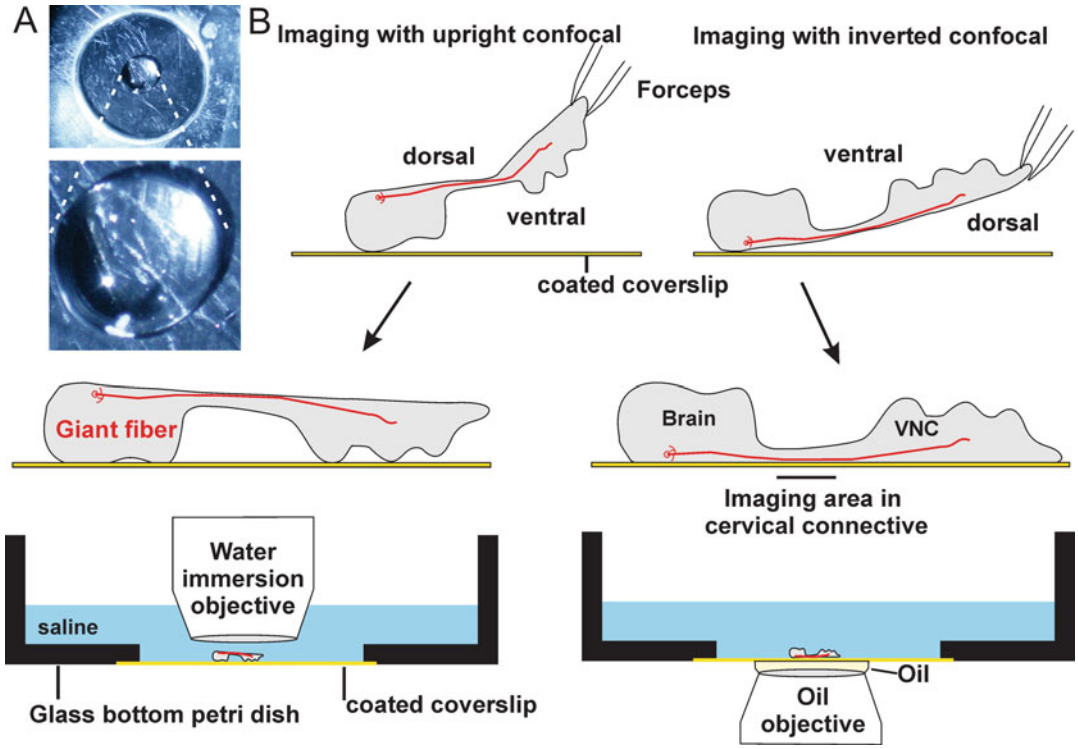

Fig. 2 Mounting CNS for live imaging. (**a**) *Drosophila* saline droplet on a coated coverslip of a glass bottom petri dish. Enlarged view of droplet of saline showing *Drosophila* CNS orientation after transfer from dissection dish with forceps into the middle of the droplet. Due to the convex shape, the CNS slides with the brain toward the coverslip. (**b**) Mounting orientation of the CNS for imaging with an upright or inverted microscope. Tension on the CC is required for straight GF during imaging, which is achieved by slightly pulling the VNC with forceps at the abdominal ganglion before lowering it onto the coated coverslip

the saline droplet, slide with the brain down to the coverslip (*see* Fig. 2a, **Note 16**).

3. Carefully push the brain with blunt-ended forceps down to adhere the anterior region of the brain to the coated coverslip (*see* **Note 17**). Gently add more *Drosophila* saline to cover the entire coverslip. Identify the dorsal and ventral side of the CNS; the dorsal side is flat, while the ventral side is not (*see* Figs. 1g, h and 2b). Use a blunt set of forceps to further manipulate the brain into the correct direction on the coverslip for imaging with an inverted (dorsal side down) or upright (ventral side down) microscope.
4. Use blunt-ended forceps to grab the abdominal ganglion (or the nerve bundles exiting the abdominal ganglion) to mount the VNC (*see* Fig. 2b). While placing the VNC down, it is essential to slightly pull and create tension onto the CC to ensure that GFs will be straight for live imaging (*see* Fig. 3a–c). Without the tension, the GFs will be winding (*see* Fig. 3d–h),

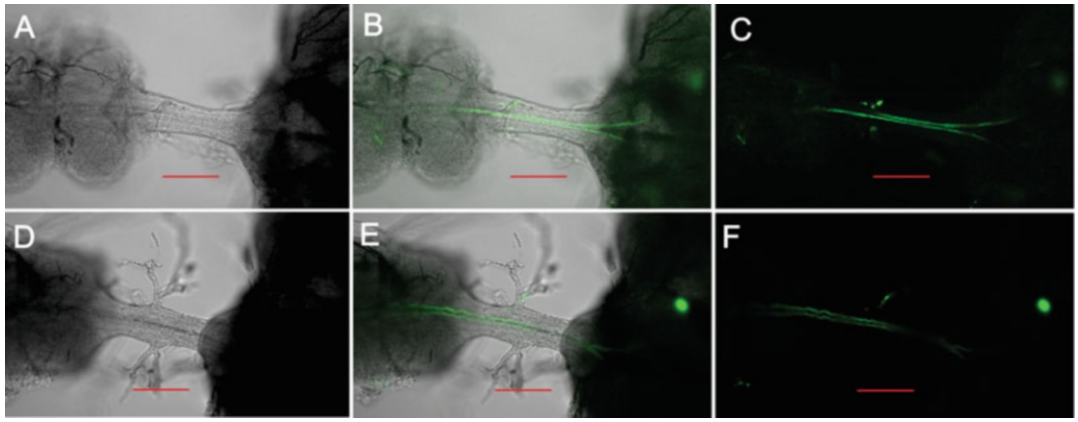

Fig. 3 Visualization of GF in CC with a Plan Fluor 20X/NA 0.75 water immersion objective. Tagged Spinster was transgenically expressed in the GFs with the GMR68A06-Gal4 line. (**a**–**c**) Show straight GF axons in a CC which was mounted with tension. (**d**–**f**) GF axons are winding in a CNS mounted with too little tension in the CC. Red scale bars are 100 μm

which will interfere with tracking of organelles, as organelles will often be moving in and out of the imaging plane (*see* **Note 18**).

5. Gently fill up the half of the glass bottom petri dish with *Drosophila* saline and move the mounted preparation to a confocal for immediate imaging (*see* **Note 19**).

3.4 Live Imaging of the Giant Fiber Axons in the Cervical Connective

1. Use a 10× or 20× objective to find the CNS under regular light illumination, center and focus on the CC (*see* Fig. 3a and **Note 20**).
2. Use the appropriate laser excitation and filters for the respective fluorophore detection and fully open the confocal pinhole to find and focus on the GF axons in confocal mode. Find and center the regions of the GF axons that are straight for approximately 30 μm or more in the CC (*see* Fig. 3).
3. Switch to a 60× or 100× objective. Since GF axons are approximately 8 μm thick in diameter, find the center plane of the axons for live imaging. Select a region of interest (ROI) that encompasses one or both GF axons with a length of 20–50 μm (*see* Fig. 4a and, **Note 21**).
4. Acquire images with a minimum of 1 frame/s and 512 pixel resolution for 2–10 min (*see* **Note 21**). However, a higher frame rate is required to reliably visualize cargoes that move faster than 1.4 μm/s. An opened pinhole size of 200–255 μm is recommended, as it allows increased signal strength and imaging of vesicle transport over a broader range of planes. Excitation laser power should be kept to a minimum (approximately

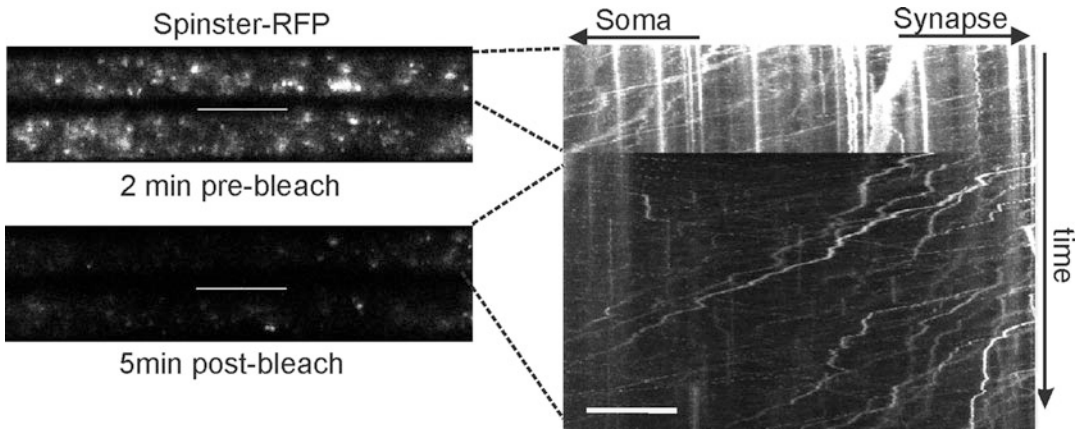

Fig. 4 Live imaging of Spinster-RFP with a CFI Plan 100×/1.1 NA water immersion lens. (Left) Regions of interest in GF axons imaged before and after a 30-s photo bleach period. (Right) Kymograph of pre and post bleach of the images acquired at 1 frame/s from the top GF. Scale bars are 10 μm.

2–10% of maximum laser power) to avoid photobleaching during imaging.

5. Photobleach with 40–50% excitation laser power for 30–60 s to improve the visibility of moving cargoes when imaging tagged-proteins localized to organelles that are frequently stationary, in the axon membrane or in the cytosol (*see* Fig. 4b).
6. Analyze videos by generation of kymographs with propriety software, such as Nikon Elements Advanced Research 4.4 used here or freeware such as ImageJ (*see* Fig. 4b and **Note 23**). While both GFs, due to their close approximation, can be imaged simultaneously, videos should be cropped to encompass only individual GFs for Kymograph analyses. Kymographs can be used to determine:
   (a) The velocities of individual organelle runs, with runs defined as a continuous movement for at least 2 μm.
   (b) The maximum net displacement of an organelle in either antero- or retrograde direction by calculating the average travel speed in μm/second during a defined imaging period (e.g., 2 min) or distance (e.g., 30 μm).
   (c) Relative number of stationary organelles in an axon segments of the imaged plane, defined as organelles that remain within their initial position ±1 μm during a defined imaging period (e.g., 2 min).
   (d) Relative flux of anterograde and retrograde organelles within the imaged plane by analyzing the total number of organelles per minute entering a bleached area or passing through an arbitrary vertical line along the GF axon per minute.

4 Notes

1. For longevity of live imaging, it is beneficial to leave the CNS and, in particular, the glial sheet surrounding it intact. Therefore, for most of the dissection, two blunt-ended forceps are preferred since they are less likely to pierce or damage the CNS, while allowing to better grab and remove the fly's exoskeleton. Fine, sharp forceps, however, are most useful for perforating the thoracic cuticula and transferring the CNS from dissection dish to imaging dish.
2. Larger Sylgard-coated dissention dishes can be used and are more stable during dissection. However, for better visibility during dissection, it is best to fully cover the entire bottom of the petri dish with *Drosophila* saline for a flat rather than convex surface. Larger petri dishes would require a larger amount of *Drosophila* saline, and small dissection dishes can be easily stabilized in place during dissection by fixing them on two sides with modeling clay.
3. It is recommended to store the *Drosophila* saline at 4 °C. However, for dissection and live imaging, we use *Drosophila* saline warmed to room temperature, since it is a more physiological temperature and temperature affects axonal transport velocity [11–14].
4. While ring light sources can be used as well, a gooseneck light source provides the advantage of modifying illumination during different steps of the dissection for better visibility of the CNS, which is difficult to see when illuminated from above due to its transparency.
5. For maximized expression of a fluorophore-tagged protein, UAS-lines crossed to strong Gal4-driver should be kept at 25 °C until aged for dissection. In addition, the Gal4-line should drive selective expression in descending neuron of interest to minimize background fluorescence from other axons during imaging. For the GFs, we found the P{GMR68A06-GAL4} line to be optimal.
6. Both Poly-L-Lysine and VECTABOND®-coated coverslips work well for mounting and stabilizing the CNS during live imaging. However, VECTABOND® adhesion is stronger and longer lasting than Poly-L-Lysine-coated coverslips, since the CNS remained reliably attached to VECTABOND®-coated but not to Poly-L-Lysine-coated coverslips over multiple days, when immunohistochemistry was performed. Coated glass bottom petri dishes can be stored for several weeks at 4 °C, but it is recommended to make only small batches of coated glass bottom petri dishes the day before or on the day of live

imaging, since adhesion capacity reduces over time. For imaging with an upright microscope, glass bottom petri dishes with a diameter of 35 mm or larger is recommended as otherwise the petri dish walls may interfere with lowering the water immersion objectives in to the medium, especially if the specimen is mounted off-center on the coverslip.

7. VECTABOND® uses acetone as a solvent, which may degrade the plastic of some brands of glass bottom petri dishes. Therefore, it is recommended to restrict the acetone treatment only to the cover slip and insulate the petri dish borders touching the coverslip with a thin layer of petroleum jelly.
8. One pin should be on the posterior end of the abdomen, the other should be placed diagonally from the posterior end of the abdomen into the thorax (*see* Fig. 1b). This provides maximum stability and prevents the fly from rotating during the dissection.
9. Ensuring that the proboscis is removed at its base and creates a hole as close as possible to the CC allows for easier removal of the entire head capsule in the next step. The second set of forceps, slightly opened, should be used to stabilize the head during removal.
10. We find that grabbing the retinas through the opening close to the CC is highly effective for removing the entire head capsule in one step. However, other previously described techniques for brain only dissection can be adapted as well [15–17]. A distinct pin-less method for brain and VNC dissection can also be viewed on the website of the HHMI Janelia Research campus (https://www.janelia.org/project-team/flylight/protocols).
11. Any air-filled sacks and cuticular pieces must be fully removed since they will interfere with the mounting process.
12. Being able to lift up the sternum plate is essential to ensure that all cuticula lateral to the CC and surrounding the VNC is removed. During this step, it is advised to use one set of forceps to further stabilize the fly in place, while the other set of forceps removes cuticula pieces. In 0- to 4-day-old adults, the CNS tends to stick to the sternum plate when lifting it up. In this case, one set of forceps should be used to "peel off" the CNS while the other set of forceps is lifting the sternum plate.
13. While lifting the CNS up, nerve bundles emanating from the abdominal ganglion into the abdomen may still connect the CNS to the preparation because they were unsevered by the removal of the cuticle surrounding the sternum plate during dissection. In this case, do not pull the CNS with the forceps but grab the nerve bundles with the forceps and use them to move the CNS away from the dissected specimen.

14. Do not pull off any nerve bundles that still emanate from the CC, which may damage the VNC, or the abdominal ganglia of the VNC. In particular, the latter can aid in proper VNC mounting.
15. Using a droplet of saline instead of covering the entire glass coverslip will ensure that the CNS will be mounted close to the center of the coverslip, which will avoid possible issues with the water immersion lens touching the borders of the petri dish. In addition, submerging a floating CNS from a flat surface is very difficult and bears the risk it sticks to the coverslip before its proper positioning.
16. Typically the CNS will come off once the forceps are lowered into the saline. However, if it remains stuck to the forceps, use a second set of forceps to gently push it off. In general, it is recommended to clean the forceps before transfer and to use the unaltered sharp set of forceps for CNS transfer to minimize the adhesive contact area.
17. Lifting off an adhered CNS will typically tear the glial sheath impacting the viability of the preparation. Since the CNS cannot be rearranged once adhered to the coverslip, it is critical to first adhere the brain into the correct direction for imaging. The CNS can be transferred with the dorsal or ventral side of the CC laying on the forceps, in which case the correct side of the brain for imaging with an upright or an inverted microscope may already be closer to the coverslip. In this case, the brain may be fixated in the saline droplet. However, for mounting the VNC, it is recommended to cover the entire coverslip with saline, since the flat surface increases visibility. Here, it is advised to keep the forceps under the VNC while adding saline to avoid that the VNC adheres to the coverslip with the CC in an unstretched manner.
18. Note that for imaging with an upright microscope, the CC is not adhered to the coated coverslip (Fig. 2b). For this preparation, the tension in the connective is not only essential for straightening the GFs but also for stability during imaging. For this preparation, it should also be ensured under the stereo microscope that the view of the CC will not be obstructed during imaging by very long nerve bundles emanating laterally from the connective. Instead of removing them, since it may damage the CC, their tips, if they are long enough, should be adhered to the coverslip.
19. Increasing saline volume aids in increasing the longevity of the preparation and is more resistant to temperature changes during imaging, which alters axonal transport [11–14]. We found that the intact CNS with minimal damage to the glial sheath is viable for imaging for at least 60 min after dissection. While not

necessary, *Drosophila* saline may be perfused with oxygen or changed multiple times to further increase the longevity of the preparation; however, we recommend to image the specimen as soon as possible after dissection.

20. In general, any type of objective can be used as long as it allows to determine the localization of the CC in the connective.
21. Parameters for optimal live imaging will need to be empirically determined for each cargo, since they depend on the type of the fluorophore, expression strength of the fluorophore, type of organelle, and the velocity of organelle to be imaged.
22. For live imaging the 60–100× objective should have a minimum of 1.1 NA, while a higher NA is preferred for improved resolution. Since oil objectives typically have a higher NA than equivalent water immersion objective, live imaging with an inverted confocal is superior for imaging of high velocity small vesicles. While larger ROIs can be selected, smaller ROIs allow for a faster image acquisition rate, which is essential for live imaging of fast-moving organelles.
23. Note that only the relative flux of antero- and retrograde organelles in the imaged plane can be analyzed, not the actual total numbers of organelles within the GFs, since not the entire diameter of the GF axons are imaged. In addition, some vesicles (small in size or low in fluorescence intensity) seen in videos often cannot be resolved from background fluorescence in kymographs.

References

1. Brady ST, Morfini GA (2017) Regulation of motor proteins, axonal transport deficits and adult-onset neurodegenerative diseases. Neurobiol Dis 105:273–282. https://doi.org/10.1016/j.nbd.2017.04.010
2. Millecamps S, Julien JP (2013) Axonal transport deficits and neurodegenerative diseases. Nat Rev Neurosci 14(3):161–176. https://doi.org/10.1038/nrn3380
3. Vagnoni A, Bullock SL (2016) A simple method for imaging axonal transport in aging neurons using the adult *Drosophila* wing. Nat Protoc 11(9):1711–1723. https://doi.org/10.1038/nprot.2016.112
4. Penserga T, Kudumala SR, Poulos R, Godenschwege TA (2019) A role for *Drosophila* amyloid precursor protein in retrograde trafficking of L1-type cell adhesion molecule Neuroglian. Front Cell Neurosci 13:322. https://doi.org/10.3389/fncel.2019.00322
5. Ramaker JM, Cargill RS, Swanson TL, Quirindongo H, Cassar M, Kretzschmar D, Copenhaver PF (2016) Amyloid precursor proteins are dynamically trafficked and processed during neuronal development. Front Mol Neurosci 9:130. https://doi.org/10.3389/fnmol.2016.00130
6. Torroja L, Chu H, Kotovsky I, White K (1999) Neuronal overexpression of APPL, the *Drosophila* homologue of the amyloid precursor protein (APP), disrupts axonal transport. Curr Biol 9(9):489–492. https://doi.org/10.1016/s0960-9822(99)80215-2
7. Boerner J, Godenschwege TA (2011) Whole mount preparation of the adult *Drosophila* ventral nerve cord for giant fiber dye injection. J Vis Exp 52:3080. https://doi.org/10.3791/3080
8. Kudumala SR, Penserga T, Borner J, Slipchuk O, Kakad P, Lee LH, Qureshi A, Pielage J, Godenschwege TA (2017) Lissencephaly-1 dependent axonal retrograde transport of L1-type CAM Neuroglian in the adult *Drosophila* central nervous system. PLoS

One 12(8):e0183605. https://doi.org/10.1371/journal.pone.0183605

9. Namiki S, Dickinson MH, Wong AM, Korff W, Card GM (2018) The functional organization of descending sensory-motor pathways in *Drosophila*. Elife 7:e34272. https://doi.org/10.7554/eLife.34272
10. Pfeiffer BD, Jenett A, Hammonds AS, Ngo TT, Misra S, Murphy C, Scully A, Carlson JW, Wan KH, Laverty TR, Mungall C, Svirskas R, Kadonaga JT, Doe CQ, Eisen MB, Celniker SE, Rubin GM (2008) Tools for neuroanatomy and neurogenetics in *Drosophila*. Proc Natl Acad Sci U S A 105(28):9715–9720. https://doi.org/10.1073/pnas.0803697105
11. Brimijoin S, Olsen J, Rosenson R (1979) Comparison of the temperature-dependence of rapid axonal transport and microtubules in nerves of the rabbit and bullfrog. J Physiol 287:303–314. https://doi.org/10.1113/jphysiol.1979.sp012660
12. Forman DS, Padjen AL, Siggins GR (1977) Effect of temperature on the rapid retrograde transport of microscopically visible intra-axonal organelles. Brain Res 136(2):215–226. https://doi.org/10.1016/0006-8993(77)90799-5
13. Grafstein B, Forman DS, McEwen BS (1972) Effects of temperature on axonal transport and turnover of protein in goldfish optic system. Exp Neurol 34(1):158–170. https://doi.org/10.1016/0014-4886(72)90196-3
14. Zhang K, Osakada Y, Vrljic M, Chen L, Mudrakola HV, Cui B (2010) Single-molecule imaging of NGF axonal transport in microfluidic devices. Lab Chip 10(19):2566–2573. https://doi.org/10.1039/c003385e
15. Kelly SM, Elchert A, Kahl M (2017) Dissection and immunofluorescent staining of mushroom body and photoreceptor neurons in adult *Drosophila* melanogaster brains. J Vis Exp 129. https://doi.org/10.3791/56174
16. Sweeney ST, Hidalgo A, de Belle JS, Keshishian H (2011) Dissection of adult *Drosophila* brains. Cold Spring Harb Protoc 2011(12):1472–1474. https://doi.org/10.1101/pdb.prot066878
17. Tito AJ, Cheema S, Jiang M, Zhang S (2016) A simple one-step dissection protocol for whole-mount preparation of adult *Drosophila* brains. J Vis Exp 118:55128. https://doi.org/10.3791/55128

Chapter 23

Drosophila Primary Neuronal Cultures as a Useful Cellular Model to Study and Image Axonal Transport

André Voelzmann and Natalia Sanchez-Soriano

Abstract

The use of primary neuronal cultures generated from *Drosophila* tissue provides a powerful model for studies of transport mechanisms. Cultured fly neurons provide similarly detailed subcellular resolution and applicability of pharmacology or fluorescent dyes as mammalian primary neurons. As an experimental advantage for the mechanistic dissection of transport, fly primary neurons can be combined with the fast and highly efficient combinatorial genetics of *Drosophila*, and genetic tools for the manipulation of virtually every fly gene are readily available. This strategy can be performed in parallel to in vivo transport studies to address relevance of any findings. Here we will describe the generation of primary neuronal cultures from *Drosophila* embryos and larvae, the use of external fluorescent dyes and genetic tools to label cargo, and the key strategies for live imaging and subsequent analysis.

Key words Live imaging, Axonal transport, Drosophila primary neurons, Motors, Organelles, Mitochondria, Kinesin, Dynein, Lysotracker, Mitotracker

1 Introduction

Neurons extend axons to communicate and innervate all parts of the body. Axons are the longest cellular protrusions, with motor neurons reaching up to a meter in humans. Axons predominantly form output synapses which are in their majority located at the distant end of the axon. The extreme spatial separation between synaptic terminals and the neuronal cell body or soma poses a logistical problem in that soma-derived proteins, RNAs, lipids, and organelles crucial for the sustainability and function of axons and their synapses need to be transported over large distances [1–3].

Supplementary Information The online version of this chapter (https://doi.org/10.1007/978-1-0716-1990-2_23) contains supplementary material, which is available to authorized users.

Alessio Vagnoni (ed.), *Axonal Transport: Methods and Protocols*,
Methods in Molecular Biology, vol. 2431, https://doi.org/10.1007/978-1-0716-1990-2_23,
© The Author(s) 2022

Long-distance axonal transport involves the coordinated action of motor proteins binding directly or indirectly (through adaptors) to the transported cargoes while walking along microtubules [2, 4–6]. For this, axonal microtubules are arranged into loose parallel bundles that run all along the axon shaft [7, 8]. Motor proteins involved in long-distance axonal transport use ATP as energy source to step along microtubules; they include dynein/dynactin responsible for retrograde movements and certain members of the kinesin family for anterograde transport (kinesin-1, −2, −3, −4 [3, 9, 10]). Apart from antero- and retrograde cargo transport, this system must also ensure the controlled release, hence delivery, of cargoes at the appropriate target sites [11, 12].

It is not surprising that many neurodegenerative diseases are linked to genetic defects in this transport machinery, thus highlighting the importance of this process for neuronal function and viability [5, 13]. Decrease in axonal transport is also considered as a widespread aging hallmark [14]. It is therefore pivotal to understand the transport machinery, its regulatory mechanisms, and the consequence of its dysfunction.

Despite the recent advances in understanding the mechanism of fast axonal transport (e.g., [15–18]), there are numerous unresolved issues in relation to the regulation of speed, directionality, selectivity of transport, targeted unloading of cargoes, and adaptation of transport to the specific cellular demands. Such complex regulatory processes are likely to involve the specific compositions of motor protein complex (e.g., type of motor protein and cargo adaptors [19, 20]), the interaction between different complexes and with other classes of microtubule binding proteins [2, 21, 22], posttranslational modifications (PTMs) of these complexes or of their microtubule tracks mediated by the orchestrating action of signaling pathways [23].

A powerful model to study transport mechanisms in its complexity is the fruit fly *Drosophila melanogaster*, which has been used for this purpose for more than two decades (e.g., [24–29]). The fundamental function and structure of *Drosophila* and vertebrate neurons is comparable [30–34], including the organization and regulation of microtubules which follow similar organizational principles as in vertebrates, in spite of the fact that neurofilaments are absent [8]. Furthermore, most motor proteins have counterparts in *Drosophila*, but there is less redundancy: while around 40 genes encode members of the kinesin super-family in vertebrates [35], only 18 kinesin coding genes cover a similar range of motor protein classes in *Drosophila* [3]. For example, kinesin light chain comprises three mouse members, but only one in *Drosophila* [3]. In addition, an arsenal of genetic tools for the manipulation of virtually every fly gene is readily available or can be efficiently generated through genomic engineering, and they can be easily targeted to

specific neurons or combined to generate loss or gain of function of different genes or tools in the same neurons or organisms [36–38].

In its majority, research in *Drosophila* neurons makes use of in vivo studies in the whole organism. However, also the use of cultured *Drosophila* primary neurons, first used half a century ago (e.g., [39, 40]) has proven a valuable complementary strategy. As is the case for mammalian primary neurons, also fly neurons give access to subcellular detail and robust and sensitive readouts and are accessible to external application of compounds such as fluorescent dyes and drugs [41–45]. Importantly, many of the observed subcellular features and dynamics are very similar to those of vertebrate neurons [46]. However, as an important advantage, primary fly neurons are accessible to the powerful combinatorial genetics mentioned above: as long as genetically manipulated embryos can generate neurons, these can be analyzed in culture. Accordingly, primary *Drosophila* neuronal cultures have been used to successfully study various different aspect of neuronal physiology [47, 48], including cell division [49], axon guidance [50–52], cytoskeletal dynamics [41, 42, 53–59], neuronal activity [60, 61], protein aggregation in neurodegenerative disease models [62], receptor signaling and trafficking [44, 52] and for the study of axonal transport [43, 63, 64]. In this method paper, we will explain primary neuronal cultures from *Drosophila* as cellular system where axonal transport can be studied efficiently.

2 Materials

1. *Drosophila* specimens: primary neuronal cultures can be performed from *Drosophila* embryos [65], late instar L3 larva [53], and late pupa [66] (*see* **Note 1**).
2. Sodium hypochlorite solution (or household bleach), diluted 1:1 with water to 50%.
3. Ultrafine sieves and brushes for the collection and cleaning of embryos.
4. Agar plates: dissolve 2–4% agar in water, boil, pour into empty plastic petri dishes (50 mm diameter), let cool down and harden.
5. 70% Ethanol in ultrapure (Milli-Q) autoclaved water.
6. Supplemented Schneider's medium pH 6.8–7.0: Combine Schneider's *Drosophila* medium with 20% non-heat-inactivated FBS. Filter-sterilize and protect from light with aluminum foil. To inactivate the serum's complement system, incubate for 3 days at 26 °C (alternatively use heat-inactivated FBS and skip the 3 days incubation at 26 °C). Add 2 μg/mL insulin (2 mg/mL insulin stock can be aliquoted and kept at −20 °C).

Use a small aliquot of medium to test the pH and adjust to 6.8–7.0 with 1 N HCl or NaOH if needed. Aliquots of 1–2 mL medium can be stored at −80 °C for 6 months. After thawing aliquots for use, filter-sterile with a 0.22-μm syringe filter and freshly add 10 U Penicillin/Streptomycin per mL medium.

7. HBSS buffer: 30 mL 10 × Hanks' Balanced Salt Solutions (GIBCO, no calcium or magnesium), 3 mL Penicillin/Streptomycin (GIBCO, 10,000 U/mL), 167 mL distilled water, 0.01 g phenylthiourea; aid to dissolve by incubating at 37 °C for 30 min, sterile filter with 0.22-μm filter. This buffer can be stored in aliquots at 4 °C for 6 months.
8. Dispersion or dissociation medium: dissolve 0.005 mg Dispase II and 0.001 mg Collagenase type V in 2 mL HBSS medium. Incubate at 37 °C for 30 min until dissolved. Filter through a 0.22-μm filter and store at 4 °C. It can be used for up to a week.
9. Pestles: small autoclavable plastic pestles for 1.5-mL microcentrifuge tubes with a tight fit.
10. Custom-made culture chambers or 35-mm glass bottom dishes (MatTek) to grow primary neurons: culture chambers can be assembled from one lead-free glass microscope slide (Menzel Gläser) with a 15-mm hole (custom-made at a workshop) and one intact slide glued together with aquarium silicone. Dry (up to 5 days) and scrape off any excess silicone. Clean with 70% ethanol followed by 100% acetone. The chambers can be reused after cleaning with acetone and autoclaving. Alternatively, use 35-mm glass bottom dishes (for example, from MatTek) with optical quality glass for microscopy. While incubation chambers and glass bottom plates can be used with inverted microscopes, incubation chambers are ideal for upright microscopes.
11. 4× concanavalin A stock solution: in a laminar flow hood, dissolve concanavalin A (conA) in ultrapure autoclaved water to a concentration of 20 μg/mL. This stock solution can be frozen in aliquots at −20 °C.
12. Treated coverslips: *Drosophila* primary neurons can grow on acetone-treated or conA-coated glass coverslip (Menzel Gläser, 24 × 24 mm, VWR international MENZBB024024A123). For acetone treatment, dip coverslips in 100% acetone, let dry and autoclave. For conA treatment, incubate coverslips with 150 μL conA at a concentration of 5 μg/mL at 37 °C for 1.5 h. Remove conA solution, wash with 150 μL sterile water, remove and dry at ~50 °C overnight. Note that the morphology of neurons changes when growing on conA [65]. When using glass bottom dishes for live imaging, treat the glass coverslip that is attached to the bottom of the dish.
13. Vaseline for sealing chambers/dishes with coverslips.

14. 100 nM LysoTracker DND-99/50 nM MitoTracker Green FM/CMXRos in supplemented Schneider's medium.
15. Fixatives: We carry out standard fixations in 4% paraformaldehyde in 0.1 M phosphate buffer (pH 7.2). To prepare 100 mL fixative, dissolve 4 g paraformaldehyde in 36 mL 0.2 M NaH_2PO_4 (warm up slightly and stir), add 14 mL 0.2 M NaH_2PO_4, and fill up with water. Adjust pH if necessary.
16. PBT: 0.3% Triton X-100 (v/v) in 1× PBS.

3 Methods

3.1 Drosophila *Embryonic Primary Neuronal Cultures (Fig. 1a–d)*

Drosophila primary neuronal cultures can be prepared from several developmental stages (embryo, larva, and pupa) [65]. In this chapter, we will discuss our protocol for primary neuronal cultures derived from whole embryos or third instar larval CNSs, in which our transport studies have been performed (Figs. 1 and 2).

1. Collect embryos (Fig. 1A.1) in vials or cages for ~15 h at 20–25 °C (the temperature can be adapted to increase the yield of stages 11–12 embryos [67], *see* **Notes 1** and **2**).
2. Dechorionate embryos (Fig. 1A.2) with 50% bleach for 90 s. Wash thoroughly with water in a sieve. Note that extended incubations as well as the quality of the bleach can affect the viability of the cultures. Carefully collect embryos with a thin paint brush from the sieve and transfer them to an agar plate.
3. Select stages 11–12 embryos (Fig. 1A.3) by autofluorescence pattern (for embryo stages *see* [67]; *see* **Note 3 a–c**). If mutant *Drosophila* stocks are used (with adequate GFP-balancers), mutant embryos can now be selected based in the absence of GFP, using a fluorescent dissection microscope. For cultures on acetone-treated glass coverslip select 10 embryos per culture (the number of embryos can be altered to achieve different densities of neurons in culture). For cultures on conA-coated glass coverslip select five embryos per culture.
4. Transfer the embryos (Fig. 1b.4, 5) into a 1.5-mL tube with a 5 μL drop of supplemented Schneider's medium using clean forceps (with 70% ethanol). From this point on the next steps will be performed in a laminar flow hood wearing gloves and with autoclaved materials whenever possible.
5. Wash the embryos (Fig. 1b.4, 5) with 70% ethanol solution for 30 s by gently inverting the tube several times.
6. Remove ethanol and wash embryos in 500 μL supplemented Schneider's medium (Fig. 1b.6). Take care not to accidentally pipette the embryos. Pipetting against a black background can help to visualize the embryos.

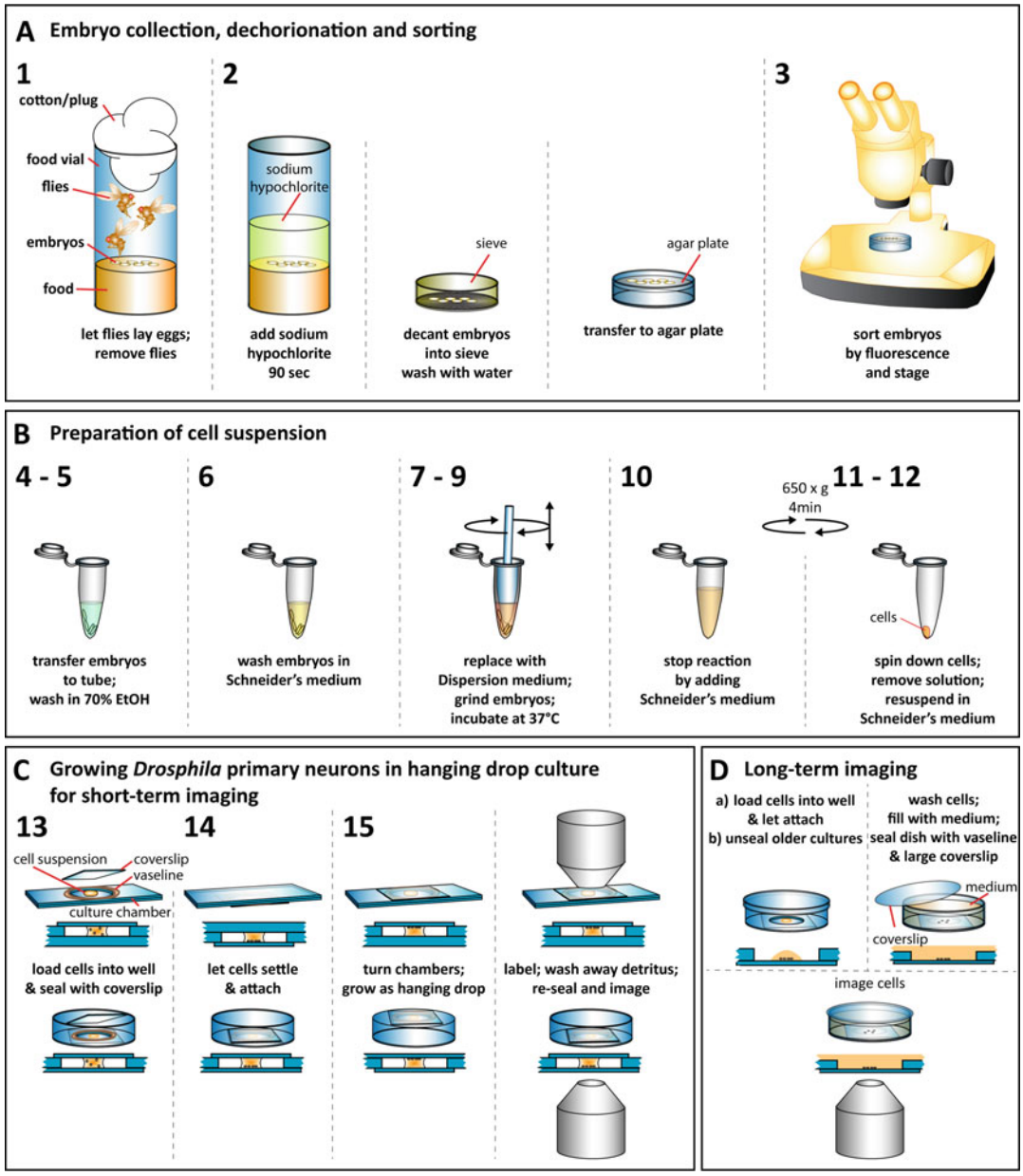

Fig. 1 Workflow to generate *Drosophila* primary neuronal cultures for short- and long-term imaging. The numbers in the figure correspond to the protocol steps in Subheading 3.3. (**a**) Diagram showing the steps for embryo collection, removal or the chorion, and selection of embryos for primary neuronal cultures. (**b**) Diagram showing the main steps to generate a suspension of primary cells from *Drosophila* embryos. Note that the protocol can be modified to use late stage 3 larval brains as well (*see* Subheading 3.3 for more detail). (**c**) Diagram showing the hanging drop culturing technique. *Drosophila* primary cells are allowed to attach to coverslips before inverting the sealed culture chambers (upper row)/glass bottom dishes (lower row). Cells are then grown the desired time in vitro (hours to days). Cultures can optionally be incubated with drugs and/or dye-based organelle/vesicle markers before medium is exchanged for imaging. (**d**) For long-term imaging, cells can be allowed to either (**a**) directly attached to coated or uncoated glass bottom dishes or (**b**) grown as hanging drop cultures in glass bottom dishes, then unsealed and Vaseline removed (*see* **c**). Cells can then be treated with drugs and/or dye-based organelle/vesicle labels. The dish is then filled up with Schneider's medium and sealed with a coverslip to prevent evaporation of the medium during long-term imaging

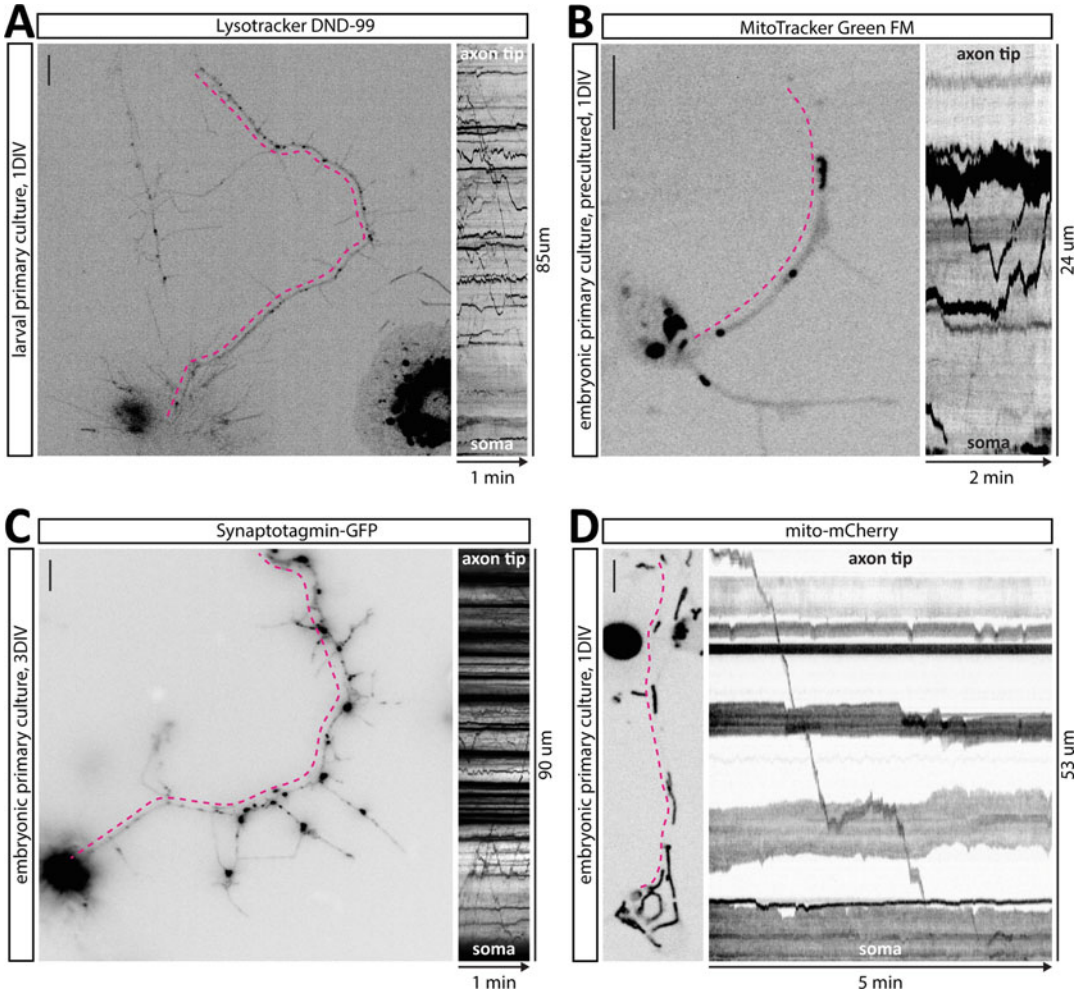

Fig. 2 Transport of vesicles and organelles in *Drosophila* primary neuronal cultures. Single frame from time-lapse movies from *Drosophila* primary neuronal cultures showing different labeled cargo (cell bodies are at the bottom of the image), and kymograph plot showing the trajectory of cargoes. (**a**) Larval primary cultures treated with the dye-based fluorescent label LysoTracker DND-99. (**b**–**d**) Embryonic primary neuronal cultures (**b**) treated with the dye-based fluorescent label MitoTracker Green FM, (**c**) expressing Synaptotagmin-GFP using the tubulin-Gal4 driver, and (**d**) expressing mito-mCherry using the elav-Gal4 driver. Magenta dashed lines mark the axon. Panels on the right in (**a**–**d**) show corresponding kymographs. Lines with positive slopes in kymographs indicate anterograde transport, lines with negative slopes retrograde transport, and horizontal lines indicate stationary objects. Scale bar in overview images is 5 μm in length

7. Replace Schneider's medium with 100 μL HBSS-based dispersion medium at RT (Fig. 1b.7–9; *see* **Note 4**).
8. Grind embryos in the tube with an autoclaved pestle to break down the embryos (Fig. 1b.7–7), use one pestle per genotype (*see* **Note 5**). At this step, there is the option to add a preculture step to reduce maternal contribution of proteins or allow for extra time for knockdowns to work (*see* Subheading 3.2).

9. Incubate the tubes with the cell dispersion for 4–7 min at 37 °C (Fig. 1b.7–9). **OPTION**: This step can be omitted leading to neurons with more complex morphologies and less isolated single neurons.
10. Stop the dispersion reaction by removing from 37 °C and adding 200 μL of supplemented Schneider's medium (Fig. 1b.10).
11. Sediment cells at 600–750 × *g* for 4 min (Fig. 1b.11, 12). Remember the orientation of the tube during centrifugation since it may be difficult to see the pellet.
12. Aspirate and discard the medium (Fig. 1b.11, 12). Make sure this step is performed promptly to avoid cell pellets resuspending in the old medium. Add 31 μL of fresh supplemented Schneider's medium per culture/chamber. Adjust volume depending on the final number of cultures (we usually prepare three cultures per condition at a time). Gently resuspend cells in Schneider's medium without generating bubbles.
13. Distribute 30 μL cell suspension either to glass bottom dishes (treated with acetone or coated with conA) and cover with a regular coverslip using Vaseline as sealant or to custom-made culture chambers and cover with a lead-free coverslips (treated with acetone or coated with conA) and seal with Vaseline (Fig. 1c.13). Note that the morphology of neurons changes when growing on conA [65].
14. Let the cells settle onto the acetone or conA treated surfaces for 2 h at 26 °C (Fig. 1c.14).
15. Flip over the incubation chambers/glass bottom dishes and grow primary neurons on top of the chamber as hanging drop cultures (Fig. 1c.15) until the desired time in vitro has been reached (*see* **Note 6**).

3.2 *Pre-culture Step for* Drosophila *Embryonic Primary Neuronal Cultures*

Cells can be cultured in a 1.5-mL tube for several days before being dispersed again and grown on coverslips in culture chambers. This step is useful in order to deplete healthy gene product deposited by heterozygous mothers in the egg cells (which otherwise carry mutations in a specific gene). Maternally contributed gene products can persist for several days and mask the homozygous mutant phenotype of embryos and larvae [68]. This step is also effective in allowing extra time for conditions of knockdowns.

1. Follow **steps 1–8** of Subheading 3.1. For this protocol, increase the number of embryos to 15 per slide and use ConA-coated coverslip.
2. After grinding the embryos, immediately add 200 μL of supplemented Schneider's medium.
3. Sediment cells at 600–750 × *g* for 4 min.

4. Aspirate the medium. Add 100 μL of fresh supplemented Schneider's medium, gently resuspend cells, and incubate in the tube for the desired time at 26 °C (1–7 days).
5. After the incubation, sediment cells at 600–750 × *g* for 4 min.
6. Aspirate Schneider's medium and add 100 μL HBSS-based dispersion medium.
7. Gently resuspend the cell pellet and incubate 4–7 min at 37 °C.
8. Continue from **step 10** of Subheading 3.1.

3.3 Third Instar Larval Brain Cultures

1. Collect 2–3 late stage 3 larvae per culture.
2. Wash larvae 3× in in 1.5 mL 70% ethanol.
3. Wash larvae 3× in 1.5 mL sterile PBS.
4. Transfer larvae into a sterile dissection dish with supplemented Schneider's medium.
5. Dissect out brains (use sterile forceps) and transfer to a 1.5-mL tube with supplemented Schneider's medium.
6. All following steps should be done in a laminar flow hood.
7. Wash brains 3× in 500 μL supplemented Schneider's medium.
8. Remove medium and replace with 100 μL dispersion medium.
9. Continue from **step 8** of Subheading 3.1.

3.4 Labeling of Cargo

The use of primary neuronal cultures to study transport allows the labeling of cargo by (a) genetically encoded tools, mostly tagged proteins or localization sequences fused with GFP or other fluorophores and (b) fluorescent chemical compounds applied to the culture media such as LysoTracker, fluoro-dextranes, and mitotracker. Here we describe the methods and tools we have been experimenting with. However, there is an arsenal of further tools that can be used to label specific cargo, such as dense-core vesicle labeled with atrial natriuretic factor-GFP (ANF-GFP), APP-positive vesicles labeled with App-YFP, Golgi vesicles labeled with GalT-RFP, endosomes labeled with Rab4-RFP, and ribonucleoprotein granules labeled with GFP-Imp to mention some [26, 29, 69].

3.4.1 LysoTracker Staining (See **Note 7**)

LysoTracker is a fluorescent probe which, due to its hydrophobic nature, diffuses into cells, and preferentially accumulates in vesicles with an acidic content. It is commonly used in vertebrate models to label late endosomes/lysosomes and to study their trafficking within cells including neurons [70–74]. LysoTracker has been used previously to label lysosomes/late endosomes in *Drosophila* primary neuronal cultures [75], *Drosophila* tissue, and cells lines [76]. Here we will describe its use in *Drosophila* primary neuronal culture (Fig. 2a, Supplementary Movie 1). Using this method, we

find LysoTracker-positive vesicles move at ~0.6–0.9 μm/s in either direction (compared to reported average speeds for lysotracker vesicles between 0.34 μm/s and 1.2 μm/s in vertebrate neurons) [77].

1. Follow Subheadings 3.1–3.3. for the generation of *Drosophila* primary neuronal cultures.
2. Prepare supplemented Schneider's medium with 100 nM LysoTracker DND-99.
3. Shortly before use, spin down solution to remove any precipitates that might have formed and could affect imaging.
4. When cells have reached the desired maturity (*see* **Note 8**), detach the coverslips from the culture chambers or glass bottom dish and wash the cells (they will be attached to the coverslips if using culture chambers or at the bottom of the glass bottom dish) and culture chambers in supplemented Schneider's medium with 100 nM LysoTracker DND-99.
5. Remove all medium and add 50–60 μL supplemented Schneider's medium with 100 nM LysoTracker DND-99 to the culture chambers/glass bottom dishes.
6. Reseal the culture chambers/glass bottom dishes with the same coverslip, a new Vaseline seal may be required.
7. Incubate for 15 min at the desired temperature.
8. Replace labeling solution with 50–60 μL label-free supplemented Schneider's medium.
9. Let cells adjust to the condition in the imaging chamber for 15 min and proceed to image the cells.

3.4.2 MitoTracker Staining

Mitochondria can be labeled by both fluorescent mitochondrial dyes including MitoTracker and genetically encoded fluorescently tagged mitochondrial proteins or tagged mitochondria-targeting sequences (such as mito-GFP [78], mito-mCherry [69]). MitoTracker is a fluorescent dye which covalently binds free sulfhydryls. It is frequently used for transport studies in vertebrate neurons [73, 79, 80], and some MitoTracker variants have previously been used in *Drosophila* tissue and in *Drosophila* cell lines to label mitochondria [81]. We experienced that MitoTracker dyes in *Drosophila* primary neuronal cultures can diminish mitochondrial dynamics slightly, as has similarly been reported for rat hippocampal neurons [82]. Nonetheless, MitoTracker easily and reliably labels mitochondria in cultured neurons, and in our studies, it is instrumental in determining the number and distribution of mitochondria at the axon, cell body, and synaptic terminals in fixed samples [43]. Here we will describe how we use MitoTracker (Fig. 2b, Supplementary Movie 2), before explaining the use of genetically encoded fluorescently tagged mitochondrial proteins in the next section.

1. Follow Subheadings 3.1–3.3. for the generation of *Drosophila* primary neuronal cultures.
2. Prepare supplemented Schneider's medium with 50 nM MitoTracker Green FM or CMXRos (note that not all MitoTracker variants will be retained after fixation).
3. Shortly before use, spin down solution to remove any precipitates that might affect the imaging.
4. Once primary neuronal cultures from the desired genotype have reached the preferred developmental stage, detach the coverslips from the culture chambers or glass bottom plates and wash the cells (they will be attached to the coverslips if using culture chambers or at the bottom of the glass bottom plates) and culture chambers in supplemented Schneider's medium with 50 nM MitoTracker Green FM/CMXRos.
5. Remove all medium and add again 50–60 μL supplemented Schneider's medium with 50 nM MitoTracker Green FM/CMXRos. Be careful as the coverslips are prone to break.
6. Replace Vaseline and reseal the culture chambers/glass bottom plates back.
7. Incubate for 15 min.
8. Remove medium and replace with regular supplemented Schneider's medium.
9. Proceed to imaging. **OPTION**: MitoTracker CMXRos-labeled cultures can be fixed by following the steps below.
10. Prewarm the standard fixative to RT. With a black permanent pen, mark the region of the culture drop on the non-cell side of the coverslip. Remove the coverslip from culture chamber and position on a piece of plasticine or a rubber block with the cells facing up in a humid chamber. If glass bottom dishes are used, detach the coverslips from the culture chambers and proceed to **step 8**.
11. Add 100–200 μL of 4% paraformaldehyde to the cells. Close the humid chamber and incubate for 30 min.
12. Remove fixative and discard adequately, wash the cultures three times with PBT. MitoTracker can be combined with immunocytochemistry, using standard protocols [83].

3.4.3 Genetically Encoded Cargo Markers (e.g., Synaptotagmin-GFP and Mito-GFP/mCherry)

Genetically encoded fluorescent tools are particularly useful to examine the dynamics of motile organelles and transport vesicles in neurons and have been used to this end during decades in vivo and in vitro studies and in various organisms including rodents, zebrafish, *Drosophila*, and *C. elegans* [84–87]. *Drosophila* examples of such tools include synaptic vesicle proteins such as GFP-fused Synaptotagmin, Synaptobrevin, and Synaptogyrin to label synapses

and synaptic transport, tagged Ras-associated binding GTPases, and Autophagy-related proteins to label endosomes and autophagosomes, respectively, and mitochondrial targeting sequences fused to fluorescent proteins (e.g., mito-GFP) to label mitochondria [43, 44, 64, 88, 89]. We have used primary cultures derived from transgenic *Drosophila* embryos expressing mito-GFP/mCherry, Synaptobrevin-GFP, and Synaptotagmin-GFP using the UAS/-Gal4 system to study the impact mutations in microtubule regulators such as Tau and spectraplakins [43] and α1-tubulin84B have on axonal transport. Here we will describe how we use genetically encoded cargo markers (*see* **Note 9**), for example, *see* Fig. 2c, d; Supplementary Movies 3 and 4. Using this method, we find Synaptotagmin-positive vesicles move at a velocity of about 1.0–1.9 μm/s.

1. Generate *Drosophila* primary neuronal cultures (Subheadings 3.1–3.3) from embryos or larvae expressing the genetically encoded cargo marker in the desired genetic background (*see* **Note 10** for suitable drivers and transfection options).
2. Once primary neuronal cultures have reached the adequate developmental stage, detach the coverslips from the culture chambers or glass bottom dishes, and wash the cells (they will be attached to the coverslips if using culture chambers or at the bottom of the glass bottom plates) and culture chambers in supplemented Schneider's medium (~60 μL). Be careful as the coverslips are prone to break. This step is important to remove debris from the cultures which may interfere with live imaging.
3. Remove all medium without disturbing the cells and add 50–60 μL fresh supplemented Schneider's medium to the chamber/dish.
4. Re-apply new Vaseline if needed and place the coverslip back in place.
5. Let the cells adjust to the imaging conditions for 30 min in the environmental chamber attached to the microscope.

3.5 Live Imaging of Neuronal Transport

Imaging neuronal transport is a delicate balancing act between sufficiently high resolution to visualize small vesicles, short exposure times to allow visualization of fast neuronal transport events and minimize exposure to avoid photo-cytotoxic effects and photobleaching. We make use of spinning disk microscopy as the systems have been specifically developed to reduce phototoxicity while providing high sensitivity.

1. Image neurons using a spinning disk confocal (SDC) microscope with environmental chamber and at least 60× magnification objective (or equivalent equipment with good sensitivity and signal to noise ratio). Ideally, set the environmental

chamber to the same conditions as the primary neurons were cultured at.

2. Use a microscope with automated z-focus control (e.g., Definite Focus system or similar), which is highly advantageous as any focus drift could shift vesicles/organelles out of focus and prevent successful tracking of their movement (*see* **Note 11**).
3. Use either eye piece widefield fluorescence, phase contrast, or SDC imaging to locate suitable cells.
4. Make sure to take note of the position of the cell body and axon/neurite tips for all imaged cells/axons to determine antero- and retrograde directionality.
5. Image with the appropriate timeframes and acquisition intervals, depending on the observed organelle/vesicle speeds, mutant conditions, labels used in the assay, and their intensity during imaging. For LysoTracker, Synaptobrevin-GFP, Synaptotagmin-GFP, and mito-GFP/mCherry, imaging timeframes in the range of 1–5 min at 0.25–1 s intervals have been used successfully. Due to the frequency of events and the slow transport component of mitochondria, imaging intervals might be expanded, and intervals prolonged for the analysis of mitochondrial transport.
6. Adjust the imaging conditions to the moving, not the stationary objects.
7. The number of cells to image depends on the frequency/number of visualized transport events. For the most part we have imaged 10–20 cells per each of the three coverslips, for statistical analysis of organelle/vesicle movements (e.g., Synaptotagmin-GFP, LysoTracker).
8. Process the imaging time series for either direct object tracking or kymograph analyses.

3.6 Analyzing Axonal Transport

1. Process the imaging time series for either direct object tracking (manual tracking plugin for ImageJ, TrackMate [90]) or kymograph generation and analyses (e.g., KymoResliceWide & Velocity measurement [91]; (http://dev.mri.cnrs.fr/projects/imagej-macros/wiki/Velocity_Measurement_Tool) or KymoAnalyzer plugins for ImageJ [92]).
2. Suitable parameters to analyze are: the number of moving objects vs stationary objects, flux (number of moving particles through a defined length of the axon over a set time), directionality of movements (fraction of anterograde vs retrograde movement), average object track velocity (total speed over the whole kymograph track of a moving object including pauses, changes in speed and direction), transport segment velocity (speed calculated for each individual segment of a kymograph

track of a moving object). A new segment within the track is defined each time there are changes in speed or direction of movement), transport run length (average length of a particle's runs), number of pauses per transport track, number of direction switches.

4 Notes

1. Any genetic combination can be used for primary cultures, these can include specimens with specific mutations, and/or expressing fluorescently tagged markers to visualize cargos. In the case of specimens carrying embryonic lethal mutations, the mutant stock will need to be balanced over a balancer chromosome which allows for the selection of mutant stage 11 embryos. For this we use the TwistGal4-UAS-GFP balancers (available in the Bloomington stock centre #6873, #6662, #6663).
2. Collection times must be adapted when changing temperatures. For example, 15 h at 25 °C will favor stage 16 but hardly yield stage 11 embryos, while 15 h at 21–23 °C will be enriched with stage 11 embryos (for stages and precise timing *see* [67]).
3. There are several factors to consider when selecting embryos:
   (a) Embryonic stages 11 would be ideal for primary neuronal cultures, at this stage most neurons in embryos are post-mitotic and are beginning axogenesis [65]. However, depending on the experimental setting, stage 15/16 might be useful, e.g., when the fluorescent signal from specific cargo is too week at younger stages (elav-Gal4-driven expression of synaptic markers is difficult to detect at stage 11).
   (b) When collecting for embryos expressing synaptic markers, select embryos with weak expression as this will facilitate imaging (strongly expressing cells will have more stationary objects that can negatively impact imaging). An inducible expression system and a short expression time might be desirable to reduce the number of labeled stationary objects.
   (c) When collecting mutant embryos against fluorescent balancers, make sure the balancer fluorescence is visible at the desired embryonic stage.
4. When using more embryos/more larval brains, adjust all volumes proportionately after grinding and before incubating at 37 °C in HBSS-based dispersion medium at RT. Do not exceed 100 µL dispersion medium in a 1.5-mL tube for the grinding step as an increased volume can lead to spillage. We

use approximately 100 μL dispersion medium per 15–30 embryos.

5. The grinding step is a key point in the protocol. Make sure to have a tight fit between tube and pestle. Using too much force might adversely affect the cultures though. However, be sure to dissociate all embryos. Any intact embryos will survive, develop into larvae, and disrupt the rest of the cultured cells. An alternative for grinding is to harvest cells from the ventral region of the embryo using a glass capillary and a micromanipulator [65], this method is considerably more laborious but may lead to purer cultures.
6. 26 °C would be the standard incubation temperature for *Drosophila* primary neurons. However, *Drosophila* primary neurons can be cultured at a range of temperatures ranging from 12 to 29 °C. For instance, incubation at 29 °C can boost UAS-Gal4 expression. Make sure controls are incubated at the same temperature. If imaging of the initial outgrowth is required, the seeding and attachment time can be reduced to 30 min. However, to get the same cell density, a 2–3 times increased amounts of embryos will be required.
7. The same protocol can be used to treat neurons with drugs and other live cell imaging fluorescent probes such as SiR-tubulin. We used 50–100 nM SiR-tubulin to label microtubules. Note that the higher end of SiR-tubulin concentrations can have effects on microtubule dynamics. A minimum of 30-min incubation will ensure microtubules are robustly labeled and can optionally be followed by a washing step with supplemented Schneider's medium but is not required, longer incubation will yield stronger labeling. Microtubules can be visualized from 45–50 min onwards. SiR-tubulin labeling of *Drosophila* primary neurons does not require Verapamil treatment. We have successfully visualized neurite outgrowth and development from primary neurons as early as 45 min in vitro up to 22 h in vitro (for long-term imaging setup, *see* Fig. 1d). For this, the cell pellet is resuspended in supplemented Schneider's medium that contains 50 nM SiR-tubulin. Other compounds (e.g., microtubule stabilizers or destabilizers, inhibitors of kinesins, kinases and phosphatases, oxidative stress inducers among others) can be added to the cell culture medium keeping in mind that each drug will need a different incubation time.
8. Axonal transport of synaptic components in *Drosophila* primary neurons can be observed already at 6 h in vitro [43]; however, we frequently image neurons at 2–3 days in vitro, so that synaptic components are robustly established and long-range transport can be observed. Primary neurons cultured from larval brains allow imaging of lysotracker after 1 day in vitro.

9. The same protocol can be used to visualize EB dynamics in neurons. Both expression of EB1-GFP or EB1-mCherry via elav-Gal4 or sca-Gal4 and transfection of neurons with pAc-EB1-mCherry have been successfully used in our laboratories [41, 42, 53, 54].
10. For UAS-Gal4-based expression of fluorescently tagged proteins in primary neuronal cultures, suitable driver lines are: sca-Gal4, elav-Gal4, tubulin-Gal4, nSyb-Gal4. Note that sca-Gal4 expression is strong in young neurons (6HIV) but decreases over time and nSyb-Gal4 is weakly expressing in young neurons but increases over time and can be robustly detected after 2–3 days in vitro (Ines Hahn, personal communication). An alternative to UAS-Gal4-based expression is transfection of neuronal cultures. We find that the actin-promotor in the pAc5.1/V5 vector variants is suitable for the expression of constructs upon transfection of primary neurons (for protocol *see* [54]). Alternatively, Gal4 expressing neurons can be transfected with UAS-constructs.
11. Be aware that due to the neurites/axons/dendrites being dynamic, they might move and leave the focal plane. ConA treatment of coverslips can be an advantage here since it increases the attachment axons.

Acknowledgments

This work was made possible through support by the BBSRC to N.S.S. (BB/M007456/1, BB/R018960/1), A.V. is funded by the BBSRC (BB/M007553/1, awarded to Andreas Prokop). The Bioimaging Facility microscopes (3i Spinning Disk Confocal/Photometrics Primer95B sCMOS camera; Andor Dragonfly Upright/Zyla 4.2 Plus sCMOS) used in this study were purchased with grants from BBSRC, Wellcome and the University of Manchester Strategic Fund. We also acknowledge the ITM Biomedical imaging facility at the University of Liverpool hosting the 3i Marianas spinning disk confocal system used for some at the studies. The Fly Facility has been supported by funds from The University of Manchester and the Wellcome Trust (087742/Z/08/Z). Special thanks go to Peter March and Steven Marsden for their help with the microscopy and to Andreas Prokop, Ryan J. H. West and Ines Hahn for helpful comments on the manuscript.

References

1. Terenzio M, Schiavo G, Fainzilber M (2017) Compartmentalized signaling in neurons: from cell biology to neuroscience. Neuron 96(3): 667–679. https://doi.org/10.1016/j.neuron.2017.10.015
2. Franker MA, Hoogenraad CC (2013) Microtubule-based transport - basic mechanisms, traffic rules and role in neurological pathogenesis. J Cell Sci 126(Pt 11):2319–2329. https://doi.org/10.1242/jcs.115030

3. Prokop A (2013) The intricate relationship between microtubules and their associated motor proteins during axon growth and maintenance. Neural Dev 8(1):17. https://doi.org/10.1186/1749-8104-8-17
4. Hirokawa N, Niwa S, Tanaka Y (2010) Molecular motors in neurons: transport mechanisms and roles in brain function, development, and disease. Neuron 68(4):610–638. https://doi.org/10.1016/j.neuron.2010.09.039
5. Sleigh JN, Rossor AM, Fellows AD, Tosolini AP, Schiavo G (2019) Axonal transport and neurological disease. Nat Rev Neurol 15(12):691–703. https://doi.org/10.1038/s41582-019-0257-2
6. Guedes-Dias P, Holzbaur ELF (2019) Axonal transport: driving synaptic function. Science 366(6462):eaaw9997. https://doi.org/10.1126/science.aaw9997
7. Kevenaar JT, Hoogenraad CC (2015) The axonal cytoskeleton: from organization to function. Front Mol Neurosci 8:44. https://doi.org/10.3389/fnmol.2015.00044
8. Prokop A (2020) Cytoskeletal organization of axons in vertebrates and invertebrates. J Cell Biol 219(7). https://doi.org/10.1083/jcb.201912081
9. Hirokawa N, Noda Y, Tanaka Y, Niwa S (2009) Kinesin superfamily motor proteins and intracellular transport. Nat Rev Mol Cell Biol 10(10):682–696. https://doi.org/10.1038/nrm2774
10. Schiavo G, Greensmith L, Hafezparast M, Fisher EM (2013) Cytoplasmic dynein heavy chain: the servant of many masters. Trends Neurosci 36(11):641–651. https://doi.org/10.1016/j.tins.2013.08.001
11. Horiuchi D, Collins CA, Bhat P, Barkus RV, Diantonio A, Saxton WM (2007) Control of a kinesin-cargo linkage mechanism by JNK pathway kinases. Curr Biol 17(15):1313–1317. https://doi.org/10.1016/j.cub.2007.06.062
12. Guedes-Dias P, Nirschl JJ, Abreu N, Tokito MK, Janke C, Magiera MM, Holzbaur ELF (2019) Kinesin-3 responds to local microtubule dynamics to target synaptic cargo delivery to the Presynapse. Curr Biol 29(2):268–282.e268. https://doi.org/10.1016/j.cub.2018.11.065
13. Guo W, Stoklund Dittlau K, Van Den Bosch L (2020) Axonal transport defects and neurodegeneration: molecular mechanisms and therapeutic implications. Semin Cell Dev Biol 99:133–150. https://doi.org/10.1016/j.semcdb.2019.07.010
14. Mattedi F, Vagnoni A (2019) Temporal control of axonal transport: the extreme case of organismal ageing. Front Cell Neurosci 13:393. https://doi.org/10.3389/fncel.2019.00393
15. Hill SE, Colón-Ramos DA (2020) The journey of the synaptic autophagosome: a cell biological perspective. Neuron 105(6):961–973. https://doi.org/10.1016/j.neuron.2020.01.018
16. Corradi E, Dalla Costa I, Gavoci A, Iyer A, Roccuzzo M, Otto TA, Oliani E, Bridi S, Strohbuecker S, Santos-Rodriguez G, Valdembri D, Serini G, Abreu-Goodger C, Baudet ML (2020) Axonal precursor miRNAs hitchhike on endosomes and locally regulate the development of neural circuits. EMBO J 39(6):e102513. https://doi.org/10.15252/embj.2019102513
17. Cheng X-T, Sheng Z-H (2021) Developmental regulation of microtubule-based trafficking and anchoring of axonal mitochondria in health and diseases. Dev Neurobiol 81(3):284–299. https://doi.org/10.1002/dneu.22748
18. Zhao J, Fok AHK, Fan R, Kwan P-Y, Chan H-L, Lo LH-Y, Chan Y-S, Yung W-H, Huang J, Lai CSW, Lai K-O (2020) Specific depletion of the motor protein KIF5B leads to deficits in dendritic transport, synaptic plasticity and memory. eLife 9:e53456. https://doi.org/10.7554/eLife.53456
19. Maday S, Twelvetrees Alison E, Moughamian Armen J, Holzbaur Erika LF (2014) Axonal transport: cargo-specific mechanisms of motility and regulation. Neuron 84(2):292–309. https://doi.org/10.1016/j.neuron.2014.10.019
20. Verhey KJ, Hammond JW (2009) Traffic control: regulation of kinesin motors. Nat Rev Mol Cell Biol 10(11):765–777. https://doi.org/10.1038/nrm2782
21. Kelliher MT, Saunders HAJ, Wildonger J (2019) Microtubule control of functional architecture in neurons. Curr Opin Neurobiol 57:39–45. https://doi.org/10.1016/j.conb.2019.01.003
22. Harterink M, Edwards SL, de Haan B, Yau KW, van den Heuvel S, Kapitein LC, Miller KG, Hoogenraad CC (2018) Local microtubule organization promotes cargo transport in C. elegans dendrites. J Cell Sci 131(20):jcs223107. https://doi.org/10.1242/jcs.223107
23. Gibbs KL, Greensmith L, Schiavo G (2015) Regulation of axonal transport by protein kinases. Trends Biochem Sci 40(10):597–610. https://doi.org/10.1016/j.tibs.2015.08.003

24. Gindhart JG Jr, Desai CJ, Beushausen S, Zinn K, Goldstein LSB (1998) Kinesin light chains are essential for axonal transport in drosophila. J Cell Biol 141(2):443–454. https://doi.org/10.1083/jcb.141.2.443
25. Reis GF, Yang G, Szpankowski L, Weaver C, Shah SB, Robinson JT, Hays TS, Danuser G, Goldstein LS (2012) Molecular motor function in axonal transport in vivo probed by genetic and computational analysis in drosophila. Mol Biol Cell 23(9):1700–1714. https://doi.org/10.1091/mbc.E11-11-0938
26. Weiss KR, Littleton JT (2016) Characterization of axonal transport defects in drosophila huntingtin mutants. J Neurogenet 30(3–4): 212–221. https://doi.org/10.1080/01677063.2016.1202950
27. Vijayakumar J, Perrois C, Heim M, Bousset L, Alberti S, Besse F (2019) The prion-like domain of drosophila imp promotes axonal transport of RNP granules in vivo. Nat Commun 10(1):2593. https://doi.org/10.1038/s41467-019-10554-w
28. Duncan JE, Goldstein LSB (2006) The genetics of axonal transport and axonal transport disorders. PLoS Genet 2(9):e124. https://doi.org/10.1371/journal.pgen.0020124
29. Medioni C, Ephrussi A, Besse F (2015) Live imaging of axonal transport in drosophila pupal brain explants. Nat Protoc 10(4):574–584. https://doi.org/10.1038/nprot.2015.034
30. Sánchez-Soriano N, Bottenberg W, Fiala A, Haessler U, Kerassoviti A, Knust E, Löhr R, Prokop A (2005) Are dendrites in *Drosophila* homologous to vertebrate dendrites? Dev Biol 288(1):126–138. https://doi.org/10.1016/j.ydbio.2005.09.026
31. Bellen HJ, Tong C, Tsuda H (2010) 100 years of drosophila research and its impact on vertebrate neuroscience: a history lesson for the future. Nat Rev Neurosci 11(7):514–522. https://doi.org/10.1038/nrn2839
32. McGurk L, Berson A, Bonini NM (2015) *Drosophila* as an *In Vivo* model for human neurodegenerative disease. Genetics 201 (2): 377–402. https://doi.org/10.1534/genetics.115.179457
33. Sánchez-Soriano N, Tear G, Whitington P, Prokop A (2007) Drosophilaas a genetic and cellular model for studies on axonal growth. Neural Dev 2(1):9. https://doi.org/10.1186/1749-8104-2-9
34. Sanes JR, Zipursky SL (2010) Design principles of insect and vertebrate visual systems. Neuron 66(1):15–36. https://doi.org/10.1016/j.neuron.2010.01.018
35. Hirokawa N, Tanaka Y (2015) Kinesin superfamily proteins (KIFs): various functions and their relevance for important phenomena in life and diseases. Exp Cell Res 334(1):16–25. https://doi.org/10.1016/j.yexcr.2015.02.016
36. Ejsmont RK, Hassan BA (2014) The little Fly that could: wizardry and artistry of drosophila genomics. Genes 5(2):385–414. https://doi.org/10.3390/genes5020385
37. Hahn I, Ronshaugen M, Sánchez-Soriano N, Prokop A (2016) Functional and genetic analysis of Spectraplakins in *Drosophila*. Methods Enzymol 569:373–405. https://doi.org/10.1016/bs.mie.2015.06.022
38. Bier E, Harrison MM, O'Connor-Giles KM, Wildonger J (2018) Advances in engineering the Fly genome with the CRISPR-Cas system. Genetics 208(1):1–18. https://doi.org/10.1534/genetics.117.1113
39. Donady JJ, Seecof RL (1972) Effect of the gene lethal (1) Myospheroid on drosophila embryonic cells in vitro. In Vitro 8(1):7–12
40. Seecof RL, Alléaume N, Teplitz RL, Gerson I (1971) Differentiation of neurons and myocytes in cell cultures made from drosophila gastrulae. Exp Cell Res 69(1):161–173. https://doi.org/10.1016/0014-4827(71)90321-1
41. Alves-Silva J, Sánchez-Soriano N, Beaven R, Klein M, Parkin J, Millard TH, Bellen HJ, Venken KJ, Ballestrem C, Kammerer RA, Prokop A (2012) Spectraplakins promote microtubule-mediated axonal growth by functioning as structural microtubule-associated proteins and EB1-dependent +TIPs (tip interacting proteins). J Neurosci 32(27): 9143–9158. https://doi.org/10.1523/jneurosci.0416-12.2012
42. Szikora S, Földi I, Tóth K, Migh E, Vig A, Bugyi B, Maléth J, Hegyi P, Kaltenecker P, Sanchez-Soriano N, Mihály J (2017) The formin DAAM is required for coordination of the actin and microtubule cytoskeleton in axonal growth cones. J Cell Sci 130(15):2506–2519. https://doi.org/10.1242/jcs.203455
43. Voelzmann A, Okenve-Ramos P, Qu Y, Chojnowska-Monga M, Del Caño-Espinel M, Prokop A, Sanchez-Soriano N (2016) Tau and spectraplakins promote synapse formation and maintenance through Jun kinase and neuronal trafficking. Elife 5:e14694. https://doi.org/10.7554/eLife.14694
44. Zschätzsch M, Oliva C, Langen M, De Geest N, Ozel MN, Williamson WR, Lemon WC, Soldano A, Munck S, Hiesinger PR, Sanchez-Soriano N, Hassan BA (2014) Regulation of branching dynamics by axon-intrinsic

asymmetries in tyrosine kinase receptor signaling. Elife 3:e01699. https://doi.org/10.7554/eLife.01699

45. Qu Y, Hahn I, Webb SED, Pearce SP, Prokop A (2017) Periodic actin structures in neuronal axons are required to maintain microtubules. Mol Biol Cell 28(2):296–308. https://doi.org/10.1091/mbc.E16-10-0727
46. Sánchez-Soriano N, Gonçalves-Pimentel C, Beaven R, Haessler U, Ofner-Ziegenfuss L, Ballestrem C, Prokop A (2010) Drosophila growth cones: a genetically tractable platform for the analysis of axonal growth dynamics. Dev Neurobiol 70(1):58–71. https://doi.org/10.1002/dneu.20762
47. Bai J, Sepp KJ, Perrimon N (2009) Culture of drosophila primary cells dissociated from gastrula embryos and their use in RNAi screening. Nat Protoc 4(10):1502–1512. https://doi.org/10.1038/nprot.2009.147
48. Küppers-Munther B, Letzkus JJ, Lüer K, Technau G, Schmidt H, Prokop A (2004) A new culturing strategy optimises drosophila primary cell cultures for structural and functional analyses. Dev Biol 269(2):459–478. https://doi.org/10.1016/j.ydbio.2004.01.038
49. Ceron J, Tejedor FJ, Moya F (2006) A primary cell culture of drosophila postembryonic larval neuroblasts to study cell cycle and asymmetric division. Eur J Cell Biol 85(6):567–575. https://doi.org/10.1016/j.ejcb.2006.02.006
50. Katsuki T, Ailani D, Hiramoto M, Hiromi Y (2009) Intra-axonal patterning: intrinsic compartmentalization of the axonal membrane in drosophila neurons. Neuron 64(2):188–199. https://doi.org/10.1016/j.neuron.2009.08.019
51. Slováková J, Speicher S, Sánchez-Soriano N, Prokop A, Carmena A (2012) The actin-binding protein canoe/AF-6 forms a complex with Robo and is required for slit-Robo signaling during axon pathfinding at the CNS midline. J Neurosci 32(29):10035–10044. https://doi.org/10.1523/jneurosci.6342-11.2012
52. Oliva C, Soldano A, Mora N, De Geest N, Claeys A, Erfurth ML, Sierralta J, Ramaekers A, Dascenco D, Ejsmont RK, Schmucker D, Sanchez-Soriano N, Hassan BA (2016) Regulation of drosophila brain wiring by neuropil interactions via a slit-Robo-RPTP signaling complex. Dev Cell 39(2):267–278. https://doi.org/10.1016/j.devcel.2016.09.028
53. Hahn I, Voelzmann A, Parkin J, Fuelle J, Slater PG, Lowery LA, Sanchez-Soriano N, Prokop A (2020) Tau, XMAP215/Msps and Eb1 jointly regulate microtubule polymerisation and bundle formation in axons. bioRxiv:2020.2008.2019.257808. https://doi.org/10.1101/2020.08.19.257808
54. Qu Y, Hahn I, Lees M, Parkin J, Voelzmann A, Dorey K, Rathbone A, Friel CT, Allan VJ, Okenve-Ramos P, Sanchez-Soriano N, Prokop A (2019) Efa6 protects axons and regulates their growth and branching by inhibiting microtubule polymerisation at the cortex. eLife 8:e50319. https://doi.org/10.7554/eLife.50319
55. Prokop A, Beaven R, Qu Y, Sánchez-Soriano N (2013) Using fly genetics to dissect the cytoskeletal machinery of neurons during axonal growth and maintenance. J Cell Sci 126(Pt 11):2331–2341. https://doi.org/10.1242/jcs.126912
56. Sanchez-Soriano N, Travis M, Dajas-Bailador-F, Gonçalves-Pimentel C, Whitmarsh AJ, Prokop A (2009) Mouse ACF7 and drosophila short stop modulate filopodia formation and microtubule organisation during neuronal growth. J Cell Sci 122(Pt 14):2534–2542. https://doi.org/10.1242/jcs.046268
57. Stephan D, Sánchez-Soriano N, Loschek LF, Gerhards R, Gutmann S, Storchova Z, Prokop A, Kadow IC (2012) Drosophila Psidin regulates olfactory neuron number and axon targeting through two distinct molecular mechanisms. J Neurosci 32(46):16080–16094. https://doi.org/10.1523/jneurosci.3116-12.2012
58. Kraft R, Escobar MM, Narro ML, Kurtis JL, Efrat A, Barnard K, Restifo LL (2006) Phenotypes of *Drosophila* brain neurons in primary culture reveal a role for Fascin in neurite shape and trajectory. J Neurosci 26(34):8734–8747. https://doi.org/10.1523/jneurosci.2106-06.2006
59. del Castillo U, Müller H-AJ, Gelfand VI (2020) Kinetochore protein spindly controls microtubule polarity in *Drosophila* axons. Proc Natl Acad Sci 117(22):12155–12163. https://doi.org/10.1073/pnas.2005394117
60. Yao W-D, Rusch J, Poo M-M, Wu C-F (2000) Spontaneous acetylcholine secretion from developing growth cones of *Drosophila* central neurons in culture: effects of cAMP-pathway mutations. J Neurosci 20(7):2626–2637. https://doi.org/10.1523/jneurosci.20-07-02626.2000
61. Küppers B, Sánchez-Soriano N, Letzkus J, Technau GM, Prokop A (2003) In developing drosophila neurones the production of gamma-amino butyric acid is tightly regulated downstream of glutamate decarboxylase translation and can be influenced by calcium. J

Neurochem 84(5):939–951. https://doi.org/10.1046/j.1471-4159.2003.01554.x

62. West RJH, Sharpe JL, Voelzmann A, Munro AL, Hahn I, Baines RA, Pickering-Brown S (2020) Co-expression of C9orf72 related dipeptide-repeats over 1000 repeat units reveals age- and combination-specific phenotypic profiles in drosophila. Acta Neuropathol Commun 8(1):158. https://doi.org/10.1186/s40478-020-01028-y
63. Narayanareddy BR, Vartiainen S, Hariri N, O'Dowd DK, Gross SP (2014) A biophysical analysis of mitochondrial movement: differences between transport in neuronal cell bodies versus processes. Traffic 15(7):762–771. https://doi.org/10.1111/tra.12171
64. Liao P-C, Tandarich LC, Hollenbeck PJ (2017) ROS regulation of axonal mitochondrial transport is mediated by Ca^{2+} and JNK in drosophila. PLoS One 12(5):e0178105. https://doi.org/10.1371/journal.pone.0178105
65. Prokop A, Küppers-Munther B, Sánchez-Soriano N (2012) Using primary neuron cultures of drosophila to analyze neuronal circuit formation and function. In: Hassan BA (ed) The making and un-making of neuronal circuits in drosophila. Humana Press, Totowa, NJ, pp 225–247. https://doi.org/10.1007/978-1-61779-830-6_10
66. Sicaeros B, Campusano JM, O'Dowd DK (2007) Primary neuronal cultures from the brains of late stage drosophila pupae. J Vis Exp 4:200–200. https://doi.org/10.3791/200
67. Campos-Ortega JA, Hartenstein V (1997) The embryonic development of Drosophila melanogaster. Springer Verlag, Berlin
68. Roote J, Prokop A (2013) How to design a genetic mating scheme: a basic training package for drosophila genetics. G3 (Bethesda, Md) 3(2):353–358. https://doi.org/10.1534/g3.112.004820
69. Vagnoni A, Bullock SL (2016) A simple method for imaging axonal transport in aging neurons using the adult drosophila wing. Nat Protoc 11(9):1711–1723. https://doi.org/10.1038/nprot.2016.112
70. Lee S, Sato Y, Nixon RA (2011) Lysosomal proteolysis inhibition selectively disrupts axonal transport of degradative organelles and causes an Alzheimer's-like axonal dystrophy. J Neurosci 31(21):7817–7830. https://doi.org/10.1523/jneurosci.6412-10.2011
71. Maday S, Wallace KE, Holzbaur ELF (2012) Autophagosomes initiate distally and mature during transport toward the cell soma in primary neurons. J Cell Biol 196(4):407–417. https://doi.org/10.1083/jcb.201106120
72. Moughamian AJ, Osborn GE, Lazarus JE, Maday S, Holzbaur EL (2013) Ordered recruitment of dynactin to the microtubule plus-end is required for efficient initiation of retrograde axonal transport. J Neurosci 33(32):13190–13203. https://doi.org/10.1523/jneurosci.0935-13.2013
73. Evans CS, Holzbaur ELF (2020) Degradation of engulfed mitochondria is rate-limiting in Optineurin-mediated mitophagy in neurons. eLife 9:e50260. https://doi.org/10.7554/eLife.50260
74. Perrot R, Julien JP (2009) Real-time imaging reveals defects of fast axonal transport induced by disorganization of intermediate filaments. FASEB J 23(9):3213–3225. https://doi.org/10.1096/fj.09-129585
75. Beaven R, Dzhindzhev NS, Qu Y, Hahn I, Dajas-Bailador F, Ohkura H, Prokop A (2015) Drosophila CLIP-190 and mammalian CLIP-170 display reduced microtubule plus end association in the nervous system. Mol Biol Cell 26(8):1491–1508. https://doi.org/10.1091/mbc.E14-06-1083
76. DeVorkin L, Gorski SM (2014) LysoTracker staining to aid in monitoring autophagy in drosophila. Cold Spring Harb Protoc 2014(9):951–958. https://doi.org/10.1101/pdb.prot080325
77. Zhao X, Chen XQ, Han E, Hu Y, Paik P, Ding Z, Overman J, Lau AL, Shahmoradian SH, Chiu W, Thompson LM, Wu C, Mobley WC (2016) TRiC subunits enhance BDNF axonal transport and rescue striatal atrophy in Huntington's disease. Proc Natl Acad Sci U S A 113(38):E5655–E5664. https://doi.org/10.1073/pnas.1603020113
78. Pilling AD, Horiuchi D, Lively CM, Saxton WM (2006) Kinesin-1 and dynein are the primary motors for fast transport of mitochondria in drosophila motor axons. Mol Biol Cell 17(4):2057–2068. https://doi.org/10.1091/mbc.e05-06-0526
79. Moutaux E, Christaller W, Scaramuzzino C, Genoux A, Charlot B, Cazorla M, Saudou F (2018) Neuronal network maturation differently affects secretory vesicles and mitochondria transport in axons. Sci Rep 8(1):13429. https://doi.org/10.1038/s41598-018-31759-x
80. Sheng Z-H (2014) Mitochondrial trafficking and anchoring in neurons: new insight and implications. J Cell Biol 204(7):1087–1098. https://doi.org/10.1083/jcb.201312123

81. Da-Rè C, Franzolin E, Biscontin A, Piazzesi A, Pacchioni B, Gagliani MC, Mazzotta G, Tacchetti C, Zordan MA, Zeviani M, Bernardi P, Bianchi V, De Pittà C, Costa R (2014) Functional characterization of drim2, the Drosophila melanogaster homolog of the yeast mitochondrial deoxynucleotide transporter. J Biol Chem 289(11):7448–7459. https://doi.org/10.1074/jbc.M113.543926
82. Wang X, Schwarz TL (2009) Imaging axonal transport of mitochondria. Methods Enzymol 457:319–333. https://doi.org/10.1016/S0076-6879(09)05018-6
83. Budnik V, Gorczyca M, Prokop A (2006) Selected methods for the anatomical study of drosophila embryonic and larval neuromuscular junctions. Int Rev Neurobiol 75:323–365. https://doi.org/10.1016/s0074-7742(06)75015-2
84. Bercier V, Rosello M, Del Bene F, Revenu C (2019) Zebrafish as a model for the study of live in vivo Processive transport in neurons. Front Cell Dev Biol 7:17. https://doi.org/10.3389/fcell.2019.00017
85. Gunawardena S, Her LS, Brusch RG, Laymon RA, Niesman IR, Gordesky-Gold B, Sintasath L, Bonini NM, Goldstein LS (2003) Disruption of axonal transport by loss of huntingtin or expression of pathogenic polyQ proteins in drosophila. Neuron 40(1):25–40. https://doi.org/10.1016/s0896-6273(03)00594-4
86. Nonet ML (1999) Visualization of synaptic specializations in live C. elegans with synaptic vesicle protein-GFP fusions. J Neurosci Methods 89(1):33–40. https://doi.org/10.1016/s0165-0270(99)00031-x
87. Surana S, Villarroel-Campos D, Lazo OM, Moretto E, Tosolini AP, Rhymes ER, Richter S, Sleigh JN, Schiavo G (2020) The evolution of the axonal transport toolkit. Traffic (Copenhagen, Denmark) 21(1):13–33. https://doi.org/10.1111/tra.12710
88. Lu W, Del Castillo U, Gelfand VI (2013) Organelle transport in cultured drosophila cells: S2 cell line and primary neurons. J Vis Exp 81:e50838. https://doi.org/10.3791/50838
89. Dey S, Banker G, Ray K (2017) Anterograde transport of Rab4-associated vesicles regulates synapse Organization in Drosophila. Cell Rep 18(10):2452–2463. https://doi.org/10.1016/j.celrep.2017.02.034
90. Jean-Yves Tineveza NP, Schindelin J, Hoopes GM, Reynolds GD, Laplantine E, Bednarek SY, Shorte SL, Eliceiri KW (2017) TrackMate: an open and extensible platform for single-particle tracking. Methods 115:80–90
91. Katrukha E (2020), KymoResliceWide plugin for ImageJ, v0.5, Zenodo https://doi.org/10.5281/zenodo.4281086. software download link: https://github.com/ekatrukha/KymoResliceWide
92. Neumann S, Chassefeyre R, Campbell GE, Encalada SE (2017) KymoAnalyzer: a software tool for the quantitative analysis of intracellular transport in neurons. Traffic (Copenhagen, Denmark) 18(1):71–88. https://doi.org/10.1111/tra.12456

Open Access This chapter is licensed under the terms of the Creative Commons Attribution 4.0 International License (http://creativecommons.org/licenses/by/4.0/), which permits use, sharing, adaptation, distribution and reproduction in any medium or format, as long as you give appropriate credit to the original author(s) and the source, provide a link to the Creative Commons license and indicate if changes were made.

The images or other third party material in this chapter are included in the chapter's Creative Commons license, unless indicated otherwise in a credit line to the material. If material is not included in the chapter's Creative Commons license and your intended use is not permitted by statutory regulation or exceeds the permitted use, you will need to obtain permission directly from the copyright holder.

Chapter 24

High-Resolution Live Imaging of Axonal RNP Granules in *Drosophila* Pupal Brain Explants

Caroline Medioni, Jeshlee Vijayakumar, Anne Ephrussi, and Florence Besse

Abstract

Dynamic and local adjustments of the axonal proteome are observed in response to extracellular cues and achieved via translation of axonally localized mRNAs. To be localized, these mRNAs must be recognized by RNA binding proteins and packaged into higher-order ribonucleoprotein (RNP) granules transported along axonal microtubules via molecular motors. Axonal recruitment of RNP granules is not constitutive, but rather regulated by external signals such as developmental cues, through pathways yet to be identified. The *Drosophila* brain represents an excellent model system where to study the transport of RNP granules as it is triggered in specific populations of neurons undergoing remodeling during metamorphosis. Here, we describe a protocol enabling live imaging of axonal RNP granule transport with high spatiotemporal resolution in *Drosophila* maturing brains. In this protocol, pupal brains expressing endogenous or ectopic fluorescent RNP components are dissected, mounted in a customized imaging chamber, and imaged with an inverted confocal microscope equipped with sensitive detectors. Axonal RNP granules are then individually tracked for further analysis of their trajectories. This protocol is rapid (less than 1 hour to prepare brains for imaging) and is easy to handle and to implement.

Key words Axonal transport, RNP granules, High resolution, Live imaging, RNA binding protein, Pupal brain explants, *Drosophila melanogaster*

1 Introduction

During development, axons must elongate and navigate through complex environments to reach targets that can be located up to dozens of centimeters away from the soma. Growing axons are guided along their path by a combination of mechanical and chemical cues sensed by their specialized tip—the growth cone—and integrated locally to produce directional decisions. As revealed by

Supplementary Information The online version of this chapter (https://doi.org/10.1007/978-1-0716-1990-2_24) contains supplementary material, which is available to authorized users.

Alessio Vagnoni (ed.), *Axonal Transport: Methods and Protocols*,
Methods in Molecular Biology, vol. 2431, https://doi.org/10.1007/978-1-0716-1990-2_24,
© The Author(s), under exclusive license to Springer Science+Business Media, LLC, part of Springer Nature 2022

recent proteomic analyses, several hundred proteins encompassing a wide range of biological functions are enriched in growth cones in vivo [1, 2], raising the question of how their accumulation to axonal tips is mediated and dynamically regulated. This question gets even more puzzling when considering that fast axonal transport cannot transport cargoes for more than few centimeters a day [3]. How then can growth cone proteomes be dynamically adjusted in response to extracellular signals? Furthermore, how can proteins with short half-lives (typically signaling and regulatory proteins [4]) accumulate distally before degradation? Onsite production of proteins via translation of mRNAs transported to axons has emerged as a key process contributing to the local regulation of axon molecular content and navigation [5, 6]. As demonstrated by pioneer work, indeed, axon tips can navigate and respond to chemical gradients when severed from the soma, a process blocked upon inhibition of translation [7, 8]. As further revealed by transcriptomics studies, hundreds to thousands of mRNAs encoding proteins with a variety of functions localize to axon shaft and/or tip [6, 9–13], where they are translated in a cue-specific manner [14, 15]. Localization of these mRNAs is regulated upon development [9, 10] and depends on the integrity of the microtubule cytoskeleton [6, 16]. Dynamic imaging of mRNAs transported to the axons of cultured neurons has shown that they undergo typical bi-directional motion, with periods of fast directional transport interspersed with pauses or switches in directionality [17–19]. Such an active transport is mediated by molecular motors, among which kinesin-1 and kinesin-2 family members [20, 21]. Over the past years, various studies have started unraveling how specific mRNAs are hooked to the transport machinery and carried along axons. These studies have revealed that mRNAs to be transported are recognized by specific RNA binding proteins and packaged into dynamic large macromolecular complexes termed ribonucleoprotein (RNP) granules [22, 23]. Connection of these complexes to the transport machinery can be mediated by the direct binding of RNA binding proteins to molecular motors [20, 21]. Alternatively, it was recently proposed that RNP granules may hitchhike on actively transported membranous organelles via their coupling through bipartite tethering proteins [24–26]. More work is now required to understand how different mRNAs are sorted to distinct transport machineries and how this is regulated during development.

Although in vitro studies have proven instrumental to dissect the molecular mechanisms underlying the transport of axonal RNP cargoes, they are not adapted to study their regulation in response to developmental cues. *Drosophila* brain has emerged as a powerful alternative model where population labeling, genetics, and drug treatment can be combined to dynamic live imaging to address these questions [27–29]. During fly metamorphosis, indeed,

microtubule-dependent axonal transport of RNP granules is triggered in specific populations of brain neurons upon programmed remodeling of their extensions [28]. This process follows a precise developmental timing and can be monitored through visualization of the distribution of Imp, a conserved RNA binding protein enriched in neuronal RNP granules [28–31]. Metamorphosis occurs in flies within an opaque pupal case preventing in vivo subcellular imaging. Yet, brain explants can be dissected from staged individuals undergoing metamorphosis and prepared for live imaging [27]. Here, we describe a protocol enabling (1) dynamic high-resolution imaging of axonal RNP granule transport in explants of maturing *Drosophila* brains and (2) quantitative analysis of RNP granule motility. This protocol is particularly adapted to the study of RNP granule transported within populations of axons in response to developmental cues and is compatible with both gene inactivation and treatment with chemical compounds.

2 Materials

2.1 Imaging Chamber Preparation

1. Nunc Lab-Tek II chambered cover glass, two wells.
2. Adhesive wells (secure-seal spacer eight wells, 9 mm diameter, 0.12 mm deep).
3. D-Polylysine solution preparation: Use sterile pipettes. Add 10 mL of sterile water to 20 mg of lyophilized D-polylysine, and agitate on a rocker for 2–3 h at room temperature (RT). Transfer the solution to a 50-mL Falcon tube, and then add another 10 mL of sterile water. Agitate again for 2–3 h at RT. Prepare aliquots of 1 mL in 1.5-mL Eppendorf tubes (store them at −20 °C; do not keep for more than 6 months).

2.2 Dissection of Pupal Brains

1. Schneider's insect medium (store at 2–8 °C and protect from light).
2. Antibiotic-antimycotic solution, stabilized, sterile-filtered, suitable for cell culture: 10,000 units of penicillin, 10 mg of streptomycin, and 25 μg of amphotericin B per mL.
3. 20-Hydroxyecdysone (prepare a 1 mg/mL solution in ethanol and store at −20 °C).
4. Culture medium: 10 mL of FBS (10%, vol/vol), 1 mL of antibiotic-antimycotic solution (1% vol/vol), adjust the final volume to 100 mL with Schneider's insect medium. Filter the medium with a vacuum filter and prepare aliquots in 2-mL cryotubes (store at 4 °C; do not keep for more than 1 week).

5. Imaging medium: add insulin (0.2 mg/mL) and 20-hydroxyecdysone (1 μg/mL) to the culture medium, under sterile atmosphere, 5 min before dissection.
6. PBS-Triton (PBT), 0.1% (vol/vol): add 0.5 mL of Triton X-100 to 499.5 mL of PBS. Mix the solution for 15–30 min using a magnetic stirrer. Store this buffer at RT.

2.3 Mounting of Brains in the Imaging Chamber

1. Gas-permeable transparent membrane.
2. Voltalef oil 10S (store at RT (15–25 °C recommended)).
3. Stainless steel ring (external diameter: 7.7 mm, internal diameter: 6.7 mm, weight: 0.7 g and height must not exceed 10 mm, can be machined in any mechanical workshop).

2.4 Image Acquisition and Analysis

1. Inverted confocal microscope equipped with ultrasensitive detectors.
2. Long-distance 40× Water Objective with a good NA (≥1.1).
3. Water-immersion oil.
4. Fiji software (https://imagej.net/Fiji) equipped with the "Bleach_correction" macro (K. Liura; https://imagej.net/Bleach_Correction) and the "Manual Tracking" plugin (F. Cordelier; https://imagej.nih.gov/ij/plugins/track/track.html).

3 Methods

The protocol is divided into five main steps (Fig. 1). Briefly, Drosophila pupae are collected upon pupariation and aged until the desired stage (step 1). Brains are then dissected (step 2) and mounted into the imaging chamber prepared prior to dissection (step 3). Brain explants are imaged under an inverted confocal microscope (step 4) and RNP cargoes tracked on recovered movies (step 5). Trajectories of RNP granules are analyzed by generating kymographs (step 6).

3.1 Animal Collection

1. Collect ~20 white pupae (0 h after pupa formation) per condition, and transfer them to a new fly vial (*see* **Notes 1** and **2**).
2. Incubate the pupae at 25 °C for 20–30 h (or allow them to develop until time of interest) (*see* **Note 3**).

3.2 Imaging Chamber Preparation

1. Cut individual wells from an eight-well adhesive spacer.
2. Remove the liner from one side of an individual adhesive well and apply the tacky surface of the well onto the bottom of a Lab-Tek chambered cover glass. Press gently to seal the well, and remove the other liner. Repeat this operation for the second chamber of the Lab-Tek device (*see* **Note 4**).

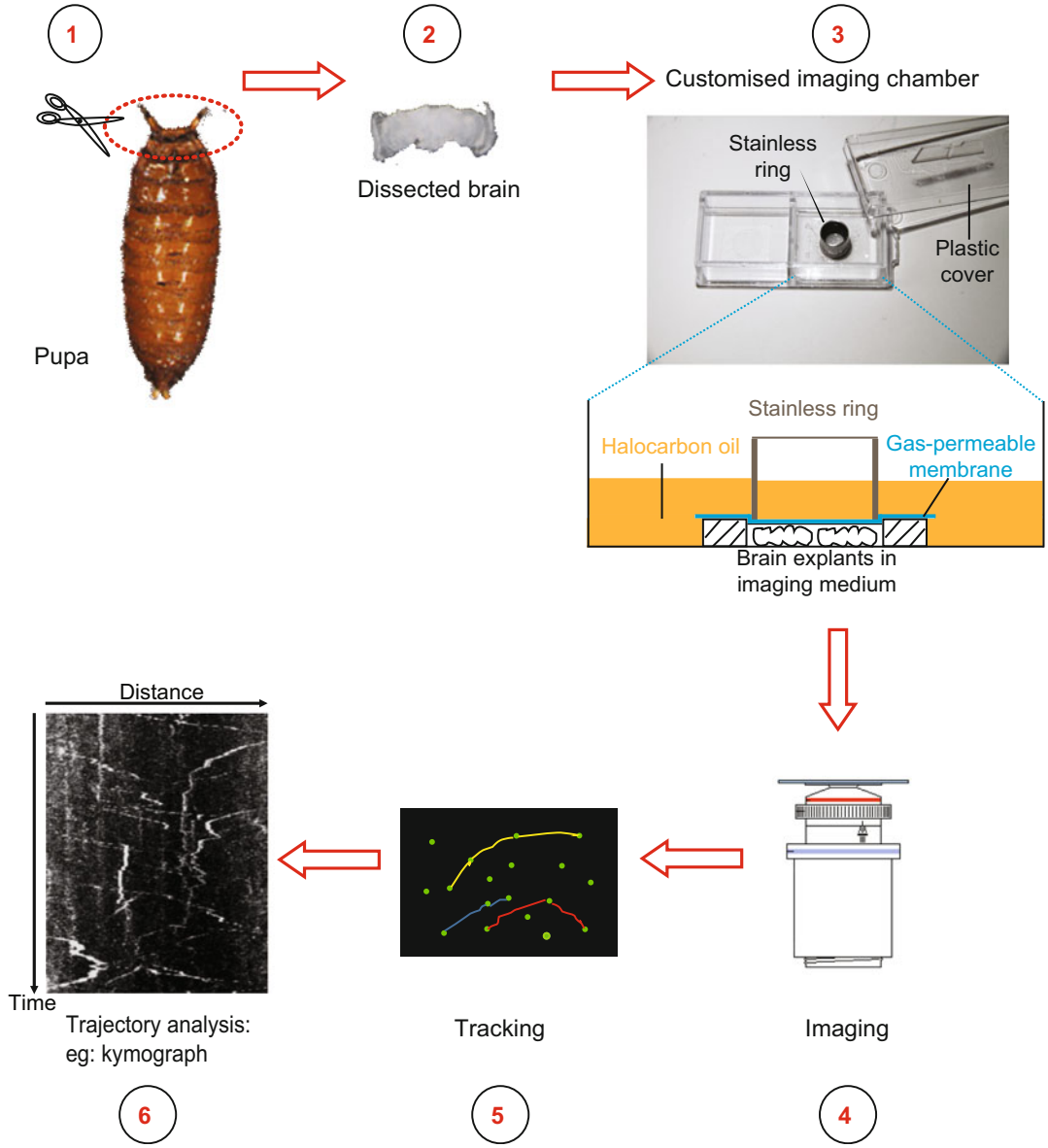

Fig. 1 From dissection to data analysis: workflow of the method. Staged pupae expressing fluorescent RNP granule markers and neuronal markers are collected (1) and brains dissected out (2). Brains are then mounted in the imaging chamber (3), with the correct orientation to image axons. Axonal transport is imaged from ex vivo brain explants, with an inverted confocal microscope (4). Motile RNP granules are manually tracked using Fiji (5). Axonal trajectories are analyzed via kymographs (6)

3. Coat the wells with a drop of D-polylysine solution and incubate for 1 h at RT (*see* **Note 5**).
4. Wash the wells twice with sterile water. Dry water traces using small pieces of absorbent paper.

3.3 Dissection of Pupal Brains (Fig. 1, Steps 1 and 2)

1. Five minutes before dissection, prepare the imaging medium by adding insulin and 20-hydroxyecdysone to the culture medium (*see* **Note 6**).
2. Pipette ~500 μL of imaging medium into the center of a 60-mm petri dish and, using one pair of forceps, carefully place the pupa in the drop of medium.
3. Dissect the pupal brains as described in [27].
4. After dissection of ~10 pupae, use a pipette fitted with a 200-μL tip previously neutralized in PBS/0.1% Triton to collect brains in ~50 μL of clean imaging medium. Gently expel the brains into a clean drop of imaging medium in the same petri dish. Repeat this rinsing step three to four times (*see* **Note 7**).
5. (Optional) If you are performing drug treatment, prepare an independent aliquot of culture medium supplemented with 20-hydroxyecdysone, insulin, and the drug of choice (e.g., colchicine, a drug that blocks microtubule polymerization). Use a pipette to collect the brains in ~50 μL of drug-supplemented culture medium.

3.4 Mounting of Brains in the Imaging Chamber (Fig. 1, Step 3)

1. Collect the brains using a pipette and place them inside the coated adhesive wells (~10 brains per well). The drop containing the brains must fill the well (*see* **Notes 8** and **9**).
2. Use a fluorescence stereomicroscope with appropriate filters to visualize neurons of interest. Orient the brains with forceps such that the axonal population to be imaged is in close proximity to the bottom of the well.
3. Cut a 15 mm × 10 mm piece of transparent gas-permeable membrane, rinse it with ethanol, dry it with a piece of absorbent paper, and place it on top of the adhesive well containing the dissected brains. This membrane seals the well (*see* **Note 10**).
4. Place the metal ring on top of the membrane to seal the system and maintain the brains in close proximity to the cover glass. This will prevent the brains from moving during imaging (*see* **Note 11**).
5. Pipette ~1 mL of halocarbon oil 10S using a 1000-μL end-cut tip, gently cover the transparent membrane inside the ring, and then add oil outside the ring to fill the chamber. 10S halocarbon oil prevents evaporation while enabling gas exchange. Close the Lab-Tek chamber with the plastic cover (*see* **Note 12**).
6. Wait for 30 min at 20–25 °C before imaging to allow the brains to settle in the imaging chamber. If drug treatment is performed (Subheading 3.3, **step 5**), incubate for at least 2 h to allow the drug to take effect before imaging.

3.5 Brain Imaging (Fig. 1, Step 4)

1. Image samples on an inverted confocal microscope equipped with adapted lasers, ultrasensitive detectors, and a long-distance water objective (*see* **Notes 13** and **14**).
2. Select the brain region to be imaged (*see* **Notes 15** and Fig. 2a–d).
3. Acquire images with high temporal and spatial resolution (*see* **Notes 16**, **17** and Supplementary Video 1).

3.6 Data Analysis (Fig. 1, Steps 5 and 6)

3.6.1 Image Processing

1. Using Fiji, perform Maximum Intensity Projection for each time point.
2. Correct for bleaching using the "Bleach_Correction" plugin from Fiji (select the "Histogram matching method").

3.6.2 Analysis of RNP Granule Trajectories

1. Manually track RNP granules using the "Manual tracking" plugin from Fiji (*see* **Notes 18**; Fig. 2e and Supplementary Video 2).
2. Generate kymographs using the *Image>Stacks>Reslice* function of Fiji. A new image sequence is generated. Select a time interval in which motile RNP granules can be observed using *Plugins> Stacks-Reducing>Substack Select*. Project the new substack using the *Image>Stacks>ZProject* function, and choose *Max Intensity* in the *Projection Type* Menu. This generates a 2D graph showing the position of granules in function of time.

4 Notes

1. White pupae are defined as non-motile and by the presence of both mouth hooks and everted spiracles. Be careful to manipulate the animal gently as pupae are particularly fragile at this stage.
2. In our experiments, pupae expressed a membrane-tagged red fluorescent protein (preferentially myr-RFP or CD8-RFP) that labeled the neuronal population of interest and a GFP fusion protein enriched in RNP granules.
3. We imaged axonal transport of RNP cargoes at 20–30 h after puparium formation (APF), in mushroom body γ neurons undergoing axonal regrowth.
4. Do not forget to cut the extra-edge at the border of the Lab-Tek chamber (bottom side), otherwise it will not fit on the microscope stage.
5. Do not store coated Lab-Tek chambers, otherwise the coating efficiency will decrease.
6. Prepare the imaging medium under sterile atmosphere. Keep this medium on ice while dissecting. Do not store this medium, as hormones may degrade.

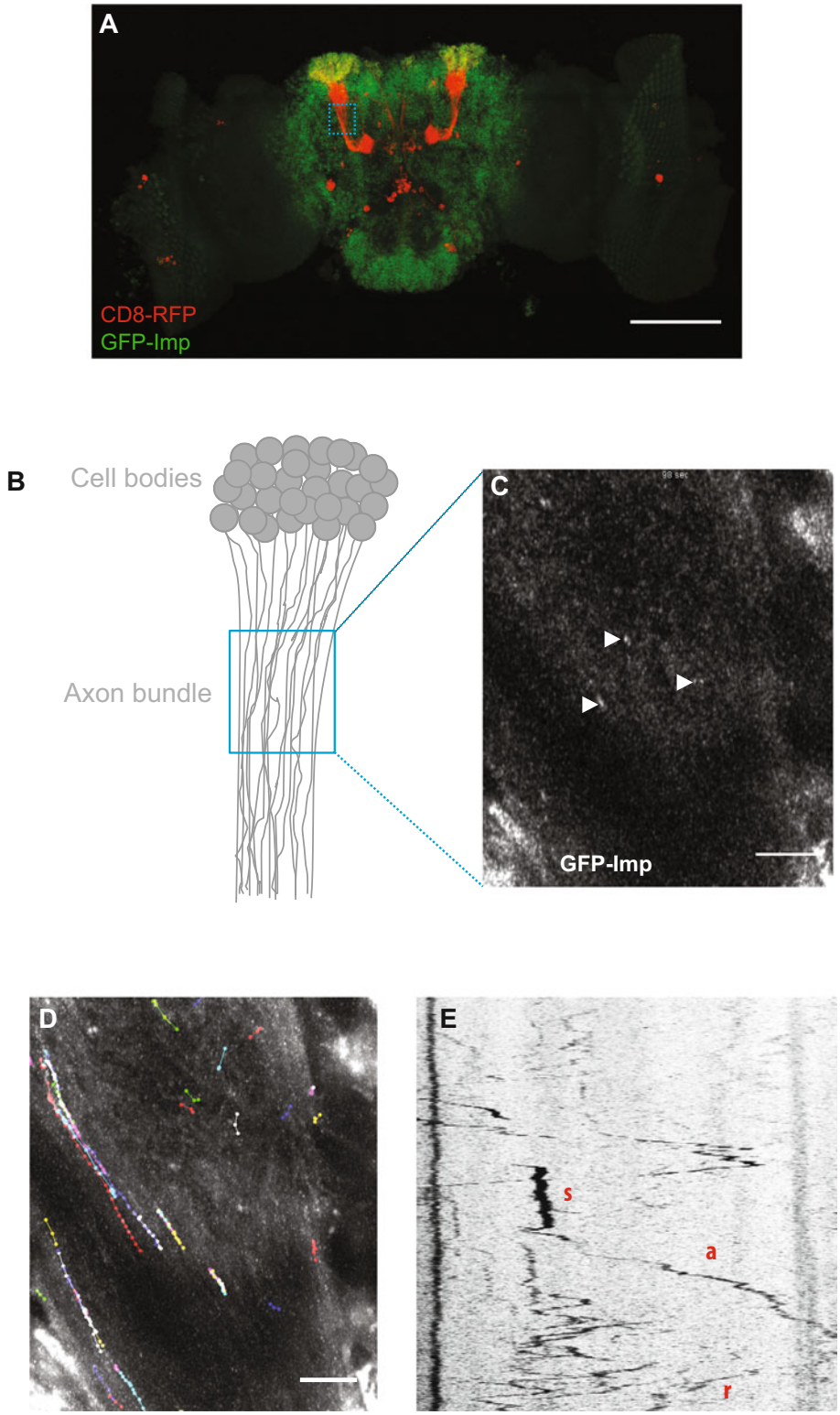

Fig. 2 Imaging of RNP granules in *Drosophila* pupal brains. (**a**) Global view of a 24 h APF *Drosophila* brain (image taken with a 10× objective). Mushroom bodies (MB) are labeled by CD8-RFP (red) and endogenous

7. Brains must be carefully cleaned after dissection. At 24 h APF, pupae contain fat particles that are autofluorescent and interfere with the imaging process.
8. Be careful to avoid excess medium, as brains may float over the edge of the well.
9. Two genotypes can be prepared in parallel when using two-well chambered cover glasses.
10. Be careful to directly cover the adhesive well with the membrane. Attempts to remove misplaced membranes would damage them, as the borders of the wells are tacky.
11. From Subheading 3.4, **step 4** onward, manipulate the chamber carefully, as the metal ring may get displaced. In case of ring displacement, correct its position with forceps before installing the chamber on the stage of the microscope.
12. Be careful when pipetting oil, as it is very viscous. Oil spillover may dirty the cover glass and interfere with imaging.
13. We used a Zeiss LSM880 confocal microscope equipped with GaAsP detectors and a 40×, 1.1 NA water immersion objective.
14. Use immersion oil with a water refractive index to avoid water evaporation while imaging.
15. We used the CD8-RFP signal to locate axonal bundles to be imaged and define the Region of Interest (ROI).
16. Combining high spatial and temporal resolution is essential to follow endogenously tagged RNP cargoes. Using the Fast Airy Scan mode of a Zeiss LSM880 confocal microscope, we acquired stacks of three images every 1.2 s for 12 min (*z*-step = 0.27 μm; pixel size = 0.05 μm).
17. We imaged the transport of RNP cargoes labeled with endogenously-expressed GFP-Imp along Mushroom Body γ neurons in pupal brains (Supplementary Video 1).
18. We tracked all granules detected for at least three consecutive time points. No selection was initially made based on the motility or the brightness of granules.

Fig. 2 (continued) Imp localization visualized using a GFP-Imp protein trap insertion (green). Complete genotype: GFP-Imp (G080); 201YGal4, UAS-CD8-RFP. Scale bar: 80 μm. (**b**) Schematic representation of MB γ neuron cell bodies and most proximal axonal region (peduncle). Axonal terminal tips are not represented. In **a** and **b** the blue rectangle indicates the axonal ROI used for imaging of GFP-Imp granules. (**c**) Image extracted from Supplementary Video 1 where GFP-Imp positive granules are highlighted (white arrowheads). (**d**) Temporal projection of RNP granule trajectories (extracted from Supplementary Video 2). Scale bars in C and D: 5 μm. (**e**) GFP-Imp granule trajectories represented on a kymograph, where distance (*x*) is represented in function of time (*y*). Note that retrograde (r), anterograde (a), and stationary (s) granules are observed

Acknowledgments

We thank I. Gaspar for his help in image acquisition and analysis. We are also grateful to L. Burger from the EMBL mechanical workshop for making the metal rings and G. Durand for the technical drawing of these rings. We thank also Y. Belyaev and S. Terjung from the EMBL microscopy platform (AMLF) for their advice in selecting the appropriate microscope for imaging. We thank W. Huebner for his daily help at EMBL, F. Brau from the IPMC imaging facility and the iBV PRISM Imaging facility for use of their microscopes and support (especially M. Mondin and S. Lachambre). C.M. was supported by short-term fellowships from EMBO, FEBS, and P3 (http://www.p-cube.eu/), and by a long-term fellowship from "Ville de Nice." J. V was funded by fellowships from the French Ministry of Research and the Foundation ARC. Development of this protocol was supported by grants (ATIP/CNRS, FRM Implantation Nouvelles Equipes, ARC Fixe, HFSP Career Development Award, ANR (ANR-15-CE12-0016), and FRM (Equipe FRM; grant #DEQ20180339161)) to F.B.

References

1. Chauhan MZ, Arcuri J, Park KK, Zafar MK, Fatmi R, Hackam AS, Yin Y, Benowitz L, Goldberg JL, Samarah M, Bhattacharya SK (2020) Multi-Omic analyses of growth cones at different developmental stages provides insight into pathways in adult Neuroregeneration. iScience 23(2):100836. https://doi.org/10.1016/j.isci.2020.100836
2. Poulopoulos A, Murphy AJ, Ozkan A, Davis P, Hatch J, Kirchner R, Macklis JD (2019) Subcellular transcriptomes and proteomes of developing axon projections in the cerebral cortex. Nature 565(7739):356–360. https://doi.org/10.1038/s41586-018-0847-y
3. Maday S, Twelvetrees AE, Moughamian AJ, Holzbaur EL (2014) Axonal transport: cargo-specific mechanisms of motility and regulation. Neuron 84(2):292–309. https://doi.org/10.1016/j.neuron.2014.10.019
4. Fornasiero EF, Mandad S, Wildhagen H, Alevra M, Rammner B, Keihani S, Opazo F, Urban I, Ischebeck T, Sakib MS, Fard MK, Kirli K, Centeno TP, Vidal RO, Rahman RU, Benito E, Fischer A, Dennerlein S, Rehling P, Feussner I, Bonn S, Simons M, Urlaub H, Rizzoli SO (2018) Precisely measured protein lifetimes in the mouse brain reveal differences across tissues and subcellular fractions. Nat Commun 9(1):4230. https://doi.org/10.1038/s41467-018-06519-0
5. Holt CE, Martin KC, Schuman EM (2019) Local translation in neurons: visualization and function. Nat Struct Mol Biol 26(7):557–566. https://doi.org/10.1038/s41594-019-0263-5
6. Turner-Bridger B, Caterino C, Cioni JM (2020) Molecular mechanisms behind mRNA localization in axons. Open Biol 10(9):200177. https://doi.org/10.1098/rsob.200177
7. Campbell DS, Holt CE (2001) Chemotropic responses of retinal growth cones mediated by rapid local protein synthesis and degradation. Neuron 32(6):1013–1026. https://doi.org/10.1016/s0896-6273(01)00551-7
8. Harris WA, Holt CE, Bonhoeffer F (1987) Retinal axons with and without their somata, growing to and arborizing in the tectum of Xenopus embryos: a time-lapse video study of single fibres in vivo. Development 101(1):123–133
9. Gumy LF, Yeo GS, Tung YC, Zivraj KH, Willis D, Coppola G, Lam BY, Twiss JL, Holt CE, Fawcett JW (2011) Transcriptome analysis of embryonic and adult sensory axons reveals changes in mRNA repertoire localization. RNA 17(1):85–98. https://doi.org/10.1261/rna.2386111
10. Zivraj KH, Tung YC, Piper M, Gumy L, Fawcett JW, Yeo GS, Holt CE (2010) Subcellular profiling reveals distinct and developmentally

regulated repertoire of growth cone mRNAs. J Neurosci 30(46):15464–15478. https://doi.org/10.1523/jneurosci.1800-10.2010

11. Andreassi C, Zimmermann C, Mitter R, Fusco S, De Vita S, Saiardi A, Riccio A (2010) An NGF-responsive element targets myo-inositol monophosphatase-1 mRNA to sympathetic neuron axons. Nat Neurosci 13(3):291–301. https://doi.org/10.1038/nn.2486
12. Medioni C, Mowry K, Besse F (2012) Principles and roles of mRNA localization in animal development. Development 139(18): 3263–3276. https://doi.org/10.1242/dev.078626
13. Taylor AM, Berchtold NC, Perreau VM, Tu CH, Li Jeon N, Cotman CW (2009) Axonal mRNA in uninjured and regenerating cortical mammalian axons. J Neurosci 29(15): 4697–4707. https://doi.org/10.1523/jneurosci.6130-08.2009
14. Cagnetta R, Frese CK, Shigeoka T, Krijgsveld J, Holt CE (2018) Rapid Cue-specific remodeling of the nascent axonal proteome. Neuron 99(1):29–46.e24. https://doi.org/10.1016/j.neuron.2018.06.004
15. Shigeoka T, Jung H, Jung J, Turner-Bridger B, Ohk J, Lin JQ, Amieux PS, Holt CE (2016) Dynamic axonal translation in developing and mature visual circuits. Cell 166(1):181–192. https://doi.org/10.1016/j.cell.2016.05.029
16. Willis DE, van Niekerk EA, Sasaki Y, Mesngon M, Merianda TT, Williams GG, Kendall M, Smith DS, Bassell GJ, Twiss JL (2007) Extracellular stimuli specifically regulate localized levels of individual neuronal mRNAs. J Cell Biol 178(6):965–980. https://doi.org/10.1083/jcb.200703209
17. Alami NH, Smith RB, Carrasco MA, Williams LA, Winborn CS, Han SSW, Kiskinis E, Winborn B, Freibaum BD, Kanagaraj A, Clare AJ, Badders NM, Bilican B, Chaum E, Chandran S, Shaw CE, Eggan KC, Maniatis T, Taylor JP (2014) Axonal transport of TDP-43 mRNA granules is impaired by ALS-causing mutations. Neuron 81(3): 536–543. https://doi.org/10.1016/j.neuron.2013.12.018
18. Knowles RB, Sabry JH, Martone ME, Deerinck TJ, Ellisman MH, Bassell GJ, Kosik KS (1996) Translocation of RNA granules in living neurons. J Neurosci 16(24):7812–7820
19. Turner-Bridger B, Jakobs M, Muresan L, Wong HH, Franze K, Harris WA, Holt CE (2018) Single-molecule analysis of endogenous β-actin mRNA trafficking reveals a mechanism for compartmentalized mRNA localization in axons. Proc Natl Acad Sci U S A 115(41):E9697–e9706. https://doi.org/10.1073/pnas.1806189115
20. Ruane PT, Gumy LF, Bola B, Anderson B, Wozniak MJ, Hoogenraad CC, Allan VJ (2016) Tumour suppressor adenomatous polyposis coli (APC) localisation is regulated by both Kinesin-1 and Kinesin-2. Sci Rep 6: 27456. https://doi.org/10.1038/srep27456
21. Fukuda Y, Pazyra-Murphy MF, Tasdemir-Yilmaz OE, Li Y, Rose L, Yeoh ZC, Vangos NE, Geffken EA, Seo HS, Adelmant G, Bird GH, Walensky LD, Marto JA, Dhe-Paganon S, Segal RA (2020) Fast transport of RNA granules by direct interactions with KIF5A/KLC1 motors prevents axon degeneration. bioRxiv 2020.02.02.931204. https://doi.org/10.1101/2020.02.02.931204
22. De Graeve F, Besse F (2018) Neuronal RNP granules: from physiological to pathological assemblies. Biol Chem 399(7):623–635. https://doi.org/10.1515/hsz-2018-0141
23. Formicola N, Vijayakumar J, Besse F (2019) Neuronal ribonucleoprotein granules: dynamic sensors of localized signals. Traffic 20(9): 639–649. https://doi.org/10.1111/tra.12672
24. Cioni JM, Lin JQ, Holtermann AV, Koppers M, Jakobs MAH, Azizi A, Turner-Bridger B, Shigeoka T, Franze K, Harris WA, Holt CE (2019) Late endosomes act as mRNA translation platforms and sustain mitochondria in axons. Cell 176(1-2):56–72.e15. https://doi.org/10.1016/j.cell.2018.11.030
25. Pushpalatha KV, Besse F (2019) Local translation in axons: when Membraneless RNP granules meet membrane-bound organelles. Front Mol Biosci 6:129. https://doi.org/10.3389/fmolb.2019.00129
26. Liao YC, Fernandopulle MS, Wang G, Choi H, Hao L, Drerup CM, Patel R, Qamar S, Nixon-Abell J, Shen Y, Meadows W, Vendruscolo M, Knowles TPJ, Nelson M, Czekalska MA, Musteikyte G, Gachechiladze MA, Stephens CA, Pasolli HA, Forrest LR, St George-Hyslop P, Lippincott-Schwartz J, Ward ME (2019) RNA granules hitchhike on lysosomes for long-distance transport, using Annexin A11 as a molecular tether. Cell 179(1):147–164.e120. https://doi.org/10.1016/j.cell.2019.08.050
27. Medioni C, Ephrussi A, Besse F (2015) Live imaging of axonal transport in drosophila pupal brain explants. Nat Protoc 10(4):574–584. https://doi.org/10.1038/nprot.2015.034
28. Medioni C, Ramialison M, Ephrussi A, Besse F (2014) Imp promotes axonal remodeling by regulating profilin mRNA during brain

development. Curr Biol 24(7):793–800. https://doi.org/10.1016/j.cub.2014.02.038

29. Vijayakumar J, Perrois C, Heim M, Bousset L, Alberti S, Besse F (2019) The prion-like domain of drosophila imp promotes axonal transport of RNP granules in vivo. Nat Commun 10(1):2593. https://doi.org/10.1038/s41467-019-10554-w
30. Leung KM, van Horck FP, Lin AC, Allison R, Standart N, Holt CE (2006) Asymmetrical beta-actin mRNA translation in growth cones mediates attractive turning to netrin-1. Nat Neurosci 9(10):1247–1256. https://doi.org/10.1038/nn1775
31. Tiruchinapalli DM, Oleynikov Y, Kelic S, Shenoy SM, Hartley A, Stanton PK, Singer RH, Bassell GJ (2003) Activity-dependent trafficking and dynamic localization of zipcode binding protein 1 and beta-actin mRNA in dendrites and spines of hippocampal neurons. J Neurosci 23(8):3251–3261

Part VII

C. elegans

Chapter 25

Analyzing the Impact of Gene Mutations on Axonal Transport in *Caenorhabditis Elegans*

Yuzu Anazawa and Shinsuke Niwa

Abstract

The development and functions of neurons are supported by axonal transport. Axonal transport is a complex process whose regulation involves multiple molecules, such as microtubules, microtubule-associated proteins, kinases, molecular motors, and motor binding proteins. Gain of function and loss of function mutations of genes that encode these proteins often lead to human axonal neuropathy. *Caenorhabditis elegans* provides a powerful genetic system to study the consequences of gene mutations for axonal transport. Here, we discuss advantages and limitations of using *C. elegans*, propose standard criteria, and describe methods to analyze the impact of gene mutations on axonal transport in *C. elegans*. To obtain solid conclusions, it is necessary to image single neurons in vivo labeled by a specific promoter and to confirm that a mutation changes the localization of a cargo. The motility parameters of the transported cargo should then be analyzed in the mutant. This method enables the axonal transport of proteins and organelles, such as synaptic vesicle precursors and mitochondria, to be analyzed.

Key words Axonal transport, *Caenorhabditis elegans*, Synapse, Synaptic vesicles, Kinesin, KIF1A, UNC-104

1 Introduction

Logistics supports human society; likewise, logistics within a cell is essential for the function and maintenance of the cell through the orchestrated delivery of membrane components, organelles, protein complexes, and mRNA [1]. Neurons are large and highly polarized cells. A neuron receives information by dendrites and transmits information to other neurons and muscles by a long process called axon. To maintain the morphology and function of neurons, a highly developed intracellular transport mechanism called axonal transport has evolved [2, 3].

Axonal transport was originally described in the mammalian nervous system [2]. Later studies showed that axonal transport is evolutionarily conserved in invertebrates such as squid and nematode [3–5]. Biochemical and genetic approaches have revealed

Alessio Vagnoni (ed.), *Axonal Transport: Methods and Protocols*,
Methods in Molecular Biology, vol. 2431, https://doi.org/10.1007/978-1-0716-1990-2_25,
© The Author(s), under exclusive license to Springer Science+Business Media, LLC, part of Springer Nature 2022

many molecules involved in axonal transport. Kinesin superfamily proteins (KIFs) and cytoplasmic dynein are molecular motors for axonal transport [6, 7]. Microtubules serve as rails for KIFs and dynein to travel along. To fine tune axonal transport, microtubule properties are regulated by posttranslational modifications (PTMs) and microtubule-associated proteins (MAPs) [8–10]. KIFs and dynein are positively and negatively regulated by direct binding of proteins and by kinase pathways [11–18].

Additional molecules continue to be suggested to be involved in axonal transport. To confirm the role of these molecules in axonal transport, genetic analyses are essential. *Caenorhabditis elegans* (*C. elegans*) provides a powerful genetic tool for neuronal cell biology [19]. The fundamental axonal transport mechanism is conserved in *C. elegans*. Protein machineries consisting of synaptic vesicles are synthesized in the cell body and then packed in specific membrane organelles called synaptic vesicle precursors (SVPs) [20]. An axonal transport kinesin for SVPs, UNC-104, was originally found by forward genetic study in *C. elegans* [4, 5]. Subsequently, KIF1A and KIF1Bβ, mammalian orthologs of UNC-104, were discovered to transport SVPs in mammalian neurons [20, 21]. We have shown that neuronal expression of a human KIF1A cDNA can rescue *unc-104* deficient worms, indicating that the fundamental mechanism of axonal transport is conserved between *C. elegans* and humans [22].

An advantage of using *C. elegans* as a tool to analyze axonal transport is that the localization of cargos in a specific neuron can be quantitatively analyzed in vivo. All the neurons in *C. elegans* have been characterized [23], and gene promoters have been identified that enable the expression of GFP-fusion cargos in specific neurons. Despite advances in in vivo imaging in the rodent brain, in vivo analysis of single cells is still very difficult. Instead, cultured neurons are widely used to study axonal transport in mammalian neurons [21, 24–26]. Mammalian cultured neurons are a mixture of several types of neuron that express different receptors and different neurotransmitters [24]. This heterogeneity sometimes makes it difficult to quantitatively compare the cargo localization in cultured neurons isolated from different genotypes. In contrast, in *C. elegans*, the localization and transport of organelles in defined neurons can be observed [17, 27–30]. The localization of organelles is very stereotypical in vivo, and individual differences are very small. Differences caused by different genotypes can be easily monitored.

Nevertheless, it should be noted that there are some limitations that must be considered when *C. elegans* is used to study axonal transport. Some cargos and organelles, such as lysosomes, are not transported to the axon in *C. elegans*, and some genes are not evolutionarily conserved [25, 29]. However, this makes it possible to do unique gain of function experiments by introducing

mammalian proteins. For example, ectopic expression of KIF1BP, a strong inhibitor of KIF1A in mammalian neurons, inhibits the axonal transport of SVPs in *C. elegans* neurons [25].

A standard way to study axonal transport is to trace the motility of cargos in mutant worms [27, 29, 31, 32]. Cargo movement can exhibit much variation, even in the same neuron in the same genetic background. Statistical differences in motility parameters can be subtle in some mutants. Therefore, simply analyzing the movement of a particle in a mutant may cause a phenotype to be overlooked or, inversely, observer bias to be introduced. To avoid these pitfalls, based on our previously published work, we suggest that the mislocalization of cargos in single or double mutants needs to be shown before analyzing motility parameters [29]. Some genes may have only a subtle effect on axonal transport. However, for these genes, double mutants can be made with previously identified axonal transport mutants [33] and the resulting phenotype assessed to see if it is enhanced or diminished. If a mutation increases axonal transport, it should suppress loss of function mutants of motor proteins and motor activators [12, 15, 22, 27]. Only when cargo mislocalization can be confirmed in mutants should motility parameters be analyzed.

2 Materials

2.1 Imaging Cargo Localization

1. Wild-type and mutant adult *C. elegans* expressing GFP-fusion cargos under *itr-1* promoter B (*Pitr-1-pB*) [34]. For synaptic vesicles, *wyIs85[Pitr-1-pB::gfp::rab-3]* is convenient.
2. Plastic plates (60-mm petri dishes).
3. Nematode growth medium (NGM) agar: 3 g NaCl, 2.5 Bactopeptone and 17 g agar are dissolved in 975 ml distilled water. After autoclaving, 1 ml cholesterol in ethanol (5 mg/ml), 1 ml M CaCl, 1 ml M MgSO, and 25 ml M potassium phosphate buffer (pH 6.0) are added in order.
4. NGM agar plates with OP50 (culture medium): store NGM agar in plates and seed with OP50 *E. coli*.
5. NGM agar plates without OP50: mix NGM with 2% agar, store in plates without OP50.
6. 5% agarose (w/v) in water: put 0.25 g agarose and 5 ml distilled water into a test tube. Heat the test tube to 95 °C using a heat block until the agarose melts (*see* **Notes 1–3**).
7. Test tubes: 16 × 125 mm disposable glass tubes.
8. Observation solution: mix 2 μl 25 mM Levamisole with 200 μl polystyrene beads (Flow Check™ Undyed Particles, 6 μm, Polysciences, 24262-5).

9. 1.5-ml plastic tube.
10. Glass slides: Glass slides, thickness (mm) 0.9–1.2, 76 × 26 mm.
11. Coverslips: Cover glass, Thickness No. 1: 0.12–0.17 mm, 22 × 22 mm or 22 × 40 mm.
12. Carl Zeiss Microscopy LSM800 system equipped with a ×40 "Plan-Apochromat" oil immersion objective (numerical aperture (N.A.) 1.4 (*see* **Note 4**).
13. Heat block that can be used at 95 °C.

2.2 Imaging Axonal Transport

1. Adult *C. elegans* expressing GFP-fusion cargos under the *mig-13* promoter (*Pmig-13*). For synaptic vesicles, *wyIs251[Pmig-13::gfp::rab-3]* is a good marker.
2. NGM agar plates with OP50.
3. NGM agar plates without OP50.
4. 5% agarose (w/v) in water.
5. Observation solution.
6. Carl Zeiss Axio Observer 7 microscope equipped with an α Plan-Fluar ×100 oil immersion objective (N.A. 1.45), Colibri 7 LED illumination system, and an ORCA-Flash4.0 V3 Digital CMOS camera (Hamamatsu) controlled through the ZEN software (*see* **Notes 5** and **6**).

2.3 Analysis of Axonal Transport

1. Fiji image processing package (https://imagej.net/Fiji) [35].
2. GraphPad Prism 7 or later.

3 Methods

In this protocol, we describe a method to show the localization of synaptic vesicles in a whole neuron, record axonal transport of SVPs, create a kymograph, and statistically analyze recorded parameters. We show how to analyze the axonal transport of SVPs; however, readers can adapt this method to any organelle or protein complex of interest by changing markers and mutants. Using this method, we have shown several genes to be involved in axonal transport of SVPs [12, 33]. We have also shown disease-associated mutations in human *KIF1A* to over-activate anterograde transport of SVPs [22].

We take advantage of the DA9 neuron to observe the localization of synaptic vesicles and analyze axonal transport. The DA9 neuron is located at the tail, making it easy to observe fluorescence-labeled vesicles without interference from the autofluorescent intestines [28, 34] (Fig. 1a). The dendrites and axon of DA9 are clearly distinct; therefore, we often use DA9 to observe the

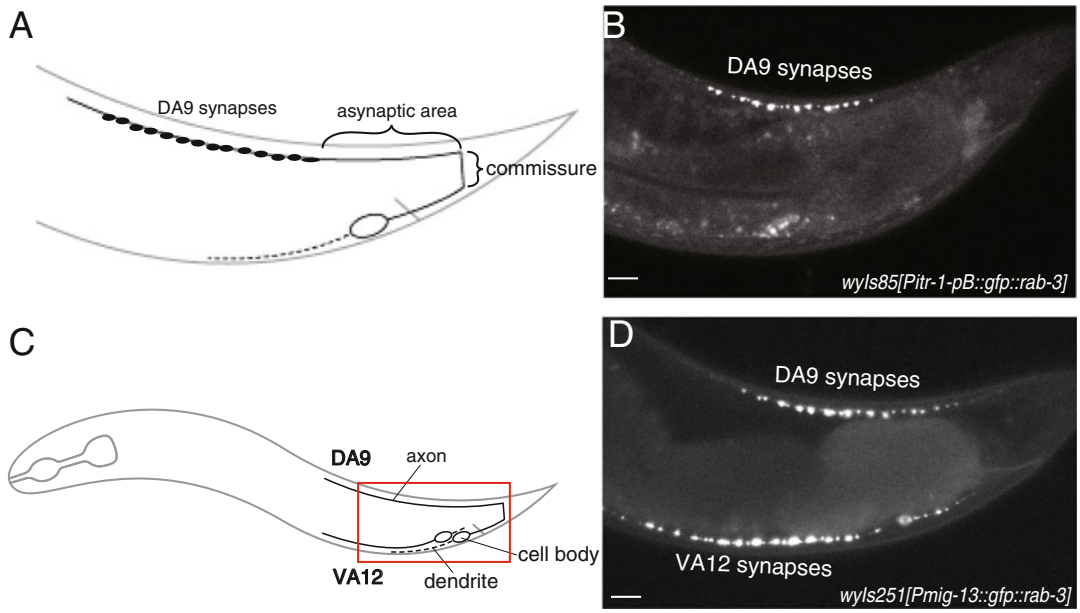

Fig. 1 The morphology of DA9 neurons and the properties of DA9 promoters. (**a**) A scheme showing the tail region and the morphology of the DA9 neuron. (**b**) A representative image of *wyIs85[Pitr-1-pB::gfp::rab-3]*. Scale bar, 10 μm. (**c**) A scheme showing the morphology of DA9 and VA12 neurons in the worm body. (**d**) A representative image of *wyIs251[Pmig-13::gfp::rab-3]*. Scale bar, 10 μm

distribution of cargos. The localization of synapses is stereotypical in DA9. Synapses are formed along the dorsal axon (Fig. 1a, b). No synapses are found in the first 30 μm of the dorsal axon, which we call the "asynaptic area" (Fig. 1a). No synapses are formed on the ventral axon or on the commissure between ventral and dorsal axon (Fig. 1a). This stereotypical morphology can be used when the distribution of synapses is statistically analyzed in wild-type and mutant animals. Two kinds of promoters are used: *itr-1* promoter B (*Pitr-1-pB*) and *mig-13* promoter (*Pmig-13*) [34, 36]. *Pitr-1-pB* expresses a GFP-fusion protein dominantly in the DA9 neuron in the tail neuronal ganglion (Fig. 1b). To observe the localization of cargos in a whole DA9 neuron, *Ptir-1-pB* is better than *Pmig-13*. However, the expression level is not very strong, and sometimes, unnecessary gut expression is seen. *Pmig-13*, however, strongly expresses GFP-fusion proteins in DA9 cell as well as in a neighboring cell, VA12 (Fig. 1c, d). Because strong expression is needed to take time-lapse images, *Pmig-13* is better while VA12 expression makes it difficult to observe cargos in the dendrites. RAB3 is a membrane protein localized to synaptic vesicles and can be used as a marker for SVPs and synaptic vesicles [21, 25, 37]. Considering these points, we use *wyis85[Pitr-1-pB::gfp::rab-3]* and *wyIs251 [Pmig-13::gfp::rab-3]* to visualize the localization of synaptic vesicles and to take time-lapse images, respectively.

For observation of dendritic transport, use of the dimmer *Pitr-1-pB* promoter or DA9-specific expression based on the Cre-loxP system is recommended [32]. The latter system is brighter but requires complicated genetics. To visualize mitochondrial transport in dendrites of DA9, we have established *jpnSi1* based on a single copy insertion and the Cre-loxP system [38]. Using this strain, localization of mitochondria can be observed in both dendrites and the axon of DA9 with more simple genetics.

For imaging axonal transport, it is very important to stop animals from moving without killing them. Nematodes can still move if only paralyzed with levamisole; therefore, we use polystyrene beads supplemented with levamisole [39]. Levamisole affects axonal transport in mechanosensory neurons [40]; however, we have not noticed strong adverse effects in the DA9 neuron if we observe the cell within 20 min after preparation.

To analyze recorded videos, we make kymographs. Kymographs are a good way to visualize how many vesicles are moving in which direction and at what speed. In this protocol, we introduce a method to make kymographs using the Fiji image processing package [35]. Although we use the "KymographBuilder" plugin bundled in Fiji, there are many other ways to create a kymograph. The approach taken should be based on the experimental objectives. Using the movies and kymographs made by this method, we compare *wyIs251* and *arl-8(wy271); wyIs251* in this protocol (Fig. 1d).

3.1 Imaging Synaptic Vesicle Localization in a Whole Neuron

1. First, confirm the mutation is relevant to axonal transport of synaptic vesicles by whole DA9 observation. Introduce the marker *wyIs85* into the mutant by crossing (*see* **Note 7**).
2. Cultivate worm strains on NGM agar plates with OP50 at 20 °C.
3. Put a tube of 5% agarose in a 95 °C heat block. Place a tube filled with distilled water in the 95 °C heat block for pipette washing (*see* **Note 8**).
4. Prepare an agarose pad on a glass slide. Put a few drops of melted 5% agarose on a glass slide using a pipette and quickly place another glass slide on the agarose perpendicular to the first slide before the agarose hardens (Fig. 2). Wash the pipette quickly in the heated distilled water to prevent clogging.
5. After the agarose hardens and becomes cloudy, carefully take off one of the glass slides. The agar will stick to either slide.
6. Transfer 20–30 adult worms to an NGM agar plate without OP50 to remove OP50 from the worms (*see* **Note 9**).
7. Put 2 μl of observation solution on the agarose pad (*see* **Note 10**).

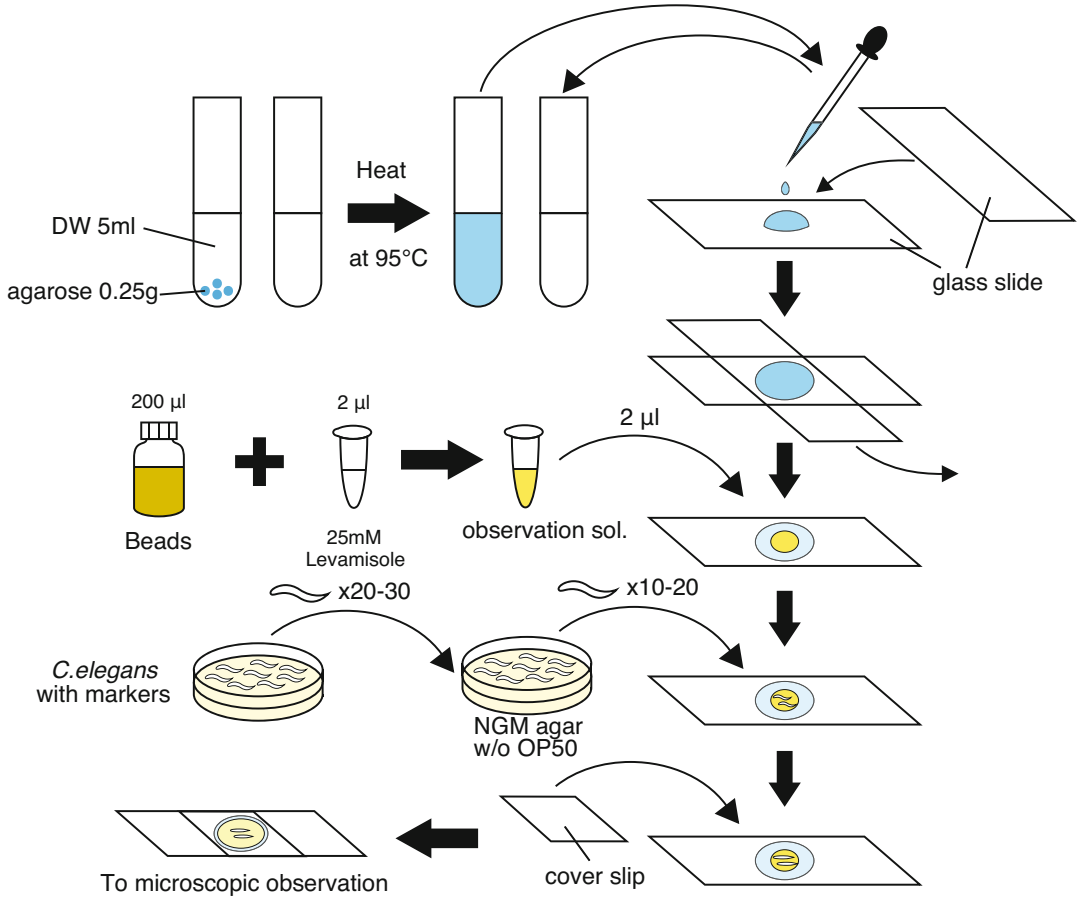

Fig. 2 Schematic flowchart showing how a sample is prepared

8. Pick up 10–20 adult worms from the NGM plate and place them in the observation solution.
9. Wait until the worms are paralyzed. After the worms stop moving, cover them with a coverslip.
10. Image worms immediately using a confocal microscope with a 40× oil immersion objective (we use a Carl Zeiss LSM800).
11. To take an image of a worm, set optimal pixel size using the microscope acquisition software. Then, set the z-stack parameters. The highest and lowest optical planes are determined and marked by the microscope acquisition software. Push the "Start Experiment" button.
12. After obtaining the z-stack images, perform an orthogonal projection and confirm the worm did not move during the imaging. If the worm moved, take z-stack images again.

13. Repeat imaging using a different worm. If it takes more than 20 min from the administration of the anesthesia (i.e., Subheading 3.1, **step 8**), prepare new samples.
14. Measure the length of the dorsal asynaptic area and the number of misaccumulated puncta in the commissure (Fig. 1b).
15. If the localization of synaptic vesicles is changed in the mutant, the mutation is predicted to affect axonal transport. Go to the next section to analyze transport parameters.
16. If the single mutant does not show clear mislocalization of synaptic vesicles, then create a double mutant with *arl-8 (wy271)*, *cdk-5(ok626)*, or another appropriate strain [18, 29]. Repeat Subheading 3.1, **steps 1–14**. If the gene is required for anterograde transport, *arl-8(wy271)* should enhance the phenotype. If the gene of interest negatively regulates axonal transport, the mislocalization of synaptic vesicles in *arl-8* should be suppressed. If the gene is essential for retrograde transport, the mutation should suppress dendritic mislocalization of synaptic vesicles found in *cdk-5(ok626)* [18]. In these cases, go to the next section to analyze dynamic parameters. If no phenotype can be observed, even by double-mutant analyses, it is safe to conclude that the gene is not important for axonal transport of synaptic vesicles.

3.2 Recording Axonal Transport

1. Introduce the marker *wyIs251* into the mutant of interest by crossing. Cultivate worm strains on NGM agar plates with OP50 at 20 °C.
2. Prepare a sample as described in Subheading 3.1, **steps 2–9** (*see* **Note 11**).
3. Image the DA9 neuron using a Carl Zeiss Axio Observer 7 microscope with a 100× oil immersion objective (N.A. 1.45), Colibri 7 LED illumination and an ORCA-Flash4.0 V3 Digital CMOS camera.
4. After setting the imaging stage, focus on the worm's tale using the bright-field light.
5. Once the tail is in focus, use the LED fluorescence to find neural vesicles in the DA9 neuron and focus on them (*see* **Note 12**).
6. Operate the microscope acquisition software to set the intensity of the LED at approximately 18% and switch to the camera.
7. Use "Live" mode and focus on the small moving vesicles. To identify them, it is necessary to magnify the image (Fig. 3a, b). If it is difficult to focus on them or see vesicle movements, quickly stop "Live" mode to prevent photobleaching and look for another worm using the bright-field light (*see* **Note 13**).

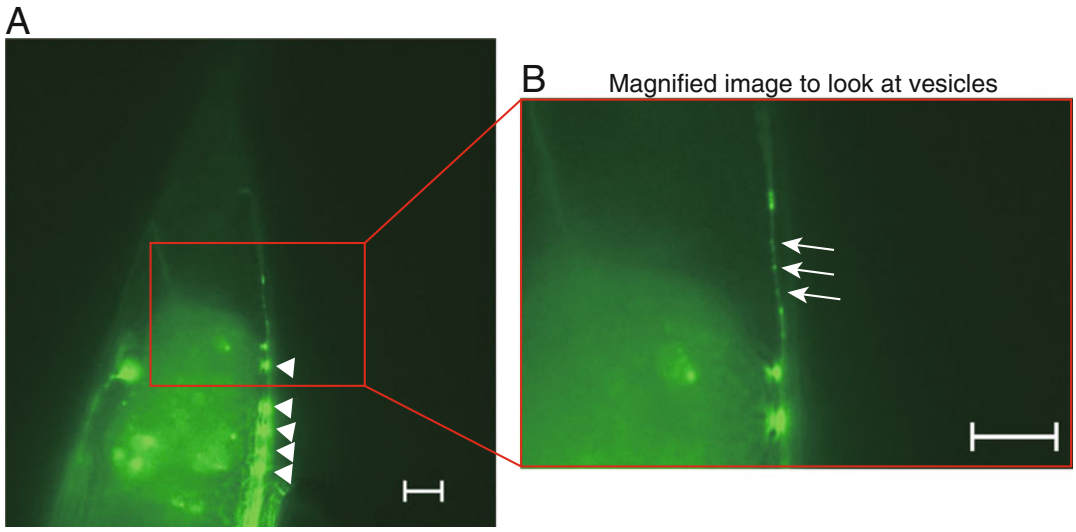

Fig. 3 Observation of synaptic vesicle precursors. (**a**) Image of a live worm tail region expressing *gfp::rab-3*. Scale bar, 10 μm. Note that strong signals from dorsal synapses (arrowheads) are saturated to enable observation of the weak signal from transported vesicles. (**b**) A magnified image. Scale bar, 10 μm. Note that small vesicles or vesicle reservoirs (arrows) can be observed

8. When a good worm is found, change the intensity of the LED light source to a minimal value at which the moving vesicles are still clearly visible.
9. Record the vesicle movements every 250 ms for a total of up to 2 min (*see* **Note 14**).
10. Image each glass slide for no more than 20 min, as constant LED exposure is deleterious to the neurons.
11. Repeat Subheading 3.2, **steps 3–11**, until sufficient time-lapse images are recorded.

3.3 Analysis of Axonal Transport

1. To visualize a movie, open the time-lapse images in Fiji software by drag-dropping the file on the Fiji icon or toolbar (Fig. 4a).
2. Select a segmented line along the axon in the movie where the movement of vesicles is clearly visible (Fig. 4b).
3. Select the image window containing the original time sequence and restore the segmented line ROI (Edit > Selection > Restore Selection).
4. Start the "KymographBuilder" plugin (Plugin > Kymograph > KymographBuilder) to generate a kymograph (Fig. 4c, d).
5. Using the movies and kymographs, compare the wild-type and mutant for various parameters. For example, the following parameters can be used.

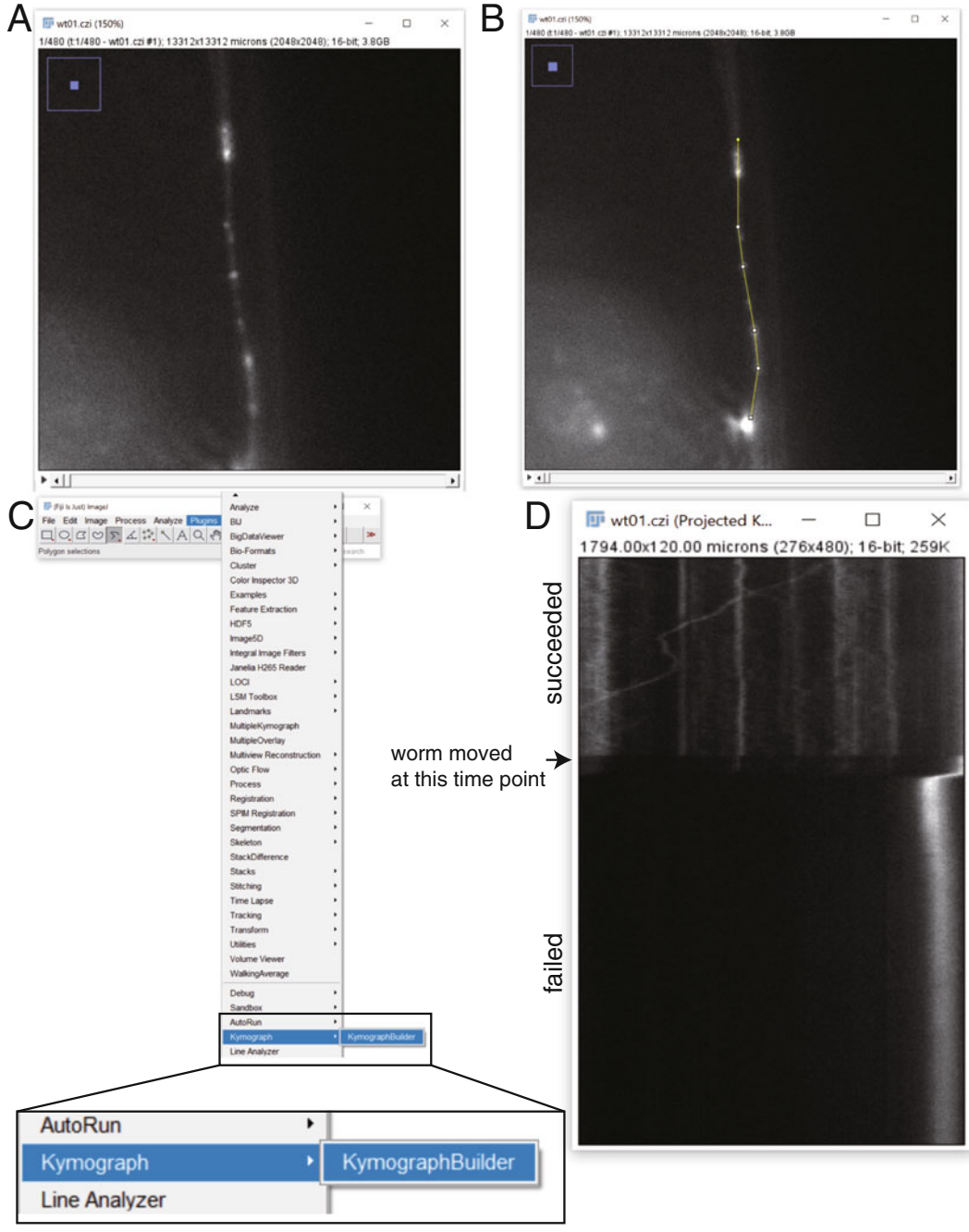

Fig. 4 Kymograph generation. (**a**) Hyper stack file opened with Fiji. (**b**) Hand-drawn line tracing an axon. (**c**) KymographBuilder plugin. (**d**) Kymograph generated by KymographBuilder plugin. Note that this example kymograph shows a region in which vesicle movement is traced properly and a region in which the trace is failed because of worm movement. Thus, worm immobilization is important for good observation

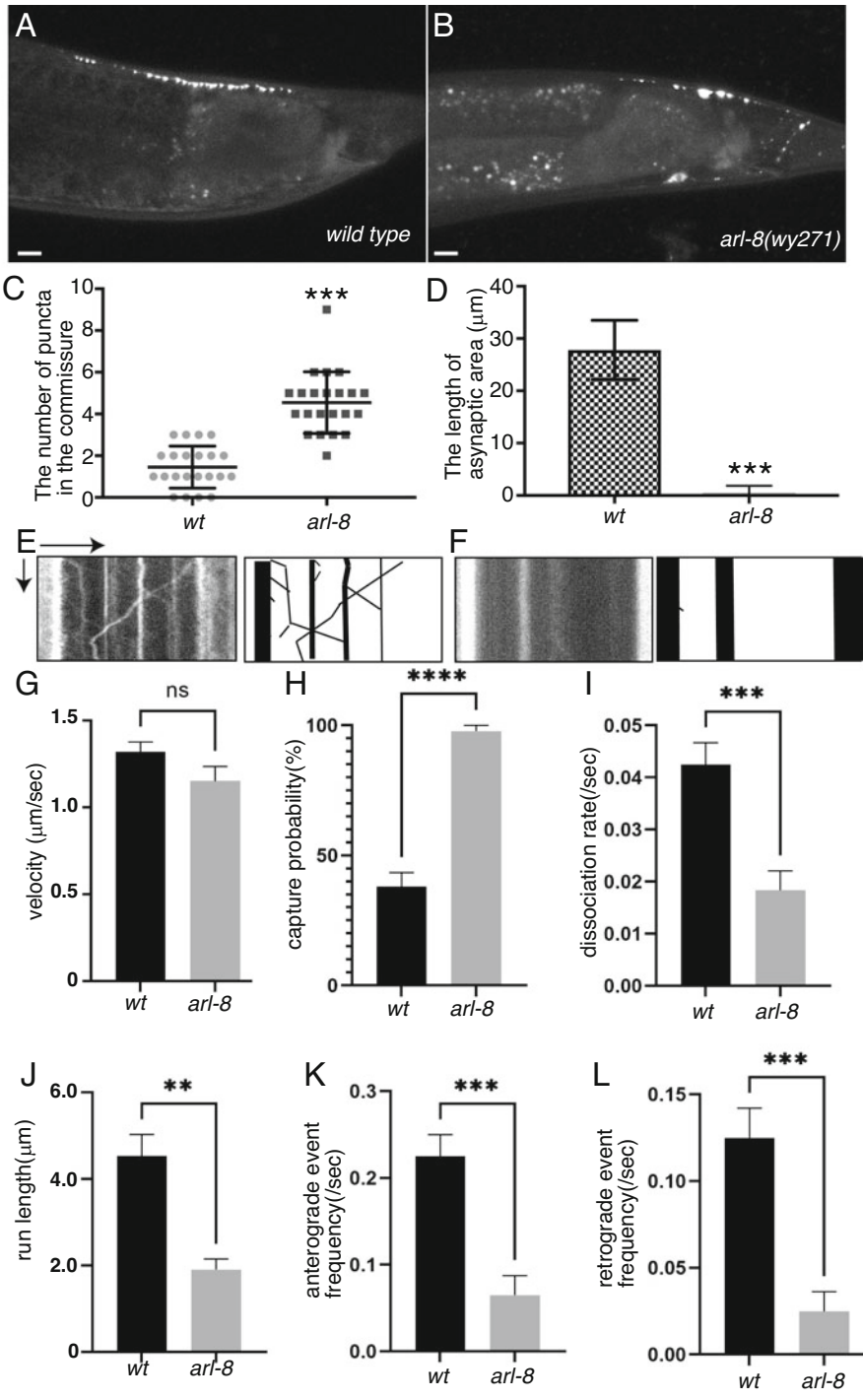

Fig. 5 A representative example of data obtained by analyzing wild-type and *arl-8* mutant animals. (**a** and **b**) Representative images showing localization of synaptic vesicles in wild type (**a**) and *arl-8(wy271)* (**b**). Scale bars, 10 μm. (**c**) A scatter dot plot of the number of RAB-3-positive puncta in the commissure between ventral and dorsal axons. The mean ± standard deviation (SD) is overlaid. ***$p < 0.001$, Student's *t*-test, $n = 20$. (**d**) Bar graphs showing the length of asynaptic regions, mean ± SD, ***$p < 0.001$, Student's *t*-test, $n = 20$. (**e** and **f**) Representative kymographs showing the motility of synaptic vesicle precursors in wild-type (**e**) and

(a) Velocity: measure the velocity of each vesicle.

(b) Dissociation rate: count the number of vesicles that dissociate from a stable punctum and divide it by the time taken and the number of stable puncta.

(c) Capture probability: count the number of mobile vesicles bypassing or captured by a stable punctum and calculate the number of captured vesicles/the total number of vesicles.

(d) Run length: measure how long the vesicles have moved without stopping.

(e) Anterograde and retrograde event frequencies: calculate the number of events moving anterogradely or retrogradely during the movie and divide it by the time taken.

As an example, we show data comparing wild-type and *arl-8(wy271)* mutant phenotypes (Fig. 5a–l).

4 Notes

1. We routinely use low-melting point agarose generally used for electrophoresis of DNA.
2. Do not use a microwave oven to prepare 5% agarose. The agarose can also be melted by autoclaving. Once melted, 5% agarose can be stored at 4 °C and can be remelted in a microwave oven.
3. After several hours of incubation at 95 °C, the agarose gradually softens. If this happens, prepare a fresh tube of 5% agarose.
4. We prefer to use an oil immersion lens because it has a higher numerical aperture and is brighter than a water immersion lens. A C-Apochromat water immersion lens (N.A. 1.2) may be used because water immersion lenses are generally better for observing living cells or animals. However, because the DA9 neuron is not localized deep in the body, an oil immersion lens works well.
5. Spinning disc confocal microscopy can be used. However, we find that the simple system for widefield microscopy described here is better for observing axonal transport in the DA9 axon

Fig. 5 (continued) arl-8(wy271) (**f**). *X* and *Y* axis bars represent 5 μm and 10 s, respectively. (**g–l**) Bar graphs showing mean ± SD values of axonal transport parameters in wild-type and *arl-8* mutant animals. Velocity of moving vesicles (**g**), capture probability (**h**), dissociation rate (**i**), run length (**j**), anterograde event frequency (**k**), and retrograde event frequency (**l**). $N = 20$ animals. $^{**}p < 0.01$, $^{***}p < 0.001$, $^{****}p < 0.0001$, Student's *t*-test

because the camera can get more signal without the spinning disc unit.

6. If the microscope is equipped with a temperature controller, set the temperature at 20 °C. If not, set the temperature of the microscope room at 20 °C.
7. *jpnSi3 [Pmig-13::loxP::stop::loxP::sng-1::gfp, Pglr-4::cre]* can be used as well [38].
8. 2% agarose instead of 5% agarose can be used. For 2% agarose, set the heat block to 60 °C instead of 95 °C. To prepare 2% agarose, one can use microwave instead of heat block or autoclave.
9. It is better not to use fresh NGM agar plates because they are wet. NGM agar plates here need to be moderately dry.
10. Levamisole (0.25 mM) in M9 buffer can be used instead.
11. Good fixation is very important for good time-lapse recording. Thus, 5% (not 2%) agarose and observation solution (not 0.25 mM levamisole) must be used for time-lapse observation. OP50 on the worm body must be removed by transferring to moderately dried NGM plate without bacteria. If remaining *E. coli* gets into the anesthesia, the worms will move, and it becomes hard to take time-lapse images.
12. The DA9 axon is usually on the dorsal side. Vesicles on the ventral side should not be recorded.
13. Moving vesicles can be found at this moment. The body angle of the worm is important for good focus and imaging. Vesicles can be clearly observed in about 2 out of 10 worms. Look for good worms as quickly as possible.
14. When in vivo force measurements are performed [41], take the movie at 100 fps.

Acknowledgments

This work was supported by JSPS KAKENHI Grant number JP20H03247, JP19H04738, and 16H06536. We deeply thank Dr. Asako Sugimoto (Tohoku University) and Niwa lab members (Tohoku University) for their helpful discussion and advice. We thank Jeremy Allen, PhD, from Edanz Group (https://en-author-services.edanz.com/ac) for editing a draft of this manuscript.

References

1. Hirokawa N, Noda Y, Tanaka Y, Niwa S (2009) Kinesin superfamily motor proteins and intracellular transport. Nat Rev Mol Cell Biol 10(10):682–696. https://doi.org/10.1038/nrm2774

2. Ochs S (1972) Fast transport of materials in mammalian nerve fibers. Science 176(4032): 252–260. https://doi.org/10.1126/science.176.4032.252
3. Brady ST, Lasek RJ, Allen RD (1982) Fast axonal transport in extruded axoplasm from squid giant axon. Science 218(4577): 1129–1131
4. Otsuka AJ, Jeyaprakash A, Garcia-Anoveros J, Tang LZ, Fisk G, Hartshorne T, Franco R, Born T (1991) The C. elegans unc-104 gene encodes a putative kinesin heavy chain-like protein. Neuron 6(1):113–122
5. Hall DH, Hedgecock EM (1991) Kinesin-related gene unc-104 is required for axonal transport of synaptic vesicles in C. elegans. Cell 65(5):837–847
6. Vale RD (2003) The molecular motor toolbox for intracellular transport. Cell 112(4): 467–480
7. Hirokawa N, Niwa S, Tanaka Y (2010) Molecular motors in neurons: transport mechanisms and roles in brain function, development, and disease. Neuron 68(4):610–638. https://doi.org/10.1016/j.neuron.2010.09.039
8. McKenney RJ, Huynh W, Vale RD, Sirajuddin M (2016) Tyrosination of alpha-tubulin controls the initiation of processive dynein-dynactin motility. EMBO J 35(11): 1175–1185. https://doi.org/10.15252/embj.201593071
9. Monroy BY, Sawyer DL, Ackermann BE, Borden MM, Tan TC, Ori-McKenney KM (2018) Competition between microtubule-associated proteins directs motor transport. Nat Commun 9(1):1487. https://doi.org/10.1038/s41467-018-03909-2
10. Janke C (2014) The tubulin code: molecular components, readout mechanisms, and functions. J Cell Biol 206(4):461–472. https://doi.org/10.1083/jcb.201406055
11. Wagner OI, Esposito A, Kohler B, Chen CW, Shen CP, Wu GH, Butkevich E, Mandalapu S, Wenzel D, Wouters FS, Klopfenstein DR (2009) Synaptic scaffolding protein SYD-2 clusters and activates kinesin-3 UNC-104 in *C. elegans*. Proc Natl Acad Sci U S A 106(46): 19605–19610. https://doi.org/10.1073/pnas.0902949106
12. Niwa S, Lipton DM, Morikawa M, Zhao C, Hirokawa N, Lu H, Shen K (2016) Autoinhibition of a neuronal kinesin UNC-104/KIF1A regulates the size and density of synapses. Cell Rep 16(8):2129–2141. https://doi.org/10.1016/j.celrep.2016.07.043
13. McKenney RJ, Huynh W, Tanenbaum ME, Bhabha G, Vale RD (2014) Activation of cytoplasmic dynein motility by dynactin-cargo adapter complexes. Science 345(6194): 337–341. https://doi.org/10.1126/science.1254198
14. Verhey KJ, Hammond JW (2009) Traffic control: regulation of kinesin motors. Nat Rev Mol Cell Biol 10(11):765–777. https://doi.org/10.1038/nrm2782
15. Kumar J, Choudhary BC, Metpally R, Zheng Q, Nonet ML, Ramanathan S, Klopfenstein DR, Koushika SP (2010) The Caenorhabditis elegans Kinesin-3 motor UNC-104/KIF1A is degraded upon loss of specific binding to cargo. PLoS Genet 6(11):e1001200. https://doi.org/10.1371/journal.pgen.1001200
16. Byrd DT, Kawasaki M, Walcoff M, Hisamoto N, Matsumoto K, Jin Y (2001) UNC-16, a JNK-signaling scaffold protein, regulates vesicle transport in *C. elegans*. Neuron 32(5):787–800. https://doi.org/10.1016/s0896-6273(01)00532-3
17. Sakamoto R, Byrd DT, Brown HM, Hisamoto N, Matsumoto K, Jin Y (2005) The Caenorhabditis elegans UNC-14 RUN domain protein binds to the kinesin-1 and UNC-16 complex and regulates synaptic vesicle localization. Mol Biol Cell 16(2):483–496. https://doi.org/10.1091/mbc.e04-07-0553
18. Ou CY, Poon VY, Maeder CI, Watanabe S, Lehrman EK, Fu AK, Park M, Fu WY, Jorgensen EM, Ip NY, Shen K (2010) Two cyclin-dependent kinase pathways are essential for polarized trafficking of presynaptic components. Cell 141(5):846–858. https://doi.org/10.1016/j.cell.2010.04.011
19. Brenner S (1974) The genetics of Caenorhabditis elegans. Genetics 77(1):71–94
20. Okada Y, Yamazaki H, Sekine-Aizawa Y, Hirokawa N (1995) The neuron-specific kinesin superfamily protein KIF1A is a unique monomeric motor for anterograde axonal transport of synaptic vesicle precursors. Cell 81(5): 769–780
21. Niwa S, Tanaka Y, Hirokawa N (2008) KIF1Bbeta- and KIF1A-mediated axonal transport of presynaptic regulator Rab3 occurs in a GTP-dependent manner through DENN/MADD. Nat Cell Biol 10(11):1269–1279. https://doi.org/10.1038/ncb1785
22. Chiba K, Takahashi H, Chen M, Obinata H, Arai S, Hashimoto K, Oda T, McKenney RJ, Niwa S (2019) Disease-associated mutations hyperactivate KIF1A motility and anterograde axonal transport of synaptic vesicle precursors. Proc Natl Acad Sci U S A 116(37): 18429–18434. https://doi.org/10.1073/pnas.1905690116

23. White JG, Southgate E, Thomson JN, Brenner S (1986) The structure of the nervous system of the nematode Caenorhabditis elegans. Philos Trans R Soc Lond Ser B Biol Sci 314(1165):1–340. https://doi.org/10.1098/rstb.1986.0056
24. Kaech S, Banker G (2006) Culturing hippocampal neurons. Nat Protoc 1(5):2406–2415. https://doi.org/10.1038/nprot.2006.356
25. Kevenaar JT, Bianchi S, van Spronsen M, Olieric N, Lipka J, Frias CP, Mikhaylova M, Harterink M, Keijzer N, Wulf PS, Hilbert M, Kapitein LC, de Graaff E, Ahkmanova A, Steinmetz MO, Hoogenraad CC (2016) Kinesin-binding protein controls microtubule dynamics and cargo trafficking by regulating kinesin motor activity. Curr Biol 26(7):849–861. https://doi.org/10.1016/j.cub.2016.01.048
26. Nakata T, Terada S, Hirokawa N (1998) Visualization of the dynamics of synaptic vesicle and plasma membrane proteins in living axons. J Cell Biol 140(3):659–674. https://doi.org/10.1083/jcb.140.3.659
27. Zheng Q, Ahlawat S, Schaefer A, Mahoney T, Koushika SP, Nonet ML (2014) The vesicle protein SAM-4 regulates the processivity of synaptic vesicle transport. PLoS Genet 10(10):e1004644. https://doi.org/10.1371/journal.pgen.1004644
28. Klassen MP, Wu YE, Maeder CI, Nakae I, Cueva JG, Lehrman EK, Tada M, Gengyo-Ando K, Wang GJ, Goodman M, Mitani S, Kontani K, Katada T, Shen K (2010) An Arf-like small G protein, ARL-8, promotes the axonal transport of presynaptic cargoes by suppressing vesicle aggregation. Neuron 66(5):710–723. https://doi.org/10.1016/j.neuron.2010.04.033
29. Wu YE, Huo L, Maeder CI, Feng W, Shen K (2013) The balance between capture and dissociation of presynaptic proteins controls the spatial distribution of synapses. Neuron 78(6):994–1011. https://doi.org/10.1016/j.neuron.2013.04.035
30. Koushika SP, Schaefer AM, Vincent R, Willis JH, Bowerman B, Nonet ML (2004) Mutations in Caenorhabditis elegans cytoplasmic dynein components reveal specificity of neuronal retrograde cargo. J Neurosci 24(16):3907–3916. https://doi.org/10.1523/JNEUROSCI.5039-03.2004
31. Mondal S, Koushika SP (2014) Microfluidic devices for imaging trafficking events in vivo using genetic model organisms. Methods Mol Biol 1174:375–396. https://doi.org/10.1007/978-1-4939-0944-5_26
32. Maeder CI, San-Miguel A, Wu EY, Lu H, Shen K (2014) In vivo neuron-wide analysis of synaptic vesicle precursor trafficking. Traffic 15(3):273–291. https://doi.org/10.1111/tra.12142
33. Niwa S, Tao L, Lu SY, Liew GM, Feng W, Nachury MV, Shen K (2017) BORC regulates the axonal transport of synaptic vesicle precursors by activating ARL-8. Curr Biol 27(17):2569–2578. e2564. https://doi.org/10.1016/j.cub.2017.07.013
34. Klassen MP, Shen K (2007) Wnt signaling positions neuromuscular connectivity by inhibiting synapse formation in C. elegans. Cell 130(4):704–716. https://doi.org/10.1016/j.cell.2007.06.046
35. Schindelin J, Arganda-Carreras I, Frise E, Kaynig V, Longair M, Pietzsch T, Preibisch S, Rueden C, Saalfeld S, Schmid B, Tinevez JY, White DJ, Hartenstein V, Eliceiri K, Tomancak P, Cardona A (2012) Fiji: an open-source platform for biological-image analysis. Nat Methods 9(7):676–682. https://doi.org/10.1038/nmeth.2019
36. Mizumoto K, Shen K (2013) Interaxonal interaction defines tiled presynaptic innervation in C. elegans. Neuron 77(4):655–666. https://doi.org/10.1016/j.neuron.2012.12.031
37. Johnston PA, Archer BT 3rd, Robinson K, Mignery GA, Jahn R, Sudhof TC (1991) rab3A attachment to the synaptic vesicle membrane mediated by a conserved polyisoprenylated carboxy-terminal sequence. Neuron 7(1):101–109. https://doi.org/10.1016/0896-6273(91)90078-e
38. Obinata H, Sugimoto A, Niwa S (2018) Streptothricin acetyl transferase 2 (Sat2): a dominant selection marker for Caenorhabditis elegans genome editing. PLoS One 13(5):e0197128. https://doi.org/10.1371/journal.pone.0197128
39. Kim E, Sun L, Gabel CV, Fang-Yen C (2013) Long-term imaging of Caenorhabditis elegans using nanoparticle-mediated immobilization. PLoS One 8(1):e53419. https://doi.org/10.1371/journal.pone.0053419
40. Mondal S, Ahlawat S, Rau K, Venkataraman V, Koushika SP (2011) Imaging in vivo neuronal transport in genetic model organisms using microfluidic devices. Traffic 12(4):372–385. https://doi.org/10.1111/j.1600-0854.2010.01157.x
41. Hayashi K, Hasegawa S, Sagawa T, Tasaki S, Niwa S (2018) Non-invasive force measurement reveals the number of active kinesins on a synaptic vesicle precursor in axonal transport regulated by ARL-8. Phys Chem Chem Phys 20(5):3403–3410. https://doi.org/10.1039/c7cp05890j

Chapter 26

Methods to Quantify and Relate Axonal Transport Defects to Changes in *C. elegans* Behavior

Syed Nooruzuha Barmaver, Muniesh Muthaiyan Shanmugam, and Oliver Ingvar Wagner

Abstract

Neuronal growth, differentiation, homeostasis, viability, and injury response heavily rely on functional axonal transport (AT). Erroneous and disturbed AT may lead to accumulation of "disease proteins" such as tau, α-synuclein, or amyloid precursor protein causing various neurological disorders. Changes in AT often lead to observable behavioral consequences in *C. elegans* such as impeded movements, defects in touch response, chemosensation, and even egg laying. Long *C. elegans* neurons with clear distinguishable axons and dendrites provide an excellent platform to analyze AT. The possibility to relate changes in AT to neuronal defects that in turn lead to quantifiable changes in worm behavior allows for the advancement of neuropathological disease models. Even more, subsequent suppressor screens may aid in identifying genes responsible for observed behavioral changes providing a target for drug development to eventually delay or cure neurological diseases. Thus, in this chapter, we summarize critical methods to identify and quantify defects in axonal transport as well as exemplified behavioral assays that may relate to these defects.

Key words Axonal transport, Kinesin, Dynein, Synaptic vesicles, Microtubules, Worm behavior

1 Introduction

Neurons are highly specialized brain cells with a well-defined cell body (soma) from which dendrites and axons emanate utilized for information processing. The delicate spatiotemporally regulated transport of metabolites and organelles from the soma to the synapses is critical for neuronal survival and proper functioning of neurotransmission. The ever-fascinating transport of cellular cargos by molecular motors in axons has caught the eyes of scientists for decades. Different types of cargos such as mitochondria, synaptic vesicle precursors, signaling endosomes, autophagosomes, lysosomes, and mRNA granules are actively transported along the axon via microtubule-based molecular motors [1]. The molecular motor kinesin (along with its regulating adaptors) is responsible for

Alessio Vagnoni (ed.), *Axonal Transport: Methods and Protocols*,
Methods in Molecular Biology, vol. 2431, https://doi.org/10.1007/978-1-0716-1990-2_26,
© The Author(s), under exclusive license to Springer Science+Business Media, LLC, part of Springer Nature 2022

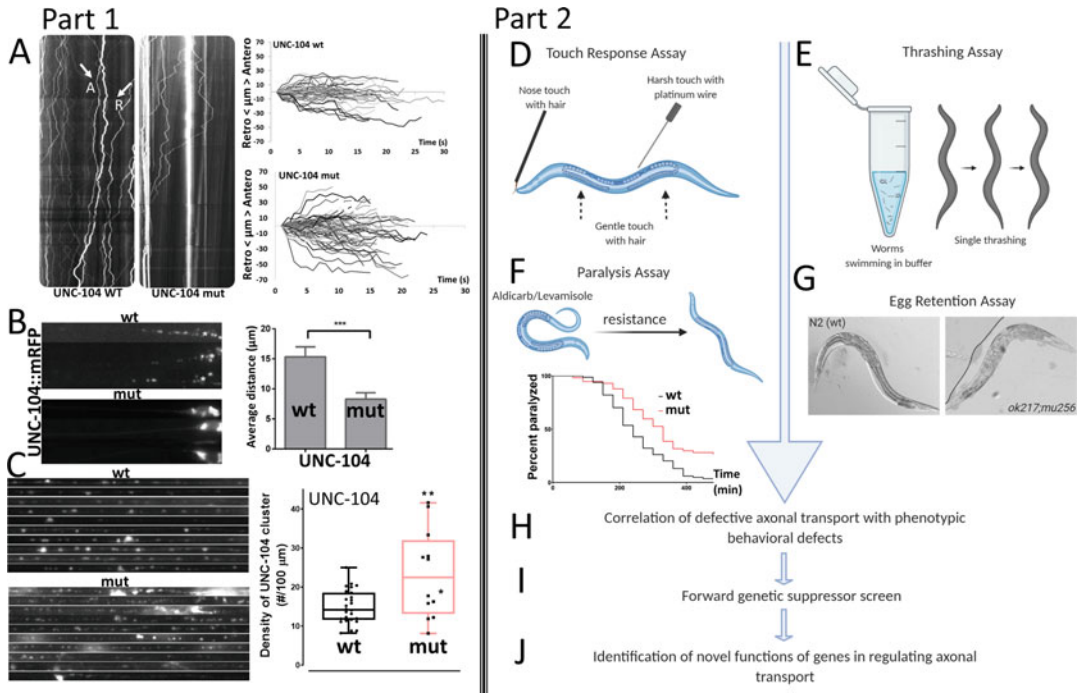

Fig. 1 Schematic diagram of the successive steps to relate axonal transport defects to changes in worm behavior. "Part 1" refers to the identification of axonal transport (AT) defects in mutants. "Part 2" refers to relating these defects to changes in worm behavior. (**a**) Kymograph analysis of UNC-104::mRFP motility in ALM neurons of wild-type and mutant worms. Right: Bullet diagram representation of motor run lengths. (**b**) Travel distances of UNC-104::mRFP in ALM neurons of wild-type and mutants (with each three representative neurons stacked on each other; cell bodies to the right). (**c**) Analysis of motor densities in sublateral neurons of wild-type and mutants (with each ten representative neurons stacked on each other). (**d**) Graphical representation of nose, harsh, and soft touch response assay. (**e**) Thrashing assay. (**f**) Aldicarb/Levamisole assay. (**g**) Egg retention assay. (**h**) Step to correlate identified phenotypic abnormality to axonal transport defects. (**i**) Screen to identify genes that may suppress this phenotype. (**j**) Functional analysis of identified genes. Student's *t*-test. $*p < 0.05$, $**p < 0.01$, $***p < 0.001$

the anterograde transport (from the soma to the distal tips of axons and dendrites), and dynein (along with its complex adaptor dynactin) is responsible for retrograde transport of the cargos [2, 3]. The bidirectional axonal transport (AT) guarantees for maintaining a diverse set of neuronal functions such as cell polarization, elongation, neuronal plasticity, brain wiring, and even learning and memory [4–6]. In light of the constant energy demands and the need of a finely tuned transport, it is not surprising that errors and disturbance in AT are causatives of various neurological diseases. Specifically, imbalance in AT may lead to the accumulation of "disease proteins" observed in pathological neurons such as tau and amyloid precursor protein in Alzheimer's disease, neurofilaments in amyotrophic lateral sclerosis (ALS), or α-synuclein in Parkinson's disease [7, 8]. Below we describe methods to quantify changes in motility of motors/cargos (Fig. 1a, b) as well as changes of motor/cargo accumulations (Fig. 1c) in nematode neurons.

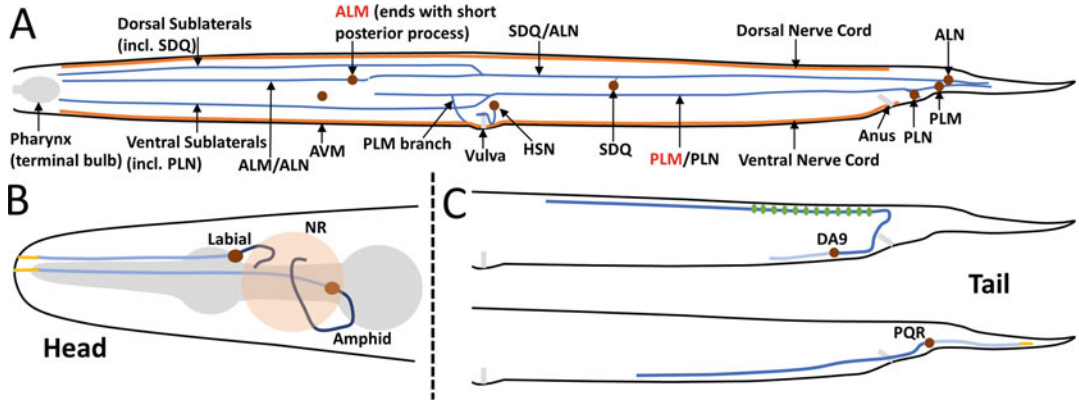

Fig. 2 (**a**) Simplified scheme of the nervous system in *C. elegans* (ALM and PLM neurons highlighted in red). Blue lines indicate neurites, and orange lines depict nerve cords. (**b**) Position and anatomy of head sensory neurons (only two neurons shown). NR = nerve ring area. (**c**) Position and anatomy of two "model neurons" in the tail. Dark blue lines = axons, light blue lines = dendrites, brown circles = soma, green lines with dots = *en passant* synapses, and yellow lines = ciliated ending in (**b**) and (**c**)

In *C. elegans*, defects in AT often result in visible changes in worm's behavior, such as defects in motor neurons, may cause uncoordinated movements, defects in mechanosensory neurons (e.g., ALM and PLM, Fig. 2a) may cause impaired touch responses, and defects in HSN neuron (Figs. 2a and 5b) function may cause egg laying defects or egg retention phenotypes. Because uncoordinated worm movements are not straightforwardly quantifiable, we discuss below the "thrashing assay" in which the worm's body bends are counted in buffer (Fig. 1e) [9, 10]. Touch response (Fig. 1d) is a more complex behavior in which the worm is capable to discriminate between gentle and harsh touch sensed by six mechanosensory neurons (ALM, PLM, AVM, and PVM, Fig. 2a) as well as nose touch mediated by at least 26 neurons [11]. Egg laying behavior is regulated by a relatively simple neuronal circuit of VA, VB, HSN, and VC motor neurons, all of them controlling vulval muscles employing acetylcholine and serotonin neurotransmitters [12, 13]. Dysfunction of these neurons often directly results in quantifiable egg retention phenotypes (Fig. 1g). The aldicarb paralysis assay (Fig. 1f) is a simple method to test for acetylcholine (ACh) neurotransmitter defects. Aldicarb is a chemical compound that can be directly absorbed by the worm and acting as an acetylcholinesterase inhibitor immediately leading to quantifiable worm paralysis (due to hyperstimulation of muscles) [14]. All these visible and easily quantifiable phenotypes can be subsequently used to develop a neuronal disease model (Fig. 1h), and importantly, subsequent suppressor screens (Fig. 1i) can be carried out. Here, a "sick" (phenotypically abnormal) worm will be exposed to a mutagen (or high-throughput RNAi knockdowns) and then progenies screened for wild-type phenotypes: "a sick worm becomes

healthy" by a mutation that suppresses the abnormal phenotype. Once a target gene has been identified (Fig. 1j), its function can be verified in higher animals and eventually used as a target to delay or cure related neurological diseases [15, 16].

2 Materials

2.1 Worm Culture

1. 5 mg/ml cholesterol in ethanol (do not autoclave).
2. 1 M KPO_4 buffer pH 6.0: 108.3 g KH_2PO_4, 35.6 g K_2HPO_4, H_2O to 1 l.
3. NGM (nematode growth medium): 3 g NaCl, 17 g agar, 2.5 g peptone, 25 ml 1 M KPO_4 buffer pH 6.0, 1 ml 1 M $CaCl_2$, 1 ml 1 M $MgSO_4$, 1 ml cholesterol, in 975 ml H_2O.
4. Plastic petri dishes (90 × 15 mm).
5. LB medium: 10 g tryptone, 5 g yeast extract, 10 g NaCl, H_2O to 1 l.
6. OP50 culture: inoculate OP50 strain in LB medium and shake overnight. Note that the uracil auxotroph *E. coli* OP50 strain acts as worm's food source.

2.2 Microinjection

1. Epifluorescence microscope with DIC contrast with a rotating stage for convenient positioning of the worm's gonads toward the microinjection needle. Microinjector, e.g., Eppendorf Femtojet express.
2. Needle puller: Sutter Instrument Micropipette Puller. Borosilicate glass capillaries (1.0 mm OD, 0.75 mm ID).
3. Stereo microscope for screening of transgenic worms.
4. 22 × 22 mm coverslips and 24 × 60 mm cover glasses .
5. Mineral oil (we suggest Sigma M5904).
6. Agarose.
7. S Buffer: 129 ml 0.05 M K_2HPO_4, 871 ml 0.05 M KH_2PO_4, 5.85 g NaCl.
8. Recovery buffer: 5 mM HEPES pH 7.2, 3 mM $CaCl_2$, 3 mM $MgCl_2$, 66 mM NaCl, 2.4 mM KCl, 4% glucose (w/v).
9. 1-ml tuberculin syringe. MultiFlex Round Tips.
10. Used transgenes: *Punc-104::unc-104::mrfp* (*C. elegans* homolog of kinesin-3 KIF1A with fused mRFP; the major fast axonal transporter of synaptic vesicles), *Punc-104::snb-1::mrfp* (synaptobrevin-1 fused with mRFP; a critical marker for synaptic vesicles), *Punc-104::rab-3::yfp* (RAB3A fused with YFP; another critical marker for synaptic vesicles), *Punc-116::unc-116::mrfp* (conventional kinesin-1 KIF5A fused with mRFP; transports organelles other than synaptic vesicles such as mitochondria or endosomes) [17, 18] (*see* **Note 1**).

2.3 Motility Assay

1. Nipkow spinning disk microscope connected to an EMCCD camera.
2. M9 Buffer: 3 g KH_2PO_4, 6 g Na_2HPO_4, 5 g NaCl, 1 ml 1 M $MgSO_4$, H_2O to 1 l. Sterilize by autoclaving.
3. NIH ImageJ free image processing software (latest version, https://imagej.nih.gov/ij/) with added "Kymo-ToolBox" plug-in.
4. Microsoft Excel, GraphPad Prism, or equivalent software to plot and statistically test the obtained data.

2.4 Behavioral Assays

1. Levamisole and aldicarb.
2. Platinum wire and eyelash attached to an appropriate holder.

2.5 Suppressor Screen

1. EMS (ethyl mesylate, methanesulfonic acid ethyl ester; toxic!).
2. 15-ml sterile polypropylene centrifuge tube.
3. EMS inactivating solution: 0.1 M NaOH, 20% w/v $Na_2S_2O_3$.

3 Methods

3.1 Worm Culture

NGM (nematode growth medium): Mix NaCl, agar, and peptone in 975 ml H_2O. Add magnetic stir bar, cover flask inlet with aluminum foil, and autoclave. After cooling down to manageable temperatures, mix the NGM using a magnetic stirrer while adding KPO_4 buffer, $CaCl_2$, $MgSO_4$, and cholesterol. Under laminar flow hood, fill the NGM solution into petri dishes (worm plates) and cool down overnight at room temperature. Prepare NGM plates with OP50 by spreading OP50 (grown overnight) culture into the center of the plates and incubate the plates at 37 °C overnight. Maintain worms at 20 °C on NGM agar plates.

3.2 Microinjection

Generating transgenic worms is essential for the following studies, and it is not uncommon that worm labs experience difficulties in microinjection. Thus, we discuss this technique in more detail, and specifically, how we modified an existing protocol [20]:

1. Prepare 2.5% agarose in *Milli-Q water*, heat it in the microwave, and mix well. With a Pasteur pipette or a P200 tip place a drop (~100 µl) of hot agarose into the center of the 24 × 60 mm cover glass. Quickly place a second 22 × 22 mm coverslip onto the drop. Note that the colder the agarose drop gets the more unevenly thick the agarose pad becomes; alternatively, two long cover slips can be used to prepare uniformly thick pads between them [21]. Once the agarose has been solidified, remove the coverslips by sliding it away sidewise; then dry at room temperature for 4–8 h until all liquid

disappears. Note that too dry agarose pads may dehydrate the worms during microinjection reducing worm recovery rate.

2. Pull fine needles (using borosilicate glass capillaries) with the micropipette puller (*see* **Note 2**). Store the needles as follows: roll a small snake of play-doh (1 cm in diameter) and press it in the center of a clean (autoclaved) glass petri dish. Carefully attach the pulled needle with its center to this play-doh snake such as the needle endings are always free and not touching the glass petri dish. Close the lid of the petri dish for long-term storage.
3. Fill few microliters of plasmid DNA (at appropriate concentrations such as 10–50 ng/μl) into a modified tuberculin syringe (*see* **Note 3**) and insert the syringe tip into the opening of the injection needle (or use MultiFlex round tips to inject DNA into the needle) and wait until the solution is drawn into the needle by capillary effect.
4. Place the loaded needle into the needle holder and mount the holder on the micromanipulator. Position the needle so that the tip is in the center of the imaging field using a 10× objective and then change to 40× objective. Once positioned, the needle should be either moved only up (away from the focal plane where the worm is focused) or only down (toward the focal plane of the focused worm). It is then necessary to break the tip of the microinjection needle, because the needle puller might produce a sealed needle; here, put a drop of mineral oil on a 24 × 60 mm cover glass and place a 22 × 22 mm coverslip on the oil. Then break the needle tip by touching it against the walls of the 22 × 22 mm coverslip (use 40× objective for monitoring). Make sure the opening of the tip is not too large to damage the worm and that the DNA solution flows smoothly.
5. Place a drop of mineral oil on a 2.5% agarose pad under a dissecting microscope and pick up one or more young adult worms (*see* **Note 4**) and use an eyelash to gently press the worm to the agarose pad to immobilize it. The worm is immobilized by the force generated by absorption of water toward the dry agarose pad from the worm. Prolonged immersion of worms in oil will damage the worm recovery rate due to dehydration as well as by lack of oxygen diffusion to the worms. Gently rotate the worm to expose the dorsal gonadal arms.
6. Transfer the above prepared worm to the microinjection microscope and orient the dorsal gonadal arms toward the microinjection needle using the rotational stage. Bring the worm in focus using a 10× objective. Switch to 40× and move the needle down to touch the cuticle near the gonad. Gently move the worm against the needle for penetration into

the gonad and use the microinjector to inject the DNA solution (*see* **Note 5**). Then move the worm away from the needle.

7. Transfer the cover glass with the microinjected worm to a dissection microscope and add few drops of S buffer (or recovery buffer) onto the animal (still immersed in oil). Pick the now floating worm and place it on an NGM plate with OP50. Screen F_1 generations for transgenic gene expression (*see* **Note 6**) and maintain separately to clone out a stable line at 20 °C.

3.3 Motor/Cargo Motility Assay

1. Pick 5–10 young adult worms into a small drop (about 10 μl) of M9 buffer placed on a 2% agarose pad (on 24 × 60 mm cover glass) and immobilize them by adding a 22 × 22 mm coverslip on top of it. Avoid using anesthetics (such as levamisole) that may interfere with axonal transport [22]. If head or tail neurons need to be investigated and worm head/tail wiggles, use 5 mM levamisole to paralyze the worm.
2. Focus on a neuron of interest (Fig. 2) and start time-lapse imaging using a Nipkow spinning disk microscope connected to an EMCCD camera for fast image acquisition rate (3–4 frames per second). We suggest obtaining a total of 1000 frames for analysis. A good starting point would be to focus near the initial axonal segment of the ALM neuron (Fig. 2a) often revealing frequent motor and cargo movements [23].
3. To convert recorded time-lapse sequences into kymographs, we suggest using ImageJ: Convert the movies to 8-bit file format, then execute "straighten" plugin to straighten curved axons in the image stacks (ImageJ → plugins → straighten → select the axon → straighten → stack). Then execute the "reslice stack" function to generate kymographs (ImageJ → plugins → reslice25). Vertical lines in a kymograph indicate stationary particles, whereas horizontally angled lines correspond to a moving particle (Figs. 3 and 4a and **Note 7**).
4. We suggest analyzing approximately 1200 moving events per experiment. An "event" is defined as an occurrence of a movement of a fluorescent particle after a reversal or a pause (Fig. 4a). The term motility is defined as a movement occurrence of any event during the time of imaging. "Run Length" is defined as a distance covered by the particle within one moving event either in anterograde or retrograde directions. Total anterograde or retrograde run length is the distance covered by the fluorescent particle in the gained kymograph. "Net Run Length" is defined as the net processivity of the particle from either anterograde or retrograde movements within a given time (total anterograde run length − total retrograde run length; meaning a positive value represents the final

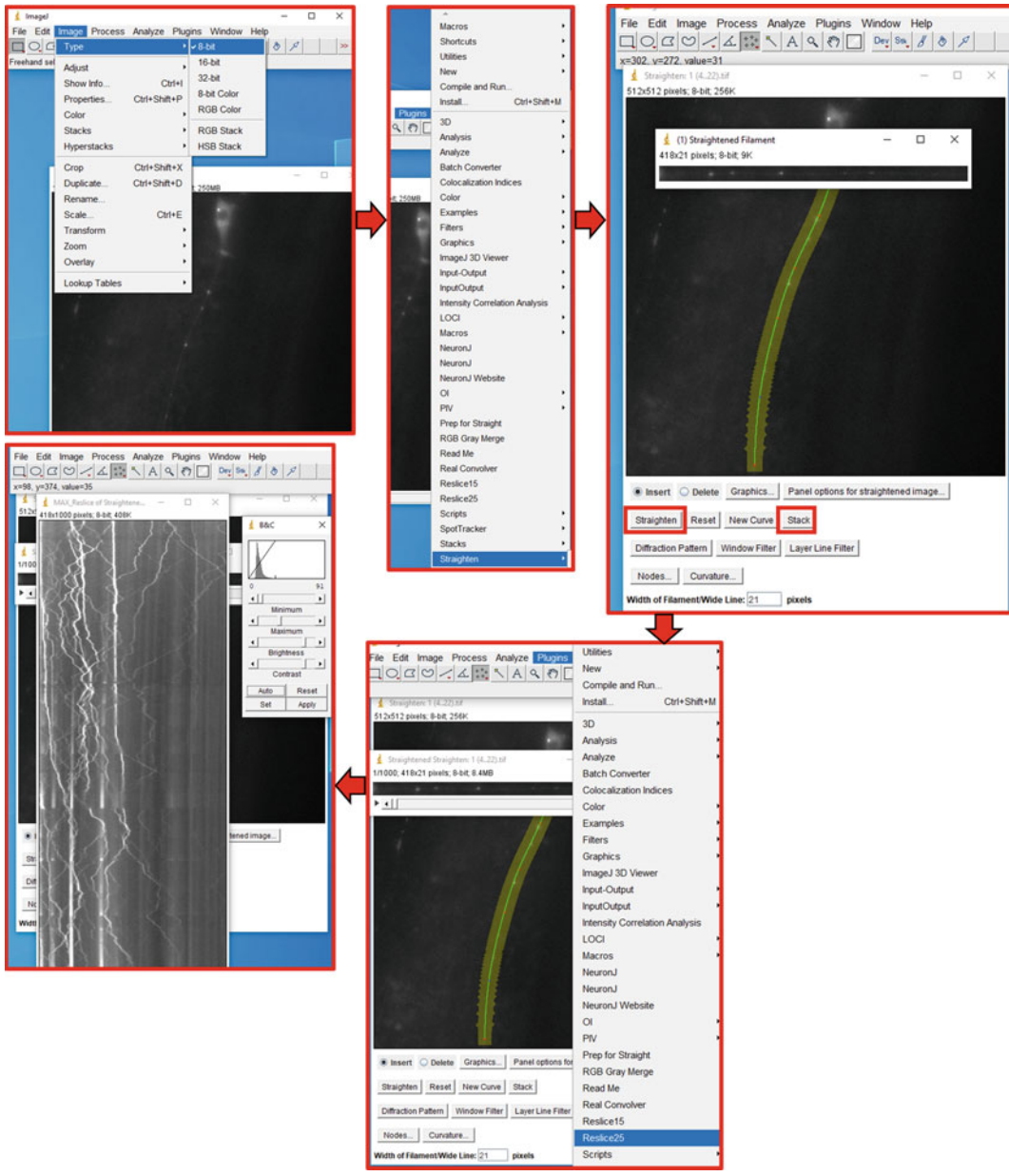

Fig. 3 Flowchart demonstrating steps to generate kymographs to quantify various parameters such as anterograde and retrograde velocity, pauses, anterograde and retrograde run length, and net run length

anterograde movement and a negative value represent the final retrograde movement). "Directional change" of a particle is defined as a change in direction within a single moving event. The slope of a moving particle is calculated to obtain the velocity of the particle in either direction (Fig. 4a).

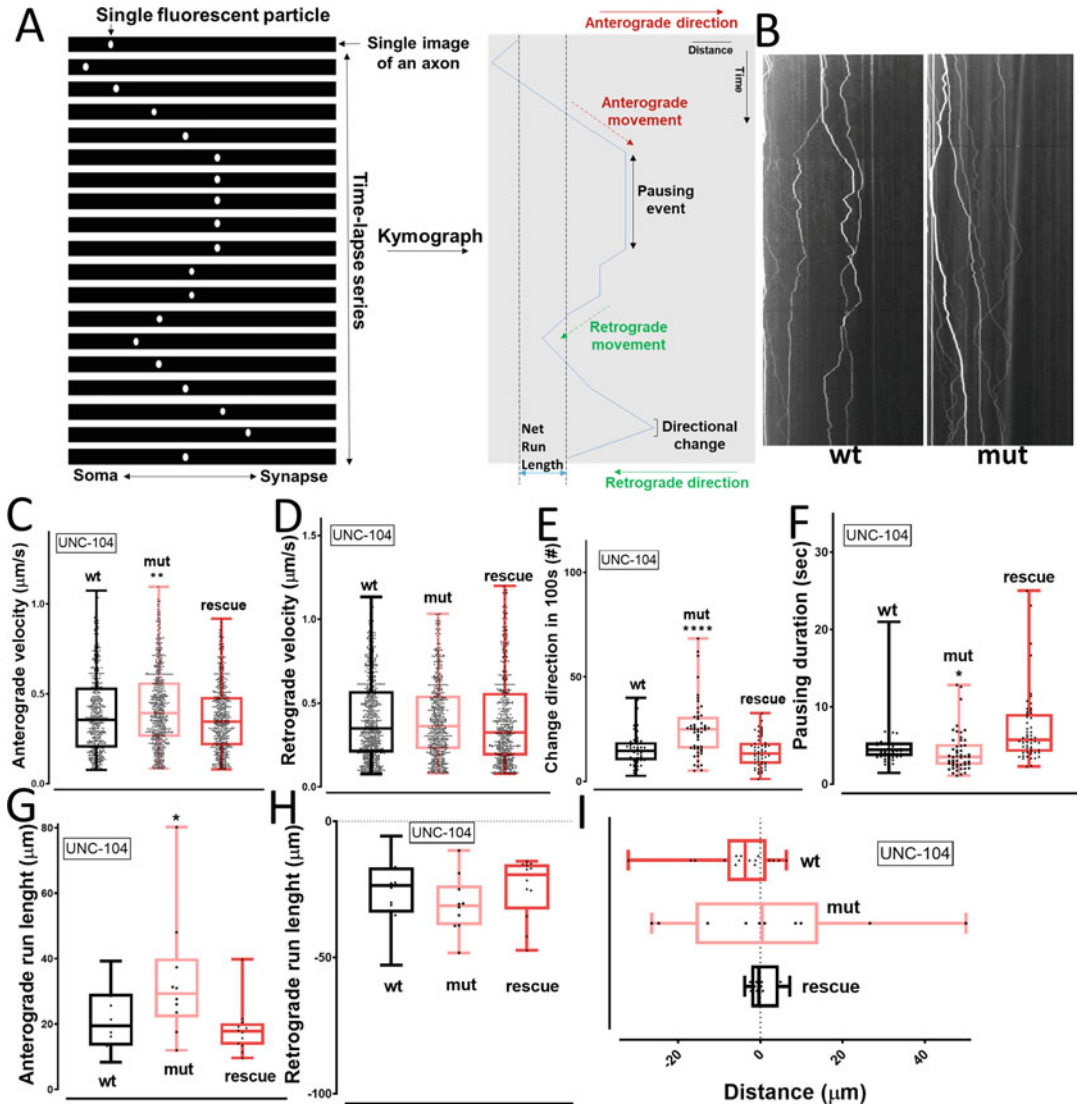

Fig. 4 Motility analysis of kinesin-3 UNC-104 in wild-type, mutants and rescue animals. (**a**) Cartoon depicting the principles of kymograph analysis and definition of quantified parameters. (**b**) Kymographs representing motility of UNC-104 in wild-type and mutant backgrounds. (**c**) UNC-104 anterograde velocities. (**d**) UNC-104 retrograde velocities. (**e**) Motor reversals (directional changes). (**f**) Motor pausing durations. (**g**–**h**) Total anterograde and retrograde run lengths. (**i**) Net run lengths. Analyzed events: $>$ 1500. One-way ANOVA with Fisher's LSD multiple comparison test ****$p < 0.0001$, ***$p < 0.001$, **$p < 0.005$, and *$p < 0.05$

5. To measure the above-mentioned parameters, we utilize a lab-build Excel sheet that can be requested from us. Here, we only need to input the coordinates of the moving particle from a kymograph which is manually selected using the "multi-point tool": ImageJ → Analyze → Measure. Alternatively, plugins such as "Kymoanalyser" can be employed to determine motility parameters [24]. We suggest plotting histograms to identify

outliers. Note that run lengths are generally more dynamic as compared to velocities often resulting in larger error bars. The reason likely lies in the complexity of this parameter including tug-of-war events, dwelling phases, motors encountering obstacles on microtubules or switching to adjacent microtubules, etc. [25]. Compelling representations of run lengths can be done in so-called bullet diagrams as shown in Fig. 1a by plotting positive (anterograde) and negative (retrograde) run lengths traces versus time.

3.4 Cargo/Motor Cluster Distribution Analysis

1. Immobilize worms as mentioned above and acquire confocal fluorescent images by focusing on the neuron of interest.
2. To analyze changes in motor/cargo distribution in neurons, we use ImageJ software:
   (a) Set the appropriate scale: ImageJ → analyze → set scale.
   (b) Convert the images to 8-bit: ImageJ → image → type → 8-bit.
   (c) Straighten the curved axons: ImageJ → plugin → straighten → execute straighten.
   (d) Apply a bit-map threshold for subsequent particle analysis: ImageJ → image → adjust → threshold (we suggest excluding particles of sizes less than 3 pixels to reject random noise).
   (e) Set required parameters for analysis: ImageJ → analyze → set measurements such as area, shape descriptors, perimeter, centroid, etc.
   (f) Execute "analyze particles."
3. Calculate density (# of particles/100 μm of neurite) using the following formula: (Total number of particles in the neurite segment/Length of that neurite segment analyzed) × 100.
4. Stack neurons on top of each other for improved visualization of the effect (Figs. 1c and 5c).
5. To measure travel distances (Figs. 1b and 5a) of particles in (straightened) neurons, we use ImageJ's "line tool" to draw a line from the proximal axon hillock to the identified distal particle.

3.5 Determining Ratios of Motor/Cargo in Soma, Axons, and Synapses

Impaired axonal transport often leads to disproportionate segregation of cargo in soma, axons, and synapses which can be quantified by calculating the amount of cargo equal to fluorescent intensities in soma, axons, and synapses (Fig. 5d). Note that the HSN neuron (Figs. 2a and 5b) reveals a large synapse for straightforward quantification of cargo accumulation.

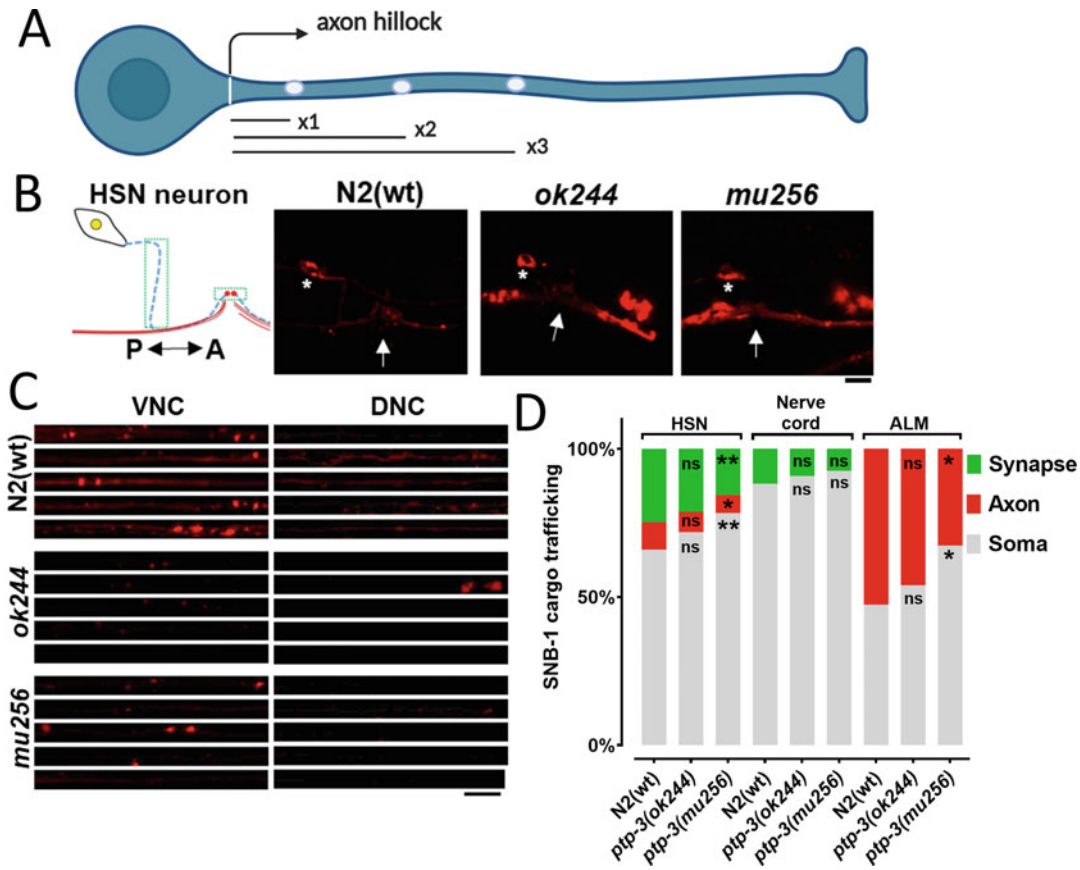

Fig. 5 Quantification of motor/cargo travel distances and accumulations in cellular compartments. (**a**) Schematic diagram of a neuron with black lines indicating the distances of a particle traveled from the axonal hillock to farther distal regions. (**b**) Cartoon of HSN neuron with its presynaptic area and representative images of SNB-1 cargo distribution in wild-type and *ptp-3* mutants. * indicates soma of HSN neuron. White arrow indicates the location of the vulva. Green boxes indicate the region used for quantification of fluorescence intensity of axons (blue dashed line) and synapses (red circles). P—posterior direction and A—anterior direction. Note that PTP-3 is a phosphatase regulating UNC-104 motor activator SYD-2. (**c**) Representative images of VNC (ventral nerve cord) and DNC (dorsal nerve cord) from different experimental groups, straightened and stacked. (**d**) Quantification (fluorescence intensity) of the amount of cargo in the cell body and the initial axonal region of ALM, nerve cord (VNC somata and DNC synapses) and HSN neurons (soma, axon and synapse). Scale bars: 10 μm. *P*-values: $*P < 0.05$, $**P < 0.01$, One-way ANOVA with Fisher's LSD multiple comparison test

1. Immobilize the worm as mentioned above and acquire confocal images of the respective regions to be analyzed.
2. Set the parameters for analysis: ImageJ → analyze → set measurements (such as area, integrated density, maximum/minimum gray value, and mean gray value).
3. Select a background region using the "rectangular tool" and subtract the background fluorescent signal: ImageJ → process → subtract background → OK.

4. Select the region of interest using the "polygon selection tool" from ImageJ and measure: ImageJ → analyze → measure.
5. Assume total fluorescence intensity as 100% (sum of soma +axon+synapse) to normalize for differences in fluorescence intensities generated by variable transgene copy number in a single neuron.
6. Calculate the amount of synaptic vesicle cargo in different cellular compartments as follows: (Fluorescence intensity in subcellular region/Total fluorescent intensity in the neuron) × 100. Examples in Fig. 5d [26].

3.6 Thrashing Assay

Quantification of worm bends in liquid ("thrashing" or lateral swimming movement) is a reliable method to evaluate the function of motor neurons that innervate the muscles. Impaired AT resulting in modulated synaptic signaling often results in changes in swimming behavior. A thrashing event is defined as bending of the body in one direction and then returning back to the original position [27–30] (Fig. 1e). Note that some authors consider half of the above-mentioned movement as a single thrash (complete change of mid body to an opposite direction from the existing position) [31].

1. Wash young adult worms with M9 buffer to remove OP50 bacteria.
2. Suspend the worms in a drop of M9 buffer placed on either NGM plate without OP50, in a multi-well plate or on a glass side (use sufficient M9 buffer to compensate for evaporation).
3. Either count body bends manually with a handheld clicker-counter or record a movie for 1 min using a dissection microscope with a digital camera attached.
4. The recorded movie can be evaluated at slower speed to properly count the number of thrashings using ImageJ or any available video player.

3.7 Touch Response Assays

1. The response to touch can be quantitatively expressed by calculating the "response percentage": (Number of times the worm responded to touch/Total number of times the worms were subjected to touch) × 100.
2. A response is scored when a worm stopped its movement, started to move from a stationary position, changed the direction of movement, does backing movement (so-called Mec response) or changed the speed of movement.
3. Nose touch: Usually performed using an eyelash by either gently touching the nose of the worm (Fig. 1d) or just placing the eyelash into the path of a moving worm. Backing

movement or immediate halt of locomotive activity is considered as a response to nose touch.

4. Gentle touch: Gentle touch is performed employing an eyelash by gently stroking the hair across the worm's body between the pharynx and vulva or between the vulva and tail.
5. Harsh touch: Here, a blunt platinum wire is used to prod a nonmoving worm just posterior to the vulva (Fig. 1d) and the response of the touch is scored.

3.8 Egg Retention Assay

1. Perform timed-egg laying with 25–30 gravid adult worms for 1 h at 20 °C in NGM OP50 plates to obtain a synchronized worm population. Let the synchronized worms grow for 88 h (majority of worms will be at L4 stage after 48 h at 20 °C). Incubate the worms for an additional 40 h for phenotypic observation of egg retention.
2. After 88 h, prepare the worms for microscopic examination (immobilize on agarose pads) of egg retention phenotype (Fig. 1g). We suggest a DIC microscope using a 10× objective. Alternatively, add a single adult worm in 10 μl of 20% bleach solution resulting in expulsion of eggs which can be counted using a dissection microscope [32].
3. Count the number of eggs using ImageJ or any other image viewer to generate a quantitative profile in control and mutant group.

3.9 Paralysis Assay

1. Prepare 5- or 6-cm NGM plates with either 0.2 mM levamisole or 1 mM aldicarb and add few drops of OP50 to the center of the plate and dry the moisture (this will help to restrict the worm motility within the OP50 lawn).
2. Add 25–40 young adult worms to these plates and score the number of worms paralyzed every 30 min for 6–8 h. Worms are considered paralyzed when no response or head movement was observed upon prodding.
3. Plot the percentage of paralyzed worms versus time as shown in Fig. 1f.

3.10 Other Behavioral Assays Related to Worm Neuron Function

Please refer to **Note 8** for other behavioral assays that may relate to impeded functioning of the nematode's nervous system.

3.11 Suppressor Screen

1. Wash identified worms with abnormal behavior from above screen thrice with M9 buffer (make sure to use plenty of L4 worms).
2. Prepare a 3 ml worm suspension in M9 buffer in a 15-ml sterile centrifuge (falcon) tube.

3. Add 1 ml of M9 buffer in a separate 15-ml tube under a hood wearing gloves. Shake EMS (toxic!) until it is no longer cloudy. Then add 20 μl EMS (designated pipette used only for EMS) to the M9 buffer.
4. Transfer the 3 ml worm suspension to the tube with EMS and rotate it for 4 h at 20 °C (the final concentration of EMS is 47 mM). Wash the worms thrice with M9 buffer and transfer the worms to the edge of the bacterial lawn on a worm plate.
5. Incubate the plate for 2–4 h and pick up late L4 worms. Remove EMS contaminations from pipettes and tubes by soaking them in the "EMS inactivating solution" for 1 day and then discard them.
6. Screen F_2 populations for wild-type phenotypes and identify the target gene by whole-genome sequencing (Fig. 1i).
7. Carry out functional analysis of the gene involved in the worm neuronal disease model (Fig. 1j).

4 Notes

1. We prefer mRFP over GFP, because GFP has been reported to oligomerize [19], likely restraining motor activity. Other popular monomeric fusions include mCherry or tdTomato.
2. Microinjection needles can be pulled into different shapes and textures by proper tuning of available machine parameters such as amount and timing of heating, cooling, and pulling velocity. Needles can be pulled into different shapes (short, brittle tips or longer, more flexible tips), and to identify best shapes for improved microinjection, some trial-and-error testing is needed. Alternatively, commercial needles are also available, e.g., Femtotips I and Femtotips II from Eppendorf.
3. Place the tip of a 1-ml tuberculin syringe over a Bunsen burner flame until it softens, then quickly pull on the tip of the syringe to produce a thin tubing that can be used for injecting DNA solution into the microinjection needles.
4. L4 worms can be identified by a white, triangular spot surrounding the vulva. Worms reach this age about 50 h after the time of egg laying at 20 °C.
5. The angle at which the microinjection needle meets the cuticle above the gonad arm should be standardized based on the user preference as well as based on the needle shape and texture. Most commonly used angles are 30° and 45°. Alternatively, align the needle parallel to the worm's body by pressing it against the surface of the worm's cuticle. It can then easily penetrate through the cuticle into the gonad by moving the

worm (via stage movements) against the needle tip. Flow of DNA solution across the gonadal arm or formation of a small bubble or swelling inside the gonad arms is an indication of successful microinjection.

6. We suggest the use of co-injection markers which are co-injected plasmids that produce visible phenotypes for convenient screening and isolation of new transgenic strains. Several co-injection markers exist such as *rol-6(su1006)* which develops a dominant roller phenotype, visible fluorescent markers such as *ttx-3p::gfp*, *myo-2p::mCherry*, *sur-5p::gfp*, and *odr-1::rfp* as well as rescue co-injection markers such as *pha-1*, *unc-119*, and *dpy-5*.
7. The cutoff value to identify a moving particle from a stationary particle is of critical importance, and it may vary between different motors and cargos. We regard a motor or synaptic vesicle as stationary if the velocity of the particle is below 0.07 μm/s and alike cutoff values have been used by others [33, 34].
8. Other behavioral assays include: determining frequency of pharyngeal pumping (regulated by coordinated neuronal activity), chemotaxis assay (we suggest quadrant assays [35]), measuring backing (Mec) response when tapping at the side of a glass worm plate, locomotion rate analysis (identifying uncoordinated movements), male mating behavior, area restricted searching (ARS), and basal slowing analysis (both related to dopamine signaling [36]).

References

1. Maday S, Twelvetrees AE, Moughamian AJ, Holzbaur EL (2014) Axonal transport: cargo-specific mechanisms of motility and regulation. Neuron 84(2):292–309. https://doi.org/10.1016/j.neuron.2014.10.019
2. Klinman E, Holzbaur ELF (2018) Walking forward with kinesin. Trends Neurosci 41(9): 555–556. https://doi.org/10.1016/j.tins.2018.07.006
3. Reck-Peterson SL, Redwine WB, Vale RD, Carter AP (2018) Publisher correction: the cytoplasmic dynein transport machinery and its many cargoes. Nat Rev Mol Cell Biol 19(7):479. https://doi.org/10.1038/s41580-018-0021-2
4. Guedes-Dias P, Holzbaur ELF (2019) Axonal transport: driving synaptic function. Science 366(6462). https://doi.org/10.1126/science.aaw9997
5. Yagensky O, Kalantary Dehaghi T, Chua JJ (2016) The roles of microtubule-based transport at presynaptic nerve terminals. Front Synaptic Neurosci 8:3. https://doi.org/10.3389/fnsyn.2016.00003
6. Zhao J, Fok AHK, Fan R, Kwan PY, Chan HL, Lo LH, Chan YS, Yung WH, Huang J, Lai CSW, Lai KO (2020) Specific depletion of the motor protein KIF5B leads to deficits in dendritic transport, synaptic plasticity and memory. Elife 9:e53456. https://doi.org/10.7554/eLife.53456
7. Sleigh JN, Rossor AM, Fellows AD, Tosolini AP, Schiavo G (2019) Axonal transport and neurological disease. Nat Rev Neurol 15(12): 691–703. https://doi.org/10.1038/s41582-019-0257-2
8. Guo W, Stoklund Dittlau K, Van Den Bosch L (2020) Axonal transport defects and neurodegeneration: molecular mechanisms and therapeutic implications. Semin Cell Dev Biol 99: 133–150. https://doi.org/10.1016/j.semcdb.2019.07.010

9. Li J, Le W (2013) Modeling neurodegenerative diseases in Caenorhabditis elegans. Exp Neurol 250:94–103. https://doi.org/10.1016/j.expneurol.2013.09.024
10. Caldwell KA, Willicott CW, Caldwell GA (2020) Modeling neurodegeneration in Caenorhabditis elegans. Dis Model Mech 13(10): dmm046110. https://doi.org/10.1242/dmm.046110
11. Schafer WR (2015) Mechanosensory molecules and circuits in *C. elegans*. Pflugers Arch 467(1):39–48. https://doi.org/10.1007/s00424-014-1574-3
12. Collins KM, Bode A, Fernandez RW, Tanis JE, Brewer JC, Creamer MS, Koelle MR (2016) Activity of the *C. elegans* egg-laying behavior circuit is controlled by competing activation and feedback inhibition. Elife 5:e21126. https://doi.org/10.7554/eLife.21126
13. Tong Zhou G, Schafer WR, Schafer RW (1998) A three-state biological point process model and its parameter estimation. IEEE Trans Signal Process 46(10):2698–2707
14. Oh KH, Kim H (2017) Aldicarb-induced paralysis assay to determine defects in synaptic transmission in Caenorhabditis elegans. Bio Protoc 7(14):e2400. https://doi.org/10.21769/BioProtoc.2400
15. Natale C, Barzago MM, Diomede L (2020) Caenorhabditis elegans models to investigate the mechanisms underlying tau toxicity in Tauopathies. Brain Sci 10(11). https://doi.org/10.3390/brainsci10110838
16. De Vos KJ, Hafezparast M (2017) Neurobiology of axonal transport defects in motor neuron diseases: opportunities for translational research? Neurobiol Dis 105:283–299. https://doi.org/10.1016/j.nbd.2017.02.004
17. Tien NW, Wu GH, Hsu CC, Chang CY, Wagner OI (2011) Tau/PTL-1 associates with kinesin-3 KIF1A/UNC-104 and affects the motor's motility characteristics in C. elegans neurons. Neurobiol Dis 43(2): 495–506. https://doi.org/10.1016/j.nbd.2011.04.023
18. Wagner OI, Esposito A, Kohler B, Chen CW, Shen CP, Wu GH, Butkevich E, Mandalapu S, Wenzel D, Wouters FS, Klopfenstein DR (2009) Synaptic scaffolding protein SYD-2 clusters and activates kinesin-3 UNC-104 in C. elegans. Proc Natl Acad Sci U S A 106(46):19605–19610. https://doi.org/10.1073/pnas.0902949106
19. Costantini LM, Fossati M, Francolini M, Snapp EL (2012) Assessing the tendency of fluorescent proteins to oligomerize under physiologic conditions. Traffic 13(5):643–649. https://doi.org/10.1111/j.1600-0854.2012.01336.x
20. Evans TC (2006) Transformation and microinjection, WormBook, ed. The C. elegans Research Community, WormBook. https://doi.org/10.1895/wormbook.1.108.1
21. Shaham S, (2006) WormBook: Methods in Cell Biology, WormBook, ed. The C. elegans Research Community, WormBook. https://doi.org/10.1895/wormbook.1.49.1
22. Kumar J, Choudhary BC, Metpally R, Zheng Q, Nonet ML, Ramanathan S, Klopfenstein DR, Koushika SP (2010) The Caenorhabditis elegans Kinesin-3 motor UNC-104/KIF1A is degraded upon loss of specific binding to cargo. PLoS Genet 6(11):e1001200. https://doi.org/10.1371/journal.pgen.1001200
23. Wu GH, Muthaiyan Shanmugam M, Bhan P, Huang YH, Wagner OI (2016) Identification and characterization of LIN-2(CASK) as a regulator of Kinesin-3 UNC-104(KIF1A) motility and clustering in neurons. Traffic 17(8): 891–907. https://doi.org/10.1111/tra.12413
24. Neumann S, Chassefeyre R, Campbell GE, Encalada SE (2017) KymoAnalyzer: a software tool for the quantitative analysis of intracellular transport in neurons. Traffic 18(1):71–88. https://doi.org/10.1111/tra.12456
25. Chen CW, Peng YF, Yen YC, Bhan P, Muthaiyan Shanmugam M, Klopfenstein DR, Wagner OI (2019) Insights on UNC-104-dynein/dynactin interactions and their implications on axonal transport in Caenorhabditis elegans. J Neurosci Res 97(2):185–201. https://doi.org/10.1002/jnr.24339
26. Shanmugam MM, Barmaver SN, Huang HY, Bayansan O, Wagner OI (2020) PTP-3 phosphatase promotes intramolecular folding of SYD-2 to inactivate kinesin-3 UNC-104 in neurons. Mol Biol Cell 31(26):2932–2947. https://doi.org/10.1091/mbc.E19-10-0591
27. Fatima S, Haque R, Jadiya P, Shamsuzzama, Kumar L, Nazir A (2014) Ida-1, the Caenorhabditis elegans orthologue of mammalian diabetes autoantigen IA-2, potentially acts as a common modulator between Parkinson's disease and diabetes: role of Daf-2/Daf-16 insulin like signalling pathway. PLoS One 9(12): e113986. https://doi.org/10.1371/journal.pone.0113986
28. Hu CC, Wu GH, Lai SF, Muthaiyan Shanmugam M, Hwu Y, Wagner OI, Yen TJ (2018) Toxic effects of size-tunable gold nanoparticles on Caenorhabditis elegans development and gene regulation. Sci Rep 8(1):

15245. https://doi.org/10.1038/s41598-018-33585-7

29. Bhan P, Muthaiyan Shanmugam M, Wang D, Bayansan O, Chen CW, Wagner OI (2020) Characterization of TAG-63 and its role on axonal transport in C. elegans. Traffic 21(2): 231–249. https://doi.org/10.1111/tra.12706
30. Hu CC, Wu GH, Hua TE, Wagner OI, Yen TJ (2018) Uptake of TiO_2 nanoparticles into C. elegans neurons negatively affects axonal growth and worm locomotion behavior. ACS Appl Mater Interfaces 10(10):8485–8495. https://doi.org/10.1021/acsami.7b18818
31. Buckingham SD, Sattelle DB (2009) Fast, automated measurement of nematode swimming (thrashing) without morphometry. BMC Neurosci 10:84. https://doi.org/10.1186/1471-2202-10-84
32. Gardner M, Rosell M, Myers EM (2013) Measuring the effects of bacteria on C. elegans behavior using an egg retention assay. J Vis Exp (80):e51203. https://doi.org/10.3791/51203
33. Li Q, Tseng KF, King SJ, Qiu W, Xu J (2018) A fluid membrane enhances the velocity of cargo transport by small teams of kinesin-1. J Chem Phys 148(12):123318. https://doi.org/10.1063/1.5006806
34. Guedes-Dias P, Nirschl JJ, Abreu N, Tokito MK, Janke C, Magiera MM, Holzbaur ELF (2019) Kinesin-3 responds to local microtubule dynamics to target synaptic cargo delivery to the Presynapse. Curr Biol 29(2):268–282. e268. https://doi.org/10.1016/j.cub.2018.11.065
35. Muthaiyan Shanmugam M, Bhan P, Huang HY, Hsieh J, Hua TE, Wu GH, Punjabi H, Lee Aplicano VD, Chen CW, Wagner OI (2018) Cilium length and Intraflagellar transport regulation by kinases PKG-1 and GCK-2 in Caenorhabditis elegans sensory neurons. Mol Cell Biol 38(7):e00612-17. https://doi.org/10.1128/MCB.00612-17
36. Cooper JF, Van Raamsdonk JM (2018) Modeling Parkinson's Disease in C. elegans. J Parkinsons Dis 8(1):17–32. https://doi.org/10.3233/JPD-171258

Chapter 27

Imaging Intracellular Trafficking in Neurons of *C. elegans*

Sravanthi S. P. Nadiminti and Sandhya P. Koushika

Abstract

Axonal transport is an essential component of neuronal function. Several neurodegenerative disorders have been associated with defects in cargo transport. Thus, studying axonal transport is important to understand such disorders. Live imaging of fluorescently labeled cargo is a prevailing technique to study properties of axonal transport. *C. elegans* is both transparent and genetically amenable, making it an excellent model system to study axonal transport. In this chapter, we describe protocols to live image several neuronal cargo in vivo in *C. elegans* neurons.

Key words *C. elegans* neurons, Axonal transport, Live imaging, In vivo imaging, Fluorescence, Microscope, Confocal microscope

1 Introduction

Neurons are polarized cells, specialized in their function to receive and transmit signals to other neurons or muscles. Neuronal function depends on long-distance transport of organelles and molecules along the microtubule track [1]. Changes to cargo transport within neurons have been linked to several neurodegenerative disorders [2]. Studying the transport and maturation of organelles [3] such as the autophagosomes [4], lysosomes [5], and synaptic vesicles [6, 7] have helped us understand mechanisms of neurodegenerative disorders.

Initial studies characterizing live axonal transport using extruded squid axoplasm were performed using widefield differential interference contrast (DIC) microscopy [8, 9]. With increasing advancements in fluorescence microscopy, live imaging using fluorescently labeled proteins is now the mainstay to study axonal transport [10–12]. Real-time tracking of intra-neuronal cargo is routinely being conducted on primary cultures of neurons [13–16]. Cultured neurons have been useful in understanding transport properties of several cargo, such as lysosomes [15, 17], endosomes [18–20], and phagosomes [21]. However, differences in number of

Alessio Vagnoni (ed.), *Axonal Transport: Methods and Protocols*,
Methods in Molecular Biology, vol. 2431, https://doi.org/10.1007/978-1-0716-1990-2_27,
© The Author(s), under exclusive license to Springer Science+Business Media, LLC, part of Springer Nature 2022

moving cargo [22] and speeds of cargo [23] are noted from cargo imaged in cell cultures and in vivo. For studies in an in vivo physiological context, live imaging of axonal transport in model organisms like *C. elegans* could prove useful [24–27]. The transparency of *C. elegans* and the ease of generating transgenic *C. elegans* expressing fluorescently tagged proteins both assist in successful in vivo live imaging. Live imaging in *C. elegans* has helped understand mechanisms of action of several proteins governing intracellular cargo transport [7, 28–32] and neuronal growth and regeneration [33–36].

Despite its importance and relevance, successful imaging of axonal transport is not without challenges. Transgenic *C. elegans* expressing fluorescently labeled proteins used for in vivo imaging pose several challenges:

1. Good transgenic lines expressing fluorescently labeled proteins—a primary concern with using fluorescently tagged proteins is that they may exhibit differences in localization compared to the endogenous protein. Such artefacts may be overcome by using low-copy integrated transgenic lines [37, 38], tagging the endogenous protein using CRISPR/Cas9 [39, 40] or by testing the in vivo behavior of the tagged proteins to ensure that they do not behave differently from the endogenous, untagged proteins [41].
2. Good signal-to-noise ratio—artefacts associated with overexpressing fluorescently tagged proteins can be overcome by using transgenes with low expression levels or tagging endogenous proteins using the CRISPR/Cas9 technology or using transgenic lines with single copy insertions. However, transgenic lines obtained from such tagging methods may not have sufficient signal intensity for live imaging of transport, depending on the expression levels of the tagged gene and the sensitivity of the imaging system. In such circumstances, standard transgenes with good expression that mirror the localization of endogenous proteins can prove useful [42, 43].
3. Speed of image acquisition—axonal transport is a dynamic process where different organelles move at different speeds, unique transport properties, or localization within the neuron. Therefore, when imaging a dynamic process such as axonal transport of organelles, it is important to choose a rate of image acquisition that captures all transport features of interest of a given cargo.

In this chapter, we describe protocols for live imaging and show examples of several markers imaged in *C. elegans* neurons. We also describe protocols to analyze the images that result from the various imaging protocols described in this chapter. Several protocols described for imaging and analysis also apply to imaging in other

contexts and model systems. We describe simple-to-follow imaging protocols that yield information about the dynamics of organellar transport, intra-axonal organellar distribution, real-time trafficking of several neuronal proteins, etc. A majority of the analyses described will utilize kymographs. Some analyses can be partly automated but most of them are manual. Described analyses are often error prone and rely on images obtained at high sensitivity settings. Hence, with each protocol, we have tried to include tips to optimize ways of imaging and analysis to get the most accurate data possible.

2 Materials

2.1 Preparation of Agarose Pads

Sigma Agarose.

Microslides.

Dropper.

Water.

2.2 Anaesthetizing C. elegans for Imaging

Pipette.

Cover slip.

C. elegans.

M9 buffer.

Sigma Sodium Azide.

Sigma Tetramisole Hydrochloride.

2.3 For Static Imaging

Widefield Fluorescence (WF) microscope fitted with a CCD or EMCCD camera with halogen or mercury arc lamp.

2.4 For Live Imaging

1. Mitochondria, actin dynamics, microtubule dynamics, and calcium imaging: WF microscope fitted with a CCD or EMCCD camera with halogen or mercury arc lamp.
2. Vesicle motion properties or live-tracking of vesicular proteins:
   (a) WF microscope fitted with a CCD or EMCCD camera with halogen or mercury arc lamp.
   (b) Confocal line scanning microscope with PMT.
   (c) Spinning Disc confocal microscope with an EMCCD camera.
3. ImageJ/Fiji.

2.5 ImageJ Plugins (and Macros)

Macro 1—For analysis of vesicle motion properties.

Macro 2—For background subtraction for intensity quantitation using ROI.

These macros can be found on GitHub: https://github.com/WormLabTifr/ImagingAxonalTransport.git

3 Methods

3.1 Culturing C. elegans for Imaging

1. Grow *C. elegans* at 20 °C on *E. coli* OP50-seeded NGM plates [44].
2. Typically, we use late L4 to 1 day adults. However, other larval stage or older animals can also be used for imaging [45].

3.2 Preparation of Agarose Pads

1. Make a 3–5% agarose solution in water (*see* **Note 1**).
2. Put a drop of the solution onto a microslide using a dropper. Avoid bubbles in the agarose pads.
3. Use another microslide to flatten the drop into a pad. Pad should be uniformly flat and thin. Let the pad rest (*see* **Note 2**).

3.3 Immobilizing C. elegans for Imaging

1. *C. elegans* can be immobilized for imaging using anesthetics or microfluidic devices [46]. The choice of immobilization depends on the developmental stage of *C. elegans* as well as the nature and duration of imaging (*see* **Note 3**).
2. For live imaging up to 10 min, we use either 3 mM or 5 mM tetramisole.
3. Add <5 μL of the anesthetic solution to the center of an agarose pad.
4. Using a sterile worm pick, transfer *C. elegans* on to the slide (*see* **Note 4**).
5. Carefully place a coverslip (*see* **Note 5**) on top of the worms. The slide is ready for imaging.

3.4 Choosing the Right Imaging System

To acquire the best images to study any kind of biological process, it is imperative to choose the right imaging system. There are several factors that influence the choice of a microscope system. A key factor in making this decision is the biological question and the nature of analysis/measurements that need to be made to address the biological question. However, the following factors are also important to consider.

1. *Phototoxicity/sample viability.*

   When imaging live animals, it is important to ensure that the sample is not damaged. Microscopes that use the least

amount of light to illuminate the sample without compromising the signal quality are preferred.

2. *Resolution.*

   For optimal live imaging, spatial and temporal resolutions are key factors in choosing an imaging system.

   (a) Spatial/lateral resolution is defined by the distance by which two objects in a sample must be separated in order for the microscope to distinguish them as separate objects. For high-quality imaging, it is important to consider (1) size of the organelle or protein complex of interest (features), (2) brightness of the fluorescent label, and (3) how close two features are in a sample. If features cannot be detected, they will not be resolved by a microscope. Therefore, a higher signal-to-noise ratio is desirable for higher resolution. For a WF microscope, lateral resolution is a function of the wavelength of light and the numerical aperture of the objective. The relation is defined in the following equation:

$$r = (0.61)\lambda / NA$$

   where r is the minimum distance between objects that need to be resolved, λ is the wavelength of light used and NA is the numerical aperture of the objective. Based on this equation, we can see that shorter wavelength of light and a higher numerical aperture result in higher resolution. This means that using fluorophores emitting shorter wavelength light such as GFP and using 1.4 or 1.5 NA objectives will provide highest spatial resolution. Spatial resolution additionally depends on the size of the camera sensor. Smaller sensor sizes would mean smaller pixel sizes. Smaller photodiode sizes in CCD cameras improve resolution but they also affect the dynamic range of the device [47].

   (b) *Temporal resolution.*

   Another factor to consider when imaging dynamic processes like axonal transport, is the speed of the process. The rate of image acquisition should be commensurate with the speed of the dynamic process. For example, while imaging transport of vesicles in axons, lower rates of acquisition might miss brief pauses in the vesicle trajectory [48]. Such errors will yield higher average velocities and run lengths for the imaged vesicles, leading to inaccuracies in data interpretation. Therefore, choosing a system equipped with a camera that can allow achieving desired frame rates without compromising signal quality for imaging dynamic processes will be greatly beneficial.

3. *Contrast.*

   Contrast often depends on the out-of-focus light from planes above and below the imaging plane. Confocal microscopes improve contrast by cutting off out-of-focus light using a pinhole. Contrast can also be improved by using brighter fluorophores or by expressing the fluorescently tagged proteins at higher concentrations. However, either choices come with their demerits (*see* Subheading 1).

4. *Thickness of the sample and z-depth penetration.*

   Biological specimens are three dimensional, and some features of interest may lie deep within the sample. Obtaining quality images deeper inside a sample is challenging because signal-to-noise ratio is affected by the scattered light and background noise. Confocal microscopes are better at imaging deep into the sample because they cut off out-of-focus light from each plane. Sometimes, systems equipped with multiphoton excitation may be preferred to confocal microscopes [49].

5. *Microscope.*

   The best imaging system will be the one that is optimized for all parameters necessary for imaging the sample to study the biological process of interest. Additionally, microscope hardware and imaging settings will also influence the quality of the final image.

   (a) *Widefield Fluorescence (WF) Microscope.*

   These microscopes are a good option especially if features in the biological sample are large and bright. When equipped with newer, better cameras, widefield microscopes can be used for sensitive live imaging. WF microscopes collect light from all z-planes in the sample, giving these systems several advantages: (a) WF microscopes are better suited for imaging fainter samples, (b) there is little phototoxicity to the sample being imaged, and (c) these are a good choice for imaging thinner samples, such as a single cell layer or thin tissue samples, where imaging along the *z*-axis is not necessary. However, a drawback of these systems is that the contrast can be poor because they collect light from all *z*-planes. However, transgenic lines expressing bright fluorophores can be reliably imaged in WF microscopes (Fig. 1c iv–vi).

   (b) *Confocal Laser Scanning Microscope (CLSM).*

   CLSMs are the best choice to get high-contrast images because they employ a single pinhole to cut off out-of-focus light from each z-plane. For the same reason, these also do better when the sample is thick and if the features of interest lie deep within the sample. Use of a single pinhole and raster scanning makes these microscopes slower and less sensitive than both WF and spinning disc (SD) microscopes. CLSMs

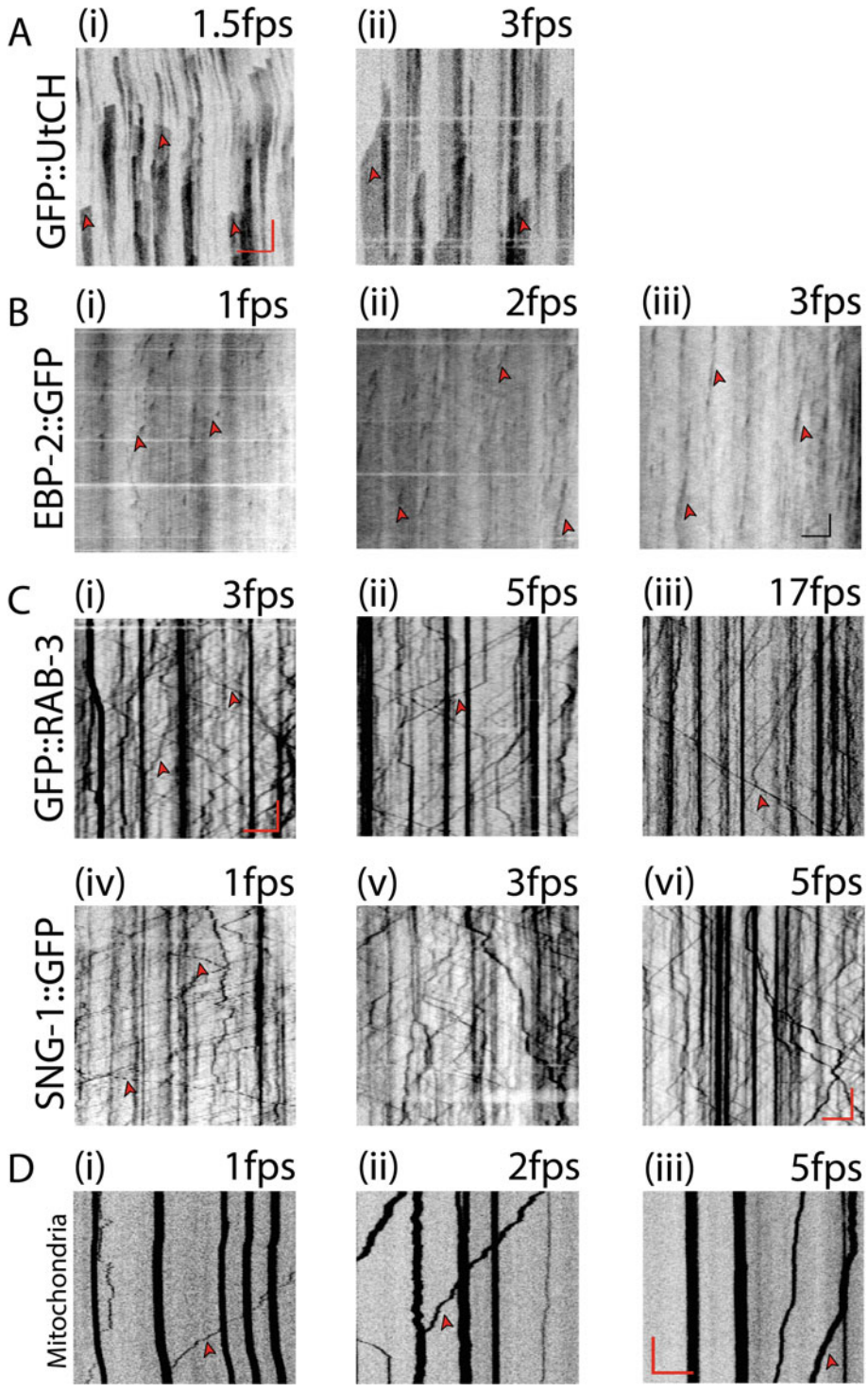

Fig. 1 Imaging intracellular organelles at different acquisition rates, shown as frames per second (fps). Kymographs from imaging (**a**) actin, marked by GFP-tagged calponin homology domain of the F-actin binding protein utrophin (GFP::UtCH), in SD microscope in *C. elegans* PLM neuron performed at (i) 1.5 fps and (ii) 3 fps. Red arrowheads point to the actin trails. (**b**) EBP-2::GFP imaged in SD microscope, to assess microtubule dynamics such as direction and speed of microtubule growth, at (i) 1 fps, (ii) 2 fps, and (iii) 3 fps; *y*-axis for this

use lasers to scan point by point in the specimen, causing phototoxicity to the sample and making them less suited for live imaging [50]. But, with the right hardware and software, they can be optimized for many kinds of live imaging. Increasing the pinhole size will allow for more light to be collected, thereby increasing sensitivity and reducing phototoxicity [51]. However, using a larger pinhole will result in more light coming from out-of-focus planes, affecting the z-resolution and contrast. CLSMs can be equipped with multiple detectors and are often fitted with photo multiplier tubes (PMTs) or high-sensitivity GaAsP detectors, or both, making possible multi-color simultaneous imaging.

(c) *Spinning Disc Confocal Microscope.*

SD microscopes differ from CLSMs in that they use not one but multiple pinholes simultaneously and are often fitted with sensitive cameras. Therefore, SD microscopes can image a large field of view at a higher temporal resolution than a CLSM, making them ideal for fast live imaging. Additionally, the incident laser illuminating the sample passes through the several pinholes of the rapidly moving spinning disc exposing the sample to low laser light for short durations of time, thereby reducing the risk of phototoxicity to the sample [52, 53, 50]. Often, out-of-focus light scatters and passes through adjacent pinholes in the spinning disk, compromising the confocality of the system. Therefore, resolution along the *z*-axis is poorer in SD microscopes as compared to CLSMs. However, the EM-CCD cameras that are often fitted with SD microscopes have higher quantum efficiency than the PMTs fitted with CLSMs, enabling more efficient and sensitive detection. Therefore, SD microscopes may offer better *xy*-resolution than CLSMs [53].

To establish parameters for live imaging, it is useful to examine the sample under a WF microscope to get an estimate of the parameters to optimize for imaging. These parameters could be the nature of fluorophore excitation and the signal, bleed-through, spatial and temporal resolution needed, effect of the duration of imaging on live samples, etc. Getting an idea about parameters to optimize for imaging before standardizing conditions on a confocal

Fig. 1 (continued) kymograph marks 25pixels. Red arrowheads point to microtubule trails. (**c**) Panels (i) to (iii) show GFP::RAB-3 imaged in a SD microscope, to assess synaptic vesicle motion properties, at (i) 3 fps, (ii) 5 fps, and (iii) 17 fps. Red arrowheads point to individual vesicles whose trajectories can be tracked clearly. Panels (iv) to (vi) show SNG-1::GFP imaged in a WF microscope at (iv) 1 fps, (v) 3 fps, and (vi) 5 fps. Red arrowheads mark the gaps in the trajectory seen at 1 fps. (**d**) Mitochondria marked by GFP targeted to mitochondrial matrix imaged in SD microscope at (i) 1 fps, (ii) 2 fps, and (iii) 5 fps. Red arrowheads point to moving mitochondria. Scale on *x*-axis is 5 μm. *y*-axis marked is 35 pixels, size in microns varies with the frame rate of each movie

system will help greatly, especially if the number of accessible microscopes and the amount of usable time are limited. Additionally, WF microscopes work well for a wide variety of imaging, some examples of which will be shared in the sections below. Therefore, it is useful to consider cheaper and more accessible microscopes before imaging on expensive systems.

Imaging *C. elegans* neurons to study dynamics of axonal transport is attractive for several reasons. (1) *C. elegans* are transparent, making in vivo imaging of fluorescently labeled proteins easy, without dissecting the animal. (2) *C. elegans* neurons are small and often have thin processes. Their cell bodies are typically 2–3 μm in thickness [54], with neuronal processes having diameters between 100 and 200 nm [55]. Therefore, while considering a suitable microscope for live imaging in *C. elegans* neurons, choosing a system that provides the best spatial resolution is preferred. While imaging of smaller cargo such as the synaptic vesicles can be done using both WF and a confocal microscope, fainter and faster vesicles can prove difficult to capture with a WF microscope. Faster vesicles may appear fainter on a camera because of reduced dwell time. A SD confocal microscope is best suited for imaging synaptic vesicles because it enables fast, high contrast, sensitive imaging. Since *C. elegans* neurons are thin, *z*-resolution is not a concern for most kinds of imaging. Imaging single cells in vivo is also easier because generating *C. elegans* transgenic lines with cell-specific expression of fluorescently labeled proteins is fairly easy.

3.5 General Steps for Live Imaging

1. Turn on either a WF or a confocal microscope depending upon the kind of imaging (*see* Subheading 3.4).
2. Locate the worm on the slide at lower magnification (4× or 10×) and switch to the desired magnification to begin imaging.
3. Specific conditions suited for each marker and the nature of data desired will decide the choice of laser power. The optimal laser power will be the lowest laser power at which the signal is not compromised, and the fluorophore does not undergo significant photobleaching for the entire duration of acquisition.

Our standardized conditions for imaging various intracellular cargo can be found in Table 1.

3.5.1 For Live Imaging of Large, Slow-Moving Organelles

1. Larger organelles such as mitochondria can be imaged in both WF and confocal microscopes (Fig. 2c).
2. Once the microscope is set up, select the laser line suitable for the fluorophore used to label mitochondria. We use a transgenic line which expresses mitochondrial matrix-targeted GFP expressed in the six touch receptor neurons [56, 57].
3. Switch to 60× or 100× magnification and focus on the mitochondria.

Table 1
Standardized imaging conditions for axonal transport on various microscopes

Microscope	Objective	Exposure time	Frame rate	Movie duration	Anesthetic used	Agarose pad percentage
Live imaging of mitochondria						
Spinning Disk confocal with EMCCD camera	60×	50–100 ms (488 nm laser)	2 fps	3 min	5 mM Tetramisole	5% agarose pads
Live imaging of microtubules						
Epifluorescence with EMCCD camera	100×	400 ms (300 EM gain)	1–2 fps	Variable	5 mM Tetramisole	5% agarose pads
Spinning Disk confocal with EMCCD camera	100×	300 ms (488 nm laser)	3 fps	3 min	5 mM Tetramisole	5% agarose pads
Live imaging of actin						
Epifluorescence with EMCCD camera	100×	600 ms, 505 EM gain	1.6 fps	3 min	5 mM Tetramisole	5% agarose pads
Spinning Disk confocal with EMCCD camera	100×	600 ms (488 nm laser)	1.6 fps	3 min	5 mM Tetramisole	5% agarose pads
Live imaging of synaptic vesicles						
Perkin Elmer Ultraview Spinning Disk confocal with Hamamatsu EMCCD camera	100×	169 ms	4.8–5 fps	5 min (*see* **Note** 7)	3 mM Tetramisole	5% agarose pads
Zeiss spinning disc with Andor iXon Ultra 897 EMCCD camera	100×	200 ms	5 fps	5 min	3 mM Tetramisole	5% agarose pads
Zeiss LSM 880	63× Frame size: 512 × 42 pixel size: 8.3 mm Zoom: 2×	Pinhole: 150.1 Pixel dwell time: 2.05 ms Scan time: 206.44 ms Cycles: 1000 Interval: 0	5 fps	5 min	5 mM Tetramisole	5% agarose pads
Live imaging of (ratiometric) calcium						
Spinning Disk confocal microscope	60× or 100×	250–300 ms	1 fps	6 min	5 mM Tetramisole	5% agarose pads

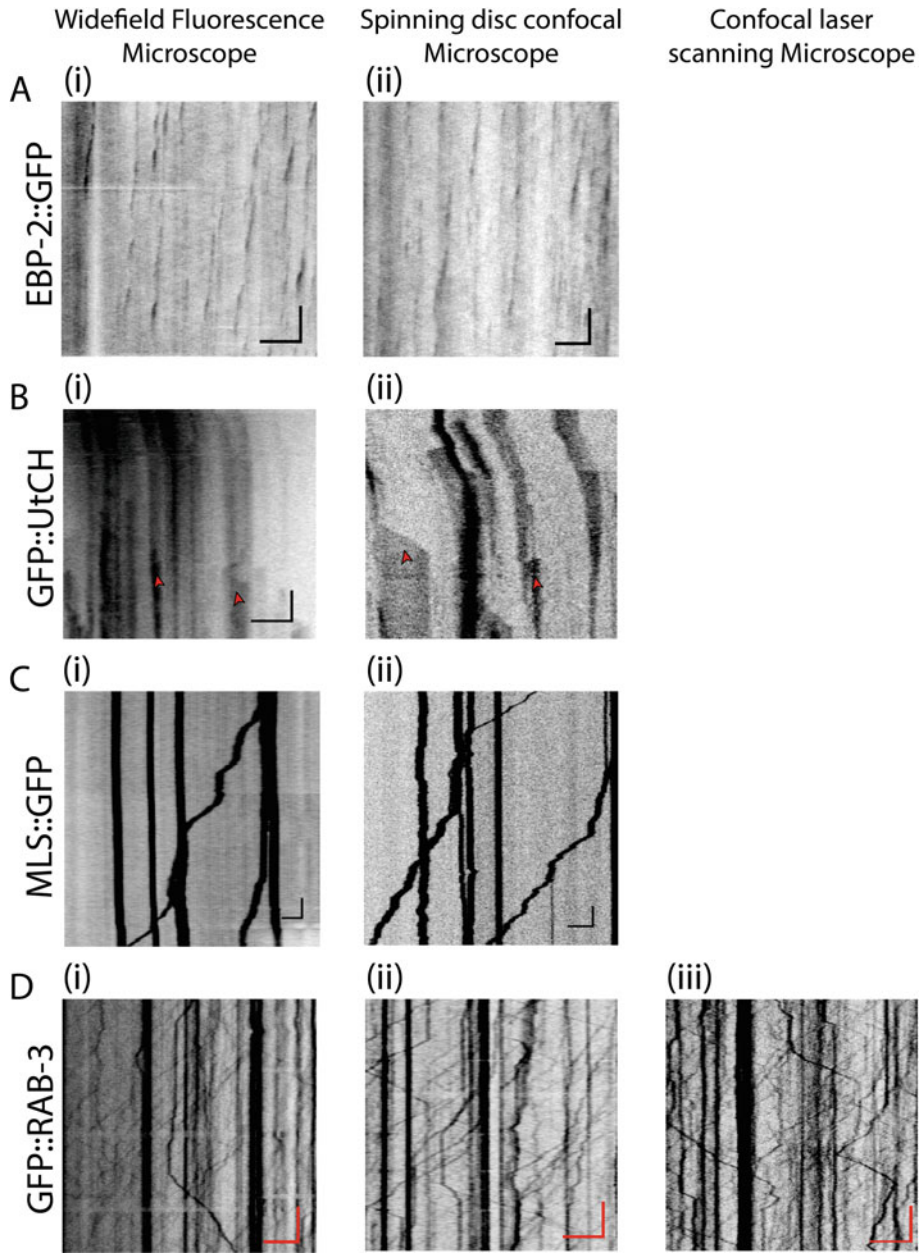

Fig. 2 Imaging in different microscope systems. Kymographs from movies obtained from imaging different markers in at least two different microscopes. (**a**) Imaging of EBP-2::GFP to assess microtubule dynamics at 3 fps in (i) WF and (ii) SD microscopes. (**b**) Imaging GFP::UtCH to assess actin growth and polymerization at 1 fps in (i) WF and (ii) SD microscopes. Red arrowheads point to some visible actin trails. (**c**) Imaging of mitochondria, marked by GFP targeted to mitochondrial matrix, in (i) WF and (ii) SD microscopes. (**d**) Imaging of GFP::RAB-3 to asses synaptic vesicle motion properties at 5 fps in (i) WF, (ii) SD, and (iii) confocal laser scanning microscopes. Scale bar on x-axis is 5 μm, scale bar on y-axis is 35 pixels which represents 11.6 s at 3 fps, 35 s at 1 fps, and 7 s at 5 fps

4. Select a suitable laser power and sensitivity for imaging (*see* **Note 6**).
5. Set imaging conditions to 2 fps (*see* **Note 6**) (Fig. 1d).
6. Acquire movies for up to 10 min in tetramisole (*see* **Notes 3** and **7**).

3.5.2 For Live Imaging of Smaller, Fast-Moving Organelles Using a WF Microscope

1. Synaptic vesicles can be imaged using a WF microscope fitted with a sensitive camera for live imaging (*see* **Note 8**) (Fig. 1c iv-vi; Fig. 2d).
2. Locate the worm on the slide at lower magnification and switch to 100× magnification and focus on the neuron.
3. Select a suitable exposure time for imaging.
4. Set imaging conditions to either 3 or 5 fps (Fig. 1c).
5. Acquire movies for up to 10 min with tetramisole.
6. Ensure that the focus does not drift during the acquisition. Correct drifts in focus by constantly adjusting the focus knob.

3.5.3 For Live Imaging of Small, Fast-Moving Organelles Using a Spinning Disc Confocal Microscope

1. At 100× magnification, focus on the neuron and select a suitable laser power for imaging (Fig. 2d).
2. Set imaging conditions to either 3 or 5 fps (*see* **Note 9**).
3. Acquire the movie for up to 10 min with tetramisole.
4. Ensure that the focus does not drift during the acquisition. Drifts in focus can be caught by monitoring the fainter moving particles and ensuring that they remain visible throughout the length of the movie. If the fainter particles are clearly visible, larger and brighter particles will be visible too, thus ensuring a focused kymograph.
5. Ensure that the worm does not drift or thrash during the acquisition. Minor drifts and linear translations can be corrected post-acquisition using the StackReg plugin in ImageJ/Fiji. However, if the animal's tail thrashes a lot, post-acquisition corrections will be harder to perform (Fig. 6b). If the animal fails to immobilize and continues to move/thrash, stop acquisition and move on to another animal.

3.5.4 For Live Imaging of Small, Fast-Moving Organelles Using a Laser Scanning Confocal Microscope

1. Once the worm is located under a 4× or 10× objective, switch to either 60× or 100× magnification and focus the neuron (Fig. 2d).
2. Choose a region of interest (ROI) that includes the neuronal process such that the frame rate for imaging is either 3 or 5 fps (*see* **Note 9**).
3. Choose an appropriate optical zoom if needed (*see* Table 1). Optical zoom is useful if the neuronal process is too thin, and the size of the ROI size cannot be changed (changing ROI size

will affect the frame rate). 2× optical zoom is typically sufficient magnification.

4. Select a suitable laser power for acquisition.
5. Adjust the time lapse settings to get 3- to 5-min movies.

3.5.5 Live Imaging of Cytoskeletal Elements

Imaging Microtubules

1. Growing microtubules can be imaged on both WF and confocal microscopes (Fig. 2a).
2. At 60× or 100× magnification, focus on the desired region of neuron.
3. Choose a suitable laser power (if using a confocal microscope) or exposure time for a lamp (if using a WF microscope).
4. Focus on the region of interest.
5. Acquire movies at from 1 to 3 fps (*see* **Note 10**) (Fig. 1b) while avoiding drifts in focus.

Imaging Actin

1. Actin dynamics can be imaged on both WF and confocal microscopes. Traditional transgenes used to label actin, such as *wyIs291* [12, 58], are quite faint and offer low contrast in WF microscopes. However, with the right settings, they can still be used to capture actin dynamics (Fig. 2b).
2. In a confocal microscope, switch to the 100× objective and focus on the desired region of the neuron.
3. Acquire movies at from 1 to 1.5 fps (*see* **Note 11**) (Fig. 1a) while avoiding drifts in focus.

3.5.6 Live Imaging of Calcium Dynamics

1. Calcium dynamics can be imaged at either 60× or 100× magnification on either a confocal or a WF microscope (Fig. 3).
2. Quantitation of changes in calcium intensity is typically done against a soluble reference fluorophore which is insensitive to stimulation/external cues that typically affect calcium levels. When imaging for intensity quantitation, it is important to check that the relevant laser lines illuminate the field of view evenly and that the background noise is random, devoid of any kind of artefacts or patterns. *See* Subheading "Checking and Correcting for Uneven Illumination, and Background Noise Artefacts or Patterns in Background Noise" for additional information on how to check and correct for such artefacts.
3. Choose appropriate imaging conditions. If performing imaging with two transgenes, follow the method listed for dual color imaging in Subheading 3.5.7.
4. Focus on the region of interest.
5. Calcium dynamics spans 3–5 s and can therefore be imaged at lower frame rates. We image calcium dynamics at 1 fps.
6. Acquire 3- to 5-min movies.

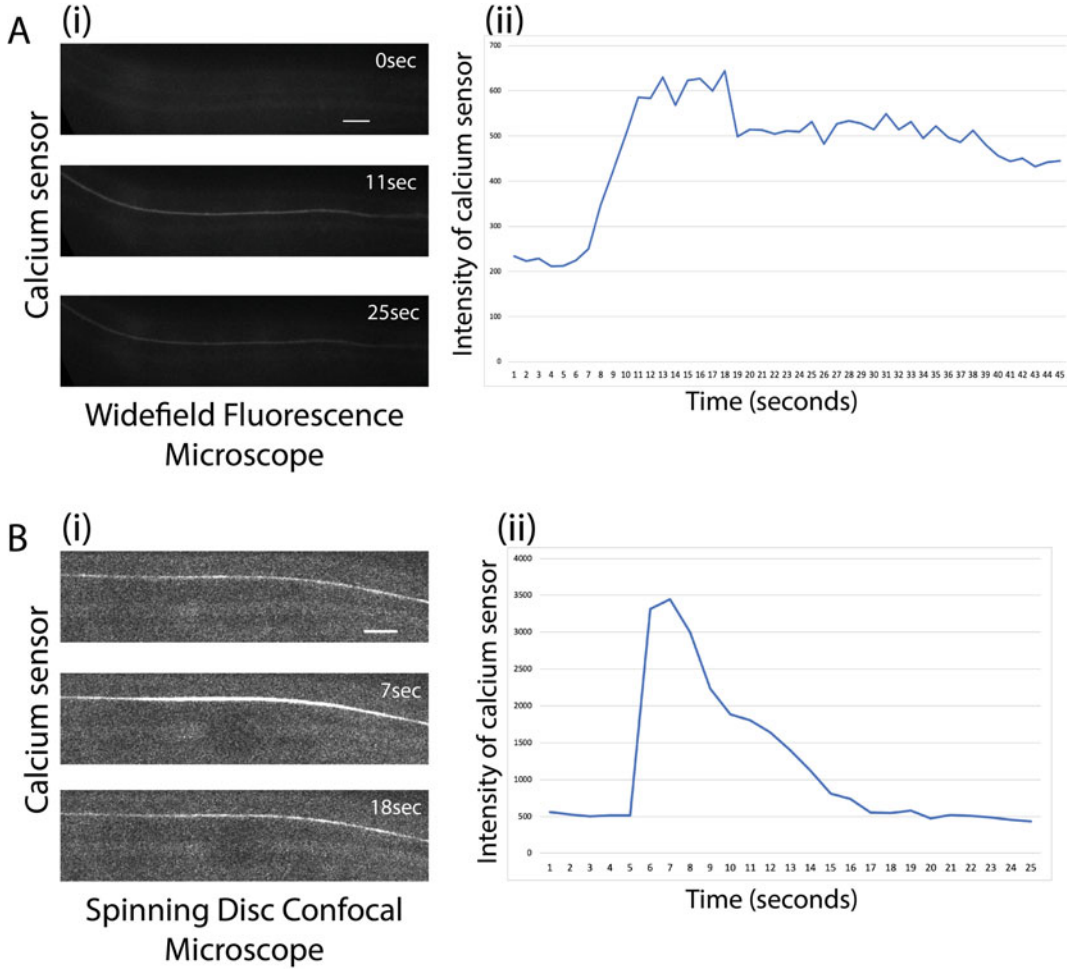

Fig. 3 Measuring intensity of calcium sensor in WF vs. SD confocal microscopes. Calcium sensor, GCamp6m, imaged in different microscopes to measure the dynamics of intensity changes in the neuron. (**a**) shows intensity measurement performed in a WF microscope under blue light. (i) Unstimulated neuron shows the least amount of fluorescence, which increases in time until it reaches baseline. (ii) A graphical representation of the rise and fall of intensity measured from the calcium sensor. (**b**) shows intensity measurement of GCamp6m performed in a SD confocal microscope. (i) Shows the change in intensity of the sensor in the neuronal process which is also represented (ii) graphically. Scale bar in **a** and **b** is 10 μm

Checking and Correcting for Uneven Illumination, and Background Noise Artefacts or Patterns in Background Noise

Fluorescent emission is usually proportional to intensity of the light illuminating the sample [59]. Therefore, if a uniformly labeled fluorescent sample appears uneven, it is most likely unevenly illuminated. Uneven illumination in the field of view will render the sample unfit for intensity measurements as the measurements will vary across the sample depending on the degree of illumination. Uniformity of illumination can be assessed using a uniformly labeled fluorescent sample, such as a film made of fluorescently labeled protein or beads [60]. Uniformity of illumination in a WF microscope will improve if it is carefully aligned for Koehler

illumination. Persistent non-uniform illumination can be corrected post image acquisition using an ImageJ/Fiji plugin for Flatfield correction, or manually as described by Wolf et al. [60].

3.5.7 Simultaneous Dual Color Live Imaging for Assessing Co-migration of Transported Cargo

1. For imaging two different fluorophores in a single neuron, choose multicamera mode for image acquisition. Cameras should be aligned such that there is no shift between the red and green channels (*see* Subheading 3.7).
2. Cross-excitation or bleed-through of signal from one channel to the other need to be examined and minimized (*see* Subheading 3.6).
3. Choose a focus such that signal from both channels is comparable (*see* **Note 12**). Focus on the fainter particles in both channels, ensuring that they can be tracked throughout the duration of the movie.
4. Acquire the movie for 3 or 5 min.

3.6 Bleed-through and Cross-Excitation in Simultaneous Dual Color Imaging

Cross-excitation occurs when a fluorophore is excited by a range of wavelengths close to its actual excitation wavelength. In dual color imaging, if the excitation wavelength of one fluorophore can also excite the other fluorophore, it results in cross-excitation. Cross-excitation may not affect analysis for co-localization or co-migration assays as these analyses are less affected by the intensity of signal, as cross-excitation only affects the recorded intensity of the fluorophore emission. Therefore, cross-excitation during imaging will affect analyses based on intensity measurements.

Bleed-through occurs when fluorescence emission from one channel is detected in another channel. For co-localization or co-migration assays, bleed-through can result in false-positive correlations. Bleed-through can be detected and avoided by adjusting the laser power and gain during image acquisition or by using a narrow band pass filter. However, using a very narrow band pass filter can reduce the signal intensity greatly. Sometimes, bleed-through is unavoidable when using extremely bright transgenic lines or when none of the aforementioned methods work. In such situations, both bleed-through and cross-excitation can be avoided by sequential imaging. SD microscopes allow for fast sequential imaging. However, achieving frame rates comparable to simultaneous imaging without compromising the signal quality is not always possible. Fortunately, images can be corrected for bleed-through and cross-excitation post-acquisition by following the protocols described in the sections below.

Post-acquisition correction for bleed-through and cross-excitation is done on kymographs made from time lapse images of the two fluorophores used for the dual color analysis. We share a protocol for correcting bleed-through and cross-excitation for dual color imaging of green and red fluorophores, where signal from the

green fluorophore bleeds through to the 561 nm channel while the red fluorophore gets cross-excited by the 488 nm laser. The implied assumptions are: (a) signal from the red fluorophore does not bleed-through to the 488 nm channel; and (b) green fluorophore does not get cross-excited by the 561 nm laser. However, the protocol can be used for any combination of fluorophores under any bleed-through/cross-excitation condition.

3.6.1 Image Acquisition for Bleed-Through Correction

1. Use *C. elegans* expressing the green fluorophore and choose the dual-color simultaneous imaging mode (Fig. 4a).
2. While keeping the red laser off, use the green laser to pick a laser power at which signal from green channel does not appear in the red channel (*see* **Note 13**).
3. If there is no laser power at which there is zero bleed-through, select the laser power at which the green fluorophore gives optimal signal.
4. With the 488 nm laser at optimum power, image in simultaneous mode while keeping the 561 nm laser switched off.
5. This movie (Movie X) will be used to calculate the percentage bleed-through from green fluorophore into the 561 nm channel.

3.6.2 Image Acquisition for Cross-Excitation Correction

1. Use *C. elegans* expressing the red fluorophore and select the single-color imaging mode.
2. Choose the laser power for 488 nm laser at which the green fluorophore gives optimal signal (from Subheading 3.6.1). Image the red transgene in the 488 nm channel using the settings that were used to get optimal signal for the green transgene (from Subheading 3.6.1). This will be Movie A.
3. Now image the same animal, in the same region, in the 561 nm channel under the optimal imaging conditions for the red fluorophore. Turn off the 488 nm laser for this imaging. This is Movie B.
4. Movies A and B will be used to calculate the extent of cross-excitation of the red fluorophore by the 488 nm laser.

3.6.3 Correcting for Bleed-Through and Cross-Excitation Post-Acquisition

Calculating Percentage Bleed-Through

1. Open Movie X on ImageJ or Fiji as a hyperstack. Split frames into two channels and generate kymographs for both these channels (*see* Subheading 3.7.1) (Fig. 4a).
2. Choose a region on a moving particle in the kymograph from the 488 nm channel and measure its intensity (Fig. 4a).
3. Copy the ROI to the same region on the kymograph from 561 nm channel and measure its intensity.

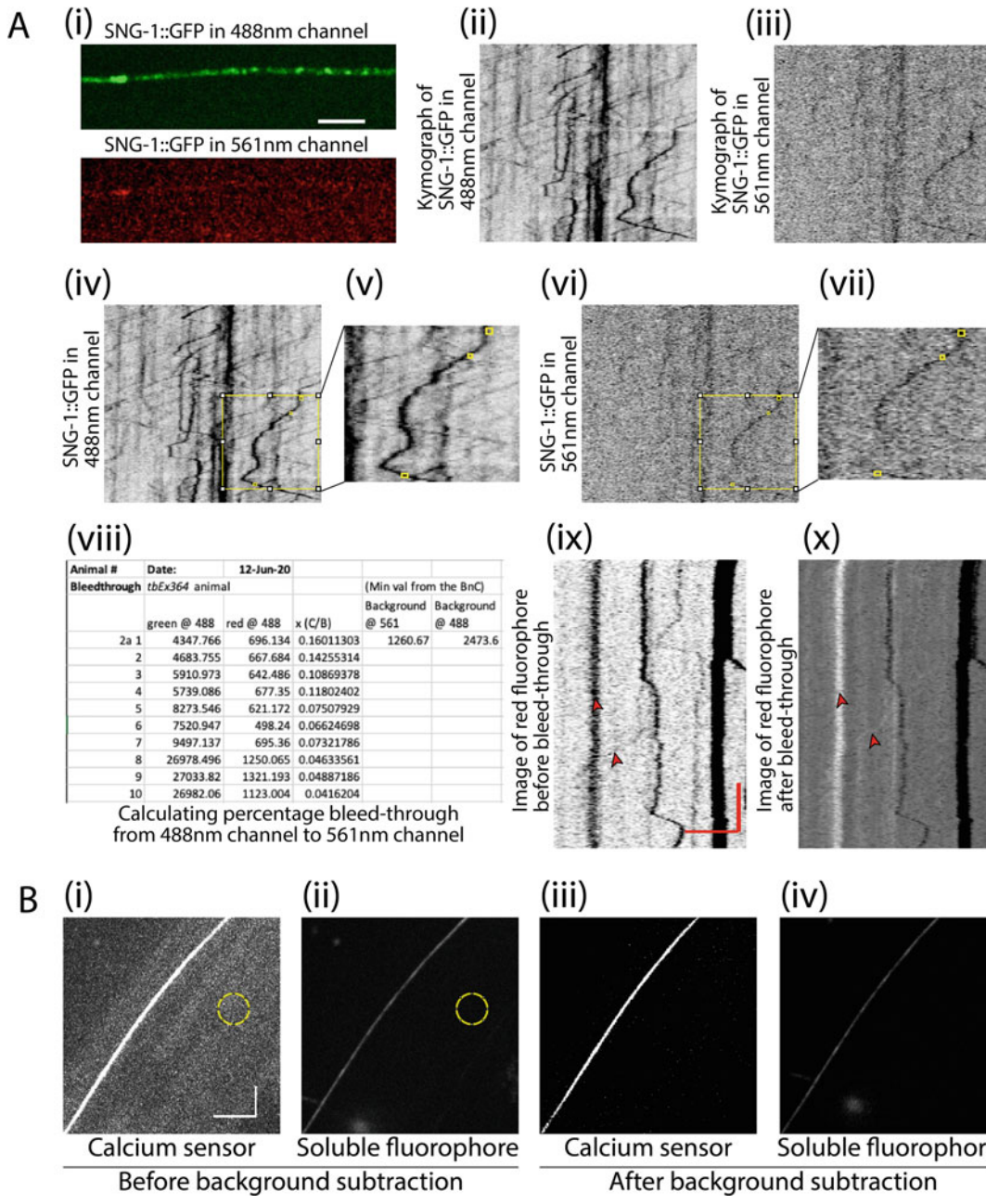

Fig. 4 Bleed-through correction and background fluorescence subtraction. (**a**) SNG-1::GFP imaged using 488 nm laser in dual-color imaging mode. Figure shows SNG-1::GFP signal in (i) 488 nm (green) channel and 561 nm (red) channel. Kymographs depicted correspond to SNG-1::GFP signal from the (ii) 488 nm channel and the (iii) 561 nm channel. Selected ROIs to measure intensity of particles in kymographs from (iv) 488 nm and (vi) 561 nm channels. Zoomed in regions chosen for ROI boxes from kymographs (ii) and (iii) are depicted in (v) and (vii), respectively. (viii) Calculations of intensity values for each ROI taken from 488 nm and 561 nm channels, to be used to calculate bleed-through percentage. (ix) Raw kymograph obtained from imaging a red fluorophore tagged protein simultaneously with SNG-1::GFP. Red arrowheads point to signal bleed-through of SNG-1::GFP into the kymograph of the red fluorophore. (x) Bleed-through corrected kymograph from (ix). Red arrowheads point to regions with zero intensity (white) which were subtracted during correction. Scale on

4. Repeat the above two steps for a total of ten different regions per kymograph pair. We typically use 10 kymograph pairs for these corrections.
5. From every measured intensity value from a 488 nm kymograph, subtract the background intensity value (minimum intensity value on the brightness/contrast scale) of that kymograph. Repeat the same for every measured value from every kymograph made from movies acquired at 561 nm. These subtracted values are the new measured values (Fig. 4a).
6. Divide the new measured intensity values from the 561 nm channel by the new measured intensity values from the 488 nm channel.
7. Calculate the average and standard deviation for these measurements. The average value is the average bleed-through of signal from the green fluorophore in the 561 nm channel.

Calculating Percentage Cross-Excitation

1. Open Movies A and B. Select a ROI and generate kymographs for the same ROI from both these movies (*see* Subheading 3.7.1). Let us call these kymographs A (red fluorophore imaged using 488 nm laser) and B (red fluorophore imaged using 561 nm laser).
2. Choose any region of a moving particle on kymograph A and measure its intensity (Fig. 4a).
3. Copy the ROI to the same region on kymograph B and measure its intensity.
4. Repeat the above two steps for a total of 10 different regions per kymograph. We typically use 10 kymographs for these corrections.
5. From every measured intensity value from kymograph A, subtract the background intensity value (minimum intensity value on the brightness/contrast scale) of that kymograph. Repeat the same for every measured value from kymograph B. These subtracted values are new measured values.
6. Divide the new measured intensity values from kymograph A by the new measured intensity values from kymograph B.
7. Calculate the average and standard deviation for these measurements. The average value is the average cross-excitation of the red fluorophore from a given transgenic line by the 488 nm laser.

Fig. 4 (continued) x-axis is 10 μm and on *y*-axis is 11.67 s. (**b**) Single frames from raw movies (before background subtraction) of simultaneous dual-color imaging of (i) calcium sensor and (ii) soluble fluorophore. The circle indicates the ROI chosen for background subtraction across all frames of the movie. Single frames from background subtracted movies of (iii) calcium sensor and (iv) soluble fluorophore. Scale on *x*-axis is 10 μm and on *y*-axis is 26.9 s

Correcting Kymographs for Bleed-Through and Cross-Excitation

1. Obtain the dual-color image as described (*see* Subheading 3.5.7).
2. Open the dual color movie in ImageJ or Fiji, split channels and get kymographs for both channels (*see* Subheading 3.7.1).
3. Kymograph from the sample imaged using 561 nm laser will need to be corrected for bleed-through and cross-excitation. We will need to subtract both the signal bleeding through from the green fluorophore into the red channel and the signal obtained due to cross-excitation of the red fluorophore by the 488 nm laser to obtain a kymograph that contains signal only from excitation of the fluorophore by the 561 nm laser.
4. Open the kymograph for the green fluorophore in ImageJ or Fiji. Go to Process > Math > Multiply...
5. In the dialog box, enter the average bleed-through value (*see* **Note 14**). For example, if the average is 0.08, enter 0.08. You will now see that only 8% of the intensity of the kymograph is visible. Save this as a separate kymograph. Let us call this kymograph "8% green kymograph." Do not close this kymograph.
6. Open the kymograph for the red fluorophore.
7. Go to Process > Image Calculator...
8. In the dialog box that opens, choose the red fluorophore kymograph as Image1 and for Image2, use the 8% green kymograph. Set the operation to Subtract. Choose to create a new window and click Ok.
9. You will now get another kymograph which will be the result of the above subtraction. This kymograph is the bleed-through corrected red fluorophore kymograph. Save this kymograph. If there is no cross-excitation, you may use this kymograph for analysis (Fig. 4a). However, in case of cross-excitation, this kymograph will need to be processed further.
10. Open the bleed-through corrected red fluorophore kymograph and go to Process > Math > Multiply... Multiply this kymograph by the average cross-excitation value (0.05) obtained in Subheading "Calculating Percentage Cross-Excitation".
11. Save the resulting kymograph (5% bleed-through corrected red fluorophore kymograph) as a separate kymograph. Do not close this kymograph.
12. Open the original bleed-through corrected red fluorophore kymograph. Go to Process > Image Calculator...
13. Subtract the 5% bleed-through corrected red fluorophore kymograph from the original bleed-through corrected kymograph. Choose to create a new window and click on Ok.

14. The resulting kymograph is the red fluorophore kymograph that has emission signal only from excitation of the fluorophore by the 561 nm laser. Save this kymograph and use it for analysis.

3.7 Analysis

3.7.1 Making a Kymograph

1. Open the movie from which you want to make a kymograph. If it is a dual color movie, split the movie into two movies corresponding to their respective channels.
2. Choose the region of the neuron which is in best focus in both the channels. Using the segmented line tool, draw a line on the region you want to be represented in your kymograph. You may choose to zoom into the movie to draw a more accurate line along the neuron. Ensure that the line covers the ROI in every frame of the movie.
3. If the line does not cover the ROI in every frame of the movie, separate the frames of the movie where the line aligns. This can be done by going to Image > Stacks > Tools > Make Substack. . . and then choosing the selected frames. This is typically required when the animal moves slightly during acquisition. Draw a different line to cover the ROI in the remaining frames.
4. If working with dual-color imaging movies, remember to make substacks of both the movies from dual color simultaneous imaging obtained after splitting.
5. Once the ROI is selected, go to Analyze > Multi Kymograph > Multi Kymograph. Choose a line width of three pixels for *C. elegans* neurons.
6. Save unprocessed kymographs. Do not adjust the brightness and contrast settings on the kymographs. Inverting the kymographs or changing their brightness or contrast will render them unusable for quantitative analyses such as corrections for bleed-through and cross-excitation correction.
7. If the animal had twitched or moved during image acquisition, substacks of the movie can be made to include frames where the animal was still. If the animal moved along the horizontal axis during the full length of the movie, the StackReg plugin in ImageJ/Fiji might be helpful in correcting the motion (Fig. 6b).

3.7.2 Annotation of Particles

1. The first step for analyzing a kymograph is annotation. Open the kymograph you wish to annotate in ImageJ or Fiji.
2. Default kymographs have white signal on black background. Invert the kymograph for analysis by pressing Ctrl+Shift+I. You can adjust the brightness and contrast of the kymograph by pressing Ctrl+Shift+C to open the brightness/contrast adjuster.

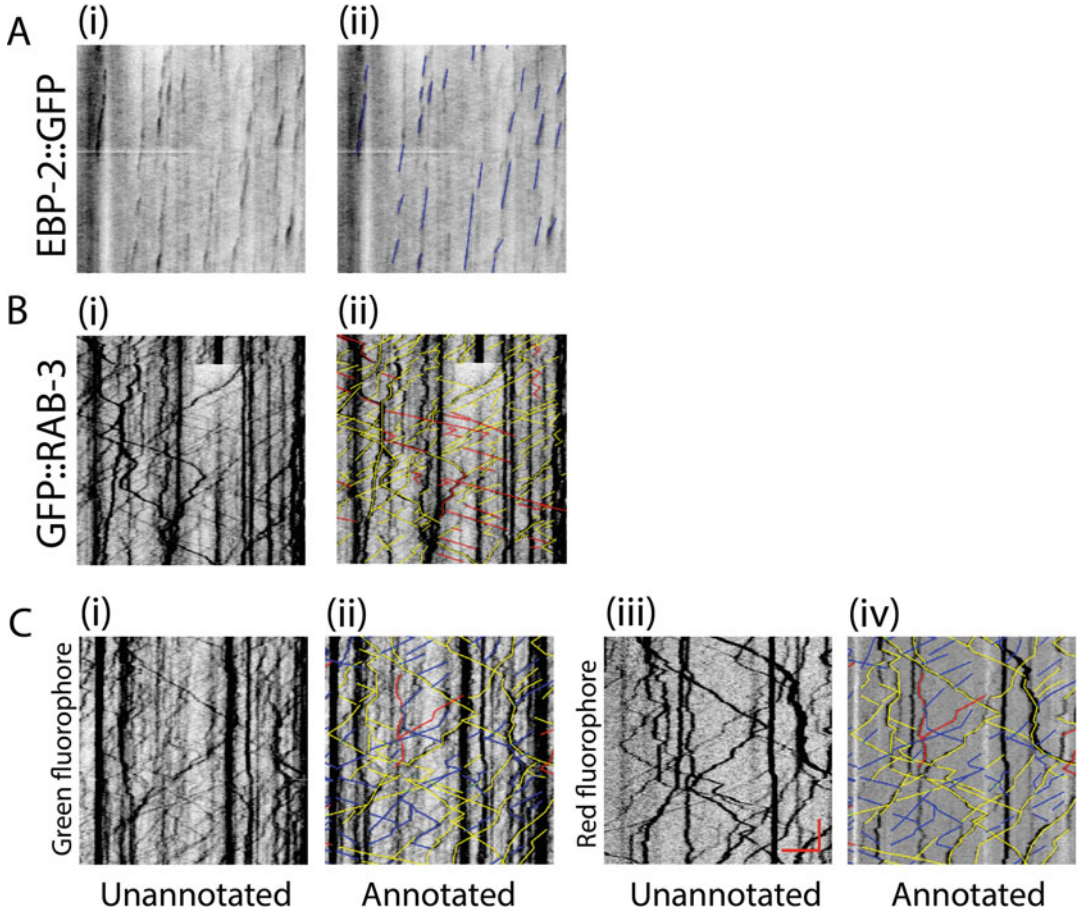

Fig. 5 Annotating particles for analysis. (**a**) Marking the EBP-2::GFP comets to assess the direction of microtubule polymerization, (i) shows an unannotated kymograph and (ii) shows the same kymograph with annotations. (**b**) Kymograph (i) and (ii) annotated kymograph, from a movie of GFP::RAB-3. Yellow annotations mark the vesicles moving in the anterograde direction (away from the cell body) and red annotations mark the vesicles moving in the retrograde direction (toward the cell body). (**c**) Kymographs depicting moving particles from dual-color simultaneous imaging of a strain simultaneously expressing both GFP-tagged and mCherry-tagged proteins. Kymograph (i) from the GFP channel and kymograph (iii) from mCherry channel. Kymographs (ii) and (iv) show the annotations performed simultaneously on kymographs (i) and (iii). Blue annotations represent particles unique to kymograph from moving GFP-tagged protein, red annotations represent particles unique to kymograph from moving mCherry-tagged protein, and yellow annotations represent moving particles common to both kymographs. Scale on *x*-axis is 5 μm and on *y*-axis is 11.67 s

3. Choose a brightness/contrast setting which allows you to see moving particles clearly. Different regions of a kymograph may need different brightness/contrast settings.
4. Using the "Segmented Line" from Line tool available in ImageJ or Fiji, mark a moving vesicle by tracing its trajectory very carefully (*see* **Note 15**). Tracing should be done very carefully for analyses involving macros or plugins, especially where characteristics of vesicle motion are being assessed (Fig. 5a, b).

5. Once done, add the trace to the ROI manager by pressing "T." Repeat for each particle you wish to annotate.
6. There will be some regions where tracking the trajectory of a particle will be very hard. These could be regions where a moving particle intercepts a stationary particle, or where two or more moving particles cross paths. When a moving particle crosses a large stationary particle, adjust the brightness/contrast at the region of intersection to track the trajectory of the moving particle accurately. The moving particle is counted as the same particle as long as it continues to have the same slope after crossing a stationary particle.
7. Sometimes, the slope of the trajectory changes when a particle crosses a stationary particle. In such cases, if the intensity remains unchanged after crossing the stationary particle, it is counted as the same particle.
8. If both slope and intensity change, especially after pauses, a particle's trajectory can be seen from the movie from which the kymograph was made, to assess whether or not it continued moving after the pause. If it cannot be determined whether the particle crossed the stationary particle, the trajectory beyond the stationary particle is considered a different particle.
9. When two or more vesicles cross paths and if both their intensities and slopes change, annotate those segments as independent trajectories.
10. Certain macros and plugins use traces stored in the ROI manager to analyze the particle trajectory, save all the traces in the ROI manager once all the particles are annotated. To save the ROI manager, in the ROI manager select More > Save...
11. When using fluorophores that tend to aggregate, such as mCherry, it is important to keep in mind that those aggregates can exhibit vesicle-like motion (Fig. 6a) [61]. Therefore, it is important to know how the movement of proteins of interest differs from the moving fluorophore aggregates, so that they are excluded from annotations.

3.7.3 Synaptic Vesicle Motion Properties

1. Analysis of vesicle motion properties such as velocities and run lengths can be done using the tsp. plugin in ImageJ/Fiji or manually (for manual velocity measurement, *see* Subheading 3.7.5).
2. More detailed analysis of vesicle motion properties can be performed using a macro we developed in our lab (Macro 1) or a published macro called KymoAnalyzer [62]. Our macro uses the traces stored in ROI manager as raw data to calculate several parameters, such as initial direction of a moving particle, particle net direction, velocity for each segment of a particle's trajectory (segment velocity), segment run length (distance a

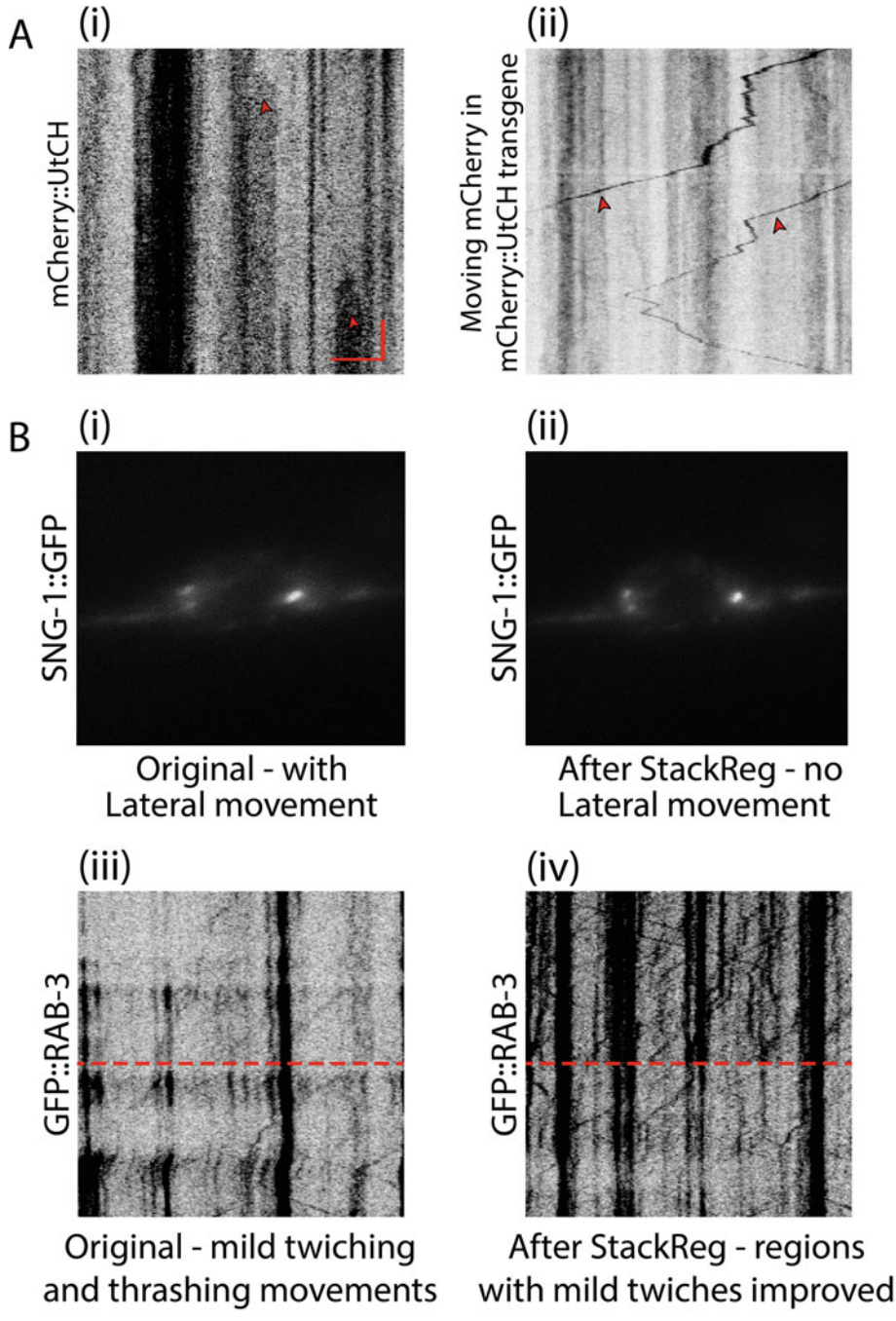

Fig. 6 Artefacts while imaging. (**a**) Kymographs from imaging actin using mCherry-tagged UtCH, mCherry::UtCH. (i) Arrowheads point to actin trails. (ii) Mobile mCherry particles moving in the kymograph from mCherry::UtCH movie. (**b**) *Z*-projection of movie from the PLM cell body expressing SNG-1::GFP in (i) an animal that moves while imaging. (ii) Z-projection of the movie after using the StackReg ImageJ/Fiji plugin. (iii) Kymograph from a movie of synaptic vesicles, tagged by GFP::RAB-3, in a moving animal. (iv) Region of kymograph affected by mild twitching (above the red dotted line) improved after using the StackReg plugin. Region of kymograph affected by twitching and body movements (below the red dotted line) not improved by the StackReg plugin

particle runs until it pauses), pause duration of each vesicle, pause frequency (number of times a vesicle pauses in its entire annotated trajectory), and the number of vesicles traveling toward (retrograde direction) and away (anterograde direction) from the cell body. Analysis using our macro is detailed below:

(a) To run the macro, open the ROI containing all traces from an annotated kymograph.

(b) Drag and drop the macro into the ImageJ or Fiji window. The macro will open in the macro editor.

(c) Click "Run." The macro will run and display all the measured parameters in a table. These values can be copied onto MS Excel or any other software used to save and analyze data.

3.7.4 Co-migration of Proteins

1. Open kymographs from one animal that are corrected for bleed-through and cross-excitation.
2. Invert both kymographs and adjust their brightness and contrast.
3. Go to Analyze > Tools > Synchronize Windows and choose "Synchronize all" to synchronize the red and green fluorophore kymographs from same animal.
4. Mark individual particles by tracing on them using the "Segmented Line" option from Line tool in ImageJ or Fiji. Once made, add this line to the ROI manager by pressing "T."
5. You may change the color and thickness of each individual line added to the ROI manager by either selecting the line on the kymograph or by choosing the line in the ROI manager and selecting "Properties" from the ROI manager. We find it useful to color the common traces from both kymographs yellow and use blue to color traces exclusive to kymograph from green fluorophore and red for traces exclusive to kymograph from the red fluorophore (Fig. 5c).
6. Once all the particles are annotated (*see* **Note 16**), go to Image > Overlay > From ROI manager to overlay all the annotated particles onto either single channel kymographs.
7. Save these kymographs separately from the original unannotated kymographs. Save the ROIs as well.
8. Calculate the percentage of traces which are common to both kymographs. This will be the percentage co-migration of the two fluorescently labeled proteins (Fig. 5c) [7].

3.7.5 Actin and Microtubule Imaging

1. For analysis of direction of polymerization of either actin or microtubule, annotate the slanting lines on the kymograph (Fig. 5a).

2. Using the annotations, density of actin/microtubule clusters (number of clusters/unit time/unit distance) [12], direction of growth (number of anterogradely moving vs retrogradely moving comets) can be performed [36, 63].
3. If assessing dynamics of actin and microtubules, lifetime of stationary tracks [12], their appearance/disappearance or velocity and length of polymerization can also be measured [36, 64].
4. Velocity measurements can be made from annotations/tracings of moving comets or the slanted signatures (Fig. 5a). Velocity measurements can be made automatically (using the tsp. plugin) or manually.
5. To measure velocity manually, draw the ROI on the slanted line and press Ctrl+M to measure the angle of the trace.
6. If performing the calculations on MS Excel, convert the angle to radiants (Default unit for angles in MS Excel is radiants. Calculations can be performed in either radiants or degrees).
7. The slope of the line will be the $\tan^{-1}$ (angle measured).
8. Multiply the slope by the frame rate of the movie and the pixel size to get the velocity of that particle.

3.7.6 Ratiometric Calcium Imaging

The following protocol describes imaging of calcium sensors to quantitate changes in calcium levels. Typically, strains used for such an imaging contain two transgenic arrays, a calcium sensor (GCamp6) and soluble mCherry, both expressed under the same promoter.

1. Open the dual-color movie in ImageJ or Fiji.
2. Subtract the background noise from either movie (*see* Subheading "Background Subtraction for Ratiometric Calcium Imaging") and split the channels. Macro 2 used for background subtraction works on unsplit movies as well.
3. For intensity measurements, select a ROI in the neuron that shows uniform changes in intensity of the calcium reporter upon stimulation.
4. Length of this ROI can vary, but the same ROI should be used on movies of both fluorophores. Add selected ROI to ROI manager.
5. In the ROI manager, go to More > Multi Measure. Save the obtained intensity measurements for that ROI in the selected channel for each frame.
6. Repeat the same with the other channel.
7. Divide the intensities obtained for the green fluorophore (calcium sensor) by those for the red fluorophore (soluble

fluorophore). Repeat this for each intensity value obtained per frame.

8. Get the mean and standard deviations for ratios of intensities across the data set. Information such as rates of rise and fall of calcium can be obtained from these data (Fig. 3).

Background Subtraction for Ratiometric Calcium Imaging

1. Open the dual color movie in ImageJ or Fiji.
2. Select a circular ROI of some diameter (we typically use a circle of diameter 25–30 μm). The size of the diameter does not matter. However, use the same ROI for all images to be processed for comparison.
3. Choose the ROI on the body of *C. elegans* that does not show intensity changes for the entire duration of the movie and is close to the region of interest (Fig. 4b).
4. Use Macro 2 in ImageJ/Fiji to obtain background subtracted images.
5. Use the background subtracted movie for intensity quantitation (Fig. 4b).

3.7.7 Motion Properties of Mitochondria and Other Moving Cargo

Analysis for assessing the motion properties of mitochondria or other moving cargo will follow the protocol described for synaptic vesicles in Subheading 3.7.3.

4 Notes

1. The percentage of agarose pad depends on factors like age of the worm and sensitivity of the worm to the mode of immobilization. Younger animals (L2 to early L4s) desiccate faster on higher percentage agarose pads (5% or more). Older animals, such as late L4s and 1-day adults, anesthetize faster on 5% agarose pads as compared to 2% or 3% agarose pads. Typically, mutants of genes that affect synaptic transmission make animals resistant to chemical anesthetics such as levamisole or tetramisole [65], so they take longer to immobilize. If imaging any such mutant, using higher concentrations of anesthetic (5 mM tetramisole, for example) with a 5% agarose pad helps immobilize animals better.
2. It is better to keep the agarose pads moisturized by placing them in a box on a wet tissue as worms desiccate on dry agarose pads. Agarose pads moisturized in this manner can be used for 3–4 h. Make sure the agarose pad's thickness is even, otherwise the worms will get room to move away when you illuminate them with light [66, 67].

3. L4 or adult animals can be imaged using either an anesthetic or a microfluidic device. However, a microfluidic device is preferred to anesthetics when imaging younger animals, especially L1 stage larvae or mutants with very low cargo flux [47]. Additionally, long-term imaging with anesthetics is known to affect the number of moving cargo and cargo motion properties [47]. Data obtained from imaging in microfluidic devices are often closer to physiological conditions. However, since most data collected from various genetic backgrounds are compared with wild-type imaged in the same conditions, the easier imaging with anesthetic immobilized animals usually suffices.
4. For live imaging in tetramisole, a maximum of two worms per slide is recommended. Long-term exposure (exposure beyond 15 min) to tetramisole affects the number of moving particles and cargo motion properties [47].
5. Place the cover slip very gently. Harsh physical handling could injure the animals, causes axon blebbing, and may affect organellar positioning or appearance.
6. Several moving mitochondria are small in size and thus imaging parameters such as the laser power, gain, and sensitivity should be optimized to capture large and bright stationary mitochondria as well as the smaller and fainter moving mitochondria. Mitochondrial movement can be imaged at either 1 or 2 fps. 2 fps is preferred because it reliably captures short pauses and rapid changes in direction of motion.
7. Typical duration for a movie is 3 or 5 min. When the animal does not immobilize in the first few minutes or if one wishes to capture either more events in the same animal or events that happen over a longer time period, one can image up to 10 min. Alternatively, two consecutive movies lasting 3 or 5 min can also be captured, as long as there is no effect of prolonged anesthetic treatment on the flux or motion properties of the organelle being imaged. We prefer capturing two consecutive movies for 5 min each instead of a single 10-min movie because with increasing time, the file size of the images increases which can sometimes be difficult to open with ImageJ/Fiji. The duration of the movie should be decided after determining the available computer system memory for ImageJ/Fiji or other image processing software used.
8. Smaller and fainter moving particles maybe missed when imaging synaptic vesicles in a WF microscope. This can be improved by using either a brighter transgenic line or increasing the intensity of excitation light. WF microscopes can be used to assess the density or intensity of stationary synaptic vesicles.
9. In vivo, synaptic vesicle proteins have an average velocity close to 1 μm/s in the anterograde direction (moving away from cell

body toward the synapse). Imaging synaptic vesicle motion properties at higher frame rates will provide greater temporal resolution and more accurate information about the duration of pauses in their trajectories [48]. However, annotation of particles on movies acquired at very high frame rates (such as 7 fps or 9 fps) can be laborious and inaccurate as at such high frame rates, the fainter particles are often not captured by the camera [47, 48] (Fig. 1c). On the contrary, low frame rates, such as 1 fps, often fail to capture parts of the vesicle trajectory and thereby features such as short pauses (Fig. 1c iv). We find that 3–5 fps achieve the best compromise between visualizing fainter moving particles and getting sufficient temporal resolution on parameters such as pause duration and frequency (Fig. 1c). However, for analyses that depend largely on observations on the presence of vesicles and not their transport properties, such as co-transport of two vesicle proteins, a rate of acquisition of 3 fps is sufficient.

10. Traditionally, EBP-2::GFP is used to characterize two properties of microtubules: (a) direction of microtubule polymerization [63] and (b) dynamics of microtubule growth and polymerization [64]. Smaller EBP-2 comets are often missed at lower frame rates (1 fps), so 3 fps is better suited for imaging to analyze direction of microtubule polymerization.
11. Fluorescently tagged calponin domain of utrophin is used to measure dynamics of actin comets such as the number of actin patches, rate of growth, and shrinkage of actin. This kind of imaging also allows us to visualize and characterize stationary actin-rich regions along the neuronal process [12, 68]. We found that imaging at lower frame rates (1 or 1.5 fps) makes distinguishing an actin comet from a stationary actin rich region easier. While quantitating changes in properties or velocities of these actin comets, we find that it is easier to catch subtle changes if the actin comets were at a 45° angle to the stationary regions. Such an angle is achieved when the frame rate is closer to 1.5 fps (600 ms exposure time). Additionally, the signal to noise ratio is higher at lower frame rates of 1–1.5 fps compared to 3 fps frame rates due to the increased exposure time.
12. When imaging two transgenic lines of dissimilar intensities, it is important to ensure that both the fluorophores are in focus for the entire duration of the movie. Fainter transgenic lines have low signal to noise ratio and, therefore, catching slight drifts in focus while imaging such lines can be hard. Therefore, it is useful to ensure that the fainter transgenic line is in focus throughout the duration of the movie.

13. Make sure to keep all the imaging settings (laser power, gain, and sensitivity) for bleed-through and cross-excitation correction identical to the settings used for the actual dual color image acquisition with both fluorophores.
14. For the percentage bleed-through or cross-excitation values, you may choose to enter just the mean value or mean value plus one or two standard deviations, depending upon how much bleed-through signal remains after correction. If assessing the same markers in several genotypes, it is advisable to choose a value that fits all genotypes.
15. Tracing a particle's trajectory using the Segmented Line tool in ImageJ/Fiji can be done by magnifying the kymograph to 200% or 300%. Magnifying the kymograph to this degree makes it appear grainy and pixelated. The optimal approach is to identify a particle at a lower magnification and tracing at a high magnification for accuracy.
16. Analysis can be done at higher magnifications, close to 300%. Since both the kymographs are synchronized, they will display similar regions. You can use the Space Bar to simultaneously navigate around both kymographs. Perform analysis only on those regions of kymographs in which the vesicles in both channels of acquisition are in focus.

References

1. Maday S, Twelvetrees AE, Moughamian AJ, Holzbaur EL (2014) Axonal transport: cargo-specific mechanisms of motility and regulation. Neuron 84(2):292–309
2. Ikenaka K, Katsuno M, Kawai K, Ishigaki S, Tanaka F, Sobue G (2012) Disruption of axonal transport in motor neuron diseases. Int J Mol Sci 13(1):1225–1238. https://doi.org/10.3390/ijms13011225
3. Chevalier-Larsen E, Holzbaur ELF (2006) Axonal transport and neurodegenerative disease. Biochim Biophys Acta 1762(11):1094–1108. https://doi.org/10.1016/j.bbadis.2006.04.002
4. Maday S, Wallace KE, Holzbaur ELF (2012) Autophagosomes initiate distally and mature during transport toward the cell soma in primary neurons. J Cell Biol 196(4):407–417. https://doi.org/10.1083/jcb.201106120
5. Lie PPY, Nixon RA (2019) Lysosome trafficking and signaling in health and neurodegenerative diseases. Neurobiol Dis 122:94–105. https://doi.org/10.1016/j.nbd.2018.05.015
6. Wang D, Chan C-C, Cherry S, Hiesinger PR (2013) Membrane trafficking in neuronal maintenance and degeneration. Cell Mol Life Sci 70(16):2919–2934. https://doi.org/10.1007/s00018-012-1201-4
7. Choudhary B, Kamak M, Ratnakaran N, Kumar J, Awasthi A, Li C, Nguyen K, Matsumoto K, Hisamoto N, Koushika SP (2017) UNC-16/JIP3 regulates early events in synaptic vesicle protein trafficking via LRK-1/LRRK2 and AP complexes. PLoS Genet 13(11):e1007100. https://doi.org/10.1371/journal.pgen.1007100
8. Brady ST, Lasek RJ, Allen RD (1982) Fast axonal transport in extruded axoplasm from squid giant axon. Science 218(4577):1129. https://doi.org/10.1126/science.6183745
9. Vale RD, Schnapp BJ, Reese TS, Sheetz MP (1985) Movement of organelles along filaments dissociated from the axoplasm of the squid giant axon. Cell 40(2):449–454. https://doi.org/10.1016/0092-8674(85)90159-X
10. Brown A (2003) Live-cell imaging of slow axonal transport in cultured neurons. Methods Cell Biol 71:305–323. https://doi.org/10.1016/s0091-679x(03)01014-8
11. Daniele JR, Baqri RM, Kunes S (2017) Analysis of axonal trafficking via a novel live-imaging

technique reveals distinct hedgehog transport kinetics. Biol Open 6(5):714. https://doi.org/10.1242/bio.024075

12. Sood P, Murthy K, Kumar V, Nonet ML, Menon GI, Koushika SP (2018) Cargo crowding at actin-rich regions along axons causes local traffic jams. Traffic 19(3):166–181. https://doi.org/10.1111/tra.12544
13. Silverman MA, Kaech S, Jareb M, Burack MA, Vogt L, Sonderegger P, Banker G (2001) Sorting and directed transport of membrane proteins during development of hippocampal neurons in culture. Proc Natl Acad Sci U S A 98(13):7051. https://doi.org/10.1073/pnas.111146198
14. Gan KJ, Silverman MA (2015) Dendritic and axonal mechanisms of Ca^{2+} elevation impair BDNF transport in Aβ oligomer–treated hippocampal neurons. Mol Biol Cell 26(6):1058–1071. https://doi.org/10.1091/mbc.E14-12-1612
15. Farías GG, Guardia CM, De Pace R, Britt DJ, Bonifacino JS (2017) BORC/kinesin-1 ensemble drives polarized transport of lysosomes into the axon. Proc Natl Acad Sci U S A 114(14):E2955–E2964
16. Bodakuntla S, Schnitzler A, Villablanca C, Gonzalez-Billault C, Bieche I, Janke C, Magiera MM (2020) Tubulin polyglutamylation is a general traffic-control mechanism in hippocampal neurons. J Cell Sci 133(3):jcs241802. https://doi.org/10.1242/jcs.241802
17. Yap CC, Digilio L, McMahon LP, Garcia ADR, Winckler B (2018) Degradation of dendritic cargos requires Rab7-dependent transport to somatic lysosomes. J Cell Biol 217(9):3141–3159. https://doi.org/10.1083/jcb.201711039
18. Soppina V, Rai AK, Ramaiya AJ, Barak P, Mallik R (2009) Tug-of-war between dissimilar teams of microtubule motors regulates transport and fission of endosomes. Proc Natl Acad Sci U S A 106(46):19381. https://doi.org/10.1073/pnas.0906524106
19. Yap CC, Winckler B (2012) Harnessing the power of the endosome to regulate neural development. Neuron 74(3):440–451. https://doi.org/10.1016/j.neuron.2012.04.015
20. Kaplan L, Ierokomos A, Chowdary P, Bryant Z, Cui B (2018) Rotation of endosomes demonstrates coordination of molecular motors during axonal transport. Sci Adv 4(3):e1602170. https://doi.org/10.1126/sciadv.1602170
21. Rai A, Pathak D, Thakur S, Singh S, Dubey AK, Mallik R (2016) Dynein clusters into lipid microdomains on phagosomes to drive rapid transport toward lysosomes. Cell 164(4):722–734. https://doi.org/10.1016/j.cell.2015.12.054
22. Smit-Rigter L, Rajendran R, Silva Catia AP, Spierenburg L, Groeneweg F, Ruimschotel Emma M, van Versendaal D, van der Togt C, Eysel Ulf T, Heimel JA, Lohmann C, Levelt Christiaan N (2016) Mitochondrial dynamics in visual cortex are limited in vivo and not affected by axonal structural plasticity. Curr Biol 26(19):2609–2616. https://doi.org/10.1016/j.cub.2016.07.033
23. Gibbs KL, Kalmar B, Sleigh JN, Greensmith L, Schiavo G (2016) In vivo imaging of axonal transport in murine motor and sensory neurons. J Neurosci Methods 257:26–33
24. Niwa S (2017) Immobilization of Caenorhabditis elegans to analyze intracellular transport in neurons. J Vis Exp (128):56690
25. Mattedi F, Vagnoni A (2019) Temporal control of axonal transport: the extreme case of organismal ageing. Front Cell Neurosci 13:393. https://doi.org/10.3389/fncel.2019.00393
26. Bhan P, Muthaiyan Shanmugam M, Wang D, Bayansan O, Chen CW, Wagner OI (2020) Characterization of TAG-63 and its role on axonal transport in C. elegans. Traffic 21(2):231–249
27. Vasudevan A, Koushika SP (2020) Molecular mechanisms governing axonal transport: a C. elegans perspective. J Neurogenet 34(3–4):282–297. https://doi.org/10.1080/01677063.2020.1823385
28. Wagner OI, Esposito A, Köhler B, Chen C-W, Shen C-P, Wu G-H, Butkevich E, Mandalapu S, Wenzel D, Wouters FS, Klopfenstein DR (2009) Synaptic scaffolding protein SYD-2 clusters and activates kinesin-3 UNC-104 in *C. elegans*. Proc Natl Acad Sci U S A 106(46):19605. https://doi.org/10.1073/pnas.0902949106
29. Zheng Q, Ahlawat S, Schaefer A, Mahoney T, Koushika SP, Nonet ML (2014) The vesicle protein SAM-4 regulates the processivity of synaptic vesicle transport. PLoS Genet 10(10):e1004644. https://doi.org/10.1371/journal.pgen.1004644
30. Rajendran L, Bali J, Barr MM, Court FA, Krämer-Albers E-M, Picou F, Raposo G, van der Vos KE, van Niel G, Wang J, Breakefield XO (2014) Emerging roles of extracellular vesicles in the nervous system. J Neurosci 34(46):15482–15489. https://doi.org/10.1523/JNEUROSCI.3258-14.2014

31. Maeder CI, Shen K, Hoogenraad CC (2014) Axon and dendritic trafficking. Curr Opin Neurobiol 27:165–170. https://doi.org/10.1016/j.conb.2014.03.015
32. Yogev S, Cooper R, Fetter R, Horowitz M, Shen K (2016) Microtubule organization determines axonal transport dynamics. Neuron 92(2):449–460. https://doi.org/10.1016/j.neuron.2016.09.036
33. Ghosh-Roy A, Chisholm AD (2010) Caenorhabditis elegans: a new model organism for studies of axon regeneration. Dev Dyn 239(5):1460–1464
34. Yan D, Jin Y (2011) Molecular and genetic approaches for the analysis of C. elegans neuronal development. Methods Cell Biol 106: 413–443
35. Basu A, Dey S, Puri D, Das Saha N, Sabharwal V, Thyagarajan P, Srivastava P, Koushika SP, Ghosh-Roy A (2017) *Let-7* miRNA controls CED-7 homotypic adhesion and EFF-1–mediated axonal self-fusion to restore touch sensation following injury Proc Natl Acad Sci U S A 114 (47):E10206. doi: https://doi.org/10.1073/pnas.1704372114
36. Kulkarni SS, Sabharwal V, Sheoran S, Basu A, Matsumoto K, Hisamoto N, Ghosh-Roy A, Koushika SP (2019) UNC-16/JIP3 negatively regulates actin dynamics dependent on DLK-1 and microtubule dynamics independent of DLK-1 in regenerating neurons. bioRxiv:484683. https://doi.org/10.1101/484683
37. Praitis V, Casey E, Collar D, Austin J (2001) Creation of low-copy integrated transgenic lines in Caenorhabditis elegans. Genetics 157(3):1217
38. Frøkjaer-Jensen C, Davis MW, Hopkins CE, Newman BJ, Thummel JM, Olesen S-P, Grunnet M, Jorgensen EM (2008) Singlecopy insertion of transgenes in Caenorhabditis elegans. Nat Genet 40(11):1375–1383. https://doi.org/10.1038/ng.248
39. Paix A, Folkmann A, Seydoux G (2017) Precision genome editing using CRISPR-Cas9 and linear repair templates in C. elegans. Methods 121:12286–12293. https://doi.org/10.1016/j.ymeth.2017.03.023
40. Stavoe AKH, Hill SE, Hall DH, Colón-Ramos DA (2016) KIF1A/UNC-104 Transports ATG-9 to Regulate Neurodevelopment and Autophagy at Synapses. Dev Cell 38(2): 171–185. https://doi.org/10.1016/j.devcel.2016.06.012
41. Moore I, Murphy A (2009) Validating the location of fluorescent protein fusions in the endomembrane system. Plant Cell 21(6): 1632–1636. https://doi.org/10.1105/tpc.109.068668
42. Nonet ML, Holgado AM, Brewer F, Serpe CJ, Norbeck BA, Holleran J, Wei L, Hartwieg E, Jorgensen EM, Alfonso A (1999) UNC-11, a Caenorhabditis elegans AP180 homologue, regulates the size and protein composition of synaptic vesicles. Mol Biol Cell 10(7): 2343–2360. https://doi.org/10.1091/mbc.10.7.2343
43. Nonet ML (1999) Visualization of synaptic specializations in live C. elegans with synaptic vesicle protein-GFP fusions. J Neurosci Methods 89(1):33–40
44. Stiernagle T (2006) Maintenance of C. elegans, WormBook, ed. The C. elegans Research Community, WormBook.https://doi.org/10.1895/wormbook.1.101.1
45. Hart, Anne C., ed. Behavior (July 3, 2006), WormBook, ed. The C. elegans Research Community, WormBook. https://doi.org/10.1895/wormbook.1.87.1
46. Mondal S, Ahlawat S, Rau K, Venkataraman V, Koushika SP (2011) Imaging in vivo neuronal transport in genetic model organisms using microfluidic devices. Traffic 12(4):372–385. https://doi.org/10.1111/j.1600-0854.2010.01157.x
47. Parry-Hill MJ Matching Camera to Microscope Resolution (trans: Davidson MW). Nikon MicroscopyU, National High Magnetic Field Laboratory, 1800 East Paul Dirac Dr., The Florida State University, Tallahassee, Florida, 32310
48. Sleigh JN, Vagnoni A, Twelvetrees AE, Schiavo G (2017) Methodological advances in imaging intravital axonal transport. F1000Res 6:200. https://doi.org/10.12688/f1000research.10433.1
49. Shimozawa T, Yamagata K, Kondo T, Hayashi S, Shitamukai A, Konno D, Matsuzaki F, Takayama J, Onami S, Nakayama H, Kosugi Y, Watanabe TM, Fujita K, Mimori-Kiyosue Y (2013) Improving spinning disk confocal microscopy by preventing pinhole cross-talk for intravital imaging. Proc Natl Acad Sci U S A 110(9):3399. https://doi.org/10.1073/pnas.1216696110
50. Jonkman J (2015) Any way you slice it-a comparison of confocal microscopy techniques. J Biomol Tech 26(2):54–65. https://doi.org/10.7171/jbt.15-2602-003
51. Borlinghaus RT(2017) Pinhole effect in confocal microscopes. Published on Leica Microsystems. https://www.leica-microsystems.com/science-lab/pinhole-effect-inconfocal-microscopes/

52. Maddox PS, Moree B, Canman JC, Salmon ED (2003) Spinning disk confocal microscope system for rapid high-resolution, multimode, fluorescence speckle microscopy and green fluorescent protein imaging in living cells. Methods Enzymol 360:597–617
53. Gräf R, Rietdorf J, Zimmermann T (2005) Live cell spinning disk microscopy. Adv Biochem Eng Biotechnol 95:57–75
54. Schafer WR (2006) Neurophysiological methods in C. elegans: an introduction. The C. elegans Research Community, Wormbook, WormBook. https://doi.org/10.1895/wormbook.1.111.1
55. Altun ZF, Hall DH (2011) Nervous system, general description. In WormAtlas. https://doi.org/10.3908/wormatlas.1.18
56. Fatouros C, Pir GJ, Biernat J, Koushika SP, Mandelkow E, Mandelkow E-M, Schmidt E, Baumeister R (2012) Inhibition of tau aggregation in a novel Caenorhabditis elegans model of tauopathy mitigates proteotoxicity. Hum Mol Genet 21(16):3587–3603. https://doi.org/10.1093/hmg/dds190
57. Sure GR, Chatterjee A, Mishra N, Sabharwal V, Devireddy S, Awasthi A, Mohan S, Koushika SP (2018) UNC-16/JIP3 and UNC-76/FEZ1 limit the density of mitochondria in C. elegans neurons by maintaining the balance of anterograde and retrograde mitochondrial transport. Sci Rep 8(1):8938. https://doi.org/10.1038/s41598-018-27211-9
58. Chia Poh H, Chen B, Li P, Rosen Michael K, Shen K (2014) Local F-actin network links synapse formation and axon branching. Cell 156(1–2):208–220. https://doi.org/10.1016/j.cell.2013.12.009
59. Waters JC (2009) Accuracy and precision in quantitative fluorescence microscopy. J Cell Biol 185(7):1135–1148. https://doi.org/10.1083/jcb.200903097
60. Wolf DE, Samarasekera C, Swedlow JR, Sluder G (2013) Chapter 14 - quantitative analysis of digital microscope images. Methods Cell Biol 114:337–367. https://doi.org/10.1016/B978-0-12-407761-4.00014-2
61. Melentijevic I, Toth ML, Arnold ML, Guasp RJ, Harinath G, Nguyen KC, Taub D, Parker JA, Neri C, Gabel CV, Hall DH, Driscoll M (2017) C. elegans neurons jettison protein aggregates and mitochondria under neurotoxic stress. Nature 542(7641):367–371. https://doi.org/10.1038/nature21362
62. Neumann S, Chassefeyre R, Campbell GE, Encalada SE (2017) KymoAnalyzer: a software tool for the quantitative analysis of intracellular transport in neurons. Traffic 18(1):71–88
63. Harterink M, Edwards SL, de Haan B, Yau KW, van den Heuvel S, Kapitein LC, Miller KG, Hoogenraad CC (2018) Local microtubule organization promotes cargo transport in *C. elegans* dendrites. J Cell Sci 131(20):jcs223107. https://doi.org/10.1242/jcs.223107
64. Ghosh-Roy A, Goncharov A, Jin Y, Chisholm Andrew D (2012) Kinesin-13 and tubulin posttranslational modifications regulate microtubule growth in axon regeneration. Dev Cell 23(4):716–728. https://doi.org/10.1016/j.devcel.2012.08.010
65. Miller KG, Alfonso A, Nguyen M, Crowell JA, Johnson CD, Rand JB (1996) A genetic selection for Caenorhabditis elegans synaptic transmission mutants. Proc Natl Acad Sci U S A 93(22):12593–12598. https://doi.org/10.1073/pnas.93.22.12593
66. Edwards SL, Charlie NK, Milfort MC, Brown BS, Gravlin CN, Knecht JE, Miller KG (2008) A novel molecular solution for ultraviolet light detection in Caenorhabditis elegans. PLoS Biol 6(8):e198
67. Gong J, Yuan Y, Ward A, Kang L, Zhang B, Wu Z, Peng J, Feng Z, Liu J, Xu XZS (2016) The C. elegans taste receptor homolog LITE-1 is a photoreceptor. Cell 167(5):1252–1263.e10
68. Ganguly A, Tang Y, Wang L, Ladt K, Loi J, Dargent B, Leterrier C, Roy S (2015) A dynamic formin-dependent deep F-actin network in axons. J Cell Biol 210(3):401–417. https://doi.org/10.1083/jcb.201506110

Part VIII

In vitro Reconstitution Assays

Chapter 28

In Vitro Reconstitution of Molecular Motor-Driven Mitochondrial Transport

Verena Puttrich, Jakub Rohlena, Marcus Braun, and Zdenek Lansky

Abstract

Intracellular trafficking of organelles driven by molecular motors underlies essential cellular processes. Mitochondria, the powerhouses of the cell, are one of the major cargoes of molecular motors. Efficient distribution of mitochondria ensures cellular fitness while defects in this process contribute to severe pathologies, such as neurodegenerative diseases. Reconstitution of the mitochondrial microtubule-based transport in vitro in a bottom-up approach provides a powerful tool to investigate the mitochondrial trafficking machinery in a controlled environment in the absence of complex intracellular interactions. In this chapter, we describe the procedures for achieving such reconstitution of mitochondrial transport.

Key words Molecular motors, Adaptor proteins, Kinesin-1, TRAK, Mitochondria, Motility assay, TIRF microscopy, Interference reflection microscopy

1 Introduction

In eukaryotic cells, intracellular directed long-range trafficking of cargoes and organelles along the cytoskeletal scaffold is essential for cellular survival. Microtubules, one of the major constituents of the cytoskeleton, are used by molecular motors, such as kinesin-1 or cytoplasmic dynein, to actively transport cargoes like mitochondria to distal regions of the cell [1]. Microtubule-based transport of mitochondria is of particular importance in highly elongated neurons, where it enables fast and efficient distribution of the organelles. Dysfunction of mitochondrial distribution is related to neurodegenerative diseases, including Alzheimer's disease, Huntington's disease, or amyotrophic lateral sclerosis [2–4]. Active trafficking of mitochondria between cells through tunnelling nanotubes [5–7] is further relevant in tumor initiation and progression [6, 8, 9].

Mitochondria are transported in bursts of motion, covering distances of tens of micrometers [10]. By hydrolyzing ATP, the

Alessio Vagnoni (ed.), *Axonal Transport: Methods and Protocols*,
Methods in Molecular Biology, vol. 2431, https://doi.org/10.1007/978-1-0716-1990-2_28,
© The Author(s), under exclusive license to Springer Science+Business Media, LLC, part of Springer Nature 2022

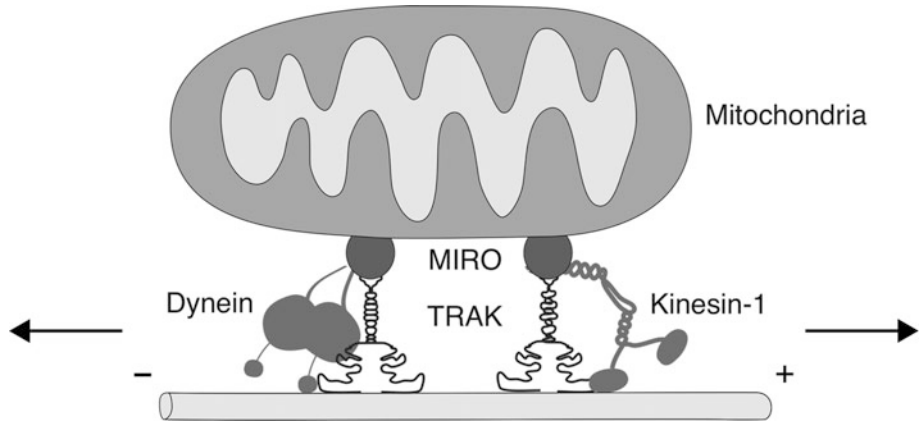

Fig. 1 Schematic representation of the mitochondrial transport machinery. The molecular motors kinesin-1 and dynein are bound to mitochondria through the adaptor proteins Miro and TRAK to drive directed long-range motion of mitochondria along microtubules

molecular motors kinesin-1 or dynein step toward the plus- or minus-ends of microtubules, respectively, to drive anterograde or retrograde mitochondrial transport [11–13]. Binding of mitochondria to molecular motors is mediated by a direct linkage through the adaptor proteins Miro (mitochondrial Rho-like guanosine triphosphate-(GTP)ase) and Milton [14–17] (Fig. 1). In mammals, Miro and Milton both have two isoforms (Miro1 and Miro2 and trafficking kinesin protein TRAK1 and TRAK2, respectively), determining mitochondrial transport characteristics. TRAK1, predominantly localized in the axon [18], is the preferred binding partner of plus end-directed kinesin-1 [18, 19], whereas TRAK2 is more abundant in dendrites and preferentially binds dynein [18], a microtubule minus-end directed molecular motor. The differential interactions of TRAK1 and TRAK2 with the oppositely directed molecular motors kinesin-1 and dynein are recognized as key players in differentially driving axonal and dendritic mitochondrial transport. Depletion of either isoform results in reduced axonal outgrowth and branching of axons and dendrites, respectively [18]. Miro, a transmembrane protein bound to the outer mitochondrial surface, directly links mitochondria to the molecular motor-TRAK complex [16]. Though preferences in molecular motor- or TRAK-binding of the mitochondrial adaptor protein Miro are to date unclear, Miro's direct involvement in mitochondrial transport renders it an important constituent of mitochondrial trafficking [20–22]. Miro1 knockout induces misplaced mitochondria in epithelial cancer cells [23], and mice deficient in Miro1 displays early signs of upper motor neuron disease phenotypes [24], demonstrating the importance of accurate mitochondrial distribution.

In this chapter, we describe the reconstitution of the kinesin-1-TRAK1 complex to drive mitochondrial transport in vitro, a technique that enables investigating the roles of the individual components of the mitochondrial transport complex in the absence of other cellular factors to disentangle the roles of the individual players in mitochondrial transport characteristics.

2 Materials

2.1 Kinesin-1 Expression and Purification

1. SF9 insect cells.
2. 6× His-tagged kinesin-1 KIF5B-plasmid in a FlexiBAC vector system for baculovirus production.
3. Escort IV transfection reagent.
4. SbfI-digested DefBac DNA.
5. ESF 921 insect cell culture medium.
6. PBS: 137 mM NaCl, 2.7 mM KCl, 10 mM Na_2HPO_4, 2 mM KH_2PO_4, pH 7.4.
7. 500 mM Na-phosphate buffer, pH 7.5: dissolve 33.49 g Na_2HPO_4 and 6.59 g NaH_2PO4 in 500 ml nanopure water (*see* **Note 1**).
8. 2 M imidazole, pH 7.5.
9. His-Trap buffer: 50 mM Na-phosphate buffer, pH 7.5, 5% glycerol, 300 mM KCl, 1 mM $MgCl_2$, 0.1% tween-20, 10 mM BME, 0.1 mM ATP.
10. Lysis buffer: 50 mM Na-phosphate buffer, pH 7.5, 5% glycerol, 300 mM KCl, 1 mM $MgCl_2$, 0.1% tween-20, 10 mM BME, 0.1 mM ATP. Before use, dissolve one tablet of Complete® protease inhibitor cocktail (Roche) in 50 ml His-Trap buffer, add 1.25 μl benzonase and 30 mM imidazole.
11. HisPur Ni-NTA Superflow Agarose beads and empty gravity flow column.
12. Wash buffer: 50 mM Na-phosphate buffer, pH 7.5, 5% glycerol, 300 mM KCl, 1 mM $MgCl_2$, 0.1% tween-20, 10 mM BME, 0.1 mM ATP, 60 mM imidazole.
13. Elution buffer: 50 mM Na-phosphate buffer, pH 7.5, 5% glycerol, 300 mM KCl, 1 mM $MgCl_2$, 0.1% tween-20, 10 mM BME, 0.1 mM ATP, 300 mM imidazole.
14. 4 mg/ml 3C PreScission protease.
15. Ultracentrifuge filter of molecular weight cut-off 100 kDa.

2.2 mCherry-TRAK1 Expression and Purification

1. HEK293T cells in suspension (concentration of 4×10^6 cells/ml).
2. TwinStrep-Flag-Halo-tagged mCherry-TRAK1-plasmid.

3. Free Style F17 medium supplemented with 0.1% Pluronic F-68 and 2 mM L-glutamine.
4. 1 mg/ml linear polyethylene imine in PBS.
5. ExCell293 serum-free medium.
6. Lysis buffer: 100 mM Tris–HCl, 10 mM NaCl, 5 mM KCl, 2 mM $MgCl_2$, 10% glycerol, pH 8.0. Before use, dissolve one tablet of Complete® protease inhibitor cocktail (Roche) in 35 ml lysis buffer and add 3 µl benzonase.
7. For assisted cell lysis: 10% Igepal-630, 4 M NaCl.
8. StrepTactin XT beads.
9. Wash buffer: 100 mM Tris–HCl, 150 mM NaCl, 1 mM EDTA, pH 8.
10. 1 mg/ml TEV protease.
11. Superose 6 10/300 GL column.
12. Mobile phase: 100 mM Tris–HCl pH 8.0, 150 mM NaCl, 2 mM $MgCl_2$, 1 mM EDTA, 0.1% tween, 10% glycerol, 1 mM DTT, 0.1 mM ATP.
13. Ultracentrifuge filter of molecular weight cut-off 100 kDa.

2.3 Isolation and MitoTracker-Labeling of Mitochondria

1. For mitochondrial isolation from cultured cells: two to three 150 mm culture dishes with 80% confluent culture of a cell line of your choice. For mitochondrial isolation from mouse liver, at least 1–2 mm diameter piece of fresh mouse liver.
2. Cell lifters and PBS.
3. Mitochondrial isolation buffer: 250 mM sucrose, 10 mM Tris, 1 mM EDTA, pH 7.6 (for cells) or 20 mM HEPES-KOH, 220 mM manitol, 70 mM sucrose, 1 mM EDTA, pH 7.4 (for mouse liver).
4. Balch-style homogenizer (for cells) or dounce tissue grinder and pestle (for mouse liver).
5. Bicinchoninin acid (BCA) assay.
6. MitoTracker Green.

2.4 Sample Preparation

1. DDS-coated coverslips (according to [25]) of 22 × 22 mm^2 and 18 × 18 mm^2 size.
2. BRB80: 80 mM PIPES, 1 mM $MgCl_2$, 1 mM EGTA, pH 6.9.
3. Microtubule polymerization: 4 mg/ml tubulin, 100 mM $MgCl_2$, 10 mM GMPCPP.
4. 1 mg/ml anti-β-tubulin antibody in PBS, store at −20 °C.
5. 10 mg/ml pluronic F-127 in BRB80: Weigh 100 mg pluronic F-127, dissolve it in 10 ml BRB80, and stir for approximately

2 h at room temperature before filtering through a 0.22-μm filter. Store at 4 °C.

6. BRB80T: 80 mM PIPES, 1 mM $MgCl_2$, 1 mM EGTA, pH 6.9, 10 μM taxol.
7. Motility buffer (*see* **Note 2**): 80 mM PIPES, 1 mM $MgCl_2$, 1 mM EGTA, pH 6.9, 10 μM taxol, 10 mM DTT, 20 mM D-glucose, 0.1% tween-20, 0.5 mg/ml casein, 1 mM Mg-ATP. Keep the solution on ice (*see* **Note 3**).
8. Oxygen scavenger buffer: mix 1 μl of 22.4 mg/ml glucose oxidase and 1 μl of 2 mg/ml catalase with 98 μl motility buffer right before imaging. Keep the solution on ice and use within 1 h.

2.5 Microscopy and Image Acquisition

1. For visualizing the kinesin-1-mCherry-TRAK1 transport complex: Inverted widefield fluorescence microscope with a total internal reflection fluorescence (TIRF) mode, equipped with a 60× or 100× oil immersion TIRF objective, a TRITC filter set, and a sensitive camera capable of single molecule detection, such as an EMCCD or sCMOS camera.
2. For visualizing mitochondria, the microscope should be equipped with an interference reflection microscopy unit [26]. Alternatively, the fluorescence signal of MitoTracker Green-labeled mitochondria can be used for the visualization of mitochondria.
3. Imaging software.

3 Methods

3.1 Kinesin-1 Expression and Purification

1. Transfect SF9 cells with 6× His-tagged kinesin-1 KIF5B-plasmid (*see* **Note 4**) using Escort IV transfection reagent and SbfI-digested DefBac DNA viral backbone to create a P1 virus stock.
2. Amplify virus from P1 virus stock to obtain P2 virus stock to then infect 500 ml SF9 insect cells (concentration of 1×10^6 cells/ml) with 5 ml P2 virus stock.
3. Incubate infected insect cells on a shaker at 180 rpm at 27 °C for 3 days.
4. Collect cells. Centrifuge at 300 × *g* for 10 min at 4 °C. Dispose supernatant, resuspend pellet in ice-cold lysis buffer (*see* **Note 5**).
5. Disrupt cells. Add 30 ml ice-cold lysis buffer to the cell pellet from 700 ml culture, slowly pipette to homogenize the solution and centrifuge the cell lysate at 45,000 × *g* for 60 min at 4 °C.

6. Equilibrate Ni-NTA agarose beads (*see* **Note 6**). Place 2 ml of 50% suspension of Ni-NTA agarose beads into a gravity flow column for 1 ml column volumes (CV). Wash the column with 5 CV ultrapure water, then equilibrate with 10 CV lysis buffer.
7. Purify by affinity chromatography. Add clarified cell lysate to the equilibrated Ni-NTA agarose column and incubate 2 h at 4 °C on a rotator. Afterwards, wash the column with 10 CV wash buffer and elute kinesin-1 with 15 CV elution buffer. Collect elution fractions of 1 ml and keep them on ice.
8. Cleavage of 6× His-tag. Pool the elution fractions that contain kinesin-1 (*see* **Note 7**) and dilute them 1:10 in 1× HisTrap buffer (*see* **Note 8**). Add 50 µl of 4 mg/ml 3C PreScission protease and incubate over night at 4 °C on a rotator. The next day, reload the cleaved kinesin-1 on a fresh equilibrated Ni-NTA agarose column of 1 ml CV, collect the flow through which contains the 6× His-tag-cleaved kinesin-1 and concentrate kinesin-1 using an ultracentrifuge filter of molecular weight cut-off 100 kDa. Aliquot to 5 µl, snap freeze in liquid nitrogen and store at −80 °C.

3.2 TRAK1 Expression and Purification

1. Transfect HEK293T cells with TwinStrep-Flag-Halo-tagged mCherry-TRAK1. Prepare two bottles of 350 ml HEK293T cells in suspension (concentration of 4×10^6 cells/ml) grown under a humidified 5% CO_2 atmosphere at 37 °C. Transfect the cells each with 17.5 ml of 700 µg DNA diluted in PBS. Add 2.1 ml of 1 mg/ml linear polyethylene imine to each DNA dilution and incubate for 10 min at room temperature. Add the mixtures to 350 ml HEK293T cells each, incubate 4 h on a shaker, add 350 ml ExCell293 medium to each, and incubate 4 days on a shaker in a humidified CO_2 atmosphere at 37 °C.
2. Collect cells. Centrifuge cells at 500 × *g* for 5 min at 4 °C. Dispose supernatant, resuspend pellet in 35 ml ice-cold lysis buffer.
3. Disrupt cells. Sonicate on ice for 5 min with 20 s pulses and 40 s pauses at 24 W/min. Add IGEPAL-630 to a final concentration of 0.2% and incubate 20 min on ice with occasional mixing. Next, add NaCl to a final concentration of 150 mM and further incubate on ice for 20 min. Centrifuge the cell lysate at 9000 × *g* for 15 min at 4 °C followed by 30,000 × *g* for 30 min at 4 °C to remove insoluble material.
4. Equilibrate StrepTactin XT beads. Place 4 ml of 50% suspension of StrepTactin XT beads into a gravity flow column (CV = 2 ml). Wash the column with 5 CV ultrapure water, then equilibrate with 5 CV lysis buffer.

5. Purify by affinity chromatography. Add clarified cell lysate to the equilibrated StrepTactin XT column and collect the flow through. Wash the column with 10 CV wash buffer.
6. Cleavage of StrepTactin-tag. Add 5 CV wash buffer containing 25 μl TEV protease (1 mg/ml) to the mCherry-TRAK1-bound StrepTactin XT column and incubate overnight at 4 °C on a rotator. The next day, collect the flow through and concentrate mCherry-TRAK1 using an ultracentrifuge filter of molecular weight cut-off 100 kDa to 500 μl for further purification steps. Keep the solutions at 4 °C throughout the procedure.
7. Purify by size exclusion chromatography. Load the cleaved and concentrated mCherry-TRAK1 sample onto a Superose 6 10/300 GL column using an aqueous mobile phase. After size exclusion chromatography, concentrate fractions containing pure mCherry-TRAK1 using an ultracentrifuge filter of molecular weight cut-off 100 kDa. Aliquot samples to 5 μl, snap freeze in liquid nitrogen and store at −80 °C.

3.3 Isolation of Mitochondria and Labeling with MitoTracker Green

3.3.1 Isolation of Mitochondria from Cultured Cells

1. Assemble the Balch-style homogenizer and place it on ice (*see* **Note 9**). Attach disposable 1 ml luer lock syringes (can be reused) and wash the homogenizer with three strokes of cold mitochondria isolation buffer (for cells) using two attached syringes. Leave the homogenizer on ice for at least 10 min to allow thorough cooling.
2. Remove culture medium and wash dishes with PBS 20 ml PBS.
3. Collect cells using cell lifter into 10 ml PBS and transfer into a 50-ml tube. Wash plates with 10 ml of PBS and combine with the cell suspension. Centrifuge for 5 min at 300 × *g* at 4 °C and discard PBS.
4. Suspend the cell pellet (ideally 30–50 × 10^6 cells) in 5 ml ice-cold isolation buffer (for cells). The optimal amount is 30–50 × 10^6 cells per 5 ml of isolation buffer.
5. Aspirate the cell suspension into one of the 1 ml disposable luer lock syringes and homogenize by passing it thrice through the homogenizer between the two syringes (there, back and there again, 2 s per stroke). After three passes, eject the homogenate into a 15-ml falcon tube on ice and aspirate another 1 ml of cell suspension.
6. Repeat **step 5** till you homogenize the whole-cell suspension in 1 ml steps and collect the homogenate in the 15-ml tube. At the end, wash the homogenizer by thrice passing 1 ml of the mitochondrial isolation buffer and add it to the 15-ml tube. Continue from **step 1** (Subheading 3.3.3).

3.3.2 Isolation of Mitochondria from Mouse Liver

1. Place the dounce tissue grinder on ice.
2. Sacrifice a mouse and collect the liver. Wash the liver in ice-cold PBS. Dissect a small piece (1–2 mm in diameter) and mince it using pointy small scissors in approximately 200 µl of ice-cold mitochondrial isolation buffer (for liver) in a 1.5-ml Eppendorf tube. Transfer the liver pieces with the buffer into the cold dounce tissue grinder using a 1000 µl cutoff pipet tip (*see* **Note 10**). Top up the grinder to 5 ml with ice-cold mitochondria isolation buffer (for liver).
3. Homogenize the liver pieces with 60 strokes of the pestle on ice (*see* **Note 11**). Transfer the homogenate into a 15-ml falcon tube on ice. Continue with **step 1** (Subheading 3.3.3).

3.3.3 Further Isolation Steps for Both Cell and Liver Mitochondria

1. Centrifuge at 800 × *g* for 5 min at 4 °C. Transfer the supernatant into a new 15-ml tube on ice. Discard the pellet, which contains non-homogenized cells, debris and nuclei.
2. Centrifuge at 3000 × *g* for 5 min at 4 °C. Transfer the supernatant into a new 15-ml tube on ice (*see* **Note 12**).
3. Centrifuge at 10,000 × *g* for 15 min to collect the mitochondrial pellet. Discard the supernatant.
4. Wash the mitochondrial pellet thrice in mitochondrial isolation buffer (for cells).
5. Resuspend the washed mitochondrial pellet in a small amount (the same volume as the pellet itself) of mitochondrial isolation buffer (for cells). Store on ice.
6. Measure the protein concentration of the mitochondrial preparation using the BCA assay.
7. Stain the mitochondria with 50 nM MitoTracker Green in mitochondrial isolation buffer (for cells) for 20 min on ice. Wash twice with the same buffer and resuspend in the minimal amount of the same buffer as above. When stored on ice, the labeled mitochondria are stable for at least 4 h.

3.4 Sample Preparation

1. Polymerize and double-stabilize microtubules. Dilute 4 mg/ml tubulin to a final concentration of 2 µM in BRB80 and add $MgCl_2$ and GMPCPP to a final concentration of 1 mM. Incubate the mixture 5 min on ice, followed by 2 h at 37 °C. After polymerization, centrifuge the microtubules for 30 min at 18,000 × *g* at room temperature and resuspend the microtubule pellet carefully in 120 µl BRB80T. Double-stabilized microtubules can be stored at room temperature for 2 weeks.
2. Assemble the flow channels. Cut five slices of parafilm of ~23 × 2 mm^2 size and place them parallel with ~2 mm distance on a 22 × 22 mm^2 DDS-coated cover glass. Place a

18×18 mm^2 DDS-coated cover glass on top and melt the parafilm homogeneously on a heating plate at 60 °C.

3. Functionalize the flow channels. Draw PBS into the flow channels by applying a droplet of PBS on one end of the flow channel and vacuum at the other end. Dilute anti-β-tubulin antibodies in PBS to 20 μg/ml, introduce them into the flow channel in the same manner and incubate for 10 min. Block the surface by introducing in 10 mg/ml pluronic F-127 and incubate for at least 1 h (*see* **Note 13**).

3.5 Reconstitution and Imaging of Mitochondrial Transport

1. Immobilize microtubules in the flow channels. Exchange the flow channel's solution by washing with 40 μl BRB80T. Pipet a droplet of BRB80T on one side of the flow channel and suck the solution through by holding a piece of filter paper on the other side. Using the same technique, introduce 8 μl of double-stabilized microtubules into the flow channel, incubate for 1–2 min. Remove unbound microtubules by washing the flow channel with 20 μl BRB80T. Flush the flow channel with 20 μl oxygen scavenger buffer to create a suitable environment for the mitochondrial transport complex.
2. Assemble the mitochondrial transport complex. Dilute kinesin-1 to 160 nM in motility buffer and mix 1 μl diluted kinesin-1 with 1 μl of 40 nM TRAK1 and 1 μl of 1 μg/μl mitochondria, incubate for 10 min on ice (*see* **Note 14**). Add 17 μl oxygen scavenger buffer to the mitochondrial transport complex and introduce the mixture into the flow channel.
3. Visualize mitochondrial transport. Use interference reflection microscopy to visualize long-range directed transport and microtubule interactions of mitochondria at frame rates of 1 s. Mitochondria appear as round objects. To confirm that the round objects are indeed mitochondria, change to the fluorescence mode using laser excitation at 488 nm. Round objects in interference reflection microscopy overlaying with a fluorescence signal excited at 488 nm represent MitoTracker green-labeled mitochondria (Fig. 2a, b).
4. Visualize individual kinesin-1-mCherry-TRAK1 transport complexes. Use laser excitation at 561 nm and total internal fluorescence microscopy to visualize kinesin-1-mCherry-TRAK1 transport complexes (*see* **Note 15** and Fig. 2c).

3.6 Data Analysis

Motility parameters of directed transported mitochondria are analyzed from movies obtained by interference reflection microscopy using the image processing software Fiji [27]. Create kymographs along microtubules where directed transport of mitochondria was observed (Fig. 3a) in order to determine motility parameters, such as:

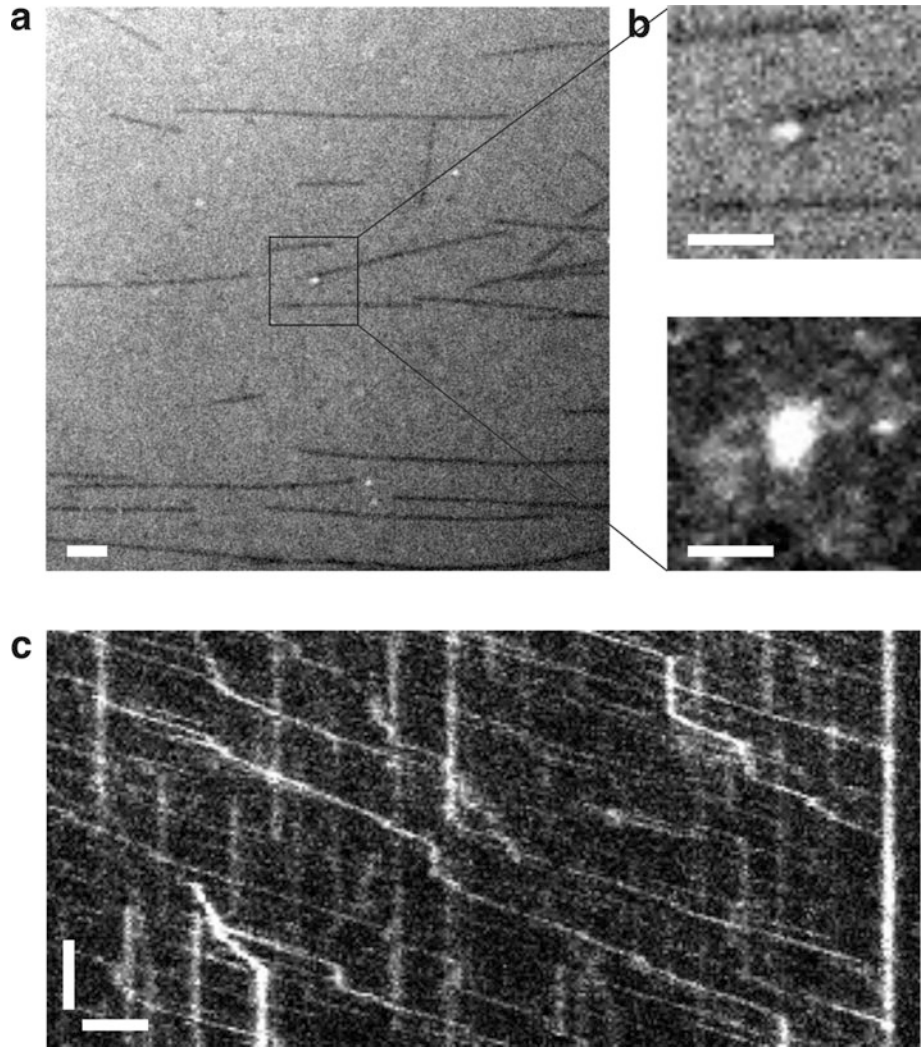

Fig. 2 Microscopy of reconstituted mitochondrial transport. (**a**) Interference reflection microscopy image showing microtubules (black) and a microtubule-bound mitochondria (white) in the middle of the field of view. Scale bar 2 μm. (**b**) Magnified image of the highlighted area in (**a**), imaged in interference reflection microscopy (top) and the respective image in fluorescence microscopy upon excitation with a laser at 488 nm (bottom). Scale bar 2 μm. (**c**) Representative kymograph showing long-range directed motion of the kinesin-1-mCherry-TRAK1 transport complexes imaged upon excitation with a laser at 561 nm for visualization of mCherry-TRAK1. Horizontal scale bar 2 μm, vertical 10 s

1. Run length. Determine the coordinates of the beginning and end of the microtubule interaction of mitochondria subjected to long-range directed transport. If a mitochondrion is either transported to the end of a microtubule or enters or leaves the field of view or if the microtubule-interaction exceeds the time of imaging, mark the event as censored. Plot the survival

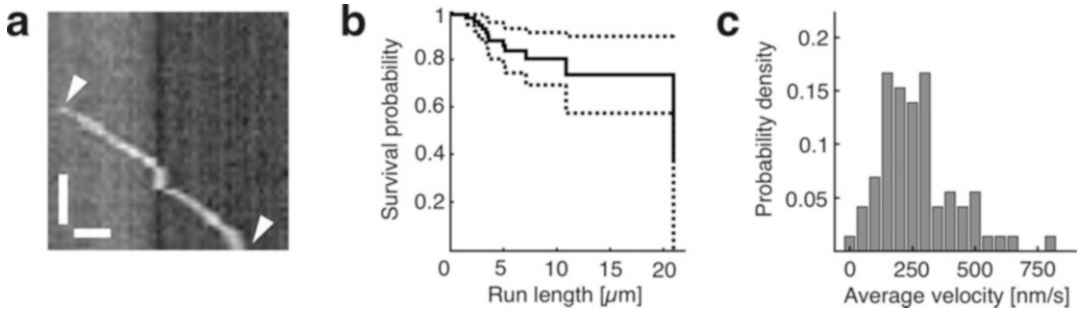

Fig. 3 Data analysis of mitochondrial transport. (**a**) Representative kymograph showing long-range directed motion of a transported mitochondrion, imaged in interference reflection microscopy. The white arrows indicate the beginning and end of the measurable microtubule interaction. As the microtubule interaction of the mitochondrion exceeds the duration of imaging, this event is denoted as censored. Horizontal scale bar 1 μm, vertical 25 s. (**b**) Survival probability of the run length of long-range directedly transported mitochondria represented by a Kaplan–Meier estimation. (**c**) Histogram of the average velocity of long-range directed transport of mitochondria

probability of the run length using a Kaplan–Meier estimation [28] (Fig. 3b).

2. Average velocity. Determine the coordinates of the beginning of the microtubule interaction of the mitochondria and the end of the directed movement and the time spent in this motion. Plot the probability density distribution of the average velocity as a histogram (Fig. 3c).
3. Landing rate. Measure the length of all microtubules present in the respective field of view, determine the overall time of the movie, and count the number of mitochondria interacting with microtubules. The landing rate is determined as the number of mitochondria–microtubule interaction events per unit length of the microtubule and unit of time.

4 Notes

1. The solubility of the reagents can be increased by slightly increasing the solutions' temperature to about 40 °C.
2. Aliquots of 10 μl of all reagents can be prepared ready-to-use at the required concentrations and stored at −20 °C.
3. For improved fluorescence imaging, it is of advantage to degas the motility buffer for 30 min on ice prior to imaging.
4. Full-length human kinesin-1 KIF5B or constitutively active KIF5B (amino acids 1–905) can be used.
5. For storage and later purification, resuspend the cell pellet in 5 ml PBS and store at −80 °C.

6. The column can be prepared during centrifugation of the cell lysate. It is important that the beads never run dry throughout the whole procedure.
7. Elution fractions containing the protein can be determined by running a sodium dodecyl sulfate (SDS) polyacrylamide gel.
8. This step is crucial and performed to reduce the concentration of imidazole in the buffer. The presence of high concentrations of imidazole would prevent protein binding to the column in the next step.
9. Any method of mitochondrial isolation that yields coupled mitochondria can be used, but we find Isobiotec Balch-style homogenizer superior to other methods when isolating mitochondria from cultured cells. The isolation of mitochondria from mouse liver gives better yields, but requires access to animals. We found that mouse mitochondria can be used with human TRAK and kinesin-1 without any problems.
10. Cutting-off the pipet tip improves the handling of the liver pieces.
11. Make sure to reach the very bottom of the grinder with each stroke.
12. This step reduces the yield but increases the purity as the discarded pellet contains smaller debris, peroxisome, and some mitochondria.
13. It is important to never introduce air into the flow channels but to keep them constantly immersed in solution. It is thus advisable to place a droplet of pluronic F-127 solution at both ends of the flow channel to prevent the flow channels from drying due to evaporation of the solution.
14. Analogously, the transport complex can be assembled using TRAK2 instead of TRAK1. For reconstituting minus-end-directed mitochondrial transport, the molecular motor dynein-dynactin complex can be used instead of kinesin-1.
15. Though kinesin-1 is unlabeled, directed movement of mCherry-TRAK1 confirms the presence of active mitochondrial kinesin-1-mCherry-TRAK1 transport complexes as TRAK1 is known to only diffuse along microtubules while not being able to undergo directed motion [29] in the absence of kinesin-1.

References

1. Tanaka Y, Kanai Y, Okada Y et al (1998) Targeted disruption of mouse conventional kinesin heavy chain kif5B, results in abnormal perinuclear clustering of mitochondria. Cell 93:1147–1158. https://doi.org/10.1016/S0092-8674(00)81459-2
2. Chang DTW, Reynolds IJ (2006) Mitochondrial trafficking and morphology in healthy and injured neurons. Prog Neurobiol 80:241–268.

https://doi.org/10.1016/j.pneurobio.2006.09.003

3. Correia SC, Perry G, Moreira PI (2016) Mitochondrial traffic jams in Alzheimer's disease—pinpointing the roadblocks. Biochim Biophys Acta Mol basis Dis 1862:1909–1917. https://doi.org/10.1016/j.bbadis.2016.07.010
4. Hsieh C-H, Shaltouki A, Gonzalez AE et al (2016) Functional impairment in Miro degradation and Mitophagy is a shared feature in familial and sporadic Parkinson's disease. Cell Stem Cell 19:709–724. https://doi.org/10.1016/j.stem.2016.08.002
5. Ahmad T, Mukherjee S, Pattnaik B et al (2014) Miro1 regulates intercellular mitochondrial transport & enhances mesenchymal stem cell rescue efficacy. EMBO J 33:994–1010. https://doi.org/10.1002/embj.201386030
6. Dong L-F, Kovarova J, Bajzikova M et al (2017) Horizontal transfer of whole mitochondria restores tumorigenic potential in mitochondrial DNA-deficient cancer cells. Elife 6:e22187. https://doi.org/10.7554/eLife.22187
7. Rustom A, Saffrich R, Markovic I et al (2004) Nanotubular highways for intercellular organelle transport. Science 303:1007–1010. https://doi.org/10.1126/science.1093133
8. Bajzikova M, Kovarova J, Coelho AR et al (2019) Reactivation of dihydroorotate dehydrogenase-driven pyrimidine biosynthesis restores tumor growth of respiration-deficient cancer cells. Cell Metab 29:399–416.e10. https://doi.org/10.1016/j.cmet.2018.10.014
9. Tan AS, Baty JW, Dong L-F et al (2015) Mitochondrial genome acquisition restores respiratory function and tumorigenic potential of cancer cells without mitochondrial DNA. Cell Metab 21:81–94. https://doi.org/10.1016/j.cmet.2014.12.003
10. Wang X, Schwarz TL (2009) The mechanism of Ca^{2+}-dependent regulation of kinesin-mediated mitochondrial motility. Cell 136:163–174. https://doi.org/10.1016/j.cell.2008.11.046
11. Brady ST (1985) A novel brain ATPase with properties expected for the fast axonal transport motor. Nature 317:73–75. https://doi.org/10.1038/317073a0
12. Vale RD, Reese TS, Sheetz MP (1985) Identification of a novel force-generating protein, kinesin, involved in microtubule-based motility. Cell 42:39–50. https://doi.org/10.1016/s0092-8674(85)80099-4
13. Vale RD, Schnapp BJ, Mitchison T et al (1985) Different axoplasmic proteins generate movement in opposite directions along microtubules in vitro. Cell 43:623–632. https://doi.org/10.1016/0092-8674(85)90234-X
14. Stowers RS, Megeath LJ, Górska-Andrzejak J et al (2002) Axonal transport of mitochondria to synapses depends on Milton, a novel drosophila protein. Neuron 36:1063–1077. https://doi.org/10.1016/S0896-6273(02)01094-2
15. Brickley K, Smith MJ, Beck M, Stephenson FA (2005) GRIF-1 and OIP106, members of a novel gene family of coiled-coil domain proteins: association in vivo and in vitro with kinesin. J Biol Chem 280:14723–14732. https://doi.org/10.1074/jbc.M409095200
16. Fransson Å, Ruusala A, Aspenström P (2006) The atypical Rho GTPases Miro-1 and Miro-2 have essential roles in mitochondrial trafficking. Biochem Biophys Res Commun 344:500–510. https://doi.org/10.1016/j.bbrc.2006.03.163
17. Glater EE, Megeath LJ, Stowers RS, Schwarz TL (2006) Axonal transport of mitochondria requires Milton to recruit kinesin heavy chain and is light chain independent. J Cell Biol 173:545–557. https://doi.org/10.1083/jcb.200601067
18. van Spronsen M, Mikhaylova M, Lipka J et al (2013) TRAK/Milton Motor-adaptor proteins steer mitochondrial trafficking to axons and dendrites. Neuron 77:485–502. https://doi.org/10.1016/j.neuron.2012.11.027
19. Brickley K, Stephenson FA (2011) Trafficking kinesin protein (TRAK)-mediated transport of mitochondria in axons of hippocampal neurons. J Biol Chem 286:18079–18092
20. Guo X, Macleod GT, Wellington A et al (2005) The GTPase dMiro is required for axonal transport of mitochondria to drosophila synapses. Neuron 47:379–393. https://doi.org/10.1016/j.neuron.2005.06.027
21. Liu X, Hajnóczky G (2009) Ca2+−dependent regulation of mitochondrial dynamics by the Miro-Milton complex. Int J Biochem Cell Biol 41:1972–1976. https://doi.org/10.1016/j.biocel.2009.05.013
22. MacAskill AF, Rinholm JE, Twelvetrees AE et al (2009) Miro1 is a calcium sensor for glutamate receptor-dependent localization of mitochondria at synapses. Neuron 61:541–555. https://doi.org/10.1016/j.neuron.2009.01.030
23. Desai SP, Bhatia SN, Toner M, Irimia D (2013) Mitochondrial localization and the persistent migration of epithelial cancer cells. Biophys J 104:2077–2088

24. Nguyen TT, Oh SS, Weaver D et al (2014) Loss of Miro1-directed mitochondrial movement results in a novel murine model for neuron disease. Proc Natl Acad Sci 111: E3631–E3640
25. Gell C, Bormuth V, Brouhard GJ et al (2010) Microtubule dynamics reconstituted in vitro and imaged by single-molecule fluorescence microscopy. Methods Cell Biol 95:221–245. https://doi.org/10.1016/S0091-679X(10)95013-9
26. Mahamdeh M, Howard J (2019) Implementation of interference reflection microscopy for label-free, high-speed imaging of microtubules. J Vis Exp:e59520. https://doi.org/10.3791/59520
27. Schindelin J, Arganda-Carreras I, Frise E et al (2012) Fiji: an open-source platform for biological-image analysis. Nat Methods 9: 676–682
28. Ruhnow F, Kloβ L, Diez S (2017) Challenges in estimating the motility parameters of single processive motor proteins. Biophys J 113: 2433–2443
29. Henrichs V, Grycova L, Barinka C et al (2020) Mitochondria-adaptor TRAK1 promotes kinesin-1 driven transport in crowded environments. Nat Commun 11:3123. https://doi.org/10.1038/s41467-020-16972-5

Chapter 29

In Vitro Reconstitution of Kinesin-Based, Axonal mRNA Transport

Julia Grawenhoff, Sebastian Baumann, and Sebastian P. Maurer

Abstract

Motor protein-driven transport of mRNAs on microtubules and their local translation underlie important neuronal functions such as development, growth cone steering, and synaptic plasticity. While there is abundant data on how membrane-bound cargoes such as vesicles, endosomes, or mitochondria are coupled to motor proteins, surprisingly little is known on the direct interactions of RNA–protein complexes and kinesins or dynein. Provided the potential building blocks are identified, in vitro reconstitutions coupled to Total Internal Reflection Microscopy (TIRF-M) are a powerful and highly sensitive tool to understand how single molecules dynamically interact to assemble into functional complexes. Here we describe how we assemble TIRF-M imaging chambers suitable for the imaging of single protein–RNA complexes. We give advice on optimal sample preparation procedures and explain how a minimal axonal mRNA transport complex can be assembled in vitro. As these assays work at picomolar-range concentrations of proteins and RNAs, they allow the investigation of molecules that cannot be obtained at high concentrations, such as many large or disordered proteins. This now opens the possibility to study how RNA-binding proteins (RBPs), RNAs, and microtubule-associated proteins act together in real-time at single-molecule sensitivity to create cytoplasmic mRNA distributions.

Key words Cytoplasmic mRNA localization, Axonal transport, Kinesins, In vitro reconstitution, Single-molecule imaging

1 Introduction

Cells spatially regulate gene expression through the active, microtubule-dependent localization and local translation of mRNAs. This is of fundamental importance for diverse processes requiring the configuration of cellular domains with distinct protein sets [1–3]. Mammalian neurons are a fascinating, well-studied model system demonstrating the importance of mRNA localization. Neurons require localized translation for development [4, 5], axonal growth cone steering [6, 7], synaptic plasticity [8], and

Julia Grawenhoff and Sebastian Baumann contributed equally to this work.

Alessio Vagnoni (ed.), *Axonal Transport: Methods and Protocols*,
Methods in Molecular Biology, vol. 2431, https://doi.org/10.1007/978-1-0716-1990-2_29,
© The Author(s) 2022

long-term memory formation [9]. To generate mRNA distributions, bidirectional microtubule (MT)-motor-based transport machines "read" localization information that is encoded in mRNA 3′UTRs. This is mediated by RBPs that bind these localization signals and potentially control mRNA–motor coupling through largely unknown mechanisms. While discoveries of biological or disease-related processes depending on mRNA transport increase [10, 11], we just begin to understand how kinesins, dynein, and mRNA cargo adaptors assemble to distribute mRNAs in neurons or mammals in general. A thorough mechanistic understanding of this process, however, is key to disentangle and potentially control the molecular causes of neurodegenerative disease and viral infections [12, 13] impairing the nervous system or mammalian cells in general. The current lack of understanding might have several causes. First, mRNA transport complexes were widely studied by co-immunoprecipitation approaches [14–17]. While this produced long lists of factors *potentially involved* in mRNA transport, such methods inform about *physical* but not *direct* interactions. Knowledge of the latter, however, is essential to understand the construction principles of mRNA transport complexes. Additionally, RBPs often contain intrinsically disordered regions [18] which tend to aggregate during isolation procedures [19] and capture non-physiological interactors. Second, loss-of-function studies are often hard to interpret; many RBPs are required for splicing, nuclear export, translation regulation, and mRNA transport while motor proteins transport vesicles, proteins, mRNAs, and organelles. Entire deletion of an RBP or motor affects several processes making an analysis of its specific contribution to mRNA transport difficult. Lastly, while omics approaches created a system-level view of mRNA localization and local translation [20, 21], they cannot reveal the biochemical processes that give rise to the system states they report. Recent advances using in vitro reconstitutions shed light on this aspect, revealing the first yeast [22, 23] and *Drosophila* [24] mRNA transport systems. However, as homologs of involved proteins are yet to be identified in mammals, still little was known about the design principles of mammalian mRNA transport complexes.

Separate publications link the microtubule plus-end-tracking protein APC to mRNA localization while others show that APC is transported by the heterotrimeric kinesin-2 KIF3AB and its cargo adaptor KAP3 (KIF3ABKAP3) in axons. These data prompted us to test whether a minimal, reconstituted APC-KIF3ABKAP3 complex is sufficient for selective transport of axonal mRNAs. To this end, we purified recombinant, SNAP-tagged [25] versions of APC as well as KIF3ABKAP3 and obtained fluorescently labeled 3′UTR fragments of the β-actin and β2B-tubulin mRNAs. TIRF-M live imaging of different combinations of these three factors (kinesin, APC, RNAs) in custom-assembled microscopy chambers (Figs. 1

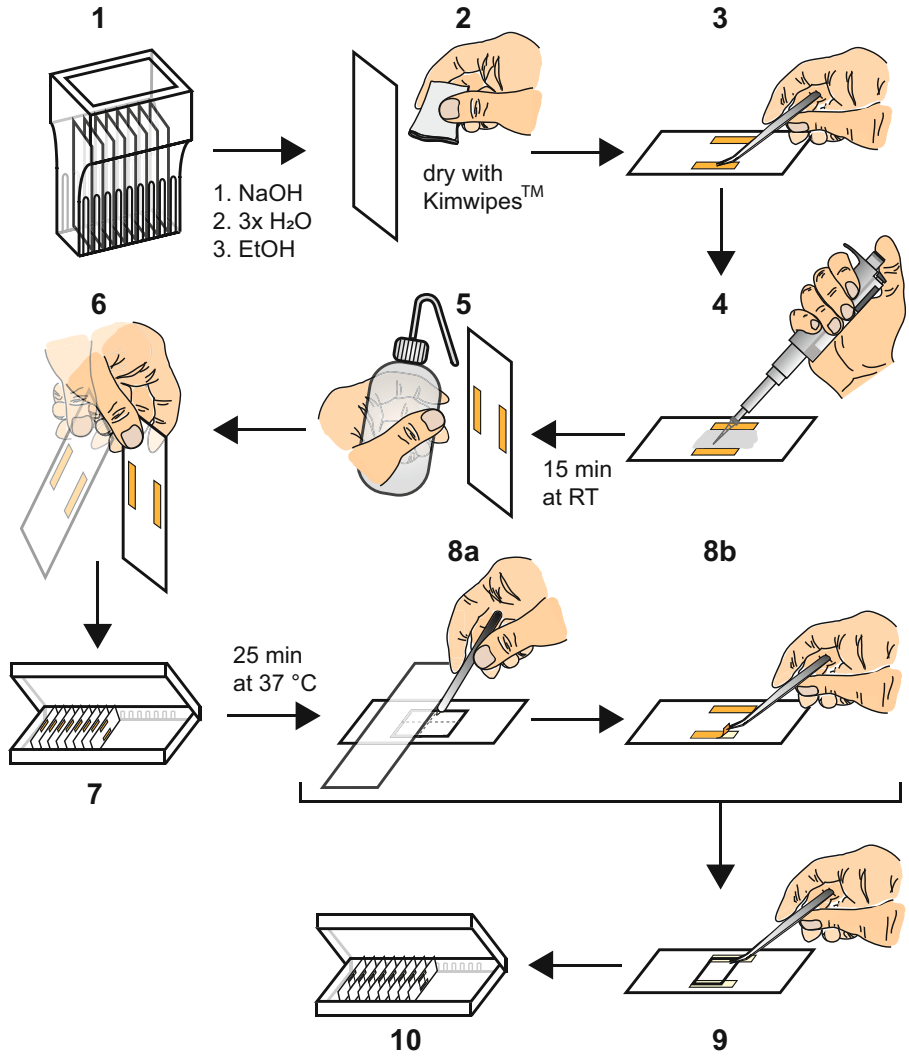

Fig. 1 TIRF-M chamber assembly. Microscopy chambers are prepared as indicated in the individual steps and described in Subheading 3.1. Considering experiment length and that chambers should be freshly made, 1 day of microscopy requires around eight chambers

and 2) allowed us to reveal their dynamic interplay and function (Fig. 3). Using the Fiji plugin Trackmate [26] (Fig. 4), we read out the dynamics (Fig. 5) and the fluorescent intensities of the reconstituted complexes. Subsequent calibration of individual intensities of the used TMR and Alexa647 dyes (Figs. 6 and 7) enables to determine the stoichiometry of reconstituted mRNA transport complexes and subcomplexes. Taken together, this approach demonstrates that the kinesin-2 adaptor KAP3 couples APC-RNA complexes to KIF3AB for processive mRNP transport along microtubules [27]. APC's selectivity of G-rich RNA sequences allows selective transport of both β-actin and β2B-tubulin 3′UTR fragments. While APC was found to be dimeric even at lowest

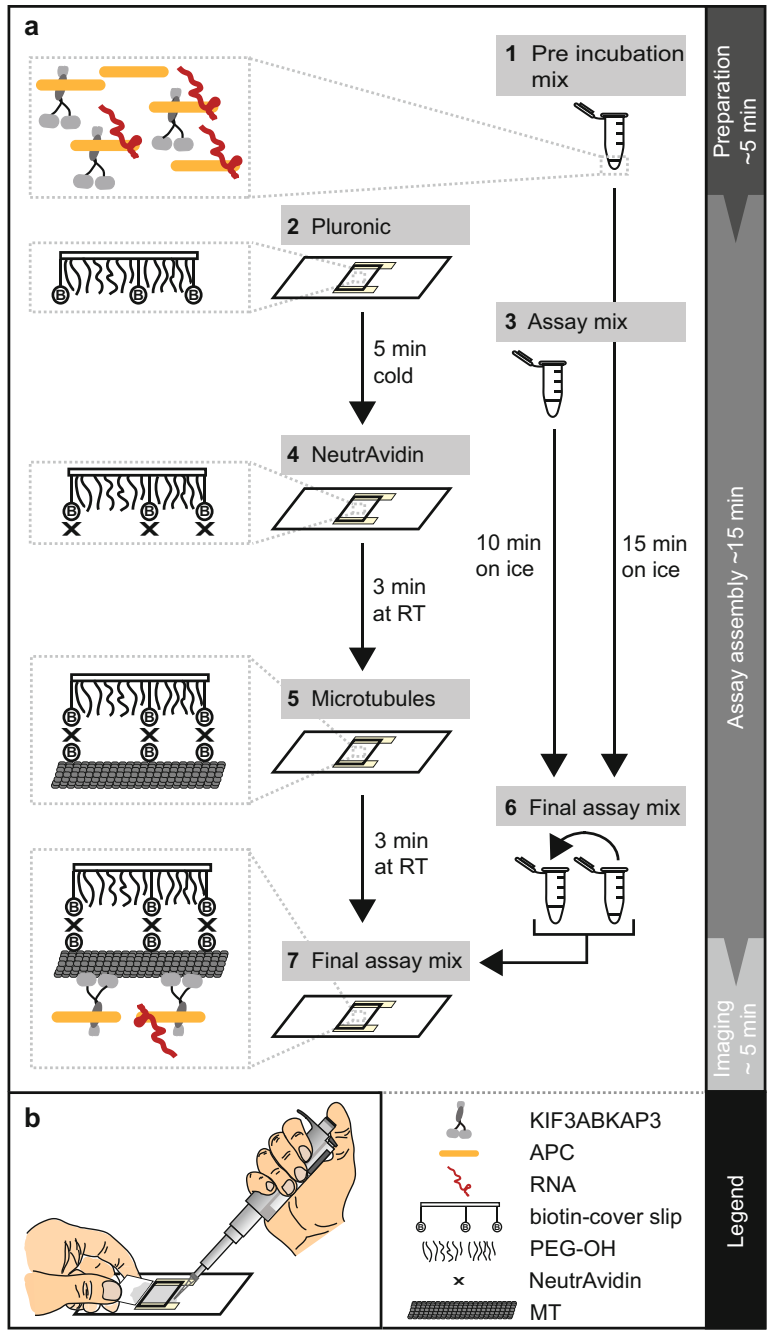

Fig. 2 TIRF-M experiment preparation. (**a**) Schematic representation of the successive steps required for TIRF-M experiment preparation. Steps are performed according to the indicated numbering. The right column (steps 1, 3, and 6) includes steps carried out in tubes on ice. The central column (steps 2, 4, 5, and 7) corresponds to steps in which different solutions are flown through microscopy chambers. Times noted next to arrows correspond to incubation times between individual steps, whereas the gray timeline on the right side corresponds to actual working time including all pipetting steps. The left column visualizes the outcome of every step, from assembly of transport complexes in solution (top) to reconstitution of full transport complexes on microtubules tethered to biotinylated coverslips (bottom). For more information, *see* Subheading 3.3. (**b**) Schematic representation of the handling of microscopy chambers. Individual solutions are pipetted next to microscopy chambers and flown through the latter with the help of small pieces of Whatman™ paper

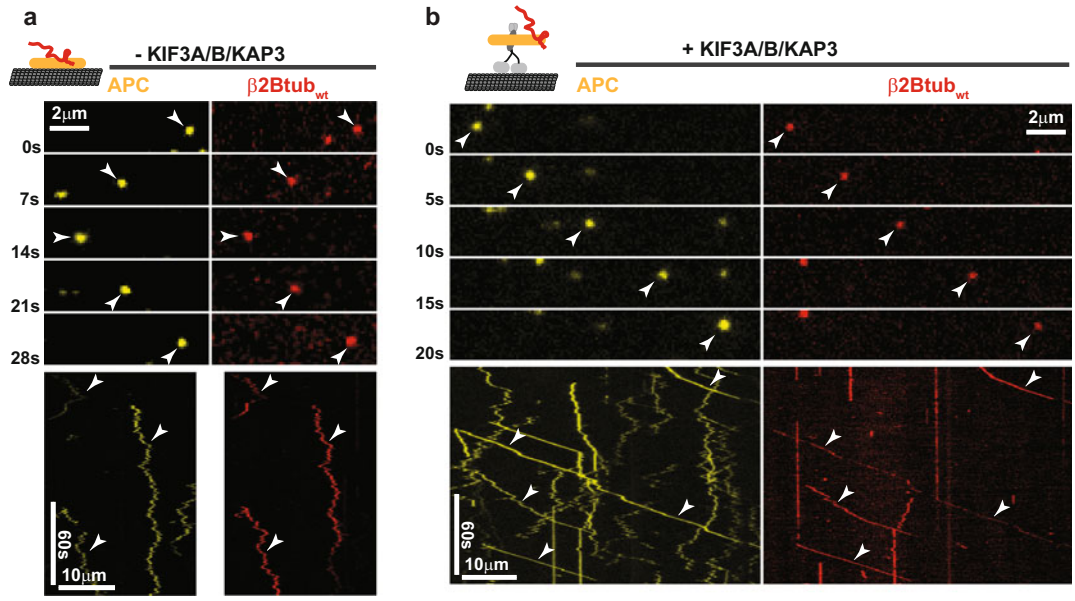

Fig. 3 In vitro reconstitution of axonal mRNA transport. (**a**) Still image series and kymographs of reconstituted APC-TMR (40 pM) and β2Btub-RNA-Alexa647 (2 nM) complexes diffusing on immobilized paclitaxel-stabilized microtubules. (**b**) Still image series and kymographs of reconstituted APC-TMR (80 pM), β2Btub-RNA-Alexa647 (2 nM), and KIF3ABKAP3 (750 pM) complexes showing both diffusive and processive movement on paclitaxel-stabilized microtubules

pM-range concentrations, it can bind one β2B-tubulin RNA per monomer. This stoichiometry and the fact that one kinesin-2 mostly carries one APC dimer lead to the observation that reconstituted mRNA transport complexes mostly carry two RNAs at saturating RNA concentrations. Interestingly, subtle variants of G-rich motifs found in β-actin and β2B-tubulin mRNAs are sufficient to fine-tune the affinity of different RNAs to the transport complex, which leads to a strong preference of β2B-tubulin mRNA transport over β-actin mRNA transport at equal concentrations.

In this chapter, we provide a detailed protocol on the reconstitution of a kinesin-based mRNA transport complex and highlight critical steps and considerations.

2 Materials

2.1 Buffers

1. 2× assay buffer stock (2× AB stock): 180 mM HEPES (Sigma #H3375), 20 mM PIPES (Sigma #P6757), 5 mM $MgCl_2$ (Sigma #M2670), 1.5 mM EGTA (Sigma #03777) in purified water (Sigma #W4502), adjusted with KOH (Sigma #P1767) to pH 6.92–6.95 (*see* **Note 1**).
2. BRB80: 80 mM PIPES, 1 mM $MgCl_2$, 1 mM EGTA, adjust with KOH to pH 6.85 with purified water (Sigma #W4502).

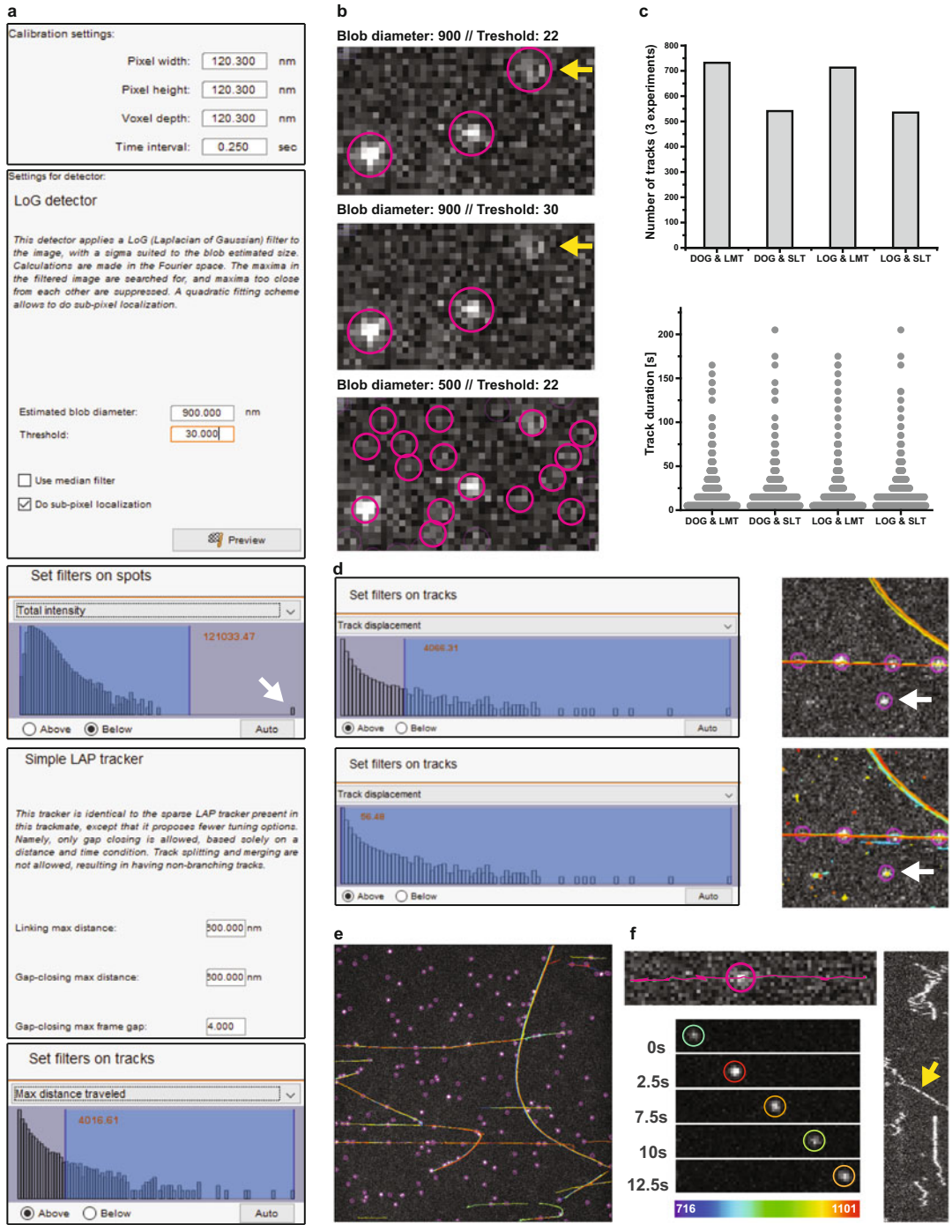

Fig. 4 Automated tracking of mRNA transport complexes. (**a**) Screenshots of Trackmate dialog boxes for important steps. The white arrow indicates an exceptionally bright spot excluded from the analysis by the chosen spot intensity cut-off. (**b**) Examples of points recognized by Trackmate depending on spot diameter and threshold settings. Magenta circles mark recognized spots at this specific time point. The yellow arrow indicates a spot that is recognized at a threshold of 22 but not at a slightly higher threshold of 30. (**c**) Comparison of number of tracks and their duration depending on detector and tracking algorithm chosen. DOG and LOG are different spot detection routines chosen to recognize fluorescent signals (*see* (**a**)). LMT and SLT

3. Filter buffers with 0.2 μm bottle top filter (Merck #S2GPU02RE) and keep in fridge for maximally 3–4 weeks (*see* **Note 2**).

2.2 Microscopy Chambers

1. Object slides (Marienfeld #101200).
2. Double-sided tape (Tesa® #05338).
3. Diamond scriber (MONOCOMP #AGT 5481-A60).
4. Tweezers (Electron Microscopy Science #78322-7(EMS 7)).
5. PLL(20)-g[3.5]-PEG(2) (SuSos AG, Duebendorf, Switzerland) in PBS (2 mg/ml).
6. 1 M NaOH solution.
7. Cover slips functionalized with PEG and Biotin-PEG (Microsurfaces Inc., USA, #Bio_01(2007134-01)).
8. 37 °C incubator.
9. Squeeze bottle with MilliQ water.
10. 100% ethanol (VWR #20821.296).
11. Kimwipes™ (Kimtech Scientific #KIMB7552).

2.3 Microtubule Polymerization

1. 180–230 μM depolymerized tubulin in BRB80 (*see* **Note 3**).
2. 180–230 μM depolymerized and biotinylated tubulin (*see* **Notes 3** and **4**) in BRB80.
3. 180–230 μM depolymerized tubulin labeled with ATTO390 (*see* **Notes 3** and **4**) in BRB80.
4. 100 mM GTP (Sigma #G8877) solution.
5. BRB80 (*see* Subheading 2.1).
6. 37 °C shaker.
7. Paclitaxel (Sigma #T7191).
8. Table centrifuge for 1.5-ml reaction tubes.

Fig. 4 (continued) refer to different tracking algorithms (*see* (**a**)). (**d**) Examples of detected tracks depending on "track displacement" cut-off. (Left) Screenshots of Trackmate with two different cut-offs. (Right) A section of a TIRF-M image with fluorescently labeled β2B-tubulin RNA transported along microtubules with the cut-offs shown in the left panel. Magenta circles mark recognized spots at this specific time point. Colored lines and dots indicate detected tracks over the whole duration of the movie. The white arrows indicate a static event that is only detected with the low track displacement cut-off. Note that in the upper panel the spot is recognized (magenta circle), but only in the lower panel, the track is marked in yellow to indicate a tracked event. (**e**) Whole frame (512 × 512 pixels) of a tracked movie at a specific time point. With the cut-off chosen, only tracks with a displacement above 4 μm are displayed. (**f**) Track example displayed as Trackmate track (upper left panel) and kymograph (right panel, yellow arrow). The lower left panel shows different time points of the respective track, exhibiting different intensities that are indicated by differently colored circles. The heatmap with numbers at the bottom indicates fluorescence arbitrary units

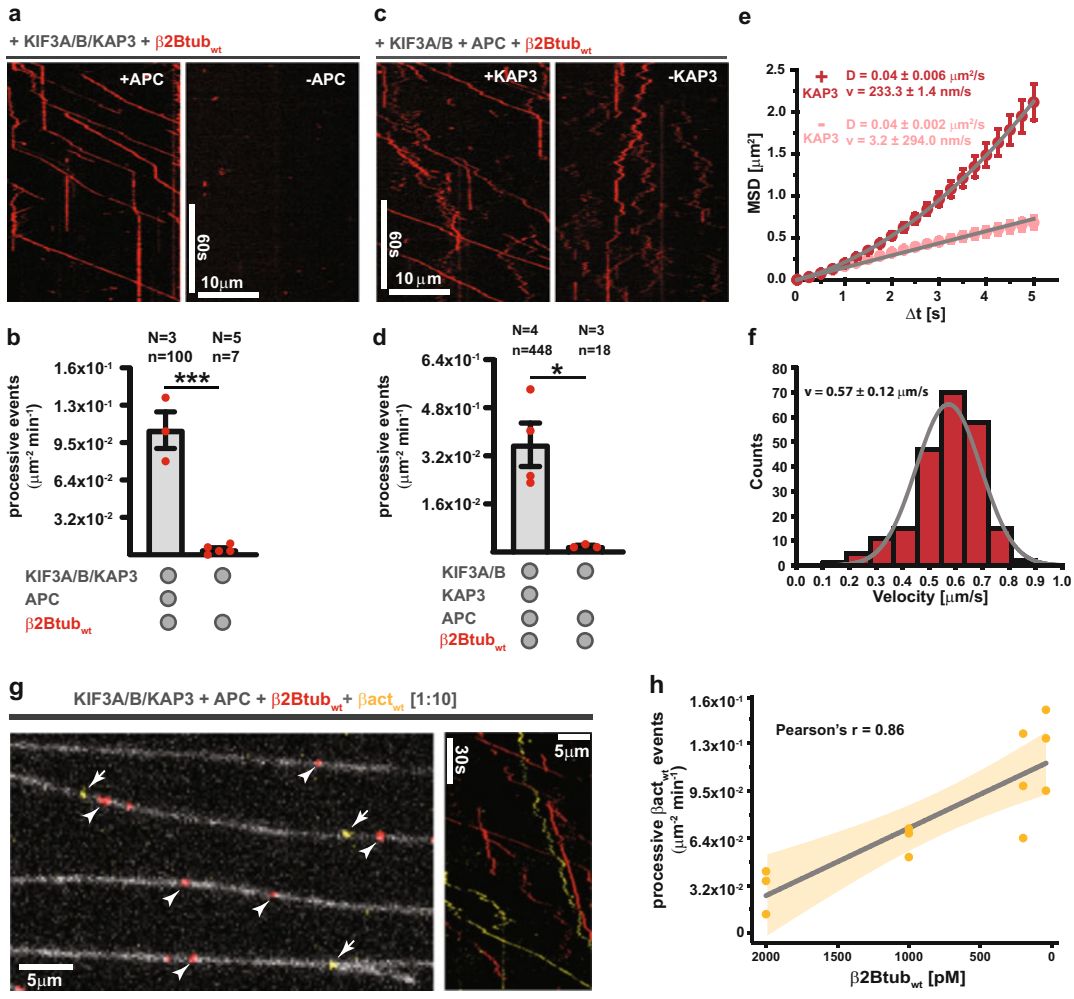

Fig. 5 Analysis of reconstituted mRNA transport complexes. (**a**) The kymographs show Alexa647-β2Btub$_{wt}$—RNA signals from TIRF-M experiments with (left) or without (right) APC. (**b**) Quantification of processive β2Btub$_{wt}$ run events in the presence and absence of APC. N: number of independent experiments, n: total number of events. Error bars: SEM. Statistical significance was evaluated with an unpaired, two-tailed *t*-test. ***$p < 0.001$. (**c**) The kymographs show Alexa647-β2Btub$_{wt}$ signals from TIRF-M experiments containing 750 pM KIF3AB, 150 pM APC, 2 nM Alexa647-β2Btub$_{wt}$, and 500 pM KAP3 (left) or no KAP3 (right). (**d**) Quantification of processive Alexa647-β2Btub$_{wt}$ run events in the presence and absence of KAP3. Error bars: SEM. Statistical significance was evaluated with an unpaired, two-tailed *t*-test. **$p < 0.01$, *$p < 0.05$. N: number of independent experiments, n: total number of events. (**e**) MSD plots of Alexa647-β2Btub$_{wt}$ motility (displacement >1.1 μm to include non-processive events in experiments lacking KAP3) from experiments shown in (**c**). (**f**) Mean instantaneous velocity distribution of processive (displacement >4 μm) Alexa647-β2Btub$_{wt}$ complexes. Gray line: A gauss fit to velocity distribution. (**g**) An overview TIRF-M image (left) and kymograph (right) showing Alexa647-β2Btub$_{wt}$ and TMR-β-actin$_{wt}$-RNA transport in the same experiments at 1:10 molar ratio (200 pM:2 nM). Arrows and arrowheads point to TMR-β-actin$_{wt}$ and Alexa647-β2Btub$_{wt}$ RNPs, respectively. (**h**) A titration of Alexa647-β2Btub$_{wt}$ from 2000 to 40 pM leads to an increase of the relative amount of TMR-β2Btub$_{wt}$ transport per experiment

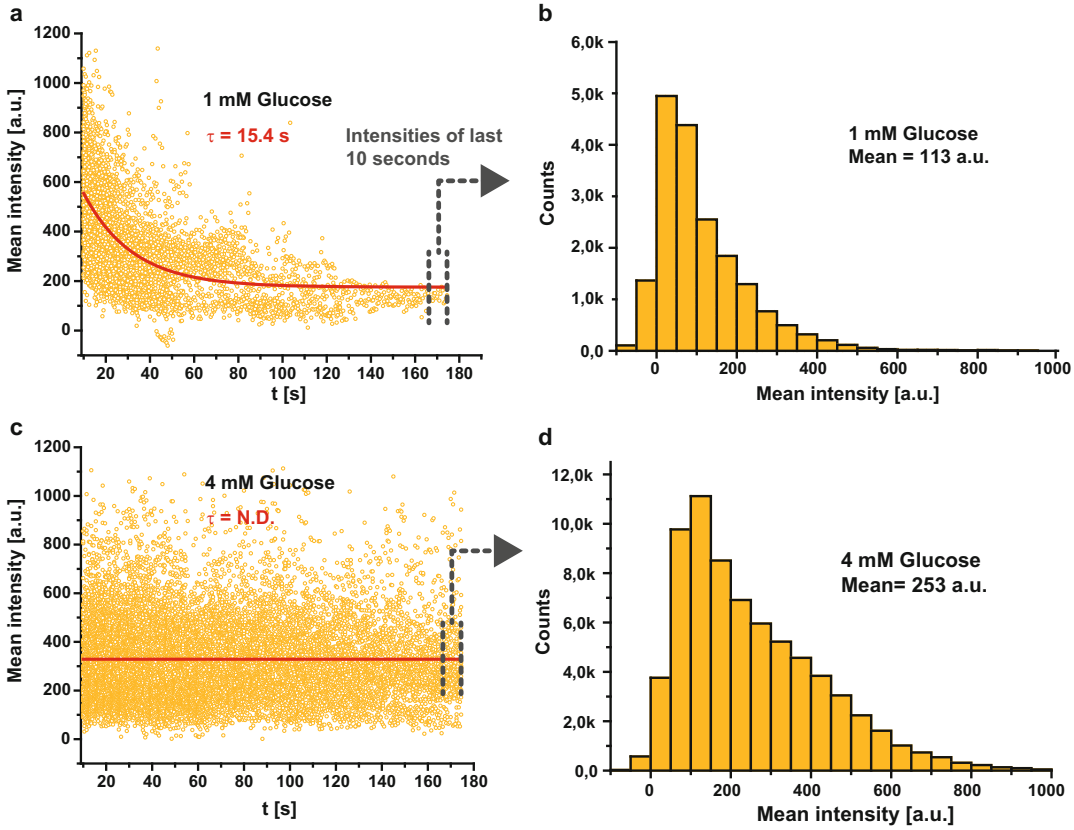

Fig. 6 Important considerations for single-molecule quantifications: bleaching conditions. (**a**) Mean spot intensities over time from a bleaching experiment of KIF3A-TMR immobilized on paclitaxel-stabilized microtubules with AMPPNP are shown. The concentration of glucose was lowered from 50 to 1 mM. (**b**) The distribution of mean spot intensities in the last 10 s of the bleaching experiment shown in (**a**). (**c**) Same experiment as in (**a**) but the concentration of glucose was only lowered from 4 mM. (**d**) The distribution of mean spot intensities in the last 10 s of the bleaching experiment shown in (**c**)

2.4 Oxygen Scavenger and Blocking Reagents

1. For each day of microscopy, prepare solutions of glucose oxidase (AMSBIO #22778.02, 20 mg/ml), catalase (Sigma #C40, 6 mg/ml), β-casein (Sigma #C6905, 5 mg/ml), and κ-casein (Sigma #C0406, 5 mg/ml) in BRB80 (*see* Subheading 2.1).
2. Spin at 80,000 rpm in tabletop ultracentrifuge and TLA120.2 rotor (Beckman Coulter) for 15 min at 4 °C and transfer supernatant (SN) into fresh 1.5-ml reaction tube (*see* **Note 5**).

2.5 TIRF Microscopy

1. iMIC (TILL Photonics, Germany) total internal reflection fluorescence (TIRF) microscope equipped with:
   (a) Three Evolve 512 EMCCD cameras (Photometrics, UK).
   (b) 100 × 1.49 NA objective lens (Olympus, Japan).
   (c) Quadband filter (405/488/561/647, Semrock, USA).

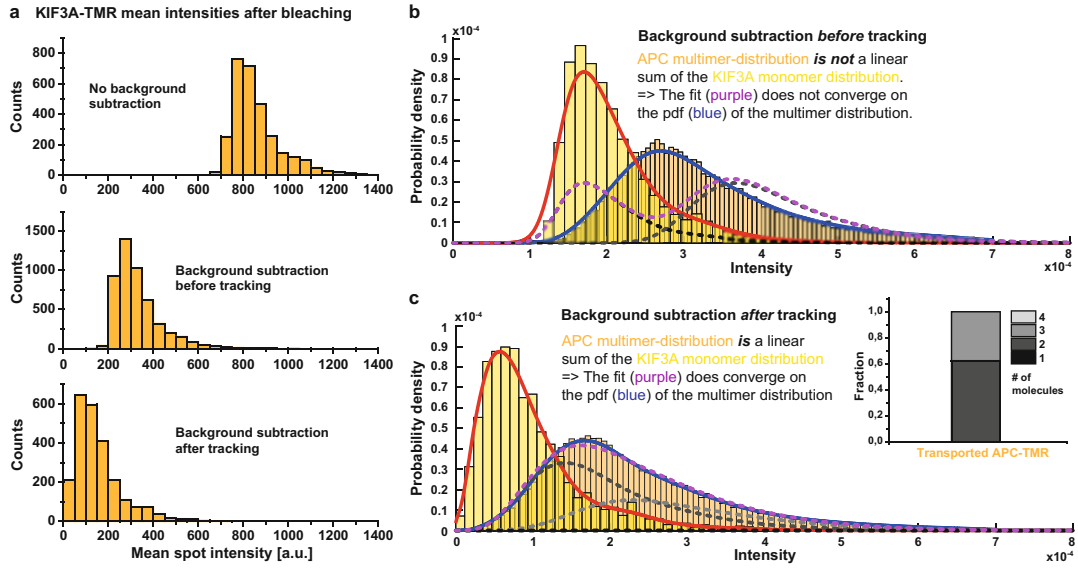

Fig. 7 Important considerations for single-molecule quantifications: background subtraction. (**a**) Mean intensity distribution of immobilized KIF3A-TMR complexes from the last 10 frames of a bleaching experiment. Upper panel: mean intensity distribution without background subtraction. Middle panel: mean intensity distribution of the same data shown in the upper panel but with intensities subtracted before tracking using the ImageJ background subtraction tool (Process > Subtract background). Lower panel: Mean intensity distribution of the same data as show in the upper panel but with background intensities subtracted manually after tracking. (**b**) Attempt to fit linear combinations of the monomeric KIF3A-TMR intensity distribution (bright yellow) obtained from data with background subtraction before tracking to intensity distribution of transported APC-TMR complexes (dark yellow). The fit (purple) does not converge on the pdf of the multimeric distribution (blue). (**c**) Fit of linear combinations of the monomeric KIF3A-TMR intensity distribution obtained from data with background subtraction after tracking to APC-TMR intensity distribution as shown in (**b**). The fit (purple) converges on the pdf of the multimeric distribution (blue). Analysis of the fraction of underlying x-meric distributions reveals that on average two to three APC monomers are transported (inset)

(d) Four different laser lines (405 nm, 488 nm, 561 nm, 639 nm).

(e) Olympus tube lens adds a post magnification of 1.33×, which results in a nominal final pixel size of 120.3 nm.

2. Pipettes 2 × 200 µl, 2 × 20 µl, 1 × 10 µl, 1 × 2.5 µl.
3. Two styrofoam boxes with lids.
4. Microscopy chamber prepared with 100 µm TetraSpeck beads (Invitrogen #T-7279).
5. Whatman™ paper (GE Healthcare #3030-917).
6. Filter tips for 10, 20, and 200 µl.
7. Aluminum blocks for reaction tubes.
8. Aluminum block for chamber on ice.
9. Aluminum block for chamber at RT.

10. NeutrAvidin (Invitrogen #A-2666) in PBS + 20% glycerol (5 mg/ml); 5 µl aliquots in PCR tubes stored at −80 °C or liquid nitrogen.
11. 10% Pluronic F-127 (Sigma #P2443) in MilliQ water.
12. 2% Methylcellulose (Sigma #M0512) in MilliQ water.
13. RNase inhibitor (Invitrogen #AM2694).
14. PEG-3350 (Sigma #1546547-1G).
15. 100 mM ATP (Sigma #A2383) solution in MilliQ water adjusted with KOH to pH 7.15.
16. β-Mercaptoethanol (Sigma #M3148).
17. 1110 mM Glucose (Sigma #G7021) solution in MilliQ water.
18. RNase-free water (ThermoFisher #AM9937).
19. 0.5-ml LoBind reaction tubes (Eppendorf #0030 108.094).
20. 1.5-ml LoBind reaction tubes (Eppendorf #0030 108.116).
21. PCR tubes (Brandt #BR78130).

2.6 Software

1. Tracking with ImageJ and Trackmate:
   (a) Fiji (ImageJ 1.52n) with Trackmate [26] and Multiple Kymograph plugins.
   (b) GraphPad Prism or Origin to plot and statistically test obtained data.
2. Analysis of mRNA transport dynamics:
   (a) GraphPad Prism or OriginLab to plot and statistically test obtained data.
   (b) MATLAB with the MSD analyzer toolbox [28] installed.

2.7 Fluorophore Intensity Calibration and Stoichiometry Measurements

1. AppNHp (AMPPNP) (Jena Bioscience #NU-407-10).
2. For all other materials refer to Subheading 2.5.

3 Methods

3.1 Microscopy Chambers

1. Two days before imaging, place object slides into glass hybridization chambers and add 1 M NaOH (Fig. 1(1)) (*see* **Note 6**).
2. Next day, wash the slides, without removing them from the chamber, three times with purified or MilliQ water (Fig. 1(1)) and discard water.
3. After adding 100% ethanol (Fig. 1(1)) into the chamber, remove slides one by one with thumb and index finger, blot

excess ethanol at the opposite (Fig. 1(2)), downward facing short edge on a tissue, quickly wipe clean with two Kimwipes™ (folded three times) on both sides (*see* **Notes 7** and **8**) and remove residual ethanol with a fresh Kimwipe™.

4. Place clean slides into object slide box to protect them from dust.
5. Cut two strips of double-sided Tesa® tape for each object slide and attach them to the edge of the laboratory bench until further use. Handle Tesa® strips with forceps.
6. Transfer two strips to each slide and position them in parallel and aligned (*see* **Note 9**) (Fig. 1(3)).
7. Pipette 4 µl PLL-PEG between the Tesa® strips with a 20-µl pipette and distribute it between the strips with the pipette tip (Fig. 1(4)).
8. Leave the slides on the bench and let PLL-PEG dry for 15 min at RT.
9. Rinse excess PLL-PEG with MilliQ water from a squeeze bottle (Fig. 1(5)) (*see* **Note 10**). Handle each slide one by one.
10. Remove excess water from the backside of each slide with a Kimwipe™ and shake off excess water with a swift move of your wrist (Fig. 1(6)). Place slides in slide box and transfer to 37 °C incubator for 20–25 min (Fig. 1(7)) (*see* **Note 11**).
11. Transfer slides into new slide box and check if each slide is dry. If not, remove residual water at edges with a Kimwipe™.
12. Cut biotinylated coverslips with a diamond cutter into four equal pieces by placing the coverslip onto an EtOH-cleaned object slide with the biotinylated side facing upward and the mark (*see* **Note 12**) in the upper left corner. Use another EtOH-cleaned object slide as a ruler and place it with one of the long edges centrally onto the coverslip. Cut with diamond cutter to obtain two equal halves. Repeat procedure with the halves to result in equal quarters (Fig. 1(8a)).
13. Remove protective layer from Tesa® strips (Fig. 1(8b)) and attach one coverslip piece to each object slide with the biotinylated surface facing the inside of the chamber. Align on one side with the Tesa® strips. Press down the coverslip gently in parts overlapping with the Tesa® strips with the backside of the tweezers (Fig. 1(9)).
14. Place slides for each experimental day in a separate box (Fig. 1(10)). Put the box into sealable plastic bag containing silica bags and store at 4 °C until 30 min before imaging session. Open the bag only after reaching RT.

3.2 Microtubule Polymerization

1. To obtain microtubules with stochastically incorporated labeled tubulin, mix together depolymerized tubulin (f.c. 30 μM), depolymerized and biotinylated tubulin (f.c. 10 μM), depolymerized and fluorescently labeled tubulin (f.c. 14 μM) as well as GTP (f.c. 4 mM) in BRB80 resulting in 25 μl total volume (*see* **Notes 13** and **14**).
2. Mix by pipetting slowly up and down and incubate at 37 °C in shaker at the lowest revolution (300 rpm) for 25 min.
3. Add 175 μl of prewarmed BRB80 containing 20 μM paclitaxel (*see* **Note 15**), pipette 2–3 times slowly up and down and incubate for 60 min at 37 °C in shaker at 300 rpm.
4. Pellet polymerized microtubules for 5 min at >16,000 × *g*. Remove SN and dissolve MTs in 30 μl BRB80 with 20 μM paclitaxel by pipetting slowly up and down until solution is homogenous (*see* **Note 16**).
5. Store MTs at RT protected from light until further use (*see* **Note 17**).

3.3 TIRF Microscopy

To make sure the overall experiment setup time does not vary between replicates, we recommend using a separate timer to record the time from thawing of reagents until imaging starts. This is especially important for sensitive proteins that might lose their activity over time after thawing.

1. On the day of microscopy, store proteins in a Dewar vessel filled with liquid nitrogen and place the latter next to the microscope.
2. Switch on the microscope, align lasers if necessary and take a reference movie with the chamber containing TetraSpeck beads.
3. Supplement 10 ml of 2× AB stock with 30 mM β-mercaptoethanol and 8 μM paclitaxel to obtain 2× AB.
   (a) Mix 480 μl 2× AB with 500 ul Pluronic and 20 μl κ-casein to obtain pluronic block buffer.
   (b) Supplement 2× AB with 8% PEG-3350 to obtain the final assay buffer 2× AB^{RNArun}.
4. Mix 5 ml of 2× AB with 5 ml RNase-free water to obtain 10 ml 1× AB.
5. Mix 5 ml 1× AB with 50 μl κ-Casein. 110 μl of 1× AB with κ-casein is mixed with 0.8 μl NeutrAvidin to obtain 110.8 μl NeutrAvidin buffer. This amount covers two consecutive experiments (*see* **Note 18**).
6. In total, tubes per day of imaging should be prepared with (*see* **Note 19**):

(a) Pluronic block buffer.
(b) 2× AB^{RNArun}.
(c) RNase-free water.
(d) Glucose (*see* **Note 20**).
(e) Methylcellulose.
(f) Glucose oxidase.
(g) Catalase.
(h) β-Casein.
(i) 1× AB.
(j) NeutrAvidin buffer.
(k) ATP (*see* **Note 21**).
(l) RNase inhibitor (*see* **Note 22**).

7. And additional tubes for each experiment:
   (a) Tube for preincubation mix (0.5-ml tube).
   (b) Tube for final assay mix (0.5-ml tube).
   (c) Tube for protein/RNA dilutions (0.5-ml tube).
   (d) Tube with 45–50 μl 1× AB for MT dilution at RT.
   (e) Tube with 110.8 μl NeutrAvidin buffer for two experiments.
8. Place all tubes in aluminum blocks on ice in a box (*see* **Note 23**).
9. Prepare a second box with ice, place a PCR aluminum block upside down onto the ice and add a piece of Parafilm, bigger than an object slide, on top of it (*see* **Note 24**).
10. Prepare the preincubation mix with 2× AB^{RNArun} (1× f.c.), RNase-free water, 2.5 mM ATP, and 0.5 U RNase inhibitor in a total volume of 10 μl (Fig. 2(1)). Mix properly and leave until further use.
11. Thaw RNA and proteins, dilute after thawing if necessary, and add immediately to preincubation mix (Fig. 2(1)) (*see* **Notes 25** and **26**). Mix quickly but gently by pipetting up and down 15× with a 10 μl pipette and incubate on ice (*see* **Notes 27** and **28**).
12. Take out a chamber from the slide box in the plastic bag, place it at RT and seal bag with the remaining slides. Take a 200 μl pipette, set to 100 μl and fill with Pluronic block buffer. Place the chamber now on the ice block and immediately flow Pluronic block buffer through the chamber (Fig. 2(2)) (*see* **Note 29**).
13. Fill assay mix tube with 2× AB^{RNArun} (1× f.c.), RNase-free water (mix 20×), glucose (50 mM f.c.), methylcellulose

(0.123% f.c.), and mix 20× with the second 200 µl pipette set to 50 µl (Fig. 2(3)) (*see* **Note 30**).

14. Add glucose oxidase (0.32 µg/ml f.c.), catalase (0.275 µg/ml f.c.), β-casein (50 µg/ml f.c.) and mix gently by pipetting up and down 20× with a 20 µl tip (Fig. 2(3)) (*see* **Note 31**).
15. After 5 min 30 s (timer counting down) of Pluronic incubation of the chamber, prepare one 200 µl pipette with 1× AB and set aside. Prepare the second 200 µl pipette with 50 µl NeutrAvidin buffer and flow it quickly through chamber. Immediately after, flow 1× AB and place on chamber on aluminum block at RT (*see* **Note 32**) (Fig. 2(4)). The incubation time of this step is 3 min.
16. After 2 min (1 min 20 s on the timer counting down), start preparing MT dilution by adding 3–6 µl of MT stock (*see* Subheading 3.2) to 1× AB to reach a final volume of 50 µl and mix gently 5×. As soon as the timer counting down beeps, flow MT dilution into chamber (Fig. 2(5)). Set timer again to count down from 3 min.
17. Add ATP (2.5 mM f.c.) to the assay mix and pipette 10× up and down with 20 µl tip.
18. After 2 min 30 s (timer counting down) of MT incubation at RT, add preincubation mix to the assay mix (Fig. 2(6)) to obtain the desired final protein and RNA concentrations in the final assay mix. As soon as the timer counting down is completed, mix the final assay mix by pipetting 10× with 200 µl pipette set to 59 µl and flow 59 µl of final assay mix through chamber (Fig. 2(7)) (*see* **Note 33**).

    Seal chamber with nail polish and begin imaging immediately (*see* **Note 34**).

3.4 Tracking with ImageJ and Trackmate

1. Load movie stack into Fiji.
2. Calibration settings: Enter pixel size and frame rate (Fig. 4a). This can also be set globally under the Fiji menu item "Image > properties" and will then apply to all movies loaded as long as Fiji is not closed.
3. Choose LoG or DoG Detector (Fig. 4a). We tested LoG and DoG detectors for our data which produced similar results (Fig. 4c).
4. Enter blob diameter and threshold: Make sure not to cut off pixels belonging to a spot if, e.g., total or mean intensities are of interest for later analysis (Fig. 4a, b) (*see* **Note 35**).
5. Hit "Preview" and use Fiji's contrast functions to manually validate that detected spots are correct. Inspect different time points to the movie in case intensities change over time.

6. Set filter on spots: After spot detection one can exclude spots (Fig. 4a) (*see* **Note 36**).
7. Choose tracker: Both the Simple Lap Tracker (SLT) and Linear Motion Tracker (LMT) worked well for our samples. The LMT found more but slightly shorter tracks (Fig. 4a, c).
8. Choose tracker tuning options that do not cause artifacts, e.g., by splitting tracks due to intensity fluctuations or link tracks that belong to different events. Also *see* **step 10** below.
9. Set filter on tracks: Setting a displacement cut-off is ideal, e.g., to include or exclude diffusive events once their characteristic displacement has been determined. We always set a minimal "track displacement" (*see* **Note 37**) cut-off of >1.1 μm to exclude molecules that stick unspecifically to the coverslip (Fig. 1d) (*see* **Notes 38** and **39**).
10. Manual control: Create kymographs along detect tracks, e.g., using Fiji's reslice option "Image > Stacks > Reslice." Check if tracks detected by Trackmate reflect number and duration of actual events. If not, adjust detector and tracking settings.
11. Export data: Hit "Analysis" button. Save tracks and spots tables for subsequent analysis of motility and intensity parameters. While the "track" files contain dynamic information, the "spot" files contain intensity information.

3.5 Analysis of mRNA Transport Dynamics

The track tables produced by Trackmate can directly be used for straightforward analysis such as determining the number of processive run events (Fig. 5a–d) or the mean velocity distribution among processive events (Fig. 5e). Importing of track files into analysis tools as MSD analyzer (MATLAB) allows computing of mean square displacement curves (Fig. 5f). For experiments with two differently labeled RNAs (Fig. 5g) in the same experiment (β2Btub$_{wt}$-Alexa647 and βact$_{wt}$-TMR), both channels can be tracked independently to later join data for comparative analysis, e.g., using OriginLab (Fig. 5h).

3.6 Fluorophore Intensity Calibration and Stoichiometry Measurements

To dissect the stoichiometry of reconstituted mRNA complexes and sub-complexes, we first determined the intensities of individual TMR and Alexa647 fluorophores coupled to a dimeric KIF3A-SNAP construct. To image these calibration probes under conditions as close to the actual transport complexes as possible, we immobilized labeled KIF3A calibration probes on paclitaxel-stabilized microtubules inside TIRF-M chambers using the ATP analog AMPPNP. While illumination settings can be kept very stable for several days depending on the microscope set up used, it is highly recommended to image both the calibration probe and the sample to be analyzed on the same day using the same imaging settings. To determine the average number of molecules in

transport complexes, we fitted linear combinations [27, 29] of the predetermined monomeric (and the resulting multimeric) fluorophore intensity distributions to the intensity distributions obtained from tracking the kinesin, APC, and RNAs.

We would like to highlight two important considerations (1). To make sure that one records single fluorophores as a calibration probe, bleaching conditions have to be properly established. We found that it requires lowering of the glucose in the TIRF-M imaging buffer from 50 to 1 mM in order to obtain image information with mostly single-fluorophores per spot in a reasonable time (Fig. 6). Once the intensities in a bleaching curve reach a stable minimum with little variation (Fig. 6a, b), one can assume that such a condition is found. Little difference in the glucose concentration can have a large effect; when using 4 mM instead of 1 mM glucose, no considerable bleaching was detected withing 3 min of imaging (Fig. 6c, d) (2). Another important aspect is how and when the image background is subtracted. We tested subtracting the background before tracking using tools included in Fiji (Process > Subtract background) and measuring the background manually [27] and subtracting it using Fiji (Process > Math > Subtract). Alternatively, we subtracted the manually measured mean background directly from the spot mean intensity values produced by Trackmate. The mean background was manually measured by averaging the mean intensity in a rectangular box at five positions of the field of view in four frames over the entire movie. This resulted in different mean intensity distributions for our KIF3A calibration samples. An example of intensity distributions obtained from immobilized KIF3A-TMR is shown in Fig. 7a. There is a notable difference in the distributions obtained when subtracting the background before and after tracking. The reason for this is that both background subtraction methods before tracking artificially increase mean spot intensities, as pixels in Fiji cannot have negative values after the "Subtract" or "Subtract background" procedure. However, there are pixels within a spot recorded by Trackmate that would have negative intensity values after mean background subtraction. When subtracting a manually measured mean background value from the spot intensity value, this problem does not occur. As a result, multimeric intensity distributions, as e.g., derived from tracking APC-TMR transported by KIF3AB-KAP3, can be fitted to linear combinations of the predetermined KIF3A-TMR intensity distribution to obtain the number of molecules in a complex (Fig. 7b, c).

1. Follow steps in Subheading 3.3.
2. Instead of using ATP, use 2.5 mM AMPPNP (f.c.).
3. Instead of using 50 mM glucose (f.c.), use 1 mM glucose (f.c.).

4. Image with the exact same settings used in the actual experiments.
5. Track TIRF-M movies with Trackmate using the same tracking parameters as before. It is important to include only tracks lasting longer than 3 s, to make sure one does not include transient, unspecifically binding molecules that have not been bleached.
6. Confirm that obtained mean spot intensities reach a stable minimum at the end of the recorded movie (Fig. 6a).
7. Use the mean spot intensity distribution from the last 10 frames of the movie as monomer fluorescence intensity calibration data set.

4 Notes

1. To keep the ionic strength of the buffer constant, it is recommended to use 1.21 g of KOH per 250 ml of buffer and confirm the correct pH, which may slightly differ with changing RT.
2. Use bottle top filters with plastic bottles to ensure buffers are free of contaminants that might originate from reused glassware.
3. The concentrations of depolymerized tubulin, depolymerized, and biotinylated tubulin as well as depolymerized and fluorescently labeled tubulin may vary. Our stock solutions commonly have concentrations around 185 μM, 184 μM, and 99 μM, respectively.
4. Tubulin is labeled according to published protocols [30].
5. If prepared for 2 days of microscopy, split in two tubes, and keep half in box with ice and place in cold room or refrigerator.
6. In general, one can prepare around eight chambers per day of microscopy. One experiment including preparation and imaging time takes about 40–45 min. After eight experiments, the buffer performance might decrease.
7. It is recommendable to clean nitril gloves with soap beforehand to prevent any dust contaminations coming from the gloves.
8. Check slides against light for any visible contaminations. In case you detect streaks or smears by eye repeat EtOH step.
9. Make sure the Tesa® strips have no dents or kinks. Turn around object slides and check if Tesa® strips are properly attached.
10. Usually one needs ~300–400 ml H_2O per six slides.
11. The incubation time increases with the amount of slides per box.

12. Commercial biotin-slips from Microsurfaces are marked at one corner.
13. The final concentration of depolymerized and biotinylated tubulin as well as depolymerized and fluorescently labeled tubulin may vary according to the labeling ratio and brightness of the fluorophore. When using ATTO390 at a labeling ratio of ~20%, the here mentioned concentrations will result in sufficient signal.
14. Depending on the desired MT density on the biotinylated coverslip and days of microscopy, the volume needs to be adjusted.
15. Keep BRB80 with paclitaxel at 37 °C and vortex extensively before adding.
16. The pellet with ATTO390-labeled microtubules appears white.
17. The best results are obtained when MTs are prepared on the day of microscopy; however, they are relatively stable for up to 2 days. This also depends on the fluorophore used.
18. Add NeutrAvidin immediately before the first of two experiments.
19. All solutions are prepared in 1.5-ml tubes unless otherwise stated.
20. Prepare 50 µl aliquots for each day of imaging in PCR tube.
21. Prepare 25 µl aliquots for each day of imaging in PCR tube.
22. Prepare a PCR tube with 2 µl per four experiments immediately before imaging. After four experiments, prepare a fresh PCR tube.
23. Styrofoam boxes with lids are convenient to prevent melting of ice and excess condensation on metal blocks. This helps keeping contaminations to a minimum.
24. The Parafilm helps removing the object slide from the block when transferred later to an aluminum block at RT.
25. Take 2–3 µl aliquot of RNA out of freezer immediately before adding to preincubation mix. Thaw RNA quickly and add first to the preincubation mix.
26. Take a PCR tube containing protein solution from liquid nitrogen and place on ice. Open tube quickly and close to prevent potential bursting of the tube. Typical protein concentrations in the preincubation mix are in the lower nanomolar range (5–50 nM). RNA concentrations range from 10 to 280 nM. The resulting concentrations within the final assay mix (*see* **step 18**) for proteins and RNAs are in the low to mid picomolar and low nanomolar range for proteins and RNA, respectively.

27. Pipetting too rapidly and excessively may denature proteins due to the air–liquid interfaces created at foam bubbles.
28. Fifteen times because the solution is viscous due to PEG-3350 and methylcellulose.
29. Be quick so that humidity cannot condense before Pluronic enters the chamber. The flow speed is comparably slow because of viscosity. To increase flow speed, change position of Whatman™ paper slightly sideways and/or lift the Whatman™ paper a tiny bit and place it on top of the first <1 mm of the coverslip. Note that at other steps such as flowing in the less viscous NeutrAvidin buffer, the flow speed may be very quick this way. In particular when flowing MTs into the chamber, you may want to keep the speed low, because it increases the amount of MTs attached to the glass.
30. First, buffer and water as well as chemicals dissolved in water are mixed before proteins are added.
31. Because of the viscosity, it is recommendable to use a smaller volume with more repetitions to mix. This way less assay mix sticks to the pipette tip.
32. If you experience a high amount of fluorescent protein or RNA sticking to the coverslip during imaging, try to decrease the amount of NeutrAvidin in the chamber by increasing flow speed or decreasing the amount of NeutrAvidin in the NeutrAvidin buffer. Be aware that less NeutrAvidin can lead to unstably attached MTs.
33. Remove excess final assay mix on both slides of the coverslip with a piece of Whatman™ paper. Be careful not to suck assay mixture out of the imaging chamber.
34. Depending on the stability of proteins and RNAs under the assay condition, it can be crucial to keep the time between chamber sealing and begin imaging as constant as possible.
35. The threshold differs depending on depending on fluorophore and concentration.
36. Usually we exclude spots above a certain intensity threshold, to exclude occasionally appearing aggregates.
37. To exclude diffusive events, either "track displacement" or "maximum distance travelled" is useful when set to >6 μm. The value might differ, depending on the molecules studied, and was experimentally determined in this case. "Max distance travelled" is included in the additional plugin "Track analysis" for Trackmate.
38. The cut-off can be as high as 2 μm, depending on the kind of molecule studied and its motion behavior. Also, it depends on the fluorophore chosen, concentration, and other settings, such as threshold and gap size.

39. Although our approach allows for rapid analysis of motility parameters, landing rates of molecular motors, for instance, can only be addressed by different means, such as manually generating and analyzing kymographs.

Acknowledgments

This work was supported by the Spanish Ministry of Economy and Competitiveness (MINECO) [BFU2017-85361-P], [BFU2014-54278-P], [BFU2015-62550-ERC], by the Juan de la Cierva-Incorporación Program [IJCI-2015-25994], the Human Frontiers in Science Program (HFSP) [RGY0083/2016], the European Research Council (ERC) [H2020-MSCA-IF-2014-659271] and the Ministerio de Ciencia, Innovación y Universidades and Fondo Social Europeo (FSE) [PRE2018-084501]. We further acknowledge support of the Spanish Ministry of Economy and Competitiveness to the EMBL partnership, "Centro de Excelencia Severo Ochoa" [SEV-2012-0208] and [SEV-2015-0533], and the CERCA Programme/Generalitat de Catalunya.
We would further like to thank Stefan Wieser and Verena Ruprecht for the helpful discussions on image analysis.

References

1. Buxbaum AR, Haimovich G, Singer RH (2015) In the right place at the right time: visualizing and understanding mRNA localization. Nat Rev Mol Cell Biol 16:95–109
2. Holt CE, Bullock SL (2009) Subcellular mRNA localization in animal cells and why it matters. Science 326:1212–1216
3. Holt CE, Martin KC, Schuman EM (2019) Local translation in neurons: visualization and function. Nat Struct Mol Biol 26:557–566
4. Litman P, Barg J, Rindzoonski L, Ginzburg I (1993) Subcellular localization of tau mRNA in differentiating neuronal cell culture: implications for neuronal polarity. Neuron 10: 627–638
5. Litman P, Barg J, Ginzburg I (1994) Microtubules are involved in the localization of tau mRNA in primary neuronal cell cultures. Neuron 13:1463–1474
6. Leung K-M, van Horck FPG, Lin AC, Allison R, Standart N, Holt CE (2006) Asymmetrical beta-actin mRNA translation in growth cones mediates attractive turning to netrin-1. Nat Neurosci 9:1247–1256
7. Lin AC, Holt CE (2007) Local translation and directional steering in axons. EMBO J 26: 3729–3736
8. Yoon YJ, Wu B, Buxbaum AR, Das S, Tsai A, English BP, Grimm JB, Lavis LD, Singer RH (2016) Glutamate-induced RNA localization and translation in neurons. Proc Natl Acad Sci U S A 113:E6877–E6886
9. Miller S, Yasuda M, Coats JK, Jones Y, Martone ME, Mayford M (2002) Disruption of dendritic translation of CaMKIIalpha impairs stabilization of synaptic plasticity and memory consolidation. Neuron 36:507–519
10. Turner-Bridger B, Caterino C, Cioni J-M (2020) Molecular mechanisms behind mRNA localization in axons. Open Biol 10:200177
11. Liao YC, Fernandopulle MS, Wang G, Choi H, Hao L, Drerup CM, Patel R, Qamar S, Nixon-Abell J, Shen Y et al (2019) RNA granules hitchhike on lysosomes for long-distance transport, using Annexin A11 as a molecular tether. Cell 179:147–164.e20
12. Hirano M, Muto M, Sakai M, Kondo H, Kobayashi S, Kariwa H, Yoshii K (2017) Dendritic transport of tick-borne flavivirus RNA by neuronal granules affects development of neurological disease. Proc Natl Acad Sci U S A 114:9960–9965
13. Pocock GM, Becker JT, Swanson CM, Ahlquist P, Sherer NM (2016) HIV-1 and

M-PMV RNA nuclear export elements program viral genomes for distinct cytoplasmic trafficking behaviors. PLoS Pathog 12:1–30

14. Dictenberg JB, Swanger SA, Antar LN, Singer RH, Bassell GJ (2008) A direct role for FMRP in activity-dependent dendritic mRNA transport links Filopodial-spine morphogenesis to fragile X syndrome. Dev Cell 14:926–939
15. Mallardo M, Deitinghoff A, Muller J, Goetze B, Macchi P, Peters C, Kiebler MA (2003) Isolation and characterization of Staufen-containing ribonucleoprotein particles from rat brain. Proc Natl Acad Sci 100: 2100–2105
16. Fritzsche R, Karra D, Bennett KL, Ang F, Heraud-Farlow JE, Tolino M, Doyle M, Bauer KE, Thomas S, Planyavsky M et al (2013) Interactome of two diverse RNA granules links mRNA localization to translational repression in neurons. Cell Rep 5:1749–1762
17. Kanai Y, Dohmae N, Hirokawa N (2004) Kinesin transports RNA. Neuron 43:513–525
18. Järvelin AI, Noerenberg M, Davis I, Castello A (2016) The new (dis)order in RNA regulation. Cell Commun Signal 14:9
19. Alberti S, Saha S, Woodruff JB, Franzmann TM, Wang J, Hyman AA (2018) A User's guide for phase separation assays with purified proteins. J Mol Biol 430:4806–4820
20. Tushev G, Glock C, Heumüller M, Biever A, Jovanovic M, Schuman EM (2018) Alternative 3′ UTRs modify the localization, regulatory potential, stability, and plasticity of mRNAs in neuronal compartments. Neuron 98:495–511. e6
21. Zappulo A, van den Bruck D, Ciolli Mattioli C, Franke V, Imami K, McShane E, Moreno-Estelles M, Calviello L, Filipchyk A, Peguero-Sanchez E et al (2017) RNA localization is a key determinant of neurite-enriched proteome. Nat Commun 8:583
22. Heym RG, Zimmermann D, Edelmann FT, Israel L, Ökten Z, Kovar DR, Niessing D (2013) In vitro reconstitution of an mRNA-transport complex reveals mechanisms of assembly and motor activation. J Cell Biol 203:971–984
23. Sladewski TE, Bookwalter CS, Hong M-S, Trybus KM (2013) Single-molecule reconstitution of mRNA transport by a class V myosin. Nat Struct Mol Biol 20:952–957
24. McClintock MA, Dix CI, Johnson CM, McLaughlin SH, Maizels RJ, Hoang HT, Bullock SL (2018) RNA-directed activation of cytoplasmic dynein-1 in reconstituted transport RNPs. Elife 7:e36312. https://doi.org/10.1101/273912
25. Zacharias DA, Violin JD, Newton AC, Tsien RY (2002) Partitioning of lipid-modified monomeric GFPs into membrane microdomains of live cells. Science 296:913–916
26. Tinevez JY, Perry N, Schindelin J, Hoopes GM, Reynolds GD, Laplantine E, Bednarek SY, Shorte SL, Eliceiri KW (2017) TrackMate: an open and extensible platform for single-particle tracking. Methods 115:80–90
27. Baumann S, Komissarov A, Gili M, Ruprecht V, Wieser S, Maurer SP (2020) A reconstituted mammalian APC-kinesin complex selectively transports defined packages of axonal mRNAs. Sci Adv 6:eaaz1588
28. Tarantino N, Tinevez J-Y, Crowell EF, Boisson B, Henriques R, Mhlanga M, Agou F, Israël A, Laplantine E (2014) TNF and IL-1 exhibit distinct ubiquitin requirements for inducing NEMO-IKK supramolecular structures. J Cell Biol 204:231–245
29. Moertelmaier M, Brameshuber M, Linimeier M, Schütz GJ, Stockinger H (2005) Thinning out clusters while conserving stoichiometry of labeling. Appl Phys Lett 87:1–3
30. Hyman A, Drechsel D, Kellogg D, Salser S, Sawin K, Steffen P, Wordeman L, Mitchison T (1991) Preparation of modified tubulins. Methods Enzymol 196:478–485

Open Access This chapter is licensed under the terms of the Creative Commons Attribution 4.0 International License (http://creativecommons.org/licenses/by/4.0/), which permits use, sharing, adaptation, distribution and reproduction in any medium or format, as long as you give appropriate credit to the original author(s) and the source, provide a link to the Creative Commons license and indicate if changes were made.

The images or other third party material in this chapter are included in the chapter's Creative Commons license, unless indicated otherwise in a credit line to the material. If material is not included in the chapter's Creative Commons license and your intended use is not permitted by statutory regulation or exceeds the permitted use, you will need to obtain permission directly from the copyright holder.

INDEX

A

Actin 13, 174, 501, 505, 508, 509, 511, 521–523, 526
Adaptor proteins 24, 245, 329, 534
Adult sensory neurons 271–287
Aging 74, 95, 108, 208, 250, 386, 430
α-tubulin N-acetyltransferase 1 (ATAT1) 208, 209, 211, 212, 217, 222
Amyloid precursor protein (APP) 5, 112, 417, 482
Anterograde transport 38, 81, 85, 92, 173, 174, 219, 223, 241, 250, 274, 275, 430, 435, 468, 472, 482
Aplysia 23–47
Aptamers 225, 226, 229, 230
Axonal organelles 95–108, 368, 369, 379, 381
Axonal transport (AT) ..... v, 3–19, 23, 24, 26, 32, 73–92, 95–108, 112–139, 145–161, 164, 172, 183, 194, 195, 199, 200, 207–223, 249–267, 271–287, 292, 311–320, 325–346, 351, 352, 354, 355, 357, 359, 361, 367–371, 373, 375, 382, 385, 386, 388, 390, 398, 402, 410, 417–427, 429–444, 452, 453, 455, 457, 465–468, 470–476, 481–495, 499, 500, 503, 507, 508, 565
Axon guidance 431
Axons 3–10, 12, 15–19, 24, 25, 30–32, 34–39, 42, 44, 50, 51, 55, 62–67, 73, 74, 83, 87–90, 92, 96, 97, 103–105, 112, 127, 145, 146, 156–158, 161, 163–165, 169–177, 182, 183, 187, 189, 193–196, 198–204, 207, 208, 213, 215, 217, 219, 220, 223, 225–236, 240, 241, 249, 251, 259, 261–263, 266, 267, 272, 274, 276, 284, 285, 291, 311, 317, 320, 325–346, 351, 352, 358, 359, 367–369, 371, 372, 377, 381, 385, 392, 394, 399, 401, 402, 418, 419, 421–423, 427, 429, 430, 435, 438, 441, 444, 451–453, 455, 465, 466, 468–470, 473–475, 477, 481–483, 486, 488, 491, 492, 503, 525, 534, 548

B

Basal forebrain cholinergic neurons (BFCNs) 249–267
Bidirectional transport 74, 249, 326
Brain 75, 78–82, 95–108, 111–139, 168, 169, 176, 213, 214, 216, 222, 250, 256, 257, 344, 355, 359, 418–421, 425, 426, 434, 437, 442, 443, 452–459, 466, 481, 482
Brain derived neurotrophic factor (BDNF) 157, 158, 210, 213, 215, 251, 253, 254, 259, 261, 266, 294, 295, 299, 312–316

C

Caenorhabditis elegans ..... v, 352, 439, 465–477, 481–495, 499–527
Caenorhabditis elegans neurons 467, 500, 507, 518
Campenot 181–204, 272
Cargoes 4, 23, 24, 74, 77, 96, 112, 113, 164, 165, 207, 223, 239, 240, 242, 245, 249, 250, 271, 274, 291, 292, 311, 325–327, 329, 331, 335, 337, 344, 352, 357, 368, 386, 401, 421, 423, 427, 430, 435, 437–440, 442, 452, 454, 457, 459, 466–468, 482, 486, 488, 491, 492, 499, 500, 503, 507, 513, 524, 525, 533, 548
Central nervous system (CNS) 28, 30, 31, 90, 112, 181, 182, 250, 251, 259, 272, 273, 368, 413, 417–427
Clathrin 165, 167, 173
Confocal microscope 18, 19, 55, 211, 213, 215–217, 222, 253, 254, 262, 277, 284, 294, 358, 388, 402, 419, 454, 455, 457, 459, 471, 501, 503, 504, 506–508, 510–512
Cranial window surgery 97–99, 105
CRISPR 5, 225, 226, 229, 500
Cryo electron tomography 203
Cultured hippocampal neurons 239–246
Cultured primary neurons 95, 225–236
Cytoplasmic mRNA localization 548
Cytoskeleton 19, 378, 452, 533
Cytosolic proteins 166, 177

Alessio Vagnoni (ed.), *Axonal Transport: Methods and Protocols*,
Methods in Molecular Biology, vol. 2431, https://doi.org/10.1007/978-1-0716-1990-2,

© The Editor(s) (if applicable) and The Author(s), under exclusive license to Springer Science+Business Media, LLC, part of Springer Nature 2022

D

Dissection 6–9, 19, 23, 27, 54, 75, 77–79, 82, 89, 90, 92, 167–169, 176, 192, 197, 211, 216, 234, 252, 253, 255–258, 265, 283, 368, 369, 371–376, 378, 380–382, 386, 412–414, 418–421, 423, 425–427, 433, 437, 453–456, 459, 487, 491, 493
Dorsal root ganglia (DRG) 182, 183, 191–194, 197, 273, 274, 276–280, 283, 284
Doryteuthis (*loligo*) *pealeii* 3, 7
Drosophila melanogaster 208, 210, 211, 215–217, 222, 430
Drosophila primary neurons 431, 432, 443
Dynein 24, 26, 164, 250, 272, 326, 327, 332, 430, 466, 482, 533, 534, 548

E

Epifluorescence microscopy 75, 76, 167, 360, 484
Ex vivo imaging 73–92, 455

F

Fast transport 164, 165, 175, 367
Fidgetin-like 1 (Fignl1) 327, 328, 330–332, 343, 345
Fimbria 73, 75–78, 81, 82, 84, 90, 92, 127
Fluorescence 19, 23, 34, 49, 54, 60, 62, 67, 104, 105, 108, 132, 164, 165, 167–169, 171–174, 177, 195, 200, 202–204, 213, 226, 230, 231, 242, 254, 265, 317, 344, 354, 355, 359, 362, 370, 371, 373–375, 377, 379–382, 389, 395, 396, 398, 413, 423, 427, 441, 442, 456, 471, 491, 492, 501, 504, 512, 513, 515, 537, 541, 542, 553, 555, 564
Fluorescence microscopy 9, 129, 132, 137, 164, 195, 198–201, 203, 253, 254, 260, 369, 372, 499, 541, 542
Fluorescent protein (FP) 5, 49, 50, 54, 96, 156, 169, 182, 198–200, 203, 220, 227, 229–231, 355, 369, 379, 457, 566
Fornix 81, 82, 127, 138
Fruit flies 430

G

Gene mutations 465–477
Giant axons, v 3–19, 112
Giant fiber (GF) 418, 419, 421–423, 427
Glial-derived neurotrophic factor (GDNF) 157, 158, 312–316

H

Herpes simplex virus (HSV) 4, 5
Herpes simplex virus type 1 (HSV-1) 5, 194, 198, 199
High resolution 272, 273, 294, 344, 402, 419, 440, 453
Hippocampal neurons 168, 176, 229, 231, 232, 242, 243, 256, 257, 438
Histone deacetylase 6 (HDAC6) 208, 211, 217, 222
Human induced pluripotent stem cell 292, 293, 312, 314, 316, 320

I

ImageJ 32, 35, 39, 41, 46, 62, 63, 83, 86, 87, 129, 158, 219, 255, 263, 264, 267, 279, 284, 285, 287, 294, 302, 331, 357, 359, 361, 388, 401, 423, 441, 485, 486, 488, 489, 491–493, 501, 502, 510, 513, 514, 517–519, 521–525, 527, 556, 560, 562
Imaging 5, 18, 19, 23–46, 49–68, 73–79, 82–85, 89, 90, 92, 95–108, 113, 120, 125–130, 135, 137, 156, 157, 161, 163–177, 182, 200, 222, 225–236, 242, 243, 245, 254, 261, 262, 265–267, 274, 279, 284, 287, 291–307, 314, 317, 326, 333–335, 343–346, 352, 354, 355, 357–362, 367–371, 373, 375–382, 385–405, 410, 412–415, 418, 419, 421–423, 425–427, 434, 438–444, 452–454, 456–460, 467, 468, 470–472, 477, 486, 500–511, 513–519, 521–527, 537, 541–543, 556, 558, 559, 561–563, 565, 566
Imaging chambers 242, 243, 294, 333, 344, 397, 401, 438, 453–456, 566
Instant structured illumination microscopy (iSIM) 293, 298, 306, 411, 414, 415
Interference reflection microscopy 537, 541–543
Intracellular transport 3, 4, 74, 182, 183, 271, 291, 386, 465
Intravital imaging 95
In vitro reconstitutions ..... v, 533–544, 547–567
In vivo imaging 73, 85, 95, 330, 331, 333, 334, 354, 386, 387, 466, 500, 507

K

KIF1A 244, 466–468, 484
KIF1Bβ 327, 330–332, 343, 345, 346, 466
KillerRed 387, 389, 391, 393, 395–397, 402
Kinesin-1 ..... 4, 5, 113, 239, 241, 242, 244, 430, 452, 484, 533–535, 537, 538, 541, 542, 544

Kinesins 4, 24, 26, 112, 113, 164, 165, 239–245, 250, 272, 274, 326, 327, 370, 430, 443, 466, 481, 534, 548, 563
Kymographs 25, 35–37, 39, 43–46, 62–65, 83, 89, 103–106, 158, 159, 171–174, 176, 200, 201, 217, 219, 223, 235, 241, 264, 275–277, 285, 287, 300–302, 306, 317, 327, 329, 331, 332, 334–340, 342, 343, 345, 346, 372, 375, 377, 388, 395, 396, 401, 402, 423, 427, 435, 441, 454, 455, 457, 459, 468, 470, 473–475, 482, 486, 488, 489, 501, 505, 506, 509, 510, 513–522, 527, 541–543, 551, 553, 554, 556, 562, 567

L

Live imaging 26, 32, 35, 37, 43, 46, 49, 55, 75, 76, 129, 168, 171, 245, 292, 304, 306, 314, 325–346, 352, 370, 387, 390, 397, 402, 410, 413, 417–419, 421, 423, 427, 432, 440, 451–459, 499–513, 525, 548
Lysosomes 24, 32, 43, 96, 213, 215, 274, 277, 326, 437, 466, 481, 499
Lysotracker 27, 32, 34, 43, 156, 210, 213, 215, 221, 277, 279, 284, 433, 435, 437, 438, 441, 443

M

Magnetic resonance imaging (MRI) 111–139
Manganese 111, 135
Mauthner cells 351–362
Microfluidics chambers 208, 211, 213, 271–286
Micropipettes 7, 10, 14, 15, 17, 19, 31, 52, 54, 55, 59–61, 98, 100, 114–118, 120–122, 124, 125, 139, 209, 265, 330, 354, 361, 378, 484, 486
Microtubule acetylation 207–223
Microtubule-based transport 533
Microtubules 4, 5, 13, 24, 96, 112, 164, 165, 173, 199, 239, 244, 249, 250, 272, 326, 368, 369, 430, 440, 443, 452, 456, 466, 490, 499, 501, 505, 506, 508, 509, 511, 519, 522, 523, 526, 533, 534, 536, 540–544, 548–551, 553, 555, 559, 562, 565
Mitochondria 9, 19, 24, 26, 32, 35, 37, 39–43, 45, 46, 74, 84, 85, 90, 95–97, 103, 104, 106, 208, 213, 215, 217, 222, 291–306, 312, 314, 317, 320, 326, 352, 354–358, 361, 368, 381, 385, 387–391, 393–404, 409, 410, 412, 438, 440, 441, 470, 481, 484, 501, 503, 506, 508, 509, 524, 525, 533, 534, 536, 537, 539–544
Mitochondrial DNA 292, 410
Mitochondrial fission 292, 293, 357
Mitochondrial functions 385–404, 409, 410
Mitochondrial transcription factor A (TFAM) .. 292, 298, 306, 410, 411
Mitotracker 27, 32, 34, 36, 43, 156, 210, 213, 215, 221, 303, 312, 433, 435, 438, 439, 536, 537, 539–541
Molecular beacons 225–229
Molecular motors 4, 24, 165, 208, 250, 271, 326, 329, 368, 452, 466, 481, 533, 534, 544, 567
Motility assay 485, 486
Motor neurons 26, 28–33, 42, 145–149, 152–156, 160, 211, 216, 311–320, 327, 329, 334, 335, 342, 344, 345, 367, 369–372, 410, 412, 413, 429, 483, 491, 534
mRNA translation 49
mRNA transport 547–567
MS2 ..... 50, 225, 226, 230–235
Myosin V 242

N

Nerve growth factor (NGF) 127, 182, 184–186, 251, 259, 274, 276, 280, 284
Neurodegeneration 251, 272, 292, 306, 351, 404
Neuromuscular junctions 74, 377
Neuronal differentiation 295, 304
Neuronal projections 112
Neurons ..... v, 4, 5, 23–47, 50, 95–97, 112, 132, 156, 163, 164, 168–171, 173, 174, 176, 177, 182, 183, 192–204, 207–215, 220, 221, 223, 225–227, 229, 231–236, 240, 241, 243, 245, 249–252, 255–257, 259, 261, 262, 265–267, 271–274, 276–280, 283, 284, 291, 292, 297, 311, 317, 325, 326, 329, 332, 333, 335, 344, 351, 352, 354, 355, 357, 359, 368, 370, 371, 374, 379–381, 385–404, 409–415, 417, 418, 423, 429–433, 436–444, 452, 453, 456, 457, 459, 465–474, 481–483, 486, 488, 491–493, 499–527, 533, 547, 548
Neuropeptides 96, 97, 370, 381
Neurotrophins 74, 156, 249–267, 327
Nucleoids 291–306, 410–414

O

Organelle density 46
Organelles 3–5, 9, 13, 23–46, 73, 74, 95–97, 103–105, 108, 156, 207, 208, 213, 215, 221, 249, 271, 272, 291, 292, 299, 311, 325, 326, 357, 368, 369, 371, 373–375, 378, 379, 382, 385–387, 393, 395, 409, 418,

422, 423, 427, 429, 434, 435, 439, 441, 452, 465, 466, 468, 481, 484, 499, 500, 503, 505, 510, 525, 533, 548
Organelle trafficking 103, 417

P

Peripheral nervous system (PNS)..... 199, 272, 273
Photoactivatable fluorescent probe (PAGFP) ... 165–167, 169, 171–175, 177
Photoactivation 165, 167–169, 171–175, 177
Photosensitizers..... 385–404
Picogreen 306
PP7..... 50, 225, 226, 230, 231
proNGF 251, 252, 254, 259, 261, 262, 266
Proteins..... 4, 5, 9, 24, 49, 50, 62, 64, 66–68, 73, 74, 96, 97, 103, 112, 138, 145–161, 164–166, 168, 171, 172, 175–177, 182, 184, 198–200, 203, 207, 211, 220, 225, 227, 229–231, 234, 236, 239, 240, 242, 244, 245, 249–251, 271, 272, 291, 292, 298, 299, 305, 312, 314, 325, 326, 331, 351, 352, 354, 357, 362, 368–370, 374, 379, 393, 402, 410, 417, 418, 423, 429–431, 435, 437–440, 444, 452, 457, 459, 465–469, 482, 499–501, 503–505, 507, 512, 515, 519, 520, 522, 525, 526, 534, 540, 544, 547, 548, 559–561, 565, 566
Pseudorabies virus (PRV) 194, 200, 201, 203
Pupal brain explants 451–460

Q

Quantitative analysis 23–47, 352, 453, 518

R

Reactive oxygen species (ROS) 389, 392–394, 409
Retinal axons 49–68
Retinal ganglion cell (RGC)..... 50, 55, 62, 66
Retrograde transport 24, 38, 46, 78, 81, 83, 85, 127, 216, 219, 223, 241, 250–252, 263, 264, 266, 272, 326, 331, 332, 343, 404, 435, 472, 482
RNA binding proteins 225, 452, 453
RNA transport..... 49–67, 225–236
RNP granules 451–459
Run lengths 158, 159, 223, 240, 327, 329, 331, 332, 334, 338, 341, 343, 373, 375, 442, 476, 482, 486, 488–490, 503, 519, 542, 543

S

Sciatic nerve..... 74, 75, 78, 79, 81–85, 90, 92, 95, 272, 386
Segmental nerves..... 367–382, 410–414
SH-SY5Y cells..... 291–306
Single-cell electroporation 353–355, 357, 360
Single-molecule imaging 50
Skeletal muscles 145, 148
Slow axonal transport 163–177
Soluble proteins 169, 171, 177
Spinning disk microscopy 327, 389, 440
Split-Venus..... 229, 231
Squid ..... v, 3–19, 112, 465, 499
Statistical parametric mapping (SPM) 113, 133, 135, 137, 138
Stem cells 182, 311–320, 386
Stereotactic injection..... 113, 121, 127, 132
Superior cervical ganglia (SCG) 182, 183, 191–195, 197–203
Supernova 387–389, 391, 393, 394, 397, 402
Super-resolution..... 46, 299, 386, 387, 401, 410, 412–414
Super-resolution radial fluctuations (SRRF) 387–390, 398, 399, 402, 403
SYBR Gold 294, 298, 300–303, 306
Synapses 5, 23–26, 46, 145, 163, 165, 292, 326, 409, 417, 429, 439, 469, 473, 481, 483, 488, 491, 492, 526
Synapsin 96, 165, 166, 169, 171–174
Synaptic vesicles..... 97, 298, 409, 439, 466–473, 475, 481, 484, 492, 495, 499, 506–510, 519, 521, 524–526

T

Tibial nerve..... 75, 78, 79, 81, 90
Time-lapse MRI 126
TIRF microscopy 555, 557, 559–561
Tracking..... 50, 63, 87, 135, 145–161, 165, 182, 200, 201, 229, 252, 254, 261–264, 274, 295, 304, 354, 371, 373, 375, 382, 422, 441, 454, 457, 499, 520, 552, 553, 556, 560, 562–564
Tract-tracing..... 112, 113
TRAK..... 534, 544
Transient transfection 231
Transport quantification 287
Tubulins..... 164, 207, 220, 249, 259, 265, 536, 540, 553, 559, 563, 565
T_1-weighted MRI 117

U

UNC-104 ..... 466, 482, 484, 489, 491

V

Velocities 24–26, 35–38, 44–46, 63, 65, 113, 158, 159, 200, 212, 219, 220, 222, 223, 240, 276, 294, 302, 317, 331, 332, 338, 340, 343, 344, 357, 361, 368, 373, 375, 382, 388, 401, 403, 423, 427, 440, 441, 476, 488–490, 494, 495, 503, 519, 523, 525, 526, 543, 554, 562
Vesicle transport 85, 239, 241, 242, 245, 371, 421
Virus 5, 96, 101, 105, 107, 181–183, 193–195, 197–201, 203, 204, 317, 537

W

Whole-mount dissection 419, 420
Wings 88, 223, 386–404, 417, 419, 420
Worm behavior 482

X

Xenopus laevis 53

Z

Zebrafish 88, 95, 325–346, 351–362, 439